Studies on the Synthesis and Characterisation of Compounds showing Colossal Magnetoresistance

A thesis submitted to the

Board of the Faculty of Physical Sciences

in partial fulfilment of the requirements

for the degree of

Doctor of Philosophy

at the

University of Oxford

by

Lauren E. Spring

Linacre College

Oxford

The Inorganic Chemistry Laboratory

Michaelmas Term, 1999

RADCLIFFE SCIENCE LIBRARY OXFORD
DEPOSITED
27 APR 2000

Abstract

The crystallographic and magnetic properties of manganese oxides belonging to the Ruddlesden Popper (RP) series, described by the formula $A_{n+1}B_nO_{3n+1}$, are presented. Compounds having n = 2, 3 and ∞ are discussed in Chapters 3, 4 and 5, respectively, their properties being studied by powder X-ray and neutron diffraction, SQUID magnetometry and magnetotransport measurements.

In Chapter 3 ($A_3B_2O_7$) it is shown that $Sr_{2-x}Nd_{1+x}Mn_2O_7$ ($0 \leq x \leq 0.5$) and $Sr_2PrMn_2O_7$ exhibit colossal, negative magnetoresistance (CMR) below 150K. The zero field resistivity signal is reduced by 2-3 orders of magnitude in a field of 14T, at ~4.2K. The compounds $Sr_2HoMn_2O_7$ and $Sr_2YMn_2O_7$ show no significant magnetoresistance. In contrast to the tetragonal Sr,Nd and Sr,Pr compositions, these compounds show a symmetry lowering to space group $P4_2/mnm$, and spin glass freezing on the Mn sublattice at ~20K.

Chapter 4 ($A_4B_3O_{10}$) focuses on A- and B-cation substitutions in the parent compound $Ca_4Mn_3O_{10-\delta}$. Substitution of Ca by Sr yields $Sr_4Mn_3O_{10-\delta}$, an orthorhombic (*Cmca*) compound, composed of trimers of face sharing octahedra. The magnetic susceptibility of this sample is interpreted in terms of direct and indirect antiferromagnetic (AFM) Mn-Mn exchange interactions. The orthorhombic (*Pbca*) RP phase $Ca_{3.95}La_{0.05}Mn_3O_{10-\delta}$ has a magnetic transition at ~114K, suggesting that the antiferromagnetic groundstate, with associated weak ferromagnetism arising through the Dzyaloshinsky-Moriya interaction observed in $Ca_4Mn_3O_{10-\delta}$, is preserved on introduction of a fraction of La^{3+} dopant cations. $Ca_{3.95}La_{0.05}Mn_3O_{10-\delta}$ displays CMR at 4K, with the resistivity signal reduced to 18% of the zero field value, in 14T. B-cation substitution yields $Ca_4Mn_2TiO_{9.93}$, an orthorhombic (*Pbca*) RP phase in which the Mn:Ti cation distribution, deduced from the combined results of anomalous dispersion X-ray experiments and neutron diffraction studies, is 59.8%(2.6):40.2%(2.6) and 70.1%(1.3):29.9%(1.3) across the 4b and 8c octahedral sites, respectively. Neutron diffraction studies at 5K show the presence of only short range magnetic interactions in this insulating material, the resistivity of which is reduced by just 10% at 75K in 14T.

Chapter 5 (ABO_3 or $A_2BB'O_6$) describes the mixed B-cation phases, La_2GaMnO_6 and Nd_2GaMnO_6, containing Mn^{3+}, $3d^4$ cations. Both are cation disordered, orthorhombic (*Pnma*) materials, and Nd_2GaMnO_6 exhibits a static, cooperative Jahn-Teller (JT) distortion. La_2GaMnO_6 contains a relatively higher proportion of dynamic, cooperative JT distortions, and as such exhibits isotropic ferromagnetism at 50K and 5K ($2.80(5)\mu_B$ per Mn aligned along y at 5K), predicted by the 'quasistatic hypothesis', which describes the correlation between electron spin configurations of neighbouring JT cations. The magnetic structure of Nd_2GaMnO_6 at 5K and 1.7K is modelled as '$A_X F_Y G_Z$' for the Mn sublattice, and 'F_Y' for the Nd sublattice, using Bertaut's notation, resulting in competing ferromagnetic and antiferromagnetic superexchange interactions on the Mn sublattice along the [010] direction of the unit cell. Both materials are highly insulating and neither displays CMR, with resistivity values in each being reduced to just 96% of the zero field value at 200K, in a field of 14T.

The work described in this thesis was carried out at the Inorganic Chemistry Laboratory and the Clarendon Laboratory at the University of Oxford, between February 1996 and November 1999, under the supervision of Dr P. D. Battle, Dr M. J. Rosseinsky and Dr J. Singleton. All the work is my own, except where stated, and has not been submitted by the author for any other degree at this, or any other university.

Lauren E. Spring

November 1999

Acknowledgements

I would like to thank my supervisors, Peter, Matt and John, for giving me the opportunity to work on the CMR collaboration. It has been a privilege to work in this area of solid state science, particularly over the last few years when there have been so many new developments in the field. The enthusiasm and insight of my supervisors have helped me keep pace with the project, and working in both physics and chemistry groups has given me a wider perspective, with which to approach the subject. I would also like to thank Dr Steve Blundell, for useful discussions and his support and encouragement throughout the project.

I am grateful to the EPSRC, and for contributions from Linacre college and Peter and Matt, towards funding for the project. The EPSRC has also provided travel grants, enabling me to present work at an MRS symposium and to perform experiments at the ILL.

A number of people have contributed to the experiments performed over the course of the project. Special thanks to members of the technical support staff in the Clarendon Laboratory, Nuclear Physics and the ICL. Graham Read has always succeeded in cutting measurable bar samples for magnetotransport, often from tiny fragments of pellet, and often with very little advance warning. Chris Goodwin's help with gold evaporation greatly improved the quality of contacts to these materials and Nenad Vranjes built an interface box for the measurements.

I would also like to thank Dr Paolo Radaelli, Dr Thomas Hansen and Dr Chiu Tang for their expertise, enabling the smooth running of the neutron diffraction and synchrotron x-ray diffraction experiments described in this thesis. In addition, Dr Phil Gee, Dr Arzhang Ardavan and Dr Anne-Katrine Klehe provided much help while I was learning how to use the magnetotransport rig, and also showed extreme patience and tact when teaching me how to solder.

The collaborative nature of the CMR project has meant I have worked with several people in the Clarendon and the ICL, all of whom have added to my enjoyment of the last few years. I have worked closely with Amalia, Julie, Jaap, Markus, Will, and more recently with Eddie, JB and Liam on the CMR project, who have been a source of inspiration and friendship. Thanks to the company of Amalia and Markus, I still miss those long evenings grappling with the intricacies of the magnetotransport rig, sometimes not knowing quite what the magnet might have to offer..... . Jaap, Eddie and Julie have accompanied me on respective Daresbury and SQUID experiments and have added to the enjoyment and the success of each. Special thanks go to Andy, Mike and more recently JB, for computer help and advice, particularly in helping me access data and write up, from overseas. Amelia, Graeme, Jorge, Mark and Peter R. have shown understanding and encouragement over the past months with

regard to writing up. Thanks also to Nicola, Caroline, JB and Dan and the current PDB Part Twos for their support....I think I have now finished with the printer! Other members of the PDB, MJR, JS and SJB groups are unfortunately too numerous to mention, but you know who you are if you ever read this.

I am very grateful to everyone who proof-read part, or all, of this thesis; the unlucky ones were Peter, Matt, John, Eddie, Tony, Amalia and John M.. Thanks particularly to the efforts of Peter, Matt and Tony over the last few months, I have been able to submit within my preferred timescale.

David deserves special thanks, as ever, for sharing the highs and lows of the last year, and for making it practically possible for me to do a large part of my writing up in the US. As usual, he has amazed and inspired me with his endless determination and his faith in me, and probably now feels like he's been through writing up twice. I think, finally, I can say I'm making this year's last trip home across the Atlantic soon.

Amalia and Radu have also helped make it possible for me to split my time between the US and Oxford this year. They have provided a temporary home in Oxford, and through their understanding and friendship, have ensured I have many happy memories of my last few months in Oxford. Helen and Tony have been a source of encouragement and advice and have provided financial support throughout my doctorate.

Finally, I would like to thank my parents. They have provided all of the opportunities as well as funding, throughout my education and have offered sound advice at all times, and this thesis is dedicated to them.

Glossary

2-D	two-dimensional
3-D	three-dimensional
Å	angström
AC	alternating current
AFM	antiferromagnetic
AMR	anisotropic magnetoresistance
°C	degrees Celsius
c.g.s	centimetre gauss second
CMR	colossal magnetoresistance
CO	charge ordering
D1b	diffractometer 1b
D2b	diffractometer 2b
DC	direct current
DE	double exchange
DM	Dzyaloshinsky-Moriya
e.g.	*exempli gratia* (Latin: for example)
et al.	*et alia* (Latin: and others)
etc.	*et cetera* (Latin: and the rest)
e.s.d	estimated standard deviation
FC	field cooled
FM	ferromagnetic
FWHM	full width at half maximum
g	gram(s)
GBMR	grain boundary magnetoresistance
GMR	giant magnetoresistance
GSAS	General Structural Analysis System
HFMR	high field magnetoresistance

HRTEM	high resolution transmission electron microscopy
i.e.	*id est* (Latin: that is to say)
ILL	Institut Laue Langevin
JT	Jahn-Teller
LFMR	low field magnetoresistance
l.h.s	left hand side
Ln	lanthanide
MI	metal-insulator
MR	magnetoresistance
OS	oxidation state
r.h.s	right hand side
RP	Ruddlesden Popper
PS	phase segregation
SANS	small angle neutron scattering
SE	superexchange
SI	International system of units
s.o.	spin-only
SQUID	Superconducting QUantum Interference Device
SRS	synchrotron radiation source
T_c	Curie temperature
T_f	(spin glass) freezing temperature
TGA	thermogravimetric analysis
T_N	Néel temperature
TOF	time-of-flight
VRH	variable range hopping
VTI	variable temperature insert
WFM	weak ferromagnetism
ZFC	zero field cooled

CHAPTER I
INTRODUCTION 1

1.1 The phenomenon of magnetoresistance 2

1.2 Structural characteristics of Ruddlesden Popper Oxides, $A_{n+1}B_nO_{3n+1}$ 7

1.3 Electronic characteristics of Ruddlesden Popper Oxides, ABO_3 ($LaMnO_3$) and $A_{1-x}A'_xMnO_3$ ($La_{1-x}Ca_xMnO_3$) 11

1.3.1 Electronic classification of stoichiometric $LaMnO_3$ 11

1.3.1.1 Crystal Field Theory 12

1.3.1.2 The Hubbard Model 13

1.3.1.3 Magnetic Exchange interactions 15

1.3.2 Electronic classification of the series $La_{1-x}Ca_xMnO_3$ 23

1.3.2.1 The Double Exchange mechanism 23

1.3.2.2 The intrinsic CMR response 25

1.3.2.3 Carrier localisation in CMR manganites 27

1.4 Electronic characteristics of n = 2 and 3 layered Ruddlesden Popper Oxides, $A_3B_2O_7$ and $A_4B_3O_{10}$ 33

1.5 Extrinsic contributions to a CMR response 40

1.6 References 43

CHAPTER II
EXPERIMENTAL TECHNIQUES 50

2.1 Synthesis by a Ceramic Route 51

2.2 Powder Diffraction 51

2.3 Powder X-Ray Diffraction 52

2.3.1 Production of X-rays and instrumentation used 52

2.3.1.1 Laboratory Siemens D5000 diffractometer 52

2.3.1.2 Laboratory Philips PW1710 diffractometer 52

2.3.1.3 Station 2.3 at the Synchrotron Radiation Source, Daresbury, UK 53

2.3.2 The intensity of reflections in a diffraction pattern 55

2.3.3 The use of anomalous dispersion in X-ray diffraction 56

2.4 Powder Neutron Diffraction 60

2.4.1 Magnetic scattering of neutrons 63

2.4.2 Production of neutrons and instrumentation used 64

2.4.2.1 Constant wavelength instrument D1b 65

2.4.2.2 Constant wavelength instrument D2b 66

2.5 Crystal Structure Analysis 67

2.5.1 Rietveld profile refinement 67

2.5.2 GSAS parameters and criteria of fit 69

2.6 DC SQUID Magnetometry 71

2.6.1 The SQUID magnetometer 71

2.6.2 Parameters measured and units used 72

2.7 Magnetotransport Measurements 74

2.8 Iodometry 76

2.9 References 78

CHAPTER III
n = 2 in $A_{n+1}B_nO_{3n+1}$
'$A_3B_2O_7$' 80

3.1 Introduction 81

3.2 Synthesis and characterisation of the compounds $Sr_2HoMn_2O_{7-\delta}$ and $Sr_2YMn_2O_{7-\delta}$ 81

3.2.1 Experimental details 81

3.2.2 Structural and magnetic characterisation of $Sr_2HoMn_2O_{7-\delta}$ and $Sr_2YMn_2O_{7-\delta}$ 84

3.2.2.1 Powder neutron and X-ray diffraction study of $Sr_2HoMn_2O_{7-\delta}$ 84

3.2.2.2 Powder neutron diffraction study of $Sr_2YMn_2O_{7-\delta}$ 95

3.2.2.3 SQUID magnetometry measurements 102

3.2.3 Discussion 104

3.3 Magnetotransport studies on the series $Sr_2LnMn_2O_{7-\delta}$ (Ln=Pr, Nd, Ho) and Y and $Sr_{2-x}Nd_{1+x}Mn_2O_{7-\delta}$ (x = 0, 0.1, 0.2 and 0.5) 108

3.3.1 Experimental details 108

3.3.2 Results 110

3.3.2.1 Summary of structural properties in the series $Sr_2LnMn_2O_{7-\delta}$ (Ln=Pr, Nd) and $Sr_{2-x}Nd_{1+x}Mn_2O_{7-\delta}$ (x = 0, 0.1, 0.2 and 0.5) 110

3.3.2.2 Magnetotransport studies on the series $Sr_2LnMn_2O_{7-\delta}$ (Ln=Pr, Nd, Ho) and Y 111

3.3.2.3 Magnetotransport studies on the series $Sr_{2-x}Nd_{1+x}Mn_2O_{7-\delta}$ (x = 0, 0.1, 0.2 and 0.5) 113

3.3.2.4 Isothermal magnetisation and magnetotransport measurements on the compounds $Sr_{1.8}Nd_{1.2}Mn_2O_{7-\delta}$ and $Sr_{1.5}Nd_{1.5}Mn_2O_{7-\delta}$ 115

3.3.3 Discussion 118

3.3.3.1 Magnetotransport studies on the series $Sr_2LnMn_2O_{7-\delta}$ (Ln=Pr, Nd, Ho) and Y 118

3.3.3.2 Magnetotransport studies on the series $Sr_{2-x}Nd_{1+x}Mn_2O_{7-\delta}$ (x = 0, 0.1, 0.2 and 0.5) 121

3.3.3.3 Isothermal magnetisation and magnetotransport measurements on the compounds $Sr_{1.8}Nd_{1.2}Mn_2O_{7-\delta}$ and $Sr_{1.5}Nd_{1.5}Mn_2O_{7-\delta}$ 126

3.4 References 129

CHAPTER IV
n = 3 in $A_{n+1}B_nO_{3n+1}$ 131
'$A_4B_3O_{10}$'

4.1 Introduction 132

4.2 Comparison of the parent compounds $Ca_4Mn_3O_{10-\delta}$ and $Sr_4Mn_3O_{10-\delta}$ 132
4.2.1 Experimental details 133
4.2.2 Structural and magnetic characterisation of $Sr_4Mn_3O_{10-\delta}$ 134
4.2.2.1 Powder X-ray diffraction 134
4.2.2.2 Magnetic measurements 139
4.2.3 Discussion 140

4.3 A-cation substitution in $Ca_4Mn_3O_{10-\delta}$ and $Sr_4Mn_3O_{10-\delta}$ 148
4.3.1 Experimental details 149
4.3.2 Structural and magnetic characterisation of $Ca_{3.95}La_{0.05}Mn_3O_{10-\delta}$ 152
4.3.2.1 Powder X-ray diffraction 152
4.3.2.2 Magnetic measurements 156
4.3.3 Discussion 165

4.4 B-cation substitution in $Ca_4Mn_3O_{10-\delta}$ and $Sr_4Mn_3O_{10-\delta}$ 170
4.4.1 Experimental details 171
4.4.2 Structural and magnetic characterisation of $Ca_4Mn_2TiO_{10-\delta}$ 176
4.4.2.1 Refinement strategy 176
4.4.2.2 Powder neutron and powder X-ray diffraction 178
4.4.2.3 Magnetic measurements 197
4.4.3 Discussion 204

4.5 References 212

CHAPTER V
$n = \infty$ in $A_{n+1}B_nO_{3n+1}$ 214
'ABO_3 ($A_2BB'O_6$)'

5.1 Introduction 215

5.2 Synthesis and characterisation of $La_2GaMnO_{6+\delta}$ and $Nd_2GaMnO_{6+\delta}$ 219

5.2.1 Experimental details 219

5.2.2 Structural and magnetic characterisation of $La_2GaMnO_{6+\delta}$ 222

5.2.2.1 Room temperature powder neutron diffraction measurements 222

5.2.2.2 SQUID magnetometry measurements 227

5.2.2.3 50K and 5K powder neutron diffraction measurements 230

5.2.2.4 Magnetotransport measurements 238

5.2.3 Structural and magnetic characterisation of $Nd_2GaMnO_{6+\delta}$ 239

5.2.3.1 290K powder neutron diffraction measurements 239

5.2.3.2 SQUID magnetometry measurements 243

5.2.3.3 5K and 1.7K powder neutron diffraction measurements 247

5.2.3.4 Magnetotransport measurements 257

5.3 Discussion 258

5.3.1 Structural and magnetic properties of $La_2GaMnO_{6+\delta}$ 263

5.3.2 Structural and magnetic properties of $Nd_2GaMnO_{6+\delta}$ 271

5.3.3 Magnetotransport properties of $La_2GaMnO_{6+\delta}$ and $Nd_2GaMnO_{6+\delta}$ 278

5.4 References 280

APPENDIX 1 283

APPENDIX 2 287

APPENDIX 3 289

SUMMARY 291

CHAPTER 1

INTRODUCTION

1.1 The phenomenon of magnetoresistance

The phenomenon of magnetoresistance (MR) is the change in electrical resistivity of a material in response to an applied magnetic field. An example of this phenomenon is shown in Figure 1.1.1. Here, the resistivity (Ωcm) of the material $La_{0.9}Ca_{0.1}MnO_3$ at a temperature of ~220K is reduced from 4000mΩcm to 1000mΩcm by the application of a magnetic field of 6T. Since the application of a magnetic field leads to a *reduction* of the signal in the compound described, the effect is *negative* magnetoresistance.

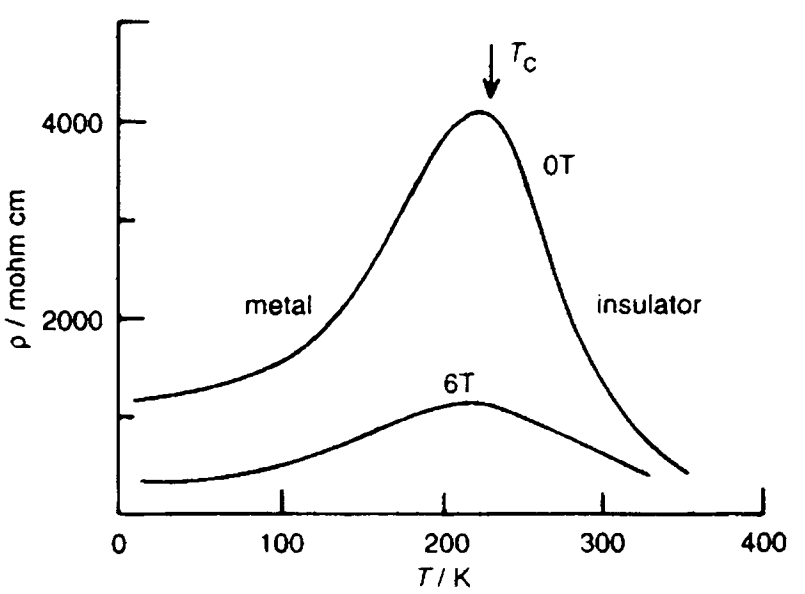


Figure 1.1.1 Resistivity as a function of temperature for $La_{0.9}Ca_{0.1}MnO_3$ at zero field and in an applied field of 6T. (Figure reproduced from reference [98]).

A common numerical definition of magnetoresistance is that given in equation 1.1.1:

$$MR\ \%\ (T,B) = -\left\{\frac{[\rho(T,B)-\rho(T,0)]}{\rho(T,0)}\right\}x100 \qquad \text{eqn. (1.1.1)}$$

Here, ρ(T,B) is the resistivity at a defined temperature, T, and magnetic field, $B = \mu_0 H$. The maximum MR (220K, 6T) ratio for $La_{0.9}Ca_{0.1}MnO_3$, described in Figure 1.1.1, is 75% using equation 1.1.1.

The variation of a measurable property (for example, electrical resistivity) with a change in magnetic field makes magnetoresistive materials useful as magnetic field sensors. Magnetic sensors have been in use in one form or another for hundreds of years. Examples range from the use of suspended magnets for navigation, to the modern day use of swipe readers for credit cards. A particularly important, current use of magnetic sensors is in thin film detectors which intercept information in the form of magnetic reversals on magnetic computer disks.

Although all metals have a small, intrinsic magnetoresistance (as a result of the Lorentz force exerted on conduction electrons in a magnetic field), the greater the magnetoresistive effect that can be generated in a material, the greater its sensory capability. A major driving force for research into magnetoresistor technology over the last decade has been the demand for more powerful computers storing information at higher packing densities on hard disks. This underlying drive, coupled with several definitive studies in the late eighties and early nineties, have fuelled intense, worldwide research over the last decade similar to that directed towards the goal of high temperature superconductivity in the eighties.

In particular, n = 2 and n = ∞ Ruddlesden Popper[1,2](RP) manganites, described by the general formula $A_{n+1}Mn_nO_{3n+1}$, and their substituted derivatives, have been studied extensively for their magnetoresistive properties over the last decade. As early as the 1950s, the work of Jonker and van Santen[3,4] identified the potential for A-cation site doping and significant structural tuning in the $A_{1-x}A'_xMnO_3$ (n = ∞) phases, preparing $La_{1-x}Ca_xMnO_3$ polycrystalline samples. They touched briefly on the electrical properties of these mixed-valent compounds; however, the observation of magnetoresistance was not reported until 1954 by Volger[5]. Volger demonstrated the proximity in temperature of the maximum magnetoresistance ratio with the ferromagnetic Curie temperature. It seems likely that the wider scientific community at that time was more aware of magnetic semiconductors such as rare earth chalcogenides, which showed extremely large magnetoresistance effects at low temperature. Interestingly, Cr-based chalcogenide spinels have formed the basis for more recent MR studies in this class of materials[6]. A handful of studies on doped $AMnO_3$ single crystals were carried out in the sixties and seventies[7-10], and Lamire and Daoudi studied the n = 2 solid solution series $Sr_{3-x}Ln_xMn_2O_7$ in 1984[11]. However, it was not until the late eighties that the real revival of interest in RP manganese-based oxides occurred.

A significant discovery was made in 1988 by Fert et al.[12]. These authors showed that the resistance of an iron-chromium superlattice fell by almost 50% when placed in a magnetic field. A comparable effect was detected in a 'magnetic sandwich structure' by Grünberg and coworkers at around the same time[13]. These observations led to use of the term 'giant magnetoresistance' (GMR), since these resistance swings were giant in comparison to those

observed in the materials which had been, and still are, utilised in many magnetoresistive devices, including data storage devices in today's PCs.

A further definitive study was made in 1989 by Kusters et al.[14], which showed that the metal-insulator (MI) transition in the compound $Nd_{0.5}Pb_{0.5}MnO_3$ occurred close to the temperature of onset of ferromagnetic (FM) order. In addition, they showed that this MI transition could be driven by an increase in applied field in the region of T_C, with the result that the resistance could be made to fall by *orders of magnitude* on application of a large enough field. This magnetotransport behaviour would become the signature for many mixed-valent manganites[15], and hinted at the complex interplay between the magnetic ground state and transport properties of these materials. Two studies of thin-film materials (the form in which several modern devices are fabricated) in the early nineties, by von Helmholt et al.[16] and Chahara et al.[17], further intensified research efforts on mixed-valent manganites, and the interest has continued until the present time. The term 'colossal magnetoresistance' (CMR) was coined by Jin et al. in 1994[18] in order to describe the remarkable ratios of magnetoresistance that could be generated in certain manganites (10^4 to 10^{11} % are claimed)[19], and to distinguish CMR materials from those such as magnetic multilayers, exhibiting GMR effects.

Despite the expectations and intense study over the last decade, the potential applications of the 'colossal' MR ratios observed in mixed-valent manganites have yet to be realised fully. A range of potential applications have been reviewed by Venkatesan[20], including the exploitation of the marked temperature dependence of resistivity in bolometers or the development of electric field effect devices. However, the application, which would have by far the most widespread impact, concerns their use in magnetoresistive read heads and magnetoresistive random access memories. Information storage in materials takes many forms, dependent upon the particular device in question. For example, in semiconductor-based memories it is stored as electrical charge, whereas for optical processing it is stored as variations in optical reflectivity or refractive index. In magnetic memories, variation in electron-spin alignment is the most widespread format for use in digital and analogue data recording. Since the early 1990s, the introduction of dual-element recording heads with

inductive write elements and magnetoresistive read elements has almost doubled the rate of areal density improvements for hard disk-drive data storage products. The principle of operation for the magnetoresistive read elements is a modulation of the sensor resistance through the MR effect which is converted then into voltage signals by passing a current through the sensor. At present, most MR sensors exploit the so-called anisotropic magnetoresistance (AMR) effect[21] in thin films of NiFe(Co) alloys. The major drawback regarding the application of CMR manganites as magnetoresistors, is the requirement for substantial magnetic fields (several Tesla) in order to achieve the desired changes in resistivity at room temperature. In comparison, a material functioning in a magnetic data storage device, such as a computer hard disk, would have to be sensitive to fields of the order of 1 millitesla at this temperature.

In the past few years, prospects of even more rapid performance improvements have been made possible by the development of sensors based on the GMR effect (also known as the spin-valve effect)[22,23], for a particular class of sensor configurations. In contrast, fields over 50,000 times greater than the Earth's magnetic field and temperatures significantly lower than room temperature are required in order to observe intrinsic CMR phenomena in mixed-valent manganites. In addition, for a thin-film device (the most widespread material form) the low field sensitivity drops as the film quality improves, suggesting defects might be a requirement for low field sensitivity.

It is possible, therefore, that the best way in which to utilise mixed-valent manganites will be *via* their low field, extrinsic MR response, rather than the intra-granular (intrinsic) CMR response[24]. As described in Section 1.5, the low field response is enhanced in systems with a high density of grain boundaries and in tunnel spin-valve structures. Thus, there is potential for the development of spin-valve devices using CMR materials as the electrodes separated by a spacer layer. Indeed, epitaxial heterostructures consisting of $La_{1-x}Sr_xMnO_3$ top and bottom electrodes separated by a conducting layer of $LaSrCoO_3$[25] have been prepared. As for the simple GMR systems comprised of magnetic multilayers mentioned above, the dominant mechanism by which the spin-valve would operate, would be by the change in spin dependent scattering of polarised free carriers in the presence and absence of a

magnetic field. However, for the manganites, a model depending on carrier transport, where the mean free path is determined by electron scattering, is only valid for $T < T_C$. Unfortunately, large series resistances have been detected across the device which have the effect of reducing the MR effect.

The significance of the almost completely spin-polarised 3d band of the ferromagnetic manganites below their Curie temperatures should not be underestimated. This property makes them useful potentially in a range of spin tunnelling devices, where they act as a source of spin-polarised electrons. Sun et al.[26] were the first to demonstrate their use in a 'trilayer spin tunnelling' device, composed of layers of $La_{0.67}Sr_{0.33}MnO_3$ separated by an intermediate layer of an insulating material such as $SrTiO_3$. Although a substantial MR effect (~ 83% change in resistance across the junction) was observed at fields of just a few millitesla at low temperatures for this device, this could not be sustained as the temperature was increased. Recent experiments[27], investigating the degree of spin polarisation of 3d sub-bands as a function of temperature, have suggested the net polarisation tends to zero as the Curie temperature is increased. Hence, a viable, room temperature spin tunnelling device would have to consist of a material with a very high Curie temperature. Layered manganites are interesting particularly since, if their magnetic properties can be tuned to give relatively high Curie temperatures, they are predisposed structurally to show magnetotunnel transport due to their intrinsic multilayer structure. These properties have been investigated as part of studies of the series $Sr_{2-x}La_{1+x}Mn_2O_7$[28,29] and the 'double' perovskite Sr_2FeMoO_6[30].

In summary, the remarkable variety of properties shown by the mixed-valent manganites, ranging from their magnetic field sensitivity to their spin polarisation below the Curie temperature, confers a large number of potential applications upon these materials. The process of 'tuning' these properties until they can be utilised in electronic devices serves also as a vehicle for understanding further a number of magnetotransport phenomena.

The materials described in this thesis are all manganese oxides, and several have been shown to display GMR or CMR. All, except the compond $Sr_4Mn_3O_{10}$[31], belong to the Ruddlesden Popper series of compounds. Section 1.3 gives an overview of the electronic

properties of the Ruddlesden Popper oxide $LaMnO_3$, (an $n = \infty$ manganite) and its A-site-doped derivatives, $La_{1-x}Ca_xMnO_3$. Together, $LaMnO_3$ and the series $La_{1-x}Ca_xMnO_3$ encompass many of the electronic and magnetic characteristics of manganites discussed in CMR-related literature, and their properties serve as a useful framework in which to define key terms. The materials described in Chapter 5 of this thesis belong to this $n = \infty$ RP series, albeit with mixed Mn/Ga B-cation site occupancy. A review of electronic properties of the lower dimensional n = 2 and n =3 layered manganites, (constituting the majority of compounds described in this thesis) follows, in Section 1.4. Section 1.5 discusses the importance of extrinsic contributions to the CMR effect, particularly relevant for polycrystalline samples, such as those described in this thesis. Firstly, however, Section 1.2 summarises some structural properties of Ruddlesden Popper oxides.

1.2 Structural characteristics of Ruddlesden Popper Oxides, $A_{n+1}B_nO_{3n+1}$

The majority of manganese oxides, for which interesting magnetoresistive phenomena have been observed belong to the Ruddlesden Popper series of compounds, with the exception of studies based on the pyrochlore, $Tl_2Mn_2O_7$[32].

Ruddlesden and Popper gave their names originally to the series of oxides defined by the formula $Sr_{n+1}Ti_nO_{3n+1}$. However, RP phases describe any intergrowth structure, in which the ratio of A- and B-site cations and oxygen (or other electronegative element) is described by the formula $A_{n+1}B_nO_{3n+1}$.

Using a 'framework' picture of ABO_3 units, the perovskite-derived RP structures may be considered in terms of the insertion of 'AO' rocksalt layers at appropriate intervals. In the ABO_3 units, corner shared BO_6 units form a network reminiscent of that in the ReO_3 structure, but with A-cations occupying the large, 12 coordinate cavities (see Figure 1.2.1). The 'intergrowth' is in the form of 'ABO_3' perovskite blocks, 'n' 'BO_6' octahedra-thick, separated by regions of 'AO' stoichiometry, the latter involving a 'rocksalt type' arrangement of cations and anions, with 9 - fold coordination of A-cations. Although RP structures can be stabilised with a number of types of cations 'A' and 'B'[33], the compounds described in this thesis all contain Mn^{3+} or Mn^{4+} on the B-cation site (albeit with a degree of substitution in

compounds described in Chapters 4 and 5) and the A-cation site is occupied by either Sr^{2+}, Ca^{2+}, La^{3+} or Nd^{3+} or combinations thereof.

Figure 1.2.1 gives a structural representation of the n=1, 2, 3 and ∞ members of the Ruddlesden Popper series $A_{n+1}B_nO_{3n+1}$:

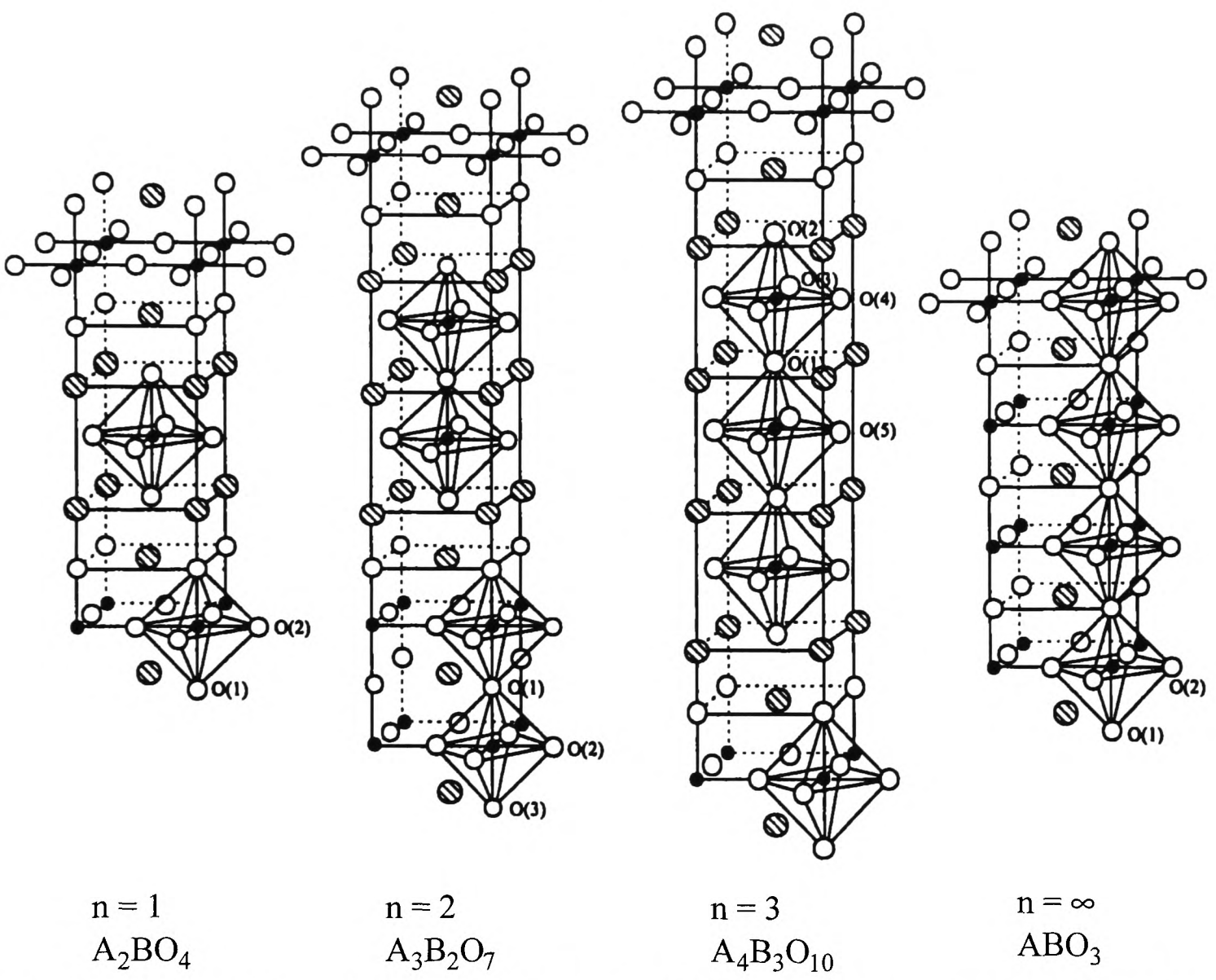


Figure 1.2.1 Representation of the crystal structures of RP $A_{n+1}B_nO_{3n+1}$ compounds, specifically the n = 1, 2, 3 and ∞ series. Oxygen anions are shown as white spheres, B-cations as black spheres and A-cations are shown as hatched spheres. (Figure reproduced from reference [46]).

In the Figure, the RP structures are represented in their 'ideal', undistorted forms, meaning n = 1, 2 and 3 members are tetragonal and are described by the *I4/mmm* space group and that n = ∞ members are described by $P\,m\bar{3}m$. The resulting numbers of crystallographically distinct oxygen anions are labelled for each structure in the Figure. It can be seen that 'n' is the number of layers of corner shared BO_6 octahedra stacked along the [001] direction, before the insertion of an 'AO' rocksalt layer and a translation of 1/2 in the [110]

direction to the next 'perovskite block'.

A measure of the degree of rotation, or tilting of octahedra, in the perovskite blocks of RP structures is given by the value of the tolerance factor, t', derived by Goldschmidt[34] and defined by the following ratio:

$$t' = \frac{(r_A + r_O)}{\sqrt{2}(r_B + r_O)} \qquad \text{eqn. (1.2.1)}$$

Here, r_A and r_B are the radii of cations A and B, respectively, and r_O is the oxygen anion radius[1]. A value t' = 1 represents the 'ideal' configuration when all neighbouring ions in the close packed array (regarded as hard spheres) are in contact. Reductions from t' = 1 result from structural distortions due to reorientations of octahedra, often to satisfy the coordination requirements of A-site cations[36].

Figure 1.2.2 illustrates the number of distinct unit cells that can be generated on departure from cubic symmetry in n = ∞ $LaMnO_3$, (the cube has length a_p).

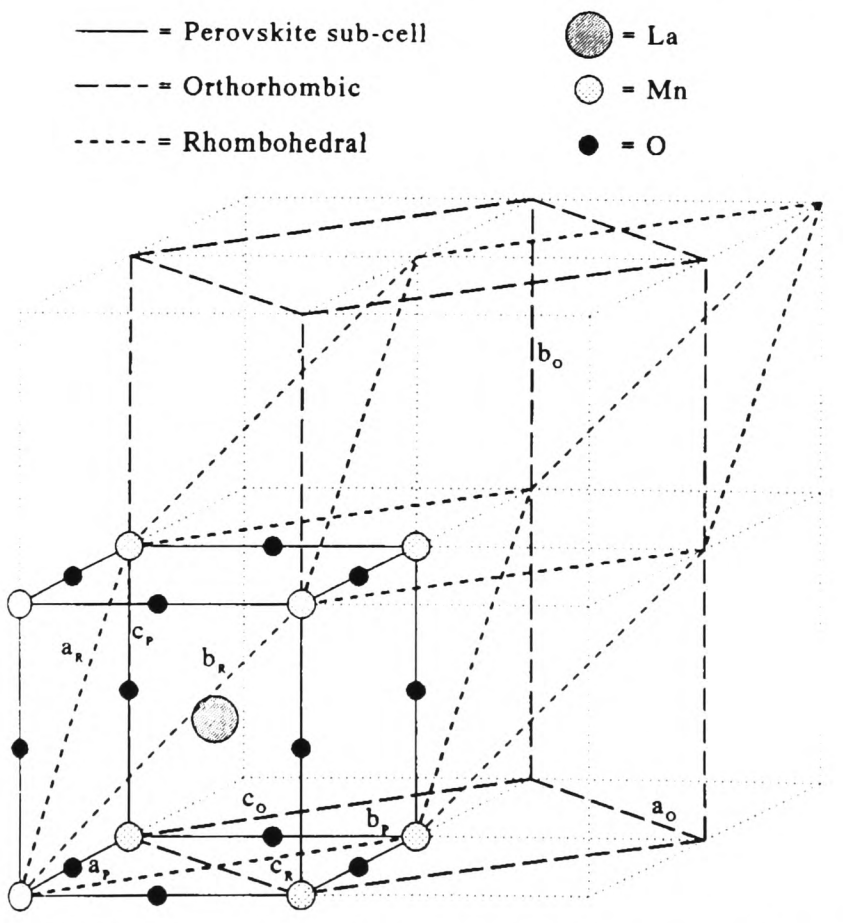


Figure 1.2.2 Examples of distinct unit cells that can be generated on departure from cubic symmetry in n = ∞ $LaMnO_3$. The subscripts 'p', 'r' and 'o' denote perovskite, rhombohedral and orthorhombic cell edges, respectively. (Figure reproduced from reference [47]).

---

[1] All ionic radii referred to in this work are values determined by Shannon and Prewitt from room temperature, ambient pressure x-ray studies[35].

The enlarged unit cell corresponding to the space group *Pnma* shown in Figure 1.2.2, has cell dimensions $a_o \approx \sqrt{2}\,a_p$, $b_o \approx 2a_p$ and $c_o \approx \sqrt{2}\,a_p$. This, particularly common, structural transition in A- and B-site doped $n = \infty$ ABO_3 phases, results from a cooperative rotation of 'BO_6' octahedra about pseudocubic [110] axes. Both compounds described in Chapter 5 were modelled successfully in the space group *Pnma*. The wide variety of structures adopted by the A-site doped $n = \infty$ ABO_3 phases (which can be formulated $A_{1-x}A'_xBO_3$) was emphasised with the identification, as recently as 1996, of the *Imma* allotype by Radaelli et al.[37].

Returning to Figure 1.2.1, the $n = \infty$ ABO_3 phases correspond to the $n = \infty$ three-dimensional limit of the RP structure type and contain only 12 coordinate A-cations, while the $n = 1$ member, A_2BO_4 is the two-dimensional K_2NiF_4 structural type containing only 9 coordinate A-cations[38,39]. The latter structure is that adopted by the superconducting oxides containing copper, $La_{2-x}Sr_xCuO_4$; however, it represents the least studied congener of the RP series with regard to magnetoresistive properties. This is because few n=1 phases have exhibited significant magnetoresistance, although the series $Sr_{1-x}La_xMnO_4$ is well studied[40], particularly for its charge ordering phenomena[41]. Recently, however, Maignan et al.[42] have claimed to observe CMR effects in the system $Ca_{2-x}Ln_xMnO_4$ (where Ln = Pr, Sm, Gd and Ho and $0 < x < 0.2$).

Indeed, the majority of CMR related studies have focussed on $n = \infty$, and layered $n = 2$ and $n = 3$ manganites, and Sections 1.3 and 1.4 give a brief review of properties which distinguish the infinite layer and reduced dimensionality systems, respectively. RP manganites are ideal systems in which to study the effects of dimensionality on electronic bandwidth (for example with increasing n from 1 to ∞). Several studies have focussed on these effects, notably those by MacChesney et al.[43], Ram et al.[44], Rao et al.[45] and more recently that by Fawcett et al.[46]. The increase of the energy bands derived largely from the Mn-3d orbitals, albeit anisotropic, is predictable considering the increase in the number of Mn nearest-neighbours, as n increases from 1 to ∞ in the series $A_{n+1}Mn_nO_{3n+1}$.

1.3 Electronic characteristics of Ruddlesden Popper Oxides, ABO_3 ($LaMnO_3$) and $A_{1-x}A'_xMnO_3$ ($La_{1-x}Ca_xMnO_3$)

1.3.1 Electronic classification of stoichiometric $LaMnO_3$

In terms of electronic classification, stoichiometric $LaMnO_3$ falls into the category of a magnetic insulator. The term magnetic insulator implies the simultaneous presence of an energy gap and unpaired electrons. The magnetic ground state of stoichiometric[47] $LaMnO_3$ corresponds to an A-type antiferromagnet, Néel temperature, $T_N \approx 140K$.

As for many 3d transition metal oxides (and particularly magnetic insulators), the description of $LaMnO_3$ raises the question of which is the best framework, one favouring localised electrons or one based upon band theory, in which to interpret the electronic properties of the material. Traditionally, the properties of transition metal oxides have been understood using crystal field theory, considering them as ionic compounds incorporating an integral number of *localised* electrons, $3d^n$, per ion. The electronic properties of the solid are interpreted then as being due to the interactions between electrons localised on atoms in the extended lattice. Indeed, the number of transition metal oxides which can be classified as simple metals (where a free electron model works well) is very small, ReO_3 and RuO_2 being examples. Spectroscopic observations, measuring the energies of crystal field and charge transfer transitions, often support the predictions of localised electron models.

However, the idea of purely localised electrons, where itinerant behaviour is prevented theoretically by inter-electron repulsion is clearly an incomplete model for many systems where the concepts of electron transfer and orbital admixtures are essential to explain certain properties. Hence, the use of band theory (in which repulsion between electrons can be represented using an average, *effective* potential) is essential, although alone it does not give a complete picture, either. Hence, intermediate models provide an optimum framework for understanding.

One such intermediate model, the Hubbard Model, is described in sub-section 1.3.1.2, briefly. Firstly, aspects of crystal field theory are discussed, since this provides the best framework in which to understand the effects of the oxygen ligand environment on the energy levels of the Mn 3d orbitals.

1.3.1.1 Crystal Field Theory

As described above, crystal field theory uses an essentially localised electron model. Therefore, each Mn^{3+} in the compound $LaMnO_3$ is regarded as having a $3d^4$ electron configuration. In an octahedral oxide ligand field, a crystal field splitting (Δ_{cf}) arises from the reduction in energy of the t_{2g} set of 3d Mn orbitals and the increase in energy of the e_g set. The filling of the t_{2g} and e_g sets by the four, 3d electrons follows the Pauli exclusion principle and occurs such that the ground states of the free ions satisfy Hund's first rule. This results in maximum S = 2, and an energy splitting, U_{ex}, between states with total spin 2 and 1. U_{ex} tends to be of a similar magnitude as Δ_{cf} for perovskites and is effectively the energy required to flip an electron spin, ($J_H = U_{ex} / 2$). Hence, the energy level diagrams (see Figure 1.3.1) focus on the lowest energy configuration (with maximum S).

For the Mn^{3+} high spin $3d^4$ electronic configuration there is a distortion of the octahedral geometry around the Mn centres as a result of the Jahn-Teller effect[48,49]. The effect of the Jahn-Teller distortion superimposed upon the crystal field splitting shown in Figure 1.3.1 (a), results in the d orbital splitting shown in Figure 1.3.1 (b), on tetragonal (apical) elongation of the octahedron.

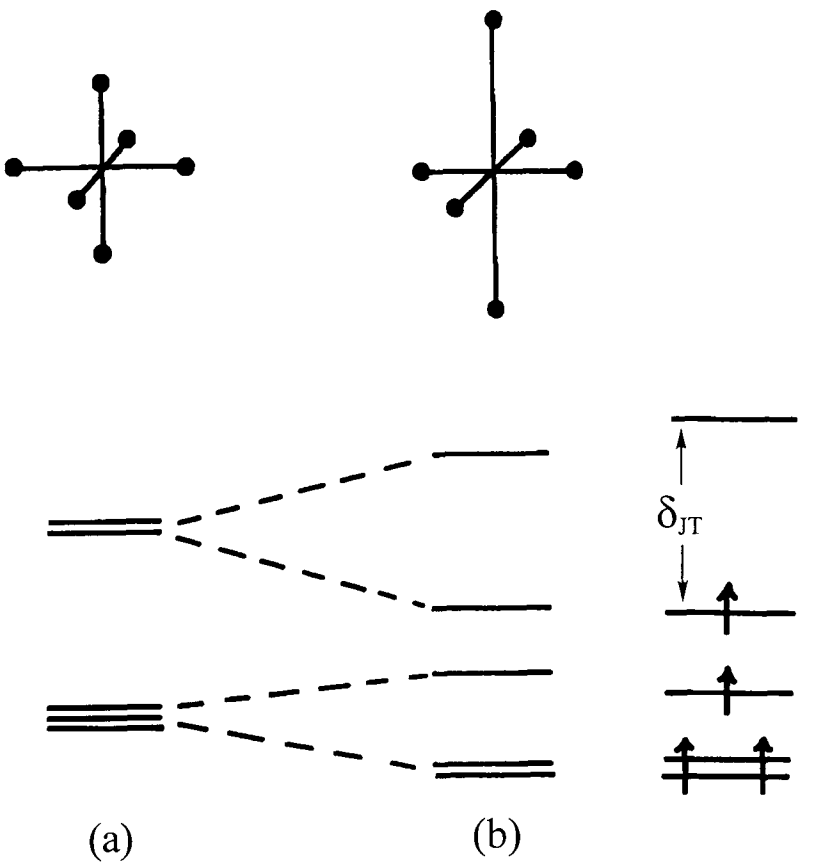


Figure 1.3.1 (a) The crystal field splitting (e.g. of Mn^{3+} 3d orbitals) in an octahedral ligand field with (b) a superimposed Jahn-Teller distortion. (Figure reproduced from reference [105]).

The Jahn-Teller crystal field interaction is denoted δ_{JT} in Figure 1.3.1, and is equal to the energy difference between the two orbitals comprising the e_g set. A *static, cooperative* Jahn-Teller effect is the decription given when the electronic configuration of the cation is uncoupled from the nuclear vibrations, and distortions around each ion in the crystal lattice are oriented in an optimum way so as to 'fit together'. The cooperative Jahn-Teller distortion which occurs in $LaMnO_3$ is discussed in more detail in sub-section 1.3.1.3. In some cases, a static, non-cooperative Jahn-Teller distortion is the more stable configuration.

When coupling between the electronic configuration and the nuclear vibrations is strong, a Jahn-Teller distortion may be described as *dynamic*. In this situation, the ground state degeneracy is removed by this coupling. The electron configurations of neighbouring cations can be imagined to resonate between two stable configurations, mediated by the lattice vibrations.

1.3.1.2 The Hubbard Model

The essence of the model, based on the ideas of Mott and Hubbard[50], assumes that the repulsion between electrons is negligible *except* when they are on the *same* atom. Within the Hubbard model, the band gap excitation in the magnetic insulator $LaMnO_3$ is predicted to arise from the process shown in equation 1.3.1:

$$Mn^{3+} + Mn^{3+} = Mn^{2+} + Mn^{4+} \qquad \text{eqn (1.3.1)}$$

or, in terms of electron configuration,

$$d^4 + d^4 = d^5 + d^3 \qquad \text{eqn. (1.3.2)}$$

The energy required to complete this process is known as the Hubbard U. It is given quantitatively by the difference between the ionisation energy (I) of one Mn^{3+} cation and the electron affinity (A) of another:

$$U = I - A \qquad \text{eqn. (1.3.3)}$$

The Hubbard model is an 'intermediate' model describing electronic structure, as it

incorporates not only the effect of electron repulsion mentioned above (albeit approximated), but also the effect of some orbital overlap which gives a small bandwidth to the states involved in the transition shown in equations 1.3.1 and 1.3.2. The half-filled band is split at the Fermi level, giving the upper-Hubbard and lower-Hubbard sub-band, corresponding to the energy of empty levels and the binding energy of occupied levels, respectively. Thus, the parameter U is shown in Figure 1.3.2 as the energy splitting for the notional situation of zero bandwidth (no orbital overlap).

Despite the many approximations necessary in the Hubbard model (for example, it is a *single-band model*) when applied to $LaMnO_3$, ignoring the effects of covalent mixing with oxygen p bands, it is used widely to help understand the properties of magnetic insulators.

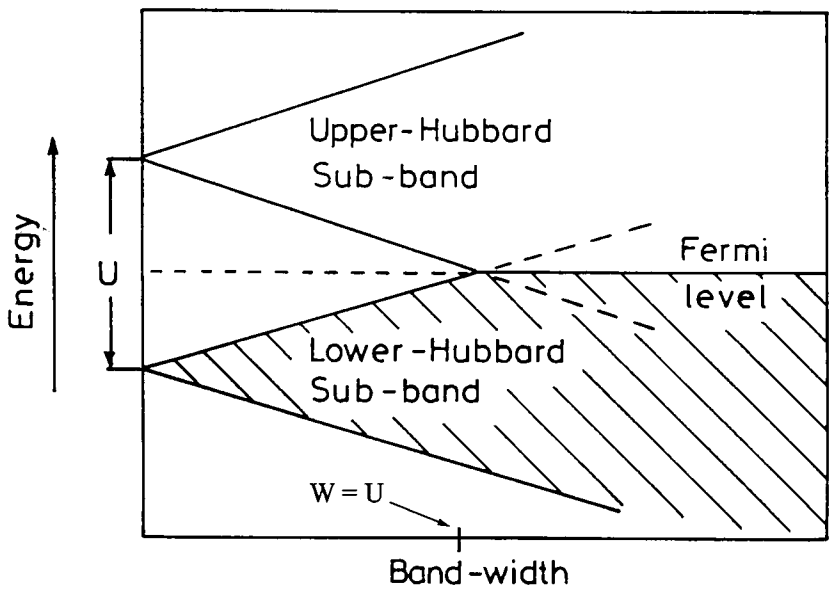


Figure 1.3.2 The energy splitting between upper-Hubbard and lower-Hubbard sub-bands, as a function of electronic bandwidth (W). (Figure reproduced from reference [105]).

As shown, as the degree of orbital overlap and the bandwidth (W) increases, the upper and lower Hubbard sub-bands extend out and, at the critical value of W = U, itinerant electron behaviour is favoured over localised behaviour as the Fermi level falls in the middle of a partially-occupied band. As long as W < U, localisation of electrons is predicted and the magnetic insulator classification holds.

The uncertainty regarding the precise nature of Hubbard sub-bands often leads to claims that many materials should be termed *charge transfer insulators*, rather than Mott Hubbard insulators[51]. For example, if the top filled level has more oxygen (p) than metal (d) character, the band gap excitation may be described more accurately as charge transfer. A charge transfer

interaction, creating a p^5d^{n+1} electronic configuration from p^6d^n, is often labelled U_{pd}. Spectroscopic measurements have given the estimations in Table 1.3.1 for the parameters introduced in this and the previous section on crystal field theory, for the compound $LaMnO_3$.

Table 1.3.1 Estimates of characteristic energies in $LaMnO_3$: (data from Coey et al.[52])

U, Mott Hubbard interaction	4.0eV	$J_H = U_{ex} / 2$	1.0eV
U_{pd}, charge transfer interaction	4.5eV	Δ_{cf}	1.8eV
		δ_{JT}	0.6eV
$W = 12t$[a]	1.0eV	$\mid J_{ij} \mid$[b]	0.001eV

[a] t is the transfer integral which determines the d-electron bandwidth, W
[b] J_{ij} are the effective exchange parameters for neighbouring manganese ions in the Heisenberg Hamiltonian $-J_{ij}(S_i \cdot S_j)$, (refer to section 1.3.1.3).

The similarity of U and U_{pd} makes the nature of the band gap controversial in the case of $LaMnO_3$ and thus the stoichiometric compound has been classified as both a Mott Hubbard insulator[53,54] and a charge transfer insulator[55-58].

1.3.1.3 Magnetic Exchange interactions

A description of the magnetic structure of $LaMnO_3$ is a useful way in which to show the occurrence of both antiferromagnetic and ferromagnetic exchange interactions and their interplay with electronic features, such as a static, cooperative Jahn-Teller effect and orbital ordering. The phenomena of paramagnetism and cooperative magnetic ordering are discussed in the first instance.

On the scale of energy separations listed in Table 1.3.1 (of the order of several electronvolts), the perturbations caused by the interactions between magnetic ions are small, typical exchange splittings being of the order of 10^{-2}eV. However, magnetic exchange interactions yield important information about chemical bonding and account for the discontinuities in magnetic susceptibility curves at magnetic transition temperatures. These discontinuities signal the onset of cooperative magnetic ordering.

Before discussing cooperative magnetic ordering, it is useful to deal with the paramagnetic state of a material. Since so few transition metal oxides are simple metals,

usually it is appropriate to interpret magnetic properties in terms of a localised electron model. Therefore, the Mn cations in $LaMnO_3$ are formulated with d^4 configurations and the total spin (S) and orbital momenta (L) are obtained (assuming a high spin configuration) using the Russell-Saunders coupling scheme. The ground state (determined by Hund's rules) is characterised by a value of J, representing total angular momentum. In the absence of a magnetic field there are (2J + 1) degenerate substates associated with the ground state. On application of a field, the substates undergo Zeeman splitting, removing their degeneracy. The population of the resulting substates follows a Maxwell Boltzmann distribution. Therefore, the magnetic dipole moment for an ion in a magnetic field is dependent upon the population of substates, which is highly temperature dependent. The summation over one mole of magnetic ions leads to the Curie Law, expressing the variation of (molar) paramagnetic susceptibility as a function of temperature, T and total angular momentum, J:

$$\chi_{mol} = \frac{N_A g^2 \mu_B{}^2 J(J+1)}{3kT} \qquad \text{eqn. (1.3.4)}$$

Since the magnetic dipole moment, μ_J, is expressed as follows,

$$\mu_J = g\sqrt{J(J+1)} \qquad \text{eqn. (1.3.5)}$$

the Curie paramagnetic susceptibility can be rewritten as follows:

$$\chi_{mol} = \frac{N_A \mu_B{}^2 \mu_J{}^2}{3kT} = \frac{C}{T} \qquad \text{eqn. (1.3.6)}$$

The quantity C in equation 1.3.6 is the Curie constant, N_A is Avogadro's constant, k is the Boltzmann constant, μ_B is the Bohr magneton and g in equations 1.3.4 and 1.3.5 is the Landé splitting factor.

For the compounds discussed in this thesis, there are two small modifications to the Curie law outlined above, to describe the paramagnetic susceptibility fully. Firstly, since the orbital motion of electrons is quenched largely in the presence of the ligand field for 3d ions, J can be replaced by S and the magnetic moment is approximated by the spin only (s.o.) value:

$$\mu_{s.o.} = g\sqrt{S(S+1)} \qquad \text{eqn. (1.3.7)}$$

Secondly, a further term, the Weiss constant, is introduced into equation 1.3.6 in order to incorporate the effect of the magnetic field the ion experiences from its neighbouring ions. The resulting Curie-Weiss expression, given in equation 1.3.8, is more appropriate for many transition metal oxides. θ is negative value for antiferromagnetic order and positive for ferromagnetic order.

$$\chi_{mol} = \frac{C}{T-\theta} \qquad \text{eqn. (1.3.8)}$$

In Chapters 3, 4 and 5, estimated Curie constants are expressed in the form $C = \frac{N}{8}\{\mu_{eff}{}^2\}$, where N is the number of moles of a particular magnetic ion per formula unit of sample.

. For certain materials, at a certain temperature, the thermal randomisation of magnetic ions, leading to the classification of the material as paramagnetic, is insufficient to compete with interactions between the magnetic moments of neighbouring ions. The result is the onset of either antiferromagnetic (AFM) or ferromagnetic (FM) order at the Néel temperature (T_N) or Curie temperature (T_C), respectively. In compounds where adjacent magnetic ions are situated sufficiently closely to one another, the *direct* exchange interaction between two ions is given to a first approximation by the following Hamiltonian:

$$H_{ij} = -J_{ij}(S_i \cdot S_j) \qquad \text{eqn. (1.3.9)}$$

The exchange parameter J is negative for antiferromagnetic interactions and positive for ferromagnetic interactions. Only one compound in the current work has metal d orbitals which are sufficiently close to overlap and for this interaction to be significant. This is $Sr_4Mn_3O_{10}$, discussed in Chapter 4.

All compounds described in this thesis (and the 'model' compound used here, $LaMnO_3$), consist of a network of Mn cations interspersed with oxide anions, diluting the inter-cation repulsion. Therefore, magnetic exchange interactions are *indirect* in nature and metal d orbital overlap occurs *via* the oxide ligand. The relative orientations of metal d and oxygen p orbitals determine the degree of overlap and thus the strength of the interaction. The nature of the

interaction (ferromagnetic or antiferromagnetic) is determined by the symmetries of overlapping metal and ligand orbitals. For the metal orbitals the interaction depends upon the electronic configuration, the nature of the ligand field and the crystal structure. Figure 1.3.3 shows a σ superexchange pathway resulting from collinear orbital overlap and a π superexchange pathway resulting from colateral orbital overlap.

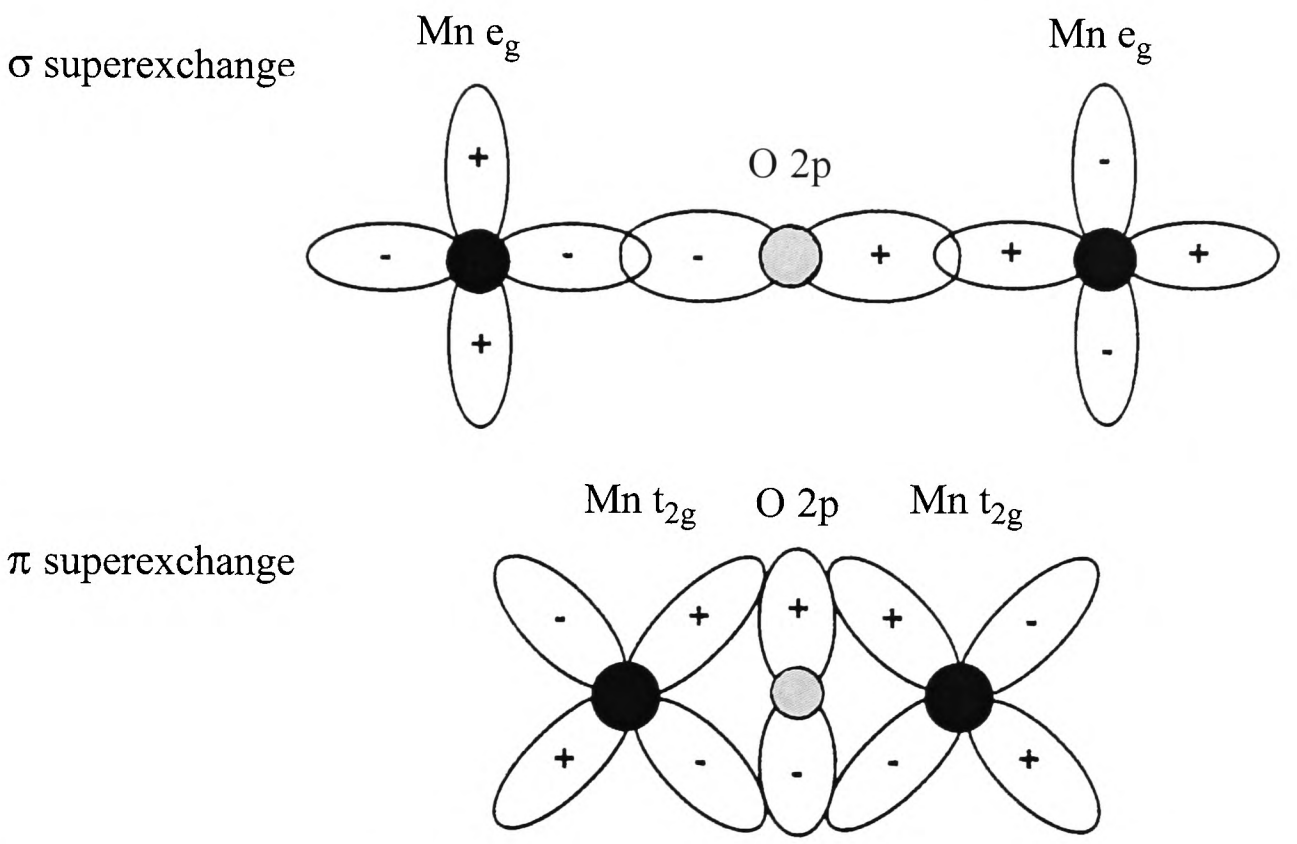


Figure 1.3.3 Superexchange pathways between nearest-neighbour Mn cations.

Detailed treatments of superexchange mechanisms are given by Goodenough[59,60], Anderson[61] and Kanamori[62,63]. Goodenough has presented[60] a framework (focussing on metal oxides with half-filled bands) in which there is a direct correlation between the strength of interatomic electronic interactions (represented by transfer energy, b), temperature, the magnetic ground state of a material and the degree of localisation of its electrons. Table 1.3.2 the nature of superexchange interactions relevant to the current work.

Table 1.3.2 The sign of nearest-neighbour superexchange interactions between Mn^{3+} and Mn^{4+}:

Superexchange pathway	Sign of dominant superexchange interaction
$Mn^{4+}\ t_{2g}^3$ - O^{2-} - $Mn^{4+}\ t_{2g}^3$	antiferromagnetic, t_{2g} - t_{2g} superexchange
$Mn^{3+}\ t_{2g}^3\ e_g^1$ - O^{2-} - $Mn^{4+}\ t_{2g}^3$	ferromagnetic, t_{2g} - e_g superexchange
$Mn^{3+}\ t_{2g}^3\ e_g^1$ - O^{2-} - $Mn^{3+}\ t_{2g}^3\ e_g^1$	AFM or FM e_g - e_g superexchange[a]

[a] d^4 - d^4 superexchange is influenced by the nature of the JT distortion (Chapter 5).

In several compounds discussed in this thesis, the interactions tabulated above exist simultaneously in the same sample as a result of the presence of mixed-valent manganese cations. This leads to the presence of competing magnetic exchange interactions. When, in addition to the competing interactions, the Mn^{4+} and Mn^{3+} cations are distributed in a random, disordered manner throughout the structure, the circumstances are present for spin glass[64] formation. The characteristics of spin glass behaviour are, firstly, the divergence between FC and ZFC curves for the measurement of susceptibility versus temperature following the cooperative freezing of spins at the temperature T_f. Secondly, there is hysteresis accompanying the M(H) loops and the loops are displaced from the origin. Finally, there is a non-zero remanent magnetisation on switching off the applied field after the sample has been cooled in a field. These properties are relevant particularly for the compounds discussed in Chapter 3 of this thesis. A comprehensive description of a 'spin glass insulator state', also relevant for the results of Chapter 3, was given by De Teresa et al.[65] for the compound $(TbLa)_{0.7}Ca_{0.3}MnO_3$.

Returning to the magnetic insulator, stoichiometric $LaMnO_3$, containing only Mn^{3+} d^4 cations; this compound is highly instructive since it shows a magnetic structure which is determined by the nature of the static, cooperative Jahn-Teller distortion and orbital ordering. It is found that *in-plane* interactions are predominantly ferromagnetic while *inter-plane* interactions are predominantly antiferromagnetic. This results in an A-type antiferromagnetic ground state.

Stoichiometric $LaMnO_3$ has the O' orthorhombic structure (*Pnma*), in which the lattice parameters have the ratio, $b/c < \sqrt{2}$. The precise nature of orbital ordering and resulting magnetic exchange interactions in $LaMnO_3$ has been considered by many authors, particularly Goodenough[66]. A number of recent studies[67-69] have lead to a detailed picture of the precise role of the e_g, ($d_{3z^2-r^2}$ and $d_{x^2-y^2}$) Mn orbitals. Understanding the complex in-plane and inter-plane exchange interactions present in stoichiometric $LaMnO_3$ relies upon identifying the *types* of occupied and empty e_g states connected with the orbital ordering. Solovyev et al.[70] gave a comprehensive account of orbital ordering in which they decomposed the e_g exchange terms into partial contributions from $d_{3x^2-r^2}$, $d_{y^2-z^2}$, $d_{3y^2-r^2}$ and

$d_{x^2-z^2}$ orbitals, the latter being linear combinations of $d_{3z^2-r^2}$ and $d_{x^2-y^2}$ type orbitals. Solovyev et al.[70] considered the nearest-neighbour in-plane exchange coupling denoted by J^1_{ab} and first neighbour interplane exchange denoted by J^1_c, and deduced the contributions listed in Table 1.3.3:

Table 1.3.3: Significant contributions to in-plane and inter-plane exchange interactions in JT distorted $LaMnO_3$ with the O' orthorhombic structure. The dominant exchange interactions are marked with an asterisk (*). Italicised orbitals denote the fact that they are empty:

	e_g superexchange	t_{2g} superexchange
[a]Contribution to J^1_{ab}	FM* $d_{3y^2-r^2}$ - $d_{y^2-z^2}$ FM* $d_{3y^2-r^2}$ - $d_{x^2-z^2}$	
Contribution to J^1_c	weak AFM $d_{3x^2-r^2}$ - $d_{3x^2-r^2}$ FM $d_{3x^2-r^2}$ - $d_{y^2-z^2}$ strong FM $d_{y^2-z^2}$ - $d_{y^2-z^2}$	AFM* t_{2g}^3 - t_{2g}^3 (d_{xz} and d_{yz})

[a] The subscripts 'ab' for the in-plane exchange and 'c' for interlayer exchange are appropriate for space group *Pbnm*, used by Solovyev et al.[70].

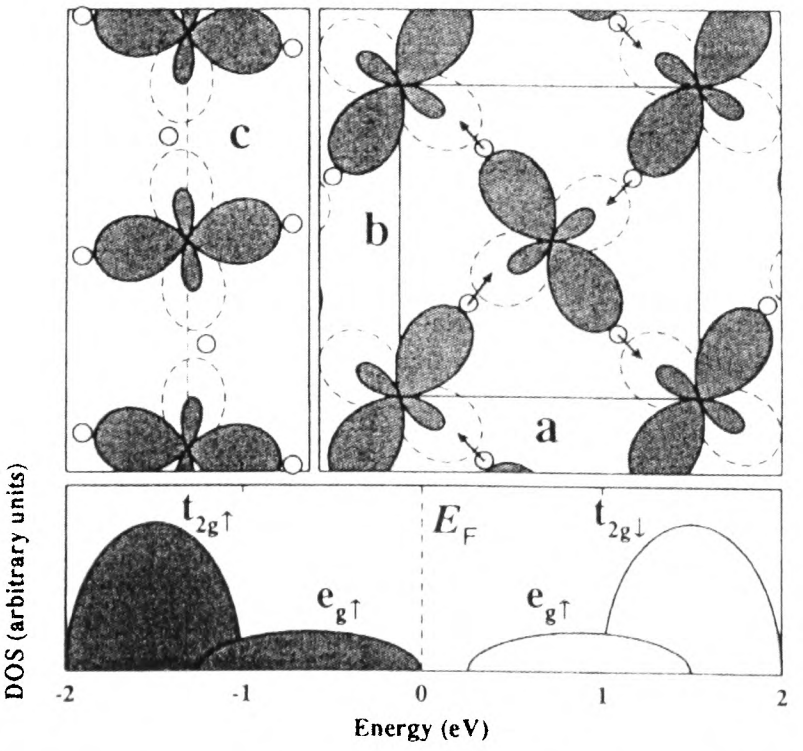


Figure 1.3.4 Pictorial representation of dominant superexchange interactions for stoichiometric $LaMnO_3$ denoted by asterisks in Table 1.3.3. The occupied $d_{3x^2-r^2}$ and $d_{3y^2-r^2}$ orbitals are shaded and the empty $d_{y^2-z^2}$ and $d_{x^2-z^2}$ are shown by dotted lines. The displacements of oxygen atoms (a signature of the orbital ordering) are represented by arrows. (Figure reproduced from reference [70]).

Hence, to summarise the results of the band-theory-based formalism used by Solovyev et al.,

the contribution to the exchange from the e_g orbitals is found to be positive for all bonds, with the magnitude of the exchange constant simply changing with distortion. For J^1_{ab}, the predominant interactions are the ferromagnetic (FM*) $d_{3y^2-r^2}$ - $d_{y^2-z^2}$ and $d_{3y^2-r^2}$ - $d_{x^2-z^2}$ pathways, where an occupied orbital on one atom is coupled with an empty one on its neighbour. Both pathways involve only e_g superexchange. For J^1_c, due to the JT distortion and subsequent emptying of $d_{y^2-z^2}$ orbitals, the FM $d_{y^2-z^2}$ - $d_{y^2-z^2}$ e_g superexchange which *would* dominate, is replaced by the antiferromagnetic t_{2g}^3- t_{2g}^3 superexchange involving d_{xz} and d_{yz} orbitals as a result of the emptying of $d_{y^2-z^2}$ states. The negative contribution from t_{2g} orbitals is found to change the sign of J_c, giving a net antiferromagnetic interlayer interaction. The detailed discussion of the case of $LaMnO_3$ presented above is helpful in understanding the arguments presented for compounds $La_2GaMnO_{6+\delta}$ and $Nd_2GaMnO_{6+\delta}$ in Chapter 5.

A further interaction which has been detected[71] in stoichiometric $LaMnO_3$ is evidenced by a weak moment along the c axis (*Pbnm*), attributed to the Dzyaloshinsky[72]-Moriya[73] (DM) interaction. This interaction is shown to be important for compounds discussed in Chapter 4. It is characterised by an antisymmetric exchange constant D_{ij} and the interaction is represented by the Hamiltonian in equation 1.3.10.

$$H = D_{ij} \cdot (S_i \times S_j) \qquad \text{eqn. (1.3.10)}$$

The effect can be significant when the inversion centre with respect to the two magnetic ions (i and j) is broken. This can occur when there is significant spin orbit coupling on the intermediate anion or on lowering of crystal symmetry. The effect manifests itself by a small canting of antiparallel moments resulting in a weak ferromagnetic moment.

The signatures of cooperative magnetic ordering and the nature of the resulting antiferromagnetic or ferromagnetic states are now discussed in more detail. An antiferromagnetic material is characterised by a sharp reduction of the molar magnetic susceptibility at the Néel temperature (T_N) and, since in a perfect antiferromagnet there should be equal numbers of magnetic ions with magnetic moments in opposing directions, the net unit cell magnetisation should tend to zero. The dependence of magnetisation on field for an antiferromagnetic is linear, without hysteresis. It is common, however, to observe non-

linear behaviour and non zero moments as a result of uncompensated moments, often as a result of the existence of domains or exchange interactions which have been 'diluted' by the presence of paramagnetic dopant ions. A definitive study detailing several types of antiferromagnetic order in perovskite oxides was made by Wollan and Koehler in 1955[74]. Antiferromagnetism is more common than ferromagnetism in transition metal oxides.

Ferromagnetism is signified by a dramatic rise in magnetic susceptibility at the Curie Temperature (T_C). This corresponds to the parallel alignment of magnetic moments on adjacent ions within finite domains. Although ferromagnetic materials exhibit a spontaneous magnetisation on the *microscopic* length-scale below the Weiss temperature θ, on a *macroscopic* length-scale, there is not necessarily a net magnetic moment in the absence of an applied magnetic field. This is because the direction of magnetisation may vary within domains comprising the bulk sample. Ferromagnetic behaviour is characterised by a non-linear dependence of magnetisation as a function of field, accompanied by hysteresis. The appearance of a net magnetisation at finite applied fields is due to the movement of Bloch walls through the material as a result of the applied field. The Bloch walls move such that domains with dominant components of magnetisation parallel to the field grow at the expense of all others. The domain wall movement is not reversible at all values of the applied field, leading to the observed hysteresis.

Finally, a particularly relevant effect for the compounds discussed in this thesis is that of the introduction of a fraction of paramagnetic ions into a magnetic array and the resulting effect on the magnetic exchange pathways. Chapters 4 and 5 both deal with B-site substitution of Mn^{n+} cations (by Ti^{4+} and Ga^{3+}, respectively) in which such paramagnetic 'impurities' are introduced with varying levels of disorder. For such cases, the issue of 'percolation limit' is raised. The percolation limit describes the case of an uninterrupted chain of magnetic ions extending throughout a crystal, containing no paramagnetic dopant cations[64]. Above the percolation limit (the critical concentration of magnetic ions), the 'magnetic backbone' supporting long range magnetic order remains intact. The percolation limit for a primitive cubic lattice (in which a cation such as Mn^{n+} has a maximum possible six magnetic neighbours) has been calculated[75,76] at 30.7%.

A case which might be considered 'intermediate' in nature between the disordered, mixed-interaction magnetic array typical of a spin glass and the long range order above the percolation limit, is that of a *cluster glass*. A cluster glass contains regions of correlated spins embedded in a spin glass matrix. Like spin glass materials, at a sufficiently low temperature, the clusters of spins freeze with random orientations. Therefore, the signatures of cluster glass behaviour are similar to those of spin glasses.

Many of the electronic properties introduced in the current section have been based on the properties of the compound $LaMnO_3$. Section 1.3.2 deals with the effect of hole doping of $LaMnO_3$, and as such, describes the essential properties of mixed-valent manganites exhibiting a 'typical' CMR response.

1.3.2 Electronic classification of the series $La_{1-x}Ca_xMnO_3$

1.3.2.1 The Double Exchange mechanism

The effect of A-site doping (with a divalent alkaline earth cation such as Ca^{2+}) is to introduce holes into the σ^* band derived from the overlap between the Mn e_g orbitals and the oxygen p orbitals. The formula of the resulting mixed-valent manganite can be written as follows,

$$(La^{3+}_{1-x}Ca^{2+}_{x})(Mn^{3+}_{1-x}Mn^{4+}_{x})O_3 \qquad \text{eqn. (1.3.11)}$$

from which it can be seen that the holes arise from a fraction of Mn^{4+} d^3 cations, present in order to maintain charge neutrality by the oxidation of a fraction of Mn^{3+} cations. Hole doping has been by far the most common form of doping reported in the literature for CMR manganites. Electron doping the other 'end member' of the $La_{1-x}Ca_xMnO_3$ series, $CaMnO_3$, has gained impetus recently, however[77], with the report of CMR properties in the series $Ca_{1-x}Ln_xMnO_3$[78].

The introduction of Mn^{4+} cations increases the tolerance factor of the perovskite structure, as well as increasing the itinerancy of the d electrons. The former effect is manifested by a gradual decrease in the orthorhombic distortion of $LaMnO_3$ as the value of x in the series $La_{1-x}Ca_xMnO_3$ increases, leading to rhombohedral or pseudocubic symmetry.

Superimposed upon this effect is the concomitant reduction in JT distortion as a fraction of Mn^{3+} d^4, with unequal occupancy of e_g orbitals, are replaced by Mn^{4+} d^3 with empty e_g orbitals. The increase in itinerancy of the d electrons manifests itself in the observation of an insulator-to-metal transition at a critical doping level, when $x \approx 0.3$. Accompanying mixed-valent Mn, is the introduction of competing, ferromagnetic, Mn^{3+} t_{2g}^3 e_g^1 - O^{2-} - Mn^{4+} t_{2g}^3 superexchange interactions[59] and, more importantly, ferromagnetic *double exchange* (DE) interactions. As shown by de Gennes[79], these ferromagnetic interactions (whether through superexchange or double exchange pathways), destabilise the antiferromagnetic ground state of the end member, $LaMnO_3$, initially manifesting themselves in spin canting, then collinear ferromagnetism at $x \approx 0.3$ in the series $La_{1-x}Ca_xMnO_3$.

Double exchange was introduced originally by Zener[80] to account for the simultaneous observation of itinerant behaviour and ferromagnetism in the mixed-valent manganites. Double exchange describes the process by which the kinetic energy contribution of e_g electrons is mediated by hopping amplitude t and a strong J_H coupling between e_g and t_{2g} spins on each of the two Mn cations involved in the 'hop'. The hole-spin scattering is minimised (and the kinetic energy of mobile carriers optimised) if the e_g electron does not have to pay an energy J_H. This is achieved if all the spins involved in the transition are parallel; hence, carriers prefer energetically to polarise the spins in their vicinity.

It is important to realise that the movement of charge carriers depends predominantly on the inherent bandwidth of the system. For example, doping the compound $LaMnO_3$ introduces holes which can move without incurring the Hubbard repulsion. Within the double exchange mechanism, the idea of an 'effective bandwidth' is introduced, in which the spin condition of Hund's rule is included. The effective bandwidth is maximised (and resistivity minimised) in the ferromagnetic state. The effect of an applied magnetic field and the observation of magnetoresistance can be rationalised now, since the field favours spin alignment and widens the effective energy band. A comprehensive review of the theoretical development of the DE mechanism is given by Bishop and Röder[81]. Anderson and Hasegawa[82] developed the mechanism significantly, multiplying the transfer integral by the spin-dependent term, $\cos\theta_{ij}/2$, where θ_{ij} is the angle between the magnetisation directions on

adjacent atoms i and j.

Figure 1.3.5 gives a schematic band structure of $La_{0.7}Ca_{0.3}MnO_3$, alongside that of the insulating $LaMnO_3$ for comparison. The most noticeable feature is the presence of a partially filled σ^* band, leading to itinerant electron behaviour. Whereas in $LaMnO_3$ the Fermi level fell in the gap between the two JT split e_g bands, for $La_{0.7}Ca_{0.3}MnO_3$ the Jahn-Teller splitting, δ_{JT}, is no longer greater than the bandwidth W. As long as the band remains Jahn-Teller split in the series $La_{1-x}Ca_xMnO_3$, the process is effectively that of doping a semiconductor until, at a critical concentration (x) of dopant ions, the carriers become delocalised, the Jahn-Teller distortion becomes dynamic and finally disappears.

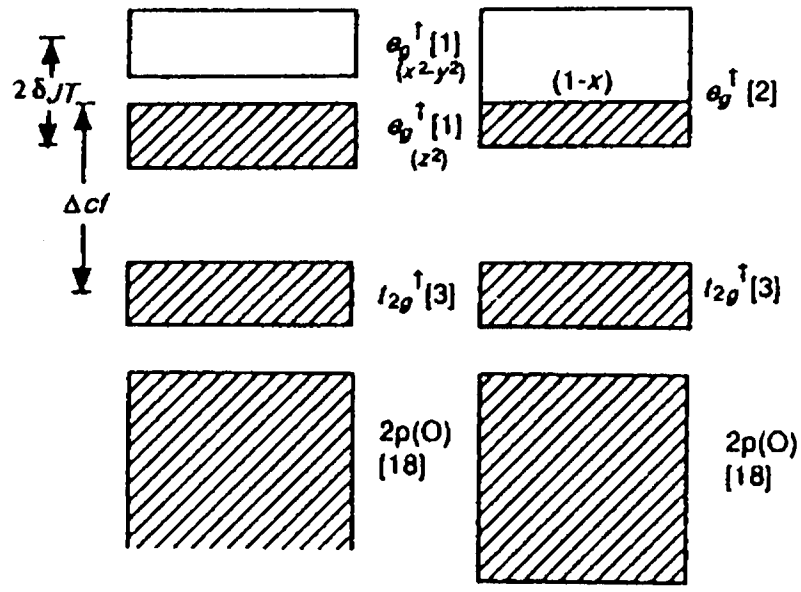


Figure 1.3.5 Schematic band structure for $La_{0.7}Ca_{0.3}MnO_3$ (r.h.s), alongside that of the insulating $LaMnO_3$ (l.h.s) for comparison. (Figure reproduced from reference [118]).

1.3.2.2 The intrinsic CMR response

The interplay between the electrical resistivity of a material and its transition to a ferromagnetic state encompassed by the double exchange mechanism is represented in Figure 1.3.6 for a thin film of the compound $La_{0.7}Ca_{0.3}MnO_3$. The correlation between resistivity, Curie temperature and the maximum magnitude of magnetoresistance reproduces the results obtained originally by Volger in 1954[5] for the mixed-valent manganites. As explained by Kusters et al. in 1989[14], the origin of the large magnetoresistance ratio is the effect of the applied magnetic field driving an increase in the Curie temperature of the material, causing the insulator-to-metal transition to occur at a higher temperature at field. The resistivity peak temperature, T_{max}, almost coincides with the Curie temperature, T_C, for doping levels in the

series $La_{1-x}Ca_xMnO_3$ around x = 0.3. The magnitude of magnetoresistance is maximum around the metal-insulator transition (T_C) and scales with the (field-induced) magnetisation such that $MR \propto (M/M_S)^2$, where M_S is the saturation magnetisation.

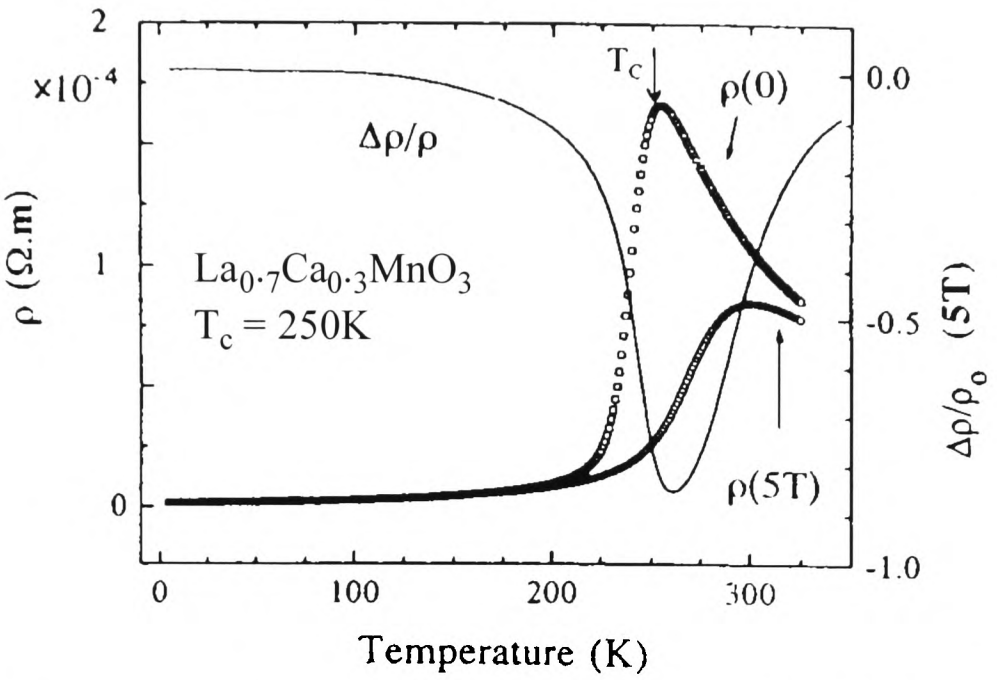


Figure 1.3.6 Resistivity as a function of temperature for $La_{0.7}Ca_{0.3}MnO_3$, at zero field and an applied field of 5T. The MR ratio as a function of temperature is also plotted. (Figure reproduced from reference [52]).

The 'intrinsic' contribution to the resistivity of $La_{0.7}Ca_{0.3}MnO_3$ in Figure 1.3.6 should be separated from 'extrinsic' contributions, governed by sample size and microstructure. Intrinsic properties are best measured on single crystals and epitaxial films and, for polycrystalline samples, the intrinsic response is strictly the 'intra-granular' contribution to a certain property.

There is a vast body of literature that has built up over the last decade in which various means of structural tuning in series such as $La_{1-x}Ca_xMnO_3$ and $La_{1-x}Sr_xMnO_3$ have been attempted, in order to optimise the CMR response. The reviews by Coey and Viret[52] and Goodenough[83] give particularly comprehensive accounts of recent advances, and the review by Ramirez[84] summarises progress throughout the mid-to-late nineties. Publications by Lanzara et al.[85] and Rao[86] help to place the recent developments regarding mixed-valent manganites in the wider context of solid state materials chemistry. The main approaches to structural tuning, have entailed altering the doping level[87], varying $\langle r_A \rangle$ both by changing the doping level and/or by changing the dopant cation[88-92] and extensive studies on B-site (Mn

cation) substitution[93-95]. It is now accepted that A-cation size mismatch, as well as the value of $\langle r_A \rangle$, is an important parameter determining electronic bandwidth. As shown by Attfield and Rodriguez-Martinez[96], at a constant value of $\langle r_A \rangle$, T_C in certain infinite layer manganites decreases as the size *difference* between distinct A-site cations increases. They have parameterised this effect using the variance (σ^2) of the A-cation radius distribution,

$$\sigma^2 = \Sigma y_i r_i^2 - \langle r_A \rangle^2 \qquad \text{eqn. (1.3.12)}$$

where y_i is the fractional occupancy of the site of the cation with radius r_i. A study by Sun et al.[97] on the system $La_{0.67-x}R_xCa_{0.33}MnO_3$ at fixed tolerance factor, also investigated the influence of cation size mismatch on electronic transport properties. Results of changing x in the series $La_{1-x}Ca_xMnO_3$ have shown CMR effects to be observed ranging from low hole densities to x = 0.5; this appears to be the density limit for the ferromagnetic phase.

Sub-section 1.3.2.3 discusses the nature of the carriers in the 'metallic' and 'insulating' regime of a mixed-valent manganite showing a 'typical' intrinsic CMR response as characterised by that shown in Figure 1.3.6. As such, this Section focusses on one of the most puzzling aspects of magnetotransport behaviour in these sytems, that of enhanced carrier localisation leading to high residual resistivities both above and below the metal-insulator transition. A model incorporating both the effects of disorder and the significance of electron-lattice interactions is required, since both have been shown to have an essential contribution, in addition to double exchange, in determining the electronic ground state of CMR manganites.

1.3.2.3 Carrier localisation in CMR manganites

Transition metal oxides at the 'metal-insulator' boundary are often termed 'marginally metallic'[98]. The majority show conductivities in the metallic state which are suggestive of a finite density of states at the Fermi level. However, the mixed-valent manganites exhibiting CMR are anomalous in that they possess very high resistivities even at low temperatures, after the metal-insulator transition, and show no significant density of states at the Fermi level. Figure 1.3.7 shows the variation in values of residual resistivity of some marginally metallic oxides over a wide temperature range, in which $La_{1-x}A_xMnO_3$ compounds are seen to

occupy the upper range of resistivity (Ωcm) values.

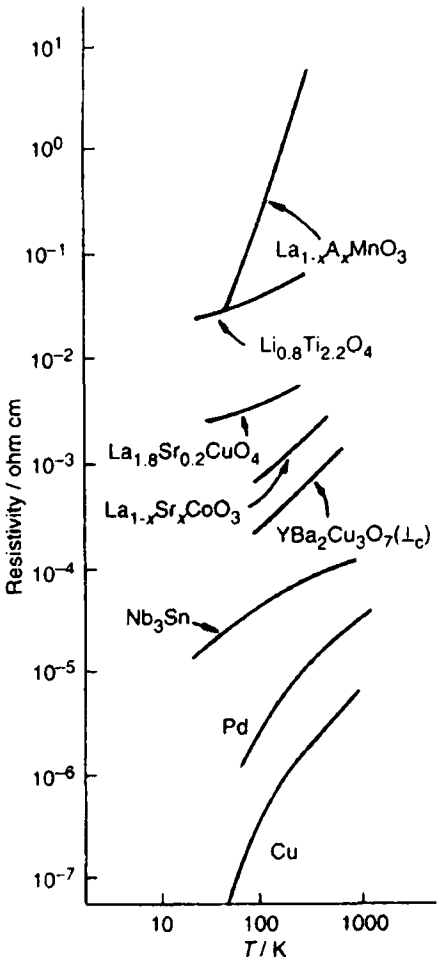


Figure 1.3.7 Resistivity as a function of temperature for a range of solid state materials. (Figure reproduced from reference [98]).

Mott[99] derived a useful experimental criterion, that of maximum metallic resistivity, ρ_{max}, at which a material may still be regarded as metallic, before the temperature coefficient of resistivity changes from being metal-like (+) to insulator-like (-). The value of ρ_{max} is approximately 1 to 10 (mΩcm) in oxide systems. Typically, the resistivities of mixed-valent manganites at the MI transition are *at least* 10mΩcm and, therefore, these materials do not obey the Mott criterion. In addition, the resistivities in the 'metallic' state (ie. below T_C) can rise as high as 10^3 - 10^4 Ωcm, and as such can be even higher than those in the insulating state (above T_C). This is not the expected behaviour following the hole doping of a 'typical' Mott insulator, which should possess mobile carriers at sufficient hole concentrations.

Turning to the 'insulating' or paramagnetic state (ie. above T_C), studies have shown that the most significant consideration, in addition to the double exchange mechanism, in describing the magnetotransport properties of the series $La_{1-x}Ca_xMnO_3$, is that of the role of phonons. Phonons are the vibrations of the crystal lattice (those of the light oxygen atoms are particularly important), and 'electron-phonon coupling' describes the interaction of charge

carriers with these vibrations. Several definitive studies have identified the significance of electron-phonon coupling in the magnetotransport behaviour of mixed-valent manganites. In particular, those of Hwang et al.[100], Millis et al.[101,102], Radaelli et al.[103], and De Teresa et al.[104]. In the studies by Hwang et al. and Radaelli et al., the authors discuss in particular the strong electron-phonon interaction arising from the Jahn-Teller splitting of the Mn 3d orbitals. Indeed, this has proven to be a highly influential feature regarding charge localisation in these systems which contain a Mn^{3+} d^4 Jahn-Teller cation. The process of localisation to form a 'Jahn-Teller polaron' can be imagined as being due to the lattice vibrations causing charge carriers to be deflected towards the vacant states in the manganese cations distributed throughout the lattice. This 'creates' a Mn^{3+} d^4 Jahn-Teller cation and strengthens the Jahn-Teller effect, inducing a local distortion of the lattice. The distortion in this case leads to 'self-trapping' of charge carriers. A Jahn-Teller polaron can form in a solid where the JT stabilisation energy is comparable to the conduction electron bandwidth, W.

The general description of a 'polaron' is that of 'the trapping of an electron or hole at one site by the local lattice polarisation which it causes'[105]. The spatial extent of the 'self -trapped' state varies, and thus may be termed either a large or small polaron, the large polaron corresponding to the more mobile electronic state. The self-trapped state of the charge carriers will exist only above the Curie temperature of a particular compound, since the onset of ferromagnetism is accompanied by an increase in the effective bandwidth, and more itinerant electronic behaviour[106,107]. This is illustrated by moving to wider bandwidth systems, where the likelihood of electron-phonon coupling is diminished. For example, the double exchange mechanism alone gives a significantly more complete description of the magnetotransport behaviour of $La_{0.7}Sr_{0.3}MnO_3$ than of $La_{0.7}Ca_{0.3}MnO_3$, the former behaving as a metal in the paramagnetic state.

De Teresa et al.[104] used the techniques of volume thermal expansion, magnetic susceptibility and small angle neutron scattering (SANS) to confirm the existence of 'magnetic polarons' in the compound $(Y\text{-}LaTb)_{0.7}Ca_{0.3}MnO_3$. The term 'magnetic polaron' in their work described a small polaron in which the trapped electron polarises the magnetic moments of the ions in its vicinity, leading to a region of short range ferromagnetic interactions.

Figures 1.3.8 (a), (b) and (c) give schematic diagrams of a small (dielectric) polaron, a Jahn-Teller polaron and a magnetic polaron, respectively:

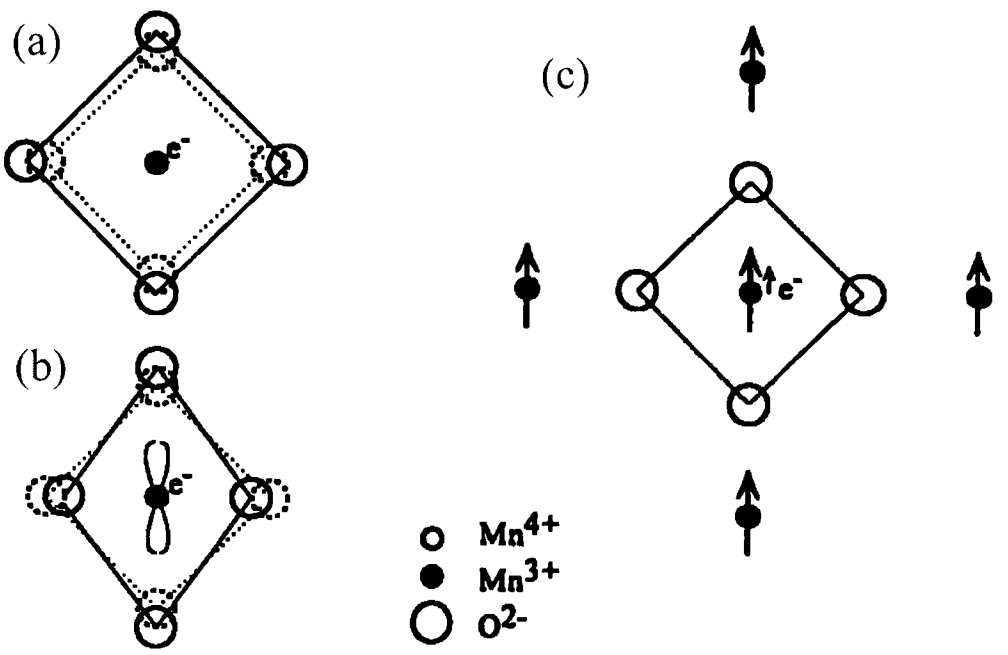


Figure 1.3.8 Schematic diagrams of (a) a small dielectric polaron, (b) a Jahn-Teller polaron and (c) a magnetic polaron. (Figure reproduced from reference [52]).

A particularly elegant means of investigating the role of electron-phonon coupling is *via* the use of isotopic substitution experiments. Here, the oxygen-16 ions are replaced at high temperature by oxygen-18. The introduction of the heavier ions should accentuate the effects of electron-phonon coupling, reducing the carrier mobility. Zhao et al. have carried out extensive studies[108,109] in which they have, indeed, demonstrated the reduction of the Curie temperature after substitution.

When polarons become sufficiently 'extended', the localisation of charge carriers in the crystal lattice leads to an electronic instability that creates short range variations in the electronic properties of the ground state. In extreme cases, these short range electronic variations can result in electronic 'phase segregation' (PS) and the term polaron is replaced by 'cluster' or 'droplet' describing a region corresponding to a particular phase. Identifying and understanding electronic phase segregation is currently one of the most active areas of CMR research[110]. An interesting issue is whether the presence of significant Jahn-Teller distortion is necessary for electronic phase segregation to occur. Calculations have suggested it is not, the implication being that PS is also expected to occur below T_C in a number of compounds. Below the respective magnetic transition temperatures, PS in a series such as $La_{1-x}Ca_xMnO_3$, for example, is expected to consist of hole-depleted AFM regions and hole-rich FM regions,

depending also on the density of charge carriers. At low values of x (~ 0.05 and 0.08) in the series $La_{1-x}Ca_xMnO_3$, PS manifests itself by the presence of FM droplets or clusters with radius 1nm, thought to correspond to hole-rich regions. In $La_{1-x}Ca_xMnO_3$, at high doping levels ($x \geq 0.5$), phase segregation is in the familiar form of charge ordering at an atomic level between Mn^{3+} and Mn^{4+}cations. Electron microscopy studies of the $La_{1-x}Ca_xMnO_3$ series with $x \geq 0.5$ have shown the existence of 'paired stripes'[111], consisting of Mn^{3+} states, interspersed with Mn^{4+} 'valleys'.

The competition between charge ordering and double exchange mechanisms in mixed-valent manganites is well documented[112,113], charge ordering often being favoured when a 1:1 ratio of Mn^{3+} and Mn^{4+} cations is present. The tendencies towards charge ordering and double exchange are both highly dependent upon $\langle r_A \rangle$, the former being favoured by small $\langle r_A \rangle$ and the latter mechanism by large $\langle r_A \rangle$[114]. A particularly informative, recent study by Uehara et al.[115] with regard to charge ordering and phase segregation, has suggested that certain low T_C (La, Pr, Ca)MnO_3 phases are electronically phase segregated into a sub-micrometre scale of insulating regions (x = 0.5 type CO) and metallic, FM domains. The aim of the study was to explain the large MR ratios observed in low T_C manganites[102,116] which are not fully accounted for within a combined double exchange/polaronic framework. Interestingly, they attribute the PS to a new type, not driven by charge segregation (on account of the large length scale, (0.5μm)), over which it occurs. They attribute the large CMR effects in their system to percolative transport through the FM domains, which is field dependent as a result of the orienting effect of the field on the relative spin directions of adjacent domains.

In considering the paramagnetic state of the mixed-valent manganites, it is useful to summarise the typical models by which the thermally activated transport (above the magnetic transition temperature) may be described. A simple, activated hopping conduction described by the relation given in equation 1.3.13 often suffices, and could be indicative of nearest-neighbour hopping, activation to a 'mobility edge'[105] or narrow gap semiconduction, for example.

$$\rho \propto \exp(E_a / k_B T) \qquad \text{eqn. (1.3.13)}$$

In many cases, however, Mott's variable range hopping (VRH) model[117], (a generalised expression of which is given in equation 1.3.14) may give a better fit to experimental data. The VRH theory was developed originally to explain electron transport in doped semiconductors, where carriers are localised by potential fluctuations associated with the dopant cation. The critical parameters dictating electron motion are the potential energy difference between two sites and the distance an electron can hop.

$$\rho \propto \exp(T_o / T)^{\gamma} \qquad \text{eqn. (1.3.14)}$$

Here, T_o is a term which is dependent upon the localisation length of the electrons and the density of states. The value of γ, characteristic of three-dimensional VRH, is 0.25, while two-dimensional VRH hopping is described when γ is 0.33. The length of 'hops' within the VRH model should be several times greater than the Mn-Mn separation distance, in mixed-valent manganites, for example.

The 'potential fluctuations' described above exist for doped magnetic semiconductors such as $La_{1-x}Ca_xMnO_3$. Within the Hubbard model described in sub-section 1.3.1.2, and in Figure 1.3.2, it can be seen that as the two Hubbard sub-bands overlap increasingly, and the gap disappears, metallic behaviour is predicted when $W > U$ for an ordered solid. In doped compounds however, there is significant disorder due to potential fluctuations arising from defects, and this produces 'Anderson localisation'[117] at the band edges. Thus, for a small overlap of the bands, the states at the Fermi level are localised and truly itinerant electron behaviour is prevented. This is exactly the regime where the VRH model might be applicable, although Coey et al. and Viret et al.[118-120] have shown that it is necessary to modify the model and include a term due to the 'magnetic localisation' of carriers in several $x = 0.3$ manganese perovskites.

Another mechanism by which conduction may occur in the thermally activated region of mixed-valent manganites, is that of the hopping of small polarons. Polarons hop from one localised state to another by emitting and absorbing phonons. Small polaron conduction can

occur also in the VRH regime; Thompson and Singh[121] have developed a theory for VRH due to small polarons in quasi-two-dimensional systems at high temperatures, establishing a $T^{-0.5}$, power law dependence.

1.4 Electronic characteristics of n = 2 and 3 layered Ruddlesden Popper oxides, $A_3B_2O_7$ and $A_4B_3O_{10}$, respectively.

The fundamental properties of mixed-valent CMR manganites have been introduced in Sections 1.3.1 and 1.3.2, within the framework of behaviour observed for n = ∞ materials, such as $LaMnO_3$ and $La_{0.7}Ca_{0.3}MnO_3$. However, since the report of CMR properties in the n = 2 manganite $Sr_{1.8}La_{1.2}Mn_2O_7$ in 1996 by Moritomo et al.[122] (50% suppression of the zero field signal in 0.3T), the n = 2 layered manganites have attracted significant interest in their own right[123]. They offer an ideal structural framework in which to investigate how CMR phenomena, observed for a particular doping level in the infinite layer systems change, on reducing the dimensionality. In fact, it is often found that band-narrowing on reducing dimensionality leads to an enhanced magnetoresistive ratio occurring at a lower Curie temperature, T_C. For example, polycrystalline $La_{0.7}Sr_{0.3}MnO_3$ showed a 40% suppression of the zero field signal in 6T, while the n = 2 analogue $Sr_{1.6}La_{1.4}Mn_2O_7$ showed 80% MR in the same field[124].

The $Sr_{1.8}La_{1.2}Mn_2O_7$ phase, studied originally by Moritomo et al.[122], undergoes a metal-insulator transition at its Curie temperature (≈ 126K) accompanied by significant, negative magnetoresistance. As such, it resembles the typical CMR response of several n = ∞ systems described within the double exchange model, despite its reduced dimensionality. However, neutron diffraction studies on the last mentioned material[125,126] revealed that MnO_6 octahedra are more severely distorted when the carrier is itinerant below T_C than when it is localised above T_C. This is in contrast to pseudocubic perovskites in which the enhanced JT distortion above T_C narrows the bandwidth and contributes strongly to carrier localisation. Indeed, closer examination of $Sr_{1.8}La_{1.2}Mn_2O_7$ and other compositions at a range of doping levels, x, in the $Sr_{2-x}La_{1+x}Mn_2O_7$ and $Sr_{2-x}Nd_{1+x}Mn_2O_7$ series, reveals numerous contrasts rather than similarities with 'typical' n = ∞ systems. For example, Battle et al.[127] have shown that colossal magnetoresistance in $Sr_2NdMn_2O_7$ and $Sr_{1.9}Nd_{1.1}Mn_2O_7$ is not

associated with bulk, three-dimensional ferromagnetic order. The differences in behaviour between n = ∞ and n = 2 systems arise often due to the *quasi*-two-dimensional, rather than three-dimensional nature of the latter systems. The following discussion outlines key properties of n = 2 layered manganites, many of which are driven by their two-dimensional nature.

The majority of studies on two-dimensional layered manganites have been performed on the $Sr_{2-x}La_{1+x}Mn_2O_7$ series[128], specifically on doping levels corresponding to x = 0[129-132], x = 0.2[133] (refer to later discussion) and x = 0.4[134-137]. Battle et al.[138] have emphasised the tendency for phase separation at the x = 0 doping level in the series $Sr_{2-x}La_{1+x}Mn_2O_7$. In comparison to the Sr, La phases, the $Sr_{2-x}Nd_{1+x}Mn_2O_7$ series has received little attention[139-143]. The properties of the $Sr_{2-x}(La_{1-z}Nd_z)_{1+x}Mn_2O_7$ series[144-149] have been shown to provide an ideal framework in which to study the crossover between '$Sr_{2-x}La_{1+x}Mn_2O_7$-like' and '$Sr_{2-x}Nd_{1+x}Mn_2O_7$-like' behaviour, at a selected, constant doping level, x. Several studies [150-152] have highlighted the degree of control of electronic properties of $Sr_{2-x}Ln_{1+x}Mn_2O_7$ materials, by the size of lanthanide dopant[153,154], and manganese oxidation state. There are also documented studies using Ca^{2+} as the alkaline earth cation in doped n = 2 manganites, in the series $Ca_{2-x}La_{1+x}Mn_2O_7$[155-160], and many more combinations of A- and B-site cations. Thus, the vast majority of magnetotransport studies on layered manganites have been carried out on 'hole doped' systems with Mn present in an oxidation state intermediate between +3 and +4. In contrast, a recent study on the series $La_{2.3-x}Y_xCa_{0.7}Mn_2O_7$, has reported a metal-insulator transition and ferromagnetism in an electron doped manganite[161].

The separation of MnO_6 octahedra along the c axis in layered materials leads to a weakening of interlayer magnetic coupling and electrical conduction in this direction. The low electrical conduction along c leads to a decoupling of in-plane and out-of-plane transport. The differences in the magnitude of resistivity within, and perpendicular to, the ab planes has been evidenced in several studies on single crystals, in particular for the phases $Sr_{1.8}La_{1.2}Mn_2O_7$[162], and $Sr_{1.6}La_{1.4}Mn_2O_7$[29]. Surprisingly, a similar order of magnitude for resistivity within, and perpendicular to, the ab planes in single crystal $Sr_{1.5}Nd_{1.5}Mn_2O_7$ was reported recently[140].

The layered nature of these materials manifests itself also in strongly anisotropic magnetic exchange interactions, for example, J_{ab}, the in-plane superexchange coupling constant is greater than the out-of-plane parameter, J_c. The small transfer integral along the z direction has implications for the nature of ferromagnetic exchange in this direction; for example, within the double exchange framework, ferromagnetism is mediated by charge carriers. Thus, the competing superexchange pathway has a relatively strong influence on the correlations along z. Several studies have highlighted the competition between antiferromagnetic superexchange interactions and ferromagnetic (super- and double exchange) interactions in n = 2 systems containing both Mn^{3+} and Mn^{4+} cations, which appears more marked than in the larger bandwidth, three-dimensional perovskites. The application of external hydrostatic pressure[160,163,164] has proved a particularly useful probe of this competition, since it neither changes the number of carriers (as doping does), nor introduces a preferred orientation of magnetic moments. The layered structure appears to accommodate the application of external pressure by changes in Mn-O bondlengths rather than tilting of MnO_6 octahedra, in contrast to several infinite layer systems. The latter point was emphasised in the study of $Sr_{1.8}La_{1.2}Mn_2O_7$ by Argyriou et al.[125] in which exchange-striction effects were interpreted as reflecting the competition between super- and double exchange.

The extent and origin of the octahedral distortion in layered manganites is a fundamental parameter in determining magnetotransport properties, as is observed for perovskite manganites. A study by Mitchell et al.[165] has characterised the extent of octahedral distortion in the stoichiometric 'parent' compound of the n = 2 layered manganites, $Sr_3Mn_2O_7$, which contains no Jahn-Teller Mn^{3+} cation. A small distortion was detected, arising from the elongation of the axial Mn-O bond directed into the rocksalt layer. The study emphasised that the steric environment alone can induce such a distortion, in the absence of the Jahn-Teller effect. The lifting of the degeneracy of Mn e_g orbitals, whatever the origin, splits them into d_{3z2-r2} and d_{x2-y2} states. A useful parameter, Δ, quantifies the irregularity of MnO_6 octahedra and is defined as 'the ratio of the averaged out-of-plane to averaged in-plane Mn-O bondlengths'. It has been shown to be an effective parameter with which to predict the anisotropy of magnetotransport behaviour, in studies of manganites with reduced

dimensionality[148]. The $d_{x^2-y^2}$ state extends along the sheet direction and has large t_{ab}, while the $d_{3z^2-r^2}$ state has a small t_c, extending along the z direction perpendicular to the MnO_2 bilayers. The respective transfer integrals t_{ab} and t_c are those for itinerant electrons for in-plane and out-of-plane conduction between nearest-neighbour Mn sites. The orbital character of conduction electrons ($d_{3z^2-r^2}$ or $d_{x^2-y^2}$) is shown to influence which is the dominant magnetic interaction in n = 2 systems. Band structure calculations by Dessau et al.[166] on single crystals of $Sr_{1.8}La_{1.2}Mn_2O_7$, have indicated that the $d_{x^2-y^2}$ orbital is slightly lower in energy than $d_{3z^2-r^2}$, but that these bands overlap significantly throughout the Brillouin zone.

The evolution of competing magnetic exchange interactions with increasing x (Mn e_g bandfilling) in the series $Sr_{2-x}La_{1+x}Mn_2O_7$, has received much attention. The results are of particular interest for comparative purposes in the current work, where the magnetotransport properties of the $Sr_{2-x}Nd_{1+x}Mn_2O_7$, series (for x = 0, 0.1, 0.2 and 0.5) are under investigation. The $Sr_{1.8}La_{1.2}Mn_2O_7$ composition particularly is well characterised, and, in addition to the onset of ferromagnetic order at $T_C \approx 126K$, several reports observed evidence of magnetic correlations existing above T_C[162,167-169]. A comprehensive study by Hirota et al.[170] has claimed to have rationalised these observations by identifying an A-type AFM phase, associated with planar, *short range* FM correlations, which persists above T_C. They have also studied the canting between ferromagnetically aligned Mn moments in adjacent planes, originally proposed by Argyriou et al.[125]. Hirota et al. also considered the compositions $Sr_{1.96}La_{1.04}Mn_2O_7$ and $Sr_{1.9}La_{1.1}Mn_2O_7$ and, as such, their results provide a useful comparison with the current treatment of $Sr_{1.9}Nd_{1.1}Mn_2O_7$ and $Sr_{1.8}Nd_{1.2}Mn_2O_7$ phases. The authors observed an A-type AFM magnetic ground state for the $Sr_{1.96}La_{1.04}Mn_2O_7$ sample, which became less stable on introduction of more La^{3+} (Mn^{3+}) with increasing x. At x = 0.2, for the $Sr_{1.8}La_{1.2}Mn_2O_7$ composition, successive (two-dimensional FM planes) have an almost FM alignment along c due to the low canting angle (6.3°) between planes, although the overall structure is still A-type AFM. The AFM structure for $Sr_{1.96}La_{1.04}Mn_2O_7$ (with no 3-D FM component) corresponds to a canting angle of 180°. Thus, for $Sr_{1.8}La_{1.2}Mn_2O_7$ 3-D FM sets in at $T_C \approx 126K$, but planar, *short range* FM correlations persisting above T_C have net AFM alignment.

These observations were interpreted using the balance between competing AFM superexchange and FM double exchange interactions, and the orbital character of conduction electrons. Ferromagnetic interactions exist within the planes, mediated by the double exchange interaction, for both $Sr_{1.96}La_{1.04}Mn_2O_7$ and $Sr_{1.8}La_{1.2}Mn_2O_7$ in Hirota's study and the $d_{x^2-y^2}$ orbitals are assumed to be stabilised, in a pseudo-2-D band. The observation of 3-D FM order relies upon the FM double exchange interaction (and/or ferromagnetic Mn^{4+} (t_{2g}^3) - O^{2-}- Mn^{3+} ($t_{2g}^3e_g^1$) superexchange interaction) competing with the AFM superexchange interaction along c. This competition proves sufficiently strong to induce 3-D ferromagnetic order in $Sr_{1.8}La_{1.2}Mn_2O_7$ but not in $Sr_{1.96}La_{1.04}Mn_2O_7$. This is attributed in the study to the enhanced value of Δ in $Sr_{1.8}La_{1.2}Mn_2O_7$ compared to that in $Sr_{1.96}La_{1.04}Mn_2O_7$ (powder neutron studies showed[148] that Δ increases from 1.00 to 1.03 on moving from $Sr_2LaMn_2O_7$ to the composition $Sr_{1.6}La_{1.4}Mn_2O_7$, consistent with the increased concentration of JT Mn^{3+} cations in the latter compound). A large value of Δ favours the hybridisation with, and stabilisation of, $d_{3z^2-r^2}$ states, contributing to electron transfer along the c axis and strengthening the FM double exchange interactions simultaneously. Charge transfer into $d_{3z^2-r^2}$, on cooling through T_C, is also consistent with the observation by Mitchell et al. that JT distortion (parameterised by Δ) becomes larger in the itinerant, FM state. Thus, the smaller value of Δ in $Sr_{1.96}La_{1.04}Mn_2O_7$ is thought to favour the AFM superexchange interaction along c and confinement of FM double exchange to within the plane. The ferromagnetic Mn^{4+} (t_{2g}^3) - O^{2-} - Mn^{3+} ($t_{2g}^3e_g^1$) superexchange interaction is also likely to compete more effectively with the antiferromagnetic Mn^{4+} (t_{2g}^3) - O^{2-} - Mn^{4+} (t_{2g}^3) superexchange interaction as the proportion of Mn^{3+} ($t_{2g}^3e_g^1$) cations increases with x. However, consideration of phases close to the composition $Sr_2LaMn_2O_7$, should involve careful examination of phase purity, in the light of results obtained by Battle et al.[138] for this material.

Equally complex interactions have been discussed for the (nominal) $Sr_{1.6}La_{1.4}Mn_2O_7$ phase[134], where it is suggested that the lattice response along the c axis is actually opposite in sign to that observed in the $Sr_{1.8}La_{1.2}Mn_2O_7$ composition. For example, it is found that on cooling through the MI transition, charge transfer into the $d_{x^2-y^2}$ state occurs. Another

significant finding in the latter study, which corroborates results observed by Battle et al.[138] for the similar $Sr_2LaMn_2O_7$ composition, is the detection of a second layered manganite phase with marginally different composition to the bulk phase.

The subtle balance between octahedral distortion, orbital stabilisation and anisotropic transfer integrals, which defines the magnetotransport properties in the n = 2 manganites has implications for the carrier localisation mechanisms expected in these systems. Evidence of small polaron formation has been linked typically to the narrowing of the two-dimensional d_{x2-y2} state with increasing temperature[171-173].

As discussed for the material $Sr_2LaMn_2O_7$[138], although the intergrowth of perovskite regions and rocksalt layers provides vast potential for structural and electronic tuning in layered manganites, it has also been shown[174] to raise significant synthetic and interpretational problems, because the layered manganites appear particularly susceptible to phase impurity. Phase impurity can be in the form of intergrowths of pseudocubic (n = ∞) perovskite structure[175] or stacking deviations, for example. Alternatively, as Battle et al. have shown[151], the ease of preparation of single n = 2 RP phase materials can be determined partially by the degree of A-site cation ordering, i.e. by the tendencies of the smaller cations to occupy the smaller 9 coordinate 'rocksalt' site and the larger cations to occupy the 12 coordinate 'perovskite block' site. Cation ordering is not an issue in infinite layer materials, where there is one distinct crystallographic site for A-cations. The presence of a high proportion of small (relatively electronegative) lanthanide cations on the 9 coordinate site of n = 2 manganites can reduce the bandwidth of the Mn-derived electrons, by competing with manganese for bonding with oxygen[150]. Even allowing for a degree of cation ordering in n = 2 systems, intrinsically the materials have site randomness arising from the presence of more than one type of A-cation. Seshadri et al.[176] emphasised the contribution of disorder to the observations of broad transitions in magnetotransport data at low temperature, both under and in the absence of a magnetic field, which then return the system to insulating behaviour.

As part of their studies into layered perovskites in 1958[2], Ruddlesden and Popper prepared the compound $Sr_4Ti_3O_{10}$. Like the n=2 compound $Sr_3Ti_2O_7$, it was shown to be

tetragonal, consisting of triple octahedral perovskite slabs displaced by a translation of 1/2 in the [110] direction, interleaved by layers of SrO, adopting the space group *I4/mmm*.

The Ca,Sr-Mn analogues of this original n = 3 phase are the subject of Chapter 4, being a logical extension of investigations into the n = 2 RP compounds, which have proved such interesting CMR systems. In comparison with the n=2 RP phases, relatively few CMR studies have been carried out on n=3 materials in the last decade, due partly to the difficulty in synthesising high quality samples containing mixed valence Mn, uncontaminated by n = 2 and n = ∞ material. The first comprehensive study on an n = 3 RP material containing Mn was the magnetic study into the series $Ca_{n+1}Mn_nO_{3n+1}$, for n=1,2,3 and ∞, by MacChesney and co-workers in 1967[43]. Their primary aim was to investigate how the insertion of non-magnetic CaO layers (with decreasing n) would influence the predominant, antiferromagnetic Mn^{4+} (t_{2g}^3) - O^{2-} - Mn^{4+} (t_{2g}^3) π superexchange interactions present in this series. MacChesney's group went on to study the chemistry of layered Sr,La manganates in 1969[177], preparing $Sr_{2.5}La_{1.5}Mn_3O_{9.98}$ in the first of several numerous studies[44] of structural and magnetic properties of this family as a function of dimensionality.

The Ca,Sr titanates and manganates are not the only examples of compounds adopting the n=3 RP structure. Shortly after the work of MacChesney et al. in 1967 came the characterisation of $Sr_4Fe_3O_{10-\delta}$ by Brisi et al.[178]. By the early eighties, the compounds $La_4Ni_3O_{10}$ and $La_4Co_3O_{10}$ had been prepared and shown to be isostructural and to have orthorhombic (*Fmmm*) symmetry[179,180](although more recent work on $La_4Co_3O_{10}$ has suggested its true symmetry is lower than *Fmmm*[181]. In the early nineties, Ba was shown to stabilise the compounds $Ba_4Pb_3O_{10}$[182] and $Ba_4In_3O_{8.5}$[183]. The difficulty in synthesising pure, n=3 materials free from intergrowths, was emphasised in a study of the vanadates, $Sr_{n+1}V_nO_{3n+1}$ (n=1,2,3 and ∞), by Nozaki and co-workers[184], in which the sample $Sr_4V_3O_{10}$ contained impurity phases of $Sr_3V_2O_7$ and $SrVO_3$. More recently,[185] the ruthenate, $Sr_4Ru_3O_{10}$ has been shown to exhibit ferromagnetism as part of ongoing investigations into the RP series $Sr_{n+1}Ru_nO_{3n+1}$.

Much of the recent work on n = 3 materials has been dominated by titanates and manganates, the former often as $Ln_2A_2Ti_3O_{10}$ cation exchange systems and the latter for their

potential CMR applications. Titanates, such as $La_2A_2Ti_3O_{10}$ (where A is an alkali metal cation), are the n=3 RP end members of solid solution series such as $La_2A_{2-x}Ti_{3-x}Nb_xO_{10}$, whilst the x=1 concentration $La_2ATi_2NbO_{10}$ containing Nb (V) belongs to the related Dion-Jacobson series[186]. Solid solutions such as these bridge the gap between Ruddlesden Popper and Dion-Jacobson compounds and are interesting in view of the changing interlayer chemistry (between the perovskite slabs) as a function of x[187]. The continuing interest in the phases $Ln_2A_2Ti_3O_{10}$ has been reaffirmed recently by detailed structural determinations of $La_2Na_2Ti_3O_{10}$ by Wright et. al.[188] and the preparation of single crystals of $Nd_2K_2Ti_3O_{10}$ by Amow et al.[189]. Lalena et al. have used a multistep, topotactic route[190] towards the phase $La_{1.93}Na_{1.12}Ca_{0.61}Ti_3O_{10}$, introducing mixed valence Ti onto the B-cation site and opening up the possibility of studying electron localisation effects in triple layered perovskites.

1.5 Extrinsic contributions to a CMR response

The two hallmarks of the predominantly intrinsic CMR response of single crystal manganites and high quality epitaxial thin films are a high MR observed at temperatures close to T_C, together with the requirement of fields of several Tesla in order to observe the 'colossal' effects. A separate, defect-mediated, '*extrinsic*' MR response is usually superimposed upon the intrinsic one; however, it is important to differentiate the effects, which have different origins and different field sensitivity. The current section outlines the origins of the extrinsic response and the models invoked to describe the role of defects.

The extrinsic MR contribution is observed typically over the temperature range $T < T_C$ and is often most pronounced at low magnetic fields, making it particularly attractive for device application. The term 'defect' in the context of the extrinsic MR response tends to describe microstructural 'discontinuities' such as dislocations or grain boundaries (GB). The micro*magnetic* structure then may be inhomogeneous *within* the grains, although it is often tied closely to the local structure. For example, in a study by Hwang et al.[191], magnetic domain boundaries were found to coincide with microstructural grain boundaries. This is expected since disruption to the local structure from the presence of grain boundaries, for instance, is

likely to interrupt the magnetic exchange pathways and cause local deviations from the value of T_C detected for the bulk sample. Thus, commonly, there are localised spatial variations of magnetisation. These spatial variations lead to changes in spin disorder that influence the resistivity through spin-dependent transport mechanisms. Evetts et al.[192] have reviewed how changes in magnetoresistance can result from changes in local magnetic order. The results emphasise the fact that x-ray and neutron diffraction measure 'average' parameters, such as Mn-O distances and O-Mn-O bond angles, and may mask a complex 'mesostructure' arising from disorder from various sources. In the same way, the mean magnetic moment averaged over a sample obtained from SQUID magnetometry studies may not reflect local spin disorder in a magnetically inhomogeneous system.

The most striking evidence for the extrinsic, low field MR contribution has come from systematic studies comparing magnetoresistance in polycrystalline, thin film and single crystal samples. In these studies the 'defects' are predominantly grain boundaries, present to the greatest extent in the polycrystalline samples. The study by Hwang et al.[191] and work by Gupta et al.[193] on samples with different characteristic grain sizes have identified a low field MR contribution as high as 20 - 30% at fields below 0.1T, ascribed to grain boundary MR. The variation of resistivity with field, at higher fields, was found to be linear with a slope almost independent of temperature, in the former study. Evetts et al.[192] have emphasised the qualitative nature of information obtained regarding the GBMR response in polycrystalline samples, where the MR behaviour is determined by a distribution of GB angles, each with different orientations to the applied field. Hence, they performed a study[194] elucidating the contribution of a single grain boundary introduced into an epitaxial film of $La_{0.7}Ca_{0.3}MnO_3$.

The origin of the GBMR response is understood most simply by considering that a strong magnetic field aligns the disordered spins in the grain boundary regions and reduces the resistance. However, experiments have identified two contributions to grain boundary magnetoresistance, one a low field (LFMR) and one a high field (HFMR) response. The low field response is due to a rotation of the magnetisation of individual grains, and the high field is responsible for the reduced polarisation of charge carriers at grain boundaries. The low field response has a characteristic hysteretic peak structure[194]. An interesting issue is the

'temperature dependence' of the LFMR contribution due to the granular nature of samples. At lower temperatures, the zero-field resistance of insulating grain boundary regions is higher. Thus, at low temperature, the effect of a strong magnetic field should be greater.

A LFMR response has also been observed in several 'magnetic tunnel junctions'. These are comprised of an insulating barrier material which is sandwiched between two layers of ferromagnetic material; for example, two layers of $La_{0.67}Sr_{0.33}MnO_3$ separated by an intermediate layer of insulating $SrTiO_3$. The potentially 'ideal' performance spin-tunnelling devices using manganites as the ferromagnetic component derives from the full spin polarisation (half-metallic) nature of these materials below their Curie temperature. This can be contrasted to the ≈ 25% net polarisation present in permalloy and ≈ 40% in nickel, cobalt and iron. The spin-polarised tunnelling of free carriers through an insulating barrier depends on the polarisation direction of the spin system on either side. For an 'ideal' performance device, the resistance should be independent of temperature and show a constant field dependence at high applied field. Spin-resolved spectroscopy experiments by Park et al.[27] have helped explain the decrease in levels of magnetoresistance that are observed typically in manganite tunnel devices as temperature is increased towards the Curie temperature. The experiments have revealed that the net polarisation of 3d sub-bands tends to zero as the Curie temperature is approached. It is suggested that the charge carriers lose their polarisation as they encounter disordered spins at interfaces[195]. This yields an interesting comparison with the role of interfaces in polycrystalline samples discussed above.

Finally, Fontcuberta[24] has pointed out that the significant dependence of LFMR on interfaces, and its rapid decay with rising temperature, are features typical of double exchange systems. Fontcuberta emphasises the interdependence of the itinerancy of the electrons and magnetic state of the material. In contrast, for manganese pyrochlores, ferromagnetism is not mediated by charge carriers but by superexchange pathways, and the low field MR response falls off less rapidly with temperature. LFMR will be discussed further in the context of magnetotransport data presented in Chapter 3.

1.6 References

[1] SN Ruddlesden, P Popper *Acta Cryst.* **1957**, *10*, 538.

[2] SN Ruddlesden, P Popper *Acta Cryst.* **1958**, *11*, 54.

[3] JH van Santen, GH Jonker *Physica* **1950**, *16*, 599.

[4] GH Jonker, JH van Santen *Physica* **1950**, *16*, 337.

[5] J Volger *Physica* **1954**, *20*, 49.

[6] AP Ramirez, RJ Cava, J Krajewski *Nature* **1997**, *386*, 156.

[7] CW Searle, S-T Wang *Can. J. Phys.* **1969**, *47*, 2703.

[8] CW Searle, S-T Wang *Can. J. Phys.* **1970**, *48*, 2023.

[9] AH Morrish, BJ Evans, JA Eaton, LK Leung *Can. J. Phys.* **1969**, *47*, 2691.

[10] LK Leung, AH Morrish, CW Searle *Can. J. Phys.* **1969**, *47*, 2697.

[11] M Lamire, A Daoudi *J. Solid State Chem.* **1984**, *55*, 327.

[12] MN Baibich, JM Broto, A Fert, F Nguyen Van Dau, F Petroff, P Eitenne, G Creuzet, A Friederich, J Chazelas *Phys. Rev. Lett.* **1988**, *61*, 2472.

[13] G Binasch, P Gruenberg, F Saurenbach, W Zinn *Phys. Rev. B* **1989**, *39*, 4828.

[14] RM Kusters, J Singleton, DA Keen, R McGreevy, W Hayes *Physica B* **1989**, *155*, 362.

[15] J Inoue, S Maekawa *Mat. Sci. and Eng.* **1995**, *B31*, 193.

[16] R von Helmholt, J Wecker, B Holzapfel, L Schultz, K Samwer *Phys. Rev. Lett.* **1993**, *71*, 2331.

[17] K Chahara, T Ohno, M Kasai, Y Kozono *Appl. Phys. Lett.* **1993**, *63*, 1990.

[18] S Jin, HM O'Bryan, TH Tiefel, M McCormack, WW Rhodes *Appl. Phys. Lett.* **1995**, *66*, 382.

[19] A Maignan, C Simon, V Caignaert, B Raveau *Solid State Commun.* **1995**, *96*, 623.

[20] T Venkatesan, M Rajeswari, Z-W Dong, SB Ogale, R Ramesh *Philos. Trans. R. Soc. London, Ser. A* **1998**, *356*, 1661.

[21] DJ Mapps *Sens. Actuators, A* **1997**, *A59*, 9.

[22] P Rodgers *New Scientist* **1996**, 34.

[23] B Dieny, VS Speriosu, S Metin, SSP Parkin, BA Gurney, P Baumgart, DR Wilhoit *J. Appl. Phys.* **1991**, *69*, 4774.

[24] J Fontcuberta *Phys. World* **1999**, *12*, 33.

[25] MC Robson, SB Ogale, R Godfrey, T Venkatesan, M Johnson, R Ramesh *Mater. Res. Soc. Symp. Proc.* **1998**, *494*, 243.

[26] JZ Sun, WJ Gallagher, PR Duncombe, L Krusin-Elbaum, RA Altman, A Gupta, Y Lu, GQ Gong, G Xiao *Appl. Phys. Lett.* **1996**, *69*, 3266.

[27] JH Park, E Vescovo, HJ Kim, C Kwon, R Ramesh, T Venkatesan *Phys. Rev. Lett.* **1998**, *81*, 1953.

[28] TG Perring, G Aeppli, T Kimura, Y Tokura, MA Adams *Phys. Rev. B.* **1998**, *58*, 14693.

[29] T Kimura, A Asamitsu, Y Tomioka, Y Tokura *Phys. Rev. Lett.* **1997**, *79*, 3720.

[30] KI Kobayashi, T Kimura, H Sawada, K Terakura, Y Tokura *Nature* **1998**, *395*, 677.
[31] RE Schmidt, J Pebler, D Babel *Eur. J. Solid State Inorg. Chem.* **1992**, *29*, 679.
[32] MA Subramanian, AP Ramirez, GH Kwei *Solid State Ionics* **1998**, *108*, 185.
[33] JS Kim, JY Lee, JS Swinnea, H Steinfink, WM Reiff, P Lightfoot, S Pei, JD Jorgensen *NIST Spec. Publ.* **1991**, *804*, 301.
[34] Goldschmidt *Mat.-Naturv. Kl.* **1926**, *2*, 117.
[35] RD Shannon, CT Prewitt *Acta Cryst. A* **1976**, *32*, 785.
[36] AM Glazer *Acta Crystallogr., Sect. B* **1972**, *28*, 3384.
[37] PG Radaelli, M Marezio, HY Hwang, SW Cheong *J. Solid State Chem.* **1996**, *122*, 444.
[38] A Daoudi, G Le Flem *J. Solid State Chem.* **1972**, *5*, 57.
[39] JF Ackerman *Mater. Res. Bull.* **1979**, *14*, 487.
[40] Y Moritomo, Y Tomioka, A Asamitsu, Y Tokura, Y Matsui *Phys. Rev. B* **1995**, *51*, 3297.
[41] Y Murakami, H Kawada, H Kawata, M Tanaka, T Arima, Y Moritomo, Y Tokura *Phys. Rev. Lett.* **1998**, *80*, 1932.
[42] A Maignan, C Martin, GV Tendeloo, M Hervieu, B Raveau *J. Mater. Chem.* **1998**, *8*, 2411.
[43] JB MacChesney, HJ Williams, JF Potter, RC Sherwood *Phys. Rev.* **1967**, *164*, 779.
[44] RAM Ram, P Ganguly, CNR Rao *J. Solid State Chem.* **1987**, *70*, 82.
[45] CNR Rao *Eur. J. Chem.* **1996**, *2*, 1499.
[46] ID Fawcett, JEIV Sunstrom, M Greenblatt, M Croft, KV Ramanujachary *Chem. Mater.* **1998**, *10*, 3643.
[47] JAM van Roosmalen, P van Vlaanderen, EHP Cordfunke, WL Ijdo, DJW Ijdo *J. Solid State Chem.* **1995**, *114*, 516.
[48] HA Jahn, E Teller *Proc. R. Soc.* **1937**, *A 161*, 220.
[49] HA Jahn *Proc. R. Soc.* **1938**, *A 164*, 117.
[50] NF Mott *Proc. Phys. Soc. Lond. A* **1949**, *62*, 416.
[51] J Zaanen, GA Sawatzky, JW Allen *Phys. Rev. Lett.* **1985**, *55*, 418.
[52] JMD Coey, M Viret *Adv. Phys.* **1999**, *48*, 167.
[53] A Chainani, M Mathew, DD Sarma *Phys. Rev. B* **1993**, *47*, 15397.
[54] JH Park, CT Chen, SW Cheong, W Bao, G Meigs, V Chakarian, YU Idzerda *Phys. Rev. Lett.* **1996**, *76*, 4215.
[55] HL Ju, HC Sohn, KM Krishnan *Phys. Rev. Lett.* **1997**, *79*, 3230.
[56] T Saitoh, AE Bocquet, T Mizokawa, H Namatame, A Fujimori, M Abbate, Y Takeda, M Takano *Phys. Rev. B* **1995**, *51*, 13942.
[57] T Arima, Y Tokura *J. Phys. Soc. Jpn.* **1995**, *64*, 2488.
[58] AE Bocquet, T Mizokawa, T Saitoh, H Namatame, A Fujimori *Phys. Rev. B* **1992**, *46*, 3771.
[59] JB Goodenough *Magnetism and the Chemical Bond*, Wiley: New York, **1963**.

[60] JB Goodenough *Progr. Solid State Chem.* **1971**, *5*, 145.
[61] OK Anderson, S Satpathy *Basic Prop. Binary Oxides, [Proc. Colloq.]* **1984**, 21.
[62] J Kanamori *J. Phys. Chem. Solids* **1959**, *10*, 87.
[63] J Kanamori, A Kotani *Core-Level Spectroscopy in Condensed Systems. [Proceedings of the 10th Taniguchi International Symposium, Kashikojima, Japan, October 19-23, 1987]*, Springer: Berlin, **1988**.
[64] JA Mydosh *Spin Glasses: An Experimental Introduction*, Taylor & Francis: London, **1993**.
[65] JM De Teresa, MR Ibarra, J Garcia, J Blasco, C Ritter, PA Algarabel, C Marquina, A del Moral *Phys. Rev. Lett.* **1996**, *76*, 3392.
[66] JB Goodenough, A Wold, RJ Arnott, N Menyuk *Phys. Rev.* **1961**, *124*, 373.
[67] LF Feiner, MO Andrzej *Phys. Rev. B* **1999**, *59*, 3295.
[68] D Feinberg, P Germain, M Grilli, G Seibold *Phys. Rev. B* **1998**, *57*, R5583.
[69] H Sawada, Y Morikawa, N Hamada, K Terakura *J. Magn. Magn. Mater.* **1998**, *177-181*, 879.
[70] I Solovyev, N Hamada, K Terakura *Phys. Rev. Lett.* **1996**, *76*, 4825.
[71] G Matsumoto *J. Phys. Soc. Jap.* **1970**, *29*, 606.
[72] I Dzyaloshinsky *J. Phys. Chem. Solids* **1958**, *4*, 241.
[73] T Moriya *Phys. Rev.* **1960**, *120*, 91.
[74] EO Wollan, WC Koehler *Physical Review* **1955**, *100*, 545.
[75] MF Sykes, JW Essam *Phys. Rev.* **1964**, *133*, A310.
[76] HL Frisch, JM Hammersley, DJA Welsh *Phys. Rev.* **1962**, *126*, 949.
[77] H Chiba, M Kikuchi, K Kusaba, Y Muraoka, Y Syono *Solid State Commun.* **1996**, *99*, 499.
[78] B Raveau, A Maignan, C Martin, M Hervieu *J. Supercond.* **1999**, *12*, 247.
[79] PG De Gennes *Phys. Rev.* **1960**, *118*, 141.
[80] C Zener *Phys. Rev.* **1951**, *82*, 403.
[81] AR Bishop, H Roder *Curr. Opin. Solid State Mater. Sci.* **1997**, *2*, 244.
[82] PW Anderson, H Hasegawa *Phys. Rev.* **1955**, *100*, 675.
[83] JB Goodenough *Aust. J. Phys.* **1999**, *52*, 155.
[84] AP Ramirez *J. Phys. Condens. Matter* **1997**, *9*, 8171.
[85] A Lanzara, NL Saini, M Brunelli, F Natali, A Bianconi, PG Radaelli *Z. Phys. B* **1997**, *104*, 699.
[86] CNR Rao *J. Mater. Chem.* **1999**, *9*, 1.
[87] P Schiffer, AP Ramirez, W Bao, S-W Cheong *Phys. Rev. Lett.* **1995**, *75*, 3336.
[88] A Urushibara, Y Moritomo, T Arima, A Asamitsu, G Kido, Y Tokura *Phys. Rev. B* **1995**, *51*, 14103.
[89] R Mahesh, R Mahendiran, AK Raychaudhuri, CNR Rao *J. Solid State Chem.* **1995**, *120*, 204.

[90] J Hejtmanek, Z Jirak, D Sedmidubsky, A Maignan, C Simon, V Caignaert, C Martin, B Raveau *Phys. Rev. B* **1996**, *54*, 11947.

[91] F Millange, A Maignan, V Caignaert, C Simon, B Raveau *Z. Phys. B* **1996**, *101*, 169.

[92] J Fontcuberta, B Martinez, A Seffar, S Pinol, JL Garcia-Munoz, X Obradors *Phys. Rev. Lett.* **1996**, *76*, 1122.

[93] F Damay, C Martin, A Maignan, B Raveau *J. Magn. Magn. Mater.* **1998**, *183*, 143.

[94] J Blasco, J Garcia, JM de Teresa, MR Ibarra, J Perez, PA Algarabel, C Marquina, C Ritter *Phys. Rev. B* **1997**, *55*, 8905.

[95] B Raveau, C Martin, A Maignan *J. Alloys Compd.* **1998**, *275-277*, 461.

[96] LM Rodriguez-Martinez, JP Attfield *Phys. Rev. B* **1996**, *54*, R15622.

[97] JR Sun, GH Rao, JK Liang *Appl. Phys. Lett.* **1997**, *70*, 1900.

[98] CNR Rao *Chem. Commun.* **1996**, 2217.

[99] NF Mott *Philos. Mag.* **1972**, *26*, 287.

[100] HY Hwang, SW Cheong, PG Radaelli, M Marezio, B Batlogg *Phys. Rev. Lett.* **1995**, *75*, 914.

[101] AJ Millis, PB Littlewood, BI Shraiman *Phys. Rev. Lett.* **1995**, *74*, 5144.

[102] AJ Millis, BI Shraiman, R Mueller *Phys. Rev. Lett.* **1996**, *77*, 175.

[103] PG Radaelli, M Marezio, HY Hwang, SW Cheong, B Batlogg *Phys. Rev. B* **1996**, *54*, 8992.

[104] JM De Teresa, MR Ibarra, PA Algarabel, C Ritter, C Marquina, J Blasco, J Garcia, A del Moral, Z Arnold *Nature* **1997**, *386*, 256.

[105] PA Cox *"Transition Metal Oxides: Introduction to their Electronic Structure and Properties"*, Oxford University Press: Oxford, **1995**.

[106] JL Garcia-Munoz, M Suaaidi, J Fontcuberta *Phys. Rev. B* **1997**, *55*, 34.

[107] H Roder, J Zang, AR Bishop *Phys. Rev. Lett.* **1996**, *76*, 1356.

[108] A Shengelaya, GM Zhao, H Keller, KA Mueller *Phys. Rev. Lett.* **1996**, *77*, 5296.

[109] GM Zhao, K Conder, H Keller, KA Mueller *Nature* **1996**, *381*, 676.

[110] A Moreo, S Yunoki, E Dagotto *Science* **1999**, *283*, 2034.

[111] S Mori, CH Chen, SW Cheong *Nature* **1998**, *392*, 473.

[112] PG Radaelli, G Iannone, DE Cox, M Marezio, HY Hwang, SW Cheong *Physica B* **1998**, *241-243*, 295.

[113] Y Tomioka, A Asamitsu, Y Moritomo, H Kuwahara, Y Tokura *Phys. Rev. Lett.* **1995**, *74*, 5108.

[114] PG Radaelli, DE Cox, M Marezio, SW Cheong *Phys. Rev. B* **1997**, *55*, 3015.

[115] M Uehara, S Mori, CH Chen, SW Cheong *Nature* **1999**, *399*, 560.

[116] V Laukhin, J Fontcuberta, JL Garcia-Munoz, X Obradors *Phys. Rev. B* **1997**, *56*, R10009.

[117] NF Mott, EA Davis *Electronic Processes in Non-crystalline Materials*, Clarendon: Oxford, **1979**.

[118] JMD Coey *Philos. Trans. R. Soc. London, Ser. A* **1998**, *356*, 1519.
[119] M Viret, L Ranno, JMD Coey *J. Appl. Phys.* **1997**, *81*, 4964.
[120] M Viret, L Ranno, JMD Coey *Phys. Rev. B* **1997**, *55*, 8067.
[121] RB Thompson, M Singh *Philos. Mag. B* **1999**, *79*, 63.
[122] Y Moritomo, A Asamitsu, H Kuwahara, Y Tokura *Nature* **1996**, *380*, 141.
[123] PD Battle, MJ Rosseinsky *Curr. Opin. Solid State Mater. Sci.* **1999**, *4*, 163.
[124] R Mahesh, R Mahendiran, AK Raychaudhuri, CNR Rao *J. Solid State Chem.* **1996**, *122*, 448.
[125] DN Argyriou, JF Mitchell, JB Goodenough, O Chmaissem, S Short, JD Jorgensen *Phys. Rev. Lett.* **1997**, *78*, 1568.
[126] JF Mitchell, DN Argyriou, CD Potter, JD Jorgensen, DG Hinks, SD Bader *Phys. Rev. B* **1997**, *55*, 63.
[127] PD Battle, SJ Blundell, MA Green, W Hayes, M Honold, AK Klehe, NS Laskey, JE Millburn, LE Murphy, et al. *J. Phys. Condens. Matter* **1996**, *8*, L427.
[128] R Seshadri, C Martin, M Hervieu, B Raveau *Chem. Mater.* **1997**, *9*, 270.
[129] JQ Li, Y Matsui, T Kimura, Y Tokura *Phys. Rev. B* **1998**, *57*, R3205.
[130] T Kimura, R Kumai, Y Tokura, JQ Li, Y Matsui *Phys. Rev. B* **1998**, *58*, 11081.
[131] R Seshadri, A Maignan, M Hervieu, N Nguyen, B Raveau *Solid State Commun.* **1997**, *101*, 453.
[132] T Hayashi, N Miura, M Tokunaga, T Kimura, Y Tokura *J. Phys. Condens. Matter* **1998**, *10*, 11525.
[133] DN Argyriou, JF Mitchell, JD Jorgensen, JB Goodenough, PG Radaelli, DE Cox, HN Bordallo *Aust. J. Phys.* **1999**, *52*, 279.
[134] DN Argyriou, JF Mitchell, PG Radaelli, HN Bordallo, DE Cox, M Medarde, JD Jorgensen *Phys. Rev. B* **1999**, *59*, 8695.
[135] Y Liu, L Sheng, DY Xing, J Dong *J. Phys. Condens. Matter* **1998**, *10*, 9747.
[136] Y Moritomo, M Itoh *Phys. Rev. B.* **1999**, *59*, 8789.
[137] D Louca, GH Kwei, JF Mitchell *Phys. Rev. Lett.* **1998**, *80*, 3811.
[138] PD Battle, DE Cox, MA Green, JE Millburn, LE Spring, PG Radaelli, MJ Rosseinsky, JF Vente *Chem. Mater.* **1997**, *9*, 1042.
[139] J Zhang, F Wang, P Zhang, X Sun, Q Yan *J. Magn. Magn. Mater.* **1998**, *190*, 166.
[140] B Garcia-Landa, MR Ibarra *Phys. Rev. B* **1999**, *60*, 5440.
[141] G Balakrishnan, MR Lees, DM Paul *J. Phys.: Condens. Matter* **1997**, *9*, L471.
[142] PD Battle, J Hepburn, JE Millburn, PG Radaelli, MJ Rosseinsky, LE Spring, JF Vente *Chem. Mater.* **1997**, *9*, 3215.
[143] PD Battle, MA Green, NS Laskey, JE Millburn, PG Radaelli, MJ Rosseinsky, SP Sullivan, JF Vente *Phys. Rev. B* **1996**, *54*, 15967.
[144] Y Moritomo, Y Maruyama, T Akimoto, A Nakamura *Phys. Rev. B* **1997**, *56*, R7057.
[145] J Zhang, F Wang, P Zhang, Q Yan *J. Phys. Condens. Matter* **1999**, *11*, 2413.

[146] J Zhang, F Wang, P Zhang, Q Yan *Solid State Commun.* **1999**, *109*, 401.

[147] Y Moritomo, A Nakamura, K Ohoyama, M Ohashi, K Hirota *J. Phys. Soc. Jpn.* **1999**, *68*, 631.

[148] Y Moritomo, Y Maruyama, T Akimoto, A Nakamura *J. Phys. Soc. Jpn.* **1998**, *67*, 405.

[149] PD Battle, N Kasmir, JE Millburn, MJ Rosseinsky, RT Patel, LE Spring, JF Vente, SJ Blundell, W Hayes, AK Klehe, A Mihut, J Singleton *J. Appl. Phys.* **1998**, *83*, 6379.

[150] PD Battle, MA Green, NS Laskey, N Kasmir, JE Millburn, LE Spring, SP Sullivan, MJ Rosseinsky, JF Vente *J. Mater. Chem.* **1997**, *7*, 977.

[151] PD Battle, MA Green, NS Laskey, JE Millburn, LE Murphy, MJ Rosseinsky, SP Sullivan, JF Vente *Chem. Mater.* **1997**, *9*, 552.

[152] AI Coldea, LE Spring, SJ Blundell, J Singleton, W Hayes *J. Phys. Condens. Matter,* **1999**, *11*, 9053.

[153] R Seshadri, C Martin, A Maignan, M Hervieu, B Raveau, CNR Rao *J. Mater. Chem.* **1996**, *6*, 1585.

[154] NH Hur *Phys. Rev. B* **1998**, *57*, 10740.

[155] M Takemoto, A Katada, H Ikawa *Solid State Commun.* **1999**, *109*, 693.

[156] K Wang, W Song, T Yu, B Zhao, M Pu, Y Sun *Phys. Status Solidi A* **1999**, *171*, 577.

[157] H Asano, J Hayakawa, M Matsui *Phys. Rev. B* **1997**, *56*, 5395.

[158] H Asano, J Hayakawa, M Matsui *Appl. Phys. Lett.* **1997**, *71*, 2303.

[159] H Asano, J Hayakawa, M Matsui *Appl. Phys. Lett.* **1996**, *68*, 3638.

[160] KV Kamenev, MR Lees, G Balakrishnan, DM Paul *Phys. Rev. B* **1997**, *56*, R12688.

[161] P Raychundhuri, C Mitra, A Paramekanti, R Pinto, AK Nigam, SK Dhar *J. Phys. Condens. Matter* **1998**, *10*, L191.

[162] Y Moritomo, A Asamitsu, H Kuwahara, Y Tokura *Nature* **1996**, *380*, 141.

[163] R Mahesh, R Wang, M Itoh *Phys. Rev. B* **1998**, *57*, 104.

[164] CF Chang, PH Chou, HL Tsay, SS Weng, S Chatterjee, HD Yang, RS Liu, CH Shen, WH Li *Phys. Rev. B* **1998**, *58*, 12224.

[165] JF Mitchell, JE Millburn, M Medarde, S Short, JD Jorgensen, MT Fernandez-Diaz *J. Solid State Chem.* **1998**, *141*, 599.

[166] DS Dessau, T Saitoh, CH Park, ZX Shen, P Villella, N Hamada, Y Moritomo, Y Tokura *Phys. Rev. Lett.* **1998**, *81*, 192.

[167] TG Perring, G Aeppli, Y Moritomo, Y Tokura *Phys. Rev. Lett.* **1997**, *78*, 3197.

[168] R Osborn, S Rosenkranz, DN Argyriou, L Vasiliu-Doloc, JW Lynn, SK Sinha, JF Mitchell, KE Gray, SD Bader *Phys. Rev. Lett.* **1998**, *81*, 3964.

[169] T Chatterji, P Thalmeier, GJ Mcintyre, R Van de Kamp, R Suryanarayanan, G Dhalenne, A Revcolevschi *Europhys. Lett.* **1999**, *46*, 801.

[170] K Hirota, Y Moritomo, H Fujioka, M Kubota, H Yoshizawa, Y Endoh *J. Phys. Soc. Jpn.***1998**, *67*, 3380.

[171] H Nakatsugawa, E Iguchi, WH Jung, F Munakata *Aust. J. Phys.* **1999**, *52*, 187.

[172] DB Romero, VB Podobedov, A Weber, JP Rice, JF Mitchell, RP Sharma, HD Drew *Phys. Rev. B* **1998**, *58*, R14737.

[173] O Chauvet, G Goglio, P Molinie, B Corraze, L Brohan *Phys. Rev. Lett.* **1998**, *81*, 1102.

[174] P Laffez, G Van Tendeloo, R Seshadri, M Hervieu, C Martin, A Maignan, B Raveau *J. Appl. Phys.* **1996**, *80*, 5850.

[175] CD Potter, M Swiatek, SD Bader, DN Argyriou, JF Mitchell, DJ Miller, DG Hinks, JD Jorgensen *Phys. Rev. B* **1998**, *57*, 72.

[176] R Seshadri, M Hervieu, C Martin, A Maignan, B Domenges, B Raveau, AN Fitch *Chem. Mater.* **1997**, *9*, 1778.

[177] JB MacChesney, JF Potter, RC Sherwood *J. Appl. Phys.* **1969**, *40*, 1243.

[178] C Brisi, P Rolando *Ann. Chim.* **1969**, *59*, 385.

[179] IB Sharma, D Singh *Indian J. Chem., Sect. A.* **1995**, *34A*, 630.

[180] C Brisi, M Vallino, F Abbattista *J. Less-Common Met.* **1981**, *79*, 215.

[181] OH Hansteen, H Fjellvag, BC Hauback *Chem. Pap.* **1998**, *52*, 7.

[182] WT Fu, RB Helmholdt *Mater. Res. Bull.* **1992**, *27*, 1371.

[183] K Mader, H Mueller-Buschbaum *J. Less-Common Met.* **1990**, *157*, 71.

[184] A Nozaki, H Yoshikawa, T Wada, H Yamauchi, S Tanaka *Phys. Rev. B* **1991**, *43*, 181.

[185] G Cao, SK McCall, JE Crow, RP Guertin *Phys. Rev. B* **1997**, *56*, R5740.

[186] M Dion, M Ganne, M Tournoux *Mater. Res. Bull.* **1981**, *16*, 1429.

[187] S Uma, AR Raju, J Gopalakrishnan *J. Mater. Chem.* **1993**, *3*, 709.

[188] AJ Wright, C Greaves *J. Mater. Chem.* **1996**, *6*, 1823.

[189] G Amow, JE Greedan *Acta Crystallogr., Sect. C: Cryst. Struct. Commun.* **1998**, *C54*, 1053.

[190] JN Lalena, BL Cushing, AU Falster, WB Simmons, Jr., CT Seip, EE Carpenter, CJ O'Connor, JB Wiley *Inorg. Chem.* **1998**, *37*, 4484.

[191] HY Hwang, SW Cheong, NP Ong, B Batlogg *Phys. Rev. Lett.* **1996**, *77*, 2041.

[192] JE Evetts, MG Blamire, ND Mathur, SP Isaac, BS Teo, LF Cohen, JL Macmanus-Driscoll *Philos. Trans. R. Soc. London, Ser. A* **1998**, *356*, 1593.

[193] A Gupta, GQ Gong, G Xiao, PR Duncombe, P Lecooeur, P Trouilloud, YY Wang, VP Dravid, JZ Sun *Phys. Rev. B* **1996**, *54*, R15629.

[194] ND Mathur, G Burnell, SP Isaac, TJ Jackson, BS Teo, JL MacManus-Driscoll, LF Cohen, JE Evetts, MG Blamire *Nature* **1997**, *387*, 266.

[195] M Ziese *Phys. Rev. B* **1999**, *60*, R738.

CHAPTER 2

EXPERIMENTAL TECHNIQUES

2.1 Synthesis by a Ceramic Route

The ceramic route was the most common route employed in preparing the polycrystalline solids described in this thesis. It involved heating a mixture of solid starting materials to temperatures between 1000°C and 1500°C in order for them to react together at a useful rate.

Stoichiometric quantities of high purity, powdered starting materials (generally oxides of rare earth and transition metal elements and carbonates of alkaline earth elements) were ground together thoroughly in a pestle and mortar. The rare earth oxides were dried at 800°C for at least six hours prior to mixing with other reagents. When the mixture consisted of a fine powder of uniform colour (usually brownish-grey), it was fired for 24 hours in an alumina crucible at 800°C to effect decarbonation.

Following decarbonation the mixture was pressed into pellets before firing at higher temperatures. Complete firing sequences and reaction times specific to particular compounds are tabulated in Chapters 3 to 5, inclusive. The heating and cooling rates between different firing temperatures were maintained at 5° /min, unless stated otherwise, and crucibles were removed directly from the furnace for reaction temperatures up to and including 1200°C. For reaction temperatures above 1200°C, the furnace was cooled at 5°/min to 1200°C and then the crucibles removed. Reactions were considered to be complete when laboratory powder X-ray diffraction patterns showed no change after successive firings under the same conditions.

In Chapter 4, Section 4.3.1, a solution-gelation-calcination route based on the Pechini[1] citrate gel process was attempted, and this synthetic route is described in detail in the relevant Section.

2.2 Powder Diffraction

Three types of radiation are used commonly in diffraction experiments on crystalline solids. These are X-rays, neutrons and electrons, all of which may have wavelengths of the order of interatomic separations. X-rays are intermediate in energy between the ultra-violet and γ -ray regions of the electromagnetic spectrum, with wavelengths of ~1Å, and may be generated in the laboratory by the bombardment of a metal target by high energy electrons.

The wave nature of neutrons and electrons is described by the following de Broglie relation, which defines a corresponding wavelength from the momentum, p , of a free particle:

$$\lambda = \frac{h}{p} = \frac{h}{mv} = \frac{h}{(2m\xi)^{1/2}} \qquad \text{eqn. (2.2.1)}$$

Here, m, v and ξ are the mass, velocity and energy of the particle, respectively. For high energy neutrons produced as a byproduct of nuclear reactions, where the 'moderator' is operated at room temperature, equation 2.2.1 gives a distribution of neutron wavelengths, including that at ~1.5Å used in the current work. The work described in this thesis, is concerned primarily with the complementary techniques of X-ray and neutron powder diffraction, which are discussed in more detail in Sections 2.3 and 2.4, respectively.

2.3 Powder X-Ray Diffraction

2.3.1 Production of X-rays and instrumentation used

2.3.1.1 Laboratory Siemens D5000 diffractometer

The Siemens D5000 diffractometer was used for collecting data for full structural refinement, often to ascertain sample quality prior to powder neutron diffraction or synchrotron X-ray diffraction measurements. Samples were sprinkled onto a silicon wafer containing a thin layer of Dow-Corning high vacuum grease and the sample holder rotated at 15rpm about an axis normal to the sample plane. Typically, data were collected over $5 \leq 2\theta/^{\circ} \leq 110$ with a step size of 0.02° and a counting time of 15 seconds per step. The D5000 utilises Bragg-Brentano or 'symmetrical' focusing geometry, and a Ge monochromator is used to remove the weaker $K\alpha_2$ and any $K\beta$ lines plus background radiation. This leaves $K\alpha_1$ radiation incident on the sample with wavelength 1.5406 Å.

2.3.1.2 Laboratory Philips PW1710 diffractometer

This diffractometer uses a PW 1729 generator and, operating in reflection geometry, was ideal for regular monitoring of the progress of sample preparations. Well-ground samples were mounted on flat aluminium plates and the surface of the powder was compacted using a

glass slide. Scans lasting 30 minutes, typically over $5 \leq 2\theta/^{\circ} \leq 70$ use continous scanning at a speed of 0.05° 2θ / s^{-1}. As with the Siemens laboratory diffractometer, electrons strike a Cu target, with a tube current of 30mA and an accelarating voltage of 40kV and the machine operates in Bragg Brentano geometry. Unlike the Siemens instrument, there is no monochromator removing the $K\alpha_2$ radiation; nevertheless, the added beam intensity as a result makes the Philips a good instrument for detecting, for example, minor traces of impurities from an overnight scan. However, the increased instrumental contribution to the diffraction profile, limits the information that can be gained from the refinement of peak shape functions.

2.3.1.3 Station 2.3 at the Synchrotron Radiation Source, Daresbury, UK

The synchrotron radiation source at Daresbury was the first in the world to be dedicated to the production and use of synchrotron radiation. It consists[2] of a linear accelerator (an 'electron gun'), a booster synchrotron and a storage ring. Electrons with energies of 2GeV are fired from the linear accelerator into the booster synchrotron, where they are accelerated to speeds approaching that of light. Then they are injected into the storage ring (an evacuated tube with a 96m circumference) where a series of magnets is used to deflect their paths. Thus, the electrons are subject to centripetal acceleration and emit electromagnetic radiation with an intensity several orders of magnitude higher than the output from conventional X-ray tubes. This synchrotron radiation is characterised by a continuous spectral distribution, a pulsed time-structure and a high degree of polarisation. The beams of synchrotron radiation are in the form of a cone in front of the electrons and are produced at each of the sixteen bending magnets and three insertion devices in the storage ring.

Station 2.3 is situated 15m tangentially from a pair of 1.2T dipole magnets where X-ray wavelengths of 0.5-3.0Å are available. The polychromatic beam, which is well collimated intrinsically (less than ~1mrad vertical divergence), is incident upon the Si (111) monochromator and the wavelength resolution is defined by the Darwin width of the crystal, which is $\Delta\lambda/\lambda = 1.7 \times 10^{-4}$. The station has a two circle diffractometer (the sample ω or θ axis with 0.2mdeg resolution and a detector 2θ axis with 0.1mdeg resolution), parallel foils, single slits assembly and motorised goniometer, and is shown schematically below.

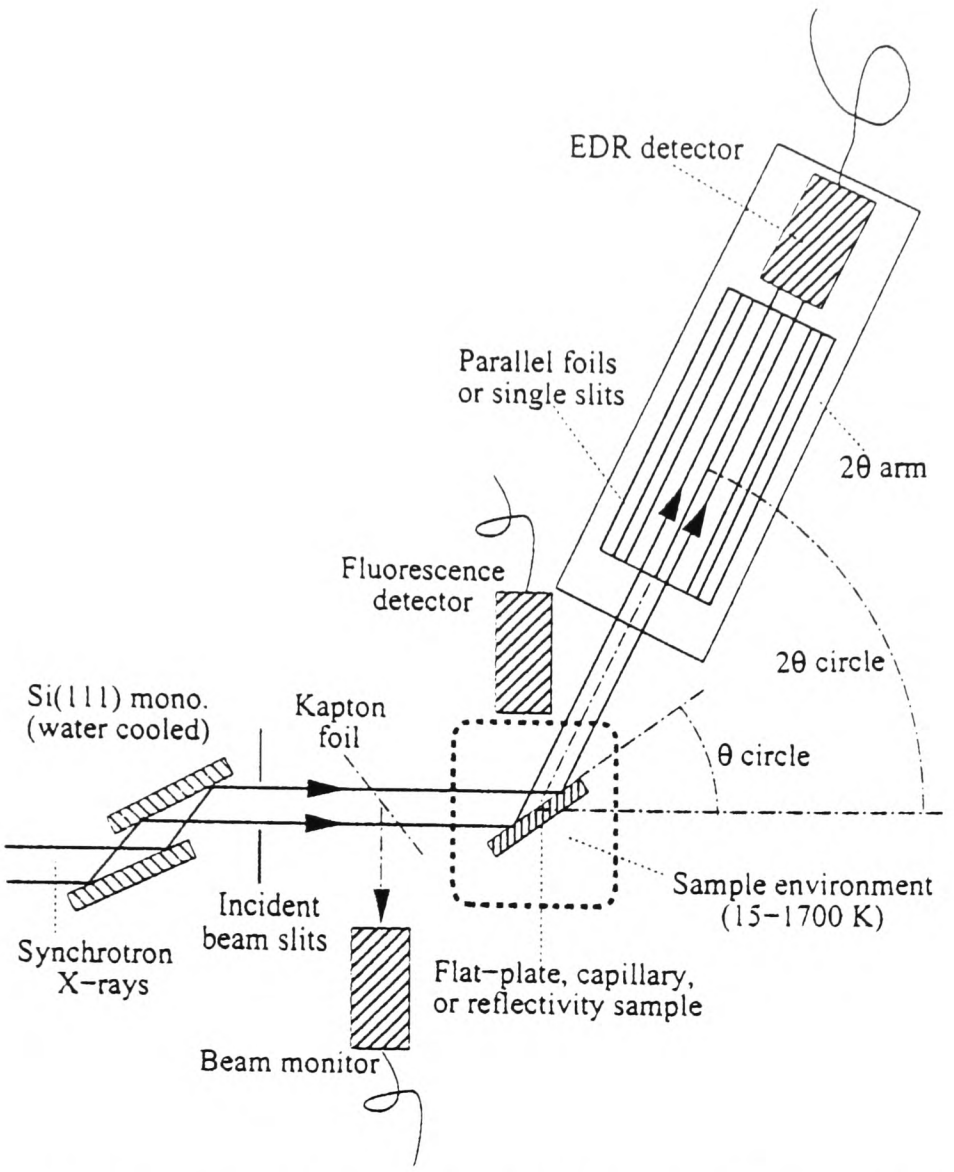


Figure 2.3.1 Schematic diagram of Station 2.3, SRS, Daresbury. (Figure reproduced from reference[2]).

The instrument is intended primarily for high resolution angular dispersive powder diffraction measurements and reflectivity studies. However, the tunability of the wavelength and the possibility of mounting a fluorescence detector 90° above the sample makes it ideal for using anomalous dispersion to solve difficult structural problems. This application is discussed in more detail in Section 2.3.3. For the flat plate powder experiments carried out in this work, the sample was sprinkled onto a silicon sample holder spread with a thin layer of vacuum grease. Then the disc-shaped sample holder was slipped into the spinner mounted on the ω-circle.

2.3.2 The intensity of reflections in a diffraction pattern

The Laue equations and Bragg's law[3] were developed using the assumption that identical atoms of unspecified scattering power were situated at each lattice point. In order to determine the total scattering amplitude of a structure (and hence the intensity of 'reflections' in a diffraction pattern), a series of summations must be made over all the constituent electrons comprising all of the atoms in the crystal or powder. The resulting 'structure factor' (F_{hkl}) (equation 2.3.1) represents the particular combination of amplitude and phase of x-radiation scattered by one unit cell in any direction in which there is a diffraction maximum.

$$F(hkl) = \sum_j f_j \exp(2\pi i(hx_j + ky_j + lz_j)) \qquad \text{eqn. (2.3.1)}$$

Here, |F(hkl)| is the amplitude of the scattered wave, and the phase of the wave scattered in the direction of the reciprocal lattice point (hkl) by an atom situated at the point (xyz) is $2\pi(hx + ky + lz)$ radians, relative to the phase of the wave scattered in the same direction by an atom at the origin.

The intensity of a diffracted beam, I, corresponding to the diffraction maximum hkl is proportional to $|F|^2$, or F(hkl) multiplied by its complex conjugate, $F^*(hkl)$, since complex notation is used. It can be shown that $F(hkl) = F^*(\overline{hkl})$ and $F^*(hkl) = F(\overline{hkl})$, hence $I(hkl) = I(\overline{hkl})$, which is itself a statement of Friedel's law[4]. Additional geometric factors and absorption corrections must be incorporated to give a complete description of the intensity of a reflection. The geometric correction, (Lp), is a combination of Lorentz and polarisation terms, and is a function of 2θ. The absorption correction is denoted (Abs) so that a general expression for Intensity, I, is:

$$I = K\,|F|^2\,(Lp)\,(Abs) \qquad \text{eqn. (2.3.2)}$$

where K is a scale factor. A further contribution to |F| is the effect from thermal vibrations of the atoms comprising the unit cell. The reduction in intensity from vibrational motion is approximated by an exponential function that has a large effect at high 2θ values. If the vibrations are nearly isotropic, the exponential factor can be written as follows:

$$\exp(-2 B_{iso} \sin^2\theta / \lambda^2) \qquad \text{eqn. (2.3.3)}$$

where B_{iso} (the temperature factor) = $8\pi^2 \langle u^2 \rangle$ and $\langle u^2 \rangle$ is the mean square amplitude of displacement of an atom from its equilibrium position. Static displacements which vary randomly from one unit cell to another may simulate vibration. Incorporating the effects of atomic vibrations gives the final expression for the corrected Intensity, I_{corr}:

$$I_{corr} = I / (Abs)(Lp) = K |F|^2 = K |F_{novib}|^2 \exp(-2 B_{iso} \sin^2\theta / \lambda^2) \qquad \text{eqn. (2.3.4)}$$

where F_{novib} is the value of F for a structure comprised of nonvibrating atoms. If the vibrations of the atoms are anisotropic, the thermal factor is described as follows:

$$\exp\left(-\frac{1}{4}\{B_{11}h^2a^{*2} + B_{22}k^2b^{*2} + B_{33}l^2c^{*2} + 2B_{12}hka^*b^* + 2B_{13}hla^*c^* + 2B_{23}klb^*c^*\}\right) \qquad \text{eqn. (2.3.5)}$$

where Bij describe a biaxial thermal ellipsoid (the components Uij of which may be refined).

2.3.3 The use of anomalous dispersion (or anomalous scattering) in X-ray diffraction

If the frequency of the incident X-ray beam is near to some of the natural frequencies of oscillation of electrons bound to the nucleus (these frequencies depend upon the atomic field strength and on the quantum state of the electron), the scattering under these conditions is called anomalous[5]. The phenomenon manifests itself by an advance of the phase of anomalously scattered radiation relative to normally scattered radiation, with the consequent modification of the atomic scattering factor, f, for the anomalous scatterer[6]. This modification is expressed as follows:

$$f \rightarrow |f| \exp(i\delta) \qquad \text{eqn. (2.3.6)}$$

where δ is the phase relative to normal scattering.

It is usual to write the modified anomalous scattering factor as follows:

$$f = f_a + \Delta f' + if'' = f' + if'' \qquad \text{eqn. (2.3.7)}$$

$\Delta f'$ and f'' are called the real and the imaginary dispersion corrections, respectively. An important issue is whether $\Delta f'$ and f'' vary as a function of 2θ. Since anomalous scattering is due to the interaction of the more tightly bound electrons of the atom with the incident radiation, the phase differences between the waves scattered by such a small volume will not be strongly dependent on scattering angle. Existing theoretical arguments suggest they are only slightly dependent upon 2θ and for the current work, the dependence of $\Delta f'$ and f'' upon energy (wavelength) will be the only concern.

While the imaginary term, f'', is always positive[5], the real term, $\Delta f'$, is negative when $\omega < \omega_0$ and positive when $\omega > \omega_0$ (where ω_0 corresponds to the frequency of a photon with just sufficient energy to eject the electron from the atom). This energy corresponds in turn to the wavelength $\lambda_0 = 2\pi c/\omega_0$, representing the absorption edge for the particular anomalous scatterer in the sample. The advantage of using synchrotron radiation is now evident, since its continuous, intense spectrum can be tuned with high precision to select a wavelength where maximum anomalous scattering is observed.

In terms of the use of anomalous scattering as a diagnostic tool, it manifests itself, through the corrections to f_a, as the cause of differences in the intensities of reflections in diffraction patterns. Specifically, it leads to a breakdown of Friedel's law for non-centrosymmetric structures, which, as described in Section 2.3.2, states that the intensity of the reflection I_{hkl} from the hkl planes is equal to the intensity of the reflection on the opposite side of the direct beam from the $\overline{hkl}$ planes, i.e $I_{\overline{hkl}}$. Appendix 1 considers in detail the effects of anomalous scattering on the structure factor, where the difference in intensities may be rationalised as a result of the complex nature of the scattering factor for the anomalous scatterer.

The most common areas of application of anomalous dispersion are twofold. Firstly, the technique provides diffraction contrast between elements which are near-neighbours in the periodic table, thereby allowing refinement of their fractional occupancies across shared crystallographic sites[7-14]. Secondly, there is often a need to distinguish between different valence states of the same cations[9,12,15] (for example, in charge ordering studies[16]) where, again, conventional X-ray diffraction does not offer adequate discrimination.

Therefore, the success of an experimental study using anomalous dispersion relies largely on the accurate determination of the values for the real and imaginary dispersion corrections for one of the elements requiring a source of diffraction contrast with another. Once these values of $\Delta f'$ and f'' have been established, and fixed in the structural model, the diffraction contrast is achieved and refinement of the parameter(s) of interest, such as a particular distribution of cations over shared sites, can begin. Wilkinson[15] has demonstrated the relative insensitivity of diffraction data to variations in f'', in contrast to the sensitivity towards $\Delta f'$[9] and this point is considered in more detail in Appendix 1.

The following discussion deals with both the shape of the functions f' and f'' and the means of determining their values at a particular energy. The intrinsic shape of functions $f'(E)$ and $f''(E)$ (where $f' = f_a + \Delta f'$ and the $f'(E)$ and $f''(E)$ notation simply reiterates the dependence of these quantities upon energy) is determined by the energies of the available final states, the probability of a transition to these states, and the lifetime of the core hole state and the outgoing photoelectron. However, the instrumental 'band pass' is also a determining factor[17,18].

In any wavelength determination, the band pass, $\Delta\lambda/\lambda$, of the monochromator is important since it controls the resolution achievable. At station 2.3, the monochromator consists of a channel-cut Si (111), which is a monolithic, double-bounce, single crystal.
The band pass[19] is given by:

$$\frac{\Delta\lambda}{\lambda} = \frac{\Delta E}{E} = [(\Delta\phi \cot\theta_B)^2 + (\Delta d/d)^2]^{1/2} \qquad \text{eqn. (2.3.8)}$$

where $\Delta\phi$ is the angular beam divergence in the scattering plane, θ_B is the monochromator Bragg angle and $\Delta d/d$ is the contribution to the divergence from the monochromator crystal. This contribution is related to the Darwin width (ω_D) for a perfect crystal by the following equation:

$$\frac{\Delta d}{d} = \omega_D \cot\theta \qquad \text{eqn. (2.3.9)}$$

and results in a wavelength resolution, $\Delta\lambda/\lambda$, of 1.7×10^{-4} for the Si (111) monochromator at station 2.3.

The energy stability of the incident X-ray beam is also an important factor in any anomalous scattering experiment. Two main sources of instability are orbit changes in the storage ring and heat loading effects on the X-ray optics. To achieve thermal stability on station 2.3, the monochromator is maintained constantly at 30.0±0.1°C using a closed circuit water bath. To counter effects of orbit instability, extra optical elements are in place which help decouple beam instability and wavelength variation.

Finally, the divergence of the scattered beam should be controlled also *via* appropriate combinations of slit system and detector. On station 2.3 the short vertical parallel foils (VPF) setup is used to reduce axial beam divergence and the incident and diffracted intensity is recorded by Harshaw scintillation counters and the enhanced dynamic range (EDR) detector.

A common technique for obtaining values for f '(E) and f "(E) is to calculate f "(E) from X-ray absorption data (using the optical theorem) and then to use the Kramers-Kronig dispersion relation[20] to obtain f '(E) from the value of f "(E)[21]. It is estimated that this method is accurate to within ± 0.2 or ± 0.3 electrons, however, it is also somewhat restrictive. This is because using the Kramers-Kronig relation involves integrating f "(E) from zero to infinity and to do this 'Cromer-Liberman' values are needed to extrapolate f "(E) to these limits. However, Cromer-Liberman[22,23] values are not available for ionic species, (only neutral atoms) and, when they are available, they are not quite accurate enough close to the edge.

Therefore, since the functions are clearly so compound-specific, (cation oxidation state and coordination environment are particularly important), by far the most ideal method for determining f '(E) and f "(E) is by accurate selection of the incident beam energy relative to the absorption edge position of the cation of interest in a 'standard' compound. This is followed then by collection of a diffraction dataset at this appropriate energy (wavelength) for both the standard *and* the sample of interest.

The correct selection of incident beam energy relative to the edge typically means selecting the low energy (high λ) side of the absorption edge for the cation of interest in order

to circumvent possible problems with absorption and fluorescence. Then, refinement of the dataset, using, for example, the GSAS Rietveld[24] code, allows the dispersion corrections to be fitted just like any other variable. These values refined for the standard are then included in an X-ray dataset (or ideally a combined neutron/X-ray dataset) from the sample and the physical quantity of interest, such as cation distributions, is itself refined. As is shown in Appendix 1, equation 1.12, diffraction data is insensitive towards variations in f " relative to the sensitivity towards $\Delta f'$. This effect was utilised in a refinement described in detail in Chapter 4. In this refinement the value of f " for Mn^{4+} was held constant at the value calculated by the programme 'FPRIME' within the GSAS[25] software package. The programme 'FPRIME' is a modified version of that written by D.T.Cromer[26] which calculates the X-ray anomalous dispersion coefficients for a particular energy. In contrast, the value of $\Delta f'$ was refined, giving a significant correction to f_{Mn4+} to yield a value of f ' ($f' = f_{Mn4+} + \Delta f'$) which provided diffraction contrast between Mn^{4+} and another tetravalent transition metal cation.

2.4 Powder Neutron Diffraction

As was shown in Section 2.2, the quantum-mechanical wave representation of neutrons is implied by the de Broglie relation (equation 2.2.1). However, it was not until 1936[27,28] that neutrons were shown to undergo diffraction from crystalline solids, as a result of the relatively recent discovery of these neutral particles. Since their discovery, neutrons have been shown to have significant advantages over X-rays in the characterisation of crystalline materials, although the fundamental drawback involving their use is, of course, their production. This either requires a nuclear reactor, such as the uranium-fuelled reactors at the Institut Laue Langevin, Grenoble or a spallation source such as ISIS, UK.

The properties which confer advantages upon the use of neutrons over X-rays arise due to the different scattering mechanism operating when neutrons, rather than X-rays, are incident on a sample. Rather than interacting with the electrons surrounding the nuclei by way of the electromagnetic force, neutrons interact by way of the strong nuclear force with the nuclei themselves. The scattering process may be regarded, in part, as the momentary capture

of the incoming neutron by the nucleus, followed by re-emission. Rather than using an atomic form factor, the neutron-nucleus interaction is described instead by a scattering length, b, (measured in femtometres, 10^{-15}m). In terms of the formulation of the structure factor equation for neutron diffraction , b would replace 'f ', by analogy with equation 2.3.1. The scattering length b is a complex variable, the real part representing elastic scattering while the imaginary part corresponds to absorption. The scattering cross section (the proportion of neutrons scattered in unit time for unit incident flux), σ_s, is proportional to the real part of the scattering length as shown:

$$\sigma_s = 4\pi b^2 \qquad \text{eqn. (2.4.1)}$$

Two further factors on which the real part of the scattering length is dependent (resulting directly from the nature of the interaction *via* the nuclear force), are the spin state of the nucleus, and the particular isotope responsible for the scattering. If an elemental constituent of a sample consists of a number of different isotopes each with a distinctive scattering length, then the coherent scattering is proportional to the average scattering length, $\bar{b}$, and the coherent cross section, σ_c , becomes $4\pi|\bar{b}|^2$. Nuclei with $I > 0$, also give rise to a range of scattering lengths, one for each of the $(2I + 1)$ nuclear spin states. Such deviations from the average scattering length tend not to be distributed in an ordered fashion, therefore cannot give rise to constructive interference and are responsible for incoherent scattering. Incoherent scattering contributes to the background scattering in most cases.

These sources of incoherent scattering have no parallel in X-ray diffraction. Points (i) to (vii) list some further differences between the two techniques, most of which favour neutron diffraction as the most comprehensive method for characterising solids (particularly oxides):

(i) The neutron scattering factor does not vary in a systematic way with atomic number unlike the X-ray form factor. Heavy atoms do not dominate a diffraction pattern (as for X-rays) and this increases the precision with which lighter elements such as oxygen are located in the structure. In particular, metal - oxygen bondlengths can be determined accurately.

Figure 2.4.1[29] shows the relationship between scattering amplitude and atomic weight for a number of elements.

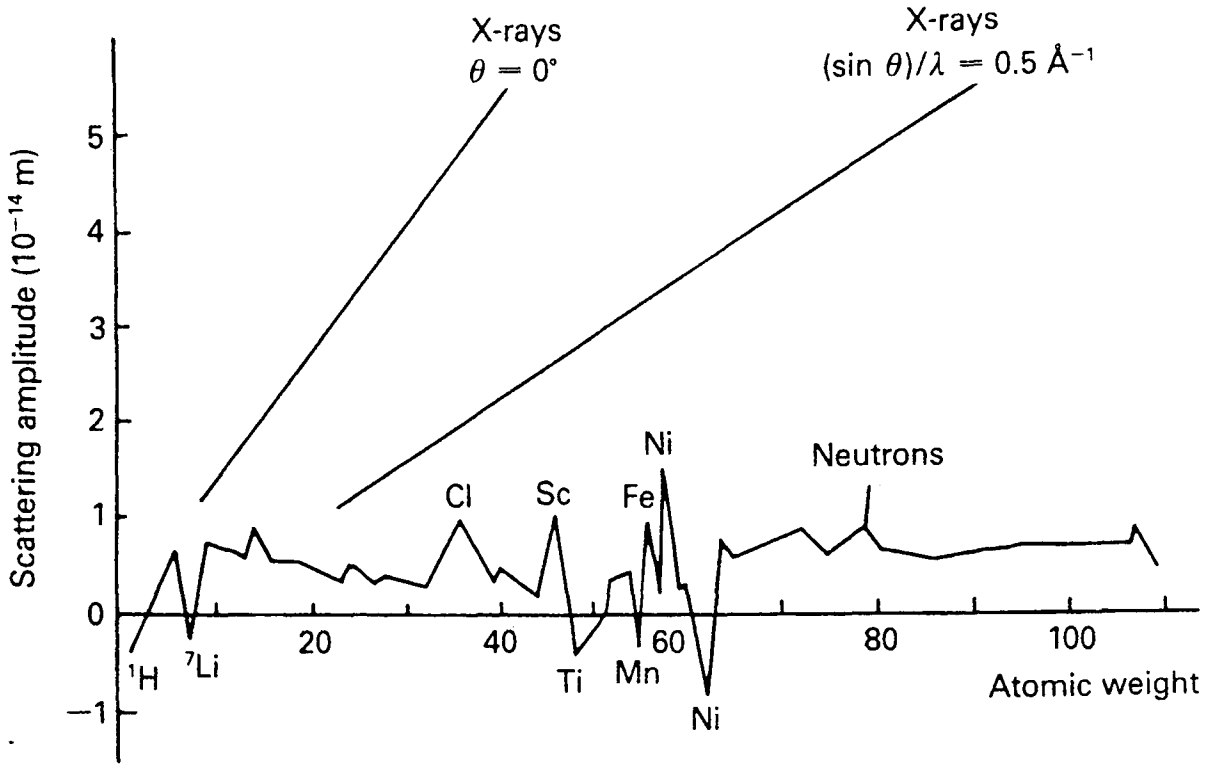


Figure 2.4.1 Comparative variation of neutron scattering lengths and X-ray atomic form factors as function of atomic weight. (Figure reproduced from reference [29])

It can be seen that elements such as Ti and Mn have negative scattering amplitudes, which occur when there is an anomalous phase change on scattering. Also, elements which may be neighbours in the periodic table still show diffraction contrast towards neutrons (for example Fe and Co have scattering lengths of 0.96 and 0.22×10^{-14}m respectively[30]).

(ii) A further, particularly useful characteristic of the elastic scattering of neutrons is the independence of the neutron scattering length of the scattering vector, K, (or $\sin\theta / \lambda$). This is because the nucleus is smaller than the neutron wavelength and hence approximates to a point source. Hence, the intra-atomic interference effects observed in X-ray scattering, are less significant.

(iii) Since the nuclear force is only effective over short distances, the probability of interaction between an incoming neutron and nuclei comprising the sample is relatively low; consequently, the neutron has a mean free path of about 1cm[29] within the solid. This is relatively large and neutron diffraction can be considered truly a probe of the bulk material, in contrast to the surface probing afforded by X-rays.

(iv) Since the beam energy for neutrons with typically useful wavelenths of ~ 1.5Å is just 40meV, radiation damage to the material is minimal compared to the potential damage in X-ray experiments. However, there is the disadvantage that certain materials will remain radioactive for a significant period of time after being in a neutron beam.

(v) Neutrons are ideal for *in-situ* studies (of real time effects, for example) in a range of environments (furnaces, cryostats) due to their low absorption cross sections.

(vi) In contrast to the number of quanta produced by laboratory X-ray sources, neutron beams are relatively weak sources. This is reflected in the large sample volumes, hence masses, which must be synthesised to obtain acceptable statistics in typical diffraction patterns.

(vii) Finally, since the neutron has an intrinsic spin (I = 1/2), it possesses a magnetic dipole moment. Therefore, it can interact with magnetic fields generated by the spin and orbital angular momenta of unpaired electrons distributed throughout the solid. If these unpaired electrons are distributed in a periodic manner (for example in ferromagnets, antiferromagnets and ferrimagnets), magnetic scattering from an ordered array of spins gives rise to magnetic Bragg peaks. Hence, the structure of magnetically ordered solids can be probed and the following Section discusses this in more detail.

2.4.1 Magnetic scattering of neutrons

For solids containing a periodic array of unpaired spins, the intensity of a set of Bragg reflections, I_{hkl} is described fully by contributions from both nuclear and magnetic scattering:

$$I(hkl) \propto K\,|F_{nuc}(hkl)|^2 + I_{mag} \qquad \text{eqn. (2.4.2)}$$

with the structure factor described by the following expression, incorporating both nuclear and magnetic contributions to the scattering:

$$F^2(hkl) = F^2_{nuc}(hkl) + \left| \sum_j \mathbf{q}_j p_j \exp(2\pi i(hx_j + ky_j + lz_j)) \right|^2 \qquad \text{eqn. (2.4.3)}$$

The structure factor for magnetic scattering depends both on the magnitude of the magnetic cross section (p) and on the magnetic interaction vector (**q**). F_{mag} is therefore a vector quantity with the summation over the 'j' magnetic atoms within the unit cell. The magnetic

cross section (p) (or scattering amplitude) is a function of the magnitude of the magnetic moment (S) and the magnetic form factor (f) and is given (for the jth atom) below:

$$p_j = 0.54 S_j f_j \times 10^{-12} \text{ cm} \qquad \text{eqn. (2.4.4)}$$

The magnetic interaction vector (**q**) for the jth atom is given as follows,

$$\mathbf{q}_j = \varepsilon(\varepsilon.\mathbf{K}_j) - \mathbf{K}_j \qquad \text{eqn. (2.4.5)}$$

which uses the notation of Halpern and Johnson[31]. The symbol $\mathbf{K}_j$ represents a unit vector in the direction of the atomic magnetic spin and ε represents a unit vector in the direction perpendicular to the reflecting planes. Thus, **q** lies in the plane of ε and **K**, is perpendicular to ε and is of magnitude sinα (where α is the angle between the vectors ε and **K**). Therefore, when α is 0° (the reflecting planes are perpendicular to the atomic spin direction), there is no magnetic contribution to the full structure factor described by equation 2.4.3.

The use of a form factor is reminiscent of X-ray scattering, and magnetic neutron scattering involves interaction with the electrons surrounding the nuclei by way of the electromagnetic force. The interaction therefore extends over longer distances than the strong nuclear forces responsible for nuclear Bragg peaks, although it is inherently weaker in nature. The combination of these factors means that the mean free path for magnetic scattering is also of the order of 1cm in solids. The use of a polarised neutron beam allows nuclear and magnetic scattering to be separated when reflections overlap in the diffraction pattern.

2.4.2 Production of neutrons and instrumentation used

All neutron diffraction data presented in this thesis were collected at the constant wavelength neutron source on instruments D1b and D2b[32,33] at the Institut Laue Langevin (ILL), Grenoble, France. The ILL is an example of a nuclear reactor based neutron source, from which neutrons are produced continuously in time, as opposed to a spallation source, such as ISIS in the UK, where the neutrons are 'pulsed'. At the ILL neutrons are a by-product of the nuclear fission process, whereas at ISIS they are a by-product of the 'spallation'

reaction as a result of high energy protons (produced from a synchrotron) bombarding a metal target of depleted uranium.

For both types of neutron source, the neutrons pass through a 'moderator' containing light molecules (eg. H_2O, D_2O, graphite) where their energies are thermalised as a result of repeated collisions and effective energy transfer with these light molecules. For a moderator held at a temperature T, the mean energy of the resulting 'thermal' neutrons is $3k_BT/2$. The high-flux reactor at the ILL has a D_2O moderator which, when held at 300K, is in equilibrium with a thermal neutron flux, with a maximum in the Maxwellian distribution of energies corresponding to $\lambda = 1.2$Å.

The next stage for neutrons produced from a reactor source is to pass through a single crystal monochromator, thus facilitating constant wavelength diffraction using detectors which scan a range of 2θ values. Collimation of the beam is achieved using Soller slits. In the case of a spallation source, neutrons are selected and analysed by a 'time of flight (TOF)' means, with a detector at a fixed scattering angle.

The following sub-sections give schematic descriptions of diffractometers D1b and D2b used for data collection at the ILL.

2.4.2.1 Constant wavelength instrument D1b

D1b is located on thermal guide H22 outside the main reactor hall. The instrument is a two-circle diffractometer and is suited ideally for experiments requiring a high neutron flux. Neutrons are collimated and are then incident on a monochromator with a take-off angle of 44.22°. Depending upon which crystal is utilised, two wavelengths are accessible. Pyrolytic graphite monochromators (002) give a wavelength of 2.52Å and provide a flux at the sample of 6.5×10^6 n cm^{-2} s^{-1}. A second wavelength of 1.28Å is available by using a germanium (311) monochromator yielding a flux at the sample of 0.4×10^6 n cm^{-2} s^{-1}. The data presented in this thesis utilised the high flux available at the 2.52Å wavelength and were collected on cooling from room temperature to 1.7K using helium to cool the sample inside a 'standard Orange ILL cryostat'.

The instrument is shown schematically in Figure 2.4.2[33,34]:

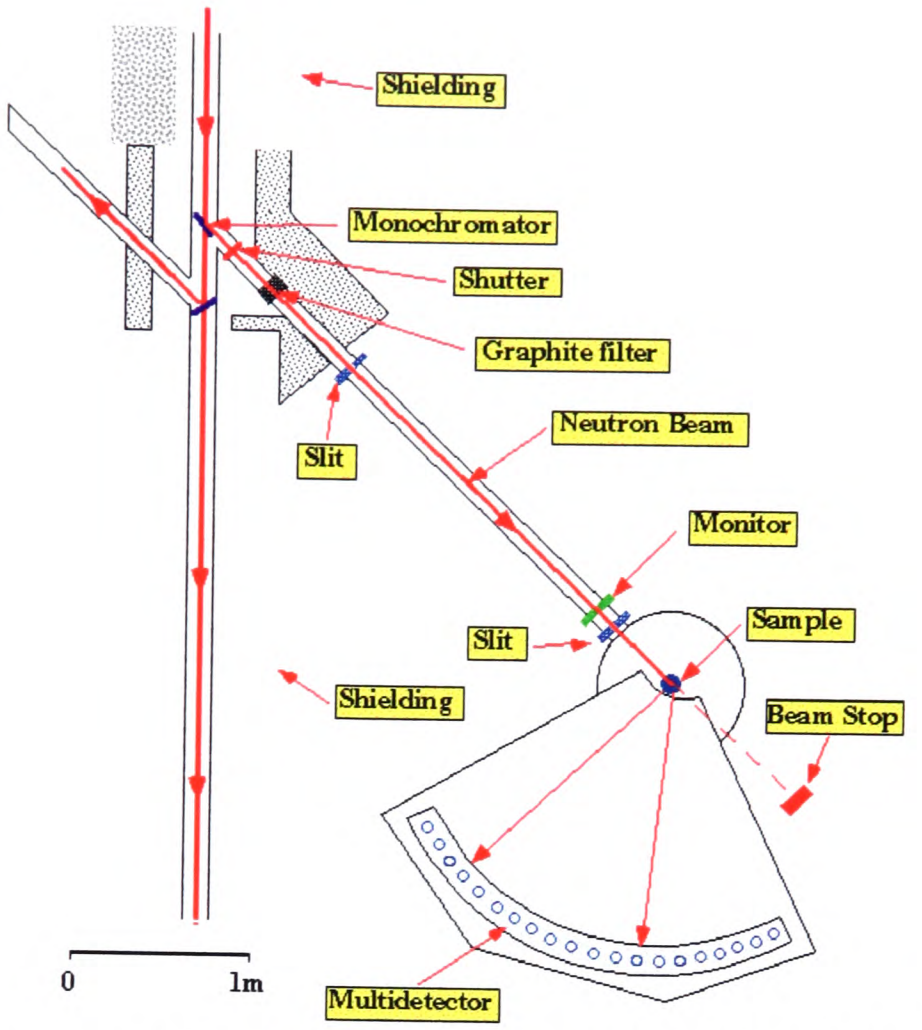


Figure 2.4.2 Schematic representation of D1b. (Figure reproduced from reference [34]).

D1b is particularly suitable for monitoring the evolution of magnetic Bragg peaks on cooling, since the high available flux means a dataset with adequate statistics covering the temperature range 1.5K to 300K can be collected in 3 to 5 hours. The instrument is equipped with a ^{3}He/Xe position-sensitive detector composed of a system of multi-electrodes with 400cells that are 0.2° apart, giving a pattern spanning an angular range of 80° in a short space of time. Measurements were made on 10g samples contained in vanadium cans and the data were collected in the $10 \leq 2\theta/° \leq 100$ range.

2.4.2.2 Constant wavelength instrument D2b

D2b is located on the thermal neutron beam also, but is inside the reactor hall. Like D1b it is a two-circle diffractometer, shown schematically in Figure 2.4.3[32,35]. The diagram shows the relatively high take-off angle of 135° for the Ge monochromator, which facilitates a high resolution, particularly in the high angle region. Relatively high intensity is achieved due to the high flux beam position of the instrument. D2b is designed to reach $\Delta d/d$ of 5×10^{-4} with perfect samples.

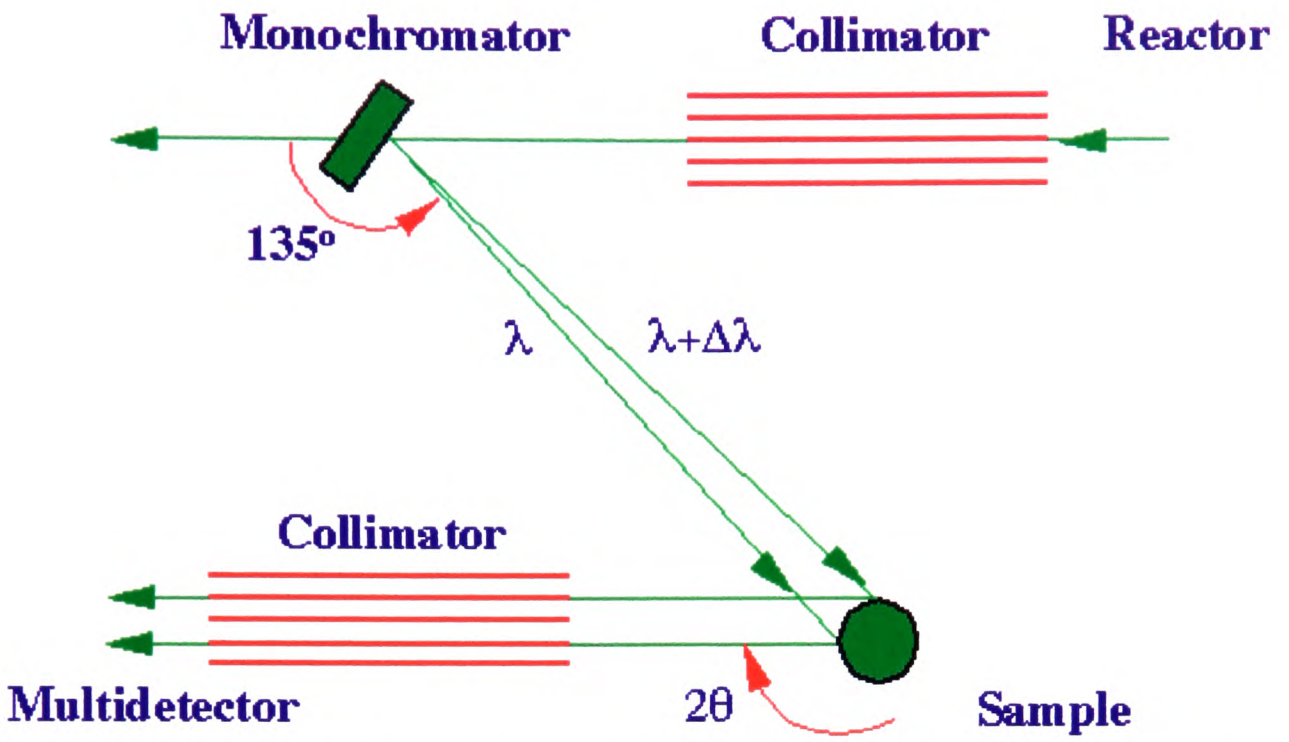


Figure 2.4.3 Schematic representation of D2b. (Figure reproduced from reference [35]).

The angular range of the diffractometer covers $5 \leq 2\theta/° \leq 165$ and the 64 counter multidetector moves on an airpad, making about 100 steps of 0.025° in 2θ, since the 64 detectors are spaced at 2.5° intervals. The duration of a scan is approximately 30 minutes and the number of scans is selected depending upon the statistics required in the pattern accounting for wavelength used (flux available) and the degree of collimation of the beam. All data collected in this work were on 5 to 10g samples contained in vanadium cans at temperatures in the range 1.5 to 295K. The typical angular range over which data were collected was for $8 \leq 2\theta/° \leq 150$.

2.5 Crystal Structure Analysis

All neutron and X-ray data presented in this thesis were analysed using the GSAS (General Structure Analysis System)[25] software package, utilising the Rietveld method of profile refinement[24,36].

2.5.1 Rietveld profile refinement

Rietveld's work in the 1960s revolutionised the method of analysis of powder neutron and X-ray diffraction data and enabled the extraction of maximum information from the pattern, provided a reasonably accurate structural model was available. His approach uses a least squares optimisation procedure which minimises the difference between the observed

and calculated *profiles*, rather than individual reflections. The method therefore alleviates the problem of extracting |F(hkl)| values from individual reflections in the cases where two or more reflections are not fully resolved. For powder data where, in addition to peak overlap due to low-symmetry structures or poor instrumental resolution, there is overlap as a result of d_{hkl} degeneracies, this is clearly advantageous. In order to consider the entire profile, the method was developed assuming that the reflections were Gaussian in shape with a term correcting for asymmetry, and that the calculated intensity at each point on the profile is obtained by summing the contributions from the Gaussians that overlap at that point.

In fact, a more comprehensive description of angular dispersive peak shapes[37] must include a range of instrumental contributions, in particular a consideration of the spectral distribution of the incident radiation and sample effects such as crystallite size and microstrain broadening. As a result, Caglioti's empirical description[38] of the full width at half maximum (FWHM), Γ_G, of peaks, is as follows:

$$\Gamma_G^2 = U\tan^2\theta + V\tan\theta + W \qquad \text{eqn. (2.5.1)}$$

This determines the minimum peak separation resolved by the instrument, but is incomplete. In addition to this Gaussian FWHM, the Lorentzian FWHM, Γ_L, (given in equation 2.5.2) is significant, since through terms Y and X (describing microstrain broadening and particle size broadening, respectively), sample effects are included in the description of the peak shape.

$$\Gamma_L = Y\tan\theta + \frac{X}{\cos\theta} \qquad \text{eqn. (2.5.2)}$$

Therefore, a more complete description of peak shape is given by a convolution of a Gaussian and Lorentzian function such as a pseudo-Voigt function, V(x)[39]. In the pseudo-Voigt function a mixing parameter, η, determines the contribution from Gaussian and Lorentzian components required to fit best the observed profile. The pseudo-Voigt function is given in equation 2.5.3, in which Γ is the resultant FWHM from convolution of Γ_G and Γ_L:

$$V(x) = \eta\left(1 + 4\left(\frac{\Delta 2\theta}{\Gamma}\right)^2\right)^{-1} + (1-\eta)\exp\left(-4\ln 2\left(\frac{\Delta 2\theta}{\Gamma}\right)^2\right) \qquad \text{eqn. (2.5.3)}$$

The profile function is then just one of many parameters contributing to the overall expression for the calculated intensity at the 'ith' step in the diffraction pattern, once the initial structural model is in place in the least squares minimisation process. Equation 2.5.4 represents y_{ci}, the calculated intensity[40] at the ith step,

$$y_{ci} = y_{bi} + s \sum_k L_k |F_k|^2 \phi(2\theta_i - 2\theta_k) P_k A \qquad \text{eqn. (2.5.4)}$$

where the quantities are denoted as follows:

y_{bi} is the background intensity at the ith step

s is the scale factor

L_k includes the Lorentz, polarisation and multiplicity factors

ϕ represents the profile function

P_k is the preferred orientation contribution

A is an absorption factor, and finally

F_k is the structure factor for the kth Bragg reflection

The summation over 'k' includes the Bragg peaks lying within a certain number of halfwidths of the profile point $2\theta_i$.

The quantity which is minimised in the least squares process (generally denoted as the residual, S_y), is the *difference* between the calculated intensity as given in equation 2.5.4 and the observed intensity at the ith step, y_i:

$$S_y = \sum_i w_i (y_i - y_{ci})^2 \qquad \text{eqn. (2.5.5)}$$

where $w_i = 1/y_i$.

2.5.2 GSAS parameters and criteria of fit

As mentioned already, the Rietveld method was applied here through use of the GSAS software programme running in Unix, developed by Larson and von Dreele[25]. It is suitable for both X-ray and neutron diffraction data from both angular dispersive and TOF data sources. Multiple datasets can be refined simultaneously which is particularly useful when complementary X-ray and neutron data are available for the same sample.

The residual, S_y, is represented slightly differently in GSAS notation, as is shown in equation 2.5.6, and the GSAS notation will be used in definitions of fitting parameters for consistency. S_y is replaced by M,

$$M = \sum w(I_o - I_c)^2 \qquad \text{eqn. (2.5.6)}$$

where I_o and I_c represent the observed and calculated intensities respectively and the weighting, w, is derived from an estimation of the background at point i.

The profile function utilised in the version of GSAS used to analyse high resolution data presented here was a slightly modified version of the Thompson-Cox-Hastings pseudo-Voigt function described by equation 2.5.3. The function used includes a resultant FWHM from convolution of Γ_G and Γ_L as previously, but where Γ_G and Γ_L have been modified in the following ways. An additional term, P, the Scherrer coefficient for Gaussian broadening, is included in the expression for Γ_G as shown in equation 2.5.7:

$$\Gamma_G^2 = U\tan^2\theta + V\tan\theta + W + \frac{P}{\cos^2\theta} \qquad \text{eqn. (2.5.7)}$$

Also, there is a modification to the Lorentzian FWHM given by equation 2.5.2 as a result of the inclusion of anisotropy coefficients X_e and Y_e for the Lorentzian Scherrer broadening and strain broadening, respectively:

$$\Gamma_L = (Y + Y_e\cos\phi)\tan\theta + \frac{X + X_e\cos\phi}{\cos\theta} + Z \qquad \text{eqn. (2.5.8)}$$

The 2θ difference is also modified for asymmetry and sample shift, giving a total of eleven profile coefficients.

The quality of fit is measured by the following functions, the first two of which, the profile R_p and the weighted profile R_{wp}, are expressed as percentages:

$$R_p = 100x\frac{\sum|I_o - I_c|}{\sum I_o} \qquad \text{eqn. (2.5.9)}$$

$$R_{wp} = 100x\left(\frac{\sum w(I_o - I_c)^2}{\sum wI_o^2}\right)^{1/2} \qquad \text{eqn. (2.5.10)}$$

The reduced χ^2 is defined as follows:

$$\chi^2 = \frac{\sum w(I_o - I_c)^2}{(N_{obs} - N_{var})} \qquad \text{eqn. (2.5.11)}$$

In addition, the 'expected R_{wp}' is given by $\frac{R_{wp}}{(\chi^2_{red})^{1/2}}$ and indicates the best R_{wp} achievable, considering the quality of the data. Lastly, a parameter as given by Durbin and Watson, denoted DWd, gives an indication of the nature of the errors in the refinement[41,42]. The Rietveld Method is reviewed in detail in the book edited by Young[43].

2.6 DC SQUID Magnetometry

DC SQUID magnetometry enables characterisation of the magnetic properties of a system, properties dependent upon the magnetic moments associated with the spin and orbital motions of electrons. The particular magnetic properties of respective samples will be discussed in more detail in the appropriate chapters. This section deals with the means of measuring magnetic moments and methods of handling the data to obtain magnetisation and magnetic susceptibility.

2.6.1 The Squid Magnetometer

In the last thirty years or so the SQUID (Superconducting QUantum Interference Device) has replaced conventional magnetometers relying on force techniques or induction based methods[44]. Its unprecedented sensitivity, (enabling detection of magnetic fields as low as 10^{-13}T such as those associated with electrical activity in the brain), means it is possible to resolve effects where the energies associated with relevant interactions are of the order of kT.

The thin film SQUID device used in the Quantum Design Model MPMS system for this work consists of a closed superconducting loop containing two Josephson junctions[44,45] in the loop's current path. The principle of operation of the SQUID relies upon the coherent

quantum tunnelling of Cooper pairs of electrons that occurs in Josephson junctions. The result is that the circulating current in the superconducting loop varies as a periodic function of an applied magnetic flux. The energy associated with the smallest change in magnetic flux the device can detect in one second, is typically about 10^{-32} joule.

The SQUID device is just one of four main components of the MPMS instrument. The other three consist of a superconducting magnet to generate large magnetic fields, a superconducting detection coil which couples inductively to the sample and a superconducting magnetic shield surrounding the SQUID. As the sample rod moves through the detection coil, its magnetic moment due to the sample induces an electric current in the detection coils. This detected change in magnetic flux is converted into a change in persistent current in the detection circuit, since the detection coils, the connecting wires and the SQUID input coil form a closed superconducting loop. The output signal recorded is, in fact, a voltage since the SQUID operates as a linear current- to -voltage converter. The instrument is configured such that variations in the voltage are proportional to the magnetic moment of the sample.

The sample (typically 5 to 100mg) was contained in a gelatin capsule mounted in a clear plastic drinking straw. The straw was attached to the sample rod using Kapton tape and the output signal for each measurement was the average of four, 6cm scans through the detection coils.

2.6.2 Parameters measured and units used

The quantity which is measured from the SQUID (whether as a function of temperature or applied field) is magnetic moment, m, given in *e*lectro*m*agnetic *u*nits (emu) in the *c*entimetre *g*ram *s*econd (c.g.s) system of units used throughout this work. It is straightforward then to convert this to magnetisation, M (always expressed per unit mass, volume or mole, etc.) by dividing by the appropriate quantity. Using c.g.s units, the magnetisation is related to the applied magnetic field, H and B, the flux density (or net local magnetic field) as shown in equation 2.6.1:

$$B = H + 4\pi M \qquad \text{eqn. (2.6.1)}$$

A useful way of treating equation 2.6.1 in the context of the SQUID measurement is to regard H as the field applied by the superconducting magnet, B as the net local field and M as the field contributed by the sample which changes the local field from H to B. The units for B are Gauss (G) in the c.g.s system and Tesla (T) in SI units[1]. The units for H are oersted (Oe) in c.g.s units and A/m in SI units. However, the units of Gauss are often used for both H and B in the c.g.s. system (since oersted and Gauss have the same dimensions).

Data collected versus temperature and field were converted to magnetisation per mole (emu per mole) by dividing by the moles of material present. Another useful quantity for the measurements versus temperature is susceptibility, χ, given by M/H, expressed per mole of material by:

$$\chi_{mol} = \frac{M(emu)xRMM(gmol^{-1})}{H(G)xmass(g)} \qquad \text{eqn. (2.6.2)}$$

The molar susceptibility is quoted in emu per mole and the value is corrected for the diamagnetic contribution (of the order of 10^{-6} emu per mole) from the sample.

Lastly, a useful way of expressing magnetisation is as Bohr magnetons (μ_B) per formula unit and this unit has been used extensively in this thesis. The Bohr magneton is the fundamental unit of magnetic dipole moment, μ, which is proportional to the angular momentum of an electron as described by equation 2.6.3:

$$\mu = -\frac{Je}{2m} \qquad \text{eqn. (2.6.3)}$$

For the lowest quantum state, μ takes the value μ_B, where μ_B is expressed as follows:

$$\mu_B = \frac{eh}{4\pi m} \qquad \text{eqn. (2.6.4)}$$

In c.g.s units, μ_B has the value of 9.2741×10^{-21} erg Oe^{-1}. Magnetisation (expressed in emu per mole) is converted to μ_B per formula unit by the following multiplication (equation 2.6.5):

---

[1] One Tesla is equivalent to 10kG.

$$\mu_B \text{ (per formula unit)} = \frac{M(emu)xRMM(gmol^{-1})}{mass(g)xN_A x\mu_B} \qquad \text{eqn. (2.6.5)}$$

2.7 Magnetotransport Measurements

The cryomagnetic system used to obtain the magnetotransport data presented in this thesis is comprised of a superconducting magnet housed in a cryostat which is a standard OXFORD model SMD10HF dewar, shown in Figure 2.7.1.



Figure 2.7.1 Cryostat surrounding the superconducting magnet, into which the cryogenic insert containing the samples was inserted.

The dewar is vacuum insulated, with a full length liquid nitrogen cooled radiation shield and a liquid helium reservoir which is in direct contact with the magnet coils. The magnet is powered by a PS1210 supply and is composed of two sets of concentric solenoids, the outer sections are wound from NbTi wire and the inner sections from Nb_3Sn wire.

In each experiment, data were collected simultaneously on three samples, in the form of sintered bars, mounted on a 24 wire cryogenic insert constructed by L. Bremer and W.

Schuster. Figure 2.7.2 gives an enlarged view of the top of the cryogenic insert (see graph paper for scale), on which three, black, sintered bars, each with two voltage contacts on their surface, are visible. The current contacts on either end of each sample are not visible in this Figure.

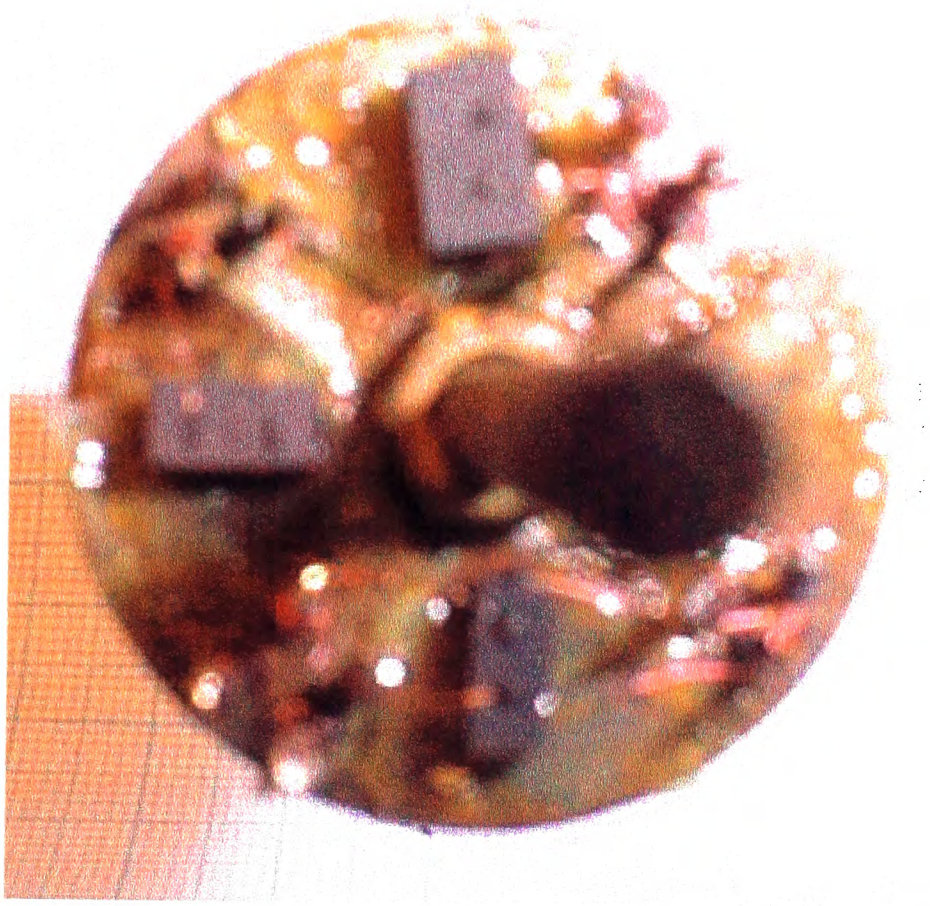


Figure 2.7.2 Enlarged view of the top of the cryogenic insert, containing three bar-shaped samples.

The insert containing the samples was not inserted directly into the magnet sample space; rather into a variable temperature insert (VTI) which fits into the cryostat and provides shielding in the form of a vacuum, from the magnet coils. Use of the VTI allowed data to be collected up to 14T, between temperatures ranging from a few Kelvin to room temperature. Inside the VTI, the sample is surrounded by helium gas at one atmosphere, providing thermal contact between it and the VTI. Heating was carried out either using the VTI heater, (a 30Ω resistor on a Cu block contained within the VTI), or using a heater wound around the Cu cap of the cryogenic insert and often by a combination of both to obtain an appreciable rate of change of temperature. Cooling was achieved *via* a flow of helium gas pulled into the sample chamber through a needle valve, by pumping. The temperature was monitored using a combination of VTI thermometer, and two thermometers (one carbon, one platinum) located on the cryogenic insert within a few centimetres of the sample.

The sintered bars were approximately 5x2x2mm in size, and were cut from 13mm or 8mm pellets using a diamond impregnated wire, by Mr G. Read. Standard four probe geometry was used during data collection, with the direct current ($\leq$ 50 μA) perpendicular to the field. For early measurements, contacts onto the sintered materials were made to Cu wires using Ag conductive paint. For later experiments, gold patches were evaporated onto the bars by Mr C. Goodwin, prior to attaching the Cu wires with Ag epoxy. This led to stronger contacts which showed less deterioration over time and with changes in temperature.

Each sample was connected, via a 24 wire interface box[2], to a Keithley 2000 multimeter, which provided the current through the sample, measured the voltage drop between the two contacts on the surface of the bar, and displayed the calculated resistance. The values of resistance were recorded by the programme 'Magneto', capable of measuring three channels (one for each sample), simultaneously.

2.8 Iodometry

Chemical analysis using iodometric titration relies upon the liberation of iodine in solution, typically from KI in the presence of a transition metal cation oxidant. The iodine is removed by reaction with thiosulphate, $S_2O_3^{2-}$, the solution of which is standardised using KIO_3 as a primary standard; hence, the oxidising power of the transition metal cation is established[46].

Typically, 50mg of well-ground, powdered sample was covered with approximately 5g (an excess) of solid KI in the bottom of a three-necked, round-bottomed flask. The flask was flushed with N_2 as the solids were dissolved in approximately 50ml of 6M HCl with vigorous stirring, (in order to minimise the risk of aerial oxidation of iodide to iodine). In order to ensure that the full oxidising power of the transition metal cation (in our case $Mn^{(2+x)+}$) was used to liberate iodine from the iodide, the sample was only dissolved in acidic solution whilst in the presence of a large excess of iodide. Finally, the strength of HCl was limited to approximately 6M, to minimise the risk of the competing, pH-dependent oxidation of HCl to Cl_2 occuring during dissolution of the sample.

---

[2] The 24 wire interface box was constructed by Nenad Vranjes.

When all the sample appeared to have dissolved, the mixture was titrated against the previously standardised thiosulphate. The titration required vigorous stirring while using a white tile to help identify the end-point, which corresponded to the loss of brown colouration of the solution as the iodine reacted with the thiosulphate. A few drops of fresh starch solution were added close to the end point. A concentration of thiosulphate solution had been chosen previously such that the titres were in the range 15 - 25ml. The titrations were repeated until at least three consistent mass/titre ratios were obtained.

Once the number of moles of thiosulphate required was calculated, the value of 'x' for the cation $Mn^{(2+x)+}$ was obtained by considering the following relations:

$$Mn^{(2+x)+} + xe^- \rightarrow Mn^{2+} \qquad \text{eqn. (2.8.1)}$$

$$Mn^{(2+x)+} + xI^- \rightarrow \frac{x}{2} I_2 + Mn^{2+} \qquad \text{eqn. (2.8.2)}$$

$$\frac{x}{2} I_2 + xS_2O_3^{2-} \rightarrow \frac{x}{2} S_4O_6^{2-} + xI^- \qquad \text{eqn. (2.8.3)}$$

2.9 References

[1] MP Pechini **1967**, US Patent No. 3 330 697.

[2] CC Tang, MC Miller, EJ MacLean *SRS Station 2.3 Manual*, CLRC, **1998**.

[3] C Hammond *The Basics of Crystallography and Diffraction*, Oxford University Press: Oxford, **1997**.

[4] AF Moodie, HJ Whitfield *Acta Crystallogr., Sect. A* **1995**, *A51*, 198.

[5] C Giacovazzo *'The Diffraction of X-Rays by Crystals' in 'Fundamentals of Crystallography'*, Oxford University Press and the International Union of Crystallography: Oxford, **1992**.

[6] D McKie, C McKie *Essentials of Crystallography*, Blackwell Scientific: Oxford, **1986**.

[7] LM Morooney, P Thompson, DE Cox *J. Appl. Crystallogr.* **1988**, *21*, 206.

[8] RS Howland, TH Geballe, SS Laderman, A Fischer-Colbrie, M Scott, JM Tarascon, P Barboux *Phys. Rev. B* **1989**, *39*, 9017.

[9] GH Kwei, RB Von Dreele, A Williams, JA Goldstone, AC Lawson, II, WK Warburton *J. Mol. Struct.* **1990**, *223*, 383.

[10] GH Kwei, RB Von Dreele, SW Cheong, Z Fisk, JD Thompson *Phys. Rev. B* **1990**, *41*, 1889.

[11] A Williams, GH Kwei, AT Ortiz, M Karnowski, WK Warburton *J. Mater. Res.* **1990**, *5*, 1197.

[12] JP Attfield *Nature* **1990**, *343*, 46.

[13] DA Perkins, JP Attfield *J. Chem. Soc., Chem. Commun.* **1991**, 229.

[14] JK Warner, AP Wilkinson, AK Cheetham, DE Cox *J. Phys. Chem. Solids* **1991**, *52*, 1251.

[15] AP Wilkinson, DE Cox, AK Cheetham *J. Phys. Chem. Solids* **1991**, *52*, 1257.

[16] Y Murakami, H Kawada, H Kawata, M Tanaka, T Arima, Y Moritomo, Y Tokura *Phys. Rev. Lett.* **1998**, *80*, 1932.

[17] LK Templeton, DH Templeton, RP Phizackerley *J. Am. Chem. Soc.* **1980**, *102*, 1185.

[18] LK Templeton, DH Templeton, RP Phizackerley, KO Hodgson *Acta Crystallogr., Sect. A* **1982**, *A38*, 74.

[19] AK Freund *X-ray Optics*, ESRF Internal Report, **1987**.

[20] JJ Hoyt, D De Fontaine, WK Warburton *J. Appl. Crystallogr.* **1984**, *17*, 344.

[21] L Kissel, B Zhou, SC Roy, SK Sen Gupta, RH Pratt *Acta Crystallogr., Sect. A* **1995**, *A51*, 271.

[22] DT Cromer, D Liberman *J. Chem. Phys.* **1970**, *53*, 1891.

[23] DT Cromer, DA Liberman *Acta Crystallogr., Sect. A* **1981**, *A37*, 267.

[24] HM Rietveld *J. Appl. Crystallogr.* **1969**, *2*, 65.

[25] AC Larson, RB von Dreele "General Structure Analysis System (GSAS)", Los Alamos National Laboratories, **1990**.

[26] DT Cromer *Acta Cryst.* **1965**, *18*, 17.
[27] DP Mitchell, PN Powers *Phys. Rev.* **1936**, *50*, 486.
[28] H Halban, P Preiswerk *C.r. hebd. Seanc. Acad. Sci. Paris* **1936**, *203*, 73.
[29] GE Bacon *Neutron Diffraction*, Clarendon Press: Oxford, **1975**.
[30] AK Cheetham, P Day *Solid State Chemistry Techniques*, Oxford University Press: Oxford, **1990**.
[31] O Halpern, MH Johnson *Phys. Rev.* **1939**, *55*, 898.
[32] AW Hewat *Mater. Sci. Forum* **1986**, *9*, 69.
[33] B Ouladdiaf *D1b Users Manual*, Institut Laue Langevin, **1997**.
[34] http://www.ill.fr/YellowBook/D1B/
[35] http://www.ill.fr/YellowBook/D2B/
[36] HM Rietveld *Acta Crystallogr.* **1967**, *22*, 151.
[37] CJ Howard *J. Appl. Crystallogr.* **1982**, *15*, 615.
[38] G Caglioti, A Paoletti, FP Ricci *Nucl. Instrum. Methods* **1958**, *35*, 223.
[39] P Thompson, DE Cox, JB Hastings *J. Appl. Crystallogr.* **1987**, *20*, 79.
[40] TM Sabine, in *The Rietveld Method*, Oxford University Press: New York, **1996**.
[41] J Durbin, GS Watson *Biometrika* **1950**, *37*, 409.
[42] J Durbin, GS Watson *Biometrika* **1951**, *58*, 1.
[43] RA Young, *The Rietveld Method*, Oxford University Press: New York, **1996**.
[44] SJ Swithenby *Contemp. Phys.* **1974**, *15*, 249.
[45] J Clarke *Scientific American* **1994**, 36.
[46] A Vogel *Inorganic Compounds: Qualitative Analysis*, Longmans: London, **1987**.

CHAPTER 3

$n=2$ in $A_{n+1}B_nO_{3n+1}$

$A_3B_2O_7$

3.1 Introduction

In comparison with the $Sr_{2-x}La_{1+x}Mn_2O_{7-\delta}$ system, there are relatively few studies[1-6] documenting the equivalent, Nd doped series $Sr_{2-x}Nd_{1+x}Mn_2O_{7-\delta}$, four members of which form part of the magnetotransport study discussed in the current chapter. The remaining compounds discussed here belong to the $Sr_2LnMn_2O_{7-\delta}$ series, (Ln=Pr, Nd, Ho and Y), and are of interest to observe the effects of changing 'Ln', and hence the mean A-site cation radius, $\langle r_a \rangle$, on crystallographic and magnetic properties of n = 2 RP phases. The current results draw parallels, with respect to the chemical pressure effect, with those obtained for the series $Sr_{2-x}(La_{1-z}Nd_z)_{1+x}Mn_2O_7$[7-9]. The $Sr_2LnMn_2O_{7-\delta}$ series is also of interest with respect to charge ordering (CO), since its members contain a 1:1 ratio of Mn^{3+}:Mn^{4+} cations. The $Sr_2LaMn_2O_7$ phase has provided interesting results regarding charge ordering in the layered manganites. For a 1:1 ratio of Mn^{3+}: Mn^{4+}, the CO model proposed by Goodenough[10] for the perovskites $La_{0.5}R_{0.5}MnO_3$, can be applied, albeit with a modification to account for the relative shift between neighbouring layers in the CO patterns in tetragonal *I4/mmm* symmetry. Li et al.[11] have established recently that CO in $Sr_2LaMn_2O_7$ below ~210K shows the same pattern of orbital ordering observed in the n = 1 compound, $La_{0.5}Sr_{1.5}MnO_4$.

The compounds $Sr_2HoMn_2O_{7-\delta}$ and $Sr_2YMn_2O_{7-\delta}$, which belong to the $Sr_2LnMn_2O_{7-\delta}$ series, were synthesised by the author. Section 3.2 focusses on the synthesis and characterisation by X-ray and neutron diffraction[12] and SQUID magnetometry, of these two samples. A discussion of the magnetotransport behaviour of $Sr_2HoMn_2O_{7-\delta}$ and $Sr_2YMn_2O_{7-\delta}$ is reserved until Section 3.3, where they are considered in relation to the rest of the $Sr_2LnMn_2O_{7-\delta}$ series.

3.2 Synthesis and characterisation of the compounds $Sr_2HoMn_2O_{7-\delta}$ and $Sr_2YMn_2O_{7-\delta}$

3.2.1 Experimental details

Large (10g) batches of the materials $Sr_2HoMn_2O_{7-\delta}$ and $Sr_2YMn_2O_{7-\delta}$ were prepared using standard ceramic techniques. Stoichiometric quantities of $SrCO_3$ (99.994%, Specpure), MnO_2 (99.999% Puratronic, Alfa) and either Y_2O_3 (99.99%, REacton) or Ho_2O_3 (99.99%, REacton) were ground together thoroughly and heated as detailed in Table 3.2.1.

Table 3.2.1 Details of the preparation of $Sr_2HoMn_2O_{7-\delta}$ and $Sr_2YMn_2O_{7-\delta}$ materials:

Compound	$Sr_2HoMn_2O_{7-\delta}$	$Sr_2YMn_2O_{7-\delta}$
Firing Temperature (°C)	Firing time	Firing time
800	26 hours, powder	32 hours, powder
1000	24 hours, 7 pellets[a,b]	42 hours, 7 pellets[a,b]
1200	24 hours, 7 pellets	120 hours, 7 pellets
1250	24 hours, 7 pellets	-
1300	17 days, 7 pellets	18 days, 7 pellets
1350	10 days, 7 pellets	10 days, 7 pellets
1400	40 hours, 7 pellets	28 hours, 2 pellets
Atmosphere	air	air
Quantity of material (g)	10g	10g

[a] All pellet diameters were 13mm and 2-3 tonnes were used during pressing.

[b] Regrinding and repelleting was carried out at each increase of the firing temperature and at least every 48 hours for longer firings at a single temperature.

The progress of both reactions was monitored by X-ray diffraction using the laboratory Philips diffractometer (λ = 1.5406Å, $3 \leq 2\theta/^\circ \leq 70$, $\Delta 2\theta = 0.05^\circ$). The protracted firing times and repeated regrindings and repelleting required reflect the sizes of the batches of sample and both reactions required the relatively high firing temperature of 1400°C to reach completion. The establishment of an approximately 3:2 ratio of the two most intense reflections (indexed as 105 and 110 in space group *I4/mmm*) in the powder pattern suggested the predominance of the n = 2 RP phase.

Powder X-ray diffraction data suitable for Rietveld analysis were collected on the laboratory Siemens (D5000) diffractometer (λ = 1.5406Å, $5 \leq 2\theta/^\circ \leq 120$, $\Delta 2\theta = 0.02^\circ$), using Cu $K\alpha_1$ radiation, operating in Bragg Brentano geometry. At the time of synthesising $Sr_2HoMn_2O_{7-\delta}$ and $Sr_2YMn_2O_{7-\delta}$, the potential coexistence of two very similar n = 2 RP phases in similar materials was known; therefore, care was taken to establish phase purity. This involved careful monitoring of the shape and the width of the 0010 Bragg peak, which would not split, should the symmetry be lower than tetragonal. The criteria used for classifying a sample as single phase, and therefore to continue characterisation by powder neutron diffraction, were when the FWHM of the 0010 reflection was $< 0.1^\circ$ (2θ) and when the complete pattern could be fitted using a single n=2 RP phase model in the Rietveld

analysis. Confirmation of n=2 RP phase purity by careful monitoring of this 0010 reflection was carried out using the synchrotron X-ray source at Station 2.3, Daresbury. The FWHM values reported for $Sr_2HoMn_2O_{7-\delta}$ and $Sr_2YMn_2O_{7-\delta}$, by fitting the 0010 reflections to a single pseudo-Voigt function, were 0.077(1)° and 0.086(1)°, respectively. In addition, a full X-ray powder diffraction pattern of $Sr_2HoMn_2O_{7-\delta}$ was collected at the SRS, with $\lambda = 1.400$ Å, $15 \leq 2\theta/^\circ \leq 100$ and step size $\Delta 2\theta = 0.01^\circ$.

Both samples were taken to the Institut Laue Langevin, Grenoble, loaded into cylindrical vanadium cans and measured on powder neutron diffractometers D1b ($\lambda = 2.520$Å, $5 \leq 2\theta/^\circ \leq 85$, $\Delta 2\theta = 0.2^\circ$) and D2b ($\lambda = 1.59412$Å, $5 \leq 2\theta/^\circ \leq 150$, $\Delta 2\theta = 0.05^\circ$). Data were collected in the temperature range $1.5 \leq T(K) \leq 293$ and analysed using the Rietveld method implemented through the GSAS software package. The following neutron scattering lengths were used: $b_{Sr} = 0.702$, $b_{Mn} = -0.373$, $b_{Ho} = 0.808$, $b_Y = 0.775$ and $b_O = 0.5805 \times 10^{-14}$m.

Data measuring magnetisation as a function of temperature were collected for both samples on a Quantum Design MPMS SQUID magnetometer. Data were collected as a function of temperature (between 5 and 300K) upon warming, after cooling the sample in zero field (ZFC) and after cooling in the measuring field (FC). A measuring field of 500G was used for each sample. All data measured as a function of field, for the Ho and Y samples, are presented elsewhere[13,14]. The details regarding magnetotransport experiments on the compounds $Sr_2HoMn_2O_{7-\delta}$ and $Sr_2YMn_2O_{7-\delta}$ are presented in Section 3.3.2.2.

Attempts to measure the mean oxidation state of Mn in the samples $Sr_2HoMn_2O_{7-\delta}$ and $Sr_2YMn_2O_{7-\delta}$ using successive iodometric titrations, yielded concordant and reproducible results[1]. The resulting values for the manganese oxidation states (OS) are given in Section 3.3.2.1 as a comparison with other members of the $Sr_2LnMn_2O_{7-\delta}$ series. Manganese oxidation states and oxygen concentrations are derived on the assumption that there are no manganese or 'A' cation site vacancies contributing to deviation from the expected oxidation state. A preferable method by which to study oxygen content is by thermogravimetric analysis (TGA); however, it did not prove possible to identify a fully reduced intermediate resulting from reduction of $Sr_2HoMn_2O_{7-\delta}$ and $Sr_2YMn_2O_{7-\delta}$ using either an Ar/H_2 mixture

[1] Ttitrations were carried out by the author and N. Kasmir.

or pure H_2. This provides an interesting contrast to the successful preparation of reduced Fe and Cu containing RP compounds, $Sr_3Fe_2O_{7-\delta}$[15] and $La_2SrCu_2O_6$[16].

3.2.2 Structural and magnetic characterisation of $Sr_2HoMn_2O_{7-\delta}$ and $Sr_2YMn_2O_{7-\delta}$

3.2.2.1 Powder neutron and powder X-ray diffraction study of $Sr_2HoMn_2O_{7-\delta}$

The observed and calculated neutron and X-ray diffraction profiles for $Sr_2HoMn_2O_{7-\delta}$ are shown in Figures 3.2.1 and 3.2.2, respectively. They are the result of a combined neutron/synchrotron X-ray refinement, enabling more precise modelling of Sr and Ho cation distributions over the 9 and 12 coordinate sites.

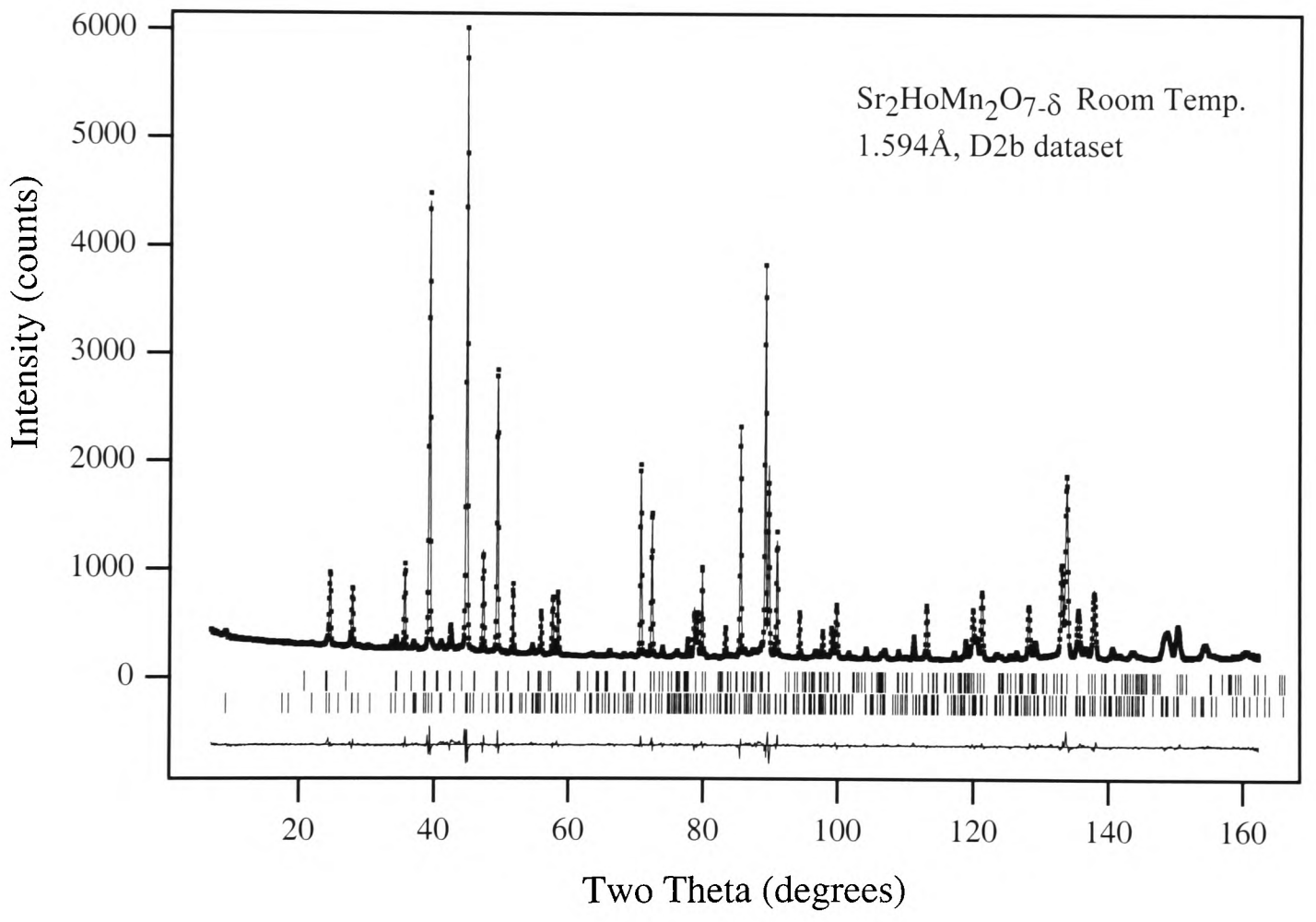


Figure 3.2.1 Observed (dots) and calculated (line) neutron powder diffraction profiles for $Sr_2HoMn_2O_{7-\delta}$ at room temperature. Upper and lower tick marks show minority and majority phases, respectively.

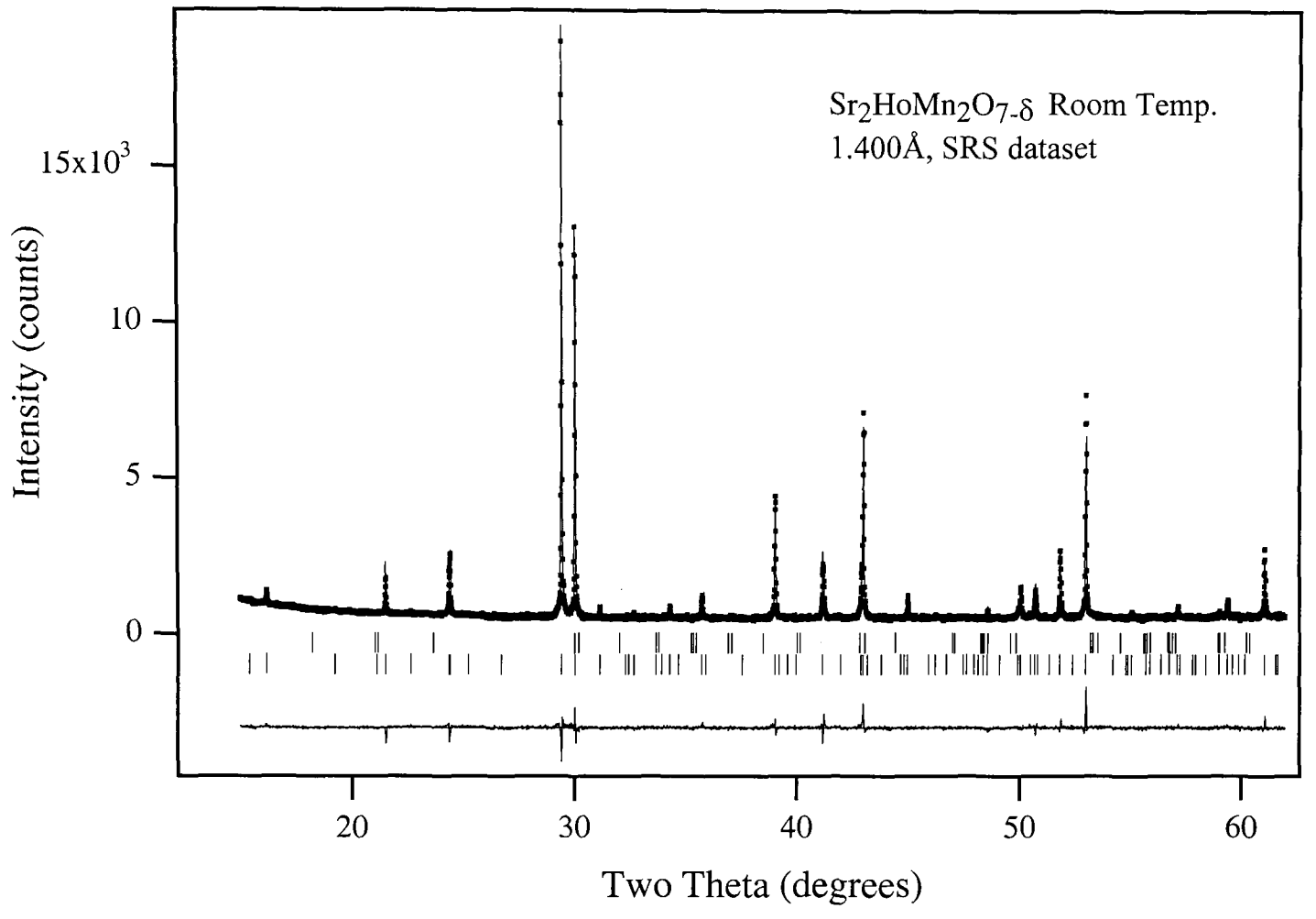


Figure 3.2.2 Observed (dots) and calculated (line) synchrotron X-ray powder diffraction profiles for $Sr_2HoMn_2O_{7-\delta}$ at room temperature. Upper and lower tick marks show minority and majority phases, respectively.

Figure 3.2.3 illustrates two sets of weak Bragg peaks in the neutron diffraction pattern for $Sr_2HoMn_2O_{7-\delta}$, which could not be indexed using the conventional *I4/mmm* cell.

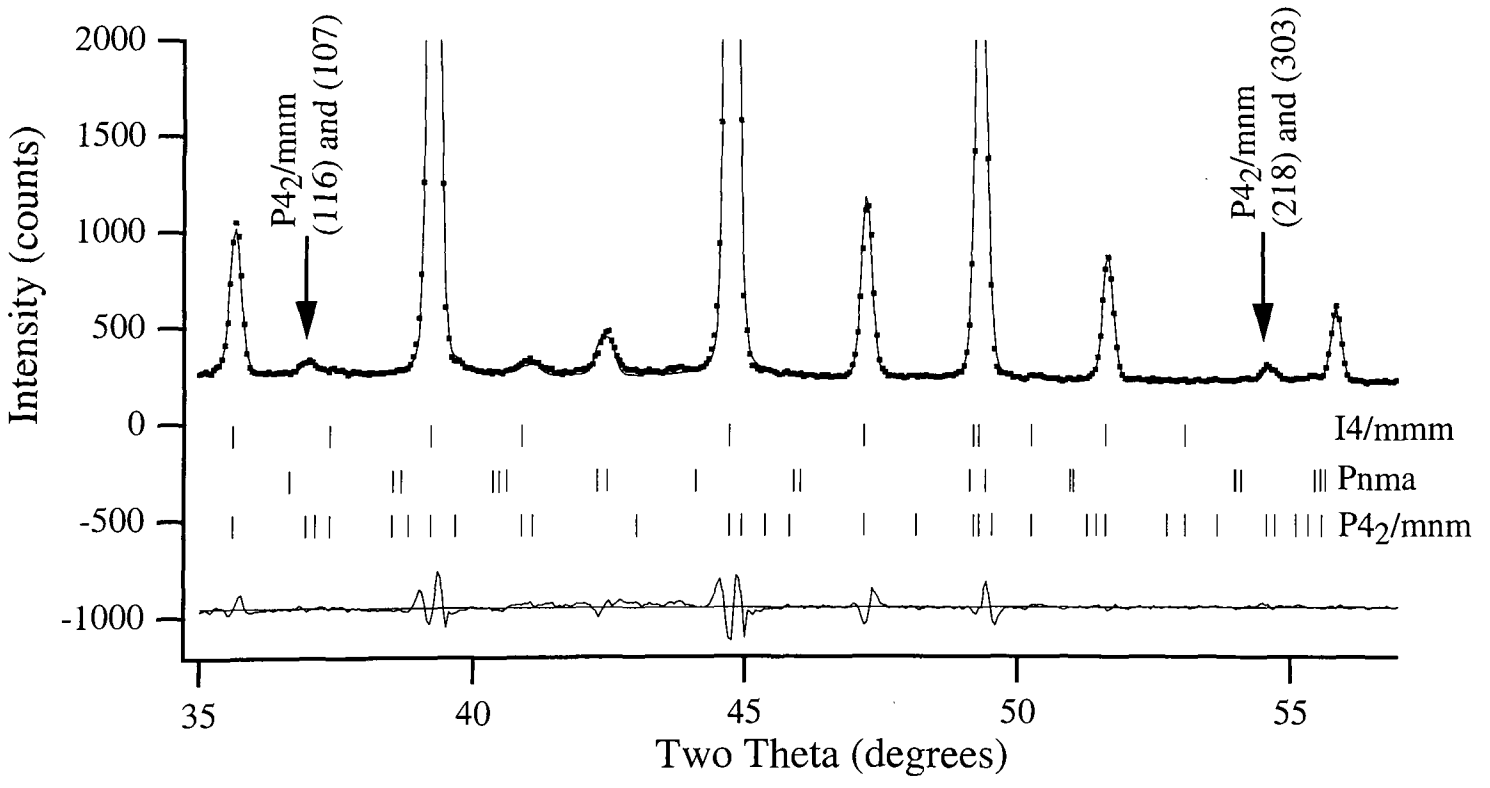


Figure 3.2.3 Enlarged view of angular region ($35 \leq 2\theta/^{\circ} \leq 57$) of the neutron diffraction profile for $Sr_2HoMn_2O_{7-\delta}$, in which tick marks for *I4/mmm*, *P4₂/mnm* and *Pnma* space groups are shown.

The presence of these additional reflections in the neutron diffraction profile, led to the modelling of $Sr_2HoMn_2O_{7-\delta}$ in the primitive tetragonal space group $P4_2/mnm$, rather than the body-centred tetragonal $I4/mmm$ cell used in a previous study[17]. The $P4_2/mnm$ model required a tetragonal unit cell of size (~5.4 by 19.9Å) for the majority, n = 2 RP phase. As shown by the upper tick marks in Figures 3.2.1 and 3.2.2, it was also necessary to include a minority phase, formulated as orthorhombic (*Pnma*) $Sr_{0.5}Ho_{0.5}MnO_3$ (cell dimensions ~5.4 x 7.8 x 5.4Å). The structural model was developed in conjunction with Dr J. Vente, and the combined neutron/synchrotron X-ray refinement converged, giving the following residual fit parameters: R_{wp} = 5.14%, R_p = 4.14%, DWd = 0.991 and χ^2_{red} = 3.841 for 84 variables.

Table 3.2.2 Structural parameters for biphasic $Sr_2HoMn_2O_{7-\delta}$ at room temperature:

Majority phase: 97.0(2)% $Sr_2HoMn_2O_{7-\delta}$ by weight

Lattice Parameters(Å) a = 5.40388(5); b = 5.40388(5); c = 19.90499(19); V = 581.265(16)Å^3

Atom	Site	Fraction (%)	x	y	z
Sr(1)[a]	4f	87.8(5)	0.2520(4)	0.2520(4)	0
Ho(2)[a]	4f	12.2(5)	0.2520(4)	0.2520(4)	0
Sr(3)[b]	8j	56.1(3)	0.2560(2)	0.2560(2)	0.18357(4)
Ho(4)[b]	8j	43.9(3)	0.2560(2)	0.2560(2)	0.18357(4)
Mn(5)	8j	100	0.2513(7)	0.2513(7)	0.40171(8)
O(6)	4g	100	0.2660(8)	0.2660(8)	0.5
O(7)	8j	100	0.2302(7)	0.2302(7)	0.2999(1)
O(8)	8h	100	0	0.5	0.1002(3)
O(9)	4e	100	0	0	0.1086(3)
O(10)	4e	100	0	0	0.4036(3)

Minority phase: 3.0(2) % $Sr_{0.5}Ho_{0.5}MnO_3$ by weight

Lattice Parameters(Å) a = 5.37694(45); b = 7.66696(90); c = 5.41007(53); V=223.029(28)Å^3

Atom	Site	U_{iso} (Å^2)	x	y	z
Sr(1)[c]	4c	0.0310(67)[d]	0.0283(58)	0.25	0.5276(39)
Ho(2)[c]	4c	0.0310(67)[d]	0.0283(58)	0.25	0.5276(39)
Mn(3)	4a	0.0180(84)	0	0	0
O(4)	4c	0.0291(127)	0.4700(100)	0.25	0.4656(98)
O(5)	8d	0.0159(48)	0.2520(123)	0.0268(27)	0.2353(68)

[a,b,c] Atomic coordinates of atoms sharing sites were constrained to be the same.

[d] Constrained to be the same

Table 3.2.3 Thermal parameters for $Sr_2HoMn_2O_{7-\delta}$ at room temperature:

Atom	U_{iso}, U_{eq}	U_{11} (Å^2)	U_{22} (Å^2)	U_{33} (Å^2)	U_{12} (Å^2)	U_{13}(Å^2)	U_{23} (Å^2)
Sr(1)	0.0075(3)[a]						
Ho(2)	0.0075(3)[a]						
Sr(3)	0.0084(2)[b]						
Ho(4)	0.0084(2)[b]						
Mn(5)	0.0010(2)						
O(6)	0.0142	0.0162(10)	0.0162(10)	0.0101(9)	-0.0021(48)	0.0000	0.0000
O(7)	0.0308	0.0305(10)	0.0305(10)	0.0314(10)	0.0055(37)	0.0063(10)	0.0063(10)
O(8)	0.0133	0.0048(20)	0.0106(22)	0.0244(20)	-0.0067(19)	0.0000	0.0000
O(9)	0.0257	0.0156(20)	0.0156(20)	0.0458(38)	0.0059(32)	0.0000	0.0000
O(10)	0.0930	0.0064(18)	0.0064(18)	0.0151(22)	0.0061(25)	0.0000	0.0000

[a,b] Constrained to be the same

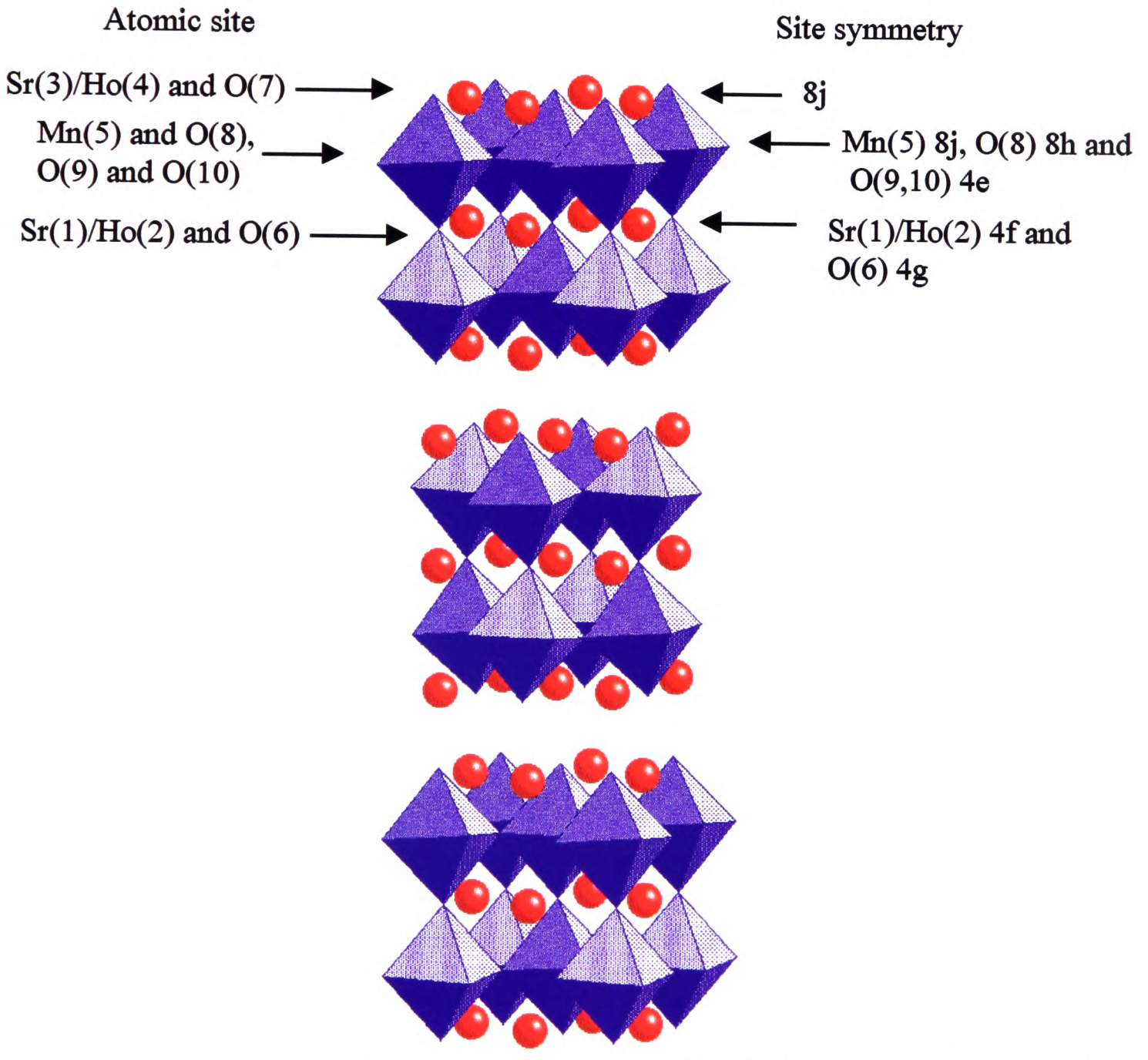
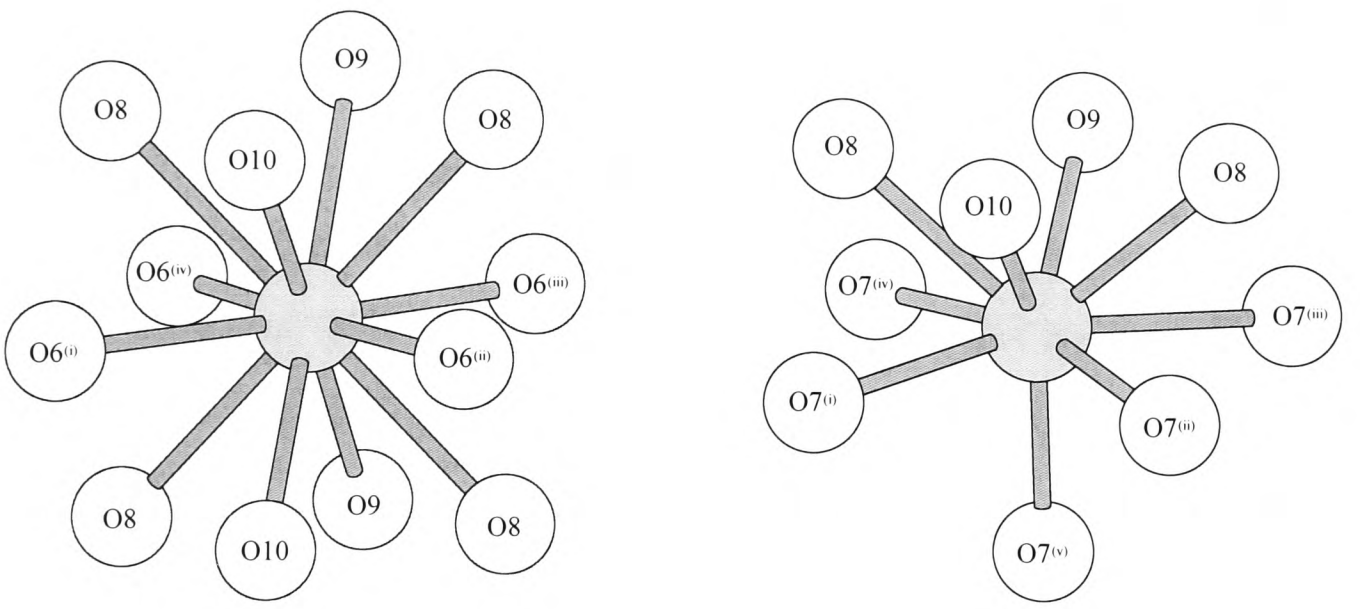


Figure 3.2.4 Polyhedral representation of the structure of $Sr_2HoMn_2O_{7-\delta}$, space group $P4_2/mnm$, in which the constituent atoms and corresponding site symmetries are labelled.

The atomic sites along with site symmetries for $Sr_2HoMn_2O_{7-\delta}$ are labelled in Figure 3.2.4. Figure 3.2.4 gives an equally accurate representation of the Y-containing phase (by replacing Ho(4) with Y(4)); however, in the Y-containing analogue, the Sr(1) site is not shared by Y cations. The presence of just one crystallographic Mn site disallows charge ordering in the *P4₂/mnm* model. Attempts to model the $Sr_2HoMn_2O_{7-\delta}$ (and $Sr_2YMn_2O_{7-\delta}$) data in orthorhombic and monoclinic space groups (which would permit charge ordering and yield distinct sites for Mn^{3+} and Mn^{4+}) failed to fit the observed profiles adequately.

The lowering of symmetry on moving to the space group *P4₂/mnm* yields a greater number of independent bondlengths around 9 and 12 coordinate A-cations. The respective 12 and 9 coordinate A-cation environments are illustrated in Figures 3.2.5.(a) and (b).



(a) (b)

Figure 3.2.5 (a) 12 coordinate Sr/Ho cation environment and (b) 9 coordinate Sr/Ho cation environment. The labelling of oxygen anions refers to bondlengths in Table 3.2.4.

The structural distortion and octahedral tilting in $Sr_2HoMn_2O_{7-\delta}$ occurs in order to satisfy the coordination requirements of the cations occupying the 9 coordinate, rocksalt site. Table 3.2.4 lists significant bond distances and angles for the majority, n = 2 RP phase in the compound $Sr_2HoMn_2O_{7-\delta}$. Comparison of Mn-O bondlengths reveals significant irregularity of MnO_6 octahedra in the Ho compound. The axial Mn-O(6) and Mn-O(7) bonds are significantly longer than the distances to equatorial O(8), O(9) and O(10) anions.

Table 3.2.4 Selected distances (Å) and angles (°) in $Sr_2HoMn_2O_{7-\delta}$ at room temperature:

Sr/Ho - O Bondlength (Å)[a]		Mn - O Bondlength (Å) or Bond Angle (°)		O - Mn - O Bond Angle (°)	
Sr(1) - O(6)$^{(i), (ii)}$	2.628(5)	Mn - O(6)	1.9595(18)	O(6) - Mn - O(7)	178.7(6)
Sr(1) - O(6)$^{(iii), (iv)}$	2.779(5)	Mn - O(7)	2.0317(28)	O(6) - Mn - O(8)	91.17(20)
Sr(1) - O(8) x 4	2.762(5)	Mn - O(8) x 2	1.9109(1)	O(6) - Mn - O(9)	92.9(4)
Sr(1) - O(9) x 2	2.897(6)	Mn - O(9)	1.912(6)	O(6) - Mn - O(10)	92.2(4)
Sr(1) - O(10) x 2	2.696(6)	Mn - O(10)	1.921(6)	O(7) - Mn - O(8)	88.83(20)
Sr(3) - O(7)$^{(i), (ii)}$	2.584(4)			O(7) - Mn - O(9)	88.3(4)
Sr(3) - O(7)$^{(iii), (iv)}$	2.861(4)	Mn - O(6) - Mn	173.4(6)	O(7) - Mn - O(10)	86.6(4)
Sr(3) - O(7)$^{(v)}$	2.3252(21)	Mn - O(8) - Mn	177.7(4)	O(8) - Mn - O(8)	177.6(4)
Sr(3) - O(8) x 2	2.531(4)	Mn - O(9) - Mn	167.6(5)	O(8) - Mn - O(9)	90.18(18)
Sr(3) - O(9)	2.460(5)	Mn - O(10) - Mn	177.7(4)	O(8) - Mn - O(10)	89.72(18)
Sr(3) - O(10)	2.547(5)			O(9) - Mn - O(10)	174.9(4)

[a] Although only Sr atoms are listed, Ho atoms share these sites in the proportions listed in Table 3.2.2.

Figure 3.2.6 illustrates the orientation of MnO_6 octahedra, viewed along a line almost parallel to the equatorial O(8)-Mn-O(8) bond in the *P4₂/mnm* cell, which best illustrates the oxide displacements leading to the deviation from the conventional *I4/mmm* cell.

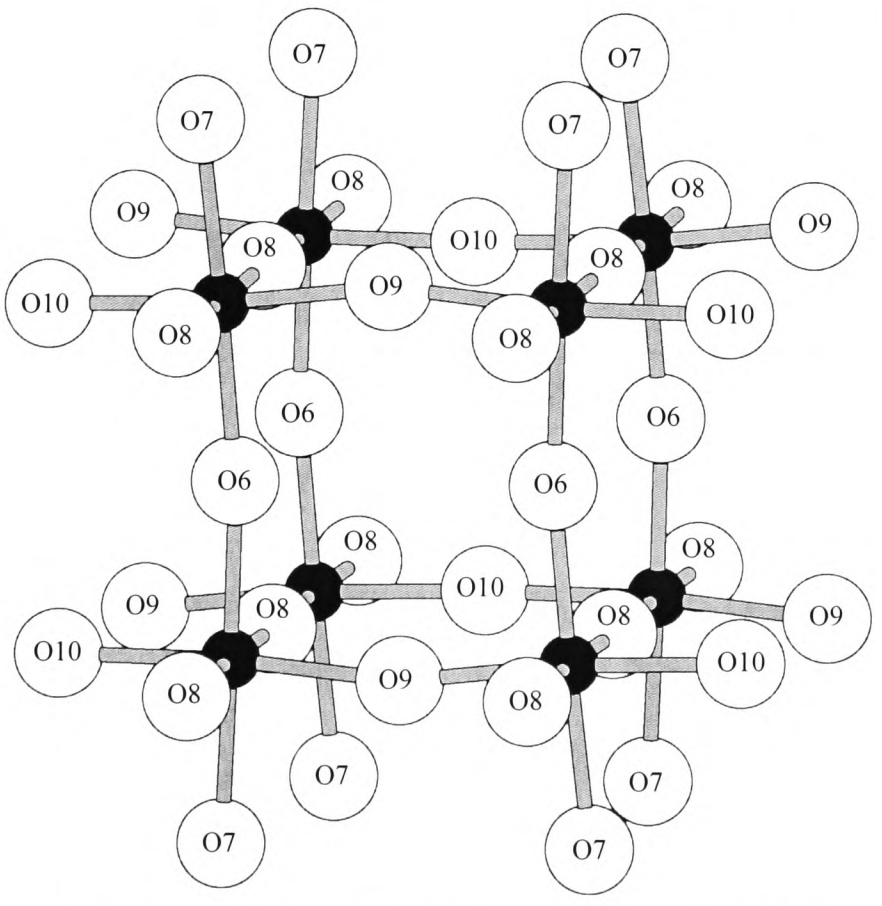


Figure 3.2.6 Representation of a bilayer of MnO_6 octahedra in $Sr_2HoMn_2O_{7-\delta}$, in which the structure is viewed along a line almost parallel to to the equatorial O(8)-Mn-O(8) bond.

As observed, there is considerable non-linearity in O-Mn-O bondlengths, and the number of independent Mn - O bondlengths allowed in the space group $P4_2/mnm$ is five, greater than the equivalent value of three in *I4/mmm*, arising from the reduction of point symmetry at the Mn site from *4mm* to *m*. The O(8)-Mn-O(8) tilt axis rotates by 90° between successive perovskite blocks, likening the nature of the structural distortion to that observed for low temperature $La_{1.875}Ba_{0.125}CuO_4$[18].

As was shown in Table 3.2.3, the best fit to the room temperature combined neutron (D2b) and X-ray (SRS) refinement for $Sr_2HoMn_2O_{7-\delta}$ involved the use of anisotropic temperature factors on the oxide sublattice. Figure 3.2.7 illustrates the enhanced motion of oxide anions using 99% thermal ellipsoids. Here $Sr_2HoMn_2O_{7-\delta}$ is shown in the same structural orientation as that in which it appears in Figure 3.2.6. For example, the structure is viewed along a direction almost parallel with the O(8)-Mn-O(8) bond. The enhanced motion of O(7) and O(9) is evident in particular, with significant displacements parallel to z in the case of O(9) (i.e. the displacement is perpendicular to the equatorial plane in it lies).

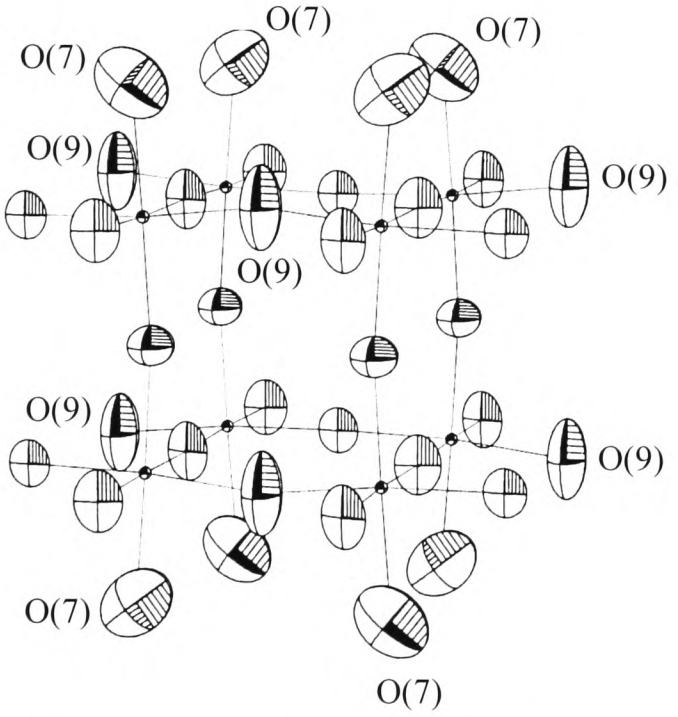


Figure 3.2.7 Representation of oxide sublattice as 99% thermal ellipsoids in room temperature $Sr_2HoMn_2O_{7-\delta}$. Certain oxygen atoms on O(7) and O(9) sites, showing enhanced motion, are labelled.

The observed and calculated neutron diffraction profile for $Sr_2HoMn_2O_{7-\delta}$ at 1.7K is shown in Figure 3.2.8.

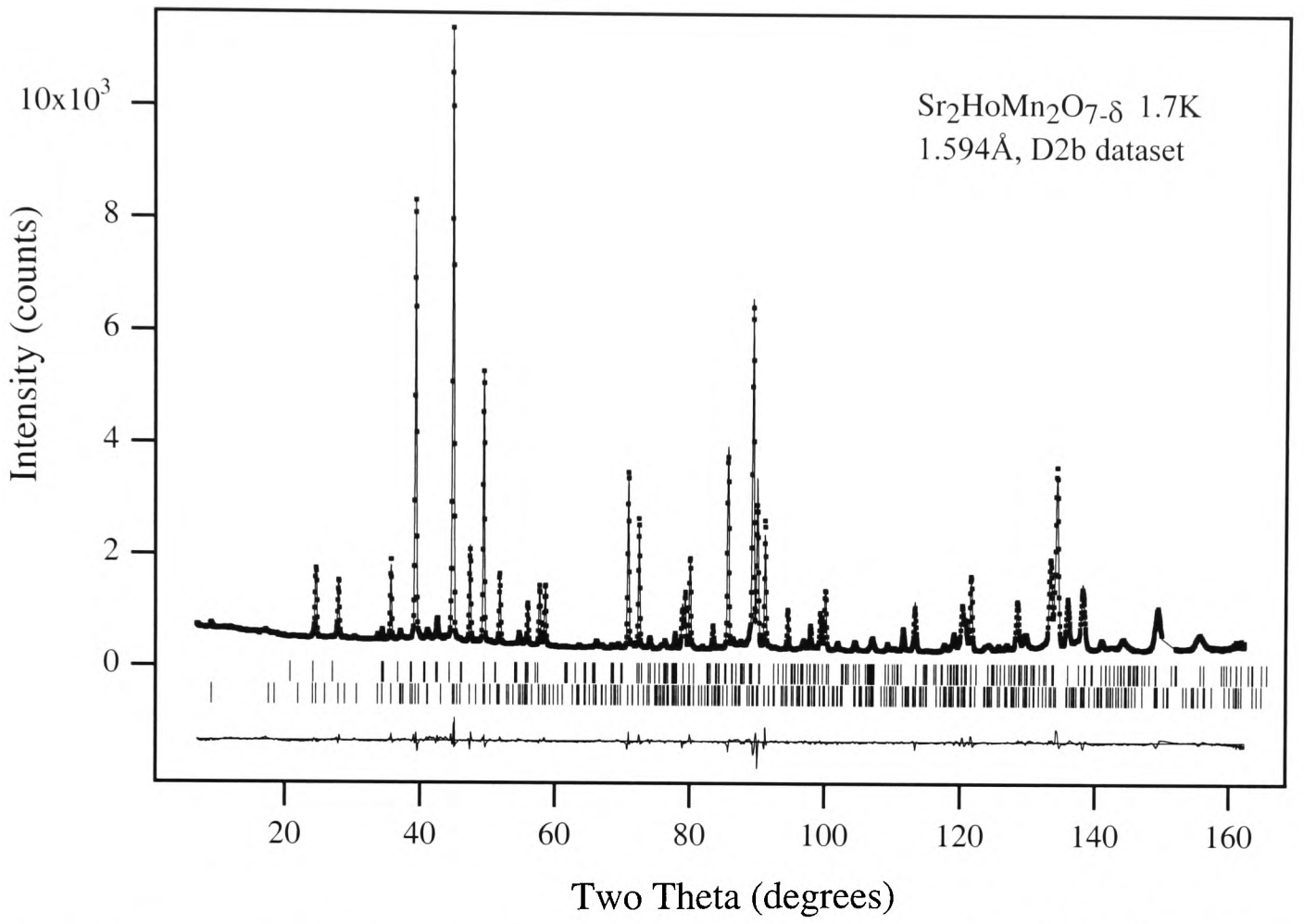


Figure 3.2.8 Observed (dots) and calculated (line) neutron powder diffraction profiles for $Sr_2HoMn_2O_{7-\delta}$ at 1.7K. Upper and lower tick marks show minority and majority phases.

Neutron diffraction data collected at 1.7K for $Sr_2HoMn_2O_{7-\delta}$ revealed no magnetic Bragg peaks, however, data collected on instrument D1b showed enhancement of diffuse scattering on reaching 2K, as shown in Figure 3.2.9:

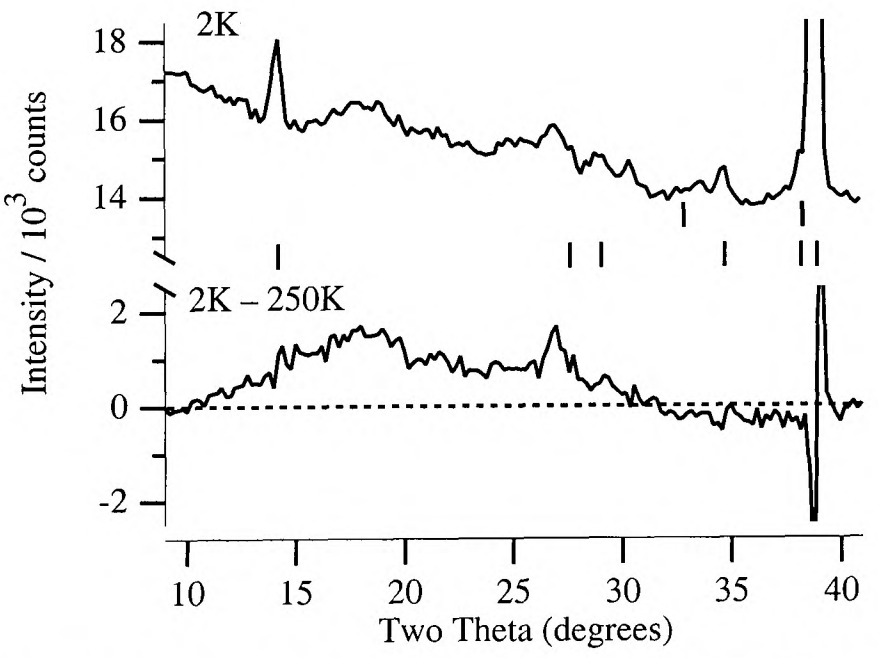


Figure 3.2.9 Enlarged view of angular region ($10 \leq 2\theta/^\circ \leq 40$) of the D1b neutron diffraction profile at 2K for $Sr_2HoMn_2O_{7-\delta}$. The result of the subtraction of the 250K intensity is also shown.

The enhancement of diffuse scattering in the angular region $15 \leq 2\theta/^\circ \leq 30$ suggests the presence of regions of correlated spins. The contribution to the low angle scattering by paramagnetic Ho cations, below $2\theta = 15^\circ$, is suggested as being responsible for the positive difference curve in the 2K - 250K subtraction. The refinement of neutron D2b data collected at 1.7K gave the following residual fit parameters: $R_{wp} = 4.29\%$, $R_p = 3.31\%$, DWd = 0.40 and $\chi^2_{red} = 9.272$ for 65 variables.

Table 3.2.5 Structural parameters for biphasic $Sr_2HoMn_2O_{7-\delta}$ at 1.7K:

Majority phase: 96.7(2)% $Sr_2HoMn_2O_{7-\delta}$ by weight

Lattice Parameters(Å) a = 5.39811(7); b = 5.39811(7); c = 19.85266(26); V = 578.498(20)Å^3

Atom	Site	Fraction (%)	x	y	z
Sr(1)[a]	4f	87.8(5)[c]	0.2533(4)	0.2533(4)	0
Ho(2)[a]	4f	12.2(5)[c]	0.2533(4)	0.2533(4)	0
Sr(3)[b]	8j	56.1(3)[c]	0.2580(2)	0.2580(2)	0.18348(7)
Ho(4)[b]	8j	43.9(3)[c]	0.2580(2)	0.2580(2)	0.18348(7)
Mn(5)	8j	100	0.2508(9)	0.2508(9)	0.4013(1)
O(6)	4g	100	0.2669(8)	0.2669(8)	0.5
O(7)	8j	100	0.2259(6)	0.2259(6)	0.2998(1)
O(8)	8h	100	0	0.5	0.0998(2)
O(9)	4e	100	0	0	0.1098(2)
O(10)	4e	100	0	0	0.4047(3)

Minority phase: 3.3(2) % $Sr_{1/2}Ho_{1/2}MnO_3$ by weight

Lattice Parameters(Å) a = 5.36620(90); b = 7.6250(19); c = 5.4110(10); V=221.406(63)Å^3

Atom	Site	U_{iso} (Å^2)	x	y	z
Sr(1)[d]	4c	0.0200(89)[e]	0.0173(111)	0.25	0.5394(65)
Ho(2)[d]	4c	0.0200(89)[e]	0.0173(111)	0.25	0.5394(65)
Mn(3)	4a	0.0707(235)	0	0	0
O(4)	4c	0.0117(14)	0.4787(131)	0.25	0.4770(82)
O(5)	8d	0.0243(82)	0.2722(69)	0.0275(36)	0.2333(101)

[a, b, d] Atomic coordinates were constrained to be the same for atoms sharing the same site.

[c] In the absence of complementary X-ray data, fractional occupancies of Sr and Ho cations were constrained at the values refined for the room temperature dataset.

[e] U_{isos} for atoms occupying the same site, were constrained to be the same.

Table 3.2.6 Thermal parameters for $Sr_2HoMn_2O_{7-\delta}$ at 1.7K:

Atom	U_{iso}, U_{eq}	U_{11} (Å^2)	U_{22} (Å^2)	U_{33} (Å^2)	U_{12} (Å^2)	U_{13}(Å^2)	U_{23} (Å^2)
Sr(1)	0.0034(3)[a]						
Ho(2)	0.0034(3)[a]						
Sr(3)	0.0045(2)[b]						
Ho(4)	0.0045(2)[b]						
Mn(5)	0.0003(3)						
O(6)	0.0139	0.0148(11)	0.0148(11)	0.0121(12)	-0.0032(44)	0.0000	0.0000
O(7)	0.0297	0.0298(13)	0.0298(13)	0.0294(12)	0.0045(34)	0.0085(11)	0.0085(11)
O(8)	0.0109	0.0031(19)	0.0087(22)	0.0208(20)	-0.0079(17)	0.0000	0.0000
O(9)	0.0154	0.0106(19)	0.0106(19)	0.0249(27)	-0.0059(28)	0.0000	0.0000
O(10)	0.0086	0.0088(19)	0.0088(19)	0.0079(20)	0.0047(23)	0.0000	0.0000

[a, b] Constrained to be the same

From comparison of Tables 3.2.3 and 3.2.6, it can be seen that thermal parameters (on the cation and anion sublattices) do not change appreciably on cooling between room temperature and 1.7K. Examination of the bond/angle data in Table 3.2.7 shows that there is also little change in structural parameters for the $Sr_2HoMn_2O_{7-\delta}$ phase on cooling to 1.7K.

Table 3.2.7 Selected distances (Å) and angles (°) in $Sr_2HoMn_2O_{7-\delta}$ at 1.7K:

Sr/Ho - O Bondlength (Å)[a]		Mn - O Bondlength (Å) or Bond Angle (°)		O - Mn - O Bond Angle (°)	
Sr(1) - O(6)$^{(i), (ii)}$	2.628(5)	Mn - O(6)	1.9631(26)	O(6) - Mn - O(7)	178.2(6)
Sr(1) - O(6)$^{(iii), (iv)}$	2.775(5)	Mn - O(7)	2.023(4)	O(6) - Mn - O(8)	90.73(21)
Sr(1) - O(8) x 4	2.752(4)	Mn - O(8) x 2	1.90868(9)	O(6) - Mn - O(9)	93.0(4)
Sr(1) - O(9) x 2	2.914(5)	Mn - O(9)	1.915(7)	O(6) - Mn - O(10)	91.6(4)
Sr(1) - O(10) x 2	2.669(5)	Mn - O(10)	1.916(7)	O(7) - Mn - O(8)	89.27(21)
Sr(3) - O(7)$^{(i), (ii)}$	2.5490(35)			O(7) - Mn - O(9)	88.8(4)
Sr(3) - O(7)$^{(iii), (iv)}$	2.892(4)	Mn - O(6) - Mn	172.8(7)	O(7) - Mn - O(10)	86.6(4)
Sr(3) - O(7)$^{(v)}$	2.3233(26)	Mn - O(8) - Mn	178.6(4)	O(8) - Mn - O(8)	178.5(4)
Sr(3) - O(8) x 2	2.530(4)	Mn - O(9) - Mn	166.8(4)	O(8) - Mn - O(9)	90.11(22)
Sr(3) - O(9)	2.453(4)	Mn - O(10) - Mn	175.9(4)	O(8) - Mn - O(10)	89.83(22)
Sr(3) - O(10)	2.545(5)			O(9) - Mn - O(10)	175.42(34

[a] Although only Sr atoms are listed, Ho atoms share these sites in the proportions listed in Table 3.2.5.

The agreement indices for the high and low temperature Rietveld refinements of $Sr_2HoMn_2O_{7-\delta}$ are encouraging, and suggest a realistic physical model has been found for the structure. The agreement parameters and refining variables at each temperature, are summarised below.

Table 3.2.8 Agreement parameters for the room temp. and 1.7K refinements of $Sr_2HoMn_2O_{7-\delta}$

Agreement parameter	Room Temperature			1.7K
	SRS 1.400Å	D2b 1.594Å	Total	D2b 1.594Å
R_{wp} (%)	6.24	3.97	5.14	4.29
R_p (%)	4.32	2.95	4.14	3.31
DWd	1.170	0.615	0.991	0.40
χ^2_{red}			3.841 (84 variables)	9.272 (65 variables)

Table 3.2.9 Refining variables for the room temp. and 1.7K refinements of $Sr_2HoMn_2O_{7-\delta}$

Refining variables (in addition to atomic coordinates, thermal parameters and fractional occupancies)	Room Temperature		1.7K
	SRS 1.400Å	D2b 1.594Å	D2b 1.594Å
Background terms (Shifted Chebyshev)	10	10	10
Profile Coefficients (pseudo-Voigt)[a]	5	4	5
Histogram scale factor	1	1	1
Wavelength (Å)	1		
Zero point		1	1

[a] Refining profile coefficients were constrained to be the same for the majority and minority phase.

3.2.2.2 Powder neutron diffraction study of $Sr_2YMn_2O_{7-\delta}$

The observed and calculated neutron diffraction profile for $Sr_2YMn_2O_{7-\delta}$ at 290K is shown in Figure 3.2.10.

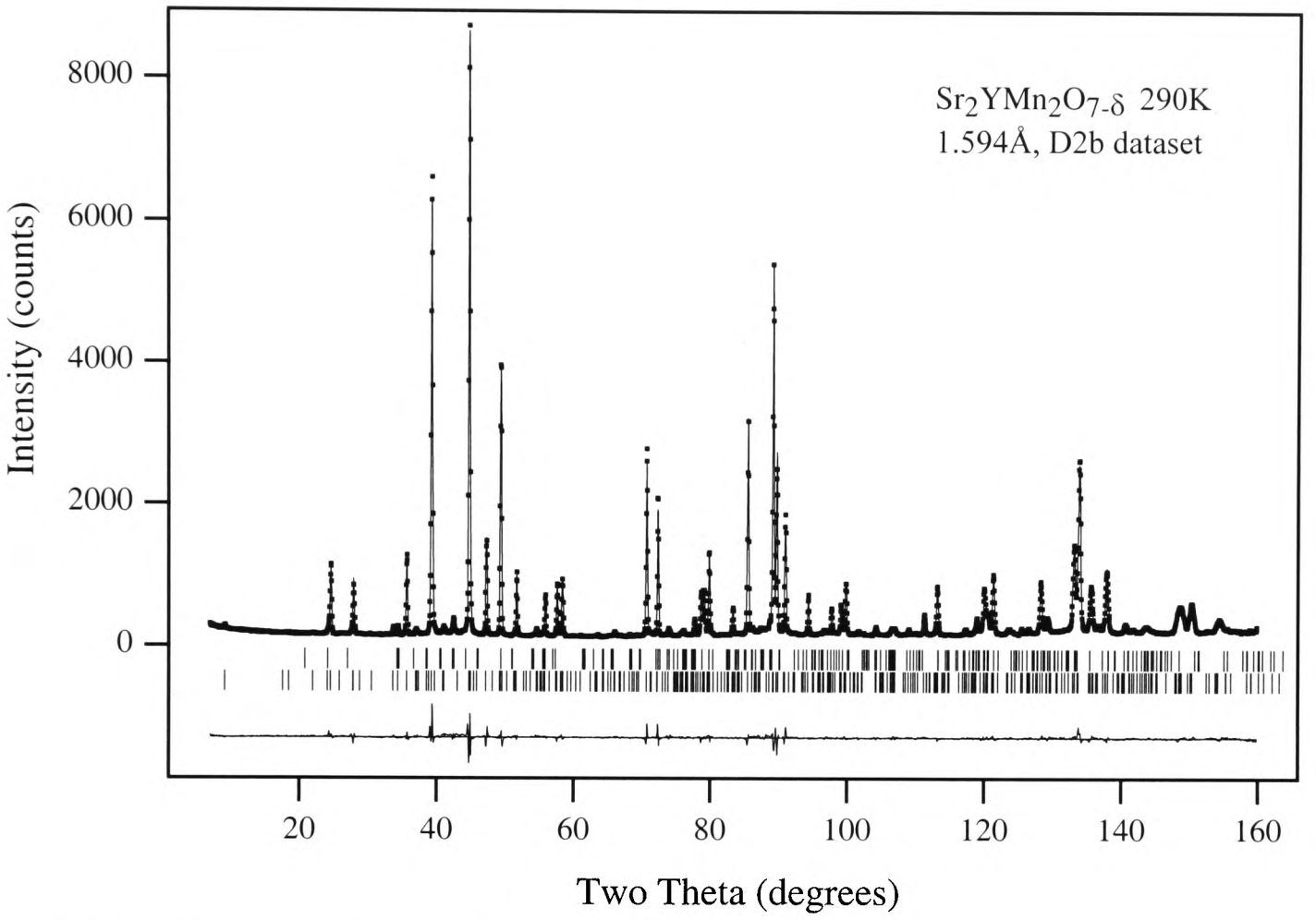


Figure 3.2.10 Observed (dots) and calculated (line) neutron powder diffraction profiles for $Sr_2YMn_2O_{7-\delta}$ at 290K. Upper and lower sets of tick marks represent minority and majority phases, respectively.

The Y sample was refined using the same structural model used to describe the Ho analogue, space group *$P4_2/mnm$*. The isoelectronic cations Sr^{2+} and Y^{3+} have similar neutron scattering lengths, therefore cation occupancies across the 9 and 12 coordinate sites were estimated for this sample. On the basis of the similar sizes of Ho^{3+} and Y^{3+} and the nature of cation ordering observed for the $Sr_2HoMn_2O_{7-\delta}$ compound, it was assumed that Y^{3+} cations in $Sr_2YMn_2O_{7-\delta}$ are located only on the 9 coordinate cation site, thereby occupying precisely half of these sites. Again, the inclusion of (~2% by weight) of perovskite $Sr_{0.5}Y_{0.5}MnO_3$ phase, space group *Pnma,* enhanced the overall quality of the fit. The refined fraction of this minority phase remained constant, on reducing the temperature to 1.7K. The fit to neutron diffraction data collected at 290K gave the following residual parameters: R_{wp} = 5.42%, R_p = 4.05%, DWd = 0.518 and χ^2_{red} = 6.954 for 65 variables.

Table 3.2.10 Structural parameters for biphasic $Sr_2YMn_2O_{7-\delta}$ at 290K:

Majority phase: 97.9(3)% $Sr_2YMn_2O_{7-\delta}$ by weight

Lattice Parameters(Å) a = 5.40456(6); b = 5.40456(6); c = 19.90536(24); V = 581.421(18)Å^3

Atom	Site	Fraction (%)	x	y	z
Sr(1)[a]	4f	100	0.2522(5)	0.2522(5)	0
Sr(3)[b]	8j	50	0.2554(3)	0.2554(3)	0.18377(7)
Y(4)[b,c]	8j	50	0.2554(3)	0.2554(3)	0.18377(7)
Mn(5)	8j	100	0.2511(10)	0.2511(10)	0.4015(1)
O(6)	4g	100	0.2641(9)	0.2641(9)	0.5
O(7)	8j	100	0.2304(8)	0.2304(8)	0.2998(1)
O(8)	8h	100	0	0.5	0.1002(4)
O(9)	4e	100	0	0	0.1074(5)
O(10)	4e	100	0	0	0.4039(4)

Minority phase: 2.1(3) % $Sr_{0.5}Y_{0.5}MnO_3$ by weight

Lattice Parameters(Å) a = 5.37762(79); b = 7.63521(162); c = 5.41794(84); V=222.457(55)Å^3

Atom	Site	U_{iso} (Å^2)	x	y	z
Sr(1)[b]	4c	0.0106(59)[d]	0.0197(7)	0.25	0.5371(44)
Y(2)[b]	4c	0.0106(59)[d]	0.0197(7)	0.25	0.5371(44)
Mn(3)	4a	-0.0030(77)	0	0	0
O(4)	4c	0.0037(83)	0.4572(76)	0.25	0.4719(68)
O(5)	8d	0.0209(72)	0.2604(102)	0.0367(29)	0.2331(87)

[a] The yttrium content on this site refined to zero hence Y(2) is not listed.

[b] Atomic coordinates of atoms sharing positions were constrained to be the same.

[c] The yttrium content was fixed at 50% on the 8j site.

[d] U_{isos} for atoms occupying the same site, were constrained to be the same.

As was observed in the Ho-containing compound, refinement of the anion sublattice using anisotropic thermal parameters improved the quality of the fit for $Sr_2YMn_2O_{7-\delta}$. The resulting (isotropic) cation thermal parameters and anisotropic oxygen values are given in Table 3.2.11 below.

Table 3.2.11 Thermal parameters for $Sr_2YMn_2O_{7-\delta}$ at 290K:

Atom	U_{iso}, U_{eq}	U_{11} (Å^2)	U_{22} (Å^2)	U_{33} (Å^2)	U_{12} (Å^2)	U_{13}(Å^2)	U_{23} (Å^2)
Sr(1)	0.0064(3)						
Sr(3)	0.0088(2)[a]						
Y(4)	0.0088(2)[a]						
Mn(5)	0.0022(3)						
O(6)	0.0153	0.0175(11)	0.0175(11)	0.0107(11)	0.0053(57)	0.0000	0.0000
O(7)	0.0328	0.0332(12)	0.0332(12)	0.0318(12)	0.0044(48)	0.0061(11)	0.0061(11)
O(8)	0.0147	0.0106(25)	0.0068(25)	0.0267(27)	-0.0065(21)	0.0000	0.0000
O(9)	0.0236	0.0105(21)	0.0105(21)	0.0498(47)	-0.0010(33)	0.0000	0.0000
O(10)	0.0108	0.0100(21)	0.0100(21)	0.0123(26)	0.0024(27)	0.0000	0.0000

[a] Constrained to be the same

The equivalent bond angles and distances that were tabulated for $Sr_2HoMn_2O_{7-\delta}$ are shown below for the Y analogue. The irregularity of MnO_6 octahedra in $Sr_2YMn_2O_{7-\delta}$ mirrors that observed in the Ho analogue. This is illustrated by the enlarged axial Mn-O(6) and Mn -O(7) bondlengths in comparison to the distances to the equatorial O(8), O(9) and O(10) anions. Labelling of all cations and anions follows the scheme introduced for the Ho analogue, as described in Figures 3.2.4 to 3.2.6.

Table 3.2.12 Selected distances (Å) and angles (°) in $Sr_2YMn_2O_{7-\delta}$ at 290K:

Sr/Y - O Bondlength (Å)[a]		Mn - O Bondlength (Å) or Bond Angle (°)		O - Mn - O Bond Angle (°)	
Sr(1) - O(6)$^{(i),(ii)}$	2.639(6)	Mn - O(6)	1.9619(25)	O(6) - Mn - O(7)	178.4(7)
Sr(1) - O(6)$^{(iii),(iv)}$	2.768(6)	Mn - O(7)	2.030(4)	O(6) - Mn - O(8)	91.07(28)
Sr(1) - O(8) x 4	2.762(6)	Mn - O(8) x 2	1.91114(17)	O(6) - Mn - O(9)	92.5(5)
Sr(1) - O(9) x 2	2.879(8)	Mn - O(9)	1.910(8)	O(6) - Mn - O(10)	91.5(4)
Sr(1) - O(10) x 2	2.691(7)	Mn - O(10)	1.920(8)	O(7) - Mn - O(8)	88.93(28)
Sr(3) - O(7)$^{(i),(ii)}$	2.589(4)			O(7) - Mn - O(9)	89.1(5)
Sr(3) - O(7)$^{(iii),(iv)}$	2.857(4)	Mn - O(6) - Mn	174.2(8)	O(7) - Mn - O(10)	87.0(5)
Sr(3) - O(7)$^{(v)}$	2.3189(26)	Mn - O(8) - Mn	177.9(6)	O(8) - Mn - O(8)	177.8(5)
Sr(3) - O(8) x 2	2.534(6)	Mn - O(9) - Mn	169.3(6)	O(8) - Mn - O(9)	90.17(24)
Sr(3) - O(9)	2.474(7)	Mn - O(10) - Mn	177.1(5)	O(8) - Mn - O(10)	89.76(24)
Sr(3) - O(10)	2.559(6)			O(9) - Mn - O(10)	176.1(5)

[a] Although only Sr atoms are listed, Y shares the Sr(3) site in a 1:1 ratio.

The observed and calculated neutron diffraction profile for $Sr_2YMn_2O_{7-\delta}$ from data collected on D2b at 1.7K is shown in Figure 3.2.11.

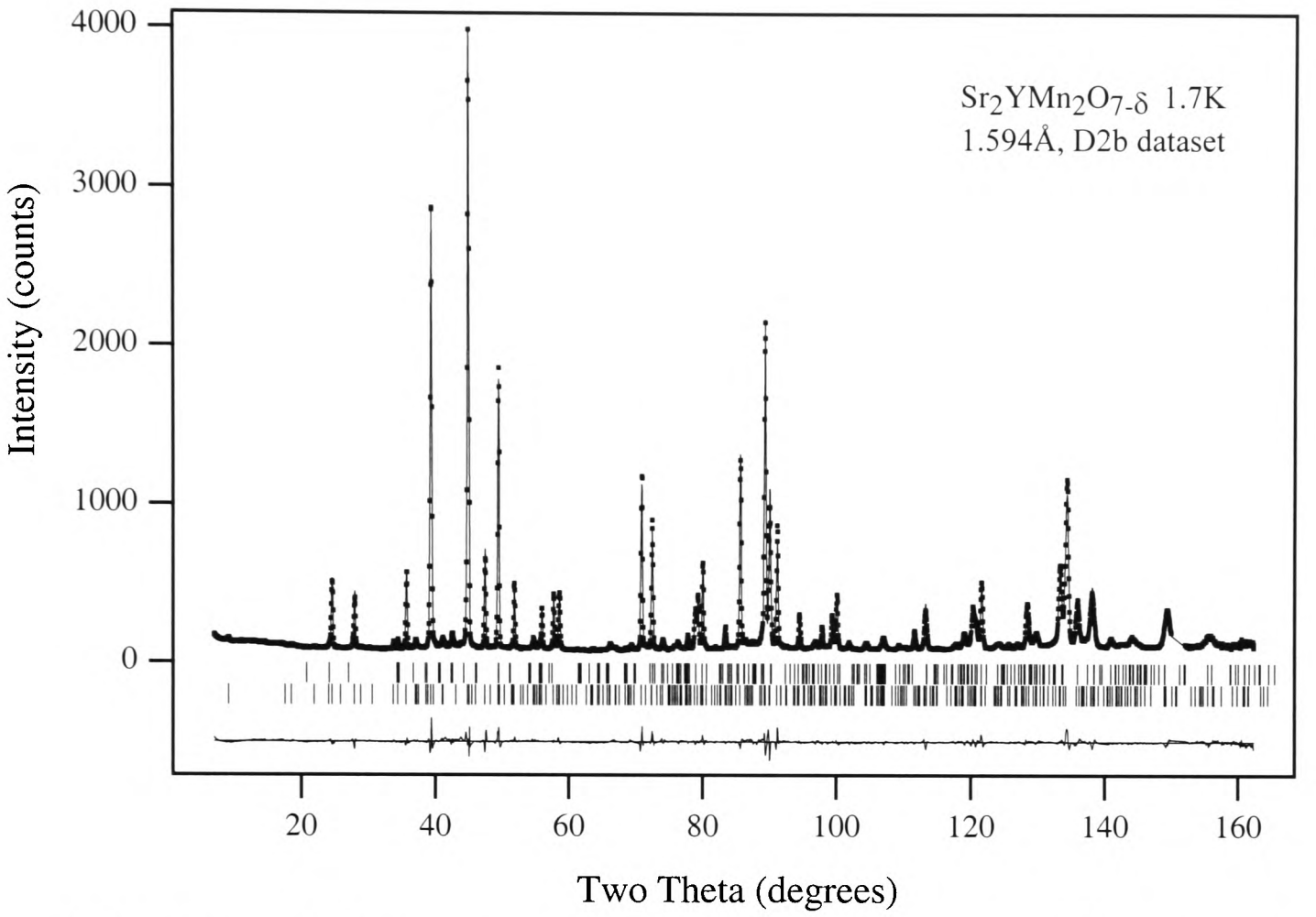


Figure 3.2.11 Observed (dots) and calculated (line) neutron powder diffraction profiles for $Sr_2YMn_2O_{7-\delta}$ at 1.7K. Upper and lower tick marks show minority and majority phases, respectively.

As for the $Sr_2HoMn_2O_{7-\delta}$ analogue, Figure 3.2.12 shows evidence of diffuse scattering suggestive of short range spin ordering in $Sr_2YMn_2O_{7-\delta}$.

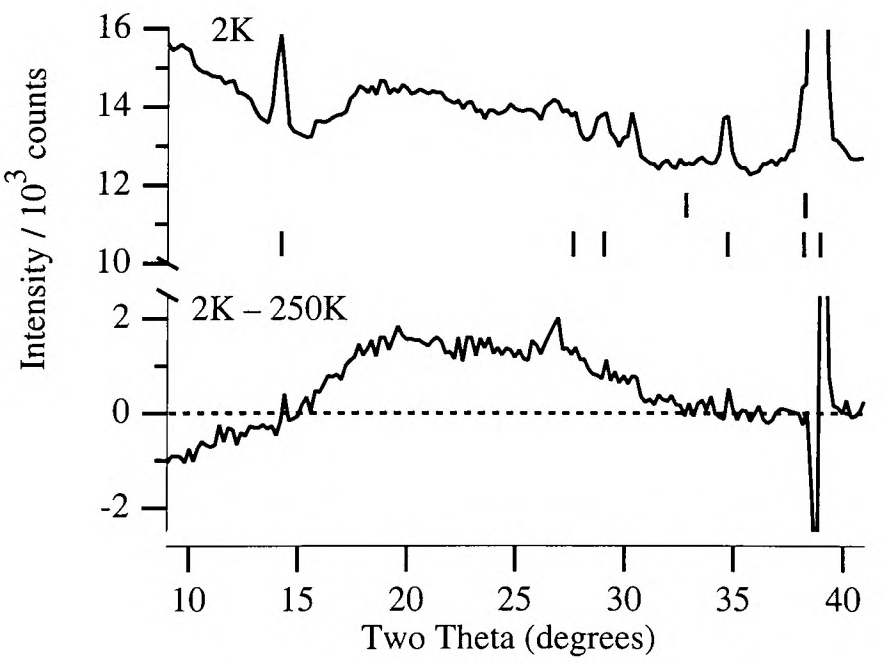


Figure 3.2.12 Enlarged view of angular region ($10 \leq 2\theta/^\circ \leq 40$) of the D1b neutron diffraction profile at 2K for $Sr_2YMn_2O_{7-\delta}$. The result of subtracting the 250K intensity is also shown.

The fit to neutron diffraction data collected on D2b at 1.7K gave the following residual parameters: R_{wp} = 5.69%, R_p = 4.43%, DWd = 0.423 and χ^2_{red} = 4.682 for 65 variables.

Table 3.2.13 Structural parameters for biphasic $Sr_2YMn_2O_{7-\delta}$ at 1.7K:

Majority phase: 98.0(3)% $Sr_2YMn_2O_{7-\delta}$ by weight

Lattice Parameters(Å) a = 5.40009(8); b = 5.40009(8); c = 19.84883(32); V = 578.812(24)Å^3

Atom	Site	Fraction (%)	x	y	z
Sr(1)[a]	4f	100	0.2530(5)	0.2530(5)	0
Sr(3)[b]	8j	50	0.2576(3)	0.2576(3)	0.18355(9)
Y(4)[b, c]	8j	50	0.2576(3)	0.2576(3)	0.18355(9)
Mn(5)	8j	100	0.2502(11)	0.2502(11)	0.4014(1)
O(6)	4g	100	0.2662(9)	0.2662(9)	0.5
O(7)	8j	100	0.2265(7)	0.2265(7)	0.3000(1)
O(8)	8h	100	0	0.5	0.1000(4)
O(9)	4e	100	0	0	0.1082(4)
O(10)	4e	100	0	0	0.4054(4)

Minority phase: 2.0(3) % $Sr_{1/2}Y_{1/2}MnO_3$ by weight

Lattice Parameters(Å) a = 5.3665(10); b = 7.6268(21); c = 5.4146(10); V=221.617(71)Å^3

Atom	Site	U_{iso} (Å^2)	x	y	z
Sr(1)[b]	4c	0.0021(69)[d]	0.0072(84)	0.25	0.5351(57)
Y(2)[b]	4c	0.0021(69)[d]	0.0072(84)	0.25	0.5351(57)
Mn(3)	4a	0.0151(130)	0	0	0
O(4)	4c	-0.0096(73)	0.4683(76)	0.25	0.4660(71)
O(5)	8d	0.0221(91)	0.2649(112)	0.0322(36)	0.2543(203)

[a] The yttrium content on this site refined to zero hence Y(2) is not listed.

[b] Atomic coordinates of atoms sharing positions were constrained to be the same.

[c] The yttrium content was fixed at 50% on the 8j site.

[d] U_{isos} for atoms occupying the same site, were constrained to be the same.

Table 3.2.14 Thermal parameters for $Sr_2YMn_2O_{7-\delta}$ at 1.7K:

Atom	U_{iso}, U_{eq}	U_{11} (Å^2)	U_{22} (Å^2)	U_{33} (Å^2)	U_{12} (Å^2)	U_{13}(Å^2)	U_{23} (Å^2)
Sr(1)	0.0041(4)						
Sr(3)	0.0075(3)[a]						
Y(4)	0.0075(3)[a]						
Mn(5)	0.0019(3)						
O(6)	0.0139	0.0176(13)	0.0176(13)	0.0144(14)	-0.0028(55)	0.0000	0.0000
O(7)	0.0297	0.0313(15)	0.0313(15)	0.0291(14)	0.0066(41)	0.0062(13)	0.0062(13)
O(8)	0.0109	0.0074(26)	0.0080(26)	0.0251(29)	-0.0064(23)	0.0000	0.0000
O(9)	0.0154	0.0069(22)	0.0069(22)	0.0293(38)	-0.0061(34)	0.0000	0.0000
O(10)	0.0086	0.0126(25)	0.0126(25)	0.0090(28)	0.0040(30)	0.0000	0.0000

[a] Constrained to be the same

Significant bond distances and bond angles are shown in Table 3.2.15. As for the $Sr_2HoMn_2O_{7-\delta}$ phase, few structural changes are brought about by the decrease in temperature to 1.7K, as evidenced by comparison with the 290K bond/angle data given in Table 3.2.12. Again, thermal parameters (on the cation and anion sublattices) do not change appreciably on cooling either.

Table 3.2.15 Selected distances (Å) and angles (°) in $Sr_2YMn_2O_{7-\delta}$ at 1.7K:

Sr/Y - O Bondlength (Å)[a]		Mn - O Bondlength (Å) or Bond Angle (°)		O - Mn - O Bond Angle (°)	
Sr(1) - O(6)$^{(i),(ii)}$	2.631(6)	Mn - O(6)	1.9598(32)	O(6) - Mn - O(7)	178.4(7)
Sr(1) - O(6)$^{(iii),(iv)}$	2.773(6)	Mn - O(7)	2.021(4)	O(6) - Mn - O(8)	90.89(31)
Sr(1) - O(8) x 4	2.755(6)	Mn - O(8) x 2	1.9094(1)	O(6) - Mn - O(9)	92.2(5)
Sr(1) - O(9) x 2	2.890(8)	Mn - O(9)	1.917(9)	O(6) - Mn - O(10)	91.2(5)
Sr(1) - O(10) x 2	2.661(7)	Mn - O(10)	1.913(9)	O(7) - Mn - O(8)	89.11(31)
Sr(3) - O(7)$^{(i),(ii)}$	2.554(4)			O(7) - Mn - O(9)	89.4(5)
Sr(3) - O(7)$^{(iii),(iv)}$	2.888(4)	Mn - O(6) - Mn	172.8(8)	O(7) - Mn - O(10)	87.2(5)
Sr(3) - O(7)$^{(v)}$	2.3240(30)	Mn - O(8) - Mn	178.2(6)	O(8) - Mn - O(8)	178.2(6)
Sr(3) - O(8) x 2	2.529(6)	Mn - O(9) - Mn	168.5(6)	O(8) - Mn - O(9)	89.97(26)
Sr(3) - O(9)	2.471(6)	Mn - O(10) - Mn	175.3(5)	O(8) - Mn - O(10)	89.97(26)
Sr(3) - O(10)	2.558(7)			O(9) - Mn - O(10)	176.6(5)

[a] Although only Sr atoms are listed, Y atoms share the Sr(3) site in a 1:1 ratio.

As for the Ho analogue, the agreement indices for the high and low temperature D2b refinements of $Sr_2YMn_2O_{7-\delta}$ are encouraging and suggest a physically realistic model has been found for the structure.

Table 3.2.16 Agreement parameters for the 290 and 1.7K refinements of $Sr_2YMn_2O_{7-\delta}$:

Agreement parameter	Room Temperature D2b 1.594Å	1.7K D2b 1.594Å
R_{wp} (%)	5.42	5.69
R_p (%)	4.05	4.43
DWd	0.518	0.423
χ^2_{red}	6.954 (65 variables)	4.682 (65 variables)

Table 3.2.17 Refining variables for the 290 and 1.7K refinements of $Sr_2YMn_2O_{7-\delta}$:

Refining variables (in addition to atomic coordinates, thermal parameters and fractional occupancies)	Room Temperature D2b 1.594Å	1.7K D2b 1.594Å
Background terms (Shifted Chebyshev)	10	10
Profile Coefficients (pseudo-Voigt)[a]	5	5
Histogram scale factor	1	1
Zero point	1	1

[a] Refining profile coefficients were constrained to be the same for the majority and minority phase each time.

3.2.2.3 SQUID magnetometry measurements

Figures 3.2.13 and 3.2.14 show molar magnetic susceptibility as a function of temperature for the samples $Sr_2HoMn_2O_{7-\delta}$ and $Sr_2YMn_2O_{7-\delta}$, respectively.

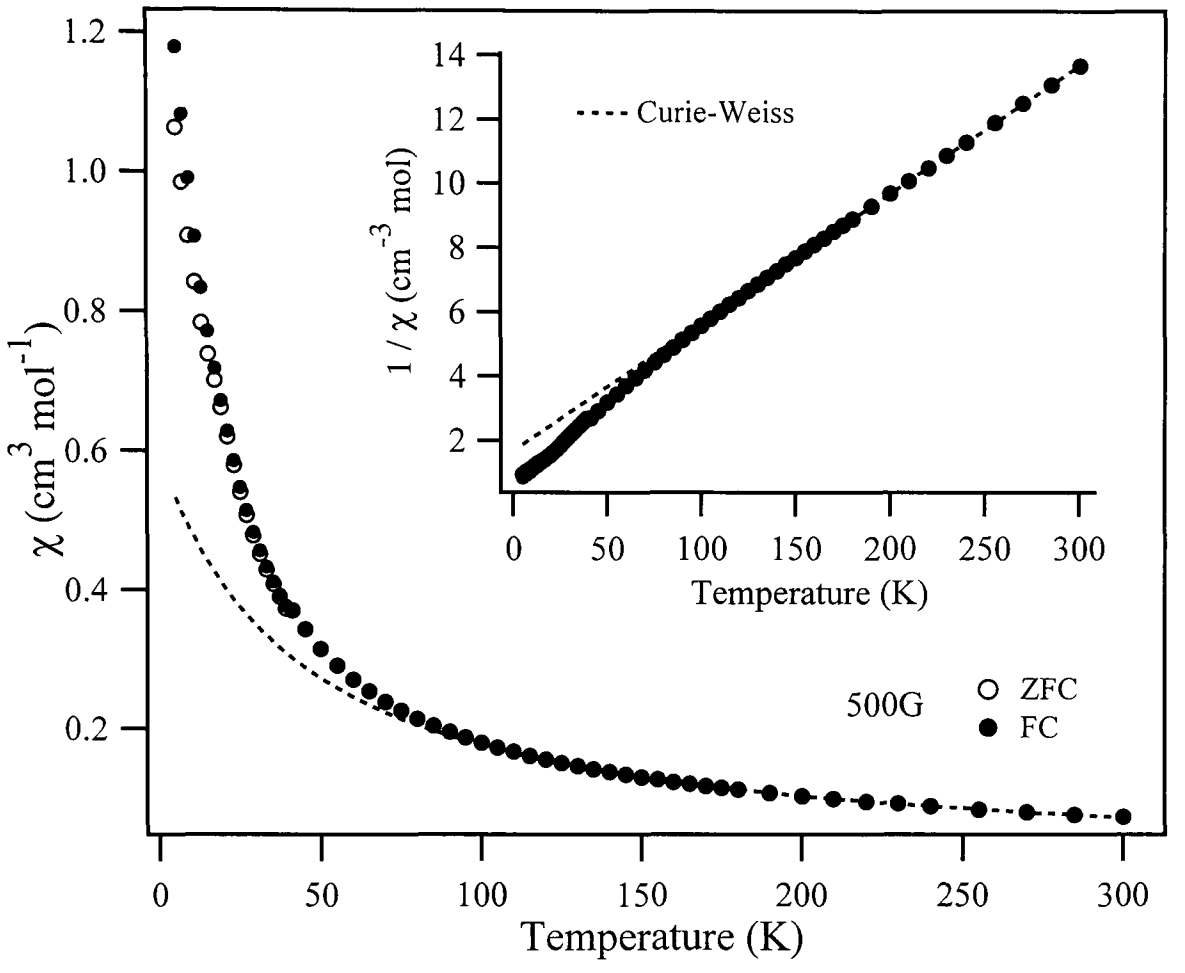


Figure 3.2.13 Molar magnetic susceptibility as a function of temperature for $Sr_2HoMn_2O_{7-\delta}$ at 500G, with an inset showing a fit of high temperature data to the Curie-Weiss law.

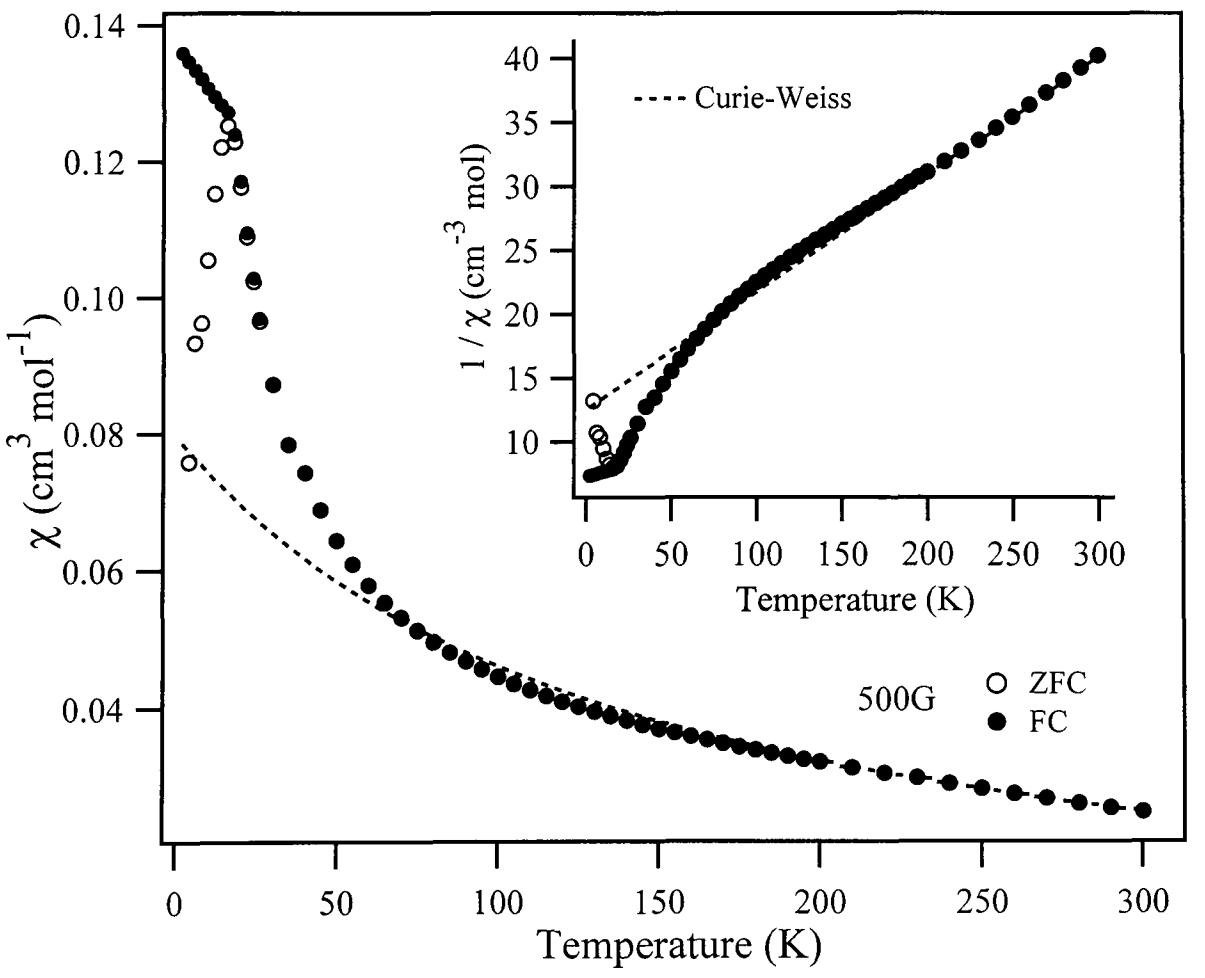


Figure 3.2.14 Molar magnetic susceptibility as a function of temperature for $Sr_2YMn_2O_{7-\delta}$ at 500G, with an inset showing a fit of high temperature data to the Curie-Weiss law.

The application of the Curie-Weiss model in the higher temperature range for each sample gave convincing fits; however, the fit applied over a wider temperature range for the Ho sample, 100-300K, as compared with 240-300K for the Y sample. Table 3.2.18 summarises the Curie-Weiss parameters obtained for each sample.

Table 3.2.18 Curie-Weiss parameters for compounds $Sr_2HoMn_2O_{7-\delta}$ and $Sr_2YMn_2O_{7-\delta}$:

Compound	Curie-Weiss range (K)	μ_{calc} / μ_B	μ_{obs} / μ_B	θ (K)	T_F (500G)
$Sr_2HoMn_2O_{7-\delta}$	100-300	12.3	13.4(2)	-33.4(7)	15
$Sr_2YMn_2O_{7-\delta}$	240-300	6.2	6.6(2)	+8(5)	17

The observed magnetic moments agree fairly well with those calculated on the basis of a simple, non-interacting ion model. The Weiss constants suggest that neither ferromagnetic nor antiferromagnetic long range interactions dominate in the temperature region where cooperative magnetic interactions exist. Low temperature, low angle data collected for $Sr_2HoMn_2O_{7-\delta}$ on instrument D1b suggest that the Ho sublattice remains paramagnetic down to 2K, dominating the low angle scattering in the neutron diffraction study. This is supported by only a marginal divergence between ZFC and FC curves for $Sr_2HoMn_2O_{7-\delta}$, as the paramagnetic signal from Ho^{3+} is retained down to the lowest measuring temperature. In contrast, there is a clear transition observed at 17K in $Sr_2YMn_2O_{7-\delta}$ with no equivalent paramagnetic tail, due to the presence of diamagnetic Y^{3+}. In summary, the temperature dependent SQUID magnetometry studies on $Sr_2HoMn_2O_{7-\delta}$ and $Sr_2YMn_2O_{7-\delta}$ are suggested as indicating spin glass behaviour for each sample. The freezing temperatures are assigned as 15K for the Ho sample and 17K for the Y sample. The spin glass freezing of the manganese moments arises from competing exchange interactions and disorder in the spatial location of Mn^{3+} and Mn^{4+} (and of Ln(Y)/Sr on the rocksalt site).

3.2.3 Discussion

The formation of single n = 2 RP phases in the Ho and Y compounds (albeit with contamination by a small amount (~ 3% by weight) of n = ∞ material) is consistent with the results of a previous study by Battle et al.[17]. In this study, it was found that single phase behaviour was exhibited in samples containing rare earths smaller than Tb. Oxide anion displacements detected in the current neutron diffraction study of $Sr_2HoMn_2O_{7-\delta}$ and $Sr_2YMn_2O_{7-\delta}$ required modelling the compounds using a primitive tetragonal unit cell in which $a \sim \sqrt{2}\, a_x$,, $c \sim c_x$ (where a_x and c_x are the unit cell parameters of the ideal, body-centred RP unit cell). Such subtle displacements of the oxide sublattice were masked in previous X-ray studies, as a result of the insensitivity of X-rays to the positions of light oxide anions.

The absence of long range magnetic order in both Ho and Y compounds is consistent with the lack of magnetic Bragg peaks in the 1.7K neutron diffraction patterns and is in contrast with the antiferromagnetic (majority) phase detected in the $Sr_2NdMn_2O_{7-\delta}$ compound at the same doping level[1]. However, on closer examination of the diffuse scattering in the region $15 \leq 2\theta/^\circ \leq 30$ in the Ho and Y phases, it is apparent that the diffuse maximum is centred at a 2θ value close to that where the 003 reflection (a magnetic Bragg peak signifying AFM order in $Sr_2NdMn_2O_{7-\delta}$) would occur. Thus, the short range magnetic order shows some similarity with the long range order detected in the Nd compound. Continuing the comparison with $Sr_2NdMn_2O_{7-\delta}$, introduction of the smaller Ho and Y cations, causes a reduction in the unit cell volume per formula unit. However, this reduction is anisotropic, largely due to the high degree of cation ordering in the latter phases and the flexibility in the n = 2 tetragonal systems for the apical Mn - O bonds to extend into the rocksalt layer.

The extent of cation ordering in the Ho and Y phases is reflected by the increase in the mean bondlength of the 12 coordinate site which has enhanced occupancy by the large Sr^{2+} in the latter compounds, compared to $Sr_2NdMn_2O_{7-\delta}$. The mean Sr/Ln - O bondlengths are, respectively, 2.712(3)Å for the majority phase of $Sr_2NdMn_2O_{7-\delta}$, and 2.754(1)Å in $Sr_2HoMn_2O_{7-\delta}$, despite the lower cationic radius of Ho^{3+} as compared to Nd^{3+}. The elongation parallel to z in $Sr_2HoMn_2O_{7-\delta}$ and $Sr_2YMn_2O_{7-\delta}$ enhances interatomic electron-electron interactions within the xy plane, relative to those along z, and accentuates the *quasi*

2-D nature of the materials. A study by Hur et al.[4] of the composition $Sr_{1.6}R_{1.4}Mn_2O_7$ (R = Gd and Nd) provided a similar contrast to that observed between $Sr_2HoMn_2O_{7-\delta}$, $Sr_2YMn_2O_{7-\delta}$ and $Sr_2NdMn_2O_{7-\delta}$. Hur et al. detected elongation of the axial Mn-O bond directed into the rocksalt layer and shortening of equatorial bonds in $Sr_{1.6}Gd_{1.4}Mn_2O_7$, relative to the values observed in $Sr_{1.6}Nd_{1.4}Mn_2O_7$.

Considering the magnetic properties of $Sr_2HoMn_2O_{7-\delta}$ and $Sr_2YMn_2O_{7-\delta}$, the absence of magnetic Bragg peaks, but the observation of diffuse scattering, points to the existence of short range correlations in these materials. The nature of these, albeit local, interactions is determined by the relative strength of competing, antiferromagnetic Mn^{4+} t_{2g}^3 - O^{2-} - Mn^{4+} t_{2g}^3 π superexchange interactions, ferromagnetic Mn^{3+} t_{2g}^3 e_g^1 - O^{2-} - Mn^{4+} t_{2g}^3 σ superexchange interactions and Mn^{3+} t_{2g}^3 e_g^1 - O^{2-} - Mn^{3+} t_{2g}^3 e_g^1 σ superexchange interactions, expected to be antiferromagnetic in the present case. The operation of ferromagnetic double exchange is not expected here, due to the low effective bandwidth of these highly distorted, cation ordered materials (refer to later discussion for transport properties).

Results of field dependent SQUID magnetisation measurements, performed by Dr J. Millburn and presented elsewhere[13,14], confirmed the spin glass characteristics of $Sr_2HoMn_2O_{7-\delta}$ and $Sr_2YMn_2O_{7-\delta}$ suggested by temperature dependent data. The behaviour observed in $Sr_2YMn_2O_{7-\delta}$ is informative particularly because, in the absence of a lanthanide magnetic moment, the spin glass freezing can be attributed solely to the response of the manganese spin system at this doping level. Thus, the less marked divergence between ZFC and FC curves and the proximity of values of T_F in $Sr_2HoMn_2O_{7-\delta}$ and $Sr_2YMn_2O_{7-\delta}$, allows the inference that the freezing involves only the Mn spin system in the Ho compound. Thus, the difference in low temperature (<15K) behaviour in magnetic susceptibility (refer to Figures 3.2.13 and 3.2.14) is due to the paramagnetic contribution of Ho^{3+}. That the paramagnetism of Ho^{3+} is preserved down to 2K has already been suggested by the low angle scattering presented in Figure 3.2.9, and this provides a further contrast to the $Sr_2NdMn_2O_{7-\delta}$ phase, where the Nd spins were interpreted as ordering at 30K. It would appear that residual Ho - Ho interactions are too weak to produce ordering and that Mn - Ho coupling is inhibited

by the spin glass freezing of Mn moments. Interestingly, returning to the work by Hur et al.[4], $Sr_{1.6}Gd_{1.4}Mn_2O_7$ showed paramagnetic behaviour which could be fitted to the Curie-Weiss law over a wide temperature range, in contrast to complex magnetic behaviour observed for $Sr_{1.6}Nd_{1.4}Mn_2O_7$. Thus, changes in structural and magnetic properties on decreasing the size of the dopant rare-earth, mirror those observed in the current study.

The characterisation of $Sr_2HoMn_2O_{7-\delta}$ and $Sr_2YMn_2O_{7-\delta}$ as spin glass materials still does not explain the nature of competing magnetic interactions present; however, since FM DE is not expected, it is likely that frustration is due to the $Mn^{3+}\ t_{2g}^3\ e_g^1$ - O^{2-} - $Mn^{4+}\ t_{2g}^3$ σ superexchange competing with antiferromagnetic $Mn^{4+}\ t_{2g}^3$ - O^{2-} - $Mn^{4+}\ t_{2g}^3$ π superexchange and $Mn^{3+}\ t_{2g}^3\ e_g^1$ - O^{2-} - $Mn^{3+}\ t_{2g}^3\ e_g^1$ σ superexchange. In addition to this competition, spin glass behaviour requires disorder. The two-dimensional square lattice is not frustrated geometrically; therefore, the root of the disorder is expected to be in the spatial location of Mn^{4+} and Mn^{3+} cations, plus the effects of Sr/Ln disorder on the rocksalt sites. The presence of short range ferromagnetic correlations in $Sr_2YMn_2O_{7-\delta}$ is not incompatible with susceptibility data, since the size and temperature dependence of the latter are consistent with frustration of antiferromagnetic exchange interactions. For example, the Weiss constant is small but positive and the observed Bohr magneton number is higher than that calculated on the basis of localised, non-interacting ions.

The observation of a disordered array of Mn^{4+} and Mn^{3+} cations, as opposed to the formation of a charge-ordered supercell, is the most surprising result of the present study. There are examples in both n = 1, n = ∞ and, indeed, in the n = 2 $Sr_2LaMn_2O_7$ phase, of charge ordering at the Mn 3.5 oxidation level, often as a result of the competition between antiferromagnetic and ferromagnetic exchange interactions. For example, the n = 1 phase $La_{0.5}Sr_{1.5}MnO_4$ undergoes charge ordering of Mn^{4+} and Mn^{3+} cations at 220K, followed by antiferromagnetic ordering at 120K[19]. In the n = ∞ system, $La_{0.5}Ca_{0.5}MnO_3$, the localisation of charge drives the transition between two magnetically ordered states. After ordering ferromagnetically at 200K, charge ordering leads to a metamagnetic transition at 160K resulting in an antiferromagnetic ground state[20]. In fact, charge ordering in n = 2 systems should be favoured over that in infinite layer systems, since the reduction of the Mn 3d

bandwidth on reducing dimensionality, favours the localisation of charge. In addition, for the $Sr_2HoMn_2O_{7-\delta}$ and $Sr_2YMn_2O_{7-\delta}$ materials, with the increase in nonlinearity of the Mn-O-Mn pathways brought about by the structural distortion, orbital overlap is reduced further.

Despite these factors, no signatures of commensurate, charge ordering were given in magnetometry measurements for either compound in the temparature range 5 - 300K. It is true that the presence of the minority, infinite layer phase does shift the oxidation state slightly from the 3.5 level; however, it is thought that the change is marginal enough not to affect the tendency for charge ordering. By analogy with the n = 1 and n = ∞ phases, charge ordering is expected to result in an antiferromagnetic ground state. Interestingly, it is possible that the cation ordering leading to the relatively large size of the 12 coordinate 'perovskite block' site in $Sr_2HoMn_2O_{7-\delta}$ and $Sr_2YMn_2O_{7-\delta}$ disfavours the transition to an antiferromagnetic ground state. For example, it was argued[1] that due to the increased occupancy of the 12 coordinate A-cation site by the large Sr cation in the minority, spin glass phase of $Sr_2NdMn_2O_{7-\delta}$, exchange-striction was not able to decrease the Mn-Mn distance parallel to z. Such a distortion would have favoured the transition to antiferromagnetic order.

Assuming that the requirements for charge ordering in $Sr_2HoMn_2O_{7-\delta}$ and $Sr_2YMn_2O_{7-\delta}$ would be the same as those identified by Li et al.[11] in $Sr_2LaMn_2O_7$, by analogy with the latter, $d_{3x^2-r^2}$ / $d_{3y^2-r^2}$ orbital ordering of Mn^{3+} accompanying the real-space ordering of 1:1 Mn^{3+} / Mn^{4+} would have to be realised. This corresponds to orbital ordering within the MnO_2 sheet. However, the octahedral distortion arising from the elongation of the apical Mn-O(7) bond in particular, confers more $d_{3z^2-r^2}$ character, than $d_{3x^2-r^2}$ / $d_{3y^2-r^2}$ character, on e_g electrons in the compounds $Sr_2HoMn_2O_{7-\delta}$ and $Sr_2YMn_2O_{7-\delta}$. A similar suppression of the CO state has been observed in the n = 1 compounds $R_{0.5}Sr_{1.5}MnO_4$, where R = '$Nd_{1-z}La_z$', and relatively large JT distortions are observed[7].

3.3 Magnetotransport studies on the series $Sr_2LnMn_2O_{7-\delta}$ (Ln=Pr, Nd, Ho) and Y and $Sr_{2-x}Nd_{1+x}Mn_2O_{7-\delta}$ (x=0, 0.1, 0.2 and 0.5).

3.3.1 Experimental details

The samples synthesised by the author which are discussed in the current section were those containing Ho and Y, as detailed above. For the remaining samples discussed in this Section, Table 3.3.1 summarises which experimentalist synthesised which sample and where information regarding sample characterisation can be found.

Table 3.3.1 Summary of information for samples, other than $Sr_2HoMn_2O_{7-\delta}$ and $Sr_2YMn_2O_{7-\delta}$, described in the current section:

Compound	Experimentalist	Synthesis and structural characterisation	Magnetometry and magnetotransport
$Sr_2PrMn_2O_{7-\delta}$	S.P.Sullivan	reference [17]	references [14] and [23]
$Sr_2NdMn_2O_{7-\delta}$	N.S.Laskey	reference [1]	references [14] and [23]
$Sr_{1.9}Nd_{1.1}Mn_2O_{7-\delta}$	N.S.Laskey	reference [1]	references [14] and [23]
$Sr_{1.8}Nd_{1.2}Mn_2O_{7-\delta}$	J.Hepburn	reference [3] (sample D)	references [3] and [23]
$Sr_{1.5}Nd_{1.5}Mn_2O_{7-\delta}$	J.E.Millburn	reference [13] (sample A)	references [13] and [23]

Several attempts by the author to grow crystals of $Sr_{1.5}Nd_{1.5}Mn_2O_{7-\delta}$, using a KCl flux technique, did not prove successful. The results of iodometric titrations to establish the oxygen content in samples other than $Sr_2PrMn_2O_{7-\delta}$ and $Sr_{1.8}Nd_{1.2}Mn_2O_{7-\delta}$, are listed in Table 3.3.2.

Magnetotransport data were collected for $Sr_2NdMn_2O_{7-\delta}$ and $Sr_{1.9}Nd_{1.1}Mn_2O_{7-\delta}$ by the author and Dr M. Honold, and later measurements on $Sr_{1.8}Nd_{1.2}Mn_2O_{7-\delta}$, $Sr_{1.5}Nd_{1.5}Mn_2O_{7-\delta}$, Ho and Y samples were carried out by the author and A.Coldea. In each case, data were collected on sintered bars, approximately 5x2x2mm in size, (which had been cut from 13mm pellets) using the apparatus described in Chapter 2.7. Standard four probe geometry was used, with the direct current ($\leq$ 50 μA) perpendicular to the field. For the measurements on $Sr_2NdMn_2O_{7-\delta}$, $Sr_{1.9}Nd_{1.1}Mn_2O_{7-\delta}$ and $Sr_2PrMn_2O_{7-\delta}$, contacts onto the sintered materials were made to Cu wires using Ag conductive paint. For all other experiments, gold patches were evaporated onto the bars prior to attaching the Cu wires with

Ag epoxy. This led to stronger contacts which showed less deterioration over time and with changes in temperature. For $Sr_2NdMn_2O_{7-\delta}$ and $Sr_{1.9}Nd_{1.1}Mn_2O_{7-\delta}$, the data presented are the result of cooling in the applied field after sweeping the field to the measuring value at room temperature. For all other data presented, resistivity was measured as a function of temperature (T = 4 - 300K) whilst cooling in zero field, and for temperatures (T = 4 - 250K) whilst warming in fields up to 14T.

In order to investigate further some interesting magnetotransport behaviour observed for the compound $Sr_{1.8}Nd_{1.2}Mn_2O_{7-\delta}$ (and to perform similar experiments on $Sr_{1.5}Nd_{1.5}Mn_2O_{7-\delta}$ for comparison), resistivity as a function of field was measured for both samples. The isothermal temperatures selected were 259, 177, 82, 31 and 3.6K for the compound $Sr_{1.8}Nd_{1.2}Mn_2O_{7-\delta}$ and 273, 123, 96 and 78K for $Sr_{1.5}Nd_{1.5}Mn_2O_{7-\delta}$. The results are presented in Figures 3.3.3 and 3.3.4, respectively and more extensive data is given in reference [23]. During each field sweep, the temperature fluctuation was maintained at no more than +/- 1K. The sweeps were carried out for the lowest temperature first and warming between temperatures was performed under zero field. The field dependence of magnetisation was measured at the same isothermal temperatures (where practical), for comparison. Field cooled magnetisation isotherms were measured between +10kG and -10kG at 259, 177, 82, 31 and 5K for $Sr_{1.8}Nd_{1.2}Mn_2O_{7-\delta}$ and 273, 123, 96, 78, 30 and 5K for $Sr_{1.5}Nd_{1.5}Mn_2O_{7-\delta}$.

3.3.2 Results

3.3.2.1 Summary of structural properties in the series $Sr_2LnMn_2O_{7-\delta}$ (Ln=Pr, Nd) and $Sr_{2-x}Nd_{1+x}Mn_2O_{7-\delta}$ (x = 0, 0.1, 0.2 and 0.5).

A detailed account of the structural parameters of $Sr_2HoMn_2O_{7-\delta}$ and $Sr_2YMn_2O_{7-\delta}$ has been given above. Detailed accounts of structural properties of the remaining samples in the magnetotransport study can be found in the references listed in Table 3.3.1; however, relevant structural information is summarised in Table 3.3.2. Table 3.3.2 also lists the expected and measured mean Mn oxidation states (OS) in samples for which iodometric titration gave reproducible results. All samples show oxidation states slightly exceeding the predicted 3.5 value, corresponding to slight oxygen excess. However, oxygen contents were sufficiently close to expected values for 'δ' to be assumed zero from this point onwards. As expected, for the Sr/Nd series, the mean oxidation state reduces as the proportion of trivalent Nd (and occupancy of the e_g band) increases.

The parameter Δ in Table 3.3.2 quantifies the irregularity of MnO_6 octahedra and is equal to the ratio of the averaged out-of-plane to averaged in-plane Mn-O bondlengths. The lattice parameters of majority and minority phases in the samples considered in the magnetotransport study show the effects of changing 'Ln' in the $Sr_2LnMn_2O_7$ series and of bandfilling in $Sr_{2-x}Nd_{1+x}Mn_2O_7$.

Table 3.3.2 Significant, room temperature structural parameters for the $Sr_2LnMn_2O_7$ and $Sr_{2-x}Nd_{1+x}Mn_2O_7$ series:

Compound		Expected Mn OS	Measured Mn OS	a(Å)	c(Å)	Δ	n = ∞ phase
$Sr_2NdMn_2O_7$	65%	3.50	3.54(1)	3.8490(6)	19.9599(7)	1.021	-
	35%			3.8451(1)	20.0222(1)	1.021	
$Sr_2HoMn_2O_7$[a]		3.50	3.51(2)	5.4038(8)	19.9049(9)	1.043	3.0(2)
$Sr_2YMn_2O_7$[a]		3.50	3.51(3)	5.4045(6)	19.9053(6)	1.043	2.1(3)
$Sr_{1.9}Nd_{1.1}Mn_2O_7$	54%	3.45	3.46(1)	3.8421(7)	20.0831(7)	1.025	-
	46%			3.8456(6)	20.0266(6)	1.025	
$Sr_{1.8}Nd_{1.2}Mn_2O_7$		-	-	3.8399(7)	20.1457(4)	1.039	6.8(6)
$Sr_{1.5}Nd_{1.5}Mn_2O_7$		3.25	3.28(1)	3.8367(1)	20.3084(6)	1.064	4.6(7)

[a] Lattice parameters quoted for Ho and Y samples are those for the enlarged unit cell in the space group $P4_2/mnm$.

3.3.2.2 Magnetotransport studies on the series $Sr_2LnMn_2O_{7-\delta}$ (Ln=Pr, Nd, Ho) and Y

Figure 3.3.1 shows resistivity as a function of temperature and field, for the title compounds:

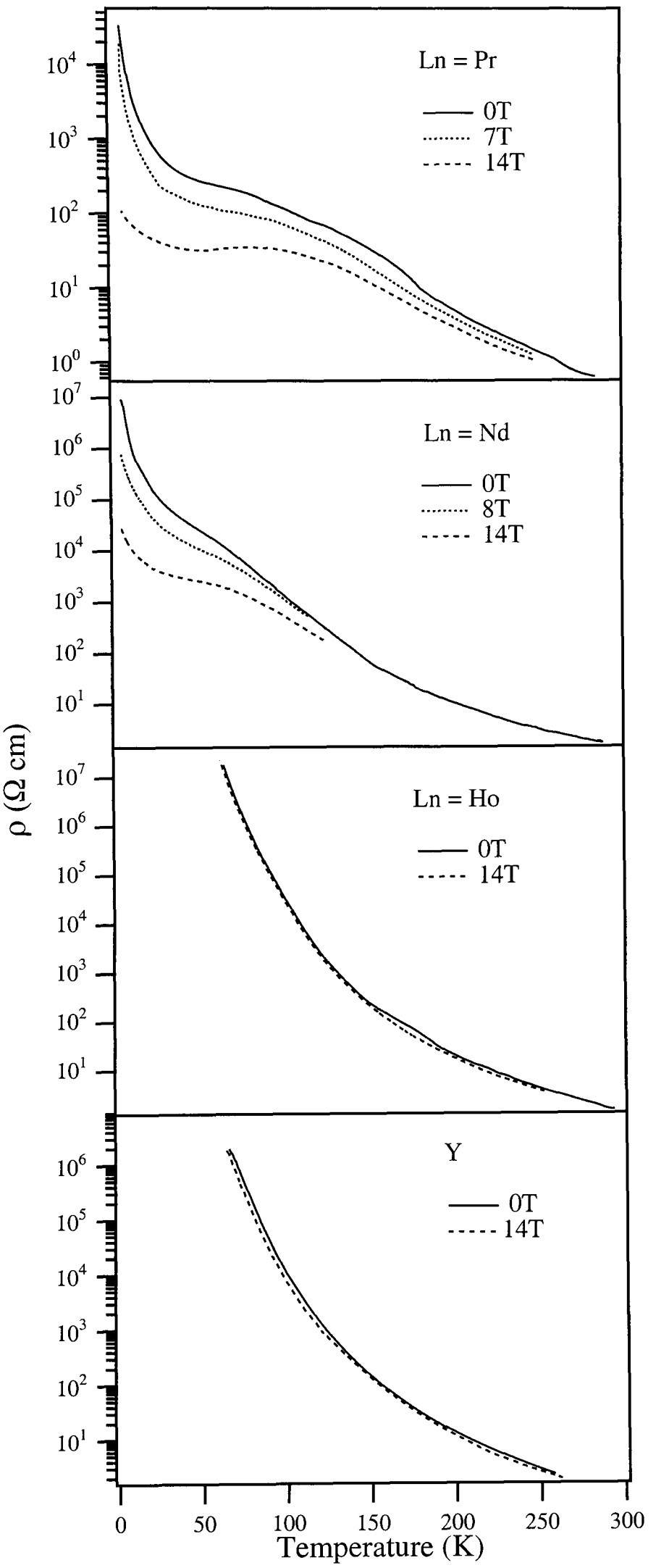


Figure 3.3.1 Resistivity as a function of temperature for the $Sr_2LnMn_2O_7$ series, at zero field and 14T for Ln = Pr, Nd, Ho and Y, with additional data at 7T for Ln = Pr and 8T for Ln = Nd.

It is apparent immediately, as for the magnetic susceptibility data shown in Appendix 2, Figure 2.1, that the four compounds can be grouped into Ho/Y and Pr/Nd pairs on account of their differing behaviour. The Ho/Y pair show thermally activated conduction throughout the entire temperature range, with minimal, almost temperature-independent values of magnetoresistance. Maximum values of negative magnetoresistance in a field of 14T were 24% for $Sr_2HoMn_2O_7$ at 125K and 32% for $Sr_2YMn_2O_7$ at 100K. It is not clear whether the spin glass freezing of the Mn sublattice would have been detected in the resistivity data for $Sr_2HoMn_2O_7$ and $Sr_2YMn_2O_7$, as the signal becomes immeasurably large below ~60K in each compound.

In contrast, the temperature dependence of resistivity for the Pr/Nd pair is characterised by three regions with differing values of the slope, (dρ/dT). Above 200K for $Sr_2PrMn_2O_7$ and 150K for $Sr_2NdMn_2O_7$, thermally activated conduction is characterised by an intermediate slope, (dρ/dT). The middle temperature region (~ 50-150K) shows a slightly reduced value of (dρ/dT) before the signal increases rapidly below 50K yielding the highest value of (dρ/dT). Both $Sr_2PrMn_2O_7$ and $Sr_2NdMn_2O_7$ exhibit colossal, negative MR below 150K, with the resistivity signal being reduced by 2-3 orders of magnitude in a field of 14T. The maximum magnetoresistance in each occurs at 4.2K, which corresponds to the maximum degree of divergence between the ZFC and FC susceptibility curves in 500G. For the Nd sample, the onset of significant magnetoresistance coincides with the divergence temperature of ZFC and FC data (however, the latter is highly field dependent). Broad, local maxima, reminiscent of a MI transition occur in the 14T resistivity datasets at 80K for $Sr_2PrMn_2O_7$ and ~75K for $Sr_2NdMn_2O_7$. For each, the general behaviour before application of the field is that of thermally activated conduction (reaching the huge value of $1x10^7$ Ωcm in the Nd sample). The zero field curve for the Pr sample does not increase sharply until about 40K and the maximum resistivity is three orders of magnitude lower than either the Nd, Ho or Y samples, at just 4×10^4 Ωcm.

3.3.2.3 Magnetotransport studies on the series $Sr_{2-x}Nd_{1+x}Mn_2O_{7-\delta}$ (x = 0, 0.1, 0.2 and 0.5)

Figure 3.3.2 shows resistivity as a function of temperature and field, for the title compounds:

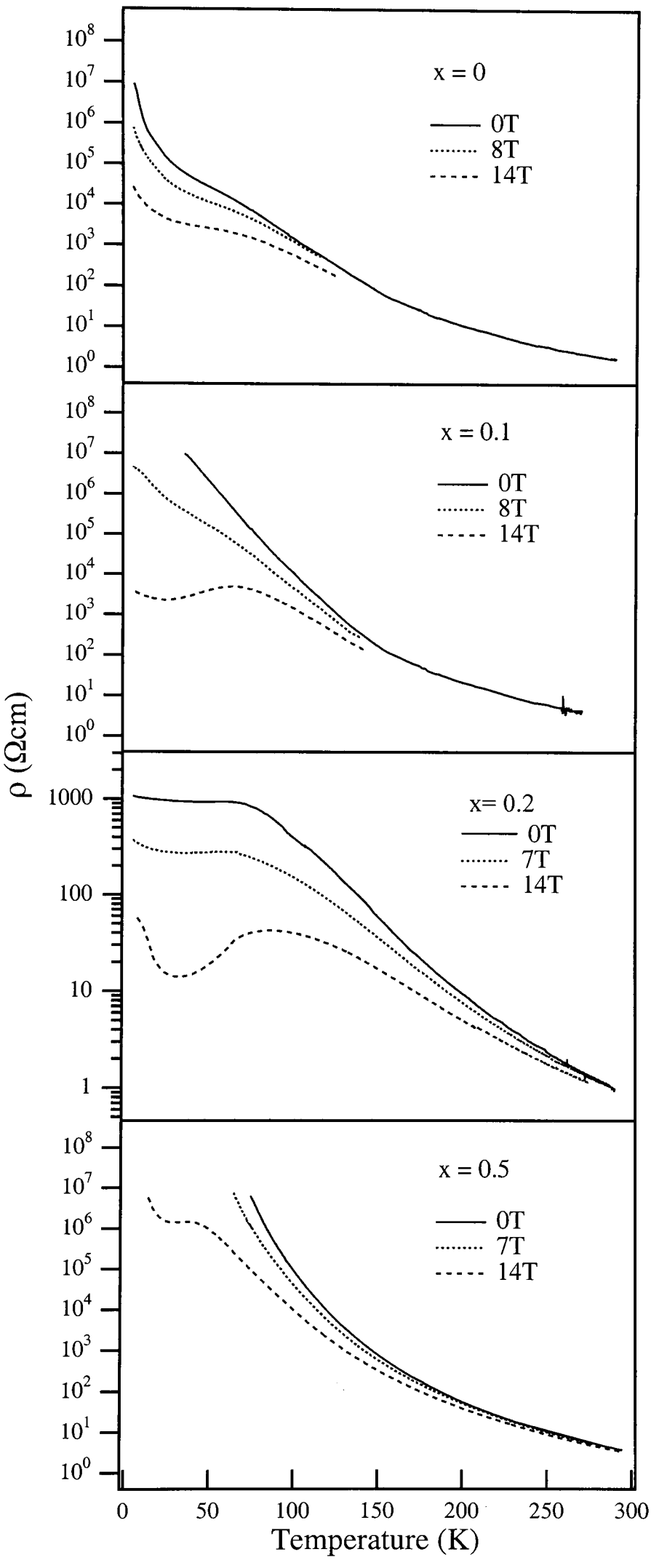


Figure 3.3.2 Resistivity as a function of temperature for the $Sr_{2-x}Nd_{1+x}Mn_2O_7$ series (x = 0, 0.1, 0.2 and 0.5), at zero field and 14T, with additional data at 8T (x = 0, 0.1) and 7T (x = 0.2, 0.5).

The immediate observation from Figure 3.3.2, is the existence of 'colossal' swings in the values of resistivity which occur below approximately 150K at all Nd^{3+} concentrations. The shape of the zero field curves is similar for x = 0.1 and x = 0.5 compositions, with $Sr_2NdMn_2O_7$ showing the three distinct regions with differing slopes, ($d\rho/dT$), as mentioned above. The zero field curve for the x = 0.2 sample has a distinctive shape, since it is much flatter below 100K, levelling off at an upper value of resistivity of $1x10^3$ Ωcm. The reason for this variation is, at present, unclear; the other samples have upper (measurable) values of zero field resistivity of the order of $1x10^7$ Ωcm. The general appearance of zero field and field data is consistent with that reported by Seshadri et al.[5] for the same composition, (x = 0.2).

For all Nd concentrations (and also for the $Sr_2PrMn_2O_7$ phase), MR approaches 100% as defined by equation 1.1.1, as the temperature is decreased towards 4.2K. The 14T data show broad, local maxima at all compositions (at temperatures of 75K for x = 0, 0.1 and 0.2 and of 50K for the x = 0.5 composition) but enter a further insulating region below a temperature of 50K.

Two major differences between the CMR properties of this series and the 'typical' intrinsic response of n = ∞ manganites such as $La_{0.7}Ca_{0.3}MnO_3$ (shown in Figure 1.3.6 in the introductory chapter), are the absence of bulk ferromagnetic order and the subsequent observation of maximum CMR ratios, at temperatures *remote* from a magnetic transition temperature. In fact, the maximum CMR ratios here were observed at the lowest measuring temperature for each sample.

3.3.2.4 Isothermal magnetisation and magnetotransport measurements on the compounds $Sr_{1.8}Nd_{1.2}Mn_2O_{7-\delta}$ and $Sr_{1.5}Nd_{1.5}Mn_2O_{7-\delta}$

Figures 3.3.3 (a) to (f) show field dependent data for the $Sr_{1.8}Nd_{1.2}Mn_2O_7$ composition. In the field dependent resistivity data (parts (a) and (b)), there is a change of curvature between data at 259 and 82K, with the 177K curve appearing almost linear with field. There is significant hysteresis at temperatures of 31 and 3.6K with the effect being most pronounced for the latter temperature. The data at 31K are particularly interesting since, not only do they show an anomaly in the region of 8 - 12T, but the rapid fall off of resistivity with fields under 1T suggests a LFMR response. A similar LFMR response is evidenced at 82 and 3.6K, although the effect is slightly less marked at these temperatures. The field dependent magnetisation data (parts (c) to (f)) show significant non-linearity at all measuring temperatures, and the 31 and 5K data exhibit significant hysteresis, with M(H) loops symmetrical about the origin.

Figures 3.3.4 (a) to (f) show the results of similar experiments on the $Sr_{1.5}Nd_{1.5}Mn_2O_7$ phase, albeit at different isothermal temperatures. Here, the resistivity data (parts (a) and (b)) show a change in curvature at some temperature between 273 and 123K. It did not prove possible to measure this sample at isothermal temperatures lower than 78K, due to the magnitude of the resistivity; so investigation of the presence of the low field, low temperature response observed at 31K in the $Sr_{1.8}Nd_{1.2}Mn_2O_7$ composition, was likewise impossible. The slight non-linearity of the isothermal magnetisation begins at 273K and becomes well-established for lower temperatures, where hysteresis is observed, as for the $Sr_{1.8}Nd_{1.2}Mn_2O_7$ sample.

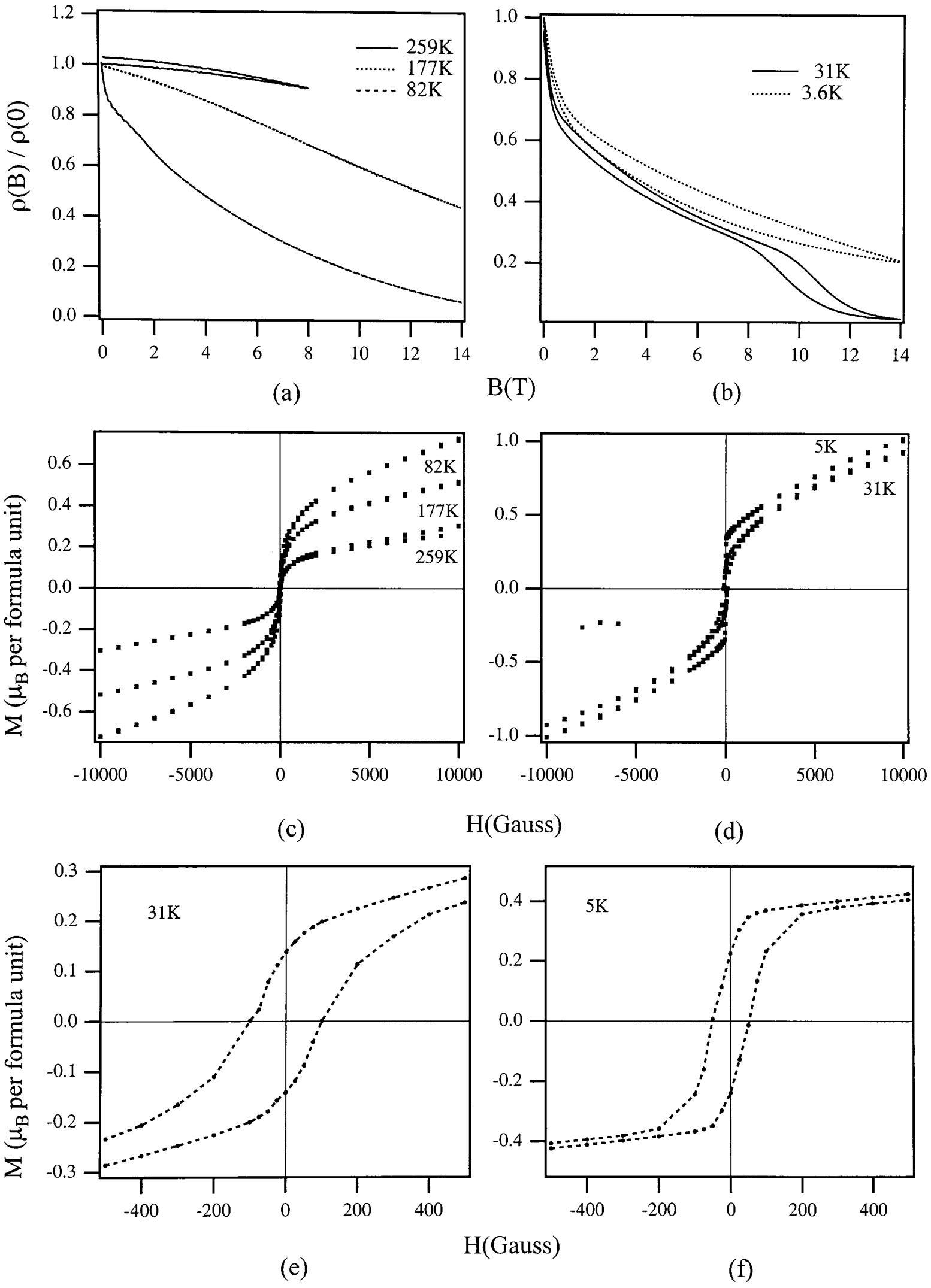


Figure 3.3.3 Field dependence of normalised resistivity (a) at 259, 177 and 82K (b) at 31 and 3.6K for $Sr_{1.8}Nd_{1.2}Mn_2O_7$. Field dependence of magnetisation (c) at 259, 177 and 82K (d) at 31 and 5K for $Sr_{1.8}Nd_{1.2}Mn_2O_7$. Graphs (e) and (f) show enlarged views of the region (-500≤Field(G)≤500) in the magnetisation measurements at 31 and 5K, respectively.

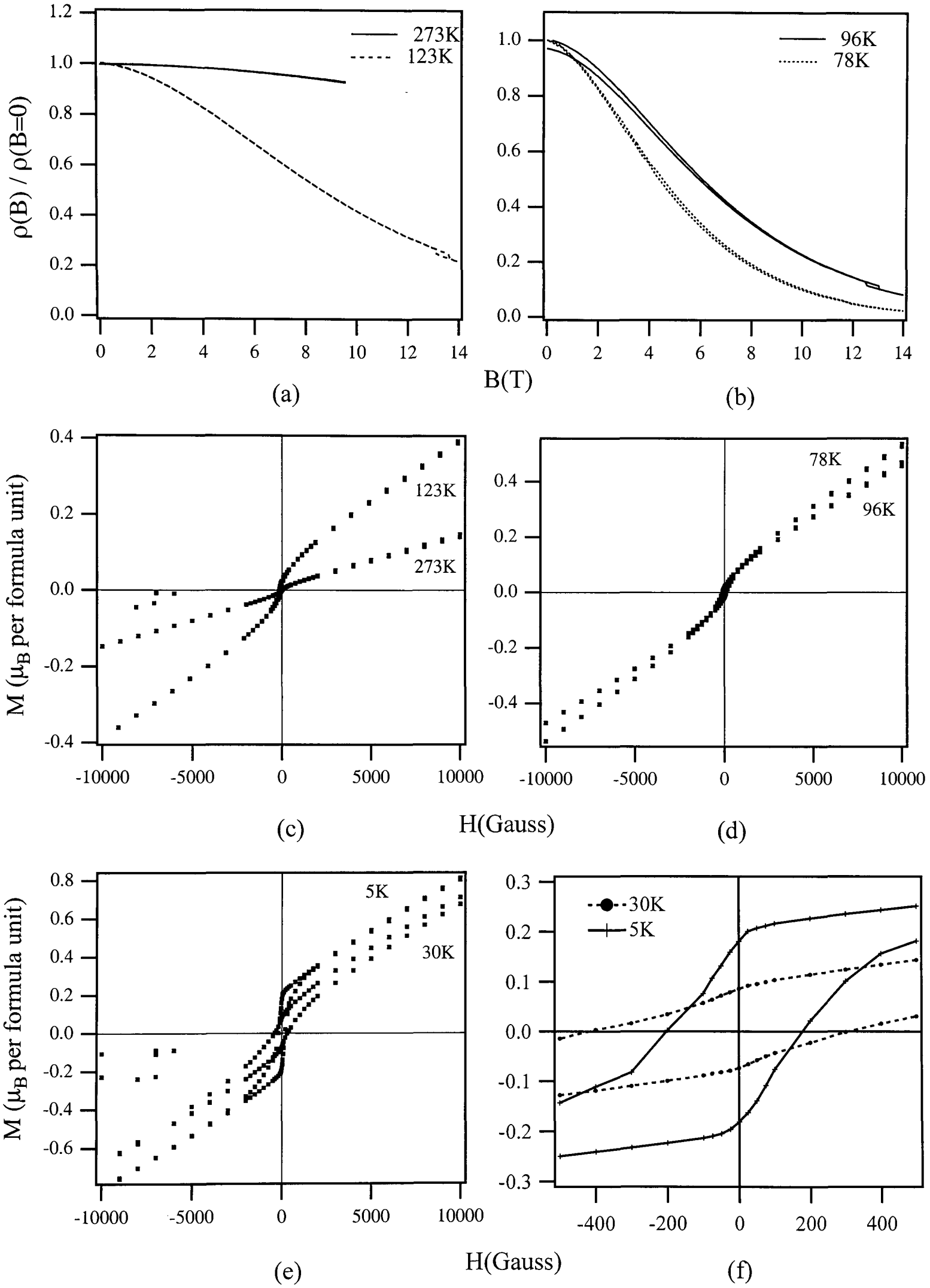


Figure 3.3.4 Field dependence of normalised resistivity (a) at 273 and 123K, (b) at 96 and 78K for $Sr_{1.5}Nd_{1.5}Mn_2O_7$. Field dependence of magnetisation (c) at 273 and 123K, (d) at 96 and 78K and (e) 30 and 5K for $Sr_{1.5}Nd_{1.5}Mn_2O_7$. Graph (f) shows an enlarged view of the region (-500≤Field(G)≤500) in the magnetisation measurements at 30K and 5K.

3.3.3 Discussion

3.3.3.1 Magnetotransport studies on the series $Sr_2LnMn_2O_7$ (Ln=Pr, Nd, Ho) and Y

For the series $Sr_2LnMn_2O_7$, the ratio of Mn^{4+} to Mn^{3+} is unity and broad changes in the magnetotransport behaviour are attributed to the effects of changing Ln. This will vary the internal pressure, changing the lattice parameters, and hence the electronic bandwidth.

SQUID magnetometry data as a function of temperature for compounds other than the Ho and Y samples were collected by Dr J. Millburn, and the data in measuring fields of 100G or 500G are presented in Appendix 2, Figure 2.1, alongside those for the Ho and Y samples, for comparative purposes. The Pr/Nd pair exhibit a complex variation of magnetic susceptibility with temperature in a field of 500G, with significant divergence between ZFC and FC curves, resulting in part from the presence of two discrete phases and competing magnetic exchange interactions across much of the temperature range. It was not possible to fit data for either Pr or Nd compound using the Curie-Weiss law over any temperature range. The magnetisation behaviour in $Sr_2NdMn_2O_7$ has been discussed in detail elsewhere[14], where the absence of clear evidence of bulk ferromagnetism or metamagnetism in fields up to 50kG was emphasised. The local maximum at ~140K coincides with the Néel temperature of the majority phase shown to undergo antiferromagnetic ordering in neutron diffraction studies[1]. Neutron studies also detected a minority spin glass phase ($T_F < 50K$). Nd moments order antiferromagnetically below 30K and at intermediate temperatures ($30 \leq T(K) \leq 140$) freeze in a spin-glass-like fashion and are likely to contribute to the hysteretic behaviour. The peak in the signal around 210K was attributed to superparamagnetic or (small ferromagnetic) clusters.

The observed behaviour in $Sr_2PrMn_2O_7$, such as the maximum in molar susceptibility at 143K and subsequent divergence in the ZFC and FC curves, likens the behaviour of the Pr sample with that of $Sr_2NdMn_2O_7$[14]. Although powder neutron diffraction data are not available for $Sr_2PrMn_2O_7$ to test for the presence of antiferromagnetic order, the similarity in their structural parameters[17] and the observation of CMR in both $Sr_2PrMn_2O_7$ and $Sr_2NdMn_2O_7$ (refer to Figure 3.3.1) suggests that the magnetic interactions are probably very similar in the two samples.

Thus, in summarising the contrasts between the Pr/Nd and Ho/Y pairs, the former give rise to complex magnetisation behaviour despite showing no bulk ferromagnetic behaviour, display negative CMR below 150K, were refined in the tetragonal space group *I4/mmm* and shown to consist of two discrete n = 2 RP phases. The latter compounds are spin glasses, exhibit Curie-Weiss behaviour at high temperatures, show minimal, temperature-independent, negative magnetoresistance and adopt distorted RP structures (space group $P4_2/mnm$). These distorted structures involve a high degree of Ln or Y/Sr ordering and are contaminated by n = ∞ minority phases. A comparison of the magnetic properties of $Sr_2HoMn_2O_{7-\delta}$ and $Sr_2YMn_2O_{7-\delta}$ with those of $Sr_2NdMn_2O_{7-\delta}$ was also considered in Section 3.2.3.

Table 3.3.2 confirms the minimal extent of deviations from ideal stoichiometry for all members of the series. The cation ordering (of the smaller Ho^{3+} and Y^{3+} onto the 9 coordinate rocksalt site) facilitates the elongation of the Jahn-Teller distorted apical Mn - O bond. The increasing values of the parameter Δ, on progressing from $Sr_2NdMn_2O_{7-\delta}$ to $Sr_2YMn_2O_{7-\delta}$ in Table 3.3.2, emphasise the elongation of MnO_6 octahedra along the c axis and the resulting, predicted stabilisation of the $d_{3z^2-r^2}$ state relative to the $d_{x^2-y^2}$ state, favouring charge localisation. Indeed, the predictions are borne out in the transport behaviour observed in Figure 3.3.1, where the resistivity becomes immeasurably large for Ho and Y phases below about 60K. The same effect has been observed in a number of studies[9,21,22] on compounds belonging to the series $(La_{1-z}Nd_z)_{1+x}Sr_{2-x}Mn_2O_7$, where it has been shown that by increasing z, and hence decreasing $\langle r_A \rangle$, the MnO_6 octahedra elongate along the c axis, modifying the crystal field around the e_g state.

In addition to the effect of the size of Ho^{3+} and Y^{3+}, their increased electronegativity, when compared to the larger Pr^{3+} and Nd^{3+}, means they compete more effectively with manganese for bonding with oxygen, accentuating the reduction of the bandwidth of Mn-derived electrons. The above-mentioned localising effects appear to outweigh the delocalising effect of the increased orbital overlap that should be induced by the relatively short Mn-Mn distances in the ab plane. Unfortunately, the biphasic (two n = 2 RP phases) nature of $Sr_2PrMn_2O_7$ and $Sr_2NdMn_2O_7$ complicates the discussion of the overall trend in cation ordering, as Ln is reduced in size.

The fitting of zero field resistivity curves below 150K, using a thermally activated hopping model, is described by Coldea et al.[23], and yields activation energies which support the narrowing of the electronic bandwidth with reduction in $\langle r_A \rangle$. For example, E_A in both $Sr_2HoMn_2O_{7-\delta}$ and $Sr_2YMn_2O_{7-\delta}$ is ~ 126meV, compared to the values of 112 and 101meV for Pr and Nd samples, respectively. A similar variation of activation energy with cation size was reported by Seshadri et al.[5], for the series of compounds $Sr_{1.8}R_{1.2}Mn_2O_{7-\delta}$ (for R = La, Pr and Nd). In the study by Coldea et al.[23], E_A is plotted as a function of Δ, and a linear dependence is observed, directly correlating activation energy with the degree of axial elongation of MnO_6 octahedra. A significant anisotropy in the zero field resistivity of Ho and Y samples was suggested by the use of the generalised VRH mechanism, with exponent γ = 0.66, to fit zero field resistivity data in the temperature range 70-275K. Similar behaviour was observed in the superconducting single crystal $PrBaCu_3O_7$, in which confinement of carriers in the planes was postulated[24].

The requirements for CMR in $Sr_2LnMn_2O_7$ phases are discussed in more detail in the next section; however, it is likely that the observation of CMR is dependent upon the formation of localised regions of spin correlation. It appears, however, that once $\langle r_A \rangle$ has reached a critically low value at this particular doping level, the magnetic ground state and electronic bandwidth are no longer predisposed to support CMR. Thus, the 14T resistivity remains activated throughout the entire temperature range in Ho and Y samples, at a value marginally lower than the zero field data. Studies on the series $Sr_{2-x}Tb_{1+x}Mn_2O_7$[14] have suggested that increasing the concentration of a rare earth cation, which is too small to support CMR, will not encourage delocalisation of the e_g electrons, an idea backed up by the paramagnetic, insulating nature of $Sr_{1.6}Gd_{1.4}Mn_2O_7$ at a variety of applied magnetic fields[4]. Thus, beyond a critical degree of distortion involving the tilting of the MnO_6 octahedra comprising the bilayers, it appears that the Mn 3d bandwidth reduces irreversibly, favouring charge localisation, no matter what the applied field. It should be noted that, as shown by Attfield and Rodriguez-Martinez[25], A-cation size mismatch, as well as the value of $\langle r_A \rangle$, is an important parameter determining electronic bandwidth. Thus, the trends observed in the

transport behaviour of the $Sr_2LnMn_2O_7$ series described above, cannot be explained solely as a result of changing $<r_A>$.

Finally, the results of the HRTEM study carried out by Sloan et al.[26] emphasise the importance of differentiating between bulk and surface homogeneity when considering phase purity in the polycrystalline samples discussed here. Using neutrons (λ~1.5Å), the average bulk of the particles is probed, whereas the microscopy study monitored defects or intergrowths occurring in relatively thin crystallites at, or close to, the surface in larger particles. The detection of intergrowths, with $n \geq 5$ for the $Sr_2NdMn_2O_7$ and $Sr_2HoMn_2O_7$ phases, was surprising particularly for the former compound, since no higher homologue impurities had been detected in the neutron study. It is likely that the defects were too small to give a coherent diffraction pattern at 1.5Å. However, it should be noted that even 'disordered' crystallites (those containing defects or intergrowths) were found to contain ~95% volume fraction of unperturbed n = 2 structure. It is likely that the potential existence of defect or intergrowth structures is directly proportional to the size (in grams) of the sample.

3.3.3.2 Magnetotransport studies on the series $Sr_{2-x}Nd_{1+x}Mn_2O_7$ (x = 0, 0.1, 0.2 and 0.5).

For the series $Sr_{2-x}Nd_{1+x}Mn_2O_7$, the mean manganese oxidation state decreases from 3.5 at x = 0 to 3.25 at x = 0.5 and the series is of interest to observe the effects of bandfilling, although by changing the concentration of Nd^{3+}, $<r_A>$ also changes marginally. The series is of particular interest as a comparison with the well characterised $Sr_{2-x}La_{1+x}Mn_2O_7$ series, where metallic behaviour and three dimensional ferromagnetic ordering are observed for the x = 0.2 and 0.4 compositions, and the CMR properties resemble those of the infinite layer materials. The evolution of metallic properties and ferromagnetic ordering as x increases across the La series is attributed to the increasing competition of the ferromagnetic double exchange interaction with the antiferromagnetic Mn^{4+} (t_{2g}^3) - O^{2-} - Mn^{4+} (t_{2g}^3) π superexchange interaction.

The $Sr_{2-x}Nd_{1+x}Mn_2O_7$ samples (x = 0, 0,1, 0.2 and 0.5) were shown to be tetragonal, biphasic compounds[1,3,13]. At the x = 0 and 0.1 doping levels, a mixture of spin glass and antiferromagnetic behaviour was observed, while for x = 0.2, 0.5, no long range magnetic order was detected. The degree of Sr/Nd cation ordering over 9 and 12 coordinate sites is minimal in

all four samples in comparison with that observed for the Ho/Y materials. All samples exhibited CMR below 150K with MR ratios which increased as the temperature was reduced. The fitting of zero field resistivity curves above 150K, using a thermally activated hopping model, gave activation energies, E_A, of 110meV for $Sr_{1.9}Nd_{1.1}Mn_2O_7$ and 143meV for $Sr_{1.5}Nd_{1.5}Mn_2O_7$. Interestingly, the latter value exceeds those obtained for the $Sr_2HoMn_2O_7$ and $Sr_2YMn_2O_7$ samples.

SQUID magnetometry data presented in Appendix 2, Figure 2.2, suggests that the evolution of ferromagnetic interactions with increasing x in $Sr_{2-x}Nd_{1+x}Mn_2O_7$ apparently occurs on a more localised scale, compared to the La series. As shown in the Figure, complex magnetic behaviour, observed for $Sr_2NdMn_2O_7$, is reproduced across the series as the concentration of electrons in the Mn e_g orbital is increased. The local maximum observed at approximately 210K in the $Sr_2NdMn_2O_7$ sample is not reproduced in the other phases. The origin of the successive maxima is unclear at present for the $Sr_{1.8}Nd_{1.2}Mn_2O_7$ and $Sr_{1.5}Nd_{1.5}Mn_2O_7$ phases; however, the increase in the signal between 250 and 300K in each sample suggests the formation of regions of ferromagnetic spin correlation. The existence of short range spin correlations would be consistent with the results of neutron diffraction measurements, which have ruled out the presence of bulk ferromagnetic order in any of the four samples. Interestingly, AC susceptibility data reported[27] for single crystals of $Sr_{1.5}Nd_{1.5}Mn_2O_7$ and $Sr_{1.5}Pr_{1.5}Mn_2O_7$ are similarly complex, containing successive maxima and revealing highly anisotropic behaviour. In a more recent study of single crystal $Sr_{1.5}Nd_{1.5}Mn_2O_7$ by García-Landa et al.[28], magnetisation data are presented at 500G with the field applied along the c direction and along a direction within the ab plane. Although these data cannot be compared directly with those for polycrystalline $Sr_{1.5}Nd_{1.5}Mn_2O_7$ in the present study, it is interesting to note the series of successive maxima in magnetisation observed for both compounds. In the single crystal study, an abrupt increase in magnetisation close to 300K was ascribed to FM ordering of intergrowths in the crystal structure. The increase of the signal for polycrystalline $Sr_{1.5}Nd_{1.5}Mn_2O_7$ described in the present study occurs more gradually with decreasing temperature, and ferromagnetic correlations are

ascribed, albeit short range, to the majority n = 2 RP phase in this material[2]. Magnetisation measurements carried out on $Sr_{1.6}Nd_{1.4}Mn_2O_7$ by Hur et al.[4] in a field of 5kG, also revealed complex behaviour containing successive local maxima, attributed to ferromagnetic clusters and a magnetically frustrated spin glass state. Moritomo et al.[22] presented the in-plane component of susceptibility, χ_{ab}, for crystals of $Sr_{2-x}Nd_{1+x}Mn_2O_7$ for x = 0, 0.1 and 0.2 in their study of the series $(La_{1-z}Nd_z)_{1+x}Sr_{2-x}Mn_2O_7$.

The differences in the evolution of ferromagnetic interactions in $Sr_{2-x}Nd_{1+x}Mn_2O_7$ and $Sr_{2-x}La_{1+x}Mn_2O_7$ series as a function of x which is suggested in the present study, were also observed in work by Zhang et al.[8,9] on the series $La_{1.2-z}Nd_zSr_{1.8}Mn_2O_7$. These authors show the crossover between $La_{1.2}Sr_{1.8}Mn_2O_7$-type and $Nd_{1.2}Sr_{1.8}Mn_2O_7$-type behaviour as z reaches 0.5 to 0.6. For z increasing from 0.1 to 0.5, FM exchange interactions were weakened, and frustration of magnetic ordering occurred, with concomitant localisation of electrons. On reaching z = 0.5, insulating behaviour was observed; however, magnetic frustration and the spin scattering of electrons were suppressed by an applied field, driving a MI transition and leading to high MR ratios. The enhanced low temperature MR effect in x = 0.5 and x = 0.6 samples was ascribed to the field induced MI transition. Considering the explanation for the increasing importance of FM DE interactions and their competition with AFM SE interactions in $Sr_{1.8}La_{1.2}Mn_2O_7$ as compared with $Sr_{1.96}La_{1.04}Mn_2O_7$ by Hirota et al.[29], it is puzzling as to why 3-D ferromagnetism does not develop in the same way as a function of x in the series $Sr_{2-x}Nd_{1+x}Mn_2O_7$.

The differences observed between the La and Nd series must stem from differences in the strengths of the competing, nearest-neighbour exchange interactions resulting in each mixed-valent system. These are an antiferromagnetic $Mn^{4+}\ t_{2g}^3$ - O^{2-} - $Mn^{4+}\ t_{2g}^3$ π superexchange interaction, a ferromagnetic $Mn^{3+}\ t_{2g}^3\ e_g^1$ - O^{2-} - $Mn^{4+}\ t_{2g}^3$ σ superexchange interaction and a $Mn^{3+}\ t_{2g}^3\ e_g^1$ - O^{2-} - $Mn^{3+}\ t_{2g}^3\ e_g^1$ σ superexchange interaction, the sign of the latter of which is dependent upon the existence of a Jahn-Teller distortion and

---

[2] Care was taken to confirm that the perovskite impurity was not responsible for features observed in the magnetisation in polycrystalline $Sr_{1.5}Nd_{1.5}Mn_2O_7$. Three compositions in the series $Nd_{1-x}Sr_xMnO_3$ were synthesised by Dr J Millburn[13], the reported cell volumes for which were close to the refined impurity cell volume. The magnetisation behaviour of these three phases did not contain features corresponding in position, or magnitude, to those observed for $Sr_{1.5}Nd_{1.5}Mn_2O_7$.

concomitant orbital ordering. For the relatively large bandwidth La compounds, the ferromagnetic double exchange interaction predominates at certain temperatures and levels of hole doping. For the Nd series, it is not likely that a double exchange interaction is dominant. Perhaps the apical Mn-O bond extends into the rocksalt layer lengthens to such an extent, as 'z' increases in the series $La_{1.2-z}Nd_zSr_{1.8}Mn_2O_7$, that inter-plane coupling is weakened to too great an extent for FM DE to compete effectively with AFM SE along z. Battle et al.[1] have solved the magnetic structure for the majority, antiferromagnetic phases in $Sr_{2-x}Nd_{1+x}Mn_2O_7$ (x = 0, 0.1) and, indeed, shown that ferromagnetic interactions are dominant within ab planes, while antiferromagnetic alignment is established along c, between the two layers of MnO_6 comprising a bilayer.

Rather than exhibiting long range ferromagnetic order, in the series $Sr_{2-x}Nd_{1+x}Mn_2O_7$, the enhanced magnetic moments appear to be due to regions of the compounds where the ferromagnetic Mn^{3+} t_{2g}^3 e_g^1 - O^{2-} - Mn^{4+} t_{2g}^3 σ superexchange interaction is competing effectively with the antiferromagnetic Mn^{4+} t_{2g}^3 - O^{2-} - Mn^{4+} t_{2g}^3 π superexchange interaction as the proportion of Mn^{3+} (t_{2g}^3 e_g^1) cations increase with x. The consistently high values of resistivity across the entire temperature range at zero field and 14T support the absence of double exchange, associated with metallic properties. Thus, the smaller size of Nd^{3+} compared with La^{3+}, the increased tendency for cation ordering and the influence of the rare earth moment in the $Sr_{2-x}Nd_{1+x}Mn_2O_7$ all appear to frustrate long range magnetic order of any sign. They do not inhibit CMR, however, and it appears that, up to a certain level of doping induced magnetic inhomogeneity, the extent of field-restored local magnetic order increases and, consequently, so does the MR ratio[9], through the reduced spin dependent scattering of carriers. A recent report[30] on the effects of replacing La with a magnetic rare earth ('R') in $(La_{1-x}R_x)_{0.67}Sr_{0.33}MnO_3$ on transport properties, has emphasised the potential additional scattering by the magnetic moment of the rare earth cation.

The importance of *local*, rather than *bulk*, or *average* magnetic structure is confirmed by the observation of CMR in both ordered (x = 0, 0.1) and non-ordered materials (x = 0.2, 0.5) in the series $Sr_{2-x}Nd_{1+x}Mn_2O_7$. It is possible that it is the minority, spin glass phase for the x = 0 and x = 0.1 compositions that is responsible for the CMR. It is more likely,

however, (considering the results for the x = 0.2[3] and 0.5[13] compositions which do not possess a spin glass phase), that local magnetic inhomogeneity is responsible for the effect. It would appear that the localised, spin-aligned clusters are strongly susceptible to an applied magnetic field in terms of their spatial extent and/or the relative misorientation between spins belonging to neighbouring clusters. Evetts et al.[31] have considered in detail the defect related (in the present case 'doping related') changes in the local magnetisation, causing changes in local spin disorder, that link to the resistivity through one of several spin dependent transport mechanisms. The presence of magnetic frustration and irreversibility in $Sr_2HoMn_2O_7$ and $Sr_2YMn_2O_7$ is clearly not sufficient alone, to induce CMR properties. The local magnetic inhomogeneity must be combined with an effective bandwidth large enough for a field-induced 'pseudo MI' transition to occur.

These ideas liken the behaviour in the present study to that observed by De Teresa et al.[32], who defined a 'spin glass insulator state' in their work on the compound $La_{2/3}Ca_{1/3}Mn_{1-x}Al_xO_{3-x}$. In their study, the effect of substitution of Mn with Al induces a magnetically disordered state, bringing about the coexistence of metallic and insulating regions, the latter of which are affected by the application of a magnetic field. The present study provides evidence that similar magnetically disordered states exist in the $Sr_{2-x}Nd_{1+x}Mn_2O_7$ series, whether from the detection of spin glass phases or observation of diffuse scattering, signifying short range spin correlations. The important parameters determining magnetotransport behaviour are then the local magnetic coherence length and the mean free path of the electron in a spin aligned region. The observation of broad, low temperature, local maxima in the 14T resistivity data may correspond to successive spin polarised regions extending in volume at different temperatures, leading to increased delocalisation of e_g electrons and a concomitant reduction in resistivity. Therefore, regions of spin correlation may be regarded as magnetic polarons, which are extended on application of the magnetic field, when spin alignment is favoured.

Another interesting observation for the $Sr_{2-x}Nd_{1+x}Mn_2O_7$ series is that compositions in which neutron diffraction studies detected minority n = 2 and n = ∞ material all show CMR and a similar variation in resistivity at both 0 and 14T. This supports the hypothesis that in

each case it is one of the n = 2 bulk phases responsible for the CMR effect. However, results of the HRTEM study detected intergrowths with n≥5 for $Sr_2NdMn_2O_7$, when no higher homologue impurities had been detected in the neutron study. Thus, the importance of probing local, as well as average structure is emphasised, and the significance of multiple phases on transport behaviour still is not understood fully.

Extrinsic contributions towards the MR response at low temperatures, in the series $Sr_{2-x}Nd_{1+x}Mn_2O_7$, are highly likely due to the polycrystalline nature of the samples. The presence of physical strain and disorder lead to spin disordered grain boundary regions (which may or may not coincide with magnetic domains) which contribute to the zero field resistivity. Since the zero field resistance of these grain boundary regions is greater at low temperature, and an applied magnetic field aligns the disordered spins in the grain boundary regions, this could account for the relatively greater effect of the magnetic field at low temperature. The dependence of the magnetoresistance ratio on temperature, in the series $Sr_{2-x}Nd_{1+x}Mn_2O_7$, has been plotted by Coldea et al.[23] and it is apparent that it reaches a maximum for the lowest measuring temperature for x = 0, 0.1 and 0.5 compositions. For the compound $Sr_{1.8}Nd_{1.2}Mn_2O_7$, the MR ratio reaches a maximum at 30K, the temperature of onset of ordering of Nd moments in the x = 0 and x = 0.1 compositions. The extrinsic contributions to the MR response in $Sr_{1.8}Nd_{1.2}Mn_2O_7$ are discussed in more detail in the following section.

3.3.3.3 Isothermal magnetisation and magnetotransport measurements on the compounds $Sr_{1.8}Nd_{1.2}Mn_2O_7$ and $Sr_{1.5}Nd_{1.5}Mn_2O_7$

As explained above, neutron diffraction studies have ruled out the presence of a bulk ferromagnetic phase in any of the four samples in the $Sr_{2-x}Nd_{1+x}Mn_2O_7$ series and it is likely that spin correlation exists on a local scale (perhaps through polaron formation) or is restricted to two dimensional ordering within the perovskite bilayers. The size of the 'jump' at high temperature in the molar susceptibility data presented in Appendix 2, Figure 2.2, and the size of the magnetisation per formula unit, suggest that the ferromagnetic clusters are present in their greatest concentration in the x = 0.2 composition. The observation of diffuse scattering at

low temperature in the neutron diffraction study on the x = 0.2 composition[3] is consistent with the development of regions of correlated spins.

It is interesting to note certain correlations between the field dependence of resistivity and the field dependence of magnetisation for samples $Sr_{1.8}Nd_{1.2}Mn_2O_7$ and $Sr_{1.5}Nd_{1.5}Mn_2O_7$. Data presented in Figure 3.3.3 for the $Sr_{1.8}Nd_{1.2}Mn_2O_7$ phase indicate non-linearity at all the chosen measuring temperatures in the isothermal magnetisation data, suggesting the presence of cooperative magnetic interactions. Hysteresis is most noticeable towards lower temperatures (≤ 82K) and exists over the greatest range of field in the 31K dataset. The onset of hysteresis in the isothermal magnetisation measurements coincides with the onset of a distinctive low field MR effect in isothermal field dependent resistivity sweeps. In the 82, 31 and 3.6K measurements, a rapid fall off of resistivity is observed in fields under 1T. A similar low field effect, in the compound $Sr_{1.6}La_{1.4}Mn_2O_7$, was attributed to spin polarised tunnelling between layers[33], suggesting that regions of parallel spin alignment in $Sr_{1.8}Nd_{1.2}Mn_2O_7$ might be restricted to layers, with rocksalt intergrowths providing the insulating tunnelling barrier. Spin polarised tunnelling between grains has also been shown to be significant for infinite layer and n = 2 granular materials[34,35]. There is no similar rapid fall off of resistivity observed for the $Sr_{1.5}Nd_{1.5}Mn_2O_7$ sample at the temperatures measured, which range from 273 to 78K. A low field MR effect of up to 30% at 10K was observed (when the field was applied parallel to c), for both ρ_{ab} and ρ_c components in the single crystal sample of $Sr_{1.5}Nd_{1.5}Mn_2O_7$ prepared by García-Landa et al.[28]. Due to the highly resistive nature of our sample at low temperature, it is not possible to compare the low field effects in the single crystal and polycrystalline samples in this temperature regime.

The observation of the most marked low field effect in the $Sr_{1.8}Nd_{1.2}Mn_2O_7$ composition, together with the fact that ferromagnetic clusters are proposed to be present in their greatest concentration in this compound (compared to x = 0, 0.1 and 0.5 samples), suggests that these two features may be related. An evaluation of the presence and dimensions of magnetic clusters for the $Sr_{1.8}Nd_{1.2}Mn_2O_7$, $Sr_{1.5}Nd_{1.5}Mn_2O_7$, $Sr_2HoMn_2O_7$ and $Sr_2YMn_2O_7$ compositions was carried out by A.Coldea and is described in detail in reference [23]. It is shown that a good correlation exists between the size of magnetic clusters and the

maximum ratio of (high field) magnetoresistance observed. It is difficult to quantify the contribution of magnetic clusters to the low field effect. All the samples described here are polycrystalline and have had similar annealing conditions suggesting that grain dimensions should be similar. However, only the x = 0.2 composition shows a significant low field effect, suggesting that granularity alone, whether leading to spin-dependent transport across grain boundaries or inter-grain tunnelling mechanisms, is insufficient to explain the observed effects. This might suggest that spin polarised tunnelling between layers contributes to the low field effect in $Sr_{1.8}Nd_{1.2}Mn_2O_7$. The low field and high field contributions to the magnetoresistance of $Sr_{1.8}Nd_{1.2}Mn_2O_7$ have been separated[36,37] by A.Coldea[23], and both components are plotted as a function of temperature in reference [23]. The low field contribution was shown to reach 27% at 10K, while the high field contribution reaches 82% at 80K in a field of 14T. It is still difficult, however, to assign the particular origin for the low field effect, even after removing the high field component.

Changes in curvature of field dependent resistivity are observed for both $Sr_{1.8}Nd_{1.2}Mn_2O_7$ and $Sr_{1.5}Nd_{1.5}Mn_2O_7$ between high and low temperature regimes. These refer to temperatures above and below ~175K in $Sr_{1.8}Nd_{1.2}Mn_2O_7$ and above and below ~123K in $Sr_{1.5}Nd_{1.5}Mn_2O_7$. Similar changes between 'convex' and 'concave' shapes of curve have been interpreted, in other CMR materials, to be indicative of different transport mechanisms operating in the high and low temperature states[38]. A particularly noticeable feature in the field dependent resistivity data presented for $Sr_{1.8}Nd_{1.2}Mn_2O_7$ is the anomaly around 8 - 10T, which could indicate a change in canting angle of Mn moments, and is likely to be induced by changes in the orientations of Nd moments at this particular temperature, by analogy with behaviour observed in the $Sr_2NdMn_2O_7$ and $Sr_{1.9}Nd_{1.1}Mn_2O_7$ materials[1]. As described by Coldea et al.[23], this anomaly in field dependent resistivity is reproduced in the field dependence of magnetisation for $Sr_{1.8}Nd_{1.2}Mn_2O_7$, measured at 31K up to 15T using an extraction magnetometer inserted in the 17T superconducting magnet. The behaviour observed for $Sr_{1.8}Nd_{1.2}Mn_2O_7$ in particular, suggests these materials would benefit from more extensive investigations into the LFMR response, perhaps as a function of grain size, if this can be controlled in a systematic way by the synthetic conditions.

3.4 References

[1] PD Battle, MA Green, NS Laskey, JE Millburn, PG Radaelli, MJ Rosseinsky, SP Sullivan, JF Vente *Phys. Rev. B* **1996**, *54*, 15967.

[2] PD Battle, SJ Blundell, MA Green, W Hayes, M Honold, AK Klehe, NS Laskey, JE Millburn, LE Murphy, et al. *J. Phys. Condens. Matter* **1996**, *8*, L427.

[3] PD Battle, J Hepburn, JE Millburn, PG Radaelli, MJ Rosseinsky, LE Spring, JF Vente *Chem. Mater.* **1997**, *9*, 3215.

[4] NH Hur, J-T Kim, KH Yoo, YK Park, JC Park, EO Chi, YU Kwon *Phys. Rev. B* **1998**, *57*, 10740.

[5] R Seshadri, C Martin, A Maignan, M Hervieu, B Raveau, CNR Rao *J. Mater. Chem.* **1996**, *6*, 1585.

[6] J Zhang, F Wang, P Zhang, X Sun, Q Yan *J. Magn. Magn. Mater.* **1998**, *190*, 166.

[7] Y Moritomo, A Nakamura, K Ohoyama, M Ohashi, K Hirota *J. Phys. Soc. Jpn.* **1999**, *68*, 631.

[8] J Zhang, F Wang, P Zhang, Q Yan *J. Phys. Condens. Matter* **1999**, *11*, 2413.

[9] J Zhang, F Wang, P Zhang, Q Yan *Solid State Commun.* **1999**, *109*, 401.

[10] JB Goodenough *Phys. Rev.* **1955**, *100*, 564.

[11] JQ Li, Y Matsui, T Kimura, Y Tokura *Phys. Rev. B* **1998**, *57*, R3205.

[12] PD Battle, JE Millburn, MJ Rosseinsky, LE Spring, JF Vente, PG Radaelli *Chem. Mater.* **1997**, *9*, 3136.

[13] JE Millburn *D.Phil Thesis,* University of Oxford **1997**.

[14] PD Battle, MA Green, NS Laskey, N Kasmir, JE Millburn, LE Spring, SP Sullivan, MJ Rosseinsky, JF Vente *J. Mater. Chem.* **1997**, *7*, 977.

[15] SE Dann, MT Weller, DB Currie *J. Solid State Chem.* **1992**, *97*, 179.

[16] N Nguyen, L Er-Rakho, C Michel, J Choisnet, B Raveau *Mat. Res. Bull.* **1980**, *15*, 891.

[17] PD Battle, MA Green, NS Laskey, JE Millburn, LE Murphy, MJ Rosseinsky, SP Sullivan, JF Vente *Chem. Mater.* **1997**, *9*, 552.

[18] S Katano, JA Fernandez-Baca, S Funahashi, N Mori, Y Ueda, K Koga *Physica C* **1993**, *214*, 64.

[19] W Bao, CH Chen, SA Carter, SW Cheong *Solid State Commun.* **1996**, *98*, 55.

[20] PG Radaelli, DE Cox, M Marezio, SW Cheong, PE Schiffer, AP Ramirez *Phys. Rev. Lett.* **1995**, *75*, 4488.

[21] PD Battle, N Kasmir, JE Millburn, MJ Rosseinsky, RT Patel, LE Spring, JF Vente, SJ Blundell, W Hayes, AK Klehe, A Mihut, J Singleton *J. Appl. Phys.* **1998**, *83*, 6379.

[22] Y Moritomo, Y Maruyama, T Akimoto, A Nakamura *J. Phys. Soc. Jpn.* **1998**, *67*, 405.

[23] AI Coldea, LE Spring, SJ Blundell, J Singleton, W Hayes *J. Phys. Condens. Matter,* **1999**, *11*, 9053.

[24] GA Levin, T Stein, CC Almasan, SH Han, DA Gajewski, MB Maple *Phys. Rev. Lett.* **1998**, *80*, 841.

[25] LM Rodriguez-Martinez, JP Attfield *Phys. Rev. B* **1996**, *54*, R15622.

[26] J Sloan, PD Battle, MA Green, MJ Rosseinsky, JF Vente *J. Solid State Chem.* **1998**, *138*,

[27] G Balakrishnan, MR Lees, DM Paul *J. Phys. Condens. Matter* **1997**, *9*, L471.

[28] B Garcia-Landa, MR Ibarra *Phys. Rev. B* **1999**, *60*, 5440.

[29] K Hirota, Y Moritomo, H Fujioka, M Kubota, H Yoshizawa, Y Endoh *J. Phys. Soc. Jpn.* **1998**, *67*, 3380.

[30] A Nossov, J Pierre, J Beille, V Vassiliev, B Slobodin *Eur. Phys. J. B* **1998**, *6*, 467.

[31] JE Evetts, MG Blamire, ND Mathur, SP Isaac, BS Teo, LF Cohen, JL Macmanus-Driscoll *Philos. Trans. R. Soc. London, Ser. A* **1998**, *356*, 1593.

[32] JM De Teresa, MR Ibarra, J Garcia, J Blasco, C Ritter, PA Algarabel, C Marquina, A del Moral *Phys. Rev. Lett.* **1996**, *76*, 3392.

[33] T Kimura, A Asamitsu, Y Tomioka, Y Tokura *Phys. Rev. Lett.* **1997**, *79*, 3720.

[34] A Gupta, GQ Gong, G Xiao, PR Duncombe, P Lecooeur, P Trouilloud, YY Wang, VP Dravid, JZ Sun *Phys. Rev. B* **1996**, *54*, R15629.

[35] HY Hwang, SW Cheong, NP Ong, B Batlogg *Phys. Rev. Lett.* **1996**, *77*, 2041.

[36] K Dorr, K-H Muller, K Ruck, G Krabbes, L Schulltz *J. Appl. Phys.* **1999**, *85*, 5420.

[37] L Balcells, R Enrich, J Mora, A Calleja, J Fontcuberta, X Obradors *Appl. Phys. Lett.* **1996**, *69*, 1486.

[38] J Blasco, J Garcia, JM de Teresa, MR Ibarra, J Perez, PA Algarabel, C Marquina, C Ritter *Phys. Rev. B* **1997**, *55*, 8905.

CHAPTER 4

$n=3$ in $A_{n+1}B_nO_{3n+1}$

$A_4B_3O_{10}$

4.1 Introduction

The investigation of the series $Ca_{n+1}Mn_nO_{3n+1}$ for n=1,2,3 and ∞, by MacChesney and co-workers in 1967[1], hinted at the complexity of the magnetic interactions in Ca,Mn RP phases. It is now believed these have been explained more fully[2] for the compound $Ca_4Mn_3O_{10-\delta}$, following characterisation of this material by powder neutron diffraction[1]. The magnetotransport behaviour of this compound has been investigated also, and has proved equally complex[3]. The symmetry of $Ca_4Mn_3O_{10-\delta}$ has been shown to be orthorhombic, space group *Pbca*, the presence of the relatively small Ca^{2+} cations causing tilting of the MnO_6 octahedra, reminiscent of that observed in the compounds $Ca_4Ti_3O_{10}$ (*Pbca*) and $CaTiO_3$ (*Pnma*)[4].

This chapter describes specifically the results of A- and B-cation site substitutions in the parent compound $Ca_4Mn_3O_{10-\delta}$ (presented in Sections 4.3 and 4.4, respectively). Firstly, Section 4.2 gives an overview of the parent compounds $Ca_4Mn_3O_{10-\delta}$ and $Sr_4Mn_3O_{10-\delta}$ and details the preparation of $Sr_4Mn_3O_{10-\delta}$.

4.2 Comparison of the parent compounds $Ca_4Mn_3O_{10-\delta}$ and $Sr_4Mn_3O_{10-\delta}$

In contrast to $Ca_4Mn_3O_{10-\delta}$, the compound $Sr_4Mn_3O_{10-\delta}$ is not a Ruddlesden Popper phase, belonging instead to the $Cs_4Ni_3F_{10}$ structural class[5]. In 1988, Fabry et al.[6] prepared orthorhombic crystals (space group *Cmca*) of composition $Sr_4Mn_{2.964}Pt_{0.036}O_{10}$. Later, in 1996, Rossell et al.[7] contrasted the structures of $Ca_4Mn_3O_{10}$ and $Sr_4Mn_3O_{10}$, confirming that $Sr_4Mn_3O_{10}$ belonged to the $Cs_4Ni_3F_{10}$ structural class rather than the RP class, but failing still to produce a pure compound (electron microscopy showed the presence of Mn_2O_3 and $SrMnO_3$). The preparation of $Sr_4Mn_3O_{10-\delta}$ in the current study is detailed as follows.

---

[1]The compound $Ca_4Mn_3O_{10-\delta}$ was prepared by J. Lago.[2]

4.2.1 Experimental details

$Sr_4Mn_3O_{10-\delta}$ was synthesised using a standard ceramic technique. Stoichiometric quantities of $SrCO_3$ (99.995%, Alfa) and MnO_2 (99.999% Puratronic, Alfa) were ground together thoroughly and given the heating sequence detailed in Table 4.2.1.

Table 4.2.1 Details of the furnace preparation of 1.5g of $Sr_4Mn_3O_{10-\delta}$:

Temperature (°C)	800	1000	1200	1250[b]
Firing time (hrs)	24	15	15	12
Atmosphere	air	air	air	air
Pellets[a] reground	(powder)	once	4 times	4 times

[a] The pellet diameter was 13mm and 2-3 tonnes were used during pressing.
[b] The sample was quenched from its final firing temperature of 1250°C.

The monitoring of the reaction by X-ray diffraction, using the laboratory Philips diffractometer ($3 \leq 2\theta/^\circ \leq 70$), indicated the formation of a crystalline phase after a relatively short (total) firing time, after quenching the material from a firing for 12 hours at 1250°C. Powder X-ray diffraction data suitable for Rietveld analysis were collected on the laboratory Siemens (D5000) diffractometer ($10 \leq 2\theta/^\circ \leq 100$, $\Delta 2\theta = 0.02^\circ$) in Bragg Brentano geometry.

The material was judged to be of sufficient quality to merit the collection of magnetisation data. This was done using a Quantum Design MPMS SQUID magnetometer. Data were collected as a function of temperature (between 5 and 300K) upon warming, after cooling the sample in zero field (ZFC) and after cooling in the measuring field (FC). Data were collected at fields of 100G.

Attempts were made (by the author and A.Coldea) to measure the magnetotransport of the sample using the apparatus described in Chapter 2.7. Standard four probe geometry was used, with the direct current (≤ 50 μA) perpendicular to the field. Attempts to measure resistivity versus temperature were made on cooling and on warming between room temperature and 4.2K. As usual, contacts were made by fixing copper wires to gold pads (evaporated onto the sample) using Ag epoxy.

4.2.2 Structural and magnetic characterisation of $Sr_4Mn_3O_{10-\delta}$

4.2.2.1 Powder X-ray diffraction

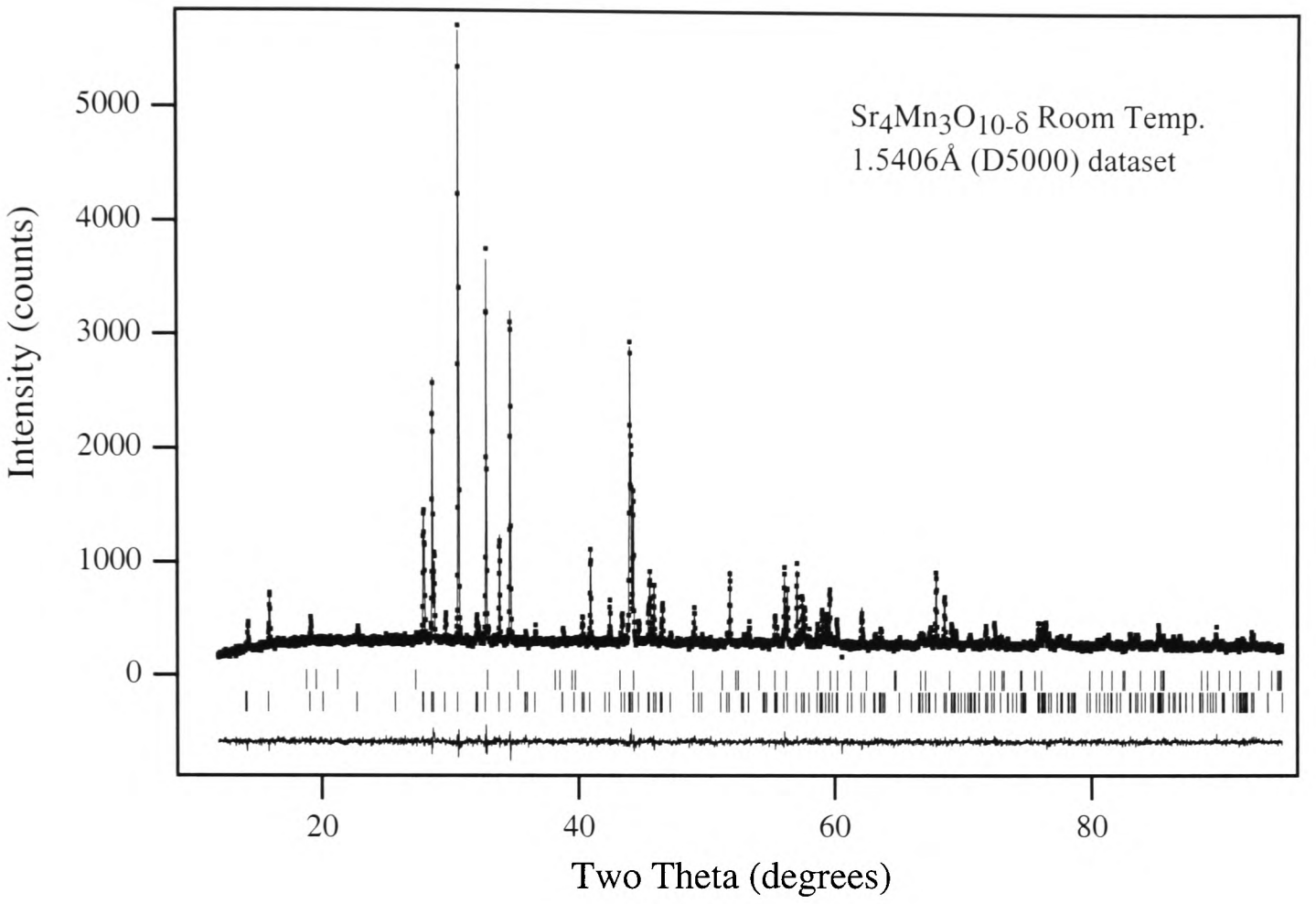


Figure 4.2.1 Observed (dots) and calculated (line) X-ray powder diffraction profiles for $Sr_4Mn_3O_{10-\delta}$ at room temperature. Upper and lower tick marks represent minority and majority phases, respectively.

The Rietveld refinement of powder X-ray diffraction data presented in Figure 4.2.1 was carried out using atomic coordinates and lattice parameters given in the earlier study by Fábry et al.[6]. The data were fitted well using the *Cmca* space group employed in this earlier study. The two sets of tick marks show that it was necessary to include a second phase (of 4H $SrMnO_3$) in the structural model in order to fit the data adequately. The phase fraction for the minority phase refined to just 0.87%; however, on careful examination of the low angle region of the pattern, it is evident that it is necessary to include this phase to account for the weak reflection at $2\theta = 27.27°$, disallowed in the orthorhombic $Sr_4Mn_3O_{10-\delta}$ pattern. The X-ray refinement converged to give the following residual fit parameters: $R_{wp} = 5.86\%$, $R_p = 4.57\%$, DWd = 1.814 and $\chi^2_{red} = 1.150$ for 40 variables.

Table 4.2.2 Structural parameters for biphasic $Sr_4Mn_3O_{10-\delta}$ at room temperature:

Majority phase, 99.13% $Sr_4Mn_3O_{10-\delta}$ by weight

Lattice Parameters(Å) a = 5.47813(8); b = 12.46744(18); c = 12.53256(19); V = 855.951(32)Å^3

Atom[a]	Site	U_{iso}, (Å^2)	x	y	z
Sr(1)	8f	0.00963(99)	0	0.4685(1)	0.1425(2)
Sr(2)	8f	0.01146(107)	0	0.2611(2)	0.3883(1)
Mn(3)	4a	0.00760(228)	0	0	0
Mn(4)	8f	0.00949(151)	0	0.1317(3)	0.1519(3)
O(5)	8f	0.00808(187)[b]	0	0.0382(11)	-0.1484(12)
O(6)	8f	0.00808(187)[b]	0	0.2755(10)	0.1502(11)
O(7)	16g	0.00808(187)[b]	0.2305(15)	0.1095(11)	0.0351(7)
O(8)	8e	0.00808(187)[b]	1/4	0.1264(16)	1/4

Minority phase, 0.87% 4H $SrMnO_3$ by weight

Lattice Parameters(Å) a = 5.45061(99); b = 5.45061(99); c = 9.08757(355)

$\alpha = 90°$; $\beta = 90°$; $\gamma = 120°$; V = 233.813(91)Å^3 Space group: *$P6_3/mmc$*

Atom	Site	U_{iso}, (Å^2)	x	y	z
Sr(1)	2a	0.005[b]	0	0	0
Sr(2)	2c	0.005[b]	1/3	2/3	1/4
Mn(3)	4f	0.005[b]	1/3	2/3	0.6132
O(4)	6g	0.005[b]	1/2	0	0
O(5)	6h	0.005[b]	-0.180	-0.360	1/4

[a] All fractional occupancies were held at 100%

[b] Constrained to be the same

The impurity phase, 4H $SrMnO_3$, was also identified by Rossell et al.[7] (along with Mn_2O_3) when they attempted to synthesise $Sr_4Mn_3O_{10-\delta}$, although they used a higher final firing temperature of approximately 1400°C. Fábry et al. used a similar final firing temperature (1200 - 1250°C) as used in the present study, although, interestingly, they were attempting originally to prepare the oxyfluoride, Sr_2MnO_3F (by a conventional method from melts using $SrCl_2$-SrF_2(-B_2O_3) as a solvent), when black crystals formed, characterised as $Sr_4Mn_{2.964}Pt_{0.036}O_{10}$. They concluded that the platinum arose from contamination by the crucible.

The structural descriptions and atom labelling schemes, introduced in Figures 4.2.2 and 4.2.3, help identification of significant bondlengths and bond angles presented later in Tables 4.2.3 and 4.2.4. As illustrated in Figure 4.2.2, the structure of $Sr_4Mn_3O_{10-\delta}$ is comprised of trimers (trinuclear units, $[Mn_3O_{12}]$) of face sharing octahedra. These corner shared trimers are arranged as 'zig-zag' layers which are parallel to the (010) plane and which are folded along the [001] direction by angles slightly above 100°.

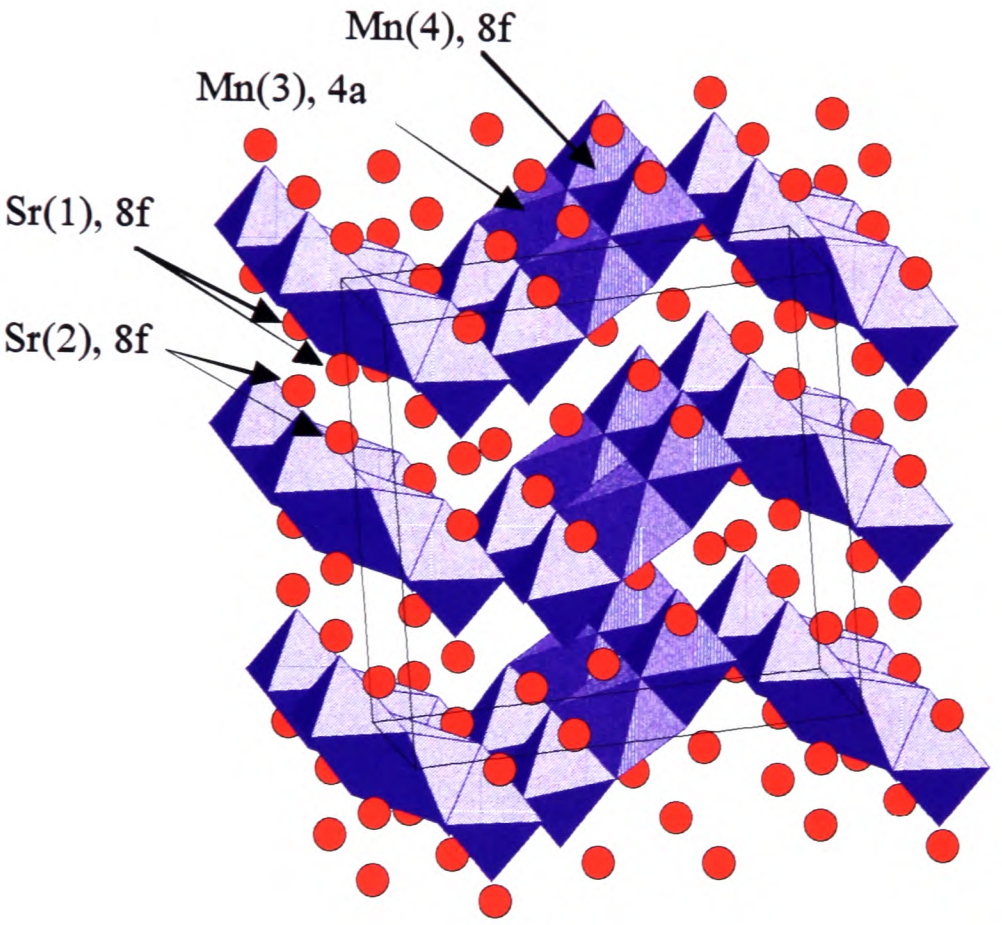


Figure 4.2.2 Polyhedral representation of the compound $Sr_4Mn_3O_{10-\delta}$ showing corner-linked trimers of face sharing octahedra along a direction close to [010]. Crystallographically distinct Sr and Mn cations, and corresponding site symmetries, are labelled.

In Figure 4.2.3, an individual trimer is represented (minus strontium cations) and the four, crystallographically distinct oxygens (O(5) to O(8)), and two distinct manganese cations, are visible. Mn(3) cations occupy the middle octahedron and Mn(4) the 'outer' or edge octahedra, two of the three terminal corners of which are shared with an outer octahedron of the next trimer. For example, in Figure 4.2.3, this corresponds to the terminal 'O(8)' anions bridging two Mn(4) cations, while 'O(6)' anions remain unshared.

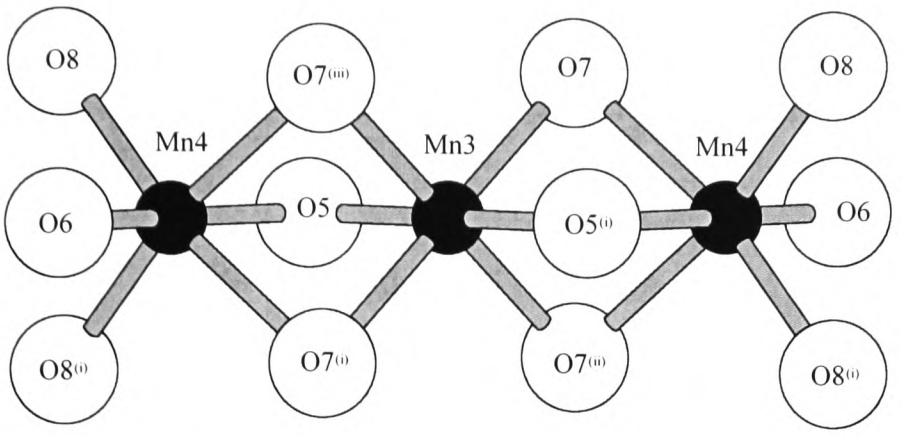


Figure 4.2.3 Arrangement of Mn-O bonds within a $[Mn_3O_{12}]$ trimer (here Sr^{2+} cations are omitted for clarity). Oxygen anions O(5), O(7) and O(8), are numbered to help identification of specific bondlengths and bond angles listed in Tables 4.2.3 and 4.2.4, respectively.

Unfortunately, since no neutron diffraction data were collected for this compound, the Sr-O and Mn-O bondlengths quoted in Tables 4.2.3 and the angles in Table 4.2.4 are accompanied by large estimated standard deviations. As is suggested by the multiplicities quoted in Table 4.2.3, Sr(1) is linked to 10 oxygen anions while Sr(2) is linked to 9 oxygens. The bond/angle data presented in Tables 4.2.3 and 4.2.4 are in good agreement with those reported in the work by Fábry et al.[6].

Table 4.2.3 Significant bondlengths (Å) in $Sr_4Mn_3O_{10-\delta}$ at room temperature:

Bond	Multiplicity	Distance(Å)	Bond	Distance(Å)
Sr(1)–O(5)	2	2.7413(6)	Mn(3)–O(5) x 2	1.921(16)
Sr(1)–O(5)	1	2.620(16)	Mn(3)–O(7) x 4	1.911(12)
Sr(1)–O(6)	1	2.408(13)		
Sr(1)–O(7)	2	2.661(12)	Mn(4)–O(5)	2.119(13)
Sr(1)–O(7)	2	2.844(9)	Mn(4)–O(6)	1.793(12)
Sr(1)–O(8)	2	2.750(14)	Mn(4)–O(7) x 2	1.953(9)
			Mn(4)–O(8) x 2	1.8415(30)
Sr(2)–O(5)	1	2.544(14)		
Sr(2)–O(6)	2	2.7873(25)	Mn(3)-Mn(4)	2.514(4)
Sr(2)–O(6)	1	2.990(15)	Mn(3)-Sr(1)	3.2940(15)
Sr(2)–O(6)	1	3.314(15)	Mn(3)-Sr(2)	3.2904(26)
Sr(2)–O(7)	2	2.583(12)		
Sr(2)–O(7)	2	2.753(12)	Mn(4)-Sr(1)	3.282(5)
Sr(2)–O(8)	2	2.775(12)	Mn(4)-Sr(1)	3.4143(28)
			Mn(4)-Sr(2)	3.2187(26)
			Mn(4)-Sr(2)	3.374(5)

Table 4.2.4 Selected bond angles (°) in $Sr_4Mn_3O_{10-\delta}$ at room temperature. Labelling refers to Figure 4.2.3:

Bond	Angle(°)	Bond	Angle(°)
O(5)–Mn(3)–O(5)^{i}	180.000(0)	O(5)^{i}–Mn(4)–O(6)	178.2(7)
O(5)–Mn(3)–O(7)	92.6(4)	O(5)^{i}–Mn(4)–O(7)	81.0(5)
O(5)–Mn(3)–O(7)^{i}	87.4(4)	O(5)^{i}–Mn(4)–O(7)^{ii}	81.0(5)
O(5)–Mn(3)–O(7)^{ii}	92.6(4)	O(5)^{i}–Mn(4)–O(8)	88.7(7)
O(5)–Mn(3)–O(7)^{iii}	87.4(4)	O(5)^{i}–Mn(4)–O(8)^{i}	88.7(7)
O(5)^{i}–Mn(3)–O(7)	87.4(4)	O(6)–Mn(4)–O(7)	97.6(6)
O(5)^{i}–Mn(3)–O(7)^{i}	92.6(4)	O(6)–Mn(4)–O(7)^{ii}	97.6(6)
O(5)^{i}–Mn(3)–O(7)^{ii}	87.4(4)	O(6)–Mn(4)–O(8)	92.5(7)
O(5)^{i}–Mn(3)–O(7)^{iii}	92.6(4)	O(6)–Mn(4)–O(8)^{i}	92.5(7)
O(7)–Mn(3)–O(7)^{i}	180.00(0)	O(7)–Mn(4)–O(7)^{ii}	80.6(5)
O(7)–Mn(3)–O(7)^{ii}	82.7(6)	O(7)–Mn(4)–O(8)	90.81(26)
O(7)–Mn(3)–O(7)^{iii}	97.3(6)	O(7)–Mn(4)–O(8)^{i}	167.5(5)
O(7)^{i}–Mn(3)–O(7)^{ii}	97.3(6)	O(7)^{ii}–Mn(4)–O(8)	167.5(5)
O(7)^{i}–Mn(3)–O(7)^{iii}	82.7(6)	O(7)^{ii}–Mn(4)-O(8)^{i}	90.81(26)
O(7)^{ii}–Mn(3)–O(7)^{iii}	180.00(0)	O(8)–Mn(4)–O(8)^{i}	96.09(21)

Table 4.2.5 Agreement parameters and refining variables for the refinement of D5000 data:

Refining variables (in addition to atomic coordinates and thermal parameters for majority phase)		Agreement parameter	
Background terms (Shifted Chebyshev)	10	R_{wp} (%)	5.86
Profile Coefficients (pseudo-Voigt)[a]	3	R_p (%)	4.57
Phase fractions	2	DWd	1.814
Zero point	1	χ^2_{red} (40 variables)	1.150
Lattice parameters	5		

[a] Refining profile coefficients were constrained to be the same for the majority and minority phase.

4.2.2.2 Magnetic measurements

Figure 4.2.4 shows the molar magnetic susceptibility of $Sr_4Mn_3O_{10-\delta}$ as a function of temperature at 100G.

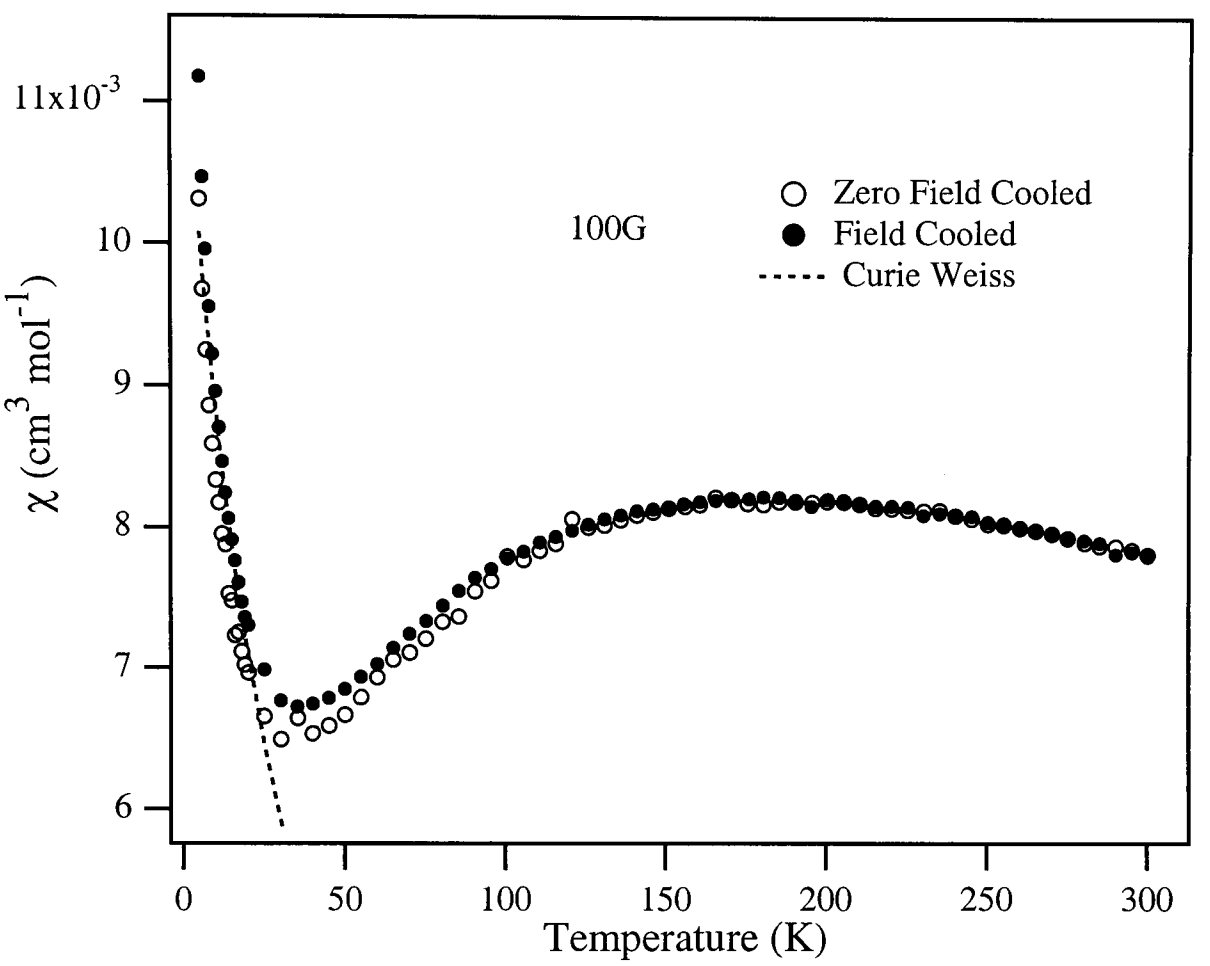


Figure 4.2.4 Molar magnetic susceptibility as a function of temperature at 100G for $Sr_4Mn_3O_{10-\delta}$.

The molar susceptibility is characterised by a broad maximum in the high temperature region, spreading from approximately 275 to 100K but reaching its absolute maximum value at 165K. The zero field cooled and field cooled curves overlie from 300 down to approximately 125K; below 125K there is a slight divergence between the two curves which is most pronounced at the local minimum of the curve, 30K. The sharp increase in the signal observed below 30K was fitted moderately well by the Curie-Weiss law (θ = -30.7(25), C = 0.359(25) cm^3 K mol^{-1}), whereas the high temperature region was not. The only significant difference in the appearance of the data collected at 1kG is the absence of any pronounced divergence between ZFC and FC signals throughout the measured 5 to 300K temperature range.

The value of the (Curie law) effective magnetic moment at 300K, calculated using equation 4.2.1, is 1.44μ_B per Mn.

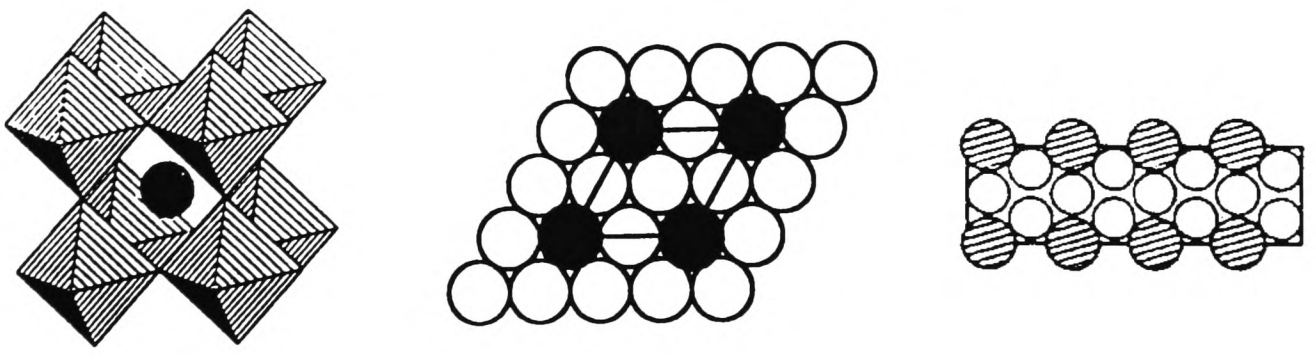
$$\mu = 2.83\ \sqrt{\chi T} \qquad \text{eqn. (4.2.1)}$$

The results of magnetotransport measurements showed that the sample was highly resistive. At approximately 110K, while cooling from room temperature to 4.2K, the voltmeter read a signal periodically, albeit unstable, corresponding to a resistance in the region of 300MΩ. However, by cooling lower to 100K, the signal disappeared. There was no evidence to suggest that the difficulties in obtaining a signal were due to poor contacts.

4.2.3 Discussion

In discussing the observed structural and magnetic properties of $Sr_4Mn_3O_{10-\delta}$ (and when comparing these properties to those of $Ca_4Mn_3O_{10-\delta}$), it is appropriate to begin with a consideration of the factors determining whether corner sharing or face sharing of octahedra predominate in a structure.

The (perovskite derived) Ruddlesden Popper structures discussed in this thesis are all based upon corner shared MnO_6 octahedra. These have been understood by considering a 'framework' picture of ABX_3 units, (where B = Mn, and X = O) from which the (n=2, n=3 etc.) RP intergrowth structures are derived by inserting 'AO' rocksalt layers at appropriate intervals. This type of representation is given in Figure 4.2.5 (a).



(a) (b) (c)

Figures 4.2.5 (a) Framework picture of generalised perovskite AMX_3, (b) Representation of the $[AX_3]$ layers with the A-cation shaded and (c) Alternative orthorhombic packing for an $[AX_3]$ array which does not occur in perovskites. (Figures reproduced from reference [5]).

In contrast to the representation shown in Figure 4.2.5 (a), when discussing $Sr_4Mn_3O_{10-\delta}$, it is more helpful to consider a 'layer' picture of ABX_3, in which the perovskite structure is viewed as deriving from the stacking of hexagonal layers of composition AX_3. The A-cations may be regarded as lying at the corners of the basal plane of a hexagonal cell, as

shown in Figure 4.2.5 (b). The oxygen anions occupy the edge and face centre positions. The way in which successive, hexagonal AX_3 layers stack upon one another determines whether corner shared or face shared octahedral interstices result. If the layers are stacked in a three-layered sequence, *abcabcabc*, a close packed structure of cubic symmetry (corner shared octahedra) results. Conversely, if a two-layered sequence, *abababab,* is preferred, a hexagonally close packed structure containing face shared octahedra results. These are the two structural extremes, although the latter stacking sequence, *abababab*, is only found in a limited number of oxides, all of which contain Ba as the A-site cation; for example, $BaNiO_3$ which often denotes the structural type[8]. Often, an additional form of nomenclature accompanies the molecular formula, in which a number indicates the layers in the unit cell and a letter indicates the symmetry. For example, the $BaNiO_3$ structural type is accompanied by 2H.

The structure of $Sr_4Mn_3O_{10-\delta}$ represents one of a number of structures [9] in which neither corner nor face sharing of octahedra is dominant completely, but instead where a mixture of hexagonal and cubic stacking exists. The structure belongs to the $Cs_4Ni_3F_{10}$ type[5]; the latter was found to be isostructural with $Ba_4(Ti,Pt)_3O_{10}$[10] which was characterised as early as 1948. In further contrast to a typical RP oxide encountered until now, the packing of cations and anions *within* the close packed layers in $Sr_4Mn_3O_{10-\delta}$ is not based entirely upon the hexagonal array of $[AX_3]$ (here $[SrO_3]^{2-}$) shown in Figure 4.2.5 (b). Instead, anion-deficient close packed layers represented by $[Sr_4O_{10\ 2}]^{6-}$ are of a mixed type; one part is the hexagonal array as is common in perovskites but the other is the alternative, orthorhombic packing for an $[AX_3]$ composition which does not occur in perovskites. The particular packing arrays are associated with two different orientations of the trimer; the orthorhombic pattern is present when the trimer is oriented approximately along $[0\bar{1}1]$, whereas the hexagonal array predominates when the trimer is oriented along the [011] direction. Figures 4.2.5 (b) and (c) give the distinctive types of close packing for the $[AX_3]$ composition. The hexagonal array is that shown in (b) and the orthorhombic arrangement is shown in (c) for comparison. The structure of $Cs_4Ni_3F_{10}$ (adopted by $Sr_4Mn_3O_{10-\delta}$) is described fully in the work presented by Schmidt et al.[5].

In comparison with the relatively complex structure adopted by $Sr_4Mn_3O_{10-\delta}$, $Ca_4Mn_3O_{10-\delta}$ is an n=3 RP oxide[2], comprised of corner sharing MnO_6 octahedra (albeit undergoing tilting to give orthorhombic symmetry). Thus, the effect of changing the A-site cation size on moving from Ca to Sr accounts for the significant structural changes between $Ca_4Mn_3O_{10-\delta}$ and $Sr_4Mn_3O_{10-\delta}$. This is illustrated also by considering the nature of the octahedra in the compounds $CaMnO_3$, 4H $SrMnO_3$ and 2H $BaMnO_3$ (completely corner shared, partially corner shared and partially face shared and fully face shared, respectively). The effect is illustrated well for some fluorides, by considering that $CsMnF_3$ has the hexagonal barium titanate structure, whereas $KMnF_3$ has a perovskite structure. Indeed, the size of the A-site cation is the most important factor controlling whether face sharing of octahedra (and the resultant, short B-B-cation separation distances) are tolerated. Clearly, the presence of a large A-site cation such as Ba causes a greater separation of the AX_3 layers, and maximises the distance apart the B-site cations are across the shared octahedral face. Even so, the magnitude of this separation distance (typically ~2.50Å) is significantly less than the B-cation separation distance across a B - X - B vertex linkage.

Structures adopting face sharing octahedra often show other features which occur so as to minimise cation-cation repulsion across the shared triangular face. For example, there is usually a displacement of the B-site cations occupying the terminal (face) shared octahedra of a polynuclear unit in order to minimise the repulsion between the cations in the face sharing unit. Indeed, this is observed in the compound in this study. From reference to Table 4.2.3 and Figure 4.2.3, although the Mn(3)-O bondlengths are all the same within error (approximately 1.92Å), the list of Mn(4)-O bondlengths shows two anomalous values. These are the high value of 2.119(13)Å for the Mn(4)-$O(5)^i$ bond and the short length of the Mn(4)-O(6) bond at 1.793(12)Å, confirming the displacement of the terminal Mn(4) cations towards the terminal, unshared face of the trimeric unit. The resulting Mn(3)-Mn(4) intercation separation distance is 2.514(4)Å, which, interestingly, is longer than the Mn-Mn separation distance of 2.40Å in 2H $BaMnO_3$, where the infinite chains of face shared octahedra do not offer the possibility of an equivalent displacement towards an unshared face[11]. An additional effect, often detected by neutron diffraction experiments on compounds containing face shared

octahedra, is the contraction of the triangle of oxygen anions comprising the shared face further into the path of the repulsive B-site cations in order to dilute further this repulsion. Clearly, only having X-ray diffraction data on the present compound limits the information available on precise oxygen positions.

It has also been suggested[12] that face sharing of octahedra can be stabilised by the presence of transition metal cations with unpaired electrons in the polyhedral unit, that can lead to a favourable bonding interaction which competes with the repulsive force between like-charged cations. For example, in the work on $Cs_4Ni_3F_{10}$ presented by Schmidt et al.[5], the compounds $Cs_4Mg_3F_{10}$, $Cs_4Zn_3F_{10}$ and $Cs_4Co_3F_{10}$ were studied also. It was noted that $Cs_4Mg_3F_{10}$ adopted an even larger Mg-Mg separation (274.8(2)pm) within the trinuclear unit than that observed in $Cs_4Ni_3F_{10}$ (272.7(1)pm), even though the magnesium compound had the smallest cell volume and octahedral distances of the entire series. After detailed analysis it was concluded that the intercation repulsion was reduced significantly for the Ni (d^8) and Co (d^7) compounds relative to the closed shell Mg and Zn species. Indeed, in the crystallographic study into the compounds $Ba_4Ti_{1.81}Pt_{1.19}O_{10}$ and $Ba(Ti,Pt)O_3$ by Fischer and Tillmanns in 1981[12], it was suggested that the shortened distances between central cations in double or triple groups of face sharing octahedra relative to those in other barium titanates arose due to the substitution of some of the (d^0 Ti^{4+}) for Pt. Probably, it was with this effect in mind that Fábry et al.[6] suggested that the Pt incorporated into their $Sr_4Mn_3O_{10-\delta}$ compound was essential for the stabilisation of the structure.

In contrast with the Mn^{4+}-Mn^{4+} magnetic interactions (within the framework of corner shared MnO_6 octahedra) in $Ca_4Mn_3O_{10-\delta}$, which have been investigated by several groups[1,2,7], the magnetic properties of $Sr_4Mn_3O_{10-\delta}$ have received little attention. The magnetic properties as interpreted from the data in Figure 4.2.4 appear to show broad similarities with those of 4H $SrMnO_3$ and another system containing face shared Mn^{4+} octahedra, $Ba_6Mn_4ZnO_{15}$, studied recently by Cussen et al.[13]. As for the latter compounds, the room temperature molar magnetic susceptibility of $Sr_4Mn_3O_{10-\delta}$ is low relative to the value predicted for the spin only contribution from three moles of Mn^{4+}, d^3 cations per mole

of $Sr_4Mn_3O_{10-\delta}$. This suggests there are antiferromagnetic exchange interactions operating between Mn^{4+}, d^3 cations even at this relatively high temperature. As observed in the compound $Ba_6Mn_4ZnO_{15}$, the molar susceptibility of $Sr_4Mn_3O_{10-\delta}$ is characterised by a broad, rather than a sharp, maximum, followed by a dramatic increase in the signal at the lowest measuring temperatures, suggestive of the presence of uncoupled Mn^{4+} magnetic moments.

In order to consider the nature of antiferromagnetic exchange interactions in $Sr_4Mn_3O_{10-\delta}$, the geometry of the Mn-O framework is shown in Figure 4.2.6.

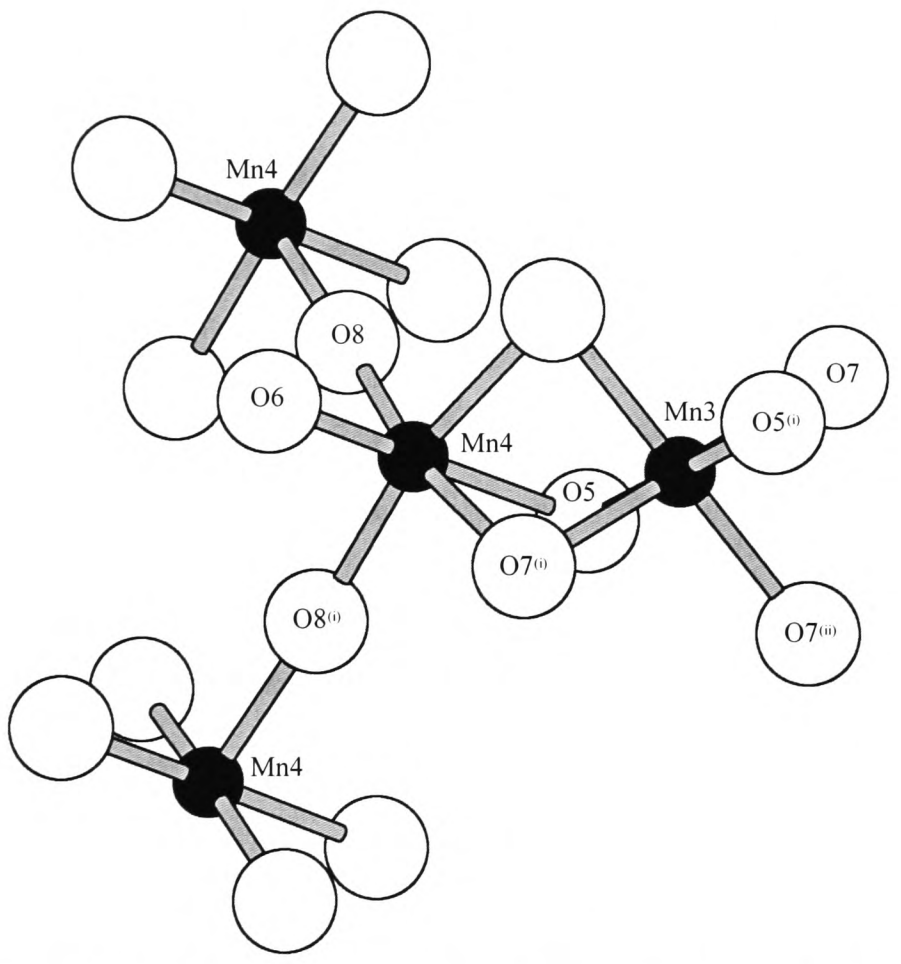


Figure 4.2.6 Geometry of Mn-O framework within the $[Mn_3O_{12}]$ trimeric unit. Oxygen anions belonging to the same trimer are labelled as in Figure 4.2.3.

The important bond angles around the Mn(4) cation occupying the terminal octahedron of the trimeric unit are as follows: the bond angles for Mn(4)-O(8)-Mn(4), Mn(4)-O(5)-Mn(3) and Mn(4)-O(7)-Mn(3) are 175.9(13)°, 76.8(5)° and 81.2(4)°, respectively.

The π superexchange interaction between the half full t_{2g} Mn orbitals through the corner sharing network is a common, *indirect* exchange mechanism for the d^3 configuration, and is antiferromagnetic, as observed in $Ca_4Mn_3O_{10-\delta}$[1,2] (albeit accompanied in this case by slight canting of spins attributed to the Dzyaloshinsky[14]-Moriya[15] interaction. The

predominant exchange interaction operating between the Mn d^3 cations *within* the trimeric unit is likely to be a *direct*, antiferromagnetic exchange interaction due to the proximity of these cations, which enables overlap of their t_{2g} orbitals. The prevalence of one particular interaction over another, and the temperature of onset of each, is an interesting issue, to which the interactions observed in 4H $SrMnO_3$ can help suggest an answer.

The magnetic behaviour in 4H $SrMnO_3$ was shown by Battle et al.[16] to involve both the indirect and direct Mn^{4+}-Mn^{4+} exchange interactions outlined above and the study identified the temperatures of onset of each, using a combination of neutron diffraction, Mössbauer spectroscopy and susceptibility measurements. It was shown that a maximum in the susceptibility at 350K corresponded to the onset of antiferromagnetic interactions between Mn cations *within* the Mn_2O_9 dimers but that long range, (inter-dimer) antiferromagnetic superexchange interactions across corner sharing Mn-O-Mn linkages did not occur until a Néel temperature of 278K.

The study mentioned above on the compound $Ba_6Mn_4ZnO_{15}$[13] identified also face shared octahedra containing d^3 cations and confirmed the predominance of antiferromagnetic interactions across the shared face between d^3 cations within polynuclear units. The study of the magnetism of $Ba_6Mn_4ZnO_{15}$ is rendered more complex by the presence of two distinct B-site cations and two coordination geometries. These are not factors in $Sr_4Mn_3O_{10-\delta}$; however, the $Ba_6Mn_4ZnO_{15}$ study emphasises the number of inter-chain exchange interactions which must be satisfied when the one dimensional interactions along the tetrameric units extend to three dimensions with sufficient lowering of temperature. With the information from these respective studies in mind, it is possible to draw broad conclusions from the observations of the magnetic behaviour in $Sr_4Mn_3O_{10-\delta}$, albeit in the absence of information from neutron diffraction data.

Considering the observed behaviour in $Sr_4Mn_3O_{10-\delta}$, the temperature dependence of molar susceptibility is characterised by a broad maximum in the higher temperature region, before the signal starts to decrease from 165K downwards in temperature. A local minimum is reached at 30K (also corresponding to the temperature at which the divergence between the ZFC and FC curves is the largest), then the signal shows a dramatic increase which continues

to the lowest measured temperature, 5K. It is probable that the reduction in the room temperature paramagnetic moment is associated with antiferromagnetic coupling between the Mn cations within the trimeric units. On lowering the temperature it is not appropriate to suggest that this short range antiferromagnetic order might extend to long range one-dimensional order, followed by long range three-dimensional order, successively. This is because, unlike in $Ba_6Mn_4ZnO_{15}$ for example, in $Sr_4Mn_3O_{10-\delta}$ polyhedral units do not occur as discrete chains separated completely by A-site cations. Instead, each trimer is connected to four others through two corner shared linkages at each terminal octahedron of the trimeric unit. Therefore, an extension of the range of antiferromagnetic correlations over more than one trimer, occurs necessarily in more than one dimension initially. Although the broad maximum peaking at 165K, followed by the steady reduction of the susceptibility, appears to represent an extension of antiferromagnetic correlations leading to a reduction in the molar susceptibility, the precise assignment of the magnetic structure would require confirmation by neutron diffraction. The value of the Curie constant, obtained from the Curie-Weiss fit to the signal between 30K and 5K, suggests that 0.192 mol of paramagnetic S = $\frac{3}{2}$ d^3 Mn^{4+} spins remain uncoupled, per mole of $Sr_4Mn_3O_{10-\delta}$ sample. The predominance of antiferromagnetic correlations over the temperature range studied is consistent with the highly insulating nature of the sample, suggested by the inability to obtain a stable reading of resistivity below the maximum, measurable value of 300MΩ. Unfortunately, any attempted explanation of the magnetic interactions operating in $Sr_4Mn_3O_{10-\delta}$ is speculative somewhat in the absence of low temperature neutron diffraction data, which would confirm whether the structure exhibits long range magnetic order.

In conclusion, the differing sizes of the Sr^{2+} and Ca^{2+} cations have far reaching consequences for the structural and magnetic properties of the systems $Sr_4Mn_3O_{10-\delta}$ and $Ca_4Mn_3O_{10-\delta}$. The r_A/r_B ratios are the most important factor in determining which structural type each compound adopts. The result is that $Ca_4Mn_3O_{10-\delta}$ belongs to the n=3 RP structural class, based on a network of corner sharing MnO_6 octahedra, tilted to provide the coordination requirements of the relatively small Ca cation, with dominant antiferromagnetic correlations between Mn^{4+}, d^3 cations across ~180° Mn-O-Mn linkages. In $Sr_4Mn_3O_{10-\delta}$, the

presence of the larger Sr cation permits some face sharing, as well as corner sharing of MnO_6 octahedra, and the $Cs_4Ni_3F_{10}$ structure is adopted. The resulting magnetic interactions appear to be based upon both *intra*-trimer and *inter*-trimer antiferromagnetic correlations which yield a highly localised electronic arrangement. $Sr_4Mn_3O_{10-\delta}$ does not appear to be a good candidate for CMR studies but its properties provide an interesting contrast to the structural and magnetic behaviour observed in n=3 RP materials.

4.3 A-cation substitution in $Ca_4Mn_3O_{10-\delta}$ and $Sr_4Mn_3O_{10-\delta}$

It was hoped to introduce mixed-valent manganese in $Ca_4Mn_3O_{10-\delta}$ by doping with low concentrations of trivalent Ln cations on the A-cation site in order to investigate the magnetotransport properties of n = 3, Mn(IV) rich RP phases. If mixed-valent Mn cations were to be tolerated in the n = 3 structure, it would be possible to proceed to higher doping levels in an attempt to reproduce the CMR properties of other RP phases containing Mn^{3+}/Mn^{4+} cations, by entering the 'double exchange regime'. The Sr solid solution series $Sr_{4-x}La_xMn_3O_{10-\delta}$ was of interest also, primarily to observe if, and when, a crossover between the $Cs_4Ni_3F_{10}$ and Ruddlesden Popper structure types would take place as a result of the changing, mean radius of the A-site cation and the increase in charge on the A-cation site. The doping levels attempted for each of the Ca and Sr series $A_{4-x}La_xMn_3O_{10-\delta}$ were x = 0.05, 0.1 and 0.5. The Sr solid solution series $Sr_{4-x}La_xMn_3O_{10-\delta}$ did not incorporate La onto either of the Sr sites within the structure, evidenced by the formation of an impurity phase indexed as La_2O_3 in each of the $Sr_{3.95}La_{0.05}Mn_3O_{10-\delta}$ and $Sr_{3.90}La_{0.10}Mn_3O_{10-\delta}$ compositions. The majority phase could still be refined as $Sr_4Mn_3O_{10-\delta}$, space group *Cmca*, in each case, suggesting that this structure can support a degree of Sr deficiency. However, on introduction of further La corresponding to x = 0.5, the $Sr_4Mn_3O_{10-\delta}$ structure could not be stabilised and a complicated diffraction pattern resulted.

It was found also that it is extremely difficult to stabilise the n=3 RP structure in the $Ca_{4-x}La_xMn_3O_{10-\delta}$ series, containing mixed-valent manganese. Of the three La concentrations studied (x=0.05, 0.1 and 0.5), only the attempt using x = 0.05 appears to have incorporated La^{3+} into the structure. The samples at the x = 0.1 and x = 0.5 doping level gave diffraction patterns dominated by n = 2 and n = ∞ material under a range of synthetic conditions. Therefore, the bulk of this section focusses on the preparation and characterisation of $Ca_{3.95}La_{0.05}Mn_3O_{10-\delta}$.

The relatively few CMR studies into $A_{4-x}Ln_xMn_3O_{10-\delta}$ solid solution series currently in the literature reflects the difficulties in preparation of mixed-valent Mn, n=3 RP compounds. Comprehensive studies appear to be limited to one by Witte et al. in 1998[17] for polycrystalline samples of $Ca_{4-x}Ln_xMn_3O_{10-\delta}$, using x=0.01 and 0.1, and two publications by

Asano's group[18,19]; the latter group have concentrated on synthesising thin films of (nominal) concentration $Ca_{1.9}La_{2.1}Mn_3O_{10}$ (using single target magnetron sputtering techniques) on which to extend their CMR studies started on n = 2 phases at the same doping level. The lack of convincing evidence of sample purity in these studies makes it difficult to evaluate the dominant contributions to the magnetic and transport data presented in each case.

4.3.1 Experimental details

$Ca_{3.95}La_{0.05}Mn_3O_{10-\delta}$ is the only compound described in this thesis for which a (non-standard) ceramic synthesis, based on the Pechini[20] citrate gel process, was attempted. This is one of several[21-23] solution based methods available for preparing polycrystalline samples which offers increased homogeneity (for example, when a uniform distributuion of the dopant through the lattice is required) and usually requires lower final firing temperatures and shorter reaction times.

Stoichiometric quantities of $CaCO_3$ (99.995%, Alfa), MnO_2 (99.999% Puratronic, Alfa) and dried La_2O_3 (99.99%, REacton, Johnson Matthey) were ground thoroughly and dissolved in 2-6M HNO_3 in a 1litre beaker. Although the starting solution of HNO_3 was 2M, additional 5ml quantities of acid were added to complete dissolution of the solids, with vigorous stirring. In total, approximately 28mmol of cationic reactants (Ca^{2+}, Mn^{4+}, La^{3+}) were present for the preparation of 2g of the target material. Hence, a slight excess of 28mmol (~6g) of the complexing agent, citric acid, was dissolved in 100ml distilled H_2O and this solution added to the solution of metal ions. The solution was adjusted to pH ~4 by addition of ammonia solution (to prevent the precipitation of alkaline earth metal nitrates during concentration of the solution) and then concentrated by gentle heating using a hot plate. During heating, 2-3ml ethyleneglycol were added as a gelling agent and gradually the solution became more viscous, signalling the esterification of the hydroxy acid, yielding eventually a brownish, slightly frothy, gelatinous precursor. Care had to be taken at this point to prevent self-ignition of the mixture; this was avoided by careful control of the heat setting and keeping to a minimum the amount of nitric acid added initially. The precursor was then scraped from the beaker into a large crucible, and given the heat treatment detailed in Table 4.3.1. During the

first heat treatment between 25 and 450°C, at approximately 210°C, ignition of the carbonaceous material occurred, accompanied by an expansion of the precursor, as NO_x and CO_2 gases are evolved. The resulting ash (containing the appropriate quantities of metal cations) was ground thoroughly and returned to the furnace as a powder and heated slowly from to 25 to 650°C, and subsequently as tabulated.

Table 4.3.1 Details of furnace preparation of $Ca_{3.95}La_{0.05}Mn_3O_{10-\delta}$:

Temperature (°C)	25→450	25→650	800	1000	1200	1150	1330
Firing time (hrs)	heated at 2°/min	heated at 2°/min[b]	22	40	20	60	36
Atmosphere	air	air	air	air	air	air	air
Pellets[a] reground	powder	powder	once	twice	once	twice	once

[a] The pellet diameter was 8mm and 2-3 tonnes were used during pressing.

[b] After the second heating to 650°C, the compound was left for 12hrs at this temperature.

It was anticipated that using the solution approach would lead to a lower final firing temperature than the 1200-1350°C values required typically for previous[24,25] RP materials (as a result of more thorough mixing of reactants in solution). However, the final firing temperature of 1330°C proved this expectation not to be the case. In a recent study by Fawcett et al.[26], it was noted that although phase formation occurred in $Ca_4Mn_3O_{10-\delta}$ (using the same Pechini related sol-gel procedure) at as low a temperature as 900°C, crystallinity improved greatly when the temperature was raised to 1000 - 1200°C.

In the present case, the X-ray diffraction patterns taken on the laboratory Philips instrument ($3 \leq 2\theta/^\circ \leq 70$), did not show the predominance of a n=3 RP phase (characterised by the evolution of the 002 reflection with a d-spacing of approximately 13.5Å), until at least 1300°C. Powder X-ray diffraction data suitable for Rietveld refinement were collected on the laboratory Siemens (D5000) instrument between $10 \leq 2\theta/^\circ \leq 120$, step size $\Delta 2\theta = 0.02^\circ$. Unfortunately, the small amount of material available resulted in a poor signal-to-noise ratio.

Magnetisation data as a function of field and temperature were collected for the sample on a Quantum Design MPMS SQUID magnetometer. Data were collected as a function of temperature (between 5 and 300K) upon warming, after cooling the sample in zero field (ZFC) and after cooling in the measuring field (FC). A maximum temperature step-size of 2°

was used in the vicinity of the magnetic transition (90-130K) observed in the 'parent' compound, $Ca_4Mn_3O_{10-\delta}$. Magnetisation data versus field were collected at temperatures of 300, 200, 100, 60 and 5K (in that order) by sweeping the field between 20kG and -20kG at each temperature, with field cooling between temperatures. For temperatures below the magnetic transition (60K and below), the temperature was raised to 200K each time before cooling back down to the measuring temperature.

Magnetotransport data were collected (by the author and A.Coldea) on a sintered bar, approximately 5x2x2mm in size, which had been cut from an 8mm diameter pellet, using the apparatus described in Chapter 2.7. Standard four probe geometry was used, with the direct current ($\leq$ 50 μA) perpendicular to the field. Firstly, resistivity was measured as a function of temperature while cooling the material from room temperature to 4.2K in zero field. Secondly, fixed temperatures were selected at which to sweep the applied field between 0 and 14T. The temperatures were selected to coincide with those for which isothermal magnetisation versus field data were collected; hence, 200, 100, 60 and 4K were chosen.

4.3.2 Structural and magnetic characterisation of $Ca_{3.95}La_{0.05}Mn_3O_{10-\delta}$

4.3.2.1 Powder X-ray diffraction

Figure 4.3.1 shows the observed and calculated X-ray diffraction profiles for $Ca_{3.95}La_{0.05}Mn_3O_{10-\delta}$ at room temperature.

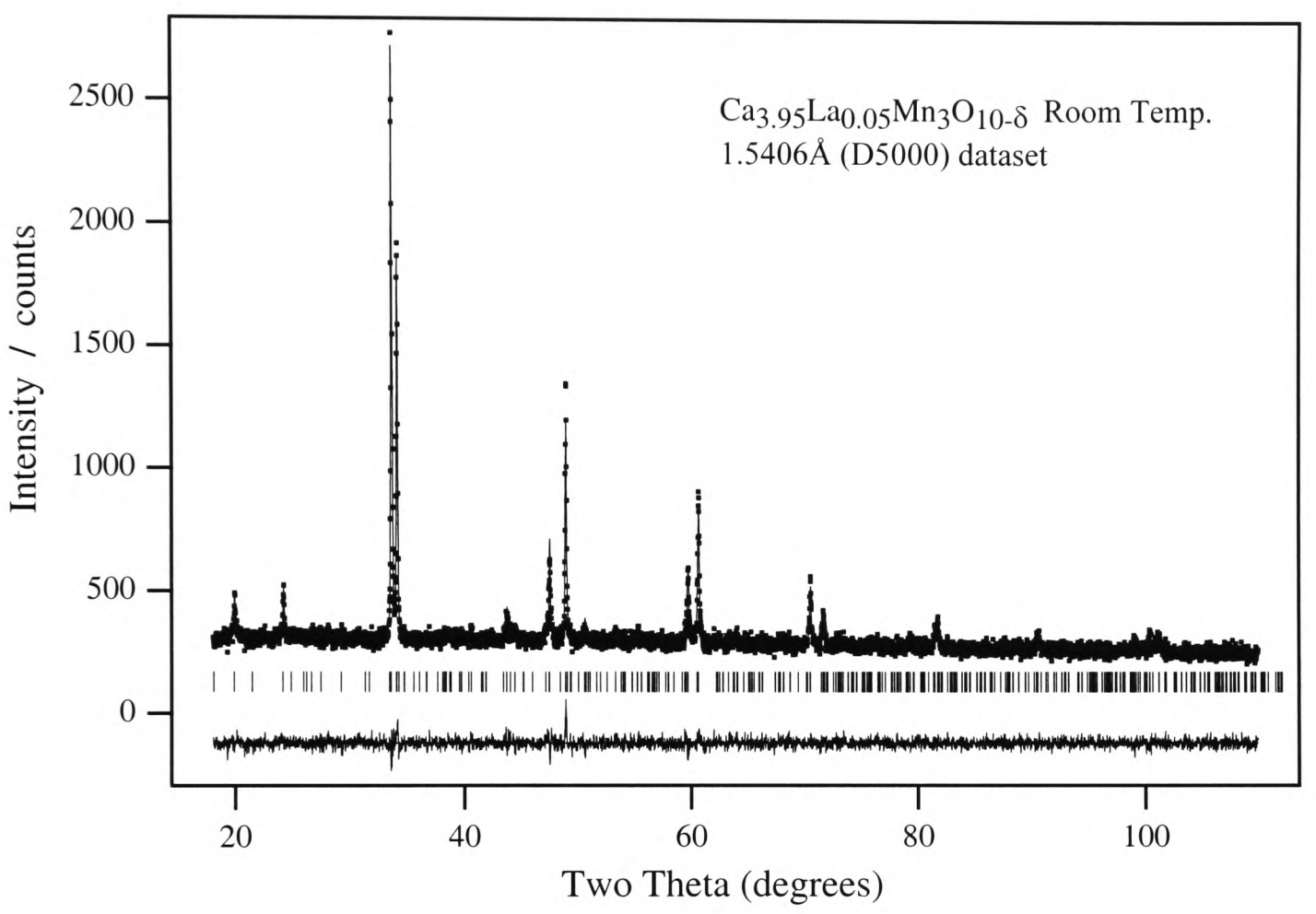


Figure 4.3.1 Observed (dots) and calculated (line) X-ray powder diffraction profiles for $Ca_{3.95}La_{0.05}Mn_3O_{10-\delta}$ at room temperature.

Considering the small modification of the structure which is likely by substitution of just 1.25% of Ca cations by La^{3+}, the space group *Pbca*, used to model the undoped sample $Ca_4Mn_3O_{10-\delta}$[2], was considered a good starting point for the structural refinement. The X-ray data were fitted adequately using this space group in a single phase model. The refinement resulted in the following residual fit parameters: R_{wp} = 5.95%, R_p = 4.77%, DWd = 1.852 and χ^2_{red} = 1.084 for 58 variables. Crystallographic parameters are given in Tables 4.3.2 to 4.3.4, and Figure 4.3.2 gives a labelling scheme denoting A-site, manganese and oxygen atoms in order to help identification of particular bondlengths and bond angles listed in Tables 4.3.3 and 4.3.4, respectively.

---

[2] All comparisons between the observed properties of $Ca_{3.95}La_{0.05}Mn_3O_{10-\delta}$ with those of the undoped phase, $Ca_4Mn_3O_{10-\delta}$, are made with 'sample P' of the latter, prepared by J.Lago and described in detail in reference [2].

Table 4.3.2 Structural parameters of $Ca_{3.95}La_{0.05}Mn_3O_{10-\delta}$ at room temperature:

$Ca_{3.95}La_{0.05}Mn_3O_{10-\delta}$

Lattice Parameters(Å) a = 5.27201(52); b = 5.26565(55); c = 26.8182(25); V = 744.490(201)Å^3

Atom	Site	U_{iso} (Å^2)	x	y	z
Ca(1)[a]	8c	0.0085(38)	0.4942(70)	0.4984(78)	0.07580(5)
Ca(2)[b]	8c	0.0000(46)	-0.0001(81)	-0.0064(77)	0.2097(3)
La(3)[a]	8c	0.0085(38)	0.4942(70)	0.4984(78)	0.07580(5)
La(4)[b]	8c	0.0000(46)	-0.0001(81)	-0.0064(77)	0.2097(3)
Mn(5)	4b	0.0339(66)	0	1/2	0
Mn(6)	8c	0.0044(41)	0.4968(66)	0.0005(73)	0.1484(3)
O(7)	8c	0.0019(46)	0.4621(121)	-0.0062(206)	0.0655(12)
O(8)	8c	0.0019(46)	0.5406(153)	-0.0538(120)	0.2239(11)
O(9)	8c	0.0019(46)	0.7823(159)	0.2233(177)	0.1281(13)
O(10)	8c	0.0019(46)	0.2393(183)	0.7495(166)	0.1496(13)
O(11)	8c	0.0019(46)	0.3178(131)	0.3081(140)	-0.0056(27)

[a,b] Atomic positions and U_{isos} of atoms sharing the same site, were constrained to be the same.

Table 4.3.3 Selected distances (Å) in $Ca_{3.95}La_{0.05}Mn_3O_{10-\delta}$ at room temperature:

Bond	Distance, Å	Bond	Distance, Å	Bond	Distance, Å
Ca1/La3–O(7)	2.65(12)	Ca2/La4–O(8)	2.42(8)	Mn(5)–O(7)	1.770(33)x2
Ca1/La3–O(7)	2.65(12)	Ca2/La4–O(8)	2.92(8)	Mn(5)–O(11)	1.89(9) x2
Ca1/La3–O(7)	2.42(6)	Ca2/La4–O(8)	2.89(7)	Mn(5)–O(11)	1.96(9) x2
Ca1/La3–O(7)	2.88(6)	Ca2/La4–O(8)	2.46(8)	Mn(6)–O(7)	2.231(35)
Ca1/La3–O(9)	2.52(5)	Ca2/La4–O(8)	1.810(35)	Mn(6)–O(8)	2.057(30)
Ca1/La3–O(9)	2.18(6)	Ca2/La4–O(9)	2.50(8)	Mn(6)–O(9)	1.99(9)
Ca1/La3–O(10)	2.73(7)	Ca2/La4–O(9)	3.01(6)	Mn(6)–O(9)	1.95(10)
Ca1/La3–O(10)	2.68(6)	Ca2/La4–O(10)	2.43(7)	Mn(6)–O(10)	1.89(9)
Ca1/La3–O(11)	2.57(7)	Ca2/La4–O(10)	2.75(5)	Mn(6)–O(10)	1.81(9)
Ca1/La3–O(11)	3.18(7)				
Ca1/La3–O(11)	2.37(7)				
Ca1/La3–O(11)	3.01(6)				

Table 4.3.4 Selected bond angles (°) in $Ca_{3.95}La_{0.05}Mn_3O_{10-\delta}$ at room temperature:

Bond	Angle (°)	Bond	Angle (°)
O(7)–Mn(5)–O(7)	179.972(0)	O(8)–Mn(6)–O(9)	105.5(31)
O(7)–Mn(5)–O(11)	91.(4)	O(8)–Mn(6)–O(9)	96.0(21)
O(7)–Mn(5)–O(11)	88.2(31)	O(8)–Mn(6)–O(10)	88.0(30)
O(11)–Mn(5)–O(11)	89.9(14)	O(8)–Mn(6)–O(10)	99.3(19)
		O(9)–Mn(6)–O(9)	85.0(15)
Mn(6)–O(9)–Mn(6)	144.9(25)	O(9)–Mn(6)–O(10)	163.6(21)
Mn(6)–O(10)–Mn(6)	178.(4)	O(9)–Mn(6)–O(10)	96.(4)
Mn(5)–O(11)–Mn(5)	150.5(23)	O(9)–Mn(6)–O(10)	84.(4)
		O(9)–Mn(6)–O(10)	163.8(24)
		O(10)–Mn(6)–O(10)	90.6(15)

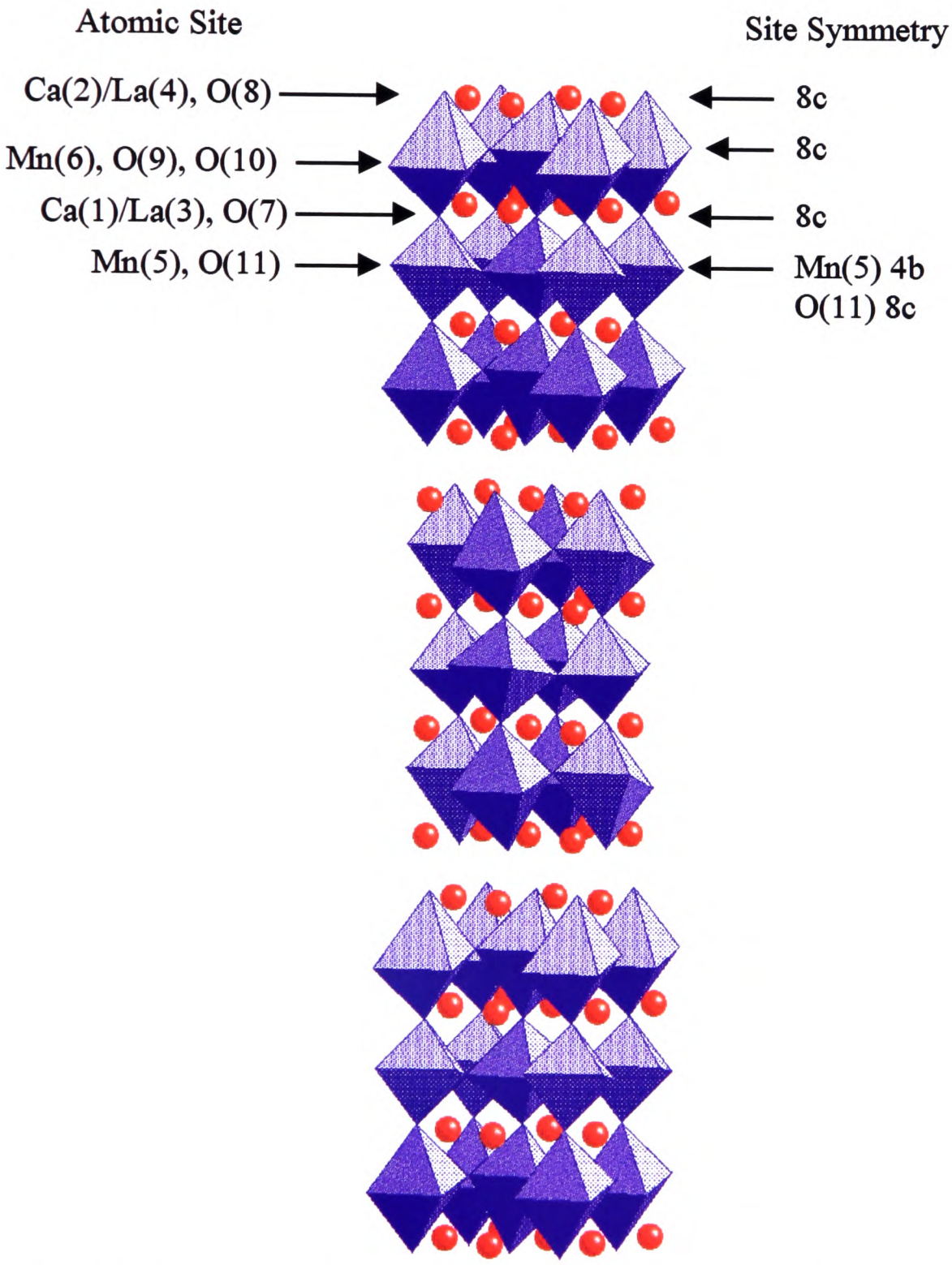


Figure 4.3.2 Polyhedral representation of the compound $Ca_{3.95}La_{0.05}Mn_3O_{10-\delta}$.

Table 4.3.5 Agreement parameters and refining variables at room temperature:

Refining variables (in addition to atomic coordinates and thermal parameters)		Agreement parameter	
Background terms (Shifted Chebyshev)	20	R_{wp} (%)	5.95
Profile Coefficients (pseudo-Voigt)	4	R_p (%)	4.77
Lattice parameters	3	DWd	1.852
Histogram scale factor	1	χ^2_{red} (58 variables)	1.084
Zero point	1		

The fit parameters given in Table 4.3.5 are encouraging, although the low signal-to-noise ratio in the data presented in Figure 4.3.1 and the lack of precise Ca/La-O and Mn-O bondlengths and angles from neutron data mean that a detailed study of structural parameters is not possible. Thus, features suggesting differences or similarities with the parent compound $Ca_4Mn_3O_{10-\delta}$, should not be taken too seriously. However, it is interesting to note that the refined unit cell volume of 749.490(201)Å^3 for $Ca_{3.95}La_{0.05}Mn_3O_{10-\delta}$ is larger than the value refined from a similar D5000 scan on $Ca_4Mn_3O_{10-\delta}$, 742.64(10)Å^3. This is consistent with the presence of a fraction of the larger La^{3+} A-site cation and the partial reduction of a fraction of $Mn^{4+}$to Mn^{3+}, notwithstanding differing oxygen stoichiometries for the two samples. Unfortunately, neither $Ca_{3.95}La_{0.05}Mn_3O_{10-\delta}$ nor $Ca_4Mn_3O_{10-\delta}$ gave concordant results on successive attempts to determine their oxygen stoichiometry by iodometric titration. The small amount of $Ca_{3.95}La_{0.05}Mn_3O_{10-\delta}$ material available limited the number of titration attempts that were made.

Referring to the structural data presented in Table 4.3.3, noticeable features are the highly contracted nature of the Mn(5)-O(7) bond (1.770(33)Å), compared to the equivalent bond in $Ca_4Mn_3O_{10-\delta}$ (1.903(4)Å) and the long Mn(6)-O(7) (2.231(35)Å) and Mn(6)-O(8) (2.057(30)Å) bonds, compared to the equivalent values in $Ca_4Mn_3O_{10-\delta}$ which are (1.921(6)Å) and (1.891(5)Å), respectively. The remaining Mn-O bondlengths listed are approximately the same as the equivalent ones in the parent compound.

4.3.2.2 Magnetic measurements

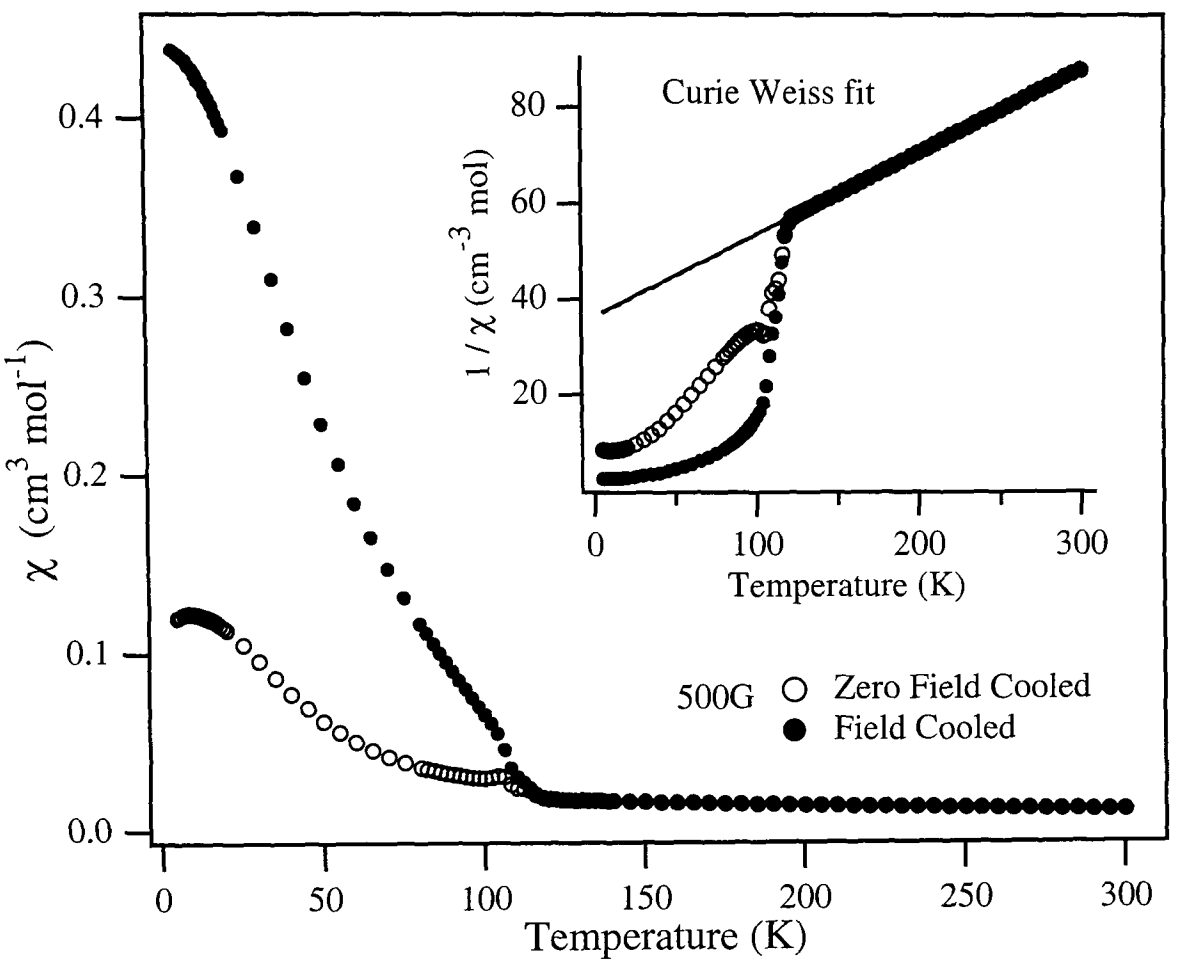


Figure 4.3.3 Molar magnetic susceptibility as a function of temperature at 500G for $Ca_{3.95}La_{0.05}Mn_3O_{10-\delta}$ with an inset showing a fit of high temperature data to the Curie-Weiss law.

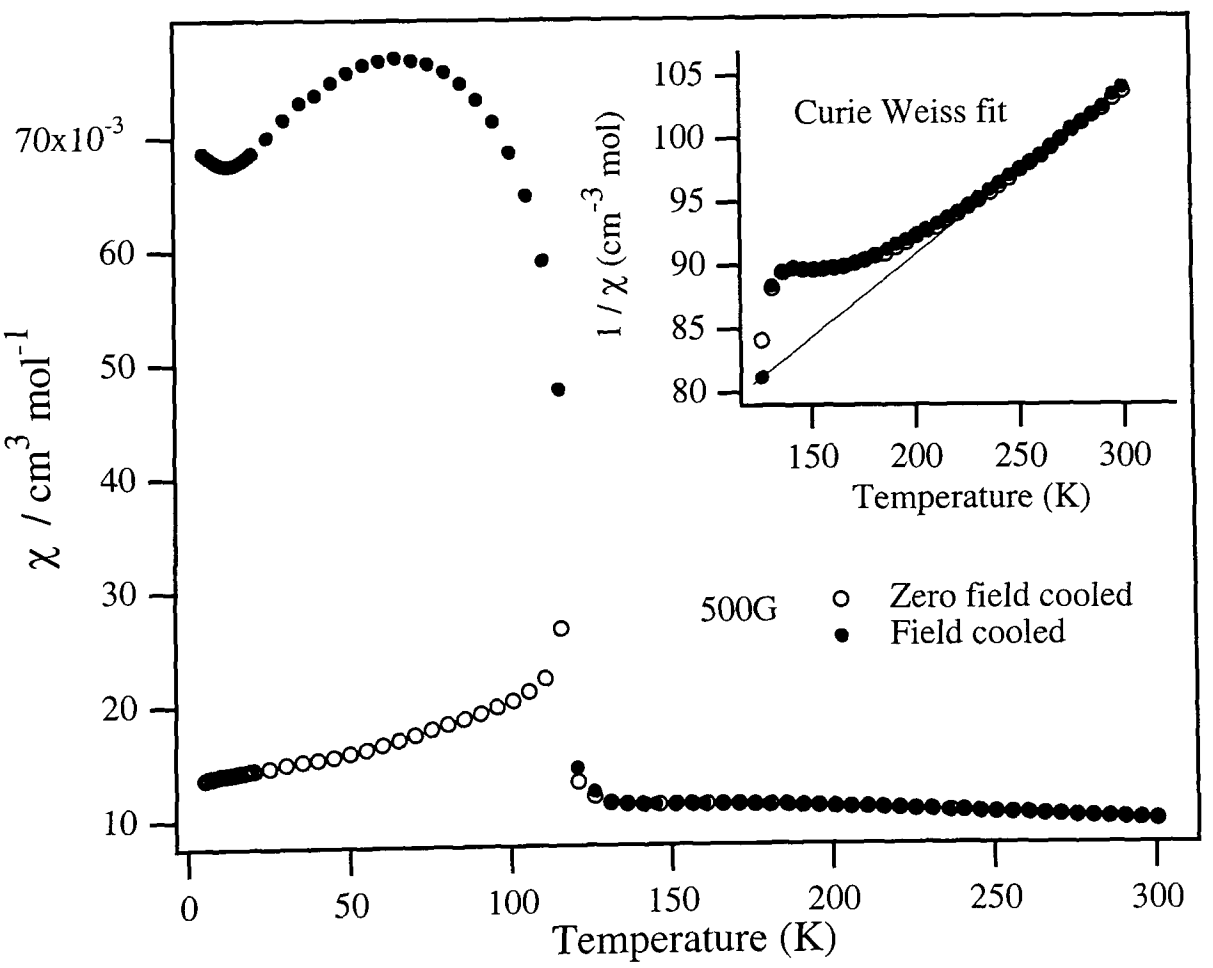


Figure 4.3.4 Comparison of molar magnetic susceptibility of undoped $Ca_4Mn_3O_{10-\delta}$ at 500G.

The variation of molar susceptibility with temperature for $Ca_{3.95}La_{0.05}Mn_3O_{10-\delta}$ (as shown in Figure 4.3.3) shows broad similarities to that observed for $Ca_4Mn_3O_{10-\delta}$ in the same field. The equivalent data measured for the latter sample are presented in Figure 4.3.4, for comparison. For each sample there is a magnetic phase transition in the region 110K-120K, followed by a dramatic increase of the signal, suggesting the onset of ferromagnetic interactions. The magnetic transition in $Ca_{3.95}La_{0.05}Mn_3O_{10-\delta}$ appears slightly more gradual than that in $Ca_4Mn_3O_{10-\delta}$, and the extent of divergence between ZFC and FC signals is not as great as in the latter sample. Figure 4.3.5 shows an enlarged view of the magnetic transition in the temperature range 80-150K for $Ca_{3.95}La_{0.05}Mn_3O_{10-\delta}$.

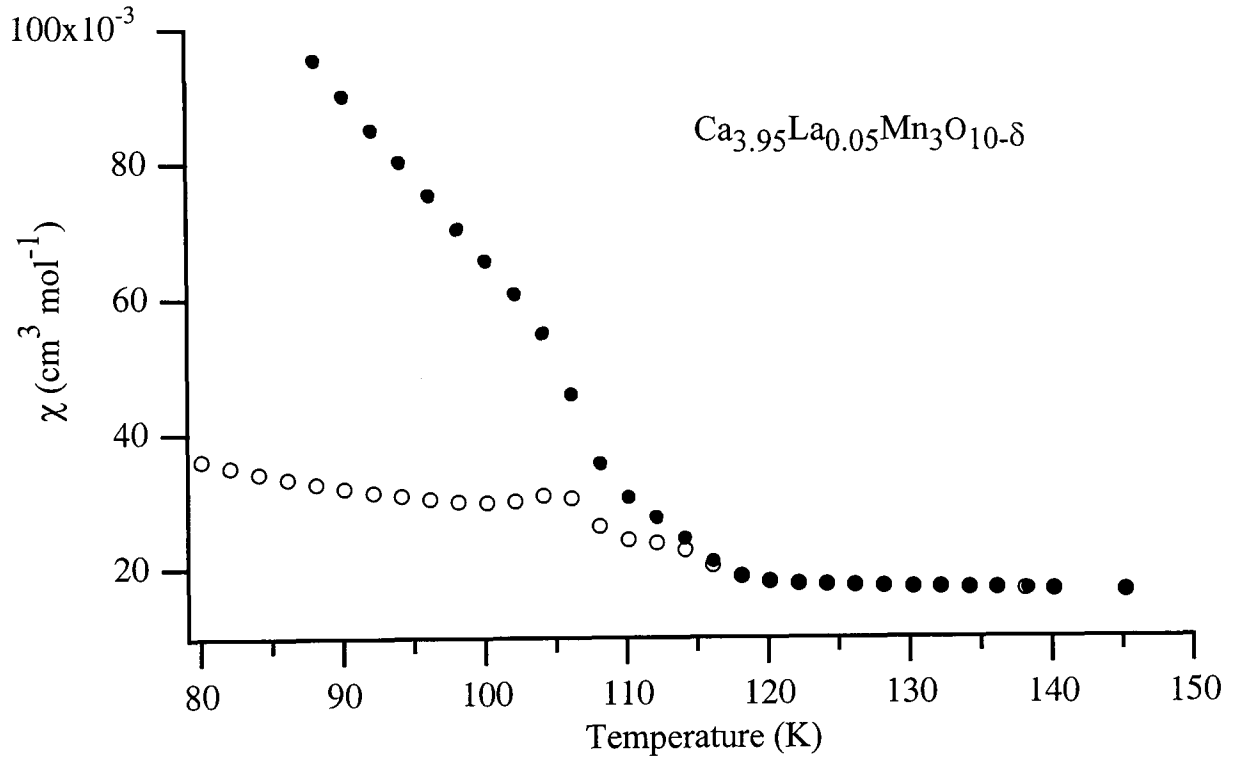


Figure 4.3.5 Enlarged view of molar magnetic susceptibility of $Ca_{3.95}La_{0.05}Mn_3O_{10-\delta}$ in the temperature region of the magnetic transition.

It can be seen that the FC signal begins to rise sharply at 114K, with concomitant divergence between FC and ZFC curves. There is a slight cusp at approximately 106K, before the signal continues to rise less steeply with temperature, to the lowest measured temperature, 5K. Unlike that observed for $Ca_4Mn_3O_{10-\delta}$, there is no broad maximum in the molar susceptibility of $Ca_{3.95}La_{0.05}Mn_3O_{10-\delta}$ for the FC signal in the temperature range 20-100K. It is significant that the ZFC signal continues to increase below 106K, rather than showing the down-turn observed for $Ca_4Mn_3O_{10-\delta}$ below the magnetic transition temperature. The rate of increase of the FC signal with temperature exceeds that of the ZFC curve at all times.

Figure 4.3.6 illustrates the difference in appearance of the magnetisation (μ_B per formula unit) above the magnetic transition temperature, in $Ca_4Mn_3O_{10-\delta}$, and $Ca_{3.95}La_{0.05}Mn_3O_{10-\delta}$. The increased magnitude of the signal for the $Ca_{3.95}La_{0.05}Mn_3O_{10-\delta}$ compound in the temperature range shown is apparent immediately. In addition, the lack of the broad maximum in the La^{3+} doped sample (occurring at T~155K in $Ca_4Mn_3O_{10-\delta}$), suggests the absence of antiferromagnetic correlations confined to the trilayer perovskite blocks in $Ca_{3.95}La_{0.05}Mn_3O_{10-\delta}$.

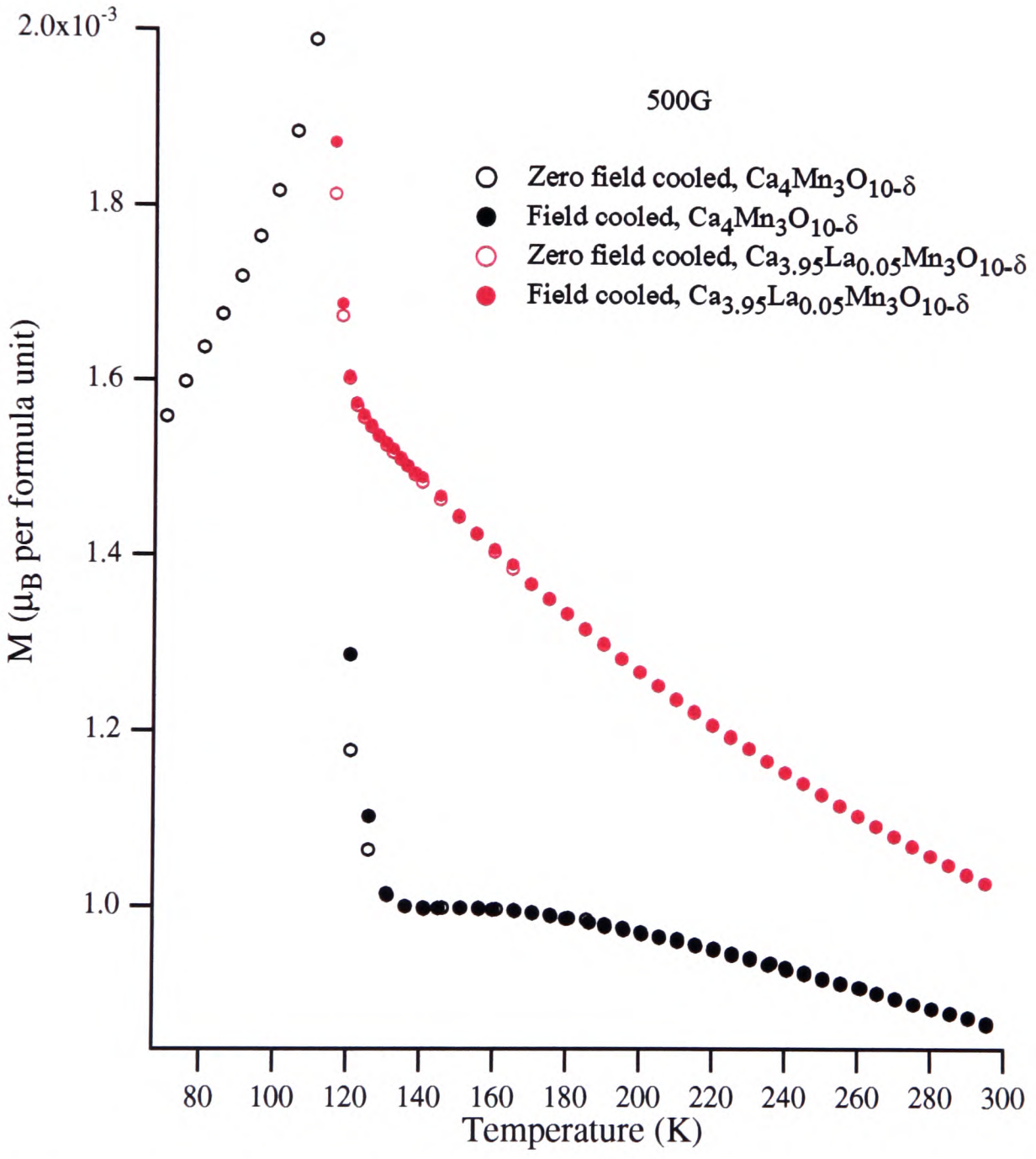


Figure 4.3.6 Comparison of magnetisation as a function of temperature, above the magnetic transition temperature, for $Ca_4Mn_3O_{10-\delta}$ (black markers), and $Ca_{3.95}La_{0.05}Mn_3O_{10-\delta}$ (purple markers).

The small magnitude of the magnetisation at 5K ($\mu_{ferro} = 1.3x10^{-2}$ μ_B per Mn) for $Ca_{3.95}La_{0.05}Mn_3O_{10-\delta}$ suggests that ferromagnetic interactions may be confined to small

clusters, and/or are associated with a canting of antiferromagnetically aligned moments. The higher temperature region of the data was fitted to the Curie-Weiss expression; the fit parameters are summarised in Table 4.3.6:

Table 4.3.6 Curie-Weiss fit parameters for $Ca_{3.95}La_{0.05}Mn_3O_{10-\delta}$:

Temperature range (K)	C_m (cm^3 K mol^{-1})	θ(K)	Estimated C_m (cm^3 K mol^{-1})
265 - 300	5.88(5)	-216.9(4)	5.68

The negative value of θ(K) obtained from the Curie-Weiss fit is indicative of antiferromagnetic interactions. The fit results in a molar Curie constant which is not significantly different than that calculated in equation 4.3.1 on the basis of a simple, non-interacting ion model for the magnetism. This suggests that interatomic magnetic interactions are significant throughout the entire measured temperature range. Equation 4.3.1 gives an estimated molar Curie constant of 5.68 (cm^3 K mol^{-1}) assuming the presence of 2.95 moles of the Mn^{4+}, d^3 cation per mole of $Ca_{3.95}La_{0.05}Mn_3O_{10-\delta}$ and 0.05 moles of the Mn^{3+}, d^4 cation, using the spin only moments for these respective cations. This assumes that any mixed valency on the B-cation site is due to the presence of the trivalent dopant, La^{3+} and that the mean Mn oxidation state is +3.983.

$$C_m(\text{estimated}) = \frac{1}{8}\left\{0.05(\mu_{eff}Mn^{3+})^2 + 2.95(\mu_{eff}Mn^{4+})^2\right\} \qquad \text{eqn. (4.3.1)}$$

The magnetisation isotherms presented in Figure 4.3.7 are consistent with $Ca_{3.95}La_{0.05}Mn_3O_{10-\delta}$ possessing a small spontaneous magnetisation below the magnetic transition temperature of ~116K. The three isotherms at 100, 60 and 5K all show hysteresis, while the data collected at 200 and 300K are linear with field and show no hysteresis. The shape of M(H) loops are in good, qualitative agreement with the undoped, parent compound, $Ca_4Mn_3O_{10-\delta}$. For $Ca_{3.95}La_{0.05}Mn_3O_{10-\delta}$, there is no evidence of asymmetry about the origin of M(H) loops showing hysteresis (i.e. those collected at, and below, 100K).

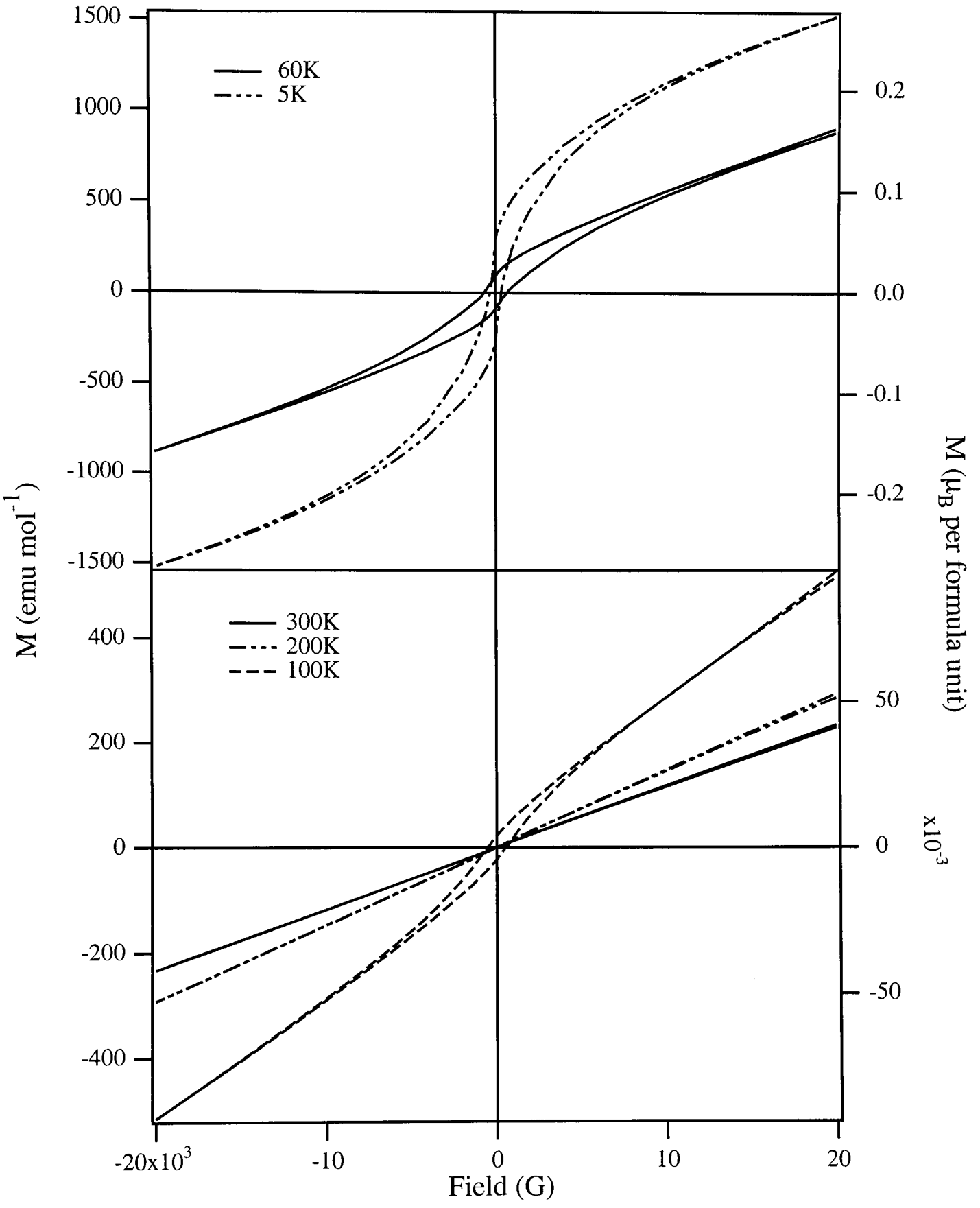


Figure 4.3.7 Magnetisation as a function of field, between 20 and -20kG, at temperatures of 300, 200, 100, 60 and 5K for $Ca_{3.95}La_{0.05}Mn_3O_{10-\delta}$.

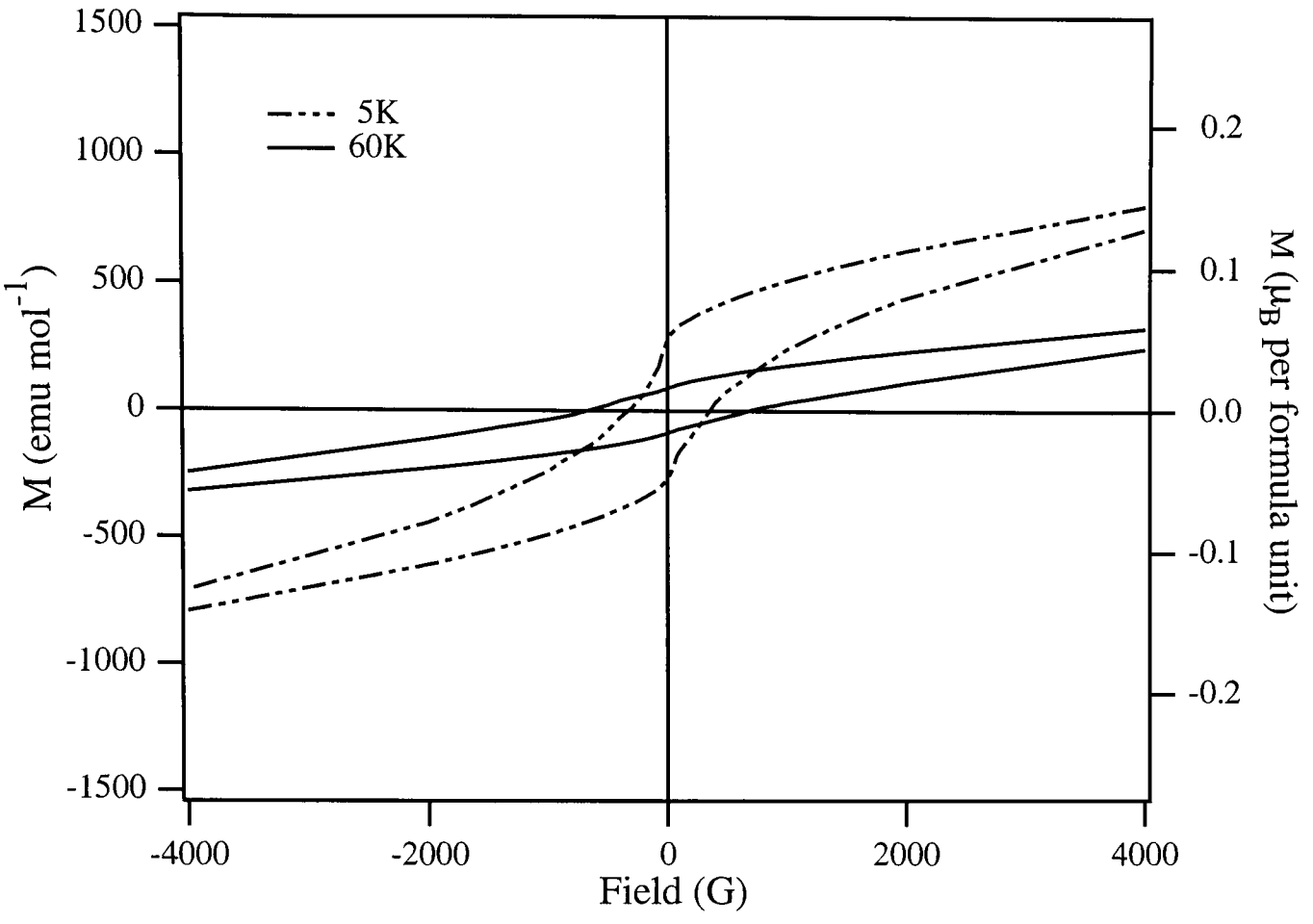


Figure 4.3.8 Enlarged view of the (-4000≤ Field(G) ≤ 4000) region of field dependent magnetisation for $Ca_{3.95}La_{0.05}Mn_3O_{10-\delta}$ at temperatures of 60 and 5K.

The magnetotransport behaviour of the sample $Ca_{3.95}La_{0.05}Mn_3O_{10-\delta}$ is shown in Figure 4.3.9. The temperature dependence of resistivity shown in the inset suggests thermally activated transport, although the sample was not so insulating at low temperature such that it could not be measured down to 4.2K, which was the case for $Ca_4Mn_3O_{10-\delta}$. The magnetotransport data for the latter sample are given for comparison in Figure 4.3.10. Although it is not clear from the inset in Figure 4.3.10, $Ca_4Mn_3O_{10-\delta}$ could be measured only down to ~25K using the methods described in Chapter 2.7.

The observed ratios of negative magnetoresistance of $Ca_{3.95}La_{0.05}Mn_3O_{10-\delta}$ and $Ca_4Mn_3O_{10-\delta}$ increase with field. Isotherms measured at 60K and above, show a similar shape of variation for the two samples. Interestingly, the magnetoresistance is greater for $Ca_4Mn_3O_{10-\delta}$ than for $Ca_{3.95}La_{0.05}Mn_3O_{10-\delta}$ at 60K and 14T (the signals are reduced to ~60% and ~80% of the zero field values for the respective compounds). However, the maximum value of magnetoresistance for the two samples is that observed for $Ca_{3.95}La_{0.05}Mn_3O_{10-\delta}$ at 4K; the signal is reduced to just 18% of the zero field value on application of a field of 14T.

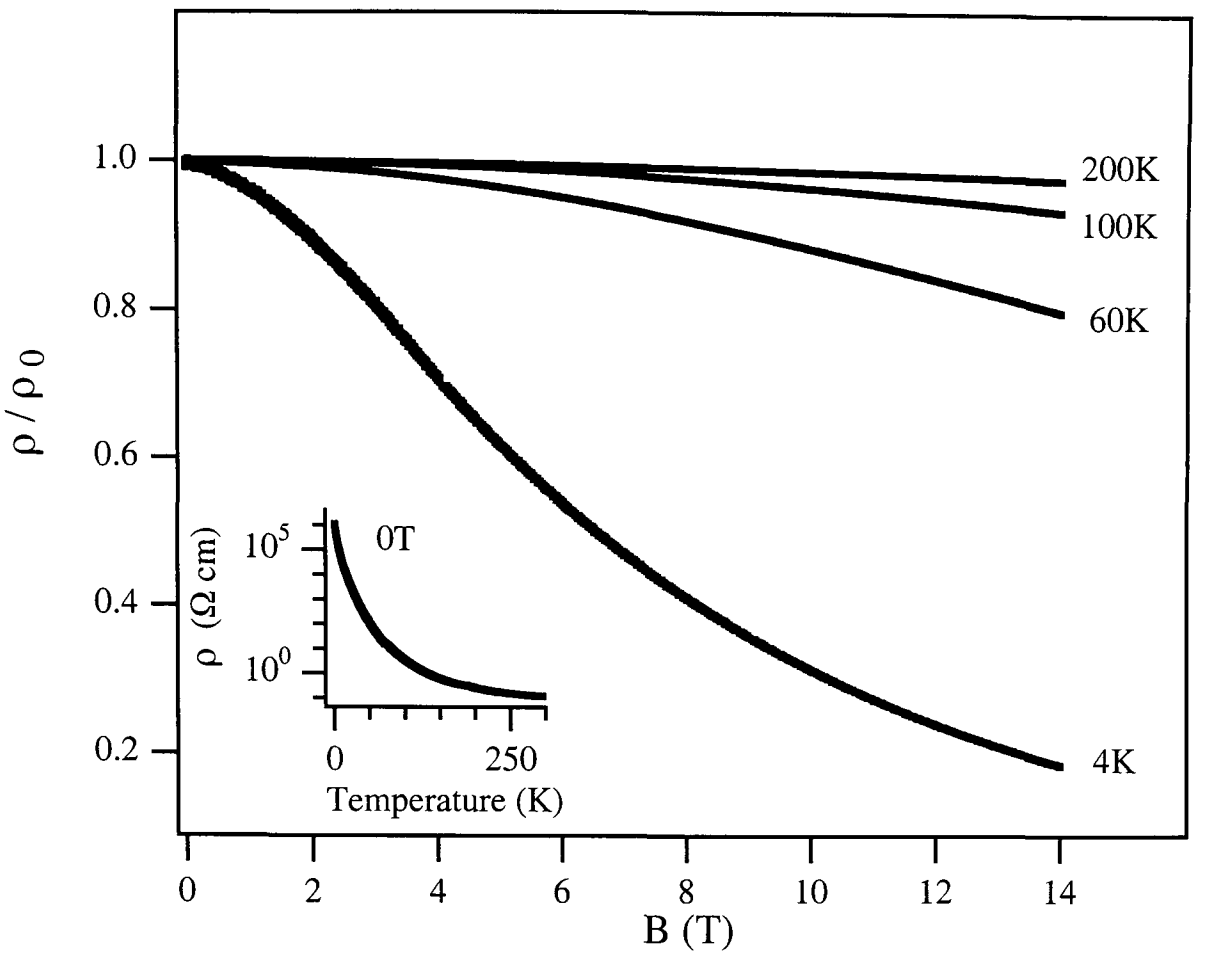


Figure 4.3.9 Field dependence of the normalised resistivity ρ(B)/ρ(0) at 200, 100, 60 and 4K for $Ca_{3.95}La_{0.05}Mn_3O_{10-\delta}$. The inset shows the temperature dependence of resistivity at zero field.

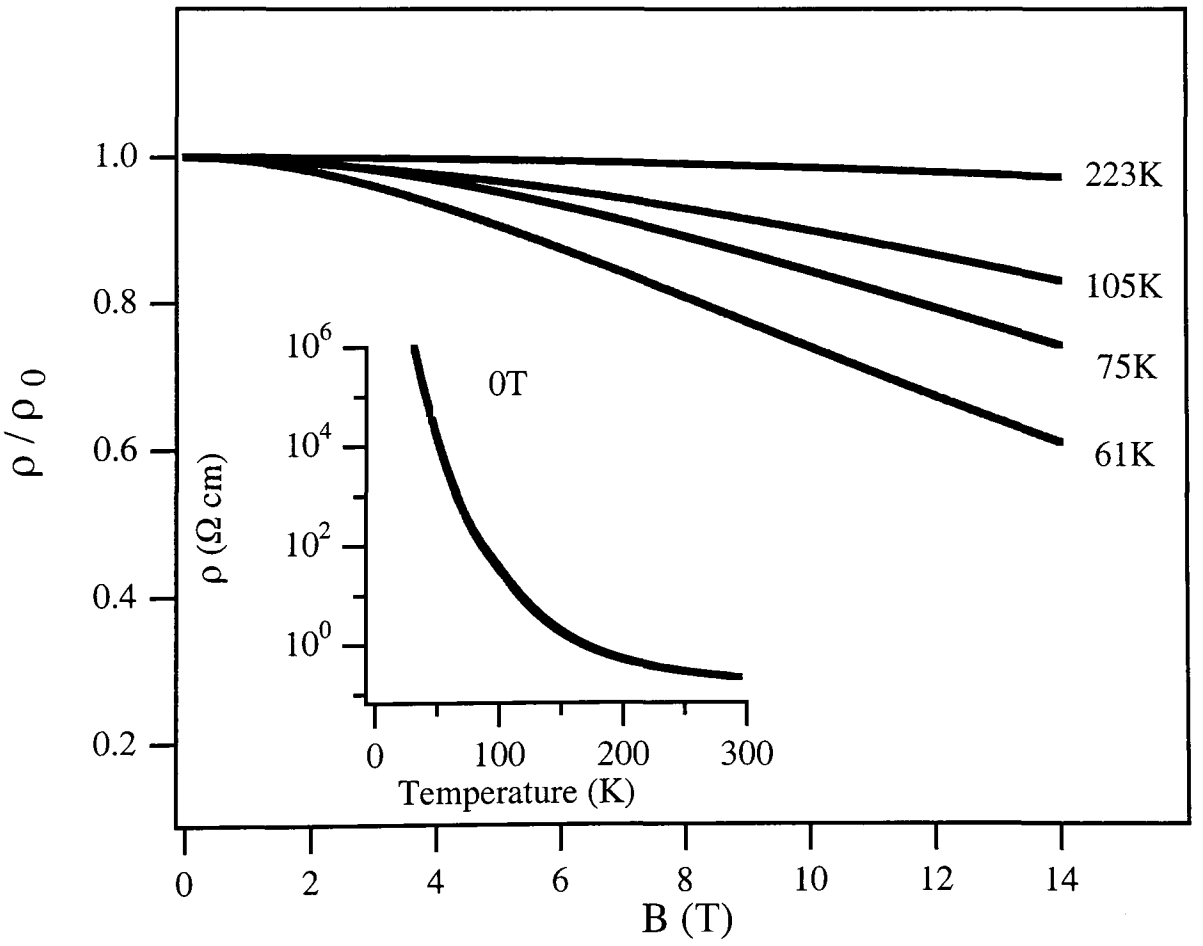
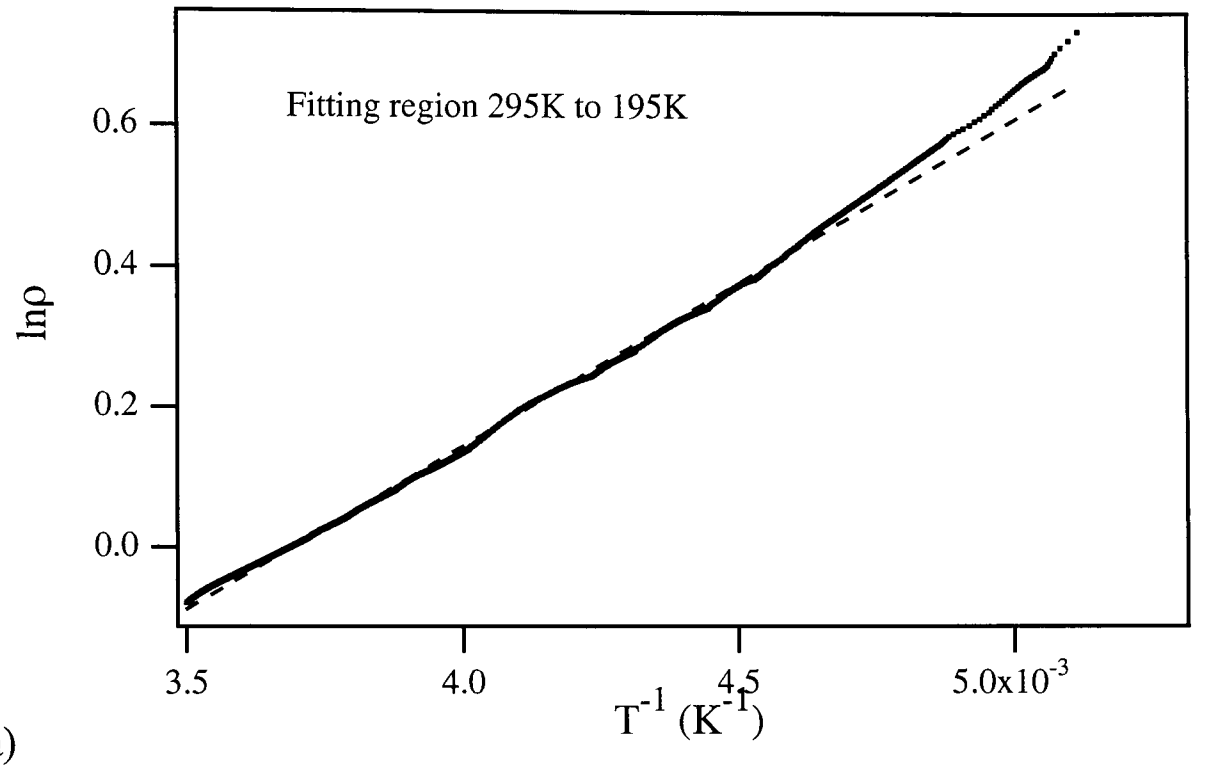


Figure 4.3.10 Field dependence of the normalised resistivity ρ(B)/ρ(0) at 223, 105, 75 and 61K for $Ca_4Mn_3O_{10-\delta}$. The inset shows the temperature dependence of resistivity at zero field[3].

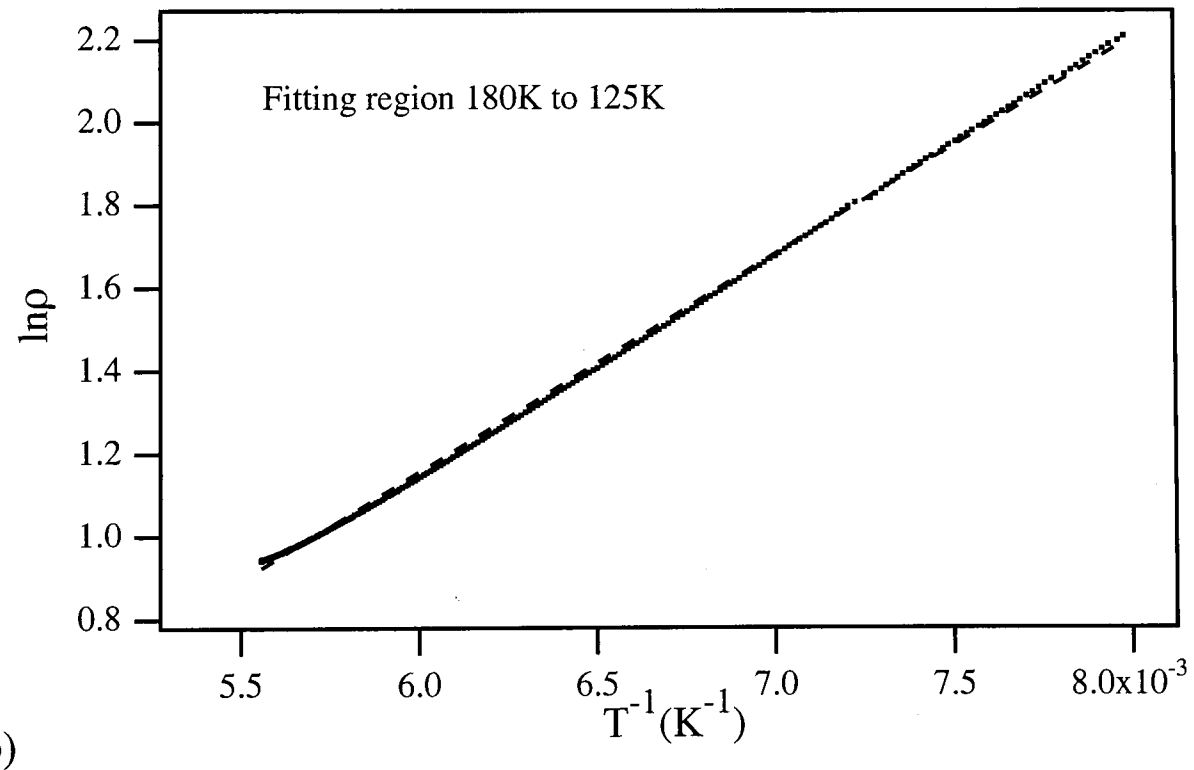
[3] Magnetotransport measurements were performed by the author and A.Coldea.

It proved possible to model the resistivity data for $Ca_{3.95}La_{0.05}Mn_3O_{10-\delta}$ between 295K and 125K using a thermally activated conduction law (equation 4.3.2), albeit in two separate regions, as shown in Figures 4.3.11 (a) and (b).

$$\rho \propto \exp(E_a / k_B T) \qquad \text{eqn. (4.3.2)}$$



(a)



(b)

Figures 4.3.11 Fits of resistivity data for $Ca_{3.95}La_{0.05}Mn_3O_{10-\delta}$ to the $\rho \propto \exp(E_a / k_B T)$ law in the temperature regions (a) 295 to 195K and (b) 180 to 125K.

Between the temperatures of 123 and 40K, the data were fitted well by the two dimensional form of Mott's variable range hopping expression[27] given in equation 4.3.3.

$$\rho \propto \exp(T_o / T)^{1/3} \qquad \text{eqn. (4.3.3)}$$

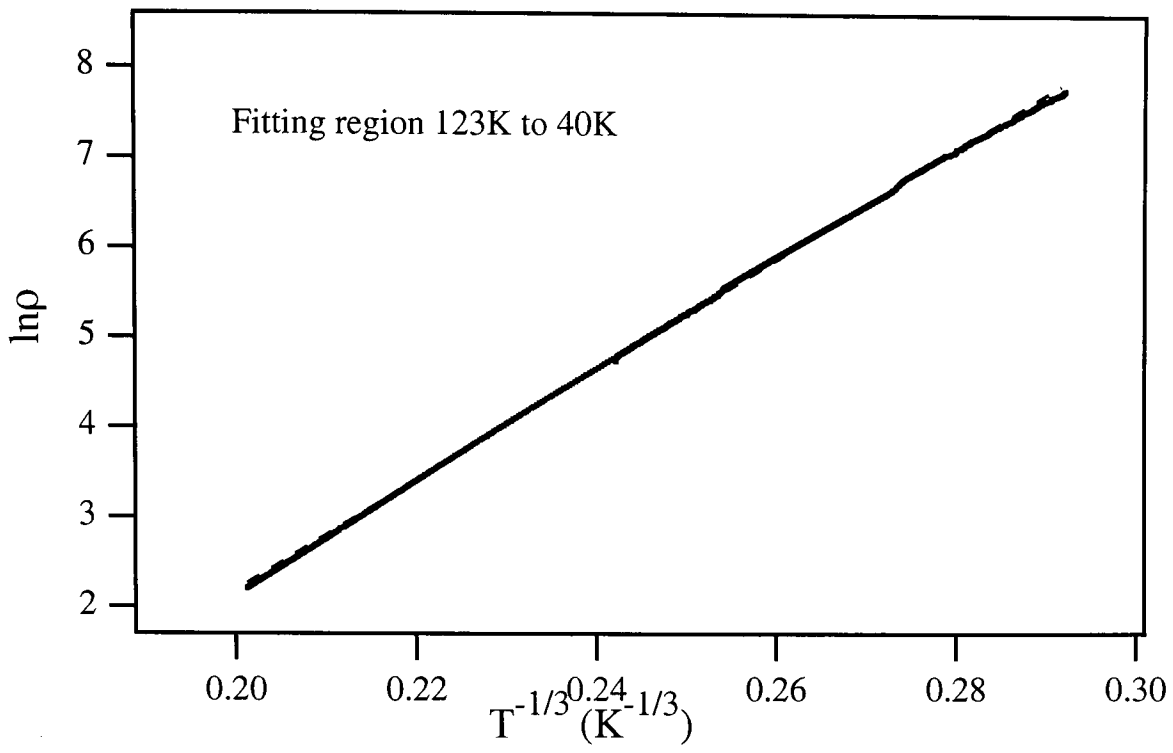


Figure 4.3.12 Fit of resistivity data for $Ca_{3.95}La_{0.05}Mn_3O_{10-\delta}$ to the $\rho \propto \exp(T_o / T)^{1/3}$ law in the temperature region 123 to 40K.

The fit parameters for the three regions shown in Figures 4.3.11 and 4.3.12 are given in Table 4.3.7, along with the models used and resulting fit parameters for $Ca_4Mn_3O_{10-\delta}$ for comparison[4].

Table 4.3.7 Fit parameters for $Ca_{3.95}La_{0.05}Mn_3O_{10-\delta}$ (parameters for $Ca_4Mn_3O_{10-\delta}$ are tabulated, for comparison):

Compound	Temperature range (K)	Model used	Parameter[a]
$Ca_{3.95}La_{0.05}Mn_3O_{10-\delta}$	295 to 195	$\rho \propto \exp(E_A / k_BT)$	$E_A = 40.13$meV
$Ca_{3.95}La_{0.05}Mn_3O_{10-\delta}$	180 to 125	$\rho \propto \exp(E_A / k_BT)$	$E_A = 45.10$meV
$Ca_{3.95}La_{0.05}Mn_3O_{10-\delta}$	123 to 40	$\rho \propto \exp(T_o / T)^{1/3}$	$T_o = 2.34 \times 10^5$K
$Ca_4Mn_3O_{10-\delta}$	300 to 200	$\rho \propto \exp(E_A / k_BT)$	$E_A = 42.12$meV
$Ca_4Mn_3O_{10-\delta}$	110 to 40	$\rho \propto \exp(T_o / T)^{1/3}$	$T_o = 1.25 \times 10^6$K

[a] $1eV = 1.6022 \times 10^{-19}J$

[4] The fitting of the resistivity data for $Ca_4Mn_3O_{10-\delta}$ was carried out by A.Coldea and is described in detail in reference [3].

4.3.3 Discussion

The quality of diffraction data available makes detailed interpretation of the structural properties of $Ca_{3.95}La_{0.05}Mn_3O_{10-\delta}$ impossible; however, there are several factors suggesting that a small proportion of La^{3+} has indeed been incorporated into the structure. The increase in the unit cell volume, compared to that measured for $Ca_4Mn_3O_{10-\delta}$ on the same laboratory diffractometer, is one of these factors. The increased values of the Ca(1) and Ca(2) shell radii would be consistent with the presence of a fraction of the larger La^{3+} cation on this site. The increased ratio of the averaged out-of-plane to averaged in-plane Mn-O bondlengths in the outer octahedron of the perovskite block in $Ca_{3.95}La_{0.05}Mn_3O_{10-\delta}$, compared to that observed in $Ca_4Mn_3O_{10-\delta}$, is consistent with the presence of the Jahn-Teller Mn^{3+} cation. Considering the low percentage (statistical) occupancy of La^{3+} of 12 and 9 coordinate sites in the structural model, it was not possible to refine any degree of Ca/La ordering which altered significantly the quality of the fit.

The temperature dependence of molar susceptibility and field dependence of the magnetisation of $Ca_{3.95}La_{0.05}Mn_3O_{10-\delta}$ is similar qualitatively to that observed in $Ca_4Mn_3O_{10-\delta}$. The increase in susceptibility at ~115K and the small magnitude of the magnetisation at 5K ($\mu_{ferro} = 1.3x10^{-2}\ \mu_B$ per Mn) in $Ca_{3.95}La_{0.05}Mn_3O_{10-\delta}$ suggests that the essential features of the behaviour observed in $Ca_4Mn_3O_{10-\delta}$ have been preserved after the introduction of a fraction of La^{3+}. For example, the transition appears to signify the onset of weak ferromagnetic interactions due to canting of predominantly antiferromagnetically aligned spins through the Dzyaloshinsky[14]-Moriya[15] interaction, as was observed for $Ca_4Mn_3O_{10-\delta}$.

However, Figure 4.3.6 suggests that the nature of magnetic interactions, above the transition temperature of ~115K, is qualitatively different from the nature of those for $Ca_4Mn_3O_{10-\delta}$, after the introduction of a fraction of La^{3+}[28]. The presence of the broad maximum at T ~ 155K in $Ca_4Mn_3O_{10-\delta}$ (also detected by Fawcett et al.[26] in a study of the same compound), was ascribed to antiferromagnetic correlations which were confined to individual trilayers of MnO_6 octahedra, with magnetic exchange interactions intermediate between 2-D and 3-D in nature. It was suggested that the applied magnetic field might be

responsible for the small ferromagnetic component at temperatures above the transition, as it would induce the ordering of ferromagnetic moments present from the DM interactions within the individual trilayers, themselves associated with the antiferromagnetic correlations. It would appear that the antiferromagnetic correlations confined to the trilayer above 115K are suppressed following the introduction of La^{3+}, and therefore the mechanism for canting to give weak ferromagnetic moments is absent also. Thus, the increased magnitude of the magnetisation for $Ca_{3.95}La_{0.05}Mn_3O_{10-\delta}$ over the undoped sample is likely to be due to the direct influence of Mn^{3+} cations, if the weak ferromagnetism arising from the DM interaction is suppressed. However, the low value of magnetisation in the M(H) measurement at 5K (~ 0.3 μ_B per formula unit), and the fact that the signal does not saturate, confirms that the concentration of Mn^{3+} cations is below the percolation level for long range ferromagnetic order. Thus, weak ferromagnetism appears to be responsible for the dramatic rise in molar susceptibility at 115K, by analogy with the behaviour in $Ca_4Mn_3O_{10-\delta}$. It is possible that, superimposed upon the weakly-canted moments associated with the DM mechanism, are localised clusters where ferromagnetic Mn^{3+} t_{2g}^3 e_g^1 - O^{2-} - Mn^{4+} t_{2g}^3 σ superexchange interactions (from the increased concentration of Mn^{3+} cations), destabilise the antiferromagnetic groundstate existing due to the predominant Mn^{4+} t_{2g}^3 - O^{2-} - Mn^{4+} t_{2g}^3 π superexchange interactions. The size of the resistivity at all temperatures, the absence of a metal-insulator transition and of long range 3-D ferromagnetic order confirms that the double exchange mechanism is unlikely to compete effectively with superexchange interactions of either sign in $Ca_{3.95}La_{0.05}Mn_3O_{10-\delta}$.

The variation in molar magnetic susceptibility below T_N following the divergence of FC and ZFC signals appears different also to that in $Ca_4Mn_3O_{10-\delta}$, although the magnetic behaviour in this temperature region has been shown[28] to be strongly dependent upon the annealing treatment of the sample. The absence, in the FC signal for $Ca_{3.95}La_{0.05}Mn_3O_{10-\delta}$, of the broad maximum (~70K) in the molar susceptibility of $Ca_4Mn_3O_{10-\delta}$, is a notable feature, although the significant divergence between ZFC and FC signals is retained. One explanation for the disordered magnetic behaviour below T_N in $Ca_4Mn_3O_{10-\delta}$, suggested in the work by Lago et al., was an inhomogeneous distribution of the distortion that gives rise to the

weak ferromagnetism. Similar disorder in $Ca_{3.95}La_{0.05}Mn_3O_{10-\delta}$ could manifest itself by the presence of small antiferromagnetic domains where the antiferromagnetic superexchange interactions are 'diluted' by the presence of Mn^{3+} cations, responsible for the uncompensated magnetic moments at domain surfaces. The associated weak ferromagnetism may be restricted to domains also. The continued increase in the ZFC curve for $Ca_{3.95}La_{0.05}Mn_3O_{10-\delta}$, down to the lowest measuring temperature, could be explained by the presence of uncompensated magnetic moments at domain surfaces. Also, contributing to the irreversibility of magnetic behaviour below T_N would be the competition between ferromagnetic Mn^{3+} t_{2g}^3 e_g^1 - O^{2-} - Mn^{4+} t_{2g}^3 σ superexchange interactions and the predominant, Mn^{4+} t_{2g}^3 - O^{2-} - Mn^{4+} t_{2g}^3 π superexchange interactions.

The compound $Ca_{3.95}La_{0.05}Mn_3O_{10-\delta}$ is a Mn(IV) rich manganite, and as such it is useful to compare the magnetic properties observed in the current study with those obtained by Maignan et al.[29] for the compound $Ca_{1-x}Sm_xMnO_3$. The concentration most comparable in their study, with $Ca_{3.95}La_{0.05}Mn_3O_{10-\delta}$, is that with minimal cation substitution, corresponding to x = 0.05. The electron density corresponding to this doping level was insufficient to observe the transition at a temperature of ~110K in the $\rho(T)$ curve observed for higher Sm^{3+} concentrations ($> x = 0.075$) which coincided with the appearance of a ferromagnetic component in magnetisation measurements. It is not surprising, by comparison, that no such transition was observed in the magnetotransport data for $Ca_{3.95}La_{0.05}Mn_3O_{10-\delta}$, which corresponds to a lower electron density than that in $Ca_{0.95}Sm_{0.05}MnO_3$. It was found that the $Ca_{1-x}Sm_xMnO_3$ materials with $0 < x \leq 0.12$, are cluster glasses at low temperature and in low magnetic fields, where the frequency dependence of AC susceptibility curves confirmed the presence of dynamic effects linked to frozen magnetic domains.

As shown in Table 4.3.7, the conduction mechanism in $Ca_{3.95}La_{0.05}Mn_3O_{10-\delta}$ in the temperature regions 295 to 195K and 180 to 125K, appears to be thermal activation of carriers. The activation energy is slightly higher in the region corresponding to lower temperature (i.e. 45.10meV as opposed to 40.13meV), but both values are comparable to that observed for $Ca_4Mn_3O_{10-\delta}$ between 300K and 200K (42.12meV). These activation energies are slightly lower than typical values obtained for n = 2 layered manganites, which tend to be

of the order of 100meV[30]. This observation may reflect the wider bandwidths associated with the n = 3 compounds, as a result of an (average) 5.5 nearest-neighbours surrounding each Mn atom as opposed to the 5 nearest-neighbours in the n = 2 compounds. The conduction mechanism appears to change on lowering the temperature further, and, between 123 and 40K, is best described by two-dimensional VRH, suggesting the confinement of charge carriers to the ab plane. As such, this model is similar to the behaviour suggested for $Ca_4Mn_3O_{10-\delta}$ in the temperature region 110 to 40K. It is noteworthy that in each compound, the conduction mechanism appears to change at around the temperature of the magnetic transition. The values of E_A of 40-45 meV for $Ca_{3.95}La_{0.05}Mn_3O_{10-\delta}$ agree well with that obtained for $Ca_{3.99}La_{0.01}Mn_3O_{10-\delta}$ in the study by Witte et al.[17], who focussed on the region of Mn valence (v) $3.97 < v < 4.0$. They reported an E_A of 41 meV in the region above T_N, and reported also the modelling of transport data below T_N using a Mott VRH expression[27], although with an exponent of 0.25.

The magnetoresistance ratios shown at equivalent temperatures (eg. 60K) by $Ca_4Mn_3O_{10-\delta}$ and $Ca_{3.95}La_{0.05}Mn_3O_{10-\delta}$ are greater for the former compound. For example, the resistivity is reduced to just 80% of its zero field value at 60K and 14 T in $Ca_{3.95}La_{0.05}Mn_3O_{10-\delta}$, but is reduced to 60% of its zero field value at the same temperature and field in $Ca_4Mn_3O_{10-\delta}$. It is interesting to note that the proposed existence of antiferromagnetic domains (possessing canted moments leading to WFM), bordered by discrete Mn^{3+} cations, leads apparently to a reduction in MR ratios over the majority of the temperature range. It is possible, therefore, that the introduction of this quantity of Mn^{3+}, through substitution of such a small amount of Ca^{2+} for La^{3+}, has disrupted the range over which the weak ferromagnetic component is stabilised, but has not increased the electron density sufficiently in order to strengthen a FM double exchange mechanism to compensate, thereby reducing the MR ratio, compared to that observed in $Ca_4Mn_3O_{10-\delta}$. This idea would appear consistent with the transport data, only until the measurement at 4K for $Ca_{3.95}La_{0.05}Mn_3O_{10-\delta}$ is considered. Here, the resistivity was measurable down to the lowest measuring temperatures, probably on account of the presence of mixed-valent Mn cations, where carriers can move without incurring the Hubbard repulsion, U. However, in contrast

with the lower MR ratios observed at 60K and above in $Ca_{3.95}La_{0.05}Mn_3O_{10-\delta}$ (in comparison with $Ca_4Mn_3O_{10-\delta}$), a high MR ratio was observed in $Ca_{3.95}La_{0.05}Mn_3O_{10-\delta}$ at 4K. The resistivity was reduced to just 18% of its zero field value in an applied field of 14T. This corresponds to the largest MR ratio that has been observed in a n = 3 layered manganite by the present author. However, the significance of extrinsic contributions to the MR response (LFMR) at this low temperature, cannot be ruled out.

4.4 B-cation substitution in $Ca_4Mn_3O_{10-\delta}$ and $Sr_4Mn_3O_{10-\delta}$

A feature of the n=3 RP materials, which it was hoped to utilise in studies of B-site cation substitution, is the presence of two, crystallographically distinct, octahedral sites in the perovskite blocks. This feature does not occur for the n=1,2 or ∞ structures and means that, when at a ratio of 2:1 (eg. for the compound $Ca_4Mn_2FeO_{10-\delta}$), the distinct B-site cations are in the same proportion as the crystallographically distinct octahedral sites. By using neutron diffraction in the case of the Mn,Fe compound, it proved possible to investigate the degree of cation ordering across octahedral sites and the resulting structural and magnetic properties for both $Ca_4Mn_2FeO_{10-\delta}$ and the Sr analogue[31].

Following the successful substitution of Mn for Fe (but the unsuccessful results when using Cr, Co and Ni substituents)[32], tetravalent Ti and Sn and trivalent Ga were chosen as substituents for B-site Mn cations in the present study. It was expected that the use of Ga^{3+} would induce significant oxygen deficiency in order to maintain electroneutrality. There is some precedence for the substitution of Ga^{3+} into n=3 RP compounds. In 1996, Steinfink et al., while continuing their studies[33,34] into cation substitution in the compound $Sr_3LaFe_3O_{10-\delta}$, examined the series $Sr_3LaFe_{3-x}Ga_xO_{10-\delta}$[35], characterising $Sr_3LaFeGa_2O_9$ successfully. Ti^{4+} and Sn^{4+} cations have been used widely as B-site dopants in the last few years, particularly by Raveau's group[36,37], although their studies have been restricted primarily to n=1,2 and ∞ phases.

It was found that the attempted substitution of Mn^{4+} by Sn^{4+} in $Ca_4Mn_3O_{10-\delta}$ was hampered by the stability of the $CaSnO_3$ impurity phase. Any future attempt might seek to circumvent its formation, perhaps by careful selection of starting materials (here $CaCO_3$ and SnO_2 were used). The Sn substitution reaction could not be optimised using a range of reaction conditions and atmospheres, and the samples tended to melt close to 1330°C. Unfortunately, attempts at incorporating Ga^{3+} in the n = 3 RP phase $Ca_4Mn_3O_{10-\delta}$, failed also, resulting in a complicated diffraction pattern. Again, the samples were prone to melting on approaching reaction temperatures around 1330°C.

Attempts at introducing Sn, Ga and Ti cations into $Sr_4Mn_3O_{10-\delta}$ also proved unsuccessful, although it was expected that $Sr_4Mn_3O_{10-\delta}$ might prove less amenable to

structural tuning than the $Ca_4Mn_3O_{10-\delta}$ RP phase. Again, the Ga synthesis gave a complex diffraction pattern, followed by melting of the sample above 1400°C. The Sn reaction gave a pattern in which traces of Sr_3MnSnO_7 and $SrMnO_3$ could be refined above 1400°C. The Ti substitution gave a complicated pattern, with evidence for the formation of $Sr_7Mn_4O_{15}$ as one of the impurity phases below 1400°C in air. It is likely that, with an increased concentration of Ti over Mn on the B-cation site, there would be a crossover to a RP type compound, containing only corner sharing 'BO_6' octahedra, in the light of the prevalence of $Sr_{n+1}Ti_nO_{3n+1}$ RP compounds[38,39].

The remainder of this section focuses on the successful preparation and characterisation of $Ca_4Mn_2TiO_{10-\delta}$, and the use of anomalous dispersion in X-ray diffraction measurements to quantify the degree of Ti^{4+}/Mn^{4+} ordering across octahedral sites.

4.4.1 Experimental details

The material was prepared using standard ceramic techniques. Stoichiometric quantities of $CaCO_3$ (99.995%, Alfa), MnO_2 (99.999% Puratronic, Alfa) and TiO_2 (99.995% Puratronic, Alfa) were ground together thoroughly and given the heat treatment detailed in Table 4.4.1.

Table 4.4.1 Details of furnace preparation of 5g of $Ca_4Mn_2TiO_{10-\delta}$:

Temperature (°C)	800	1000	1200	1250	1275
Firing time (hrs)	36	24	60	40	84
Atmosphere	air	air	air	air	air
Pellets[a] reground	(powder)	once	4 times	4 times	4 times

[a] The pellet diameter was 13mm and 2-3 tonnes were used during pressing.

The progress of the reaction was monitored by X-ray diffraction, collected on the laboratory Philips diffractometer ($3 \leq 2\theta/^{o} \leq 70$), and was shown to require a similar heating sequence as a 1g batch of the same material synthesised previously. Rietveld refinement of a dataset collected on the laboratory D5000 instrument (in space group *Pbca*, as was used to model synchrotron X-ray data collected for the smaller batch) confirmed that the compound was of sufficient quality to measure at station 2.3, SRS, Daresbury.

Since one of the main interests of this study in compounds of the type $A_4B_{3-x}B'_xO_{10}$ was to establish whether there is any B/B' cation ordering over octahedral sites (and the resulting effects on structural and magnetic properties), it was of particular interest to refine the fractional occupancies of Mn^{4+} and Ti^{4+} over the 4b and 8c octahedral sites (space group *Pbca*). However, the respective X-ray atomic scattering factors and neutron scattering lengths for Mn and Ti are too similar to provide adequate diffraction contrast between these two cations (see Table 4.4.2). Therefore, it was impossible to refine fractional occupancies using either conventional X-ray diffraction data or neutron diffraction data alone, or a combination of the two. Thus, it was necessary to make use of anomalous X-ray scattering.

Table 4.4.2 X-ray and neutron scattering amplitudes for Mn and Ti atoms:

Atom	Atomic form factor, f ($2\theta=0^o$)	Neutron scattering length (fm)
Mn	25	-3.73
Ti	22	-3.44

As described in Chapter 2.3.3, the optimum method for refining dispersion corrections from X-ray data is to measure the material of interest alongside a 'standard'. This standard compound should contain one of the cations being distinguished in the sample of interest in (ideally) the same coordination environment in which it occurs in the sample. Since diffraction contrast between Mn^{4+} and Ti^{4+} was required in the compound $Ca_4Mn_2TiO_{10-\delta}$, either of the Mn^{4+} or Ti^{4+} absorption edges could be selected in order to introduce anomalous scatterers into the sample. The Mn^{4+} edge was selected for two main reasons. Firstly, 4H $SrMnO_3$ was available as a good 'standard' material, since it was known to be highly stoichiometric under the preparation conditions used and Mn^{4+} was present in a similar coordination environment as that in which it occurs in $Ca_4Mn_2TiO_{10-\delta}$. Secondly, the tabulated Mn K edge position was 1.89643Å, as opposed to the value of the Ti K absorption edge wavelength of 2.4973Å. The respective edge positions of the tetravalent cations are close to the neutral atom values, hence 1.89643Å was selected since it corresponded to a higher incident photon flux on station 2.3, SRS.

For confirmation that $SrMnO_3$ was an appropriate standard (that the absorption edges of Mn^{4+} in standard and sample coincided) it was necessary to measure the absorption edge positions of both at the beamline. As can be seen from Figure 2.3.1, Station 2.3 is equipped with a fluorescence detector, which can be mounted 90° above the sample (particularly for anomalous scattering studies) to identify the edge position. Both standard and sample were measured on a flat-plate sample holder which was loaded onto the spinner mounted on the ω-circle. Maximum illumination of the each material was achieved by moving the omega circle to 5°. Then, a 2θ region remote from any Bragg peaks was selected (91°), over which the background could be observed as a function of energy (providing a good indication of the magnitude of the fluorescence signal). The energy was scanned by changing the monochromator angle, after calculation of the approximate value of monochromator angle which corresponded to a wavelength of 1.89Å. This meant scanning over the following ranges, for sample and standard consecutively:

Table 4.4.3 Identifying edge positions for standard, $SrMnO_3$ and sample, $Ca_4Mn_2TiO_{10-\delta}$:

Compound	Monochromator angle (mdeg.)	Step size (°)	Counting time (sec.)
$Ca_4Mn_2TiO_{10-\delta}$	17.48 - 17.64	0.001	10
4H $SrMnO_3$	17.50 - 17.65	0.001	2

Figure 4.4.1 shows the resulting fluorescence signals for sample and standard, coinciding as required. The value for both the respective edges lie close to a monochromator angle of 17.56°, as shown.

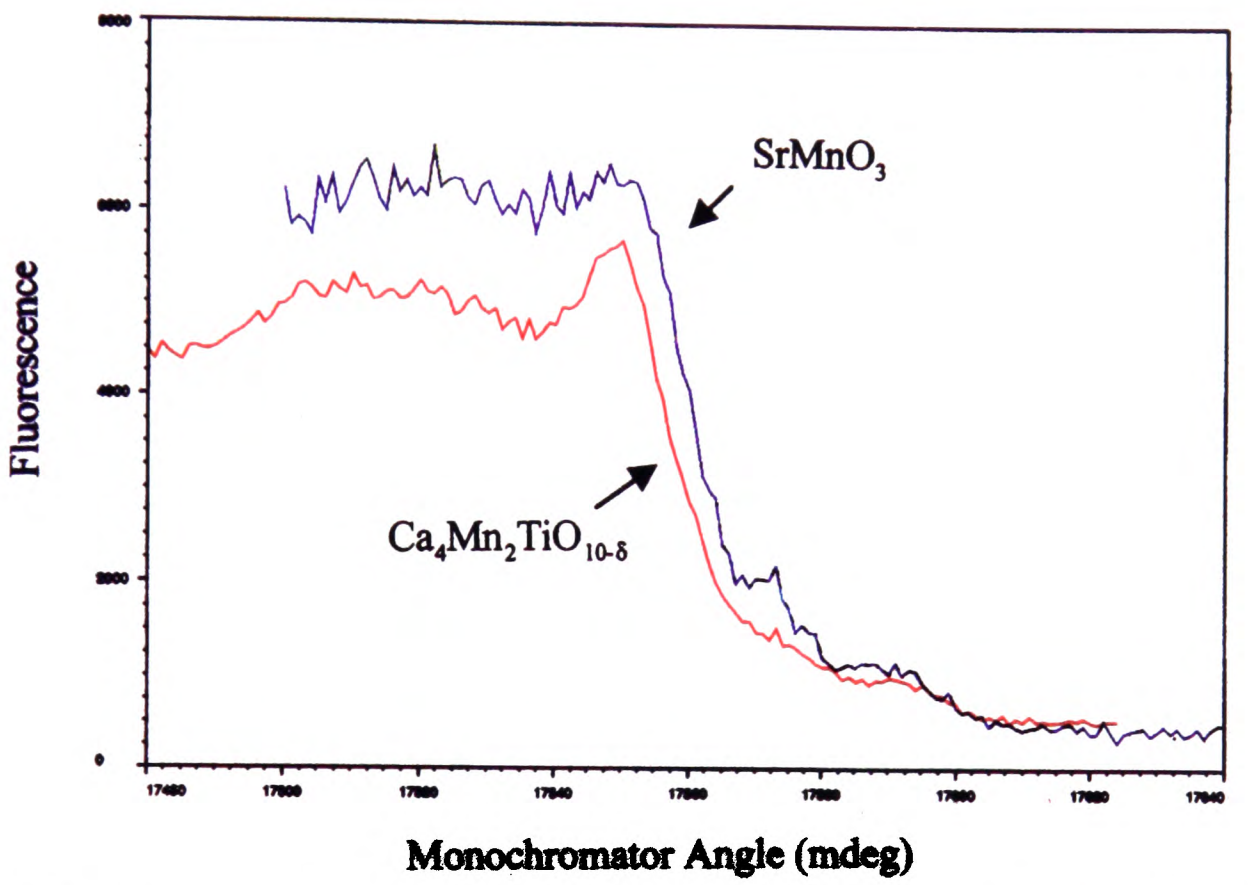


Figure 4.4.1 Fluorescence signal as a function of monochromator angle on Station 2.3, for standard, $SrMnO_3$ (blue line) and sample, $Ca_4Mn_2TiO_{10-\delta}$ (red line).

Since it was necessary to measure on the low energy side of the edge itself, a monochromator angle of 17.57° was selected, which corresponded to λ_{meas} of 1.8930Å and a monochromator energy of 6.5505 keV, calculated from the Si standard. Subsequently, datasets were collected for standard, and sample, at λ_{meas} of 1.8930Å.

The relatively low flux condition of the 'edge' datasets at the wavelength of ~ 1.89Å for both standard and sample meant these datasets alone could not be used for refinement of accurate structural models and thermal parameters. Indeed, the 'edge' datasets are meant only to complement additional datasets (from which the structural model is determined), so that the value of $\Delta f'$ (for Mn^{4+} in the present case) can be refined.

The additional datasets were, firstly, in the case of the sample, $Ca_4Mn_2TiO_{10-\delta}$, that collected at 295K on D2b at the ILL. The sample was loaded into a cylindrical vanadium can and the following experimental parameters used: $\lambda = 1.594$Å, $8 \leq 2\theta/° \leq 150$, $\Delta 2\theta = 0.05°$. Powder neutron data were analysed using the Rietveld method as implemented by the GSAS

software package, using the following neutron scattering lengths: $b_{Ca} = 0.490$, $b_{Mn} = -0.373$, $b_{Ti} = -0.344$ and $b_O = 0.581 \times 10^{-14}$m. Secondly, in the case of the sample, $Ca_4Mn_2TiO_{10-\delta}$, a synchrotron X-ray dataset was collected at 1.40Å, the optimum wavelength for high incident photon flux on Station 2.3. For the standard, $SrMnO_3$, an additional dataset was collected at SRS, again at 1.40Å. A summary of datasets collected, which were relevant for obtaining the fractional occupancies of Mn^{4+} and Ti^{4+} over 4b and 8c octahedral sites in $Ca_4Mn_2TiO_{10-\delta}$, is given in Table 4.4.4. The SRS datasets were collected, in the order (ii) to (v) as shown, over two days of beamtime, and the D2b dataset for $Ca_4Mn_2TiO_{10-\delta}$ was collected a few weeks later on the same batch of sample, unchanged from the X-ray study.

Table 4.4.4 Relevant datasets for determination of Mn^{4+} and Ti^{4+} octahedral site distributions:

Compound	Instrument	Refined angular range($2\theta/^o$)	Approximate wavelength (Å)	Temperature (K)
(i) $Ca_4Mn_2TiO_{10-\delta}$	D2b, ILL	12 - 148	1.594	295K
(ii) $Ca_4Mn_2TiO_{10-\delta}$	2.3, SRS	20 - 120	1.400	room temp.
(iii) $Ca_4Mn_2TiO_{10-\delta}$	2.3, SRS	20 - 120	1.890	room temp.
(iv) 4H $SrMnO_3$	2.3, SRS	20 - 120	1.890	room temp.
(v) 4H $SrMnO_3$	2.3, SRS	15 - 100	1.400	room temp.

In addition to the data collections detailed above, a neutron diffraction experiment was performed at 5K on D2b ($\lambda = 1.5940$Å, $8 \leq 2\theta/^o \leq 150$, $\Delta 2\theta = 0.05^o$) for $Ca_4Mn_2TiO_{10-\delta}$. It did not contribute to the refinement of the anomalous dispersion correction and was useful simply as a means of examining the low temperature structural and magnetic behaviour in $Ca_4Mn_2TiO_{10-\delta}$.

Magnetisation data as a function of field and temperature were collected for $Ca_4Mn_2TiO_{10-\delta}$ on a Quantum Design MPMS SQUID magnetometer. Data were collected as a function of temperature (between 5 and 300K) upon warming, after cooling the sample in zero field (ZFC) and after cooling in the measuring field (FC). The measuring fields were 100G, 500G and 1kG; however, only the 100G and 1kG are presented due to the similarity of the behaviour at 500G and 1kG. The magnetisation was measured as a function of field at temperatures of 300, 100, 30, 10 and 5K (in that order) by sweeping the field between 20kG

and -20kG at each temperature, with field cooling between temperatures. These temperatures were selected from examination of the data collected as a function of temperature.

Magnetotransport data were collected (by the author and A. Coldea) on a sintered bar, approximately 5x2x2mm in size, (which had been cut from a 13mm diameter pellet) using the apparatus described in Chapter 2.7. Standard four probe geometry was used, with the direct current ($\leq$ 50 μA) perpendicular to the field. Firstly, resistivity was measured as a function of temperature while cooling the material from room temperature to 4.2K in zero field. The resistivity signal became immeasurably large below approximately 70K. Secondly, fixed temperatures were selected (200, 150, 100 and 75K), at which to sweep the applied field between 0 and 14T. The temperatures were selected (as far as was possible practically), to coincide with those for which isothermal magnetisation versus field data were available. The low temperature magnetisation isotherms (at 30, 10 and 5K) could not be reproduced because of the immeasurably large resistivities at these temperatures (which were not made measurable by the application of 14T). Field sweeps at temperatures above 200K were not attempted. During each field sweep, the temperature fluctuation was maintained at no more than +/- 1K. The sweeps were carried out for the lowest temperature first and warming between temperatures were performed under zero field.

4.4.2 Structural and magnetic characterisation of $Ca_4Mn_2TiO_{10-\delta}$

4.4.2.1 Refinement strategy

Equations 1.7 to 1.12 in Appendix 1 show that once the appropriate datasets have been collected, only $\Delta f'$ is sensitive to refinement and this can be carried out in the programme FPRIME[40] within the GSAS[41] software package. Therefore, f'' was held at the default value calculated by the programme for the incident wavelength of 1.893Å, which was 2.81 electrons per Mn. Refinement of $\Delta f'$ to give a significant correction to f_{Mn4+} to yield f' ($f' = f_{Mn4+} + \Delta f'$) would ultimately allow discrimination between Mn^{4+} and Ti^{4+}. The basic refinement strategy was to obtain $\Delta f'$ from refinement of the 'edge' dataset for the standard, then to insert this value into the sample refinement, thereby providing the necessary diffraction contrast between Mn^{4+} and Ti^{4+} for refinement of their site occupancies in the

structure. However, first, the 'edge' wavelength had to be established precisely in the refinement of the sample (and then inserted into the 'edge' dataset for the standard), using the reliable structural model afforded by the availability of neutron diffraction data for $Ca_4Mn_2TiO_{10-\delta}$.

Thus, referring to Table 4.4.4, the room temperature D2b dataset for the sample was refined first, in order to obtain a reliable structural model. The use of neutron data, collected to an angle of $2\theta = 148°$, allowed refinement of accurate thermal parameters, since the rapid decrease of the atomic scattering factor with $(\sin\theta/\lambda)$ observed in X-ray diffraction does not occur in neutron scattering. The preliminary structural model (with reliable parameters for lighter atoms such as oxygen), obtained from refinement of the $Ca_4Mn_2TiO_{10-\delta}$ 1.594Å D2b neutron dataset at 295K, was used as a basis for refinement of the $Ca_4Mn_2TiO_{10-\delta}$ SRS 1.40Å X-ray dataset. This allowed refinement of the wavelength of the incident radiation of the 1.40Å dataset while using a reliable structural model for the sample (albeit still with a statistical distribution of Mn^{4+}/Ti^{4+} cations across the two octahedral sites). The wavelength refined to the value 1.400012(16)Å, not deviating significantly from the calibrated value, as expected.

Next, a second histogram, that from the 1.89Å 'edge' dataset for $Ca_4Mn_2TiO_{10-\delta}$, was included in the 1.40Å X-ray refinement in order to refine the value of the '1.89Å' wavelength. This value refined to 1.892951(16)Å, which was in agreement with the expected value. This value could now be fixed, with confidence, in the refinement of the standard, since the experimental setup had not changed between consecutive measurements (refer to the order of measurements given in Table 4.4.3). Consequently, the dataset collected at 1.892951(16)Å for $SrMnO_3$ was used in a two histogram refinement, the other histogram being that collected at the high incident flux 1.40Å setting. The value of $\Delta f'(Mn^{4+})$ refined for the 1.892951Å histogram in this two-wavelength X-ray refinement of the standard, was -9.040(49) electrons per Mn^{4+}, and a significant improvement to the fit of this histogram was observed on letting $\Delta f'(Mn^{4+})$ refine. It is encouraging to note the excellent agreement between the value of $\Delta f'(Mn^{4+})$ at a monochromator energy of 6.55 keV obtained by the author, and that obtained by Murakami et al.[42] in a recent charge ordering study on the compound $La_{0.5}Sr_{1.5}MnO_4$.

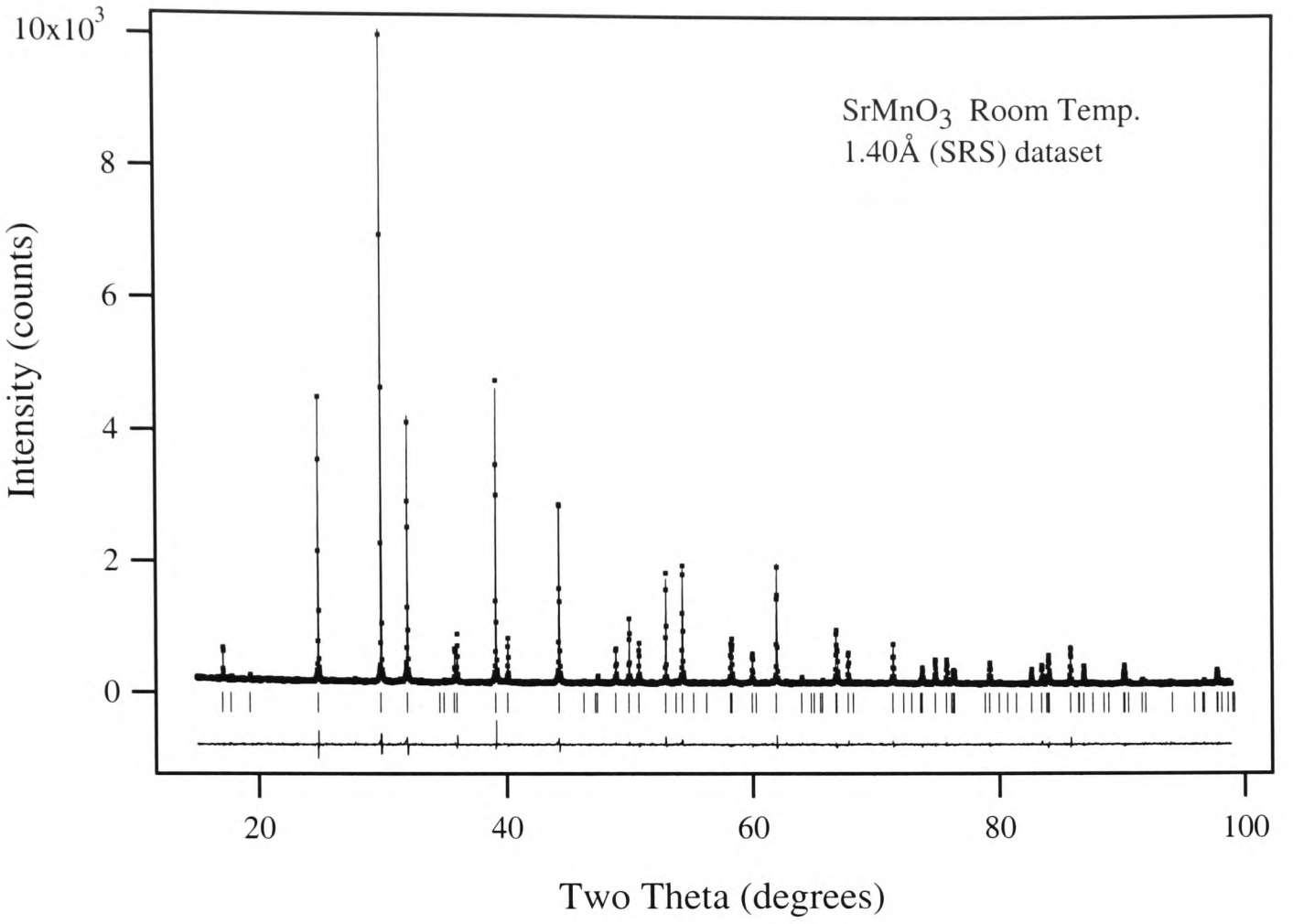
This agreement suggests that 4H $SrMnO_3$ was an effective choice of standard, despite the slightly differing Mn coordination environment afforded by the presence of face sharing MnO_6 octahedra.

Finally, the value of $\Delta f'$ of -9.040(49) electrons per Mn^{4+} was fixed in the 1.892951Å histogram, in the three histogram refinement of $Ca_4Mn_2TiO_{10-\delta}$, (the other two histograms being the D2b 1.594Å neutron dataset and the 1.40Å SRS dataset, respectively). The combination of neutron and X-ray datasets was essential not only to establish the degree of ordering of Mn^{4+} and Ti^{4+} across octahedral sites, but also to help locate precise positions for these transition metal cations. Without the X-ray data, the negative neutron scattering length of Mn (-3.73fm) would result in a low net scattering length for transition metal sites and would mean that parameters for the 4b and 8c positions had little influence in the overall quality of the fit. The crystallographic data obtained for the standard will be described first, followed by that of the sample at room temperature, and 5K, respectively.

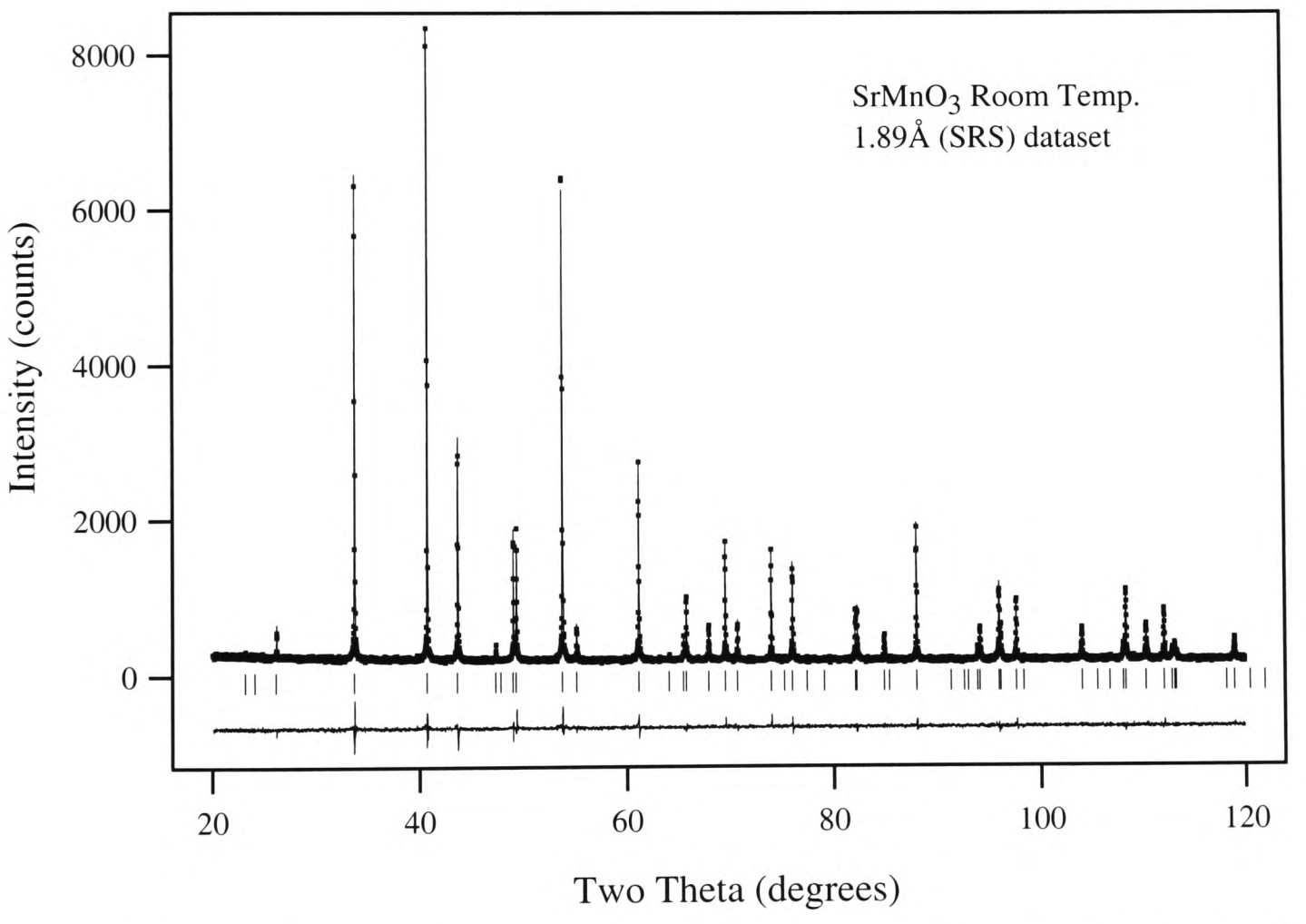
4.4.2.2 Powder neutron and powder X-ray diffraction

The synchrotron X-ray datasets collected at two wavelengths (~1.40Å and ~1.89Å respectively), for the standard, $SrMnO_3$, are presented below. Despite the shift in the scale of 2θ (as a result of the differing wavelengths at which data were collected) in Figures 4.4.2 (a) and (b), it is possible to observe differences in the relative intensities of several reflections in the two patterns, as a result of the introduction of anomalous scatterers into the sample, at the 'edge' wavelength (~1.89Å).

The standard, $SrMnO_3$, was prepared in the laboratory by Dr E. Cussen and the starting parameters used in the refinement were based upon those determined by Battle et al.[16] for a different batch of $SrMnO_3$ material, prepared under similar synthetic conditions. The refined atomic positions and lattice parameters modelling the data using the space group *$P6_3/mmc$* agree well with the reported values in previous studies on the material[43]. The two-histogram synchrotron X-ray refinement converged, giving the following residual fit parameters: R_{wp} = 6.49%, R_p = 5.26%, DWd = 1.704 and χ^2_{red} = 1.328 for 37 variables.



(a)



(b)

Figures 4.4.2 Observed (dots) and calculated (line) synchrotron X-ray diffraction profiles for $SrMnO_3$ (a) at room temperature and 1.40Å, and (b) at room temperature and 1.89Å.

Table 4.4.5 Structural parameters for 4H $SrMnO_3$ at room tempertaure:

4H $SrMnO_3$, $\Delta f' = -9.040(49)$ electrons per Mn^{4+}

Lattice Parameters(Å) a = 5.44809(2); b = 5.44809(2); c = 9.07818(4)

$\alpha = 90°$; $\beta = 90°$; $\gamma = 120°$; V = 233.359(2)Å^3 Space group: *$P6_3/mmc$*

Atom[a]	Site	U_{iso}, (Å^2)	x	y	z
Sr(1)	2a	0.0124(3)	0	0	0
Sr(2)	2c	0.0084(3)	1/3	2/3	1/4
Mn(3)	4f	0.0061(4)	1/3	2/3	0.6132(1)
O(4)	6g	0.0108(6)[b]	1/2	0	0
O(5)	6h	0.0108(6)[b]	-0.1801(3)	-0.3602(7)	1/4

[a] All fractional occupancies were held at 100%

[b] Constrained to be the same.

Table 4.4.6 Agreement parameters for the SRS X-ray refinement of 4H $SrMnO_3$:

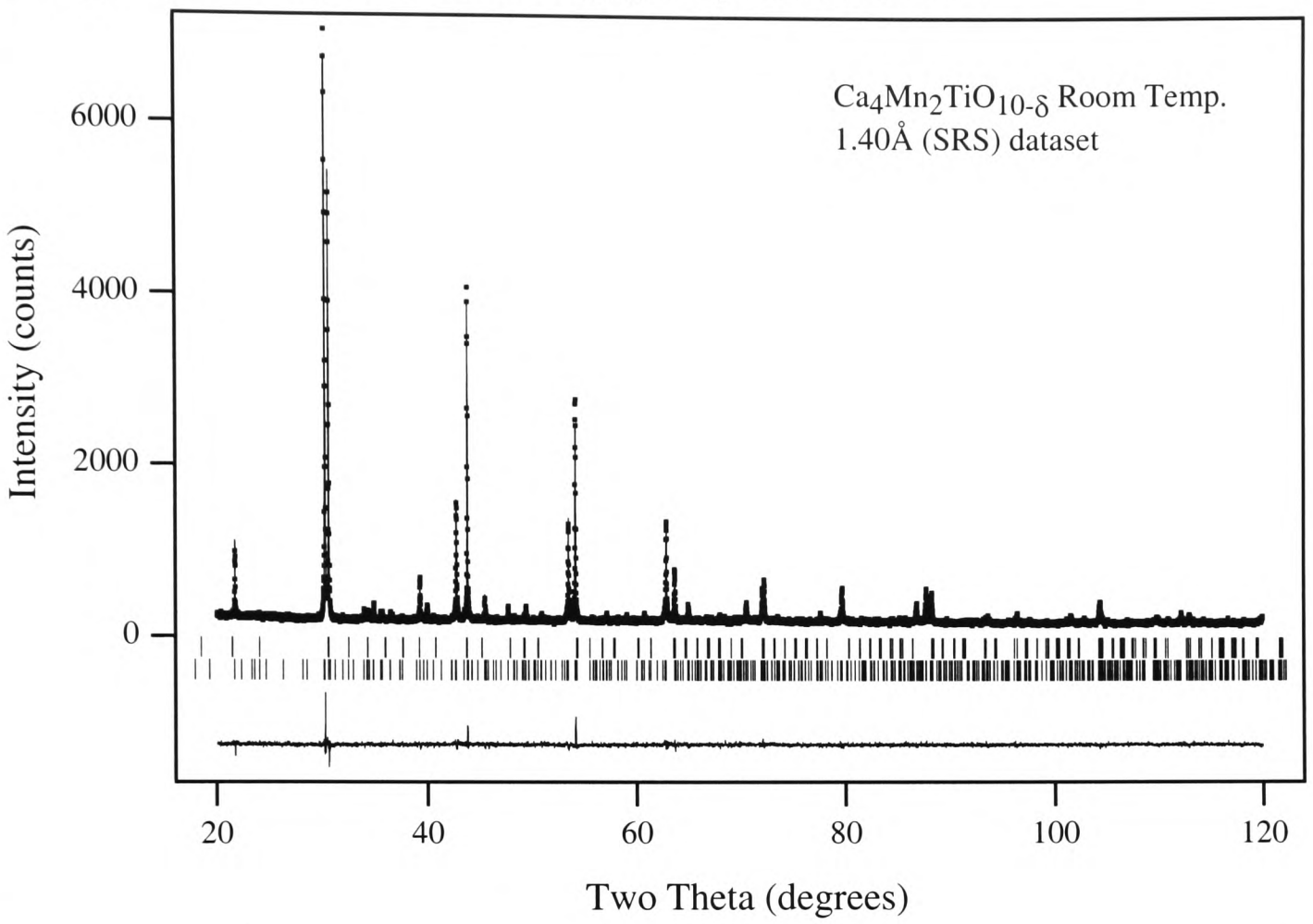
Agreement parameter	1.40Å SRS histogram	1.89Å SRS histogram	Total
R_{wp} (%)	6.00	7.03	6.49
R_p (%)	4.71	5.63	5.26
DWd	1.700	1.708	1.704
χ^2_{red} (37 variables)			1.328

Table 4.4.7 Refining variables for the SRS X-ray refinement of 4H $SrMnO_3$:

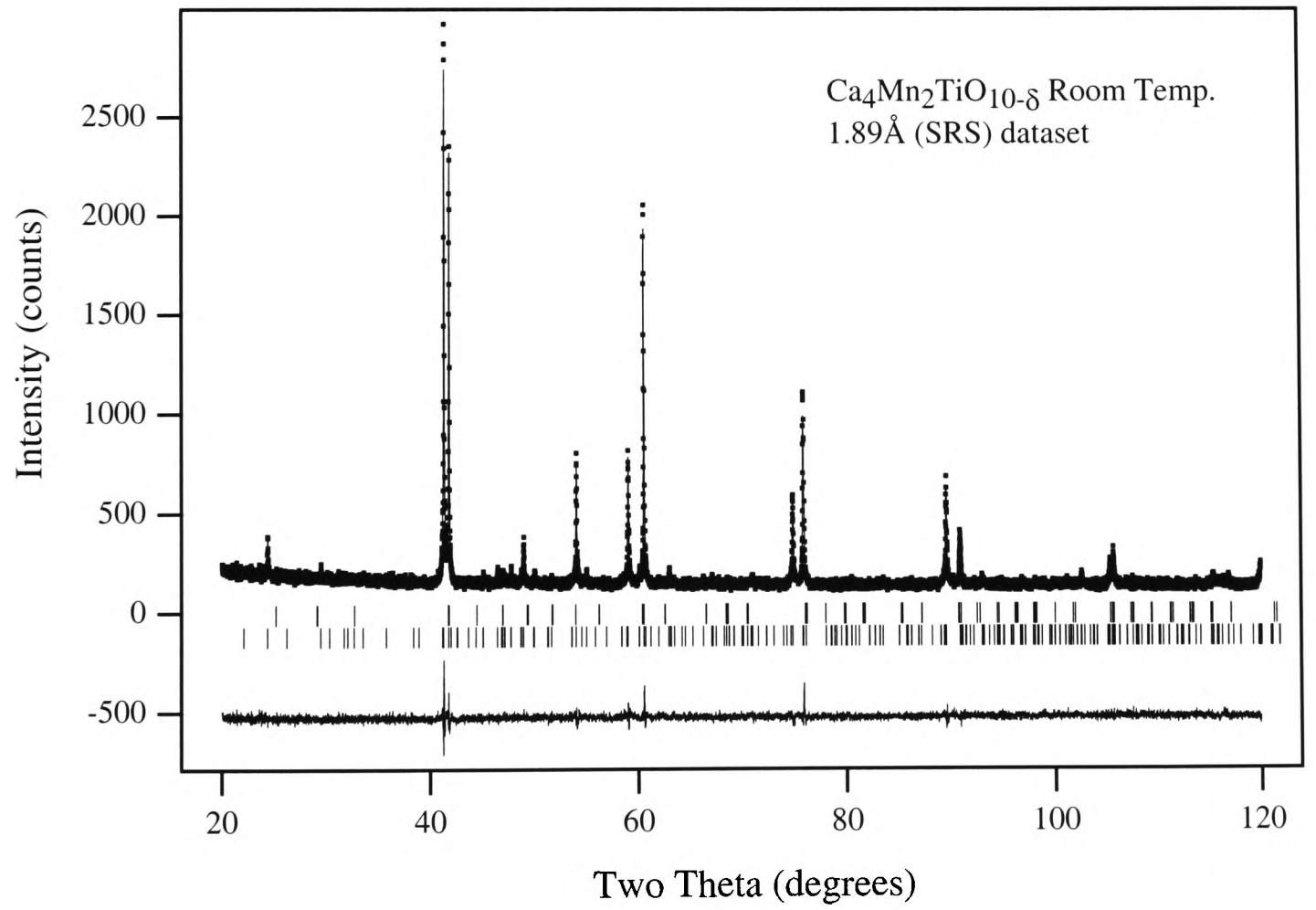
Refining variables (in addition to atomic coordinates and thermal parameters)	1.40Å SRS histogram	1.89Å SRS histogram
Background terms (Shifted Chebyshev)	8	8
Profile Coefficients (pseudo-Voigt)[a]	4	5
Histogram scale factor	1	1
Wavelength (λ / Å)	1	
$\Delta f'$(Mn)		1

[a] The height of the sample was refined through the 'shift' profile coefficient

The synchrotron X-ray datasets collected at two wavelengths (~1.40Å and ~1.89Å, respectively), for the sample, $Ca_4Mn_2TiO_{10-\delta}$, are presented below.

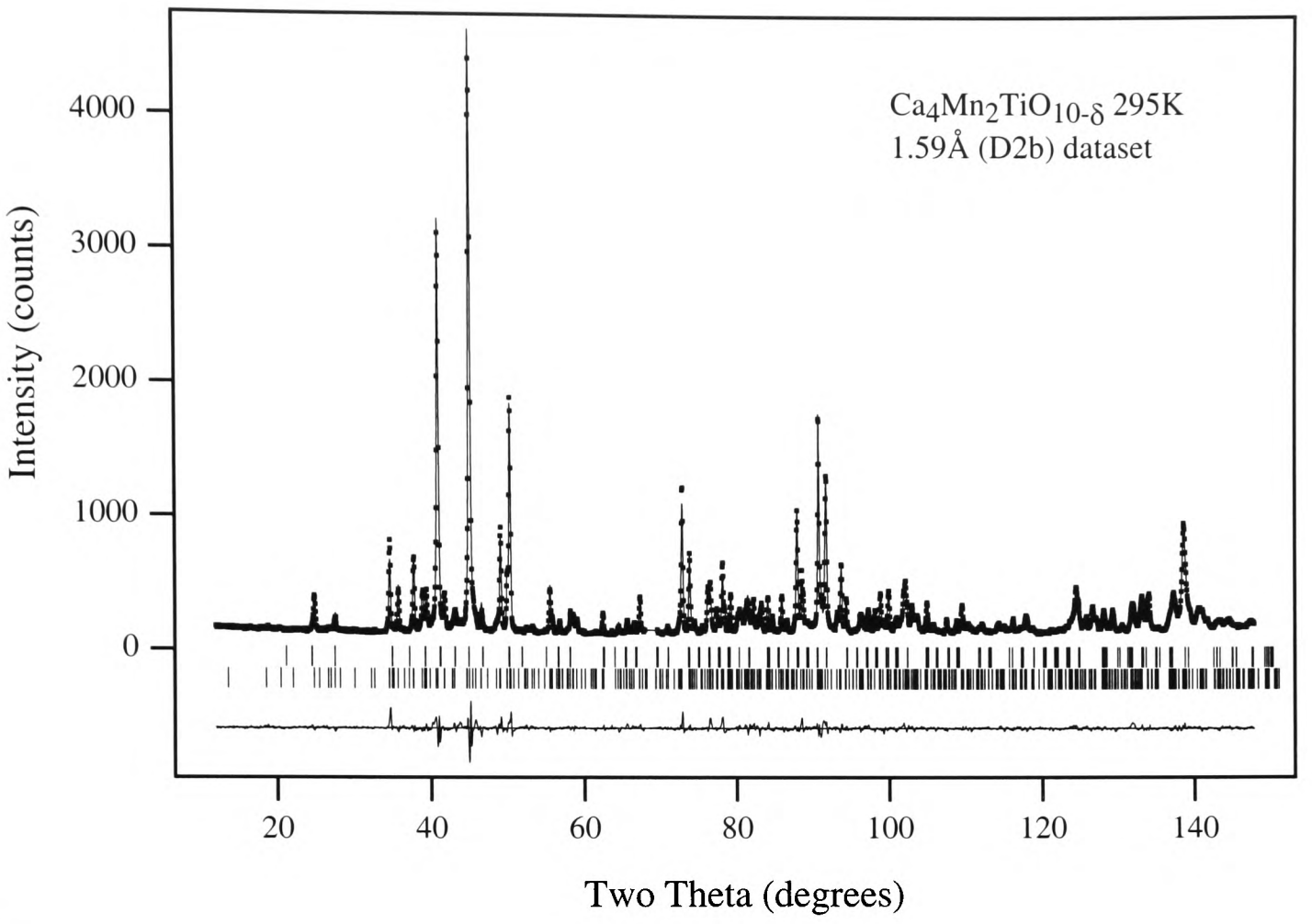


(a)



(b)

Figures 4.4.3 Observed (dots) and calculated (line) synchrotron X-ray diffraction profiles for $Ca_4Mn_2TiO_{10-\delta}$ at room temperature (a) at 1.40Å, and (b) at 1.89Å.



(c)

Figure 4.4.3 (c) Observed (dots) and calculated (line) neutron diffraction profile for $Ca_4Mn_2TiO_{10-\delta}$ at room temperature, refined in parallel with the two X-ray histograms presented in Figures 4.4.3 (a) and (b). In (a), (b) and (c), upper and lower tick marks represent minority and majority phases, respectively.

The differing intensities between the 1.40Å and 1.89Å datasets (as a result of the introduction of anomalous scatterers into the sample at the higher wavelength) can be observed from Figures 4.4.3 (a) and (b) by careful examination of the intensity of the reflections corresponding to the lower set of tick marks for the majority, $Ca_4Mn_2TiO_{10-\delta}$ phase.

Refinement of the 295K neutron dataset confirmed $Ca_4Mn_2TiO_{10-\delta}$ was modelled best using the space group *Pbca*, and the resulting diffraction pattern is shown in Figure 4.4.3 (c). However, there were significant differences in the observed and calculated profiles using a single phase $Ca_4Mn_2TiO_{10-\delta}$ model. A 24-hour scan over the poorly fitted angular regions using the laboratory Philips diffractometer, followed by use of an X-ray powder pattern database, identified a potential impurity as $CaMnO_{3-\delta}$ (with $\delta = 0.02$)[44]. The inclusion of a fraction of $CaMnO_{2.98}$ in the structural model for the Philips X-ray refinement provided the required intensity in the 33.2 and 48.4° (2θ) angular regions ($\lambda = 1.5406$Å). The impurity

phase was formulated as $CaMn_{2/3}Ti_{1/3}O_{2.98}$ in the refinement of the 295K neutron dataset, with significant improvement to the fit (R_{wp} reduced from 6.67% in the single phase model to 5.92% in the biphasic model). The fraction of this minority phase refined to 1.13%. The impurity is present in too low a concentration to establish the ratio of Mn^{4+}:Ti^{4+} it contains, or its oxygen content, and so the cation ratio was fixed at that for the majority phase (ie. 2:1) and δ was left at 0.02. The overall stoichiometry of the majority n=3 material dictates that if there is a concentration, albeit low, of n=∞ impurity, there should be also a trace of (most likely) n=2 RP material. The refinement of the profile coefficient representing the anisotropy coefficient for strain broadening, 'Y_e', in equation 2.5.8 to a non-zero value, improving significantly the fit in the 295K neutron data, may reinforce this suggestion. The anisotropic strain broadening term was modelled through Y_e assuming the principal strain axis to be [001] (ϕ in equation 2.5.8 is the angle between this axis and the reciprocal-lattice vector of the Bragg reflection) and may reflect strain caused by intergrown domains of n=2 RP material.

Having established a precise structural model using the D2b neutron dataset, the two synchrotron X-ray histograms were introduced into the refinement, as detailed in the description of the refinement strategy above. The value of $\Delta f'$ of -9.040(49) electrons per Mn^{4+} was fixed in the 1.892951Å histogram, with the result that it was possible to refine fractional occupancies across 4b and 8c octahedral sites. In attempting to establish the distributions of Mn^{4+} and Ti^{4+} across octahedral sites, in the three-histogram refinement of $Ca_4Mn_2TiO_{10-\delta}$, the values of U_{iso} for both transition metal sites (4b and 8c) were set first to one common value and the fractional occupancies of Mn^{4+} and Ti^{4+} refined then from statistical distributions. However, it was found that when individual U_{iso} values were set for distinct 4b and 8c sites, the fractional occupancies of Mn^{4+} and Ti^{4+} did not change (within error) and so distinct U_{iso} values were preferred. The effect of allowing the distributions of Mn^{4+} and Ti^{4+} across octahedral sites to refine, was a reduction in R_{wp} in the 1.892951Å histogram from 8.84% to 7.72% as the final value. The resultant (total) residual fit parameters in the three-histogram refinement were as follows: R_{wp} = 6.62%, R_p = 5.64%, DWd = 1.308 and χ^2_{red} = 1.253 for 120 variables.

Table 4.4.8 Sructural parameters for biphasic $Ca_4Mn_2TiO_{10-\delta}$ at room temperature:

Majority phase, 98.87% $Ca_4Mn_2TiO_{10-\delta}$ by weight

Lattice Parameters(Å) a = 5.31411(5); b = 5.31148(5); c = 26.91376(21); V = 759.662(16)Å^3

Atom	Site	Fraction (%)	x	y	z
Ca(1)	8c	100	0.5011(5)	0.4792(6)	0.07000(9)
Ca(2)	8c	100	-0.0036(6)	0.0130(8)	0.20432(6)
Mn(3)	4b	59.8(2.6)[a]	0	1/2	0
Ti(4)	4b	40.2(2.6)[a]	0	1/2	0
Mn(5)[c]	8c	70.1(1.3)[b]	0.4992(7)	0.0011(7)	0.14111(7)
Ti(6)[c]	8c	29.9(1.3)[b]	0.4992(7)	0.0011(7)	0.14111(7)
O(7)	8c	100	0.4425(3)	0.0017(5)	0.06987(9)
O(8)	8c	100	0.5432(5)	-0.0124(6)	0.21117(6)
O(9)	8c	96.3(0.8)	0.7809(7)	0.2210(6)	0.13265(9)
O(10)	8c	100	0.2178(5)	0.7790(6)	0.14743(8)
O(11)	8c	100	0.2874(6)	0.2909(6)	-0.00860(8)

Minority phase[d], 1.13% $CaMn_{2/3}Ti_{1/3}O_{2.98}$ by weight

Lattice Parameters(Å) a = 5.31647(109); b = 5.30808(118); c = 7.52849(136)
V = 212.456(51)Å^3 Space group: *Pbnm*

Atom	Site	Fraction (%)	x	y	z
Ca(1)	4c	100	-0.007	0.035	0.25
Mn(2)	4b	66.67	0.5	0	0
Ti(3)	4b	33.33	0.5	0	0
O(4)	4c	100	0.081	0.492	0.25
O(5)	8d	100	-0.284	0.293	0.027

[a,b] Fractional occupancies were initially set with statistical distribution (66.67% : 33.33%, Mn : Ti) across octahedral sites 4b and 8c

[c] Atomic coordinates were constrained to be the same for atoms occupying the same site

[d] Atomic coordinates, fractional occupancies and U_{iso} values (0.005(Å^2)) were held constant for the minority phase.

As shown in Table 4.4.8, there is (albeit slight) preferential ordering of Ti^{4+} cations onto the central layer in the triple octahedron block (site symmetry 4b) in $Ca_4Mn_2TiO_{10-\delta}$. The refined oxygen fractional occupancies give a value of δ in $Ca_4Mn_2TiO_{10-\delta}$ of 0.07. The oxygen deficiency arises from the O(9) site, an equatorial anion in the outer layer of octahedra. From this point onwards, $Ca_4Mn_2TiO_{10-\delta}$ is formulated as $Ca_4Mn_2TiO_{9.93}$.

Table 4.4.9 Thermal parameters for $Ca_4Mn_2TiO_{9.93}$ at room temperature:

Atom	U_{iso}, U_{eq}	U_{11} (Å^2)	U_{22} (Å^2)	U_{33} (Å^2)	U_{12} (Å^2)	U_{13}(Å^2)	U_{23} (Å^2)
Ca(1)	0.0132	0.0086(15)	0.0142(17)	0.0166(10)	-0.0036(11)	0.0064(20)	-0.0054(23)
Ca(2)	0.0121	0.0057(18)	0.0282(23)	0.0022(9)	-0.0057(16)	-0.0063(10)	0.0035(16)
Mn(3)	0.0034(6)[a]						
Ti(4)	0.0034(6)[a]						
Mn(5)	0.0064(4)[b]						
Ti(6)	0.0064(4)[b]						
O(7)	0.0036(4)						
O(8)	0.0063(5)						
O(9)	0.0143	0.0168(15)	0.0084(14)	0.0176(12)	-0.0123(11)	0.0011(11)	0.0044(11)
O(10)	0.0145	0.0109(13)	0.0148(15)	0.0176(11)	-0.0101(11)	-0.0004(10)	0.0001(10)
O(11)	0.0063(5)						

[a, b] Constrained to be the same.

Figure 4.4.4 represents the thermal parameters described above, as (99%) ellipsoids..

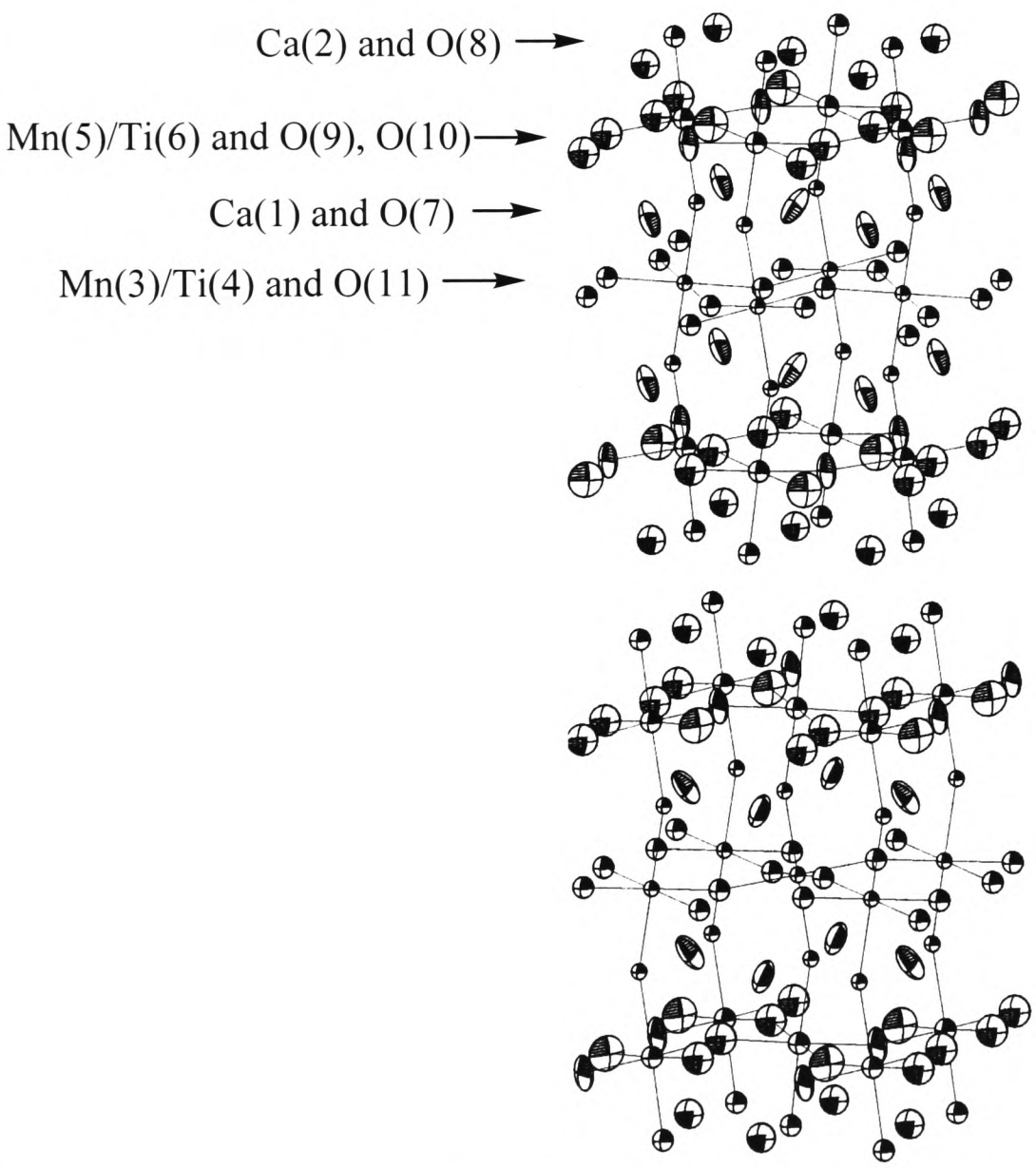


Figure 4.4.4 Representation of atoms as 99% thermal ellipsoids in room temperature $Ca_4Mn_2TiO_{9.93}$.

The relatively large anisotropic displacements of O(9) and O(10) are evident from the enlarged ellipsoids corresponding to these sites. The O(9) site is where the oxygen vacancies occur, hence this outer layer of octahedra is proposed to contain the small fraction of Mn^{3+} cations present in this sample. The 12 and 9 coordinate cations, Ca(1) and Ca(2), respectively, are also described by anisotropic displacement parameters as shown in Table 4.4.9. The Ca(1) ellipsoids in particular, show significant elongation in a direction approximately parallel to the z axis, perpendicular to the planes in which they are situated.

Figure 4.4.5 gives a polyhedral representation of the structure of $Ca_4Mn_2TiO_{9.93}$ at 295K. The labelling of atomic sites is identical to that used in the previous Figure; however, the nature of octahedral tilting in *Pbca* is better illustrated in the polyhedral diagram.

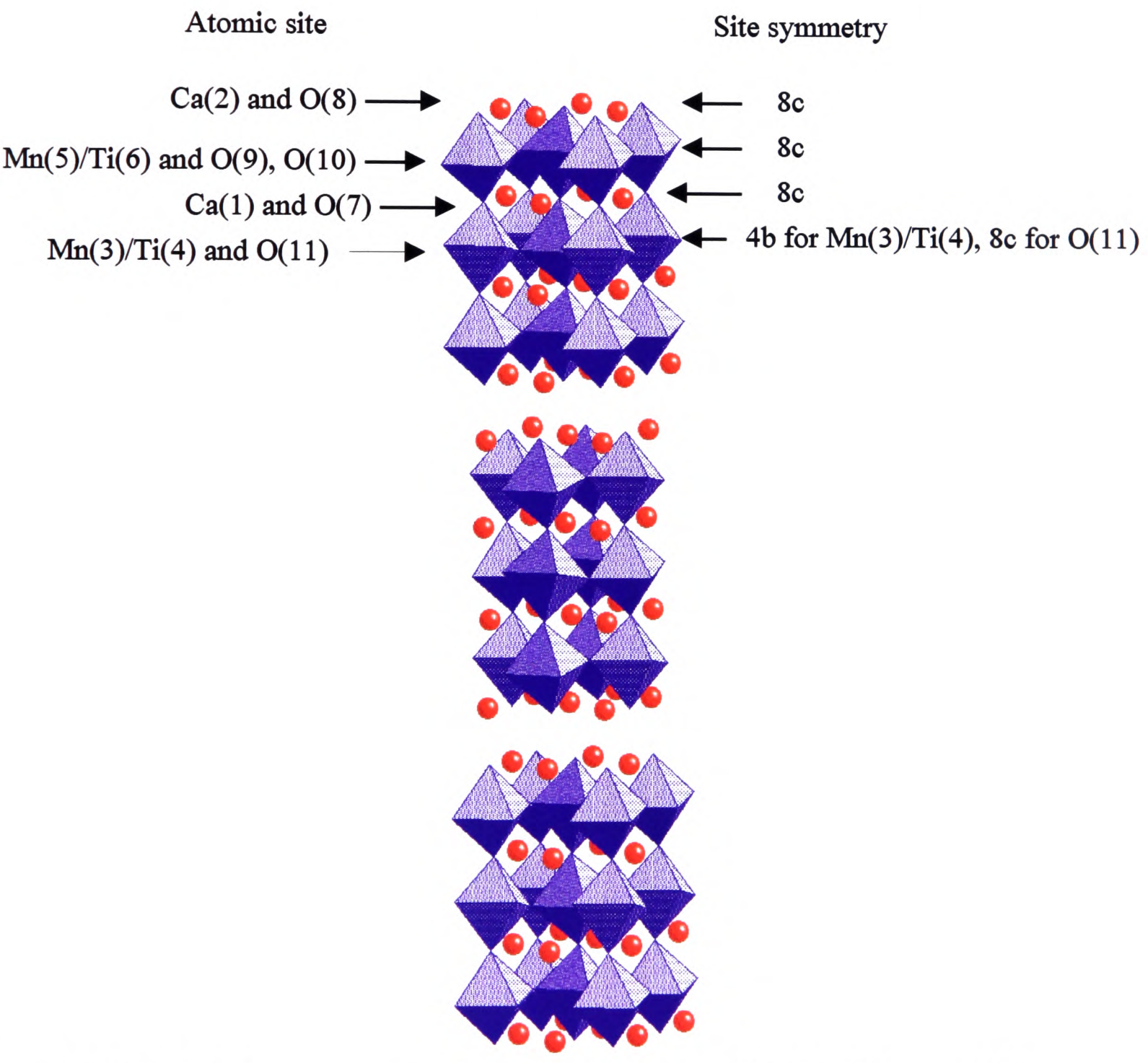
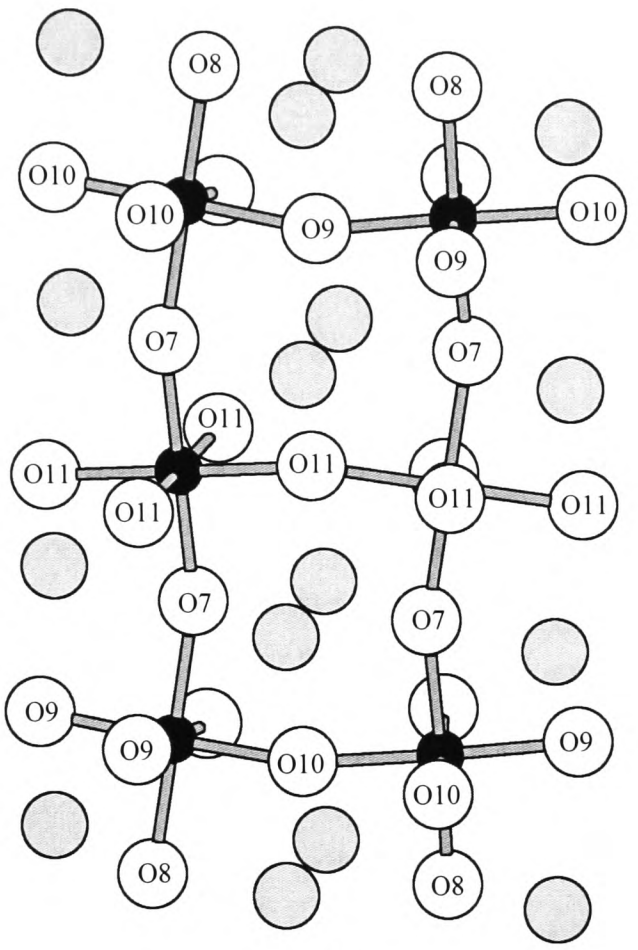
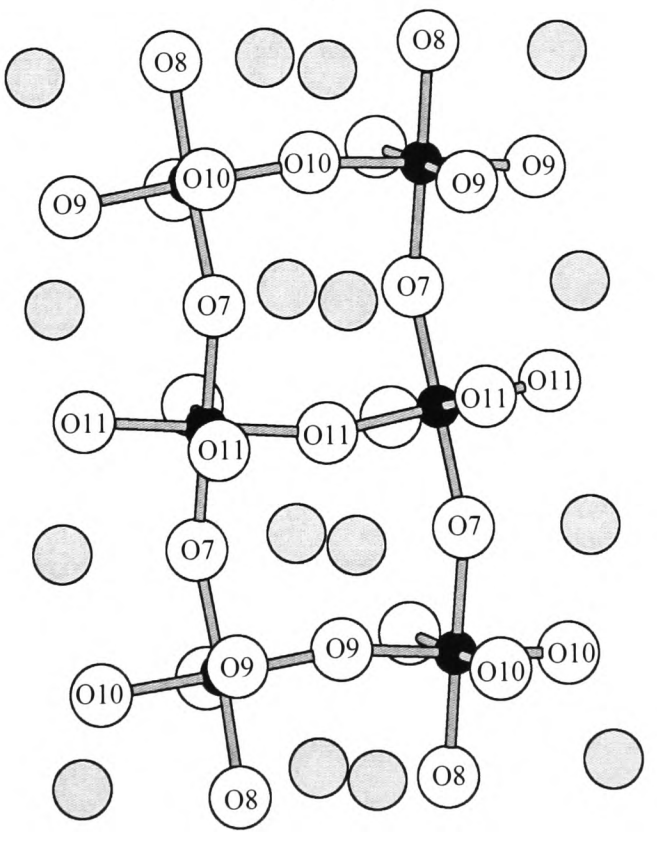


Figure 4.4.5 Polyhedral representation of the crystal structure of $Ca_4Mn_2TiO_{9.93}$ at 295K.

Figures 4.4.6 (a) and (b) give a more detailed view of the orientation of octahedra within the triple octahedron blocks represented in the polyhedral diagram in the previous Figure. Labelling is appropriate for specific bondlengths and bond angles listed in Table 4.4.10.



(a)



(b)

Figures 4.4.6 The orientation of octahedra within the triple octahedron block in $Ca_4Mn_2TiO_{9.93}$, viewed along directions (a) close to [110] and (b) $[1\bar{1}0]$, respectively

Table 4.4.10 Selected distances (Å) and angles (°) of $Ca_4Mn_2TiO_{9.93}$ at 295K:

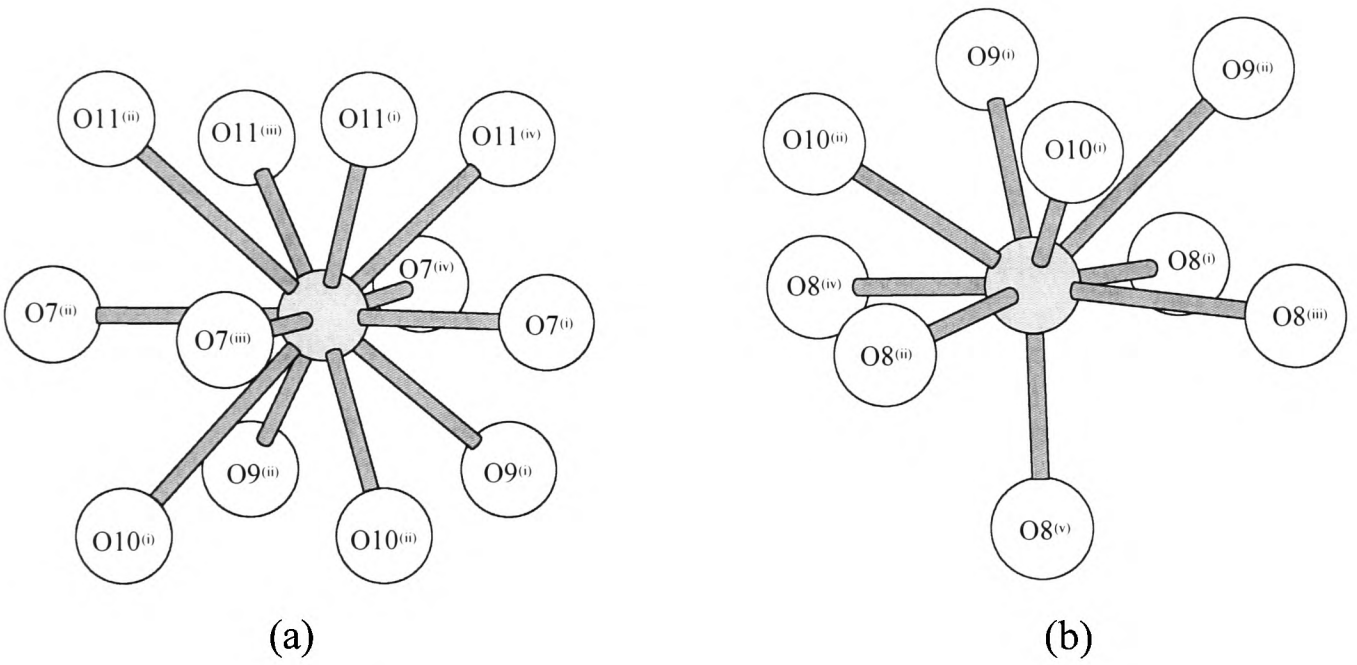
Ca(1)–O(7)^{i}	2.555(5)	Ca(2)–O(8)^{i}	2.419(4)	Mn(3)[a]–O(7)	1.9051(24)x2
Ca(1)–O(7)^{ii}	2.793(5)	Ca(2)–O(8)^{ii}	2.915(4)	Mn(3)–O(11)	1.903(5) x2
Ca(1)–O(7)^{iii}	2.3610(31)	Ca(2)–O(8)^{iii}	2.805(6)	Mn(3)–O(11)	1.928(5) x2
Ca(1)–O(7)^{iv}	2.9586(30)	Ca(2)–O(8)^{iv}	2.536(6)	Mn(5)–O(7)	1.9409(32)
Ca(1)–O(9)^{i}	2.633(4)	Ca(2)–O(8)^{v}	2.2919(23)	Mn(5)–O(8)	1.9013(27)
Ca(1)–O(9)^{ii}	2.415(4)	Ca(2)–O(9)^{i}	2.501(4)	Mn(5)–O(9)	1.912(5)
Ca(1)–O(10)^{i}	3.024(4)	Ca(2)–O(9)^{ii}	2.880(4)	Mn(5)–O(9)	1.905(6)
Ca(1)–O(10)^{ii}	2.613(4)	Ca(2)–O(10)^{i}	2.297(4)	Mn(5)–O(10)	1.912(6)
Ca(1)–O(11)^{i}	2.6012(35)	Ca(2)–O(10)^{ii}	2.578(5)	Mn(5)–O(10)	1.881(5)
Ca(1)–O(11)^{ii}	3.0933(35)				
Ca(1)–O(11)^{iii}	2.341(4)				
Ca(1)–O(11)^{iv}	2.666(4)				

O(7)–Mn(3)–O(7)	180.000(0)	O(8)–Mn(5)–O(9)	92.59(19)
O(7)–Mn(3)–O(11)	89.68(10)	O(8)–Mn(5)–O(9)	90.77(20)
O(7)–Mn(3)–O(11)	88.81(10)	O(8)–Mn(5)–O(10)	89.11(18)
O(11)–Mn(3)–O(11)	89.02(4)	O(8)–Mn(5)–O(10)	90.89(18)
		O(9)–Mn(5)–O(9)	89.02(16)
O(7)–Mn(5)–O(8)	177.20(30)	O(9)–Mn(5)–O(10)	178.24(16)
O(7)–Mn(5)–O(9)	90.17(16)	O(9)–Mn(5)–O(10)	90.67(22)
O(7)–Mn(5)–O(9)	88.76(17)	O(9)–Mn(5)–O(10)	90.48(23)
O(7)–Mn(5)–O(10)	88.14(17)	O(9)–Mn(5)–O(10)	178.32(16)
O(7)–Mn(5)–O(10)	89.59(19)	O(10)–Mn(5)–O(10)	89.79(16)
Mn(3)–O(11)–Mn(3)	157.44(13)	Mn(5)–O(9)–Mn(5)	160.51(23)
Mn(3)–O(7)–Mn(5)	161.85(16)	Mn(5)–O(10)–Mn(5)	162.87(23)

[a] Although only Mn(3) and Mn(5) cations are listed in Table 4.4.10, Ti(4) and Ti(6) cations share the transition metal sites in the proportions quoted in Table 4.4.8.

It is instructive to compare key structural parameters obtained for $Ca_4Mn_2TiO_{9.93}$ with equivalent values reported for the undoped, parent compound $Ca_4Mn_3O_{10-\delta}$ and, as far as possible due to the differing symmetry, with the Fe substituted compound $Ca_4Mn_2FeO_{9.75}$[31]. Considering the Ca cation coordination environments, as was observed in $Ca_4Mn_3O_{10-\delta}$ there is a large variation in values of Ca-O bondlengths for the tilted octahedral arrangement characteristic of orthorhombic symmetry, evidenced by the parameters listed in

Table 4.4.10. For example, considering the Ca(1) cation in the perovskite block in $Ca_4Mn_2TiO_{9.93}$, the shortest bond is that between Ca(1) and one of the 'equatorial' O(11) anions, measuring 2.341(4)Å. However, in order to complete the 12-fold coordination at this site, it is necessary to consider a sphere with radius 3.093(4)Å to reach the most remote O(11) anion surrounding Ca(1). The latter distance is more typical of a Ca-Mn separation distance. In comparison, Ca(2)-O bondlengths show less variation, ranging between 2.291(2) and 2.915(4), the latter setting the radius of the 9 coordinate shell. These values are comparable to the upper limits for Ca-O distances in $Ca_4Mn_3O_{10-\delta}$ (3.056(5) and 2.902(6)Å for 12 and 9 coordinate sites, respectively). The coordination environments for Ca(1) and Ca(2) are shown in Figures 4.4.7 (a) and (b).



(a) (b)

Figure 4.4.7 The distribution of oxygen anions around (a) Ca(1), the 12 coordinate and (b) Ca(2), the 9 coordinate A-cation.

The Mn/Ti-O bondlengths may be compared with the values in $Ca_4Mn_3O_{10-\delta}$, $Ca_4Mn_2FeO_{9.75}$ and to those in the mixed A-site cation compound $K_2Nd_2Ti_3O_{10-\delta}$[45]. There was no evidence of octahedral distortion resulting from displacement of Ti^{4+} cations from the centres of outer octahedra of the perovskite block, known to be prevalent for d^0 cations[46]. Attempts were made to model such a displacement by splitting the Ti(6), however, this failed to give any significant improvement to the fit.

In $Ca_4Mn_2TiO_{9.93}$ the central layer of octahedra in the perovskite blocks appears slightly less regular than those in the undoped sample, $Ca_4Mn_3O_{10-\delta}$. The degree of distortion can be quantified with the parameter $(r_{ax} - r_{eq})/(r_{ax} + r_{eq})$ which takes the value of 0.00272 for

$Ca_4Mn_2TiO_{9.93}$ and 0.00157 at room temperature in $Ca_4Mn_3O_{10-\delta}$. The mean Mn(3)-O bondlength in $Ca_4Mn_2TiO_{9.93}$ is 1.912Å, somewhat longer than that for $Ca_4Mn_3O_{10-\delta}$, (1.899Å), which is to be expected after the introduction of the larger Ti^{4+} cation. The ionic radii for Ti^{4+} and Mn^{4+} in octahedral geometry are 0.605 and 0.530Å, respectively[47]. In $Ca_4Mn_2TiO_{9.93}$ the apical Mn(3)-O(7) and two of the Mn(3)-O(5) bondlengths are the same essentially and it is the second Mn(3)-O(5) distance that causes the variation, whereas in $Ca_4Mn_3O_{10-\delta}$ the equatorial Mn-O distances are equal and the apical bondlength is increased slightly. The Mn(3)/Ti(4) cations are constrained by the 4b site symmetry to be central in distorted octahedra.

The outer octahedra in $Ca_4Mn_2TiO_{9.93}$ are less regular than the central octahedra, a pattern observed also in $Ca_4Mn_3O_{10-\delta}$ and $Ca_4Mn_2FeO_{9.75}$. The spread in Mn(5)-O bondlengths is between 1.940(3)Å for Mn(5)-O(7) and 1.881(5)Å for two of the equatorial Mn(5)-O(10) bonds; however, this degree of variation (0.059Å) is only slightly greater than that observed in $Ca_4Mn_3O_{10-\delta}$ (0.054Å). The mean Mn(5)-O bondlength is 1.909Å, lower than for the middle octahedron, consistent with the lower percentage occupancy of this site by the larger Ti^{4+} cation. The parameter $(r_{ax} - r_{eq})/(r_{ax} + r_{eq})$ takes the value of 0.00487 for the outer octahedron. The isotropic displacement parameter for the transition metal site 8c, corresponding to the outer octahedron, is about twice the value for the middle octahedron.

For both orthorhombic compounds, $Ca_4Mn_2TiO_{9.93}$ and $Ca_4Mn_3O_{10-\delta}$, the length of the apical Mn/Ti-O bond extending from the outer octahedron into the rocksalt layer is shorter than the opposite apical bond directed into the perovskite block. The level of oxygen nonstoichiometry refined allows the presence of 0.14 moles of the Mn^{3+} d^4 cation per mole of $Ca_4Mn_2TiO_{9.93}$. This Jahn-Teller ion would be expected to occupy preferentially the outer octahedra of the triple layer, where the inherent lack of symmetry would allow elongation of the octahedron into the rocksalt layer. Indeed, this is where the Mn^{3+} cations appear to be located, since this is where the oxide anion vacancies (from the equatorial O(9) sites) occur. The deviation of O-Mn-O bond angles away from 180° and 90° in $Ca_4Mn_2TiO_{9.93}$ (giving a measure of the degree of octahedral tilting) is very similar to that observed in $Ca_4Mn_3O_{10-\delta}$.

This is confirmed by comparison of the data in Table 4.4.10 with that presented for sample P in reference [2].

A summary of refinement agreement parameters and refining variables in the room temperature, three-histogram refinement of $Ca_4Mn_2TiO_{9.93}$, are tabulated below.

Table 4.4.11 Agreement parameters for the room temperature combined neutron (D2b) and X-ray (SRS) refinement of $Ca_4Mn_2TiO_{9.93}$:

Agreement parameter	1.40Å SRS histogram	1.89Å SRS histogram	1.59Å D2b histogram	Total
R_{wp} (%)	6.98	7.72	5.92	6.62
R_p (%)	5.56	6.15	4.58	5.64
DWd	1.706	1.785	0.607	1.308
χ^2_{red} (120 variables)				1.253

Table 4.4.12 Refining variables for the room temperature combined neutron (D2b) and X-ray (SRS) refinement of $Ca_4Mn_2TiO_{9.93}$:

Refining variables (in addition to atomic coordinates, thermal parameters and fractional occupancies)	1.40Å SRS histogram	1.89Å SRS histogram	1.59Å D2b histogram
Background terms (Shifted Chebyshev)	5	5	30
Profile Coefficients (pseudo-Voigt)[a]	5	4	7
Histogram scale factor	1	1	1
Zero point			1

[a] Refining profile coefficients were constrained to be the same for the majority and minority phase, other than 'ptec' which was set to zero for the minority phase.

The observed and calculated neutron diffraction profiles for $Ca_4Mn_2TiO_{9.93}$ at 5K, are shown in Figure 4.4.8.

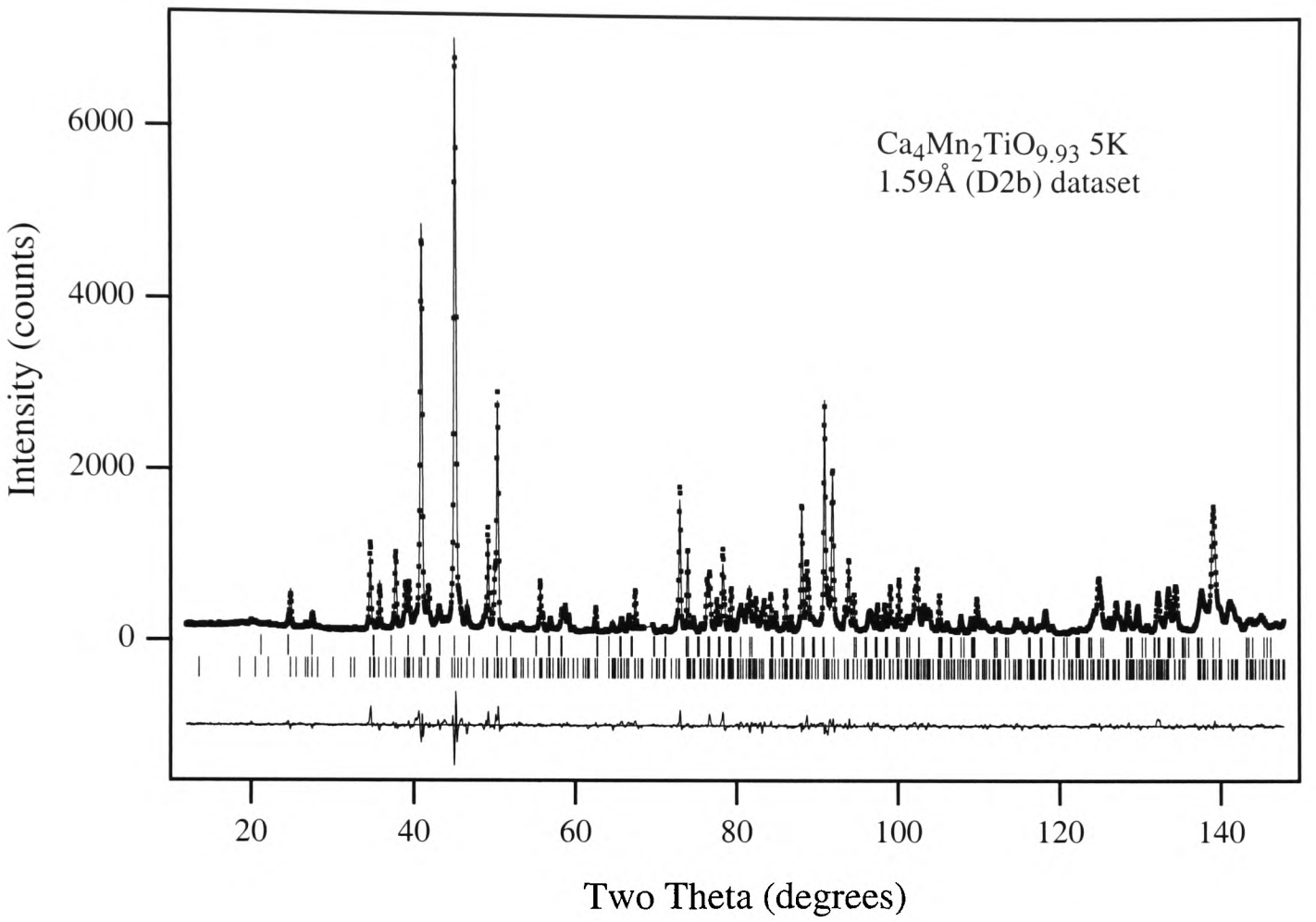
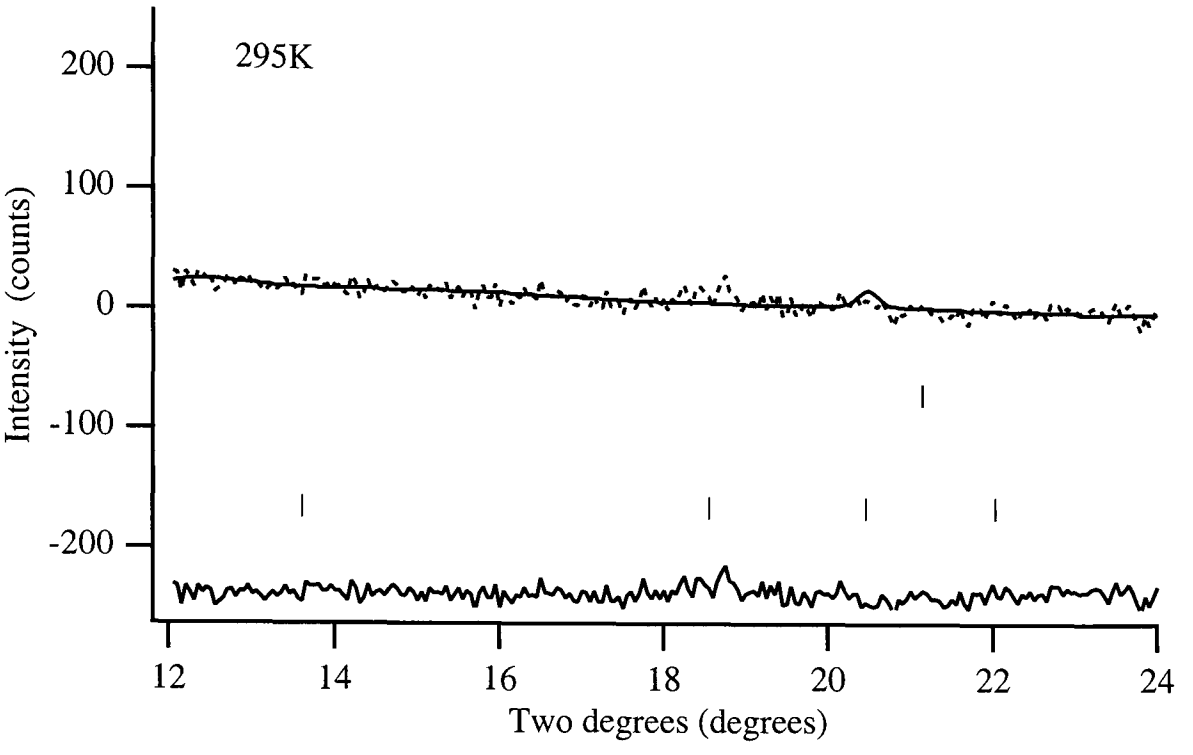


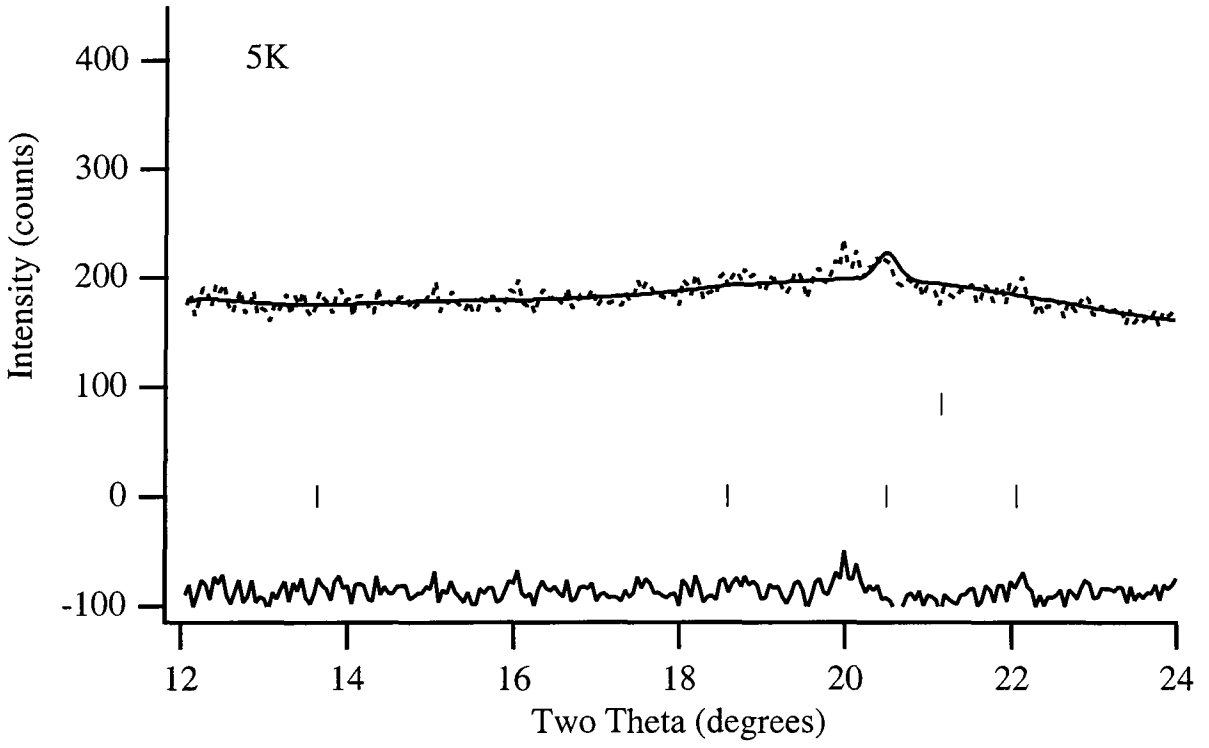
Figure 4.4.8 Observed (dots) and calculated (line) neutron powder diffraction profiles for $Ca_4Mn_2TiO_{9.93}$ at 5K. Upper and lower tick marks represent minority and majority phases, repectively.

The refinement of the low temperature (5K) D2b dataset shown in Figure 4.4.8, employed the same starting structural model (containing the same level of $CaMn_2TiO_{2.98}$ impurity and distribution of Mn/Ti over octahedral sites). This Mn/Ti distribution was held constant in the refinement; however, all other parameters (including the level of impurity) were refined, as in the 295K dataset. The resultant fit parameters in the single-histogram refinement of $Ca_4Mn_2TiO_{9.93}$ at 5K were as follows: R_{wp} = 5.63%, R_p = 4.32%, DWd = 0.482 and χ^2_{red} = 6.232 for 120 variables. The evolution of magnetic Bragg peaks on reducing the measuring temperature to 5K, thought possible by analogy with the antiferromagnetic $Ca_4Mn_3O_{10-\delta}$ and $Ca_4Mn_2FeO_{9.75}$, did not occur.

However, Figures 4.4.9 (a) and (b) give enlarged views of the 12-24° angular region of the neutron diffraction pattern obtained at 5K. The presence of a broad maximum, although not representing a large increase in intensity, is just visible in the 5K pattern. This diffuse scattering is consistent with the development of regions of correlated spins within the sample.



(a)



(b)

Figures 4.4.9 Enlarged view of the 12-24° angular region of the neutron diffraction profile of $Ca_4Mn_2TiO_{9.93}$ at (a) 295K and (b) 5K. Upper and lower tick marks represent minority and majority phases, respectively.

Table 4.4.13 Structural parameters for biphasic $Ca_4Mn_2TiO_{9.93}$ at 5K:

Majority phase, 98.87% $Ca_4Mn_2TiO_{9.93}$ by weight

Lattice Parameters(Å) a = 5.30497(14); b = 5.30469(14); c = 26.86191(64); V = 755.926(50)Å^3

Atom	Site	Fraction (%)	x	y	z
Ca(1)	8c	100	0.5015(9)	0.4764(14)	0.06991(26)
Ca(2)	8c	100	-0.0041(12)	0.0150(17)	0.20413(18)
Mn(3)	4b	59.8(2.6)[a]	0	1/2	0
Ti(4)	4b	40.2(2.6)[a]	0	1/2	0
Mn(5)[b]	8c	70.1(1.3)[a]	0.5029(15)	0.0085(18)	0.14097(25)
Ti(6)[b]	8c	29.9(1.3)[a]	0.5029(15)	0.0085(18)	0.14097(25)
O(7)	8c	100	0.4403(6)	0.0019(8)	0.07013(20)
O(8)	8c	100	0.5455(9)	-0.0130(11)	0.21131(12)
O(9)	8c	96.3(0.8)	0.7830(11)	0.2215(10)	0.13220(16)
O(10)	8c	100	0.2158(9)	0.7782(10)	0.14764(15)
O(11)	8c	100	0.2845(11)	0.2937(10)	-0.00924(15)

Minority phase[c], 1.13% $CaMn_{2/3}Ti_{1/3}O_{2.98}$ by weight

Lattice Parameters(Å) a = 5.31292(260); b = 5.29771(240); c = 7.51185(359)

V = 211.431(99)Å^3 Space group: *Pbnm*

Atom	Site	Fraction (%)	x	y	z
Ca(1)	4c	100	-0.007	0.035	0.25
Mn(2)	4b	66.67	0.5	0	0
Ti(3)	4b	33.33	0.5	0	0
O(4)	4c	100	0.081	0.492	0.25
O(5)	8d	100	-0.284	0.293	0.027

[a] Fractional occupancies were constrained at the values refined from the room temperature dataset.

[b] Atomic coordinates were constrained to be the same for atoms occupying the same site

[c] Atomic coordinates, fractional occupancies and U_{iso} values (0.005Å^2) were held constant for the minority phase.

At 5K, lattice parameters are all contracted relative to the room temperature values with percentage reductions in length as follows: a has reduced by 0.172%, b by 0.128% and c by 0.193%. The larger reduction of a, as compared to b, results in the low temperature structure having essentially equal a and b lattice parameters within the quoted error margins.

Table 4.4.14 Thermal parameters of $Ca_4Mn_2TiO_{9.93}$ at 5K:

Atom	U_{iso}, U_{eq}	U_{11} (Å^2)	U_{22} (Å^2)	U_{33} (Å^2)	U_{12} (Å^2)	U_{13}(Å^2)	U_{23} (Å^2)
Ca1	0.0084	0.0028(29)	0.0160(40)	0.0066(22)	-0.0018(20)	0.0054(34)	-0.0054(37)
Ca2	0.0082	0.0017(35)	0.0240(50)	-0.0008(22)	-0.0052(29)	-0.0060(19)	-0.0045(27)
Mn3[a]	-0.0002(16)						
Ti4[a]	-0.0002(16)						
Mn5[b]	0.0027(11)						
Ti6[b]	0.0027(11)						
O7	-0.0005(8)						
O8	0.0013(10)						
O9	0.0085	0.0122(26)	0.0034(25)	0.0099(22)	-0.0083(18)	-0.0000(19)	0.0028(18)
O10	0.0101	0.0072(23)	0.0101(26)	0.0129(20)	-0.0129(20)	0.0000(18)	0.0003(16)
O11	0.0031(10)						

[a,b] Constrained to be the same

The $U_{equivalent}$ values for Ca(1), Ca(2), O(9) and O(10) reduce only to approximately two-thirds of their room temperature values when refined in the 5K D2b dataset (Table 4.4.14). Table 4.4.15 summarises the agreement parameters and refining variables for the 5K neutron refinement of $Ca_4Mn_2TiO_{9.93}$.

Table 4.4.15 Agreement parameters and refining variables for the 5K D2b refinement of $Ca_4Mn_2TiO_{9.93}$:

Agreement parameter	1.59Å D2b histogram	Refining variable	1.59Å D2b histogram
R_{wp} (%)	5.63	Background terms (Shifted Chebyshev)	30
R_p (%)	4.32	Profile Coefficients (pseudo-Voigt)[a]	7
DWd	0.482	Histogram scale factor	1
χ^2_{red} (120 variables)	6.232	Zero point	1

[a] Refining profile coefficients were constrained to be the same for the majority and minority phase, other than 'ptec' which was set to zero for the minority phase.

Table 4.4.16 lists the equivalent bondlengths and bond angles for $Ca_4Mn_2TiO_{9.93}$ at 5K, as were tabulated for the structure 295K.

Table 4.4.16 Selected distances (Å) and angles (°) of $Ca_4Mn_2TiO_{9.93}$ at 5K. The superscripts relate to the oxygens numbered as in Figures 4.4.7 (a) and (b):

Ca(1)–O(7)^{i}	2.538(10)	Ca(2)–O(8)^{i}	2.401(7)	Mn(3)^{a}–O(7)	1.910(5)x2
Ca(1)–O(7)^{ii}	2.807(10)	Ca(2)–O(8)^{ii}	2.926(7)	Mn(3)–O(11)	1.881(8) x2
Ca(1)–O(7)^{iii}	2.348(5)	Ca(2)–O(8)^{iii}	2.816(12)	Mn(3)–O(11)	1.948(7) x2
Ca(1)–O(7)^{iv}	2.964(5)	Ca(2)–O(8)^{iv}	2.521(12)	Mn(5)–O(7)	1.932(8)
Ca(1)–O(9)^{i}	2.619(8)	Ca(2)–O(8)^{v}	2.292(5)	Mn(5)–O(8)	1.906(8)
Ca(1)–O(9)^{ii}	2.408(8)	Ca(2)–O(9)^{i}	2.492(8)	Mn(5)–O(9)	1.882(10)
Ca(1)–O(10)^{i}	3.036(8)	Ca(2)–O(9)^{ii}	2.889(8)	Mn(5)–O(9)	1.914(11)
Ca(1)–O(10)^{ii}	2.607(8)	Ca(2)–O(10)^{i}	2.290(8)	Mn(5)–O(10)	1.961(11)
Ca(1)–O(11)^{i}	2.605(8)	Ca(2)–O(10)^{ii}	2.567(8)	Mn(5)–O(10)	1.851(11)
Ca(1)–O(11)^{ii}	3.108(7)				
Ca(1)–O(11)^{iii}	2.330(8)				
Ca(1)–O(11)^{iv}	2.639(8)				

O(7)–Mn(3)–O(7)	180.000(0)	O(8)–Mn(5)–O(9)	93.8(4)
O(7)–Mn(3)–O(11)	88.63(18)	O(8)–Mn(5)–O(9)	90.2(4)
O(7)–Mn(3)–O(11)	89.98(17)	O(8)–Mn(5)–O(10)	88.0(4)
O(11)–Mn(3)–O(11)	88.72(7)	O(8)–Mn(5)–O(10)	91.4(4)
		O(9)–Mn(5)–O(9)	89.6(4)
O(7)–Mn(5)–O(8)	174.6(7)	O(9)–Mn(5)–O(10)	177.6(5)
O(7)–Mn(5)–O(9)	91.3(4)	O(9)–Mn(5)–O(10)	92.5(5)
O(7)–Mn(5)–O(9)	88.1(4)	O(9)–Mn(5)–O(10)	88.7(5)
O(7)–Mn(5)–O(10)	86.9(4)	O(9)–Mn(5)–O(10)	177.2(6)
O(7)–Mn(5)–O(10)	90.1(4)	O(10)–Mn(5)–O(10)	89.18(35)
Mn(3)–O(11)–Mn(3)	156.83(22)	Mn(5)–O(9)–Mn(5)	158.6(5)
Mn(3)–O(7)–Mn(5)	160.56(32)	Mn(5)–O(10)–Mn(5)	163.7(5)

[a] Although only Mn(3) and Mn(5) cations are listed in Table 4.4.16, Ti(4) and Ti(6) cations share the transition metal sites in the proportions quoted in Table 4.4.13.

Using the parameter $(r_{ax} - r_{eq})/(r_{ax} + r_{eq})$ to quantify distortion, the degree of distortion of both middle and outer octahedra comprising the perovskite block decreases with temperature, only marginally in the case of the outer octahedron, however. The parameter $(r_{ax} - r_{eq})/(r_{ax} + r_{eq})$ takes the value of 0.00118 for the middle octahedron and 0.00445 for the outer octahedron at low temperature.

4.4.2.3 Magnetic measurements

The variation of molar magnetic susceptibility with temperature in $Ca_4Mn_2TiO_{9.93}$ is shown in Figure 4.4.10.

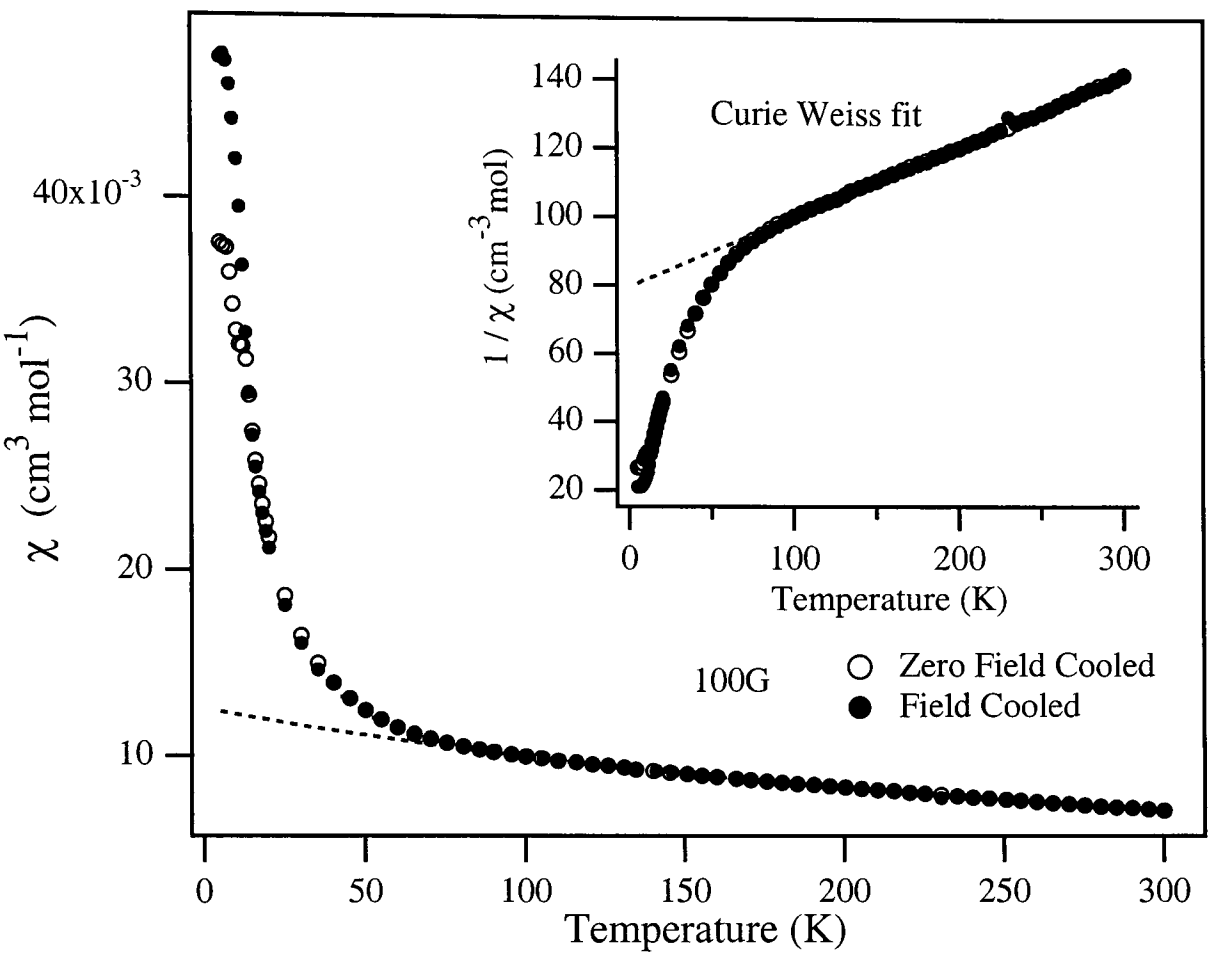
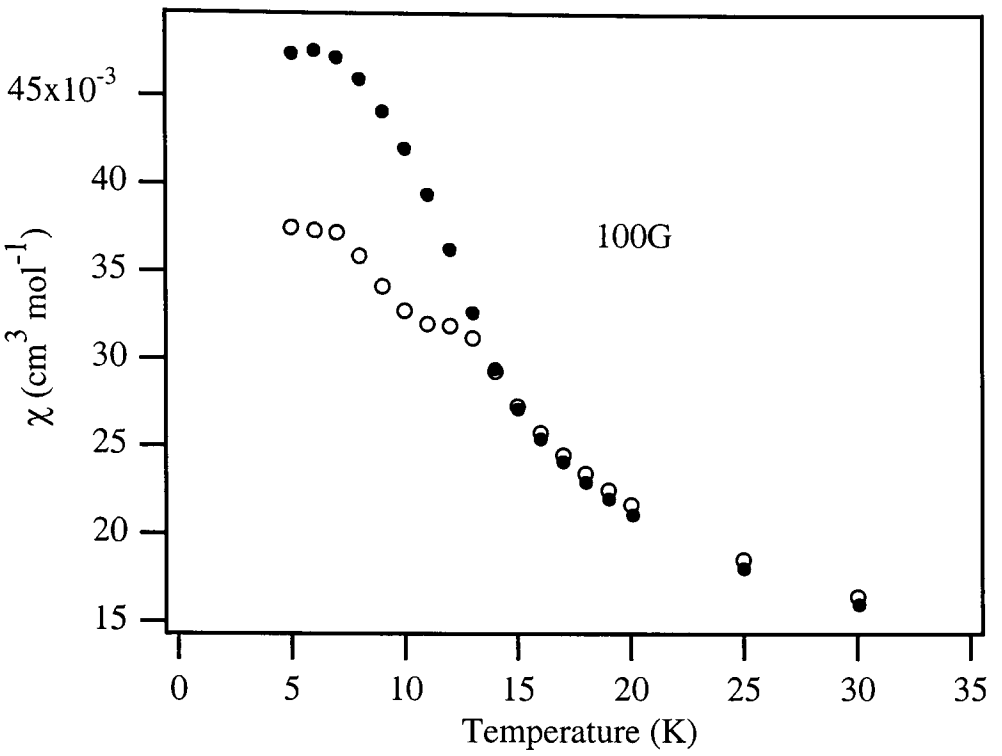


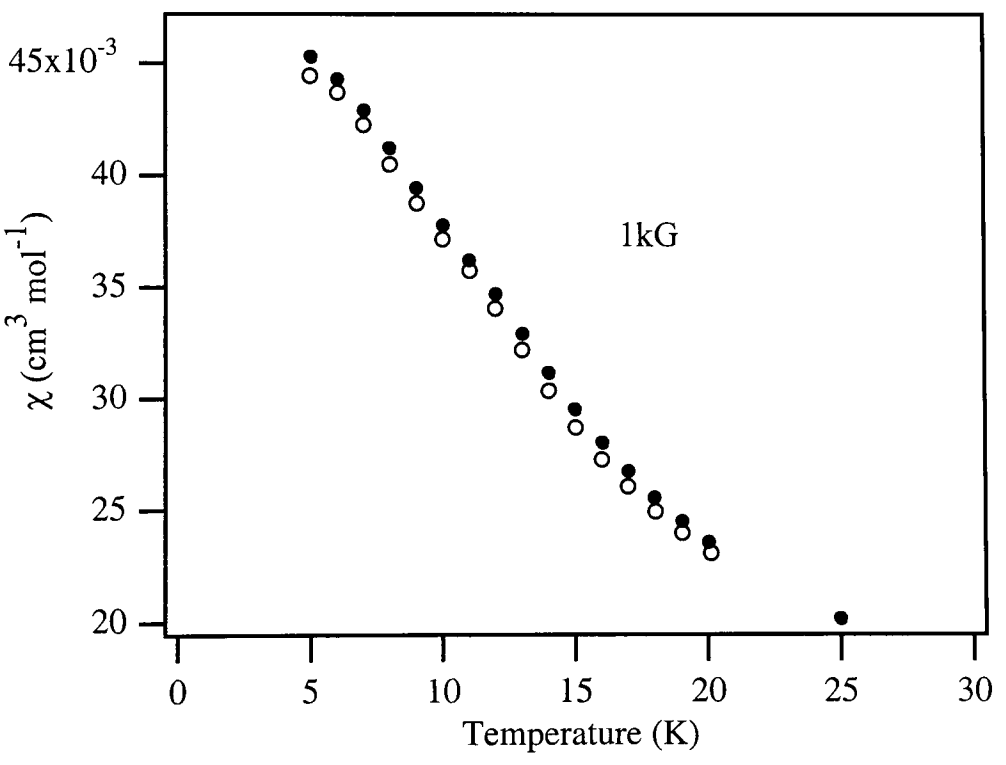
Figure 4.4.10 Molar magnetic susceptibility as a function of temperature for $Ca_4Mn_2TiO_{9.93}$ in a field of 100G, with an inset showing a fit of the high temperature data to the Curie-Weiss law.

The absence of a magnetic transition in the temperature range 100-120K in the data presented in Figure 4.4.10, is highly significant. This is because it indicates that the presence of the Ti^{4+} dopant has disrupted severely the Mn-Mn antiferromagnetic superexchange interactions responsible for the observed G-type magnetic cell in the undoped sample, $Ca_4Mn_3O_{10-\delta}$, which displays a magnetic transition at ~115K. In agreement with the absence of a transition in magnetic susceptibility, the neutron diffraction study of $Ca_4Mn_2TiO_{9.93}$ conducted at 5K confirmed the absence of long range antiferromagnetic order. Unlike that observed in $Ca_4Mn_3O_{10-\delta}$, there is no broad maximum, at about 60K, in the molar susceptibility of $Ca_4Mn_2TiO_{9.93}$ at 100G either, although both ZFC and FC signals do appear to show local maxima at 7-9K, after divergence of the two signals at 13K. The ZFC signal continues to rise after the divergence at 13K. The application of a field of 1kG was

sufficient to remove almost the divergence between ZFC and FC signals observed below 13K at 100G as shown in Figures 4.4.11 (a) and (b).



(a)



(b)

Figures 4.4.11 Low temperature region of molar magnetic susceptibility for $Ca_4Mn_2TiO_{9.93}$ at (a) 100G and (b)1kG.

The Curie-Weiss model, applied to data in the temperature range 245 to 300K, gave the following fit parameters.

Table 4.4.17 Curie-Weiss fit parameters for the 100G data for $Ca_4Mn_2TiO_{9.93}$:

Temperature range (K)	C_m (cm^3 K mol^{-1})	θ(K)	Estimated C_m (cm^3 K mol^{-1})
245 - 300	4.70(6)	-365.0(87)	3.89

The highly negative values of θ(K) suggest antiferromagnetic interactions; however, the molar Curie constant gives an observed magnetic moment significantly larger than that calculated in equation 4.4.1 on the basis of a simple, non-interacting ion model for the magnetism. This is not physically sensible and suggests that interatomic magnetic interactions are significant throughout the entire measured temperature range. The estimated value of C_m of 3.89 (cm^3 K mol^{-1}) is calculated assuming the presence of 1.86 moles of the Mn^{4+}, d^3 cation per mole of $Ca_4Mn_2TiO_{9.93}$ and 0.14 moles of the Mn^{3+}, d^4 cation, using the spin-only moments for these respective cations. This assumes that the Ti cation remains as Ti^{4+}, d^0 and also that there are no A- or B-cation site vacancies.

$$C_m(\text{estimated}) = \frac{1}{8}\left\{0.14(\mu_{eff}Mn^{3+})^2 + 1.86(\mu_{eff}Mn^{4+})^2\right\} \qquad \text{eqn. (4.4.1)}$$

The magnitude of the magnetisation (2.125×10^{-3} μ_B per Mn) at 5K and 500G (the 500G data are not shown due to their similarity with the 1kG data) is almost identical to that observed in $Ca_4Mn_3O_{10-\delta}$ at the same temperature and field.

The field dependence of magnetisation at five temperatures is presented below in Figure 4.4.12. The behaviour at 300K, 100 and 30K is represented by a linear dependence upon field (characteristic of antiferromagnetic or paramagnetic behaviour) with no hysteresis evident. At 10K and 5K, however, there is a small degree of curvature in the variation of magnetisation with field and finite width hysteresis loops are evident, which, interestingly, are symmetrical about the origin.

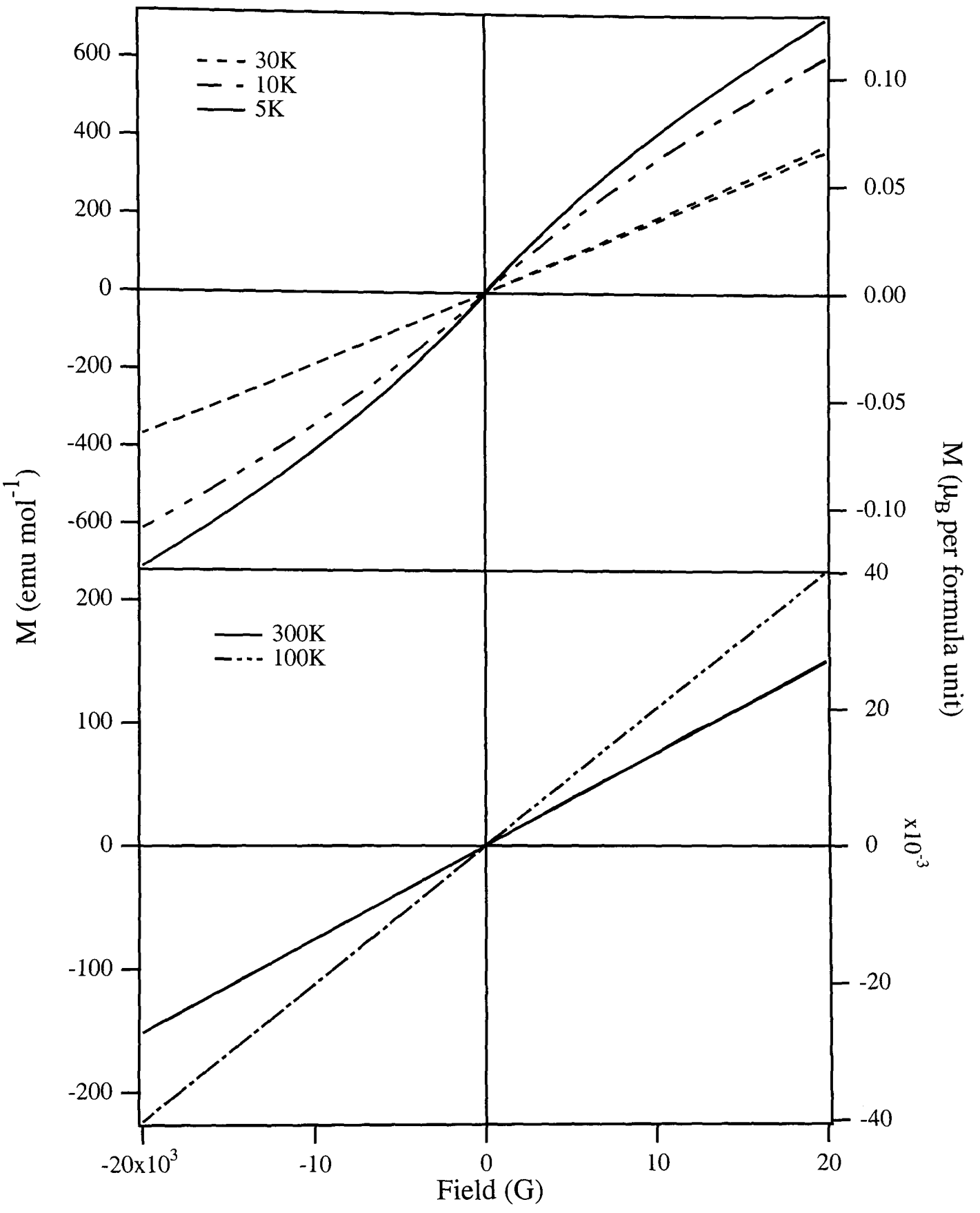


Figure 4.4.12 Field dependence of magnetisation for $Ca_4Mn_2TiO_{9.93}$ between 20 and -20kG, at temperatures of 300, 100, 30, 10 and 5K.

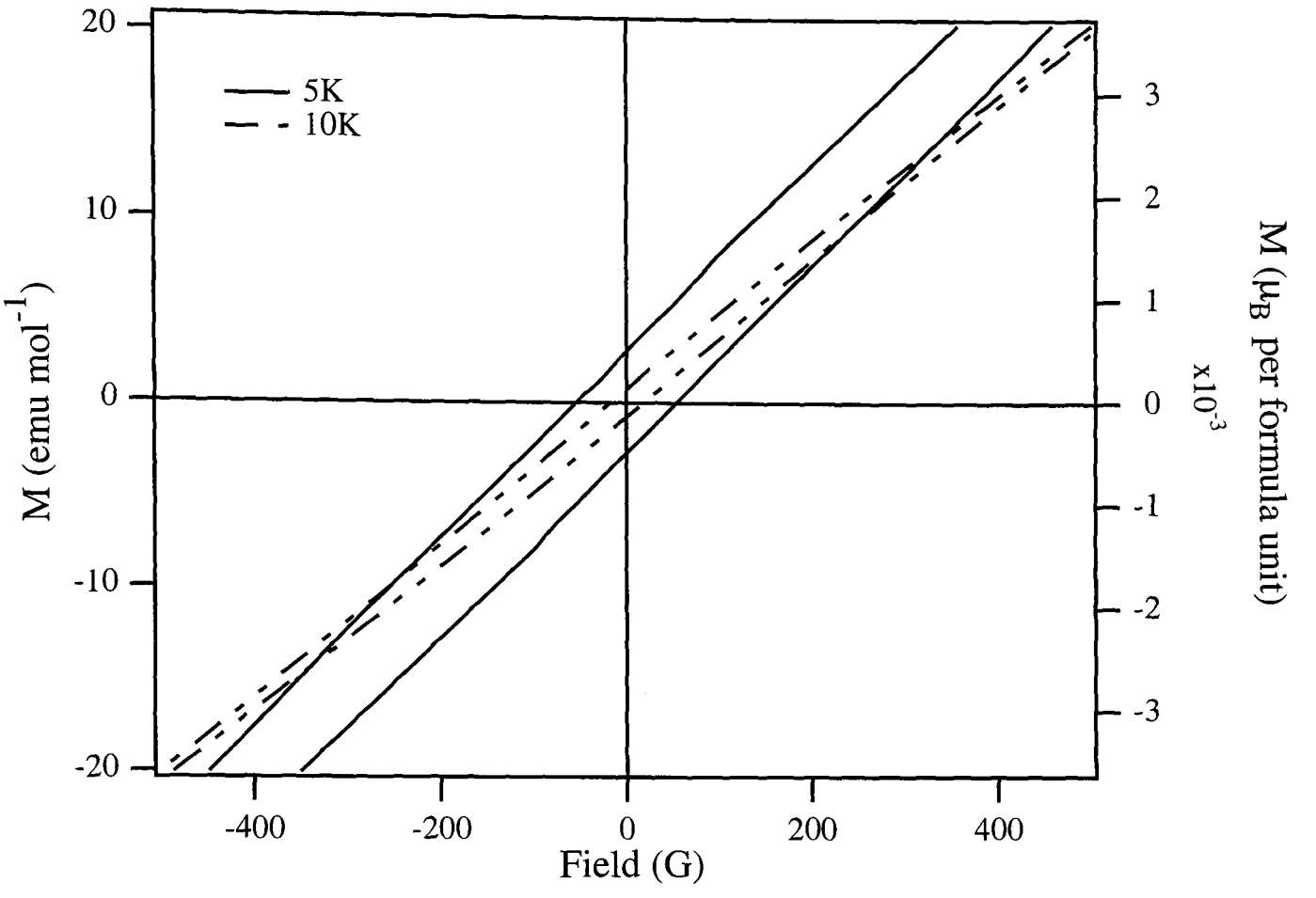


Figure 4.4.13 Enlarged view of the low field (-500≤ Field(G) ≤ 500) region of field dependent magnetisation for $Ca_4Mn_2TiO_{9.93}$, at temperatures of 10 and 5K.

The magnetotransport behaviour of $Ca_4Mn_2TiO_{9.93}$, as a function of field at four different temperatures, is shown in Figure 4.4.14. The temperature dependence of resistivity shown in the inset indicates activated transport. The sample resistance reached an immeasurably high value (~300MΩ) by a temperature of 70K. The magnetotransport data for the undoped sample may be referred to in Figure 4.3.10 in the previous Section, for comparison. Although it is not clear from the inset in Figure 4.3.10, $Ca_4Mn_3O_{10-\delta}$ could only be measured down to ~25K using the apparatus described in Chapter 2.7.

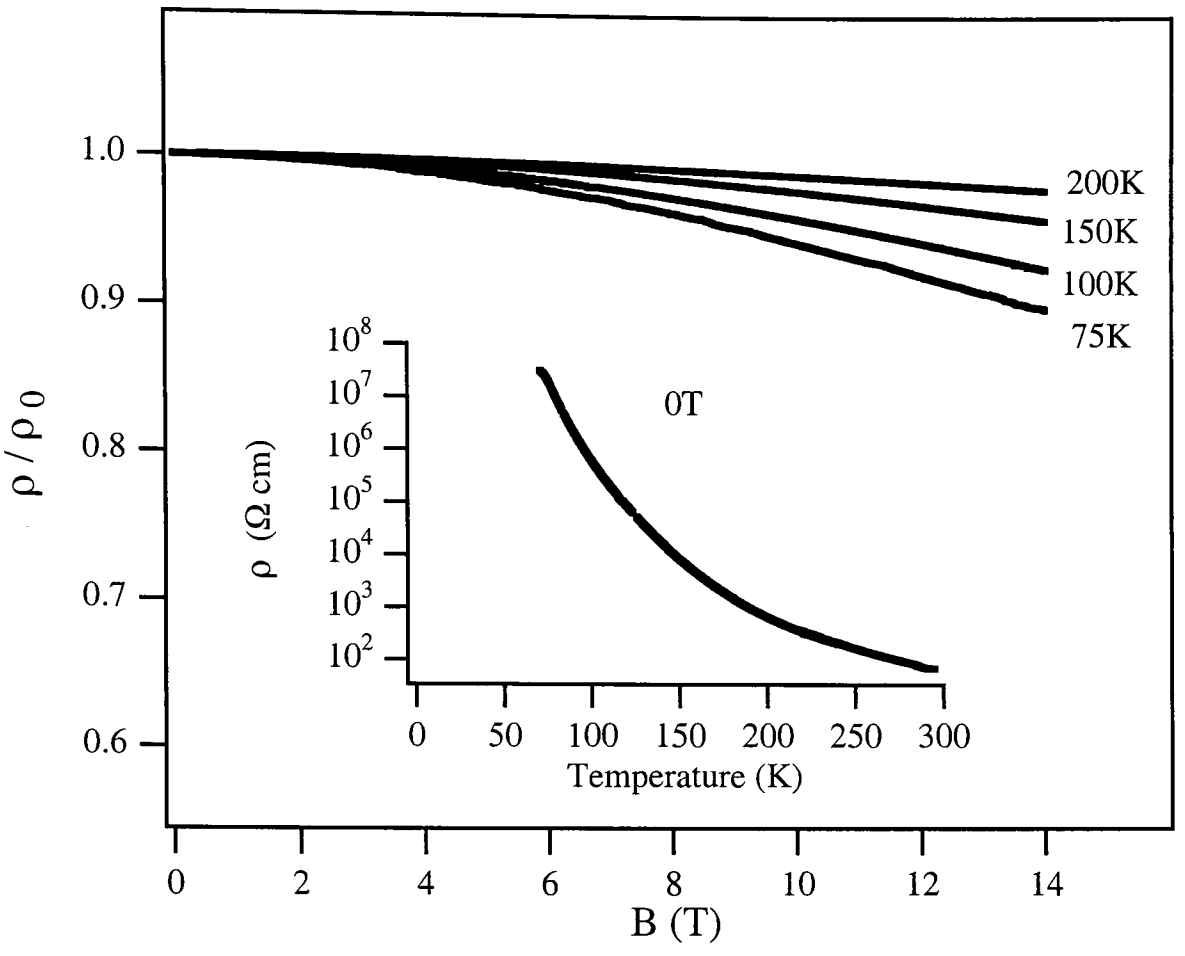
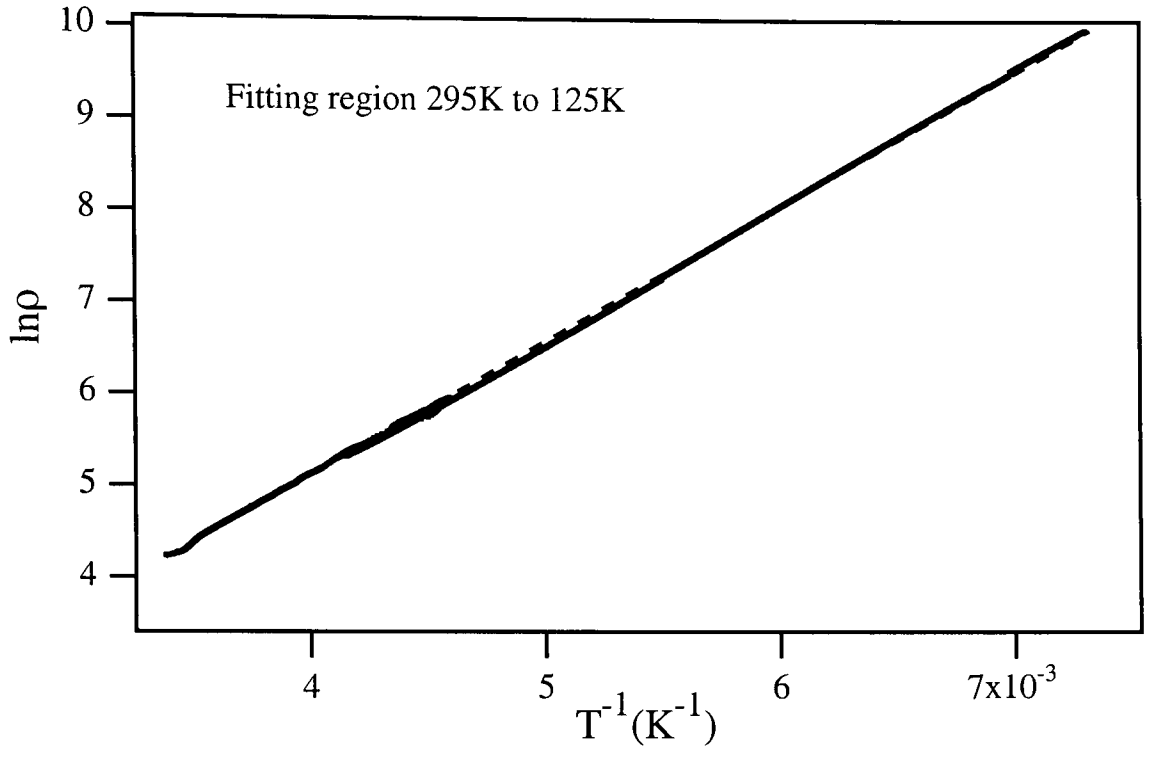


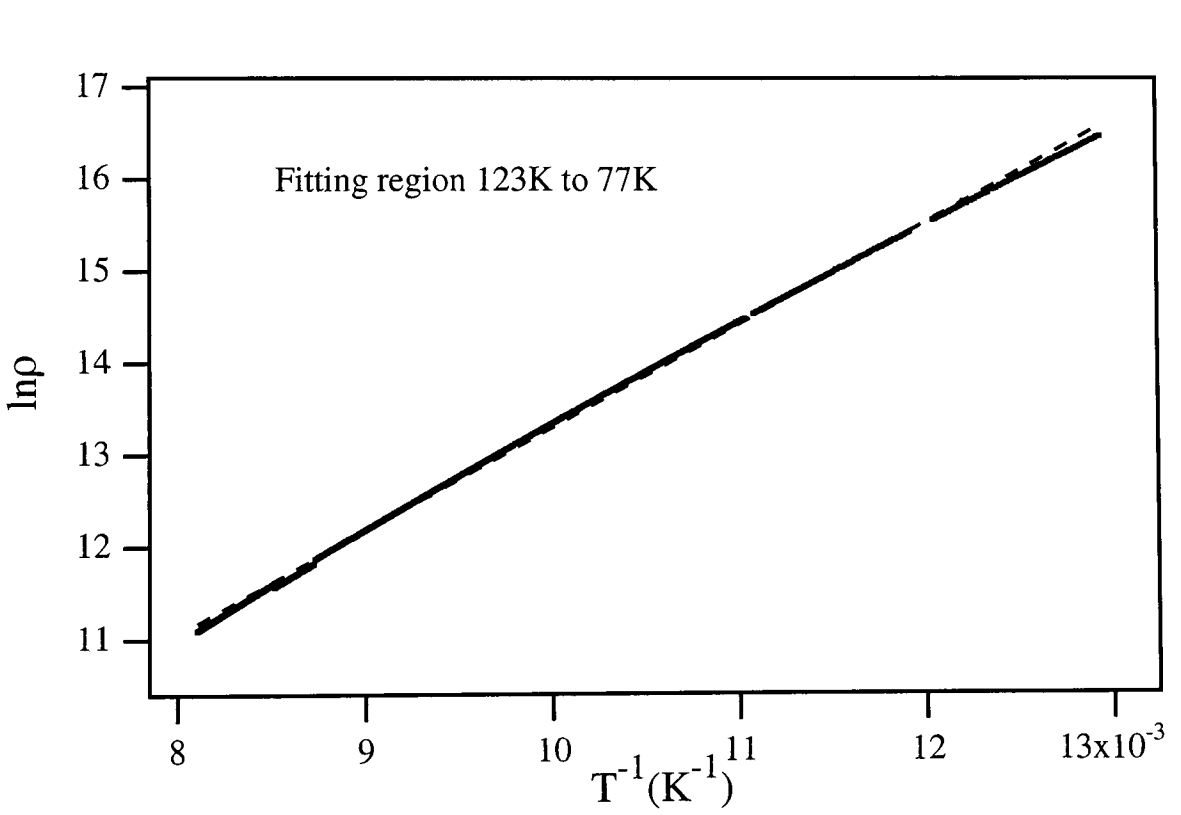
Figure 4.4.14 Field dependence of normalised resistivity ρ(B)/ρ(0) at temperatures of 200, 150, 100 and 75K for $Ca_4Mn_2TiO_{9.93}$. The inset shows the temperature dependence of resistivity at zero field.

The ratio of negative magnetoresistance of both $Ca_4Mn_2TiO_{9.93}$ and $Ca_4Mn_3O_{10-\delta}$ increases with field, and isotherms measured at 60K and above show a similar shape of variation for the doped and undoped samples. Where the isotherms have roughly coinciding temperatures for the doped and undoped samples, (ie. 75K and ~100K) the magnetoresistance is greater for $Ca_4Mn_3O_{10-\delta}$ than for $Ca_4Mn_2TiO_{9.93}$ (for example the signals are reduced to ~75% and ~90% of the zero field values at 75K and 14T for the respective compounds).

It proved possible to model the temperature dependence of resistivity for $Ca_4Mn_2TiO_{9.93}$ between 295 and 125K and 123 and 77K using a thermally activated conduction law (equation 4.3.2), as shown in Figures 4.4.15 (a) and (b):



(a)



(b)

Figure 4.4.15 Fits of resistivity data for $Ca_4Mn_2TiO_{9.93}$ to the $\rho \propto \exp(E_a / k_B T)$ law, (a) between 295 and 125K and (b) between 123 and 77K.

Table 4.4.18 Fit parameters for thermally activated conduction in $Ca_4Mn_2TiO_{9.93}$:

Temperature range (K)	Model used	Parameter[a]
295 to 125	$\rho \propto \exp(E_A / k_B T)$	$E_A = 126.60$meV
123 to 77	$\rho \propto \exp(E_A / k_B T)$	$E_A = 96.21$meV

[a] $1eV = 1.6022X10^{-19}J$

4.4.3 Discussion

The preparation and characterisation of $Ca_4Mn_2TiO_{9.93}$, detailed above, demonstrates that it is possible to substitute one third of the Mn^{4+} cations in $Ca_4Mn_3O_{10-\delta}$ for Ti^{4+} and quantify the degree of ordering of the two cations over distinct octahedral sites using anomalous X-ray scattering.

The successful preparation of the Mn/Ti-containing compound is not surprising considering the stability of the Mn- and Ti-containing analogues; nor is the orthorhombic symmetry surprising, since both $Ca_4Mn_3O_{10-\delta}$ and $Ca_4Ti_3O_{10-\delta}$ have been modelled using the space group *Pbca*. The structural properties of $Ca_4Mn_2TiO_{9.93}$ show many parallels with the undoped sample, $Ca_4Mn_3O_{10-\delta}$; however, the magnetic properties do not. Both $Ca_4Mn_2TiO_{9.93}$ and $Ca_4Mn_3O_{10-\delta}$ provide interesting contrasts to n=3 RP compounds $K_2Nd_2Ti_3O_{10-\delta}$ and $Ca_4Mn_2FeO_{9.75}$, both of which retain the ideal tetragonal symmetry and possess high levels of local, structural disorder.

The anomalous scattering study showed, (through the intensity differences at the 1.89Å SRS wavelength and the subsequent evaluation of $\Delta f'$ for Mn^{4+}), that adequate diffraction contrast could be gained between Mn^{4+} and Ti^{4+} to evaluate their distributions across 4b and 8c octahedral sites. The resulting, preferential occupancy by Ti^{4+} of the 4b site gave it an approximately 40% share of this site as opposed to 30% occupancy of the 8c site. It should be noted that the presence of 0.14 moles of Mn^{3+} present per mole of $Ca_4Mn_2TiO_{9.93}$ (as a result of oxygen non-stoichiometry) and the presence of the $CaMn_{2/3}Ti_{1/3}O_{2.98}$ impurity, each introduce a small error into the anomalous dispersion analysis, although the degree of error is difficult to quantify. Table 4.4.19 summarises the differences in Mn^{4+} : B^{4+} cation distributions over the two distinct octahedral sites in B-site substituted phases, $Ca_4Mn_2BO_{10-\delta}$ where B = Ti^{4+} and Fe^{4+}.

Table 4.4.19 Comparison between Ti and Fe distributions in $Ca_4Mn_2BO_{10-\delta}$:

B-cation	Mn^{4+} : B^{4+} distribution across site 4b	Mn^{4+} : B^{4+} distribution across site 8c
Ti^{4+}	59.8(2.6) : 40.2(2.6)	70.1(1.3) : 29.9(1.3)
Fe^{4+}	42.4 : 57.6(4)	78.8 : 21.2(2)

As well as increasing the mean B-cation-O bondlengths relative to the values observed in $Ca_4Mn_3O_{10-\delta}$, the presence of the d^0 Ti^{4+} cation introduces the possibility of increased distortion of octahedra due to the tendencies for d^0 and d^{10} cations to displace from the centre of their coordination spheres[46]. Although displacement effects as distinct as those displayed in $K_2Nd_2Ti_3O_{10-\delta}$ and $Ca_4Ti_3O_{10-\delta}$ were not reproduced in $Ca_4Mn_2TiO_{9.93}$, due only to partial occupancy of octahedra by Ti^{4+}, the effect may have contributed to the relative lengths of apical Mn(5)-O(7) and Mn(5)-O(8) bonds. In $K_2Nd_2Ti_3O_{10-\delta}$, the local distortion of the outer TiO_6 octahedron resulted in a Ti-O bondlength directed into the rocksalt layer of 1.734Å as opposed to the bondlength of 2.291Å directed into the perovskite block. The equivalent bondlengths in $Ca_4Mn_2TiO_{9.93}$ are 1.901(3)Å for the apical bond directed into the rocksalt layer and 1.940(3)Å for the bond directed into the perovskite block. Although, clearly, the effect is not as marked, this variation in apical bondlengths is twice that observed in $Ca_4Mn_3O_{10-\delta}$ where no d^0 cation is present. The effect is even more interesting due to the likely occupancy of the outer octahedra in $Ca_4Mn_2TiO_{9.93}$ by the 0.14 moles of Mn^{3+} present per mole of $Ca_4Mn_2TiO_{9.93}$. These d^4 Jahn-Teller cations are likely to show the reverse tendency of lengthening and shortening the Mn(5)-O(8) and Mn(5)-O(7) bonds, respectively, according to previous studies[2,31].

$Ca_4Mn_3O_{10-\delta}$ and $Ca_4Mn_2TiO_{9.93}$ show many structural similarities; however, both compounds provide an interesting structural contrast to the tetragonal compounds $K_2Nd_2Ti_3O_{10-\delta}$ and $Ca_4Mn_2FeO_{9.75}$, from which a pattern begins to emerge regarding the mechanisms available to satisfy the 9 and 12 fold coordination requirements of small Ca (or K and Nd) A-site cations. In $Ca_4Mn_3O_{10-\delta}$ and $Ca_4Mn_2TiO_{9.93}$, the cooperative tilting of octahedra and the concomitant reduction of the ideal tetragonal symmetry provides the necessary oxygen coordination spheres around Ca. In $Ca_4Mn_2FeO_{9.75}$, it was argued[31] that the aperiodic strain present as a result of the Jahn-Teller Fe^{4+} t_{2g}^3 e_g^1 cations on the outer octahedra, plus that due to the disordered arrangement of Mn and Fe cations, were sufficient to induce significant displacive disorder on the oxygen sublattice. This local displacive disorder, producing effectively a rotation of BO_6 octahedra, was sufficient to provide the correct distribution of oxygen anions around both Ca sites. In $Ca_4Mn_2TiO_{9.93}$, it appears

that, although the cation disorder (due to the lower preference of Ti^{4+} for one octahedral site over another) is greater than in the Fe compound, the absence of a significant proportion of Jahn-Teller cations favours the concerted transition to orthorhombic symmetry. The enhanced displacements at the O(9) and O(10) sites in $Ca_4Mn_2TiO_{9.93}$ as shown in Figure 4.4.4, appears to be related to the presence of oxide vacancies and the presence of Mn^{3+} cations on the adjacent transition metal site. On the grounds of Ti^{4+} and Mn^{4+} cation disorder alone, the O(11) site would be expected to show slightly greater static disorder.

The importance of local disorder on the oxygen sublattice for a compound adopting tetragonal symmetry (as shown in $Ca_4Mn_2FeO_{9.75}$) was emphasised also in the study of $K_2Nd_2Ti_3O_{10-\delta}$ by Amow et al.[45]. Assuming statistical distribution over 9 and 12 coordinate A-cation sites in this compound, the mean, weighted A-site cation radius is 1.41Å compared to the value for Ca of 1.26Å; therefore, the requirement for tilting of octahedra may not be as great to meet the coordination needs of the A-site cations. However, it was concluded in this study that octahedral tilting appeared to be disordered or incoherent in nature, as suggested by the strongly anisotropic oxygen atom displacement parameters. Local octahedral distortions due to the displacements of Ti away from the centre of their coordination spheres were reported also. In $Ca_4Ti_3O_{10-\delta}$, although the tendency for Ti displacements to cause local distortions of octahedra is present, the absence of Jahn-Teller cations and lack of a disordered cation array on the B-sites appears to favour the concerted orthorhombic distortion, over local distortions.

Although it is possible to rationalise the factors governing the structural relationships between $Ca_4Mn_2TiO_{9.93}$, $Ca_4Mn_2FeO_{9.75}$ and $Ca_4Mn_3O_{10-\delta}$, the mixed Mn/Ti compound appears to differ from the undoped and Fe doped materials in terms of its magnetic properties. Both $Ca_4Mn_2FeO_{9.75}$ and $Ca_4Mn_3O_{10-\delta}$ showed G-type antiferromagnetic order within the triple layer of octahedra comprising the perovskite block (although for the Fe compound the central layer of manganese-poor octahedra remained magnetically disordered). In contrast, the absence of well defined magnetic Bragg peaks in the 5K D2b diffraction pattern shows that such long range antiferromagnetic order is not present in the

$Ca_4Mn_2TiO_{9.93}$ compound. However, the diffuse scattering observed does suggest that there are regions of correlated spins.

It is instructive to review the magnetic exchange interactions present in each of the compounds, $Ca_4Mn_2TiO_{9.93}$, $Ca_4Mn_2FeO_{9.75}$ and $Ca_4Mn_3O_{10-\delta}$, in order to rationalise the differences in magnetic behaviour. The observation of insulating, rather than metallic, behaviour in each of the three compounds precludes any significant contribution from double exchange. $Ca_4Mn_3O_{10-\delta}$ was shown to undergo a transition to an antiferromagnetic state at ~115K, with concomitant spontaneous magnetisation developing as a result of the DM mechanism[14,15]. This explained the dramatic rise in the susceptibility observed at 115K, although the magnitude of the spontaneous magnetisation was measured at just $2x10^{-3}$ μ_B per Mn at 5K and 500G. In this compound the antiferromagnetic t_{2g} - t_{2g} π interactions are dominant between Mn^{4+} cations with a d^3 configuration. The DM mechanism is operative since the tilting of octahedra removes the centre of inversion at oxygen sites, producing neighbouring spins which are no longer collinear and allowing a non-zero antisymmetric coupling term to exist. The resulting canting of antiferromagnetically aligned sublattices within the G-type structure relative to each other produces the weak ferromagnetism.

In $Ca_4Mn_2FeO_{9.75}$, in addition to the antiferromagnetic t_{2g} - t_{2g} π interactions between Mn^{4+} cations, there was the potential for competing, ferromagnetic superexchange interactions between a half-occupied e_g orbital on Fe^{4+} (or the small amount of Fe^{3+} present) with the empty e_g orbital on Mn^{4+}. The retention of the ideal tetragonal symmetry for this compound removed the potential for weak ferromagnetism through the DM interaction. The Fe^{4+}/Fe^{3+} distributions in this compound were shown to be influential with regard to which of the competing magnetic interactions predominated. No ordered moment was observed on the (Fe rich) B-cation sites comprising the central layer of octahedra in the perovskite block, suggesting that the net interaction between a Mn^{4+} d^3 cation and a Fe^{4+} d^4 cation was negligible. However, with Fe^{n+} comprising just 25% of B-cations in the outer octahedra of the perovskite block, it was possible for the antiferromagnetic t_{2g} - t_{2g} π interactions between Mn^{4+} cations to predominate and G-type antiferromagnetic ordering was observed in these layers.

With these observations in mind, the competing interactions likely for a Mn^{4+} cation array (containing 0.14 mols of Mn^{3+} per mole of $Ca_4Mn_2TiO_{9.93}$) interspersed with diamagnetic Ti^{4+}, d^0 cations, can be evaluated. The potential for weak ferromagnetism is possible theoretically, due to the symmetry of the structure, and indeed Lago et al.[28] suggested that weak FM was associated with the short range bilayer correlations above T_N in $Ca_4Mn_3O_{10-\delta}$. Neutron diffraction studies on $Ca_4Mn_2TiO_{9.93}$ revealed only short range correlations to be present in this sample. Considering the competing superexchange interactions, the antiferromagnetic Mn^{4+} t_{2g}^3 - O^{2-} - Mn^{4+} t_{2g}^3 π interactions between the numerous Mn^{4+} d^3 cations are expected to dominate, albeit regularly interspersed with Ti^{4+}, d^0 cations. Ferromagnetic Mn^{3+} t_{2g}^3 e_g^1 - O^{2-} - Mn^{4+} t_{2g}^3 σ superexchange interactions are also present as a result of oxygen non-stoichiometry. Interestingly, the 'dilution' of the antiferromagnetic t_{2g} - t_{2g} π interactions between the numerous Mn^{4+} d^3 cations is exacerbated by the lower degree of preferential occupation of one particular transition metal site over the other by Ti^{4+}. For example, such was the site preference of the Fe cations for the central layer of octahedra (as shown in Table 4.4.19), that their low occurrence on the outer octahedra permitted a solid solution of 80% manganese occupation to preserve a magnetically ordered backbone. The absence of long range antiferromagnetic order in $Ca_4Mn_2TiO_{9.93}$ would suggest that just 60% and 70% occupancy by Mn^{n+} in the central and outer octahedra respectively, is, however, insufficient to preserve similar magnetic order. The percolation limit for a primitive cubic lattice (in which a cation such as Mn^{n+} has a maximum possible of six magnetic neighbours) as is the case here, has been calculated[48,49] at 30.7%, hence Mn^{4+} cation concentrations of 60% and 70% in both middle and outer octahedra are above this limit. A comparison between $Ca_4Mn_2FeO_{9.75}$ and $Ca_4Mn_2TiO_{9.93}$, purely on the grounds of percolation limit, fails to take into consideration the effects on Mn^{4+} t_{2g}^3 - O^{2-} - Mn^{4+} t_{2g}^3 superexchange interactions resulting from the orthorhombic distortion in the latter compound. Rather than long range antiferromagnetic order, short range antiferromagnetic correlations exist in $Ca_4Mn_2TiO_{9.93}$, accounting for the nature of the Curie-Weiss parameters in the high temperature region fit to susceptibility data, and the observation of diffuse scattering in the 5K neutron diffraction pattern.

The low temperature SQUID magnetometry data, (in particular the magnetisation isotherms at 5 and 10K) are informative. Unlike the case of the Fe compound, it appears that uncoupled magnetic moments do not freeze in a spin glass transition at low temperature (explaining the lack of a finite width hysteresis loop that is displaced from the origin at either 5 or 10K). This is consistent with a lower degree of magnetic frustration in the mixed Mn/Ti compound due to the diamagnetic character of Ti^{4+} and the lower concentration of d^4 cations which introduce competing ferromagnetic interactions. However, there is still divergence between the ZFC and FC susceptibility curves at 100G (although this is almost eliminated by application of a field of 500G or higher). This, together with the observations of a magnetisation per Mn cation at 5K and 500G that is comparable to the value observed in $Ca_4Mn_3O_{10-\delta}$, and the hysteresis observed in the 5 and 10K magnetisation isotherms, require explanation.

In trying to predict the effect of tetravalent dopants such as Ti^{4+} on Mn exchange interactions, a study by Raveau et al.[37] gives a useful insight. Their study observed the effect of tetravalent dopants (including Ti^{4+}) on the Mn exchange interactions in $Pr_{0.5}Sr_{0.5}MnO_3$, where the mean Mn oxidation state was +3.5. It was found for phases $Pr_{0.5}Sr_{0.5}Mn_{1-x}Ti_xO_3$ that increasing x destroyed the antiferromagnetic ordering at the benefit of the ferromagnetic state. This is to be expected perhaps, where there is a significant proportion (50%) of Mn^{3+} as in this study. In our compound there is just ~0.07% per outer octahedron (assuming all Mn^{3+} is confined to the octahedral site exhibiting oxygen deficiency) and it is therefore unlikely that this could produce the features in the magnetisation mentioned above, even when the antiferromagnetic Mn^{4+} t_{2g}^3 - O^{2-} - Mn^{4+} t_{2g}^3 interactions have been diluted by the presence of Ti^{4+}.

It is more likely that either weak ferromagnetism is induced by the DM mechanism as in $Ca_4Mn_3O_{10-\delta}$, or that small antiferromagnetic domains (characteristic of a compound such as $Ca_4Mn_2TiO_{9.93}$ where the superexchange interactions are 'diluted' by the presence of a non-magnetic dopant cation) contain uncompensated magnetic moments at their surfaces which are responsible for the hysteresis observed at 5 and 10K. These uncompensated moments will be more numerous, the smaller the sizes of the antiferromagnetic domains. The

irreversibility of magnetic behaviour may be evidence, alternatively, for the blocking of clusters of spins below a temperature of ~13K. The compound would benefit from more extensive magnetometry measurements, both DC and AC, in order to establish the true nature of the magnetic ground state. It has been assumed throughout the discussion of the magnetic interactions present in $Ca_4Mn_2TiO_{9.93}$ that the $CaMn_{2/3}Ti_{1/3}O_{2.98}$ impurity (or the possible presence of n=2 intergrown material) do not contribute.

The magnetotransport behaviour of the Ti-doped phase shows evidence of insulating behaviour characteristic of a material dominated by (albeit short range) magnetic interactions and localised electrons. Table 4.4.20 summarises the activation energies extracted from fitting the temperature dependence of resistivity for the undoped, Ti doped and Fe doped samples, to a thermally activated conduction law:

Table 4.4.20 Fitting parameters for thermally activated conduction in n = 3 RP phases:

Compound	Model	Temperature range (K)	E_A (meV)[a]
$Ca_4Mn_3O_{10-\delta}$	$\rho \propto \exp(E_A / k_BT)$	300-200	42.12
$Ca_4Mn_2FeO_{9.75}$	$\rho \propto \exp(E_A / k_BT)$	285-200	210
$Ca_4Mn_2FeO_{9.75}$	$\rho \propto \exp(E_A / k_BT)$	200-130	150
$Ca_4Mn_2TiO_{9.93}$	$\rho \propto \exp(E_A / k_BT)$	295-125	126.60
$Ca_4Mn_2TiO_{9.93}$	$\rho \propto \exp(E_A / k_BT)$	123-77	96.21

[a] $1eV = 1.6022X10^{-19}J$

The value of E_A of 126.60meV in the 295-125K temperature range for $Ca_4Mn_2TiO_{9.93}$ is more typical of an activation energy reported for a n = 2, rather than a n = 3, layered manganite[30]. This gives some idea of the narrowing of the bandwidth which occurs on introducing the Ti (or Fe) dopant into the Mn-O network. The introduction of energy fluctuations due to randomness introduced by the chemical substitution is one means of carrier localisation. In addition, the presence of Jahn-Teller cations, Mn^{3+} in each of the $Ca_4Mn_2FeO_{9.75}$ and $Ca_4Mn_2TiO_{9.93}$ phases provides a further source of electron localisation through electron-phonon coupling. Unlike A-site cation substitution, chemical substitution on the B-cation site in this instance does not compensate the effects of disorder with the introduction of mixed-valent Mn cations.

The lower ratios of negative magnetoresistance exhibited on Ti and Fe doping relative to the $Ca_4Mn_3O_{10-\delta}$ sample supports the observation that these particular dopants, (at the 2:1 doping level) disrupt the 3-D antiferromagnetic order, and hence the weak ferromagnetic state arising from the DM mechanism, which is expected to favour higher ratios of magnetoresistance.

4.5 References

[1] JB MacChesney, HJ Williams, JF Potter, RC Sherwood *Phys. Rev.* **1967**, *164*, 779.

[2] PD Battle, MA Green, J Lago, JE Millburn, MJ Rosseinsky, JF Vente *Chem. Mater.* **1998**, *10*, 658.

[3] AI Mihut, LE Spring, RI Bewley, SJ Blundell, W Hayes, T Jestadt, BW Lovett, R McDonald, FL Pratt, J Singleton, PD Battle, J Lago, MJ Rosseinsky, JF Vente *J. Phys. Condens. Matter* **1998**, *10*, L727.

[4] MM Elcombe, EH Kisi, KD Hawkins, TJ White, P Goodman, S Matheson *Acta Crystallogr., Sect. B* **1991**, *B47*, 305.

[5] RE Schmidt, J Pebler, D Babel *Eur. J. Solid State Inorg. Chem.* **1992**, *29*, 679.

[6] J Fábry, J Hybler, Z Jirak, K Jurek, K Maly, M Nevriva, V Petricek *J. Solid State Chem.* **1988**, *73*, 520.

[7] HJ Rossell, P Goodman, S Bulcock, RH March, SJ Kennedy, TJ White, FJ Lincoln, KS Murray *Aust. J. Chem.* **1996**, *49*, 205.

[8] Y Takeda, F Kanamaru, M Shimada, M Koizumi *Acta Crystallogr., Sect. B* **1976**, *B32*, 2464.

[9] L Katz, R Ward *Inorganic Chemistry* **1964**, *3*, 205.

[10] H Blattner, H Granicher, W Kanzig, W Merz *Helv. Phys. Acta* **1948**, *21*, 341.

[11] JJ Lander *Acta Cryst.* **1951**, *4*, 148.

[12] R Fischer, E Tillmanns *Z. Kristallogr.* **1981**, *157*, 69.

[13] EJ Cussen, JF Vente, PD Battle *J. Am. Chem. Soc.* **1999**, *121*, 3958.

[14] I Dzyaloshinsky *J. Phys. Chem. Solids* **1958**, *4*, 241.

[15] T Moriya *Phys. Rev.* **1960**, *120*, 91.

[16] PD Battle, TC Gibb, CW Jones *J. Solid State Chem.* **1988**, *74*, 60.

[17] NS Witte, P Goodman, FJ Lincoln, RH March, SJ Kennedy *Appl. Phys. Lett.* **1998**, *72*, 853.

[18] H Asano, J Hayakawa, M Matsui *Phys. Rev. B* **1997**, *56*, 5395.

[19] H Asano, J Hayakawa, M Matsui *Phys. Rev. B* **1998**, *57*, 1052.

[20] MP Pechini **1967**, US Patent No. 3 330 697.

[21] MR De Guire, WB Philipp *J. Mater. Chem.* **1993**, *3*, 571.

[22] A Douy, P Odier *Mater. Res. Bull.* **1989**, *24*, 1119.

[23] C Marcilly, P Courty, B Delmon *J. Amer. Ceram. Soc.* **1970**, *53*, 56.

[24] PD Battle, MA Green, J Lago, JE Millburn, MJ Rosseinsky, JF Vente *Chem. Mater.* **1998**, *10*, 658.

[25] PD Battle, MA Green, NS Laskey, JE Millburn, LE Murphy, MJ Rosseinsky, SP Sullivan, JF Vente *Chem. Mater.* **1997**, *9*, 552.

[26] ID Fawcett, JEIV Sunstrom, M Greenblatt, M Croft, KV Ramanujachary *Chem. Mater.* **1998**, *10*, 3643.

[27] NF Mott, EA Davis *Electronic Processes in Noncrystalline Materials (The Internation Series of Monographs on Physics)*, **1971**.

[28] J Lago, PD Battle, MJ Rosseinsky *J. Phys. Condens. Matter, submitted for publication* **1999**.

[29] A Maignan, C Martin, F Damay, B Raveau *Phys. Rev. B* **1998**, *58*, 2758.

[30] AI Coldea, LE Spring, SJ Blundell, J Singleton, W Hayes *J. Phys. Condens. Matter* **1999**, *11*, 9053.

[31] PD Battle, WR Branford, A Mihut, MJ Rosseinsky, J Singleton, J Sloan, LE Spring, JF Vente *Chem. Mater.* **1999**, *11*, 674.

[32] W Branford *Part II Thesis*, Oxford University, **1998**.

[33] JY Lee, JS Swinnea, H Steinfink, WM Reiff, S Pei, JD Jorgensen *J. Solid State Chem.* **1993**, *103*, 1.

[34] WM Reiff, JY Lee, H Steinfink *Z. Anorg. Allg. Chem.* **1992**, *616*, 172.

[35] B Shankar, H Steinfink *J. Solid State Chem.* **1996**, *122*, 390.

[36] B Raveau, C Martin, A Maignan *J. Alloys Compd.* **1998**, *275-277*, 461.

[37] A Maignan, C Martin, B Raveau *Z. Phys. B* **1997**, *102*, 19.

[38] SN Ruddlesden, P Popper *Acta Cryst.* **1957**, *10*, 538.

[39] SN Ruddlesden, P Popper *Acta Cryst.* **1958**, *11*, 54.

[40] DT Cromer *Acta Cryst.* **1965**, *18*, 17.

[41] AC Larson, RB von Dreele **1990**.

[42] Y Murakami, H Kawada, H Kawata, M Tanaka, T Arima, Y Moritomo, Y Tokura *Phys. Rev. Lett.* **1998**, *80*, 1932.

[43] K Kuroda, N Ishizawa, N Mizutani, M Kato *J. Solid State Chem.* **1981**, *38*, 297.

[44] KR Poeppelmeier, ME Leonowicz, JC Scanlon, WB Yelon, JM Longo *J. Solid State Chem.* **1982**, *45*, 71.

[45] G Amow, JE Greedan *Acta Crystallogr., Sect. C.* **1998**, *C54*, 1053.

[46] NSP Bhuvanesh, J Gopalakrishnan *J. Mater. Chem.* **1997**, *7*, 2297.

[47] RD Shannon, CT Prewitt *Acta Cryst. A* **1976**, *32*, 785.

[48] HL Frisch, JM Hammersley, DJA Welsh *Phys. Rev.* **1962**, *126*, 949.

[49] MF Sykes, JW Essam *Phys. Rev.* **1964**, *133*, A310.

CHAPTER 5

$n=\infty$ in $A_{n+1}B_nO_{3n+1}$

ABO_3 ($A_2BB'O_6$)

5.1 Introduction

A brief discussion of some electronic properties of stoichiometric $LaMnO_3$ was given in Chapter 1. The current chapter is concerned with B-site substituted derivatives of the 'parent' compounds $LaMnO_3$ and $NdMnO_3$. As such it focusses on the $n = \infty$ or 'infinite layer' end members of the RP series $A_{n+1}B_nO_{3n+1}$. In compounds $La_2GaMnO_{6+\delta}$ and $Nd_2GaMnO_{6+\delta}$, diamagnetic Ga^{3+} [Ar] $3d^{10}$ cations replace one half of Mn^{3+} [Ar] $3d^4$ cations on the B-cation site in the parent compounds. The majority of recent studies involving B-cation substitution of Mn by Al[1], In[2] and Ga[3,4] have tended to focus on hole doped phases, $Ln_{1-x}A_xMn_{1-x}B_xO_3$, (where A is an alkaline earth cation and B is the Al, In, or Ga substituent), rather than Mn^{3+}, $3d^4$ materials.

The 'parent' compound $LaMnO_3$, both in stoichiometric and nonstoichiometric forms, has been studied extensively in recent years. Tofield and Scott[5] were the first to differentiate $LaMnO_{3+\delta}$ from other lanthanum transition metal perovskites, noting its tendency towards nonstoichiometry. Van Roosmalen and Cordfunke[6] established that the oxygen excess in $LaMnO_{3+\delta}$ manifests itself in reality, as *equivalent* amounts of *cation*, La and Mn vacancies in an 'as prepared' sample, (suggesting $LaMnO_{3+\delta}$ should be formulated more accurately as $La_{3/(3+\delta)}Mn_{3/(3+\delta)}O_3$). Generally, however, nonstiochiometric $LaMnO_3$ is denoted as $LaMnO_{3+\delta}$ in the literature, with the percentage of Mn^{4+} cations given by $2 \times 100\delta$. Studies by van Roosmalen et al.[7], Arulraj et al.[8] and Töpfer et al.[9] among others, have provided much information, structural and magnetic, on a range of defect compositions. These have encompassed several different ratios of La : Mn vacancies, both greater and less than unity. Ritter et al.[10] carried out a systematic study recently into the effect of Mn^{4+} in $LaMnO_{3+\delta}$ for $\delta \leq 0.15$ (compounds contained an equal number of La and Mn vacancies). The study illustrated the continuous change from a highly distorted orthorhombic structure, towards *quasicubic* and then to a rhombohedral structure, which takes place across the series as δ (and therefore the Mn^{4+} concentration) is increased, and confirmed results of earlier studies. As reported by Töpfer et al.[9], the rhombohedral symmetry, stable at room temperature for relatively high values of δ (they report $0.10 \leq \delta \leq 0.16$), suppresses a static, cooperative Jahn-Teller (JT) distortion, since the e_g orbitals are necessarily degenerate in this symmetry.

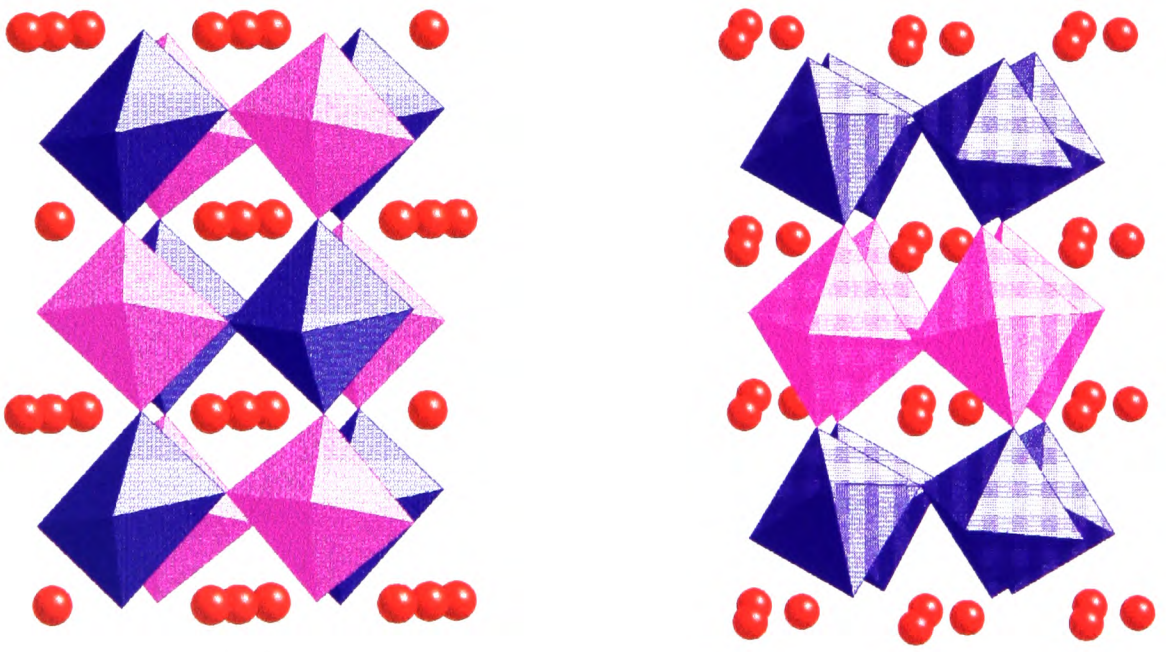
As mentioned in Chapter 1, stoichiometric $LaMnO_3$ adopts the O' orthorhombic structure (for which $\frac{b}{c} < \sqrt{2}$, in the space group *Pnma*), which is characterised by a cooperative, static Jahn-Teller distortion. The effects of orbital ordering on superexchange interactions in $LaMnO_3$ have been considered by several authors[11-14], and the nature of the approximations employed, regarding Hubbard repulsion terms and charge transfer energy, has been reviewed by Millis[15]. The results of Solovyev et al.[16] on $LaMnO_3$ are highly informative, and describe how the ordering of $d_{3x^2-r^2}$, $d_{y^2-z^2}$, $d_{3y^2-r^2}$ and $d_{x^2-z^2}$ orbitals (which are linear combinations of the JT split $d_{3z^2-r^2}$ and $d_{x^2-y^2}$ states), results in highly anisotropic Mn^{3+} t_{2g}^3 e_g^1 - O^{2-} - Mn^{3+} t_{2g}^3 e_g^1 superexchange interactions, consisting of ferromagnetic coupling within (010) planes and antiferromagnetic inter-plane coupling.

Thus, it was expected that the magnetism in $La_2GaMnO_{6+\delta}$ would depend upon how Ga^{3+} modified these anisotropic interactions and hence, on how it modified the nature and extent of the JT distortion. This in turn would depend upon its distribution in the Mn^{3+} cation array and whether any Mn^{4+} cations were present. The distribution of Ga^{3+} and Mn^{3+} could be monitored using neutron diffraction to quantify the degree of Ga^{3+} : Mn^{3+} cation ordering and test whether the O' - orthorhombic structure (of $LaMnO_3$) remained intact after the introduction of Ga^{3+}. By focussing on materials containing (nominally) only Mn^{3+} cations, structural, magnetic and magnetotransport properties would give a measure of how Mn^{3+} t_{2g}^3 e_g^1 - O^{2-} - Mn^{3+} t_{2g}^3 e_g^1 superexchange interactions in $LaMnO_3$ were dependent upon Mn^{3+} concentration and distribution, without introducing the competing ferromagnetic double exchange interaction, dominant in many mixed-valent manganites. It was of interest to compare properties observed for $La_2GaMnO_{6+\delta}$, with those obtained by Töpfer et al.[17] in a study carried out in 1997, of the series $La_2Ga_xMn_{2-x}O_6$ ($0.2 \leq x \leq 2$). Since the magnetic properties of these compounds are highly dependent on the nature of oxide displacements, it is advantageous to perform neutron diffraction experiments, in order to obtain accurate values of Mn/Ga-O bondlengths. The study by Töpfer et al. utilised only X-ray diffraction, and in addition, transport measurements were reported only at zero field.

The $Nd_2GaMnO_{6+\delta}$ sample would provide an interesting contrast with the La analogue, and help identify the effect on Mn magnetic interactions, of a magnetic rare earth

moment on the A-cation site. $NdMnO_3$ is a less well-documented 'parent' compound than $LaMnO_3$; however, it is known to exhibit oxygen non-stoichiometry like the La analogue[18], and was described by Cherepanov et al.[19] in the space group *Pbnm*. Maguire et al.[18] have carried out a detailed study of the stoichiometry and defect structure of $NdMnO_3$, concluding that defects can form on any two of the three Nd, Mn and O sublattices. Both $LaGaO_3$ and $NdGaO_3$ have been shown to adopt orthorhombic structures (space group *Pbnm*) at room temperature and below, in a recent single crystal X-ray study by Sanjuán et al.[20].

A 1:1-ordered arrangement of cations on neighbouring octahedral sites in double perovskites, may be likened to the distribution of Na and Cl in rocksalt, and is modelled in the space group $P2_1/n$,[21], as for the material La_2LiSbO_6. This type of cation ordering is represented in Figure 5.1.1 (a). Alongside, in Figure 5.1.1 (b), is the cation ordered arrangement characterised by the material La_2CuSnO_6. As shown in Figure 5.1.1.(b), La_2CuSnO_6 consists of alternating Cu-O and Sn-O layers, and this material is described by the space group $P2_1/m$[22].



(a) (b)

Figures 5.1.1 Cation ordered arrangements in (a) La_2LiSbO_6 and (b) La_2CuSnO_6. Purple and blue shading represents crystallographically distinct B-site cations.

The orthorhombic space group *Pnma* does not allow for B-site cation ordering and nor do its subgroups. Regarding the choice of axes in the orthorhombic structure, much of the literature describing the magnetic and electronic properties of $LaMnO_3$ and double perovskites

uses the *Pbnm* nomenclature. In the compounds characterised in the current chapter, *Pnma* is used consistently, and the a and c axes in *Pnma* are equivalent to the b and a axes, respectively, in literature examples employing *Pbnm*.

Ordered double perovskites, particularly those based upon mixed Fe / '4d' or '5d' B-cation arrays, have been reported widely in recent CMR literature. Kobayashi et al.[23] calculated the electronic structure of Sr_2FeMoO_6 and found the material to be half-metallic, which, combined with its high ferromagnetic ordering temperature of 415K, makes it useful potentially as a room temperature magnetoresistive device. More recently, the same group have presented evidence for intergrain tunnelling magnetoresistance existing up to room temperature in polycrystalline, half-metallic Sr_2FeReO_6[24]. Like Sr_2FeMoO_6, Sr_2FeReO_6 has an ordered, double perovskite structure (space group $P2_1/n$), with a Curie temperature in excess of 400K. Maignan et al.[25] have reported a large *intra-grain* magnetoresistance in Ba_2FeMoO_6, occurring above room temperature, as well as a low field tunnelling MR comparable to that observed for Sr_2FeMoO_6. Battle et al.[26] have investigated the system $La_{1.5}Sr_{0.5}MnRhO_6$, hence combining a 4d and a mixed-valent, 3d transition metal cation on the B-cation site. The Mn,Ga compositions described in this chapter provide an effective means by which to extend the range of double perovskites used in the study of superexchange interactions in Mn^{3+} systems.

5.2 Synthesis and characterisation of $La_2GaMnO_{6+\delta}$ and $Nd_2GaMnO_{6+\delta}$

5.2.1 Experimental details

A large, 5g batch of each material, $La_2GaMnO_{6+\delta}$ and $Nd_2GaMnO_{6+\delta}$, was prepared using a standard ceramic route. Stoichiometric quantities of Ga_2O_3 (Johnson Matthey, Grade 1), MnO_2 (99.999% Puratronic, Alfa) and the appropriate rare earth oxide (La_2O_3 99.999%, REacton or Nd_2O_3 99.99%, REacton) were ground together thoroughly and fired under the synthetic conditions detailed in Table 5.2.1. The rare earth oxides had been dried at 800°C for at least six hours prior to mixing with other reagents.

Table 5.2.1 Details of preparation of $Ln_2GaMnO_{6+\delta}$ materials (where Ln = La and Nd):

Compound	$La_2GaMnO_{6+\delta}$	$Nd_2GaMnO_{6+\delta}$
Firing Temperature (°C)	Firing time	Firing time
800	-	36 hrs, powder
850	36 hrs, powder	-
1000	12 hrs, 4 pellets[a,b]	30 hrs, 4 pellets[a,b]
1200	60 hrs, 4 pellets	22 hrs, 4 pellets
1250	-	58 hrs, 3 pellets
1300	48 hrs, 4 pellets	-
Atmosphere	air	air
Quantity of material (g)	5g	5g

[a] All pellet diameters were 13mm and 2-3 tonnes were used during pressing.

[b] Regrinding and repelleting were carried out at each increase of the firing temperature and at least every 24 hours for firings at a single temperature which exceeded 24 hours.

The progress of reactions was monitored by powder X-ray diffraction using the laboratory Philips diffractometer ($3 \leq 2\theta/° \leq 70$, $\lambda = 1.5406$Å). Powder X-ray diffraction data suitable for Rietveld analysis were collected on the laboratory Siemens (D5000) diffractometer ($10 \leq 2\theta/° \leq 120$, $\Delta 2\theta = 0.02°$) using Cu Kα_1 radiation, in Bragg Brentano geometry. Both compounds were shown to be of sufficient quality to merit the collection of powder neutron diffraction data. Prior to the neutron study, the $La_2GaMnO_{6+\delta}$ compound was characterised also in a synchrotron X-ray experiment performed at Station 2.3, SRS, Daresbury, (λ = 1.300Å, $15 \leq 2\theta/° \leq 100$, $\Delta 2\theta = 0.01°$).

Neutron diffraction experiments were performed over a range of temperatures on the instrument D2b, ILL, Grenoble. The samples were loaded in cylindrical vanadium cans and, in the case of $La_2GaMnO_{6+\delta}$, measurements were taken at 290, 50 and 5K, with λ = 1.5940Å, angular range $8 \leq 2\theta/^{o} \leq 150$, and a step size $\Delta 2\theta = 0.05^{o}$. For $Nd_2GaMnO_{6+\delta}$, data were collected at 290, 5 and 1.7K, again at λ = 1.5940Å, $8 \leq 2\theta/^{o} \leq 150$, and $\Delta 2\theta = 0.05^{o}$. Powder diffraction data were analysed using the Rietveld method, as implemented by the GSAS software package. The following neutron scattering lengths were used: $b_{Nd} = 0.769$, $b_{La} = 0.827$, $b_{Mn} = -0.373$, $b_{Ga} = 0.729$ and $b_O = 0.581 \times 10^{-14}$m. For magnetic structure determinations, the size of the magnetic moments was constrained to be the same for each Mn cation. The free ion form factors of Mn^{3+} and Nd^{3+}[27] were used to describe the angular dependence of the magnetic scattering amplitude. The magnetic structure of $Nd_2GaMnO_{6+\delta}$ was solved in conjunction with Dr E. Cussen.

Magnetometry measurements were performed on a Quantum Design MPMS SQUID magnetometer. For $La_2GaMnO_{6+\delta}$ and $Nd_2GaMnO_{6+\delta}$, data were collected as a function of temperature (between 5 and 300K) upon warming, after cooling the sample in zero field (ZFC) and after cooling in the measuring field (FC). For both $La_2GaMnO_{6+\delta}$ and $Nd_2GaMnO_{6+\delta}$ the measuring fields were 100G and 1kG, however only the 100G data are presented in Sections 5.2.2.2 and 5.2.3.3, respectively. The behaviour at 1kG differs only in the degree of divergence of ZFC and FC curves at low temperature and these data are presented in Appendix 3, Figures 3.1 and 3.2.

Magnetisation as a function of field was measured for $La_2GaMnO_{6+\delta}$ at temperatures of 300, 100, 50 and 5K (in that order) by sweeping the field between 20 and -20kG at each temperature, and cooling in field between temperatures. These temperatures were judged to represent specific regions (types of magnetic behaviour) from examination of the magnetometry data collected as a function of temperature, and coincided also (at three temperatures) with those at which powder neutron diffraction data were available. For $Nd_2GaMnO_{6+\delta}$ magnetisation isotherms were collected at 300, 30, 15 and 5K, reflecting the lower temperature of the magnetic transition in this compound relative to the La analogue. Again, the field was swept between 20 and -20kG at each temperature, with field cooling

between temperatures. At 5K, the range of the field sweep for the Nd compound was increased to +/- 50kG, in an attempt to saturate the magnetic moment.

Magnetotransport data were collected (by the author and A. Coldea) on sintered bars, approximately 5x2x2mm in size, using the apparatus described in Chapter 2.7. Standard four probe geometry was used, with the direct current (≤50μA) perpendicular to the field. Resistivity was measured as a function of temperature while cooling the material from room temperature to 4.2K in zero field. Then, fixed temperatures were selected, at which to measure the magnetoresistance of the samples at fields between 0 and 14T. The selected temperatures were 200, 150 and 114K for $La_2GaMnO_{6+\delta}$ and 200K for $Nd_2GaMnO_{6+\delta}$. During each field sweep, the temperature fluctuation was maintained at no more than +/- 1K. The sweeps were carried out for the lowest temperature first and warming between temperatures was performed under zero field. Equivalent, isothermal magnetotransport measurements at the lower temperatures selected for magnetisation field sweeps, could not be reproduced, due to the immeasurably large resistivities at these temperatures. For $Nd_2GaMnO_{6+\delta}$, it was confirmed that the application of a field of 14T in the low temperature region did not lead to a reduction in the resisitivity such that it became measurable once more. It was not possible to test this for $La_2GaMnO_{6+\delta}$ due to experimental difficulties; however, this has subsequently been tested by A.Coldea and L.Noailles for another batch of the material $La_2GaMnO_{6+\delta}$ (prepared by L. Noailles) which was measured down to 4.2K under a field of 14T. However, the signal remained immeasurably large below a temperature of approximately 100K for this batch of $La_2GaMnO_{6+\delta}$ also. For $La_2GaMnO_{6+\delta}$ and $Nd_2GaMnO_{6+\delta}$, field sweeps at temperatures above 200K were not attempted.

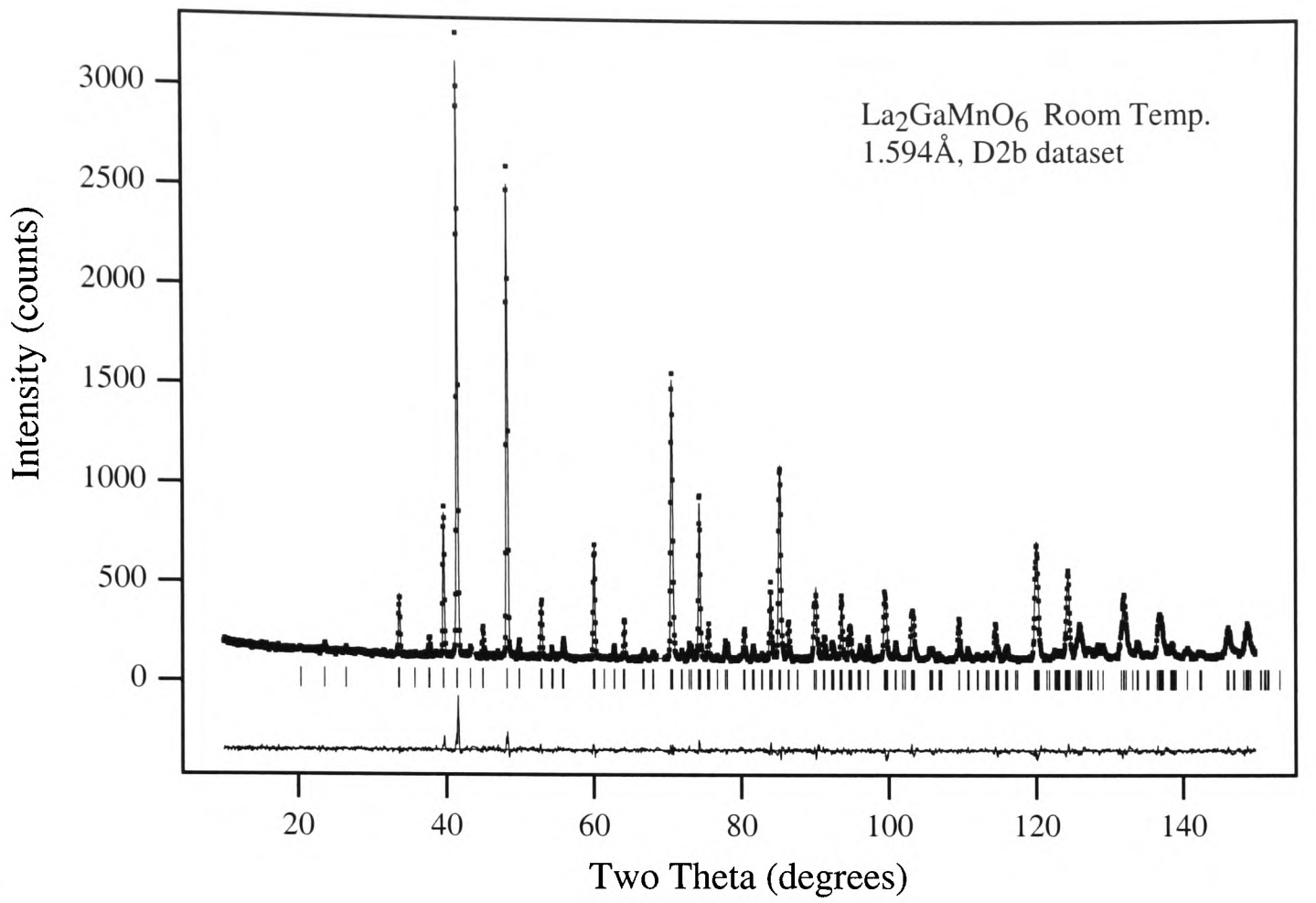
Despite numerous attempts to establish the oxygen content in the compounds $La_2GaMnO_{6+\delta}$ and $Nd_2GaMnO_{6+\delta}$ using iodometric titration, it was not possible to obtain concordant results by way of successive attempts. Following detailed analysis of X-ray and neutron diffraction data for the compound $Nd_2GaMnO_{6+\delta}$, it was decided to heat this compound further. This was in order to investigate the effects of higher firing temperatures, followed by quenching into liquid N_2, on the Mn,Ga cation distribution, phase purity and oxygen content of the sample. All further treatment and characterisation of $Nd_2GaMnO_{6+\delta}$

involving firing at a temperature in excess of 1250°C was carried out by J. Burley. The sample obtained from this further firing is referred to as 'the single phase' sample in Section 5.3.

5.2.2 Structural and magnetic characterisation of $La_2GaMnO_{6+\delta}$

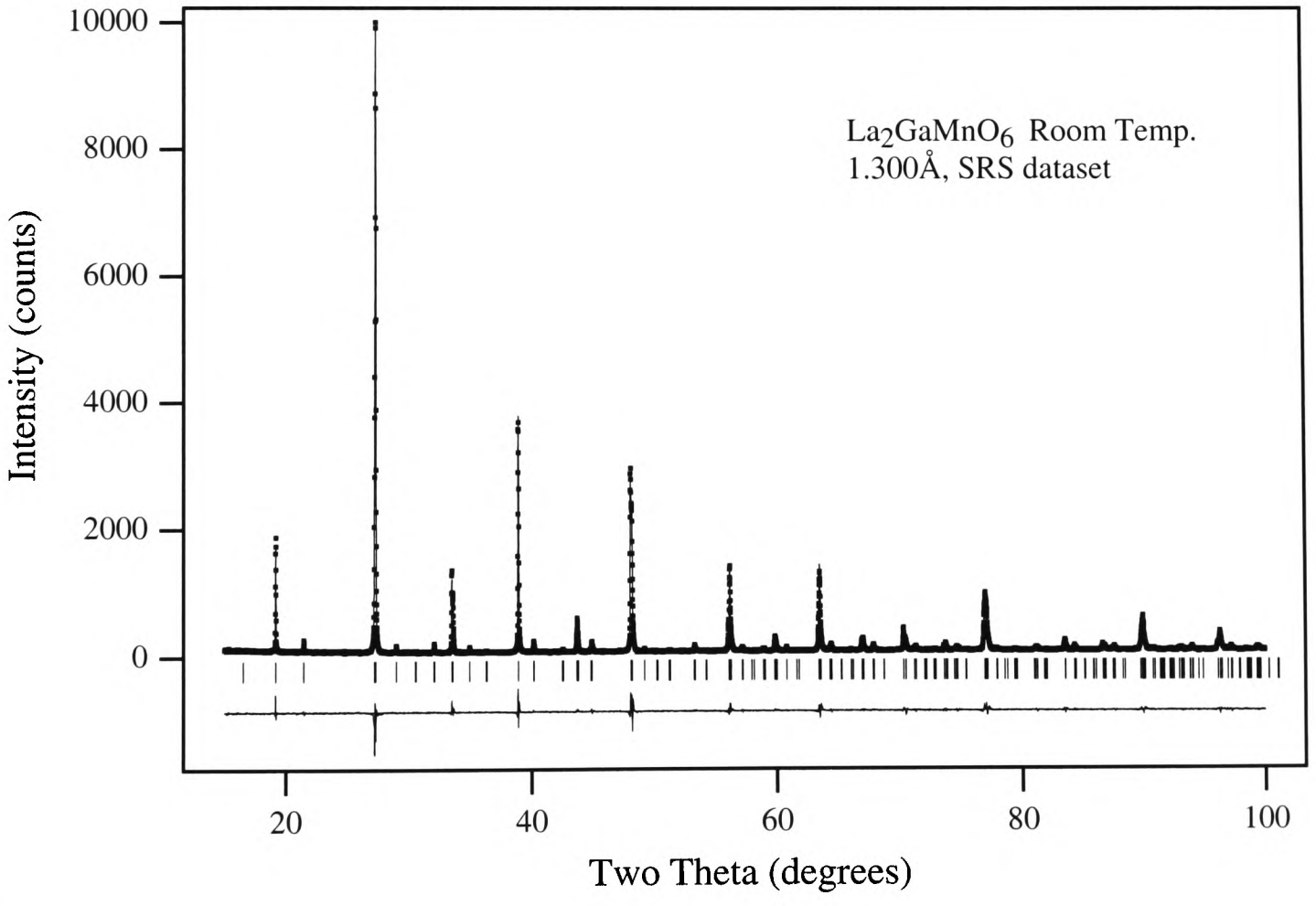
5.2.2.1 Room temperature powder neutron diffraction measurements

The observed and calculated neutron and X-ray diffraction profiles for $La_2GaMnO_{6+\delta}$ at room temperature are shown in Figures 5.2.1 (a) and (b), respectively. The two patterns are the result of a combined neutron/synchrotron X-ray refinement, enabling more precise modelling of Mn and Ga cation distributions across octahedral sites. As expected, given the crystal structures of $LaGaO_3$ and stoichiometric $LaMnO_3$, the structure was found to be orthorhombic and could be modelled using the space group *Pnma*. This implies a disordered Mn^{3+}/Ga^{3+} cation array. The combined room temperature neutron/synchrotron X-ray refinement of $La_2GaMnO_{6+\delta}$ converged to give the following residual fit parameters: R_{wp} = 7.64%, R_p = 6.09%, DWd = 1.068 and χ^2_{red} = 1.937 for 52 variables. The tendency towards B-cation ordering in double perovskites is greater when there is an appreciable (> 2 units) charge difference between two cations and when their sizes differ by more than 0.10Å. Neither of these criteria are satisfied in the Mn^{3+},Ga^{3+} pair, thus the absence of cation ordering is not surprising.



(a)

Figure 5.2.1 (a) Observed (dots) and calculated (line) neutron powder diffraction profiles for $La_2GaMnO_{6+\delta}$ at room temperature.



(b)

Figure 5.2.1 (b) Observed (dots) and calculated (line) synchrotron X-ray powder diffraction profiles for $La_2GaMnO_{6+\delta}$ at room temperature.

Tables 5.2.2 and 5.2.3 list structural and thermal parameters, respectively, obtained in

the single phase, room temperature refinement of the compound $La_2GaMnO_{6+\delta}$.

Table 5.2.2 Structural parameters for $La_2GaMnO_{6+\delta}$ at room temperature:

$La_2GaMnO_{6+\delta}$

Lattice Parameters(Å) a = 5.51122(4); b = 7.80515(6); c = 5.52947(4); V = 237.855(3)Å^3

Atom	Site	Fraction (%)	x	y	z
La(1)	4c	100	0.0217(1)	0.25	0.0049(2)
Mn(2)	4b	50	0	0	1/2
Ga(3)	4b	50	0	0	1/2
O(4)	8d	100	0.2752(3)	0.0349(2)	0.2745(3)
O(5)	4c	100	0.4919(6)	0.25	-0.0699(5)

Table 5.2.3 Thermal parameters for $La_2GaMnO_{6+\delta}$ at room temperature:

Atom	U_{iso}, U_{eq}	U_{11} (Å^2)	U_{22} (Å^2)	U_{33} (Å^2)	U_{12} (Å^2)	U_{13}(Å^2)	U_{23} (Å^2)
La(1)	0.0027(1)						
Mn(2)	0.0029(2)[a]						
Ga(3)	0.0029(2)[a]						
O(4)	0.0063	0.0101(10)	0.0050(9)	0.0038(9)	0.0003(9)	-0.0021(8)	-0.0023(9)
O(5)	0.0091	0.0168(23)	0.0064(19)	0.0041(13)	0.0000	0.0025(12)	0.0000

[a] Constrained to be the same

The compounds $La_2GaMnO_{6+\delta}$ and $Nd_2GaMnO_{6+\delta}$ were both prepared under air, rather than argon. Therefore, careful refinement of both oxygen and A- and B-site cation concentrations was carried out. As shown by the refined atomic fractions in Table 5.2.2, it was not possible to improve significantly the quality of the fit by incorporating nonstoichiometry on either the La, Mn or O sublattices. Therefore, the compound will be formulated as La_2GaMnO_6 from this point onwards. Table 5.2.3 reveals that the thermal displacement parameters for oxygen anions O(4) and O(5), are anisotropic, at room temperature.

In order to help the interpretation of bondlengths and bond angles given in Table 5.2.4 and subsequent tabulated data in this chapter, Figure 5.2.2 gives a polyhedral representation of La_2GaMnO_6, illustrating the labelling of atomic sites and site symmetry which are applicable for both La_2GaMnO_6 and $Nd_2GaMnO_{6+\delta}$ modelled in space group *Pnma*.

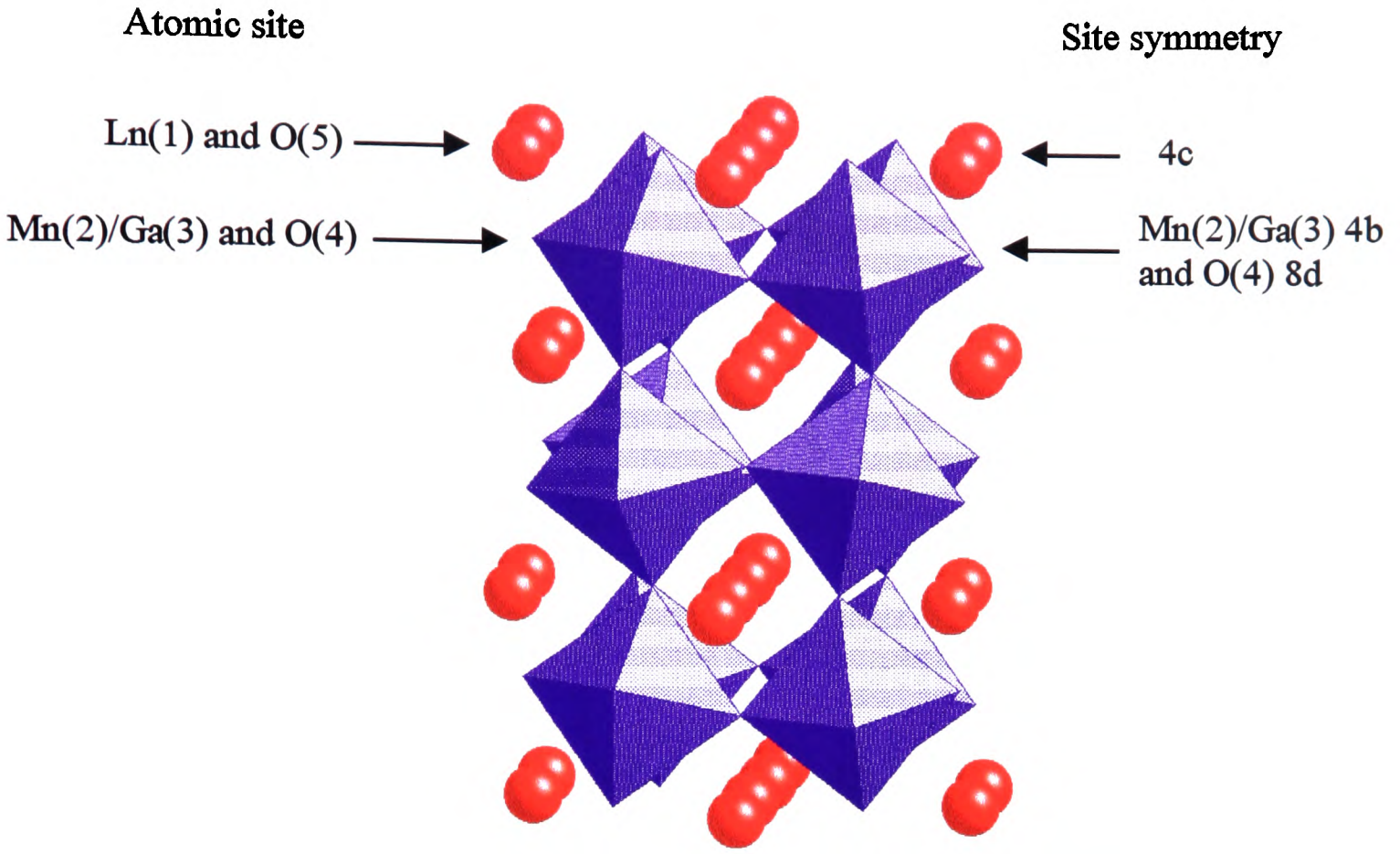
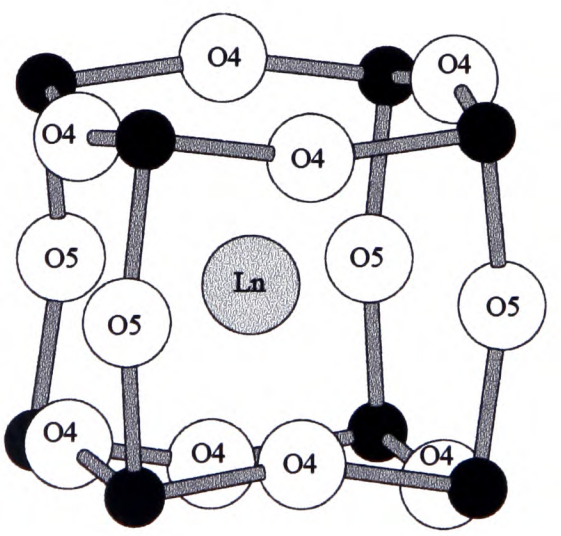


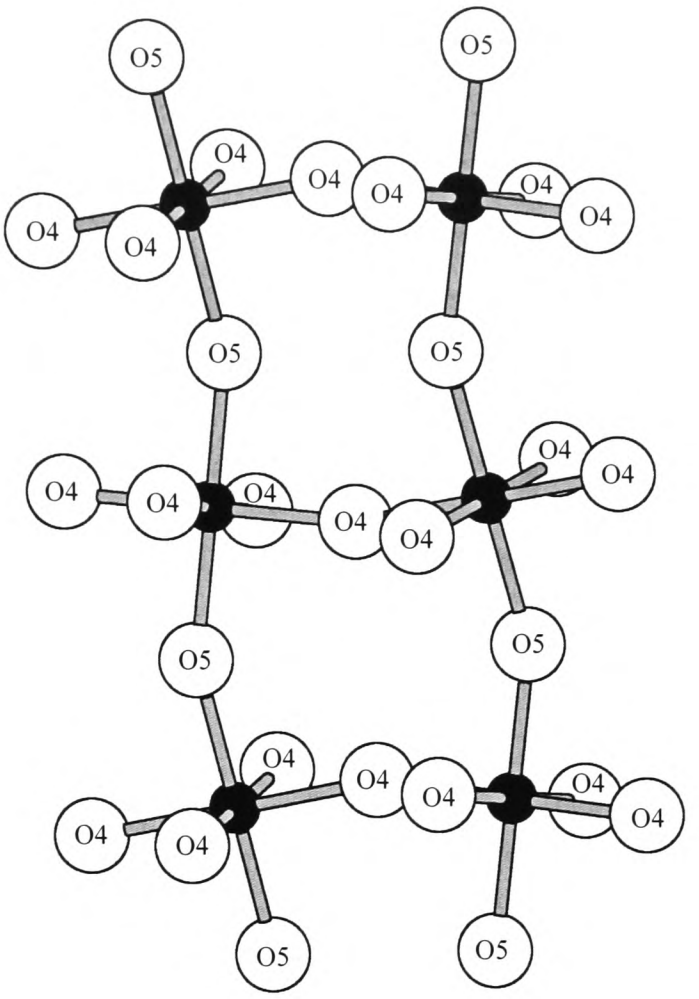
Figure 5.2.2 Polyhedral representation of the compound La_2GaMnO_6 in the space group *Pnma*, where 'b' is the long (vertical) axis. The positions and site symmetry of constituent atoms are labelled.

Figure 5.2.3 shows the geometry of the A-cation (Ln) environment, in which the 12-fold coordination, by eight O(4) and four O(5) anions, is evident.



Figures 5.2.3 Coordination environment of A-site (Ln) cations, in the *Pnma* space group.

Figure 5.2.4 illustrates more clearly, the distribution of O(4) and O(5) anions in the tilted, Ga/Mn-O_6 network of octahedra in La_2GaMnO_6



Figures 5.2.4 Distribution of O(4) and O(5) anions and tilting of octahedra in La_2GaMnO_6, modelled in space group *Pnma*.

Figures 5.2.2 to 5.2.4 are useful in identifying the significant bondlengths and bond angles given in Table 5.2.4, for the room temperature structure of La_2GaMnO_6.

Table 5.2.4 Selected distances (Å) and angles (°) for La_2GaMnO_6 at room temperature:

La - O Bondlength (Å)		Mn/Ga - O Bondlength (Å) or Angle (°)[a]	
La - O(4) x 2	2.6434(23)	Mn - O(4) x 2	1.9782(22)
La - O(4) x 2	2.7971(23)	Mn - O(4) x 2	1.9824(22)
La - O(4) x 2	3.1648(18)	Mn - O(5) x 2	1.9898(6)
La - O(4) x 2	2.4798(19)	Mn - O(4) - Mn	160.52(10)
La - O(5)	2.6239(34)	Mn - O(5) - Mn	157.43(16)
La - O(5)	2.9495(35)	O(4) - Mn - O(4)	88.712(21)
La - O(5)	2.4110(31)	O(4) - Mn - O(5)	89.75(13)
La - O(5)	3.1284(31)	O(4) - Mn - O(5)	89.99(13)

[a] Although only Mn atoms are listed, Ga shares the Mn site in a 1:1 ratio.

From Table 5.2.4, it can be seen that four La-O bondlengths are equal to, or greater than 2.949(4)Å, suggesting pseudo-eightfold coordination of La cations.

5.2.2.2 SQUID magnetometry measurements

The variation of molar susceptibility with temperature for La_2GaMnO_6 is shown in Figure 5.2.5. The sample undergoes a magnetic transition at 70K, this temperature being obtained by plotting the first derivative of susceptibility with respect to temperature, against temperature, and locating the minimum. The value of T_C and the low temperature behaviour is similar to that observed by Töpfer and Goodenough[17] in their sample containing the same concentration of Ga. The low temperature behaviour is characterised by a broad maximum in the ZFC signal, while the value of the FC signal continues to increase after the divergence between the two at 70K.

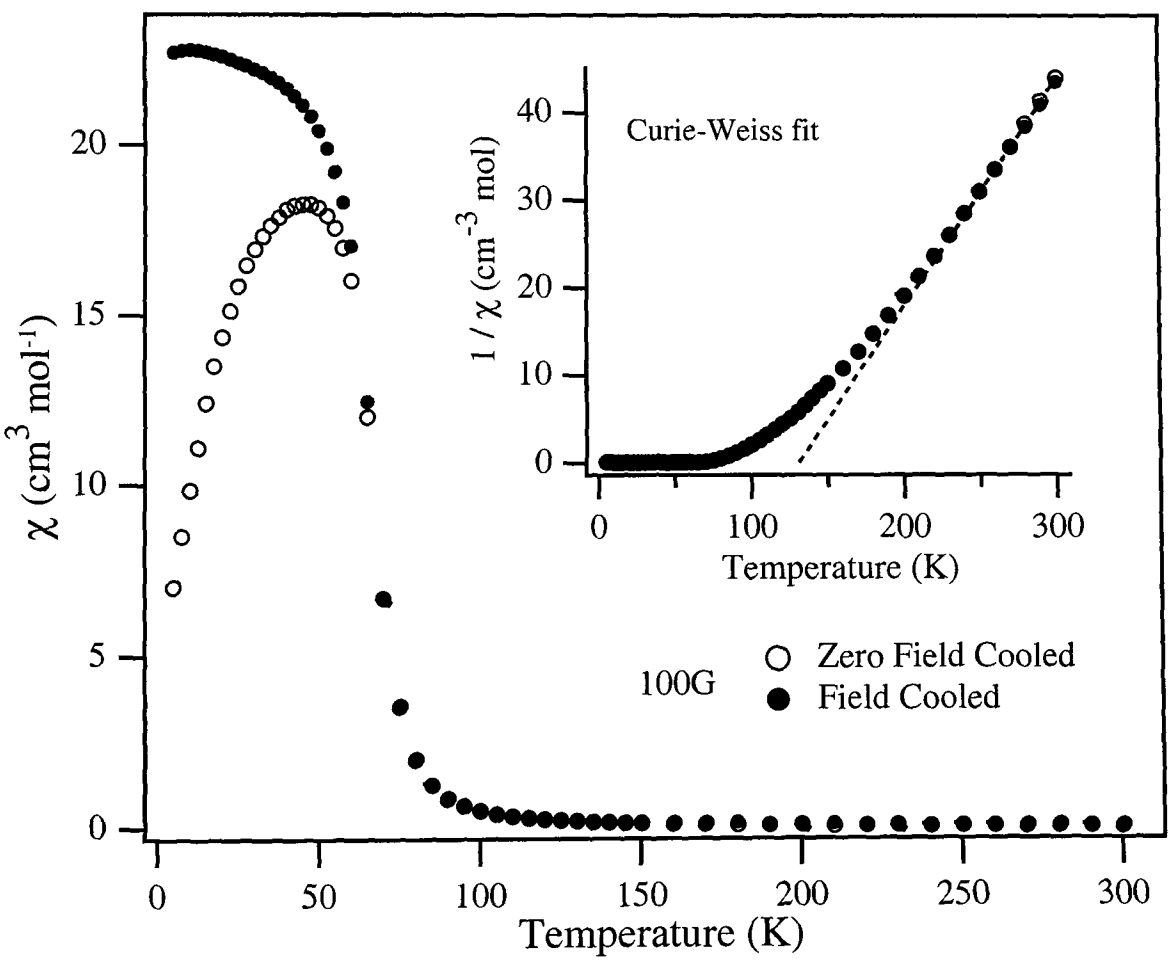


Figure 5.2.5 Molar magnetic susceptibility as a function of temperature for La_2GaMnO_6 at 100G.

The application of the Curie-Weiss model to the temperature dependence of inverse magnetic susceptibility data for La_2GaMnO_6 gives the parameters shown in Table 5.2.5.

Table 5.2.5 Curie-Weiss fit parameters for 100G data:

Compound	Temperature range (K)	C_m (cm^3 K mol^{-1})	θ(K)	Estimated C_m (cm^3 K mol^{-1})
La_2GaMnO_6	230 - 300	3.98(3)	126.65(87)	3.000

The sample exhibits a positive Weiss constant θ(K), with $\theta > T_C$, typical of a ferromagnet. The estimated value of C_m of 3.00 (cm^3 K mol^{-1}) for La_2GaMnO_6 is calculated assuming the presence of one mole of the Mn^{3+}, d^4 cation, as represented by equation 5.2.1. The observed value of C_m (cm^3 K mol^{-1}) exceeds the calculated value, and hence, gives an effective Mn magnetic moment exceeding that calculated by the spin only formula. The observed value of C_m corresponds to a value of μ_{eff} of $5.64\mu_B$ per Mn^{3+}, d^4 cation. This suggests ferromagnetic interactions exist at temperatures exceeding 70K.

$$\text{Estimated } C_m(La_2GaMnO_6) = \frac{1}{8}\left\{(\mu_{eff}Mn^{3+})^2\right\} \qquad \text{eqn. (5.2.1)}$$

The field dependence of magnetisation for La_2GaMnO_6 at four temperatures is presented below in Figure 5.2.6. The behaviour at 300K is represented by a linear dependence upon field (characteristic of antiferromagnetic or paramagnetic behaviour) with no hysteresis evident. At temperatures of 100K and below, however, there is a degree of curvature in the variation of magnetisation with field and finite width hysteresis loops are evident at 50 and 5K (albeit minimal for 50K), which are symmetrical about the origin. At 5K, the magnetisation approaches the theoretical value for parallel alignment of spins, saturating in a field of 20kG.

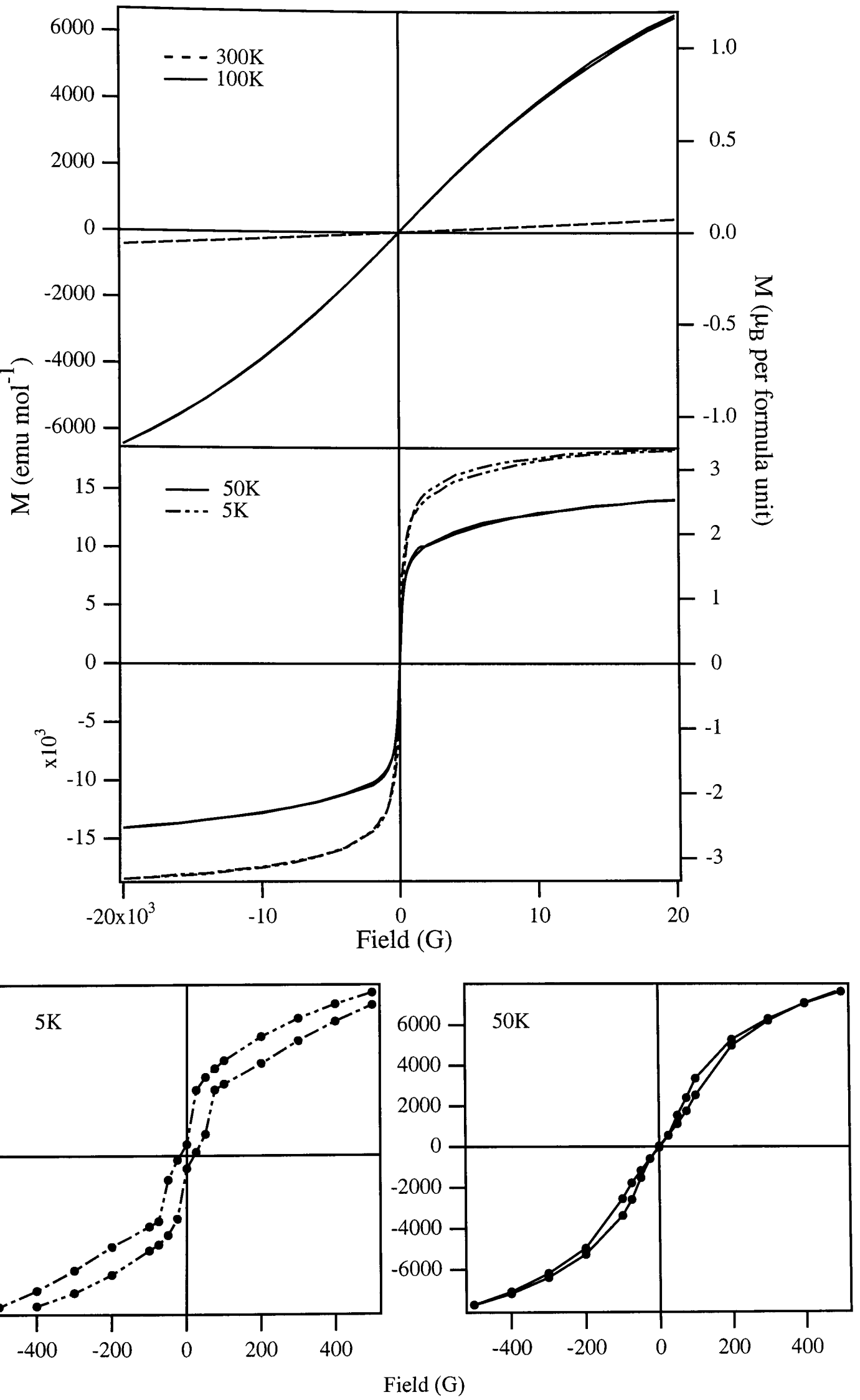


Figure 5.2.6 Magnetisation as a function of field (-20≤ Field(kG) ≤ 20) for La_2GaMnO_6 at 300, 100, 50 and 5K. Enlarged views of the region (-500≤ Field(G) ≤ 500) are shown at 5 and 50K.

Temperatures of 50K and 5K were chosen as those at which to perform low temperature neutron experiments, in order to investigate further the magnetic structure of La_2GaMnO_6. The results of experiments performed on instrument D2b, at 50 and 5K, are now presented.

5.2.2.3 50K and 5K powder neutron diffraction measurements

Figure 5.2.7 illustrates the observed and calculated neutron diffraction profile for La_2GaMnO_6 after reducing the temperature to 50K, using the space group *Pnma*. The change in intensity of the 101 and 020 nuclear reflections in particular, on lowering the temperature, required the introduction of an additional, magnetic phase in the structural model at 50K. The refinement gave the following residual fit parameters: R_{wp} = 6.88%, R_p = 5.34%, DWd = 0.952 and χ^2_{red} = 1.969 for 38 variables. The structural parameters for the nuclear and magnetic cells, are given in Tables 5.2.6 to 5.2.9 below.

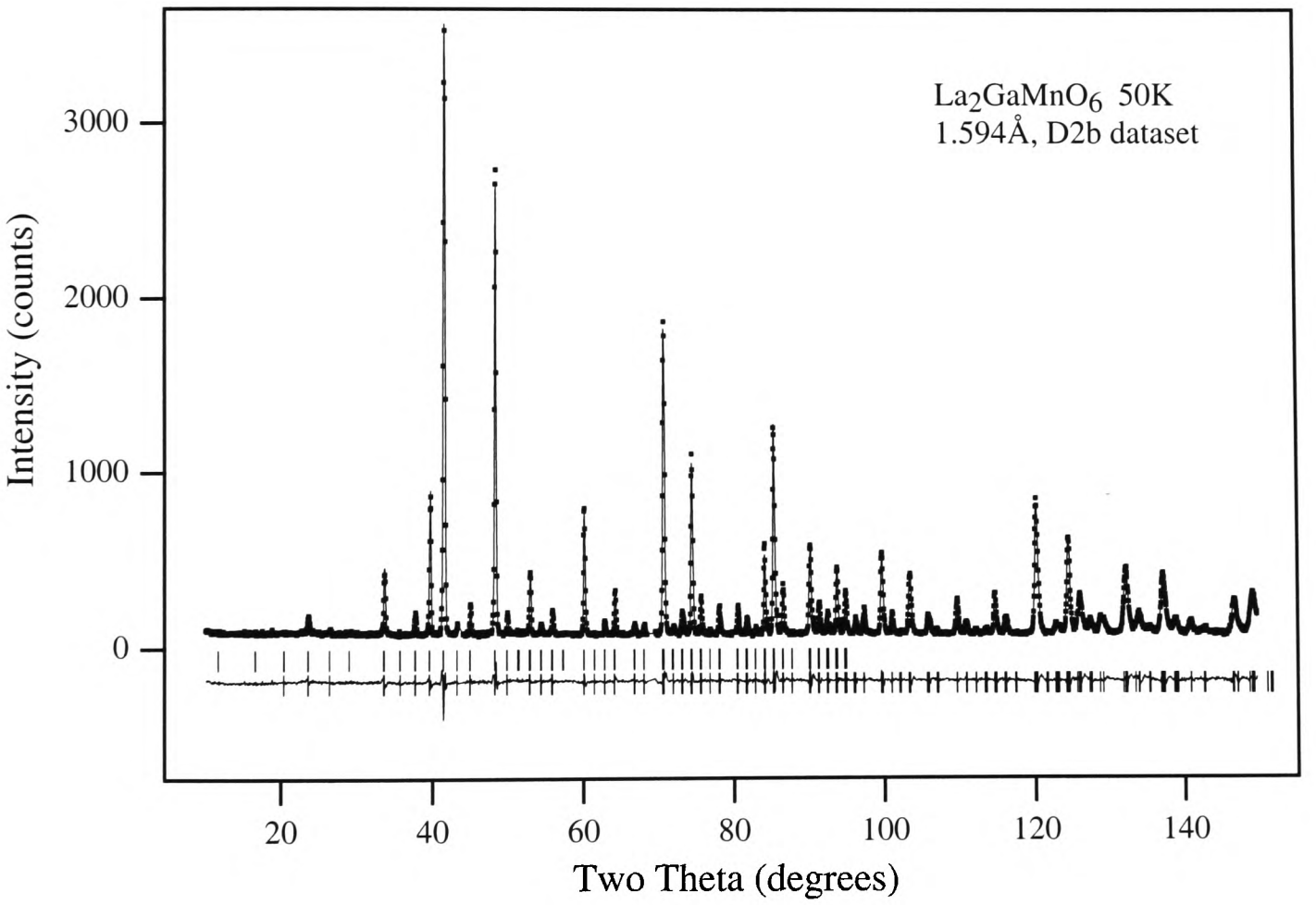


Figure 5.2.7 Observed (dots) and calculated (line) neutron powder diffraction profiles for La_2GaMnO_6 at 50K. Upper and lower sets of tick marks represent the magnetic, and nuclear Bragg peaks, repectively.

Table 5.2.6 Structural parameters for La_2GaMnO_6 at 50K:

La_2GaMnO_6

Lattice Parameters(Å) a = 5.51155(11); b = 7.79862(15); c = 5.52382(11); V = 237.428(6)Å^3

Atom	Site	Fraction (%)	x	y	z
La(1)	4c	100	0.0246(2)	1/4	0.0043(4)
Mn(2)	4b	50	0	0	1/2
Ga(3)	4b	50	0	0	1/2
O(4)	8d	100	0.2772(3)	0.0354(2)	0.2752(3)
O(5)	4c	100	0.4915(5)	1/4	-0.0702(4)

Table 5.2.7 Thermal parameters for La_2GaMnO_6 at 50K:

Atom	U_{iso}, U_{eq}	U_{11} (Å^2)	U_{22} (Å^2)	U_{33} (Å^2)	U_{12} (Å^2)	U_{13}(Å^2)	U_{23} (Å^2)
La(1)	0.0042(2)						
Mn(2)	0.0026(7)[a]						
Ga(3)	0.0026(7)[a]						
O(4)	0.0062	0.0136(9)	0.0017(8)	0.0031(7)	0.0020(9)	-0.0034(6)	0.0012(8)
O(5)	0.0087	0.0226(26)	0.0022(15)	0.0011(11)	0.0000	0.0043(9)	0.0000

[a] Constrained to be the same

Table 5.2.7 reveals little change in U_{11} within error, for both equatorial O(4), and apical O(5) oxygen anions, on reducing the temperature from room temperature to 50K. U_{33} for equatorial oxygens O(4) remains unchanged also, with U_{22} values and U_{33} for O(5) all reducing in magnitude to about one third of their room temperature values.

Table 5.2.8 Selected distances (Å) and angles (°) for La_2GaMnO_6 at 50K:

La - O Bondlength (Å)		Mn/Ga - O Bondlength (Å) or Angle (°)[a]	
La - O(4) x 2	2.6405(25)	Mn - O(4) x 2	1.9732(22)
La - O(4) x 2	2.7833(22)	Mn - O(4) x 2	1.9874(22)
La - O(4) x 2	3.1789(20)	Mn - O(5) x 2	1.9878(5)
La - O(4) x 2	2.4768(23)	Mn - O(4) - Mn	159.98(9)
La - O(5)	2.6054(30)	Mn - O(5) - Mn	157.34(15)
La - O(5)	2.9659(31)	O(4) - Mn - O(4)	88.713(19)
La - O(5)	2.4045(35)	O(4) - Mn - O(5)	89.81(12)
La - O(5)	3.130(4)	O(4) - Mn - O(5)	89.89(11)

[a] Although only Mn atoms are listed, Ga shares the Mn site in a 1:1 ratio.

The magnetic structure of La_2GaMnO_6 at 50K refined to that represented in Figure 5.2.8. It consists of ferromagnetically coupled moments, 1.76(8) μ_B per Mn, aligned along y.

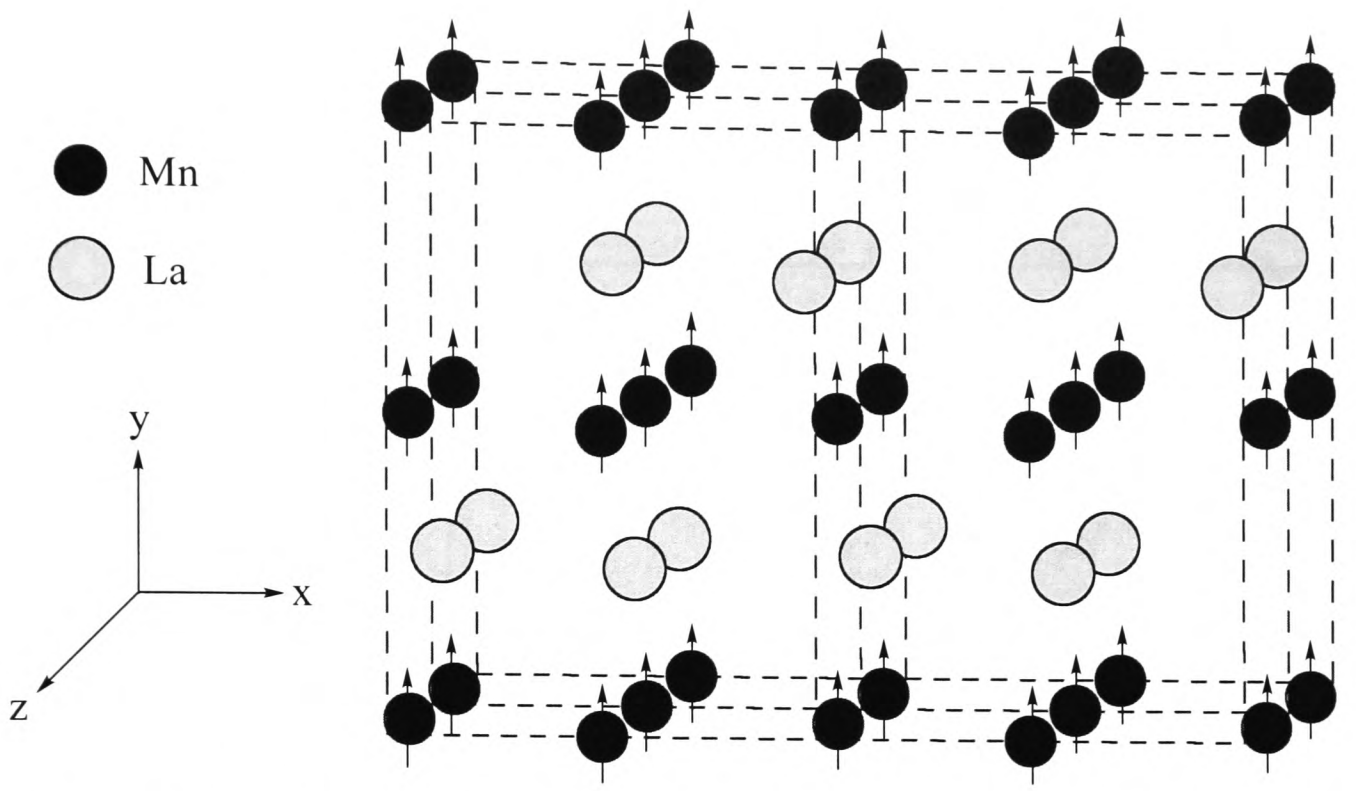


Figure 5.2.8 Magnetic structure of La_2GaMnO_6 at 50K, with the spin directions of Mn cations shown. Mn cations have 50% occupancy of the B-cation sites.

In the refinement of the magnetic structure, the lattice parameters were constrained at the values for the nuclear cell, as were temperature factors, as shown in Table 5.2.9. The space group was set at *P1*, hence, the Mn coordinates were generated according to the '4b' site symmetry in space group *Pnma*.

Table 5.2.9 Atomic coordinates and magnetic components for Mn atoms comprising the magnetic cell of La_2GaMnO_6 at 50K:

Atom	Site	Fraction (%)[a]	U_{iso} (Å^2)	x	y	z	Mx (μ_B)	My (μ_B)	Mz (μ_B)
Mn(1)	1	50	0.0026(7)	0	0	1/2	0	1.76(8)	0
Mn(2)	1	50	0.0026(7)	1/2	0	0	0	1.76(8)	0
Mn(3)	1	50	0.0026(7)	0	1/2	1/2	0	1.76(8)	0
Mn(4)	1	50	0.0026(7)	1/2	1/2	0	0	1.76(8)	0

[a] The 50% occupancy of positions in the magnetic cell reflects the disordered array of Mn and Ga across transition metal sites.

Figure 5.2.9 gives the neutron powder diffraction pattern from data collected on D2b at the lowest measuring temperature, 5K. Again, it was necessary to include the magnetic cell in the structural model, and the refinement converged to give the following residual parameters: R_{wp} = 6.14%, R_p = 4.71%, DWd = 0.791 and χ^2_{red} = 2.462 for 39 variables Structural and magnetic parameters at 5K are summarised in Tables 5.2.10 to 5.2.13.

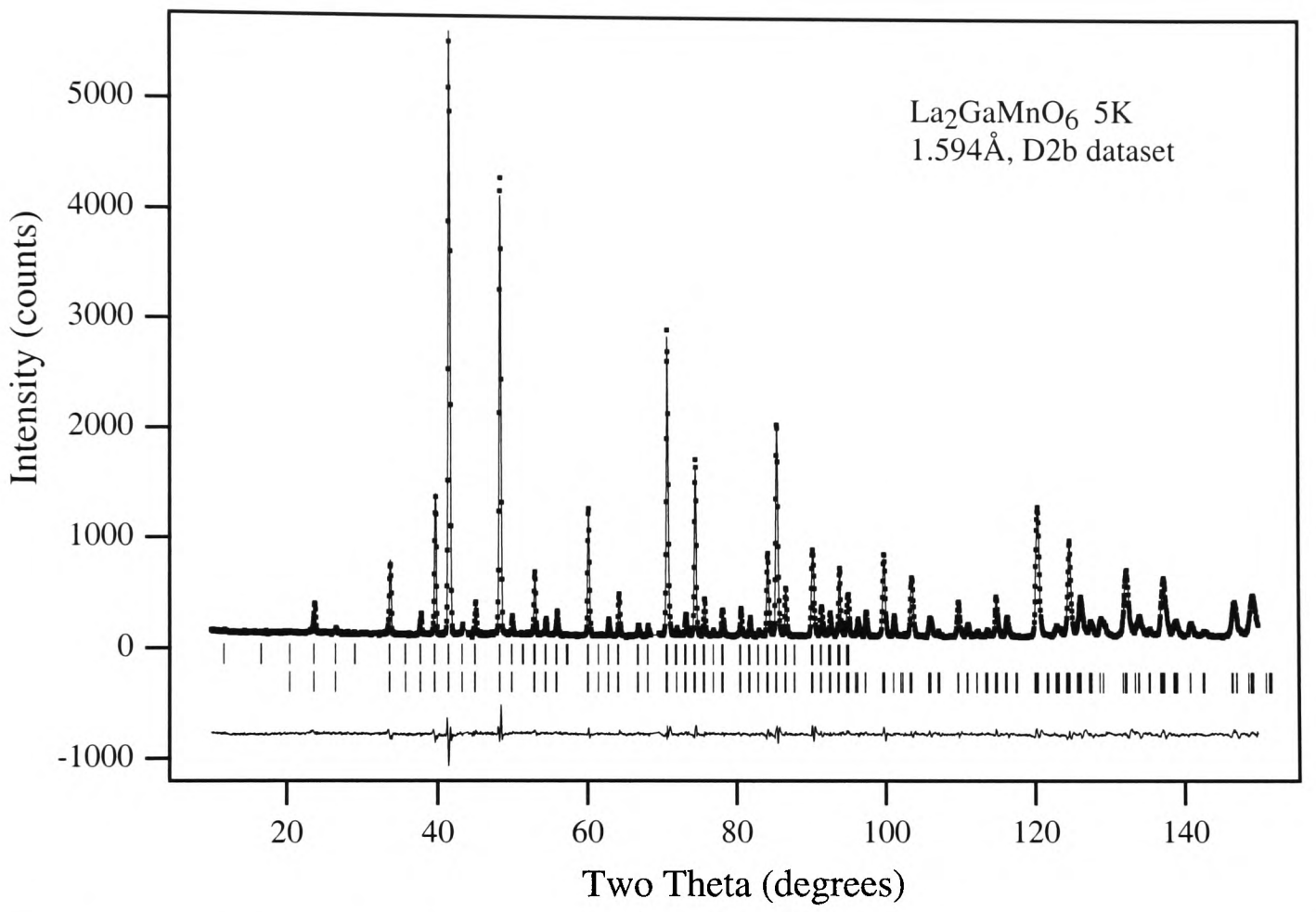


Figure 5.2.9 Observed (dots) and calculated (line) neutron powder diffraction profiles for La_2GaMnO_6 at 5K. Upper and lower tick marks refer to the magnetic and nuclear Bragg peaks, respectively.

Table 5.2.10 Structural parameters for La_2GaMnO_6 at 5K:

La_2GaMnO_6

Lattice Parameters(Å) a = 5.50980(10); b = 7.79614(15); c = 5.52206(11); V = 237.201(5) $Å^3$

Atom	Site	Fraction (%)	x	y	z
La(1)	4c	100	0.0250(2)	1/4	0.0045(4)
Mn(2)	4b	50	0	0	1/2
Ga(3)	4b	50	0	0	1/2
O(4)	8d	100	0.2768(3)	0.0351(2)	0.2754(2)
O(5)	4c	100	0.4909(5)	1/4	-0.0712(4)

Table 5.2.11 Thermal parameters for La_2GaMnO_6 at 5K:

Atom	U_{iso}, U_{eq}	U_{11} (Å^2)	U_{22} (Å^2)	U_{33} (Å^2)	U_{12} (Å^2)	U_{13}(Å^2)	U_{23} (Å^2)
La(1)	0.0034(2)						
Mn(2)	0.0033(6)[a]						
Ga(3)	0.0033(6)[a]						
O(4)	0.0054	0.0128(8)	0.0011(7)	0.0022(6)	0.0013(8)	-0.0022(6)	-0.0005(7)
O(5)	0.0095	0.0244(23)	0.0033(14)	0.0006(9)	0.0000	0.0031(8)	0.0000

[a] Constrained to be the same

Table 5.2.11 shows that U_{11} and U_{22} remain the same within error, as the values refined at the higher temperature of 50K. Values of U_{33} have decreased to approximately two thirds of their 50K values. Table 5.2.12 summarises significant bondlengths and bond angles obtained in the 5K refinement.

Table 5.2.12 Selected distances (Å) and angles (°) for La_2GaMnO_6 at 5K:

La - O Bondlength (Å)		Mn/Ga - O Bondlength (Å) or Angle (°)[a]	
La - O(4) x 2	2.6398(22)	Mn - O(4) x 2	1.9750(19)
La - O(4) x 2	2.7807(19)	Mn - O(4) x 2	1.9847(19)
La - O(4) x 2	3.1776(17)	Mn - O(5) x 2	1.9890(5)
La - O(4) x 2	2.4809(20)	Mn - O(4) - Mn	160.15(8)
La - O(5)	2.6005(27)	Mn - O(5) - Mn	157.00(13)
La - O(5)	2.9727(28)	O(4) - Mn - O(4)	88.750(17)
La - O(5)	2.3999(31)	O(4) - Mn - O(5)	89.56(10)
La - O(5)	3.1352(32)	O(4) - Mn - O(5)	89.95(10)

[a] Although only Mn atoms are listed, Ga shares the Mn site in a 1:1 ratio.

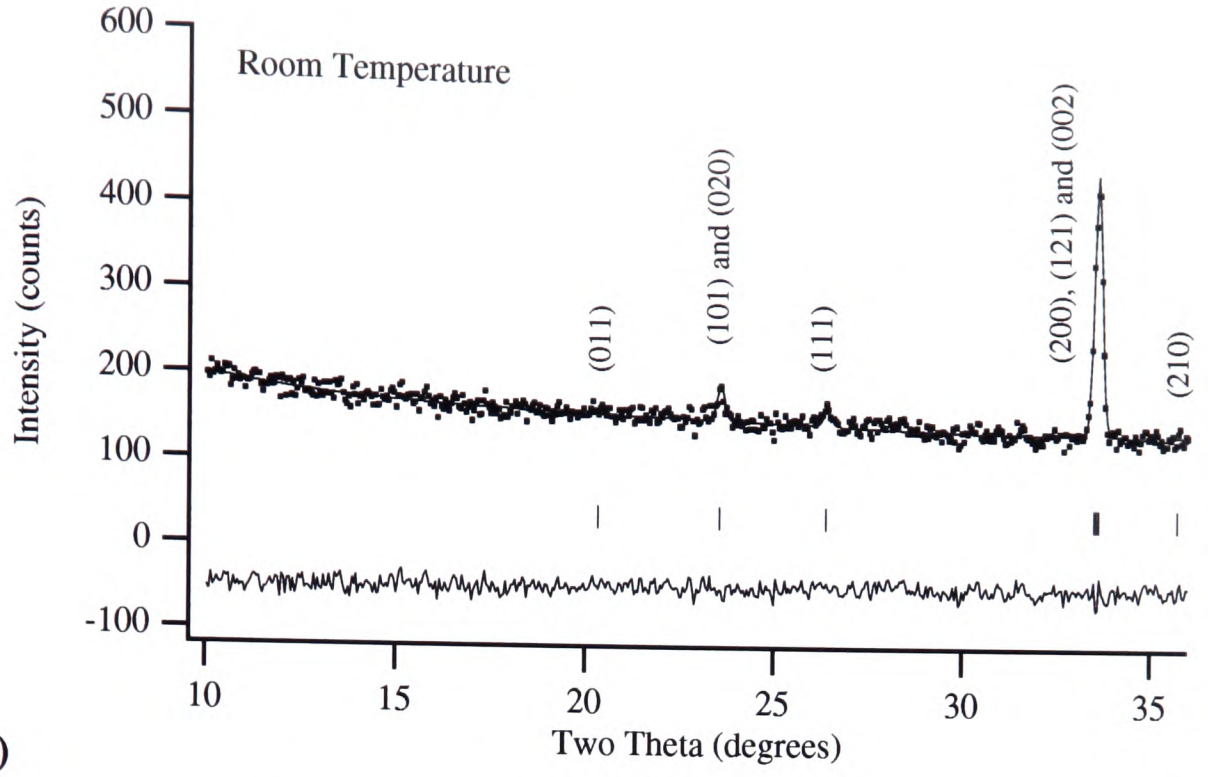
The magnetic structure at 5K remained the same as that refined at 50K, although the ferromagnetic moment was enhanced to 2.80(5)μ_B per Mn. Table 5.2.13 summarises the magnetic cell parameters obtained in the 5K model.

Table 5.2.13 Atomic coordinates and magnetic components for Mn atoms comprising the magnetic cell at 5K:

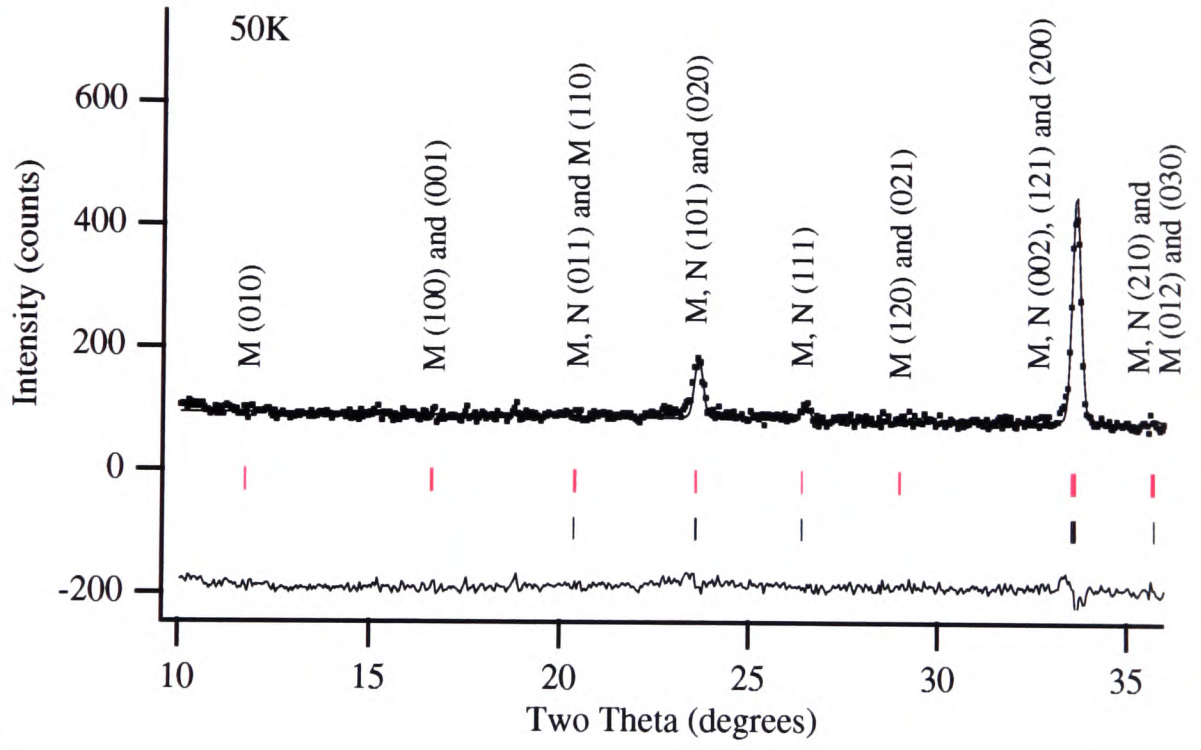
Atom	Site	Fraction (%)[a]	Uiso (Å^2)	x	y	z	Mx (μ_B)	My (μ_B)	Mz (μ_B)
Mn(1)	1	50	0.0033(6)	0	0	1/2	0	2.80(5)	0
Mn(2)	1	50	0.0033(6)	1/2	0	0	0	2.80(5)	0
Mn(3)	1	50	0.0033(6)	0	1/2	1/2	0	2.80(5)	0
Mn(4)	1	50	0.0033(6)	1/2	1/2	0	0	2.80(5)	0

[a] The 50% occupancy of positions on the magnetic cell reflects the disordered array of Mn and Ga across transition metal sites.

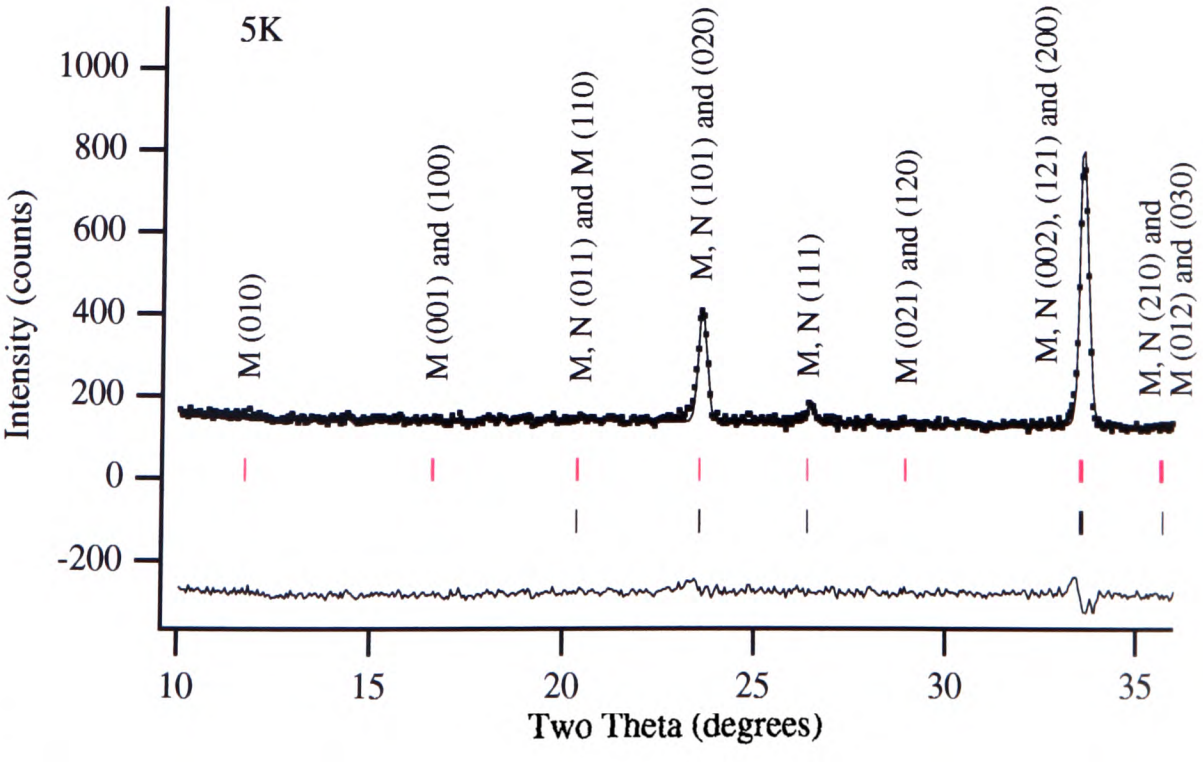
Figures 5.2.10 (a), (b) and (c) give enlarged views of the low angle region of the diffraction patterns collected at room temperature, 50 and 5K, respectively, illustrating the evolution of magnetic intensity as a function of temperature, predominantly in the 101 and 020 'nuclear' reflections denoted at 290K. All magnetic Bragg peaks in the magnetic structure at 50 and 5K, are denoted by purple tick marks in Figures 5.2.10 (b) and (c). The black set of tick marks corresponds to the nuclear reflections. The plots at the three different temperatures do not have a common scale. 'M' and 'N' denote magnetic and nuclear reflections, respectively.



(a)



(b)



(c)

Figures 5.2.10 Evolution of magnetic Bragg peaks from (a) room temp., to (b) 50K and (c) 5K.

Tables 5.2.14 and 5.2.15 summarise agreement indices and details of the refinements of La_2GaMnO_6 at room temperature, 50 and 5K.

Table 5.2.14 Agreement parameters and refining variables at room temperature, 50K and 5K:

Agreement parameter	Room Temperature			50K	5K
	SRS 1.300Å	D2b 1.594Å	Total	D2b 1.594Å	D2b 1.594Å
R_{wp} (%)	8.81	5.33	7.64	6.88	6.14
R_p (%)	6.91	4.26	6.09	5.34	4.71
DWd	1.046	1.161	1.068	0.952	0.791
Total no. variables			52	38	39
χ^2_{red}			1.937	1.969	2.462

Table 5.2.15 Refined variables at room temperature, 50K and 5K:

Refining variables (in addition to atomic coordinates, thermal parameters and fractions)	Room Temperature		50K	5K
	SRS 1.400Å	D2b 1.594Å	D2b 1.594Å	D2b 1.594Å
Background (Shifted Chebyshev)	8	10	10	10
Profile (pseudo-Voigt)[a]	4	5	4	4
Histogram scale factor	1	1	1	1
Wavelength (Å)	1			
Zero point		1	1	1

[a] Profile coefficients for the magnetic phase at 50 and 5K were constrained to the same values as for the non-magnetic phase.

5.2.2.4 Magnetotransport measurements

The magnetotransport behaviour of La_2GaMnO_6 as a function of field at three isothermal temperatures is shown in Figure 5.2.11. The observed ratio of negative magnetoresistance at 14T in La_2GaMnO_6 increases, on decreasing the isothermal measuring temperature, the signal being reduced to approximately 82% of its zero field value at 14T and 114K. The isotherm at 150K has an approximately linear variation with field, and either side of it, the 200K and 114K data show 'convex' and 'concave' shaped curves, respectively. As shown in the inset of the Figure, conductivity is thermally activated in La_2GaMnO_6, and the insulating nature of the sample means resistivity is measurable only to 112K.

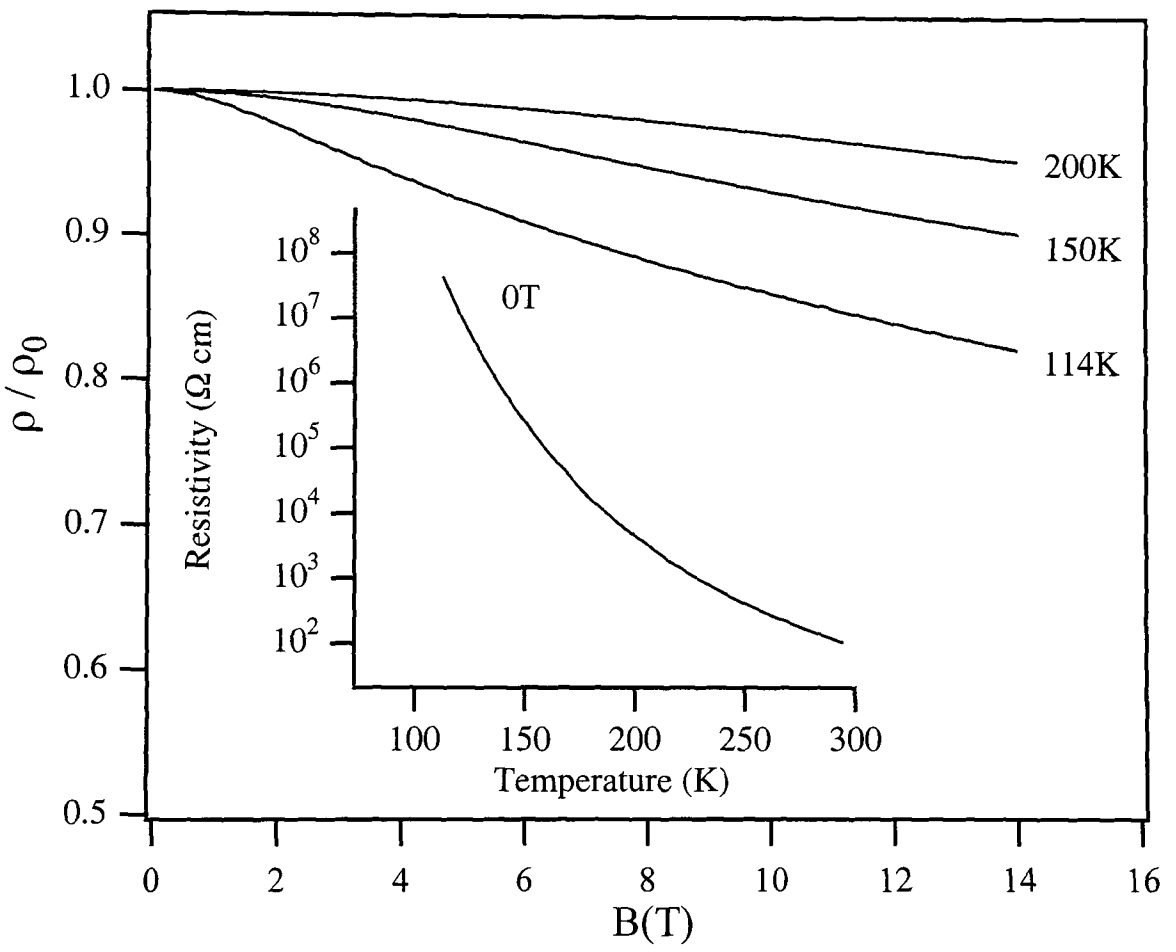


Figure 5.2.11 Field dependence of normalised resistivity $\rho(B)/\rho(0)$ at 200, 150 and 114K for La_2GaMnO_6. The inset shows the temperature dependence of resistivity at zero field.

Parameters for the fit of temperature dependent data using a thermally activated conduction law, are tabulated below. The fit is shown in Appendix 3, Figure 3.3 (a).

Table 5.2.16 Fit parameters for thermally activated conduction:

Compound	Temperature range (K)	Model used	Parameter[a]
La_2GaMnO_6	295 to 112	$\rho \propto \exp(E_A / k_B T)$	$E_A = 205.28$ meV

[a] $1eV = 1.6022X10^{-19}J$

5.2.3 Structural and magnetic characterisation of $Nd_2GaMnO_{6+\delta}$

5.2.3.1 290K powder neutron diffraction measurements

Figure 5.2.12 shows the observed and calculated neutron diffraction profile for $Nd_2GaMnO_{6+\delta}$, at a temperature of 290K.

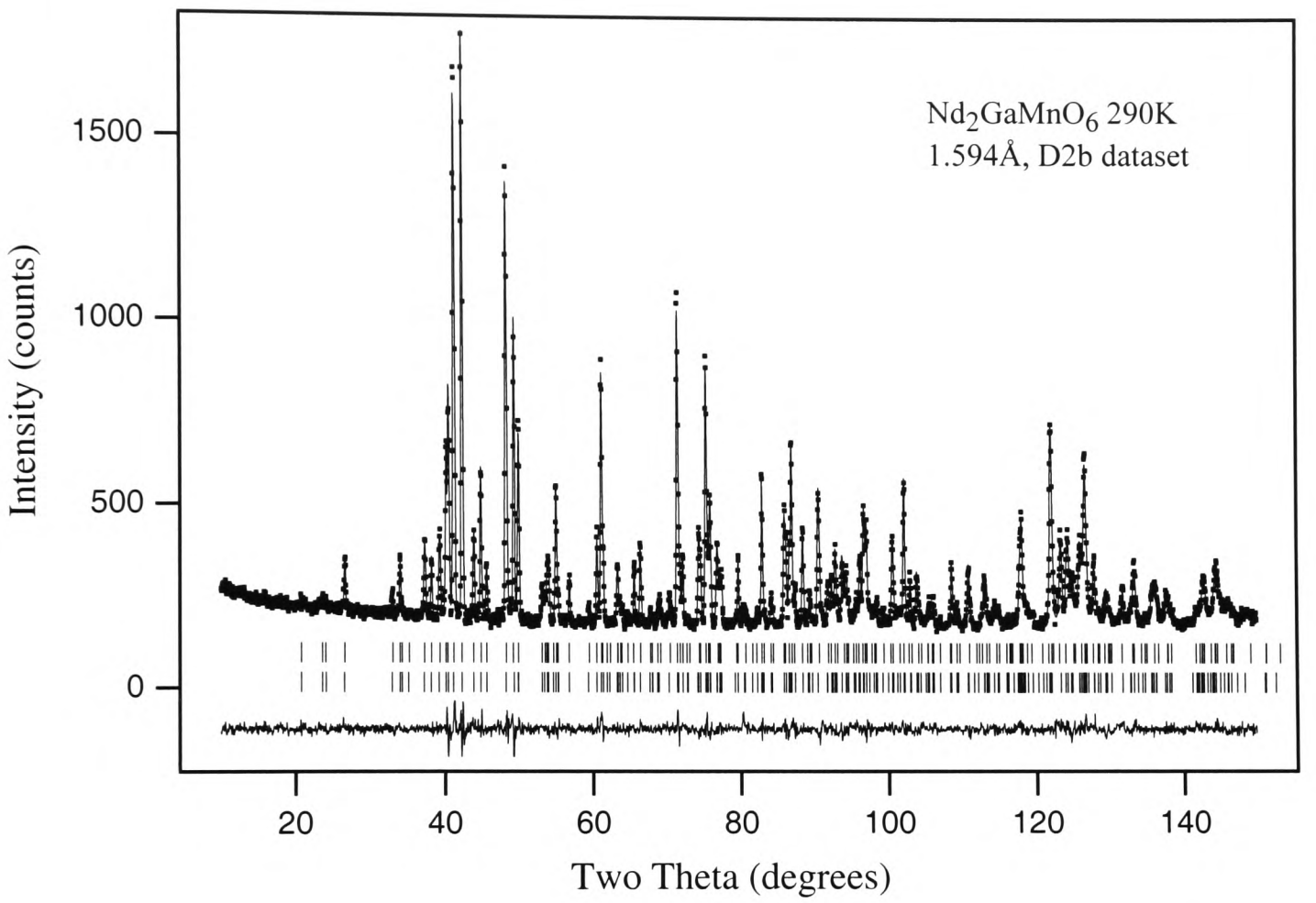


Figure 5.2.12 Observed (dots) and calculated (line) neutron powder diffraction profiles for $Nd_2GaMnO_{6+\delta}$ at 290K. Upper and lower tick marks represent minority and majority phases, respectively.

The most striking difference between the room temperature neutron diffraction profiles for La and Nd compounds, is the greater number of distinct peaks which is observed in the latter, as a consequence of the dramatic deviation between the a and c lattice parameters in $Nd_2GaMnO_{6+\delta}$. This signals enhanced distortion in the orthorhombic cell, in comparison to that present in the La analogue.

Initial attempts to model $Nd_2GaMnO_{6+\delta}$ in space group *Pnma* using a single phase model, resulted in the fit parameters R_{wp} = 5.37%, R_p = 4.10%, and χ^2_{red} = 4.194 for 46 variables. This single phase model was considered satisfactory, originally; however, careful examination of the peak shape of the 200 reflection revealed distinct asymmetry, and several

biphasic models were then investigated, in order to improve the fit to this reflection in particular. Although combinations of orthorhombic and monoclinic ($P2_1/n$) space groups were investigated, the most convincing fit to the 290K data was achieved using a biphasic model comprised of two orthorhombic phases in space group *Pnma*. The two orthorhombic phases fractions refined to the ratio 65.2(2)%:34.8(2)% by weight, and the improvement in the fit to the data can be gauged by the reduction in R_{wp} to 4.32%, with other residual fit parameters taking the following values: R_p = 3.45%, DWd = 1.316 and χ^2_{red} = 1.370 for 51 variables. Use of the space group *Pnma* indicates that the disordered arrangement of Ga^{3+} and Mn^{3+} appears to remain intact on lowering $\langle r_A \rangle$, by comparison with the La analogue. The majority, and minority phase 290K structural parameters are tabulated together below, for comparative purposes.

Table 5.2.17 Structural parameters for biphasic $Nd_2GaMnO_{6+\delta}$ at 290K:

Majority Phase, 65.2(2)% by weight

Lattice Parameters(Å) a = 5.63677(12); b = 7.65070(13); c = 5.41778(13); V = 233.643(7)Å^3

Atom	Site	U_{iso} (Å^2)	Fraction (%)	x	y	z
Nd(1)	4c	0.0038(4)	100	0.0560(3)	1/4	0.0116(6)
Mn(2)	4b	0.0030(20)[a]	50	0	0	1/2
Ga(3)	4b	0.0030(20)[a]	50	0	0	1/2
O(4)	8d	0.0048(4)	100	0.3063(3)	0.0443(3)	0.2899(5)
O(5)	4c	0.0057(7)	100	0.4801(5)	1/4	-0.0828(8)

Minority Phase, 34.8(2)% by weight

Lattice Parameters(Å) a = 5.62191(26); b = 7.66164(32); c = 5.41691(32); V = 233.323(17)Å^3

Atom	Site	U_{iso} (Å^2)	Fraction (%)	x	y	z
Nd(1)	4c	0.0114(11)	100	0.0525(9)	1/4	0.0109(15)
Mn(2)	4b	0.0069(47)[a]	50	0	0	1/2
Ga(3)	4b	0.0069(47)[a]	50	0	0	1/2
O(4)	8d	0.0176(12)	100	0.3006(10)	0.0412(7)	0.2859(15)
O(5)	4c	0.0131(17)	100	0.4842(11)	1/4	-0.0854(20)

[a] Constrained to be the same.

It was thought, perhaps, that the two phases constituting $Nd_2GaMnO_{6+\delta}$ at 290K, may contain different concentrations of Mn and Ga cations. However, as shown by Table 5.2.17, the cation occupancies in each phase refined to 50%, and fixing the fractions at values

deviating from this ratio led to instability in the refinement. Therefore, it appears that, as in La_2GaMnO_6, Ga has entered the structure randomly, and maintains a random distribution in the two discrete phases comprising the Nd sample. As for the La analogue, it was not possible to improve significantly the quality of the fit by incorporating nonstoichiometry on either the Nd, Mn or O sublattices in the 290K refinement of $Nd_2GaMnO_{6+\delta}$. Therefore, $Nd_2GaMnO_{6+\delta}$ is formulated as Nd_2GaMnO_6 from this point onwards. Although it was not possible to confirm this observation for either sample due to the irreproducibility of results of iodometric titration, reproducible results were obtained on the single phase of $Nd_2GaMnO_{6+\delta}$ obtained from further thermal treatment of the sample described here. An oxygen content in $Nd_2GaMnO_{6+\delta}$ consistent with a δ value of 0.004 was established[1], in good agreement with the diffraction data for the treated sample.

As shown from Table 5.2.15, thermal displacement parameters for oxygen anions in both phases of Nd_2GaMnO_6 at 290K are isostropic, in comparison with those in the La_2GaMnO_6 sample. The significant bondlengths and bond angles in biphasic Nd_2GaMnO_6 are given in Table 5.2.18, and all parameters presented are labelled as for the La analogue, using the atom labelling scheme introduced in Figures 5.2.2 to 5.2.4.

---

[1] Iodometric titrations were carried out by the author and J. Burley.

Table 5.2.18 Selected distances (Å) and angles (°) for biphasic Nd_2GaMnO_6 at 290K:

Majority Phase, 65.2(2)% by weight			
Nd - O Bondlength (Å)		Mn/Ga - O Bondlength (Å) or Angle (°)[a]	
Nd - O(4) x 2	2.5966(35)	Mn - O(4) x 2	1.9427(30)
Nd - O(4) x 2	2.6672(28)	Mn - O(4) x 2	2.0960(26)
Nd - O(4) x 2	3.4519(35)	Mn - O(5) x 2	1.9679(11)
Nd - O(4) x 2	2.3685(33)	Mn - O(4) - Mn	150.88(14)
Nd - O(5)	2.445(4)	Mn - O(5) - Mn	152.78(26)
Nd - O(5)	3.287(4)	O(4) - Mn - O(4)	89.75(4)
Nd - O(5)	2.362(5)	O(4) - Mn - O(5)	89.02(14)
Nd - O(5)	3.125(5)	O(4) - Mn - O(5)	89.22(11)
Minority Phase, 34.8(2)% by weight			
Nd - O Bondlength (Å)		Mn/Ga - O Bondlength (Å) or Angle (°)[a]	
Nd - O(4) x 2	2.593 (9)	Mn - O(4) x 2	1.938(8)
Nd - O(4) x 2	2.673(7)	Mn - O(4) x 2	2.074(7)
Nd - O(4) x 2	3.392(8)	Mn - O(5) x 2	1.9719(25)
Nd - O(4) x 2	2.403(9)	Mn - O(4) - Mn	153.3(4)
Nd - O(5)	2.483(8)	Mn - O(5) - Mn	152.5(6)
Nd - O(5)	3.236(8)	O(4) - Mn - O(4)	89.98(8)
Nd - O(5)	2.339(13)	O(4) - Mn - O(5)	88.92(27)
Nd - O(5)	3.133(13)	O(4) - Mn - O(5)	89.86(34)

[a] Although only Mn atoms are listed, Ga shares the Mn site in a 1:1 ratio.

The Nd cations occupying the coordination environment shown in Figure 5.2.3 have four Nd-O bondlengths in excess of 3Å (in both majority and minority phases), suggesting pseudo-eightfold coordination of Nd cations, similar to the coordination of La cations in La_2GaMnO_6. The Mn-O(4)-Mn and Mn-O(5)-Mn bond angles in Nd_2GaMnO_6 are of the order of 151°, approximately 8-9° lower than the values obtained for the La analogue. This reflects the increased structural distortion in the Nd compound, as a result of the smaller size of the Nd^{3+} cation.

5.2.3.2 SQUID magnetometry measurements

The molar magnetic susceptibility of Nd_2GaMnO_6 as a function of temperature at 100G is presented in Figure 5.2.13. Figure 5.2.14 gives an enlarged view of the low temperature (<50K) region of magnetisation, plotted as μ_B per formula unit, with the inset showing the first derivative of the (FC) signal with respect to temperature, against T(K). The inset reveals two distinct minima in the low temperature region. The first minimum appears at a temperature of 20K, coinciding with the onset of significant divergence between FC and ZFC signals. The second minimum occurs at 10K, and could represent the onset of magnetic order of Nd^{3+} cations. After the 10K minimum, the FC signal continues to increase until the lowest measuring temperature. The temperature dependence of molar susceptibility at 1kG is shown in Appendix 3, Figure 3.2.

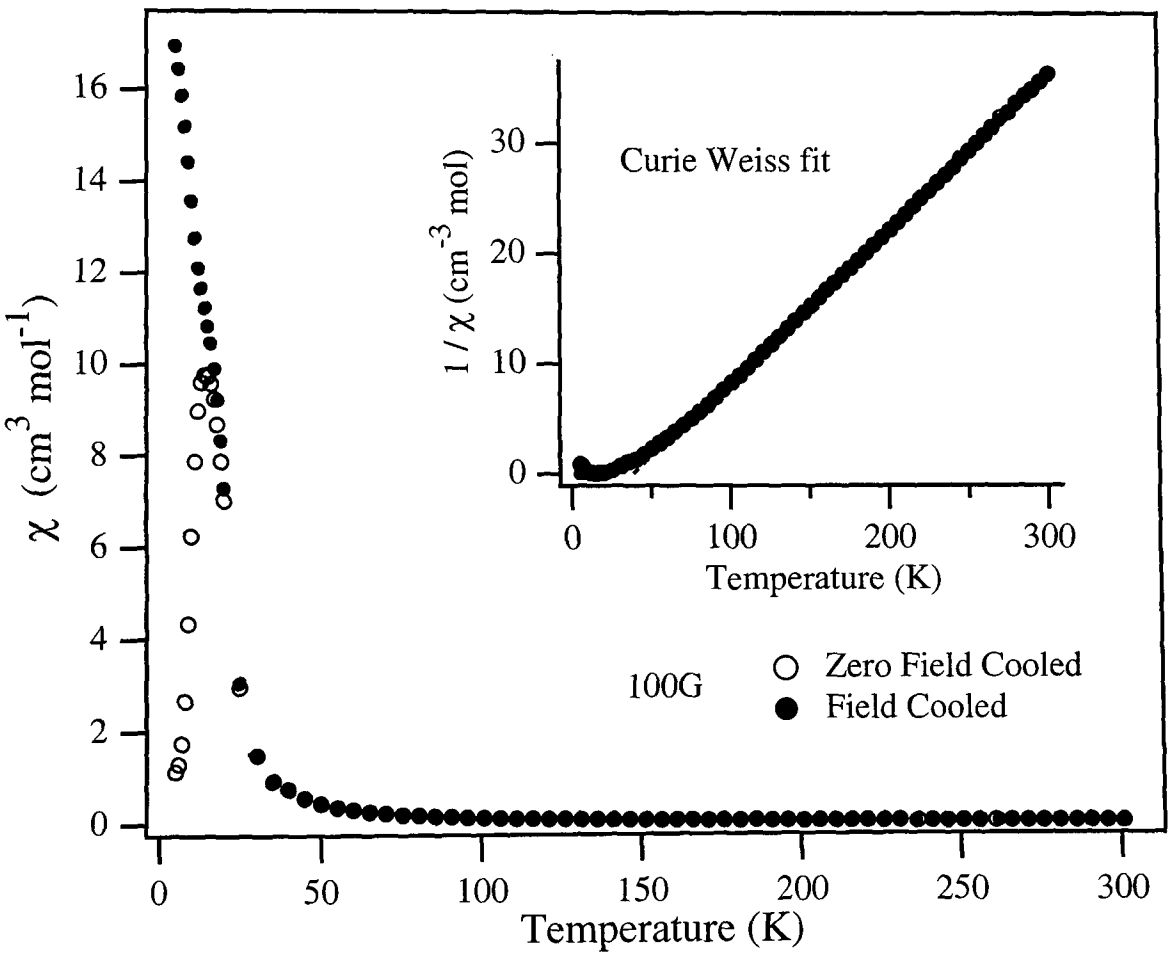


Figure 5.2.13 Molar magnetic susceptibility as a function of temperature for Nd_2GaMnO_6 at 100G.

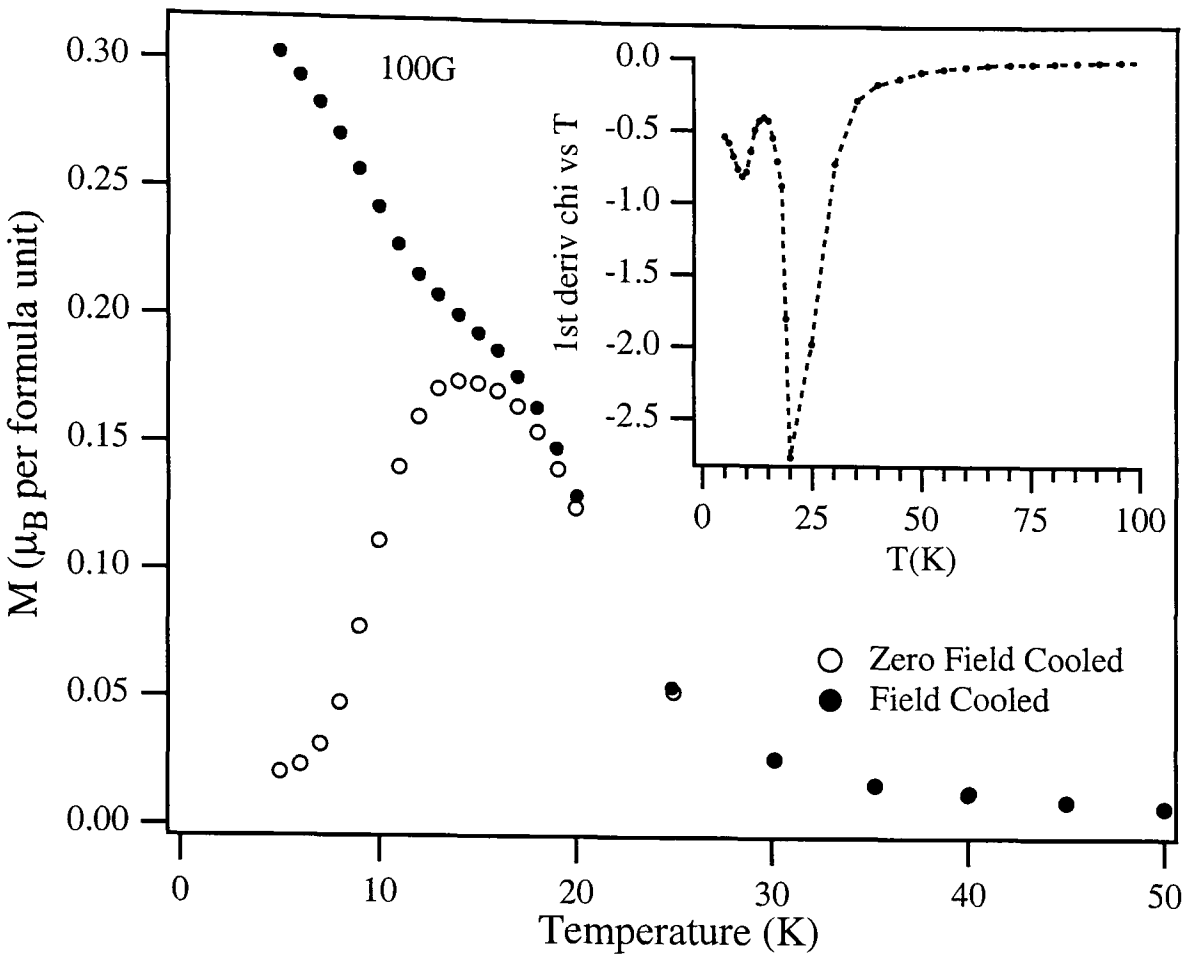


Figure 5.2.14 Magnetisation as a function of temperature for Nd_2GaMnO_6 at 100G, with an inset showing the first derivative of Chi (χ) (FC) with respect to T(K).

The application of the Curie-Weiss law for the temperature dependence of inverse magnetic susceptibility for Nd_2GaMnO_6, gives the parameters shown in Table 5.2.19.

Table 5.2.19 Curie-Weiss fit parameters for 100G data:

Compound	Temperature range (K)	C_m (cm^3 K mol^{-1})	θ(K)	Estimated C_m (cm^3 K mol^{-1})
Nd_2GaMnO_6	195 - 300	7.00(13)	45.09(34)	6.28

The fit results in a positive Weiss constant θ(K), suggesting ferromagnetic interactions, and the model is applicable over a significantly wider temperature range than in the La sample. The estimated value of C_m of 6.28 (cm^3 K mol^{-1}) is calculated assuming the presence of one mole of Mn^{3+}, d^4 cations, plus the presence of 2 moles of Nd^{3+} per formula unit (g = 0.727 for the latter), as formulated in equation 5.2.2. The observed value of C_m of 7.00 (cm^3 K mol^{-1}) exceeds the calculated value. Again, this is indicative of ferromagnetic correlations.

$$\text{Estimated } C_m(Nd_2GaMnO_6) = \frac{1}{8}\left\{(\mu_{eff}Mn^{3+})^2 + 2(\mu_{eff}Nd^{3+})^2\right\} \quad \text{eqn. (5.2.2)}$$

M(H) loops for Nd_2GaMnO_6 at five temperatures are presented in Figures 5.2.15 to 5.2.17. As in La_2GaMnO_6, the behaviour at 300K is represented by a linear dependence upon field. At 50K, there is a slight degree of curvature in the variation of magnetisation with field which is more significant by 30K; however, neither curve exhibits significant hysteresis. At 15 and 5K, curves exhibiting significant non-linearity and hysteresis are obtained.

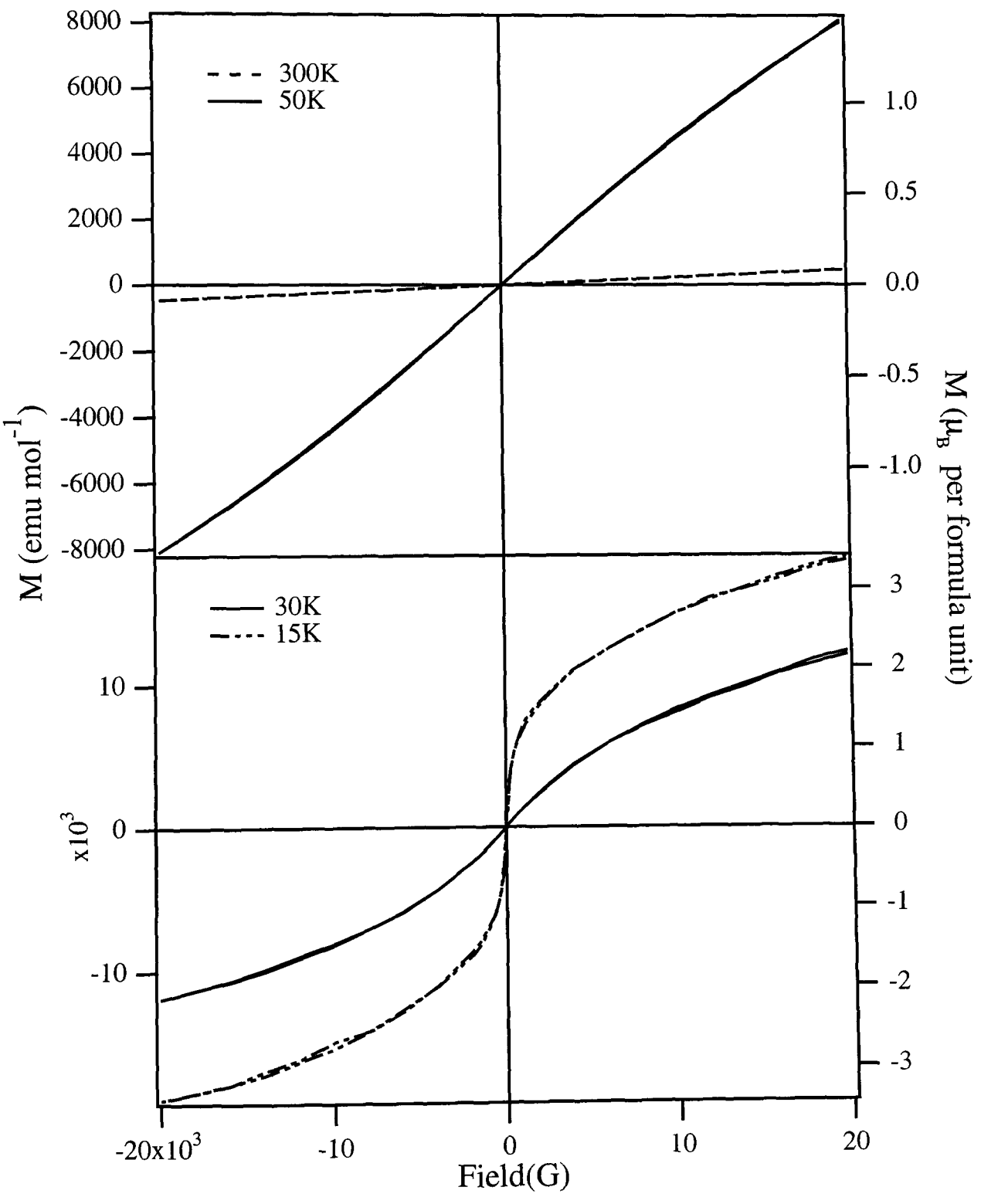


Figure 5.2.15 Magnetisation as a function of field (-20≤ Field(kG) ≤ 20) for Nd_2GaMnO_6 at 300, 50, 30 and 15K.

The magnetic moment per mole of Nd_2GaMnO_6 at 5K and 50kG reaches 5.59μ_B. As for the La analogue, there is no clear evidence of spin glass behaviour in field dependent magnetisation data.

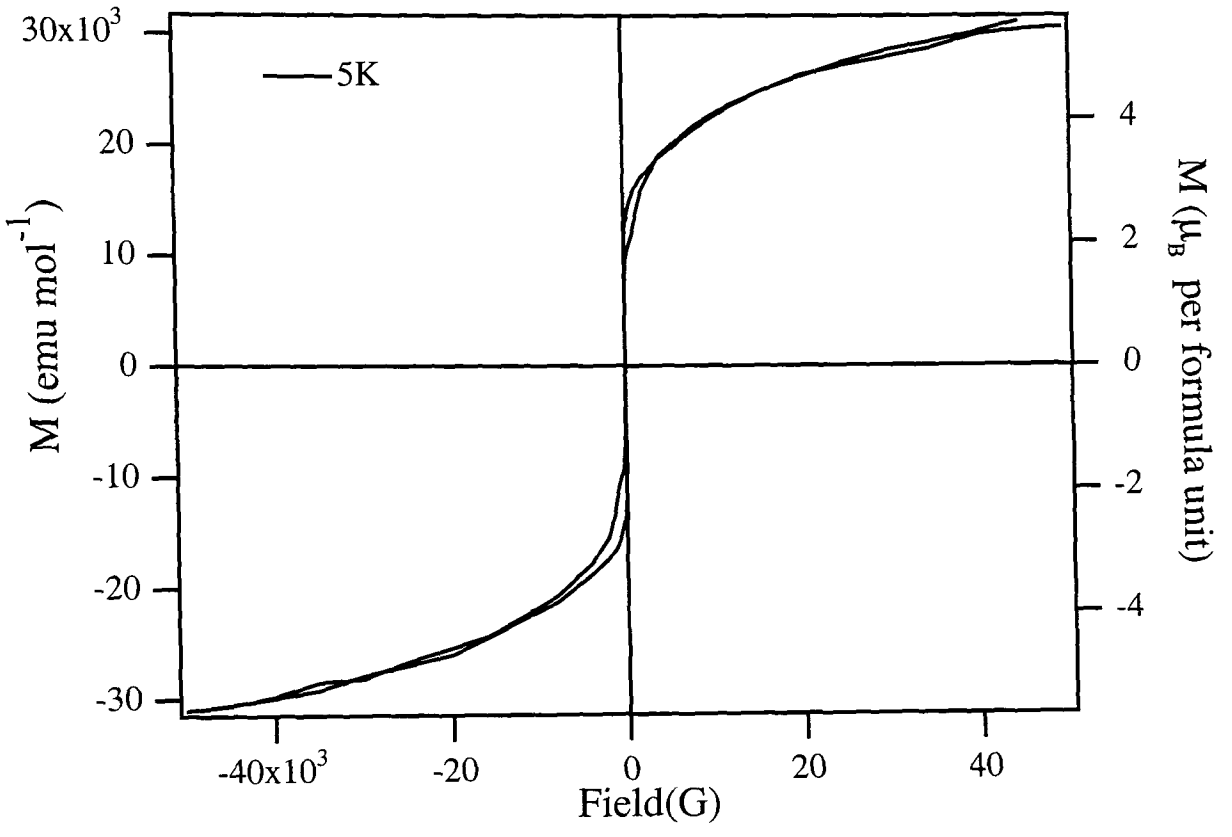


Figure 5.2.16 Magnetisation as a function of field (-50 ≤ Field(kG) ≤ 50) at 5K for Nd_2GaMnO_6.

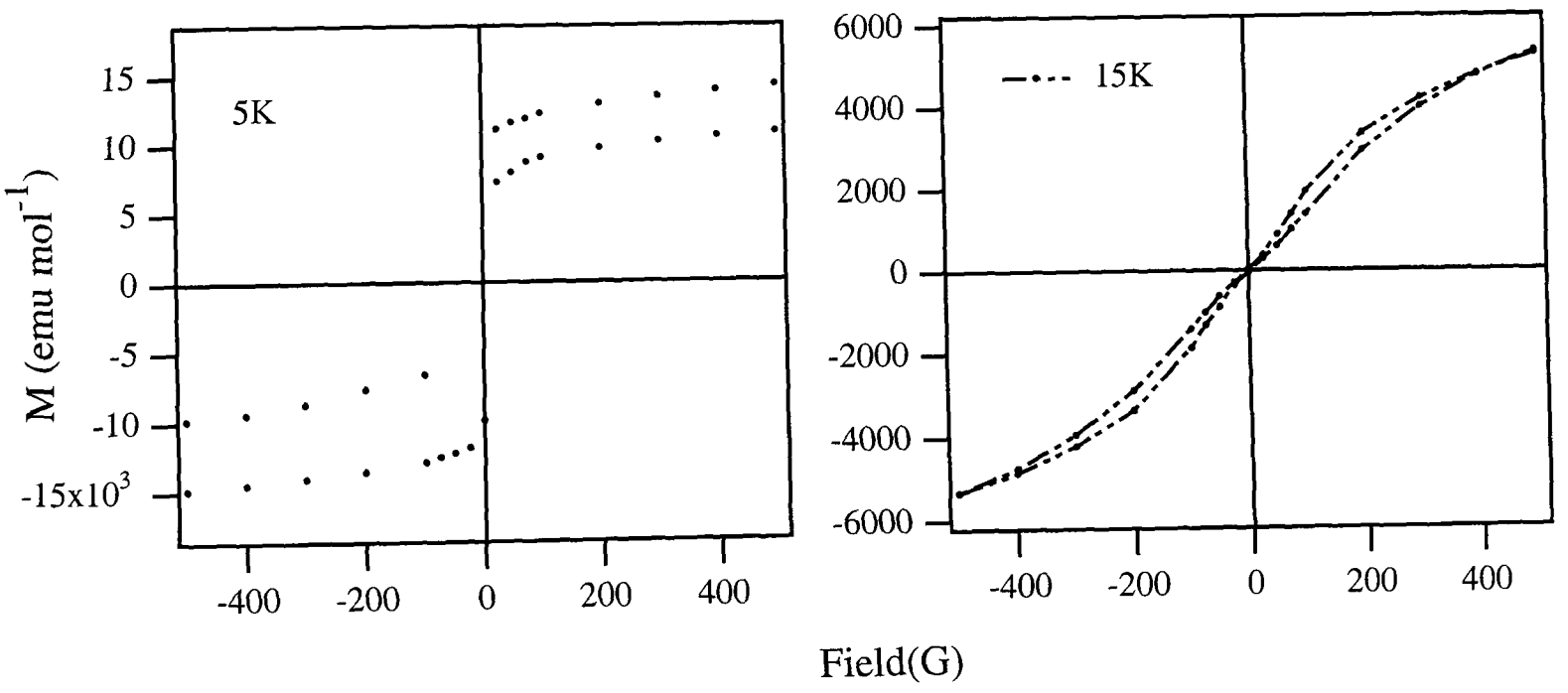


Figure 5.2.17 Enlarged view of the (-500≤ Field(G) ≤ 500) region of field dependent magnetisation for Nd_2GaMnO_6 at 15 and 5K.

Temperatures of 5K and 1.7K were those selected at which to perform low temperature neutron diffraction studies, in order to complement the magnetic data presented in this section. The lower value of 'intermediate' temperature selected for Nd_2GaMnO_6,

compared with La_2GaMnO_6, (5 as opposed to 50K), reflects the lower magnetic transition temperature in the former compound, as evidenced from SQUID magnetometry studies. The results of the 5K and 1.7K neutron diffraction experiments are presented below.

5.2.3.3 5K and 1.7K powder neutron diffraction measurements

The observed and calculated neutron diffraction profile for Nd_2GaMnO_6 at 5K presented in Figure 5.2.18, shows the presence of additional, magnetic Bragg peaks in the low angle region, the most striking of which is the 010 reflection. There is also significant enhancement of intensity in the 121 and 002 'nuclear' reflections from magnetic scattering. The phase ratio between majority and minority components, obtained from the 290K refinement, was allowed to vary, initially, in the 5K and 1.7K refinements described in this section. However, since it showed no significant deviation from the ratio established at 290K, it was fixed at the 65.2(2)%:34.8(2)% value (by weight), established at the higher temperature. The structural parameters of biphasic Nd_2GaMnO_6 at 5K are given in Table 5.2.20.

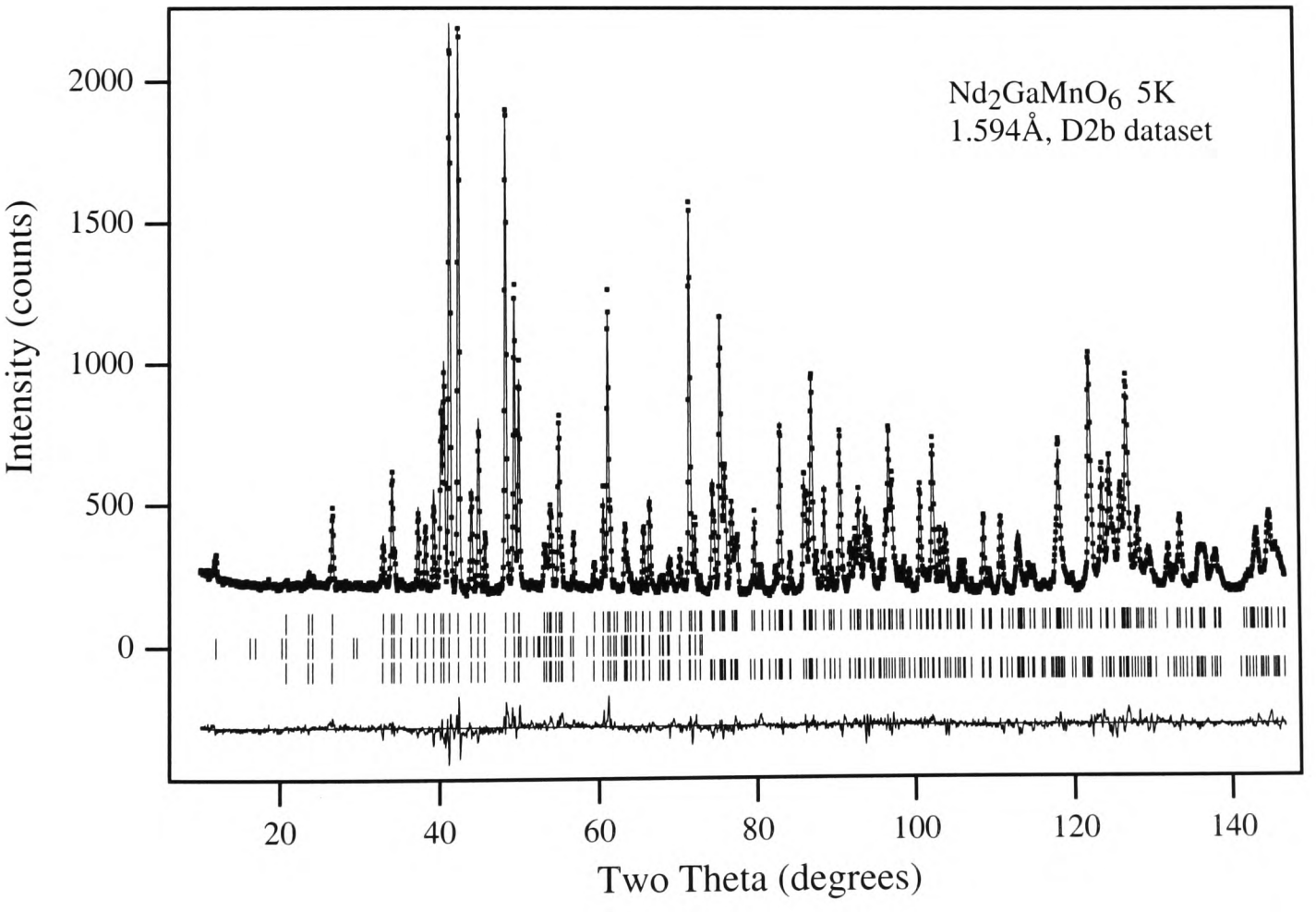


Figure 5.2.18 Observed (dots) and calculated (line) neutron powder diffraction profiles for Nd_2GaMnO_6 at 5K. Upper and lower tick marks represent minority and majority phases, respectively. The middle set of tick marks represents magnetic Bragg peaks.

Table 5.2.20 Structural parameters for biphasic $Nd_2GaMnO_{6+\delta}$ at 5K:

Majority Phase, 65.2% by weight

Lattice Parameters(Å) a = 5.63850(16); b = 7.63792(22); c = 5.41329(18); V = 233.131(17)Å^3

Atom	Site	U_{iso} (Å^2)	Fraction (%)	x	y	z
Nd(1)	4c	0.0002[a]	100	0.0570(3)	1/4	0.0117(6)
Mn(2)	4b	0.0002[a]	50	0	0	1/2
Ga(3)	4b	0.0002[a]	50	0	0	1/2
O(4)	8d	0.0029(4)	100	0.3049(3)	0.0442(3)	0.2894(6)
O(5)	4c	0.0015(6)	100	0.4791(4)	1/4	-0.0874(8)

Minority Phase, 34.8% by weight

Lattice Parameters(Å) a = 5.62427(19); b = 7.64542(33); c = 5.41228(27); V = 232.728(19)Å^3

Atom	Site	U_{iso} (Å^2)	Fraction (%)	x	y	z
Nd(1)	4c	-0.0011(9)	100	0.0557(6)	1/4	0.0117(12)
Mn(2)	4b	0.0022(23)[a]	50	0	0	1/2
Ga(3)	4b	0.0022(23)[a]	50	0	0	1/2
O(4)	8d	0.0028(7)	100	0.3053(6)	0.0421(6)	0.2885(10)
O(5)	4c	0.0018(11)	100	0.4821(8)	1/4	-0.0807(14)

[a] Constrained to be the same.

Table 5.2.21 Selected distances (Å) and angles (°) for biphasic Nd_2GaMnO_6 at 5K:

Majority Phase, 65.2% by weight			
Nd - O Bondlength (Å)		Mn/Ga - O Bondlength (Å) or Angle (°)[a]	
Nd - O(4) x 2	2.5851(9)	Mn - O(4) x 2	1.9441(5)
Nd - O(4) x 2	2.6654(6)	Mn - O(4) x 2	2.0901(4)
Nd - O(4) x 2	3.4459(6)	Mn - O(5) x 2	1.9707(5)
Nd - O(4) x 2	2.3767(8)	Mn - O(4) - Mn	151.257(2)
Nd - O(5)	2.4399(15)	Mn - O(5) - Mn	151.35(16)
Nd - O(5)	3.3022(12)	O(4) - Mn - O(4)	89.87(5)
Nd - O(5)	2.3386(17)	O(4) - Mn - O(5)	88.66(16)
Nd - O(5)	3.1470(10)	O(4) - Mn - O(5)	89.50(15)
Minority Phase, 34.8% by weight			
Nd - O Bondlength (Å)		Mn/Ga - O Bondlength (Å) or Angle (°)[a]	
Nd - O(4) x 2	2.5963(7)	Mn - O(4) x 2	1.9341(7)
Nd - O(4) x 2	2.6567(8)	Mn - O(4) x 2	2.0888(6)
Nd - O(4) x 2	3.4284(8)	Mn - O(5) x 2	1.9632(9)
Nd - O(4) x 2	2.3826(12)	Mn - O(4) - Mn	151.89(12)
Nd - O(5)	2.4499(9)	Mn - O(5) - Mn	153.58(32)
Nd - O(5)	3.2646(11)	O(4) - Mn - O(4)	89.84(13)
Nd - O(5)	2.3689(11)	O(4) - Mn - O(5)	89.20(11)
Nd - O(5)	3.1074(15)	O(4) - Mn - O(5)	89.35(21)

[a] Although only Mn atoms are listed, Ga shares the Mn site in a 1:1 ratio.

As shown from Table 5.2.21, the Nd^{3+} primary coordination sphere is comprised of eight oxide anions, a similar environment as that refined at 290K. A more detailed analysis of the temperature dependence of key structural parameters is given in Section 5.3.

The magnetic cell refined from the 5K D2b dataset is denoted by the middle set of tick marks in Figure 5.2.18. The evolution of the 010 magnetic Bragg peak at 7.65Å as the only additional magnetic reflection at 5K, (and the fact that it could be indexed using the dimensions of the existing cell), meant it would not be necessary to enlarge the original cell to account for the magnetic structure. In order for the 010 reflection to be allowed, this suggested that the serial reflection condition due to the 2_1 screw axis in the y direction had been violated.

Therefore, for the magnetic structure, this screw axis had been lost. This observation was the first clue to the solution of the magnetic structure. Since the dimensions of the nuclear and magnetic cells were known to be identical, it was possible to employ 'Bertaut's macroscopic theory[28]' as an aid to the magnetic structure solution.

The magnetic structure of Nd_2GaMnO_6 at 5K modelled as '$A_X F_Y G_Z$' for the Mn sublattice, and 'F_Y' for the Nd sublattice, (using notation derived by Bertaut), gave a good fit to the observed intensity in the low angle region shown in detail in Figure 5.2.21 (b). The magnetic structure resulting from Bertaut's '$A_X F_Y G_Z$' notation is depicted in Figure 5.2.19, and it is shown to represent competing, superexchange interactions on the Mn sublattice along the [010] direction of the unit cell. The components of the Mn moment along z refined to zero, and were fixed consequently at this value. At 5K, the magnitude of Nd moments aligned along y refined to $0.93(4)\mu_B$. The magnitude of the Mn ordered moment refined to $3.00(7)\mu_B$, oriented at an angle θ of 25.8(9)° to y. This gives components My and Mx of $2.70(8)\mu_B$ and +/- $1.31(5)\mu_B$, respectively. The Mn ferromagnetic component is $2.70(8)\mu_B$ along [010] therefore, and the competing antiferromagnetic superexchange results in an antiferromagnetic component of +/- $1.31(5)\mu_B$ along the same direction.

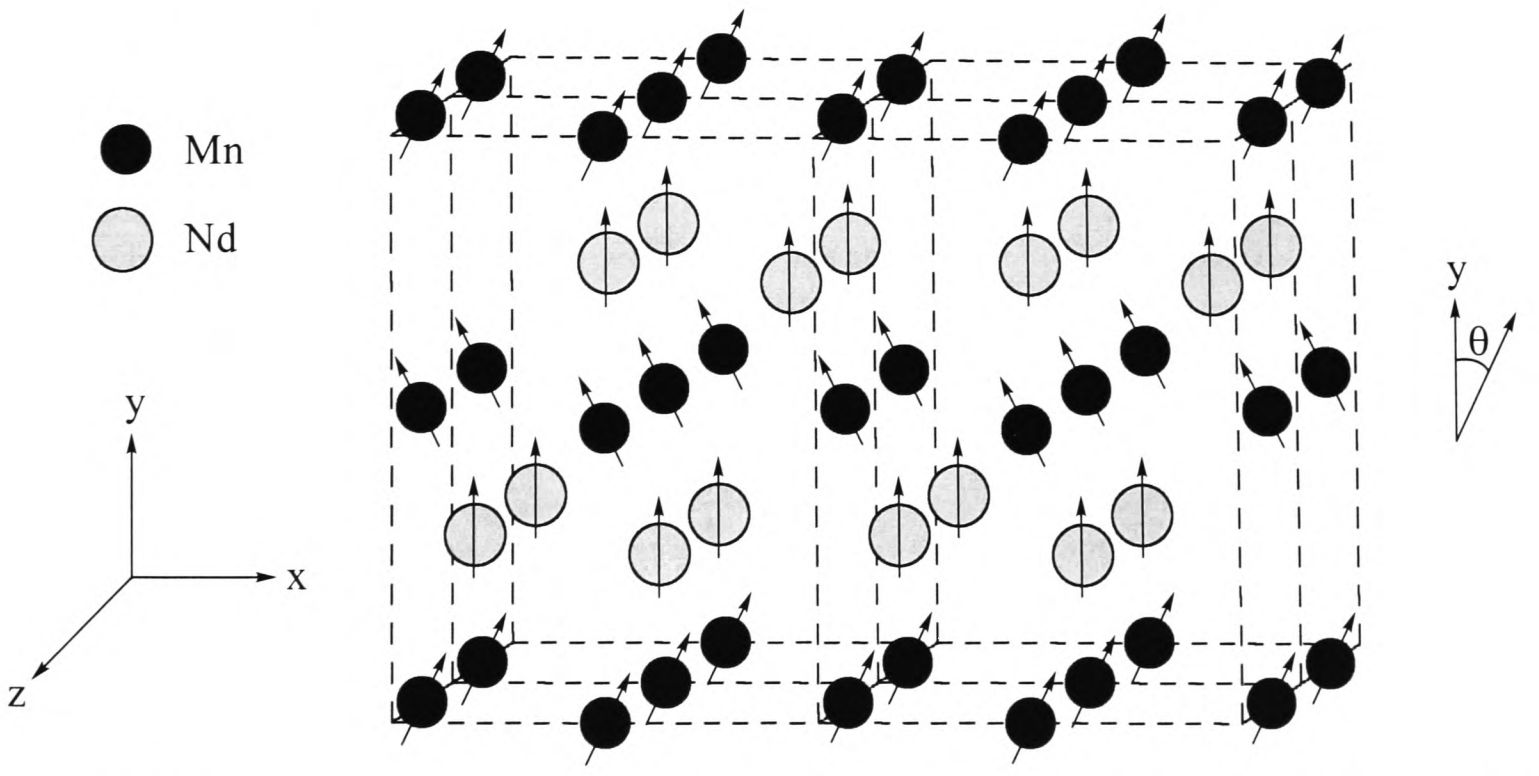


Figure 5.2.19 Magnetic structure of Nd_2GaMnO_6 at 5K in which the spin directions of Mn and Nd cations are shown by arrows.

The lattice parameters of the magnetic cell initially were allowed to refine freely;

however, this lead to instability in the refinement and they were constrained then at the values of the majority nuclear cell. In addition, appropriate constraints were imposed on atomic positions and isotropic temperature factors between the majority phase and the magnetic structure in the 5K dataset. However, the phase fraction of the magnetic cell was not reduced to 65%, as there was no evidence to suggest that the bulk of the sample does not show long range magnetic order. Therefore, all magnetic data quoted in Table 5.2.22 are per atom in the sample, not per atom in the majority phase. The space group of the magnetic cell was set at *P1*, hence the Mn and Nd coordinates were generated according to the 4b and 4c site symmetries, respectively, in space group *Pnma*.

Thus, the magnetic structure of Nd_2GaMnO_6 at 5K is somewhat different to that in La_2GaMnO_6 at the same temperature. The isotropic ferromagnetic interactions in the latter compound have been replaced by a mixture of ferromagnetic and antiferromagnetic superexchange in the Nd analogue. Table 5.2.22 summarises magnetic cell parameters refined at 5K.

Table 5.2.22 Atomic coordinates and magnetic components for Mn/Nd atoms comprising the magnetic cell in Nd_2GaMnO_6 at 5K:

Atom	Site	Fraction (%)[a]	U_{iso} (Å^2)	x	y	z	Mx (μ_B)	My (μ_B)	Mz (μ_B)
Mn(1)	1	50	0.0002	0	0	1/2	1.31(5)	2.70(8)	0
Mn(2)	1	50	0.0002	0	1/2	1/2	-1.31(5)	2.70(8)	0
Mn(3)	1	50	0.0002	1/2	1/2	0	-1.31(5)	2.70(8)	0
Mn(4)	1	50	0.0002	1/2	0	0	1.31(5)	2.70(8)	0
Nd(5)	1	100	0.0002	0.0570	1/4	0.0117	0	0.93(4)	0
Nd(6)	1	100	0.0002	0.5570	1/4	0.4883	0	0.93(4)	0
Nd(7)	1	100	0.0002	0.9430	3/4	0.9883	0	0.93(4)	0
Nd(8)	1	100	0.0002	0.4430	3/4	0.5117	0	0.93(4)	0

[a] The 50% occupancy of positions on the magnetic cell reflects the disordered array of Mn and Ga across transition metal sites.

Figure 5.2.20 shows the 1.7K neutron diffraction pattern for Nd_2GaMnO_6.

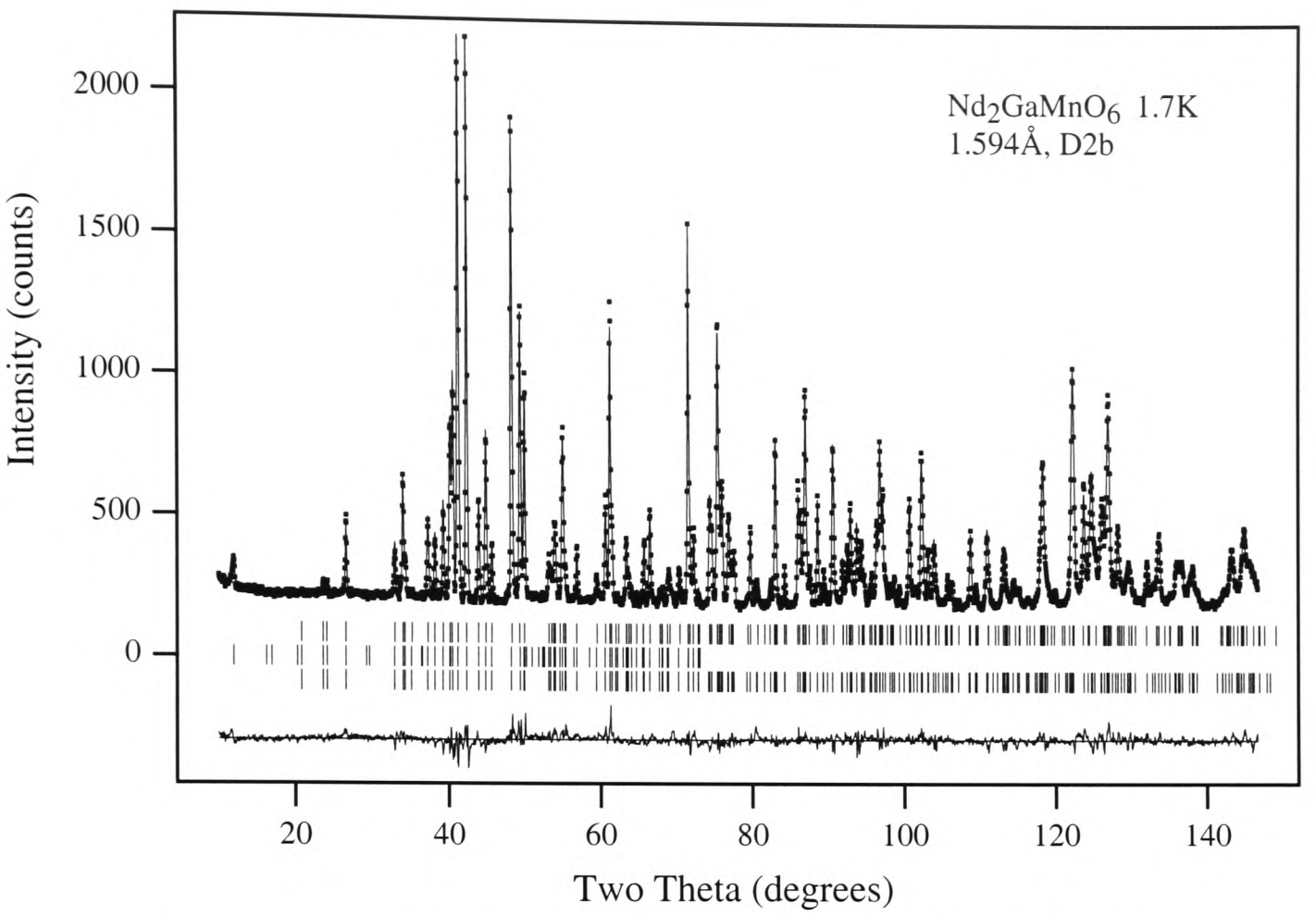


Figure 5.2.20 Observed (dots) and calculated (line) neutron powder diffraction profiles for Nd_2GaMnO_6 at 1.7K. Upper and lower tick marks denote minority and majority phases respectively. The middle set of tick marks represents magnetic Bragg peaks.

Table 5.2.23 Structural parameters for biphasic $Nd_2GaMnO_{6+\delta}$ at 1.7K:

Majority Phase, 65.2% by weight

Lattice Parameters(Å) a = 5.63618(9); b = 7.63502(16); c = 5.41107(14) ; V = 232.851(6)Å^3

Atom	Site	U_{iso} (Å^2)	Fraction (%)	x	y	z
Nd(1)	4c	0.0002[a]	100	0.0568(3)	1/4	0.0114(7)
Mn(2)	4b	0.0002[a]	50	0	0	1/2
Ga(3)	4b	0.0002[a]	50	0	0	1/2
O(4)	8d	0.0022(4)	100	0.3054(3)	0.0434(4)	0.2895(6)
O(5)	4c	0.0016(6)	100	0.4800(4)	1/4	-0.0870(8)

Minority Phase, 34.8% by weight

Lattice Parameters(Å) a = 5.62233(15); b = 7.64183(29); c = 5.41031(26); V = 232.453(11)Å^3

Atom	Site	U_{iso} (Å^2)	Fraction (%)	x	y	z
Nd(1)	4c	-0.0025(20)	100	0.0557(6)	1/4	0.0108(13)
Mn(2)	4b	-0.0002(23)[a]	50	0	0	1/2
Ga(3)	4b	-0.0002(23)[a]	50	0	0	1/2
O(4)	8d	0.0052(8)	100	0.3052(6)	0.0441(7)	0.2890(11)
O(5)	4c	0.0037(12)	100	0.4796(8)	1/4	-0.0798(15)

[a] Constrained to be the same.

Table 5.2.24 Selected distances (Å) and angles (°) for biphasic Nd_2GaMnO_6 at 1.7K:

Majority Phase, 65.2% by weight			
Nd - O Bondlength (Å)		Mn/Ga - O Bondlength (Å) or Angle (°)[a]	
Nd - O(4) x 2	2.5911(3)	Mn - O(4) x 2	1.9410(3)
Nd - O(4) x 2	2.6575(4)	Mn - O(4) x 2	2.0901(2)
Nd - O(4) x 2	3.4410(3)	Mn - O(5) x 2	1.9692(3)
Nd - O(4) x 2	2.3782(2)	Mn - O(4) - Mn	151.39(16)
Nd - O(5)	2.4437(3)	Mn - O(5) - Mn	151.54(13)
Nd - O(5)	3.2942(4)	O(4) - Mn - O(4)	89.91(11)
Nd - O(5)	2.3372(5)	O(4) - Mn - O(5)	88.65(10)
Nd - O(5)	3.1441(7)	O(4) - Mn - O(5)	89.72(11)
Minority Phase, 34.8% by weight			
Nd - O Bondlength (Å)		Mn/Ga - O Bondlength (Å) or Angle (°)[a]	
Nd - O(4) x 2	2.5897(6)	Mn - O(4) x 2	1.9387(7)
Nd - O(4) x 2	2.6654(8)	Mn - O(4) x 2	2.0880(5)
Nd - O(4) x 2	3.4358(8)	Mn - O(5) x 2	1.9622(7)
Nd - O(4) x 2	2.3728(5)	Mn - O(4) - Mn	151.257(1)
Nd - O(5)	2.4325(7)	Mn - O(5) - Mn	153.662(2)
Nd - O(5)	3.2757(9)	O(4) - Mn - O(4)	89.714(3)
Nd - O(5)	2.3706(11)	O(4) - Mn - O(5)	88.574(1)
Nd - O(5)	3.1083(15)	O(4) - Mn - O(5)	89.375(1)

[a] Although only Mn atoms are listed, Ga shares the Mn site in a 1:1 ratio.

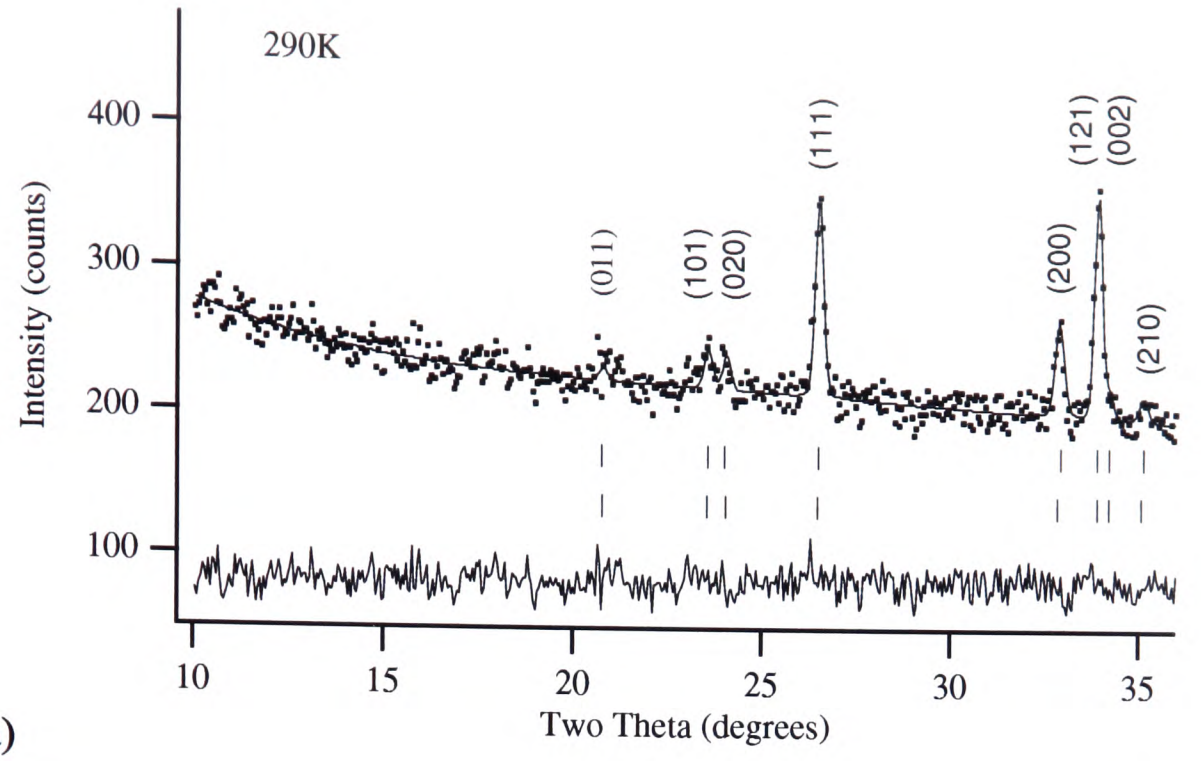
The magnetic structure of Nd_2GaMnO_6 denoted by '$A_X F_Y G_Z$' for the Mn sublattice and 'F_Y' for the Nd sublattice, and represented in Figure 5.2.19, was retained at 1.7K. The fit to the observed intensity in the low angle region is shown in Figure 5.2.21 (c). At 1.7K, the magnitude of the ordered Nd moment aligned along y refined to 0.96(4)μ_B. The magnitude of the Mn ordered moment refined to 3.15(7)μ_B, oriented at an angle θ of 26.1(9)° to y (as illustrated in Figure 5.2.19). This gives components My and Mx of 2.82(7) and +/- 1.38(4)μ_B, respectively. The 1.7K magnetic parameters are summarised in Table 5.2.25.

Table 5.2.25 Atomic coordinates and magnetic components for Mn/Nd atoms comprising the magnetic cell in Nd_2GaMnO_6 at 1.7K

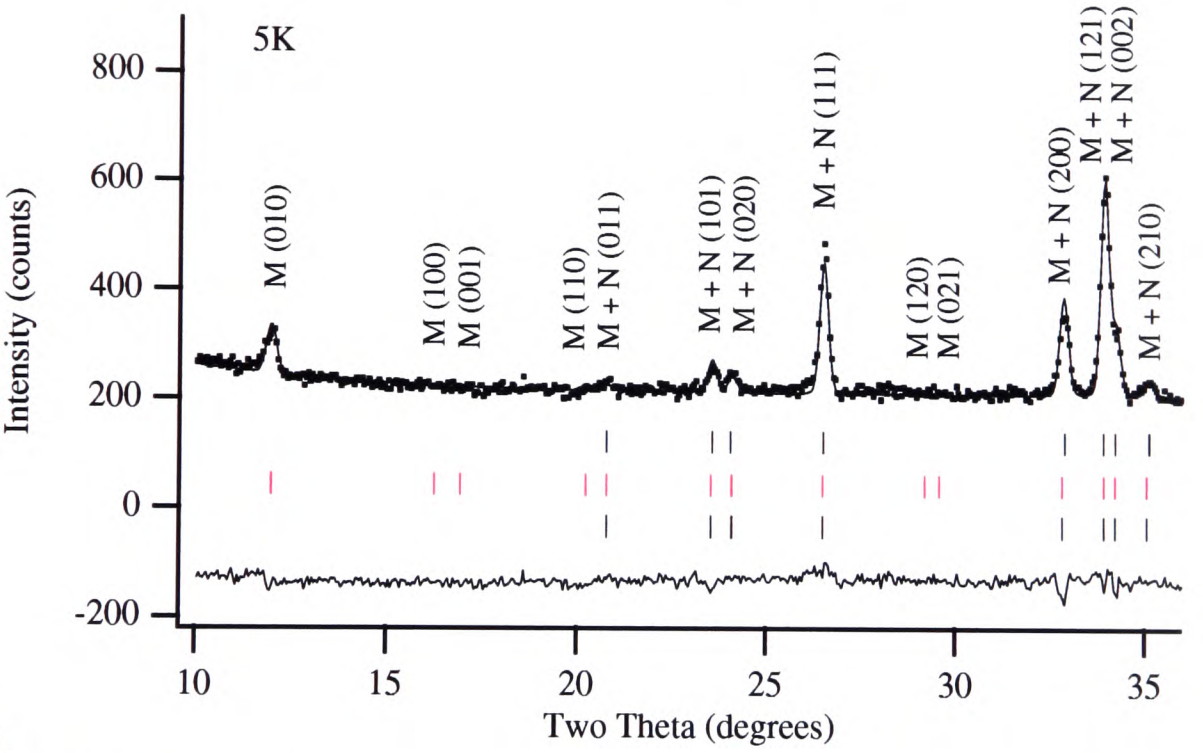
Atom	Site	Fraction (%)[a]	U_{iso} (Å^2)	x	y	z	Mx (μ_B)	My (μ_B)	Mz (μ_B)
Mn(1)	1	50	0.0002	0	0	1/2	1.38(4)	2.82(7)	0
Mn(2)	1	50	0.0002	0	1/2	1/2	-1.38(4)	2.82(7)	0
Mn(3)	1	50	0.0002	1/2	1/2	0	-1.38(4)	2.82(7)	0
Mn(4)	1	50	0.0002	1/2	0	0	1.38(4)	2.82(7)	0
Nd(5)	1	100	0.0002	0.0568	1/4	0.0114	0	0.96(4)	0
Nd(6)	1	100	0.0002	0.5568	1/4	0.4886	0	0.96(4)	0
Nd(7)	1	100	0.0002	0.9432	3/4	0.9886	0	0.96(4)	0
Nd(8)	1	100	0.0002	0.4432	3/4	0.5114	0	0.96(4)	0

[a] The 50% occupancy of positions on the magnetic cell reflects the disordered array of Mn and Ga across transition metal sites.

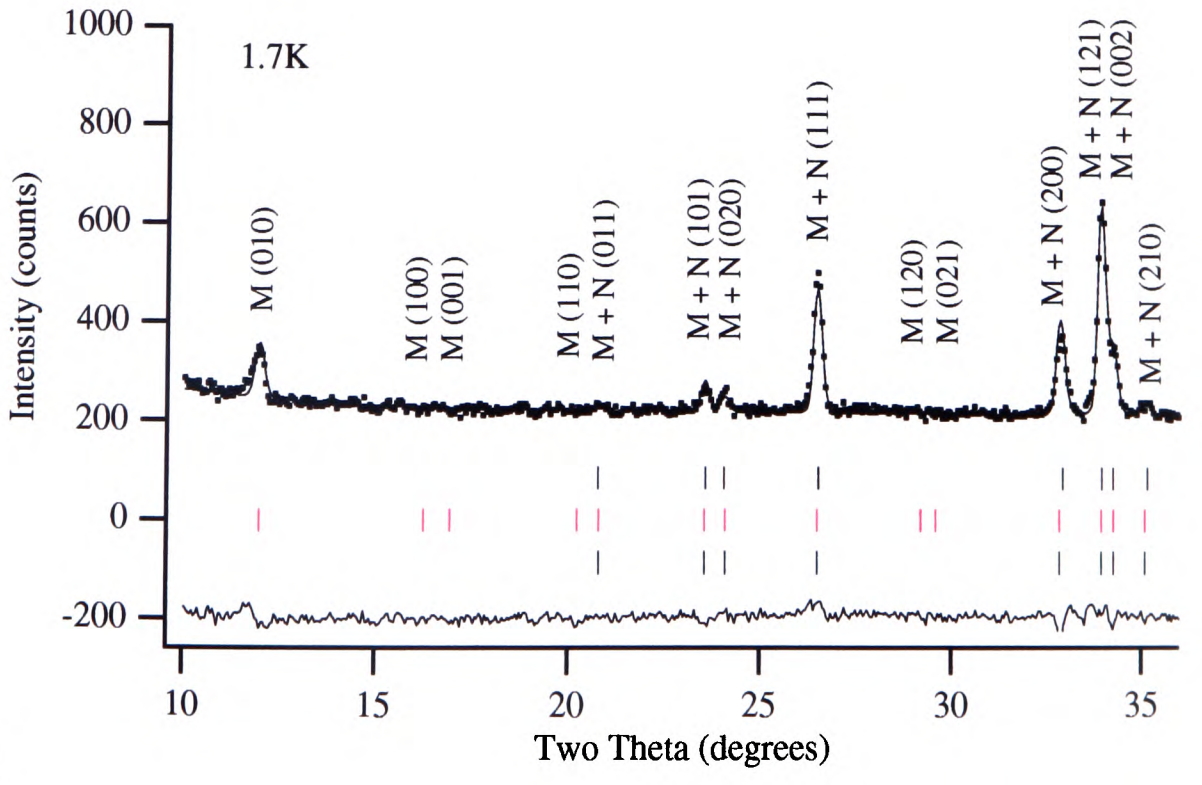
Figures 5.2.21 (a), (b) and (c) show the evolution of the magnetic Bragg peak 010, on reducing the temperature of Nd_2GaMnO_6 from 290K to 5K and finally to 1.7K. Slightly less obvious is the enhancement of intensity, due to magnetic scattering, in the regions corresponding to the nuclear reflections 121 and 002 in the 290K dataset. All allowed magnetic Bragg peaks in the magnetic structure at 5 and 1.7K, are denoted by purple tick marks in Figures 5.2.21 (b) and (c). The black (upper and lower) sets of tick marks correspond, respectively, to the nuclear reflections arising from the majority and minority phases in Nd_2GaMnO_6. The plots at the three different temperatures do not have a common scale, and 'M' and 'N' denote magnetic and nuclear reflections, respectively.



(a)



(b)



(c)

Figures 5.2.21 Evolution of magnetic Bragg peaks on reducing temperature from (a) 290K, to (b) 5K and (c) 1.7K.

Tables 5.2.26 and 5.2.27 summarise agreement indices and details of the refinements of Nd_2GaMnO_6 at 290K, 5K and 1.7K. The larger values of χ^2_{red} at the lower measuring temperatures of 5 and 1.7K, reflect the longer counting times at these temperatures (7 hours as opposed to 3.5 hours).

Table 5.2.26 Agreement parameters and refining variables at 290K, 5K and 1.7K:

Agreement parameter	290K D2b 1.594Å	5K D2b 1.594Å	1.7K D2b 1.594Å
R_{wp} (%)	4.32	4.74	4.82
R_p (%)	3.45	3.68	3.73
DWd	1.316	0.657	0.613
Total no. variables	51	46	46
χ^2_{red}	1.370	3.247	3.358

Table 5.2.27 Refining variables for the 290K, 5K and 1.7K refinements of Nd_2GaMnO_6:

Refining variables (in addition to atomic coordinates, thermal parameters and fractions)	290K D2b 1.594Å	5K D2b 1.594Å	1.7K D2b 1.594Å
Background (Shifted Chebyshev)	15	10	10
Profile (pseudo-Voigt)[a]	5	5	5
Histogram scale factor	1	1	1
Zero point	1	1	1

[a] Profile coefficients were constrained to be the same for all phases.

5.2.3.4 Magnetotransport measurements

The magnetotransport behaviour of Nd_2GaMnO_6 as a function of field at 200K is shown in Figure 5.2.22. The highly insulating nature of Nd_2GaMnO_6 did not leave a wide range of temperatures at which to record isothermal field dependent data (for example, temperature dependent data were measurable only down to 193K). The data collected at 200K illustrate minimal negative magnetoresistance, with the signal reduced to just 96% of its zero field value on application of a field of 14T.

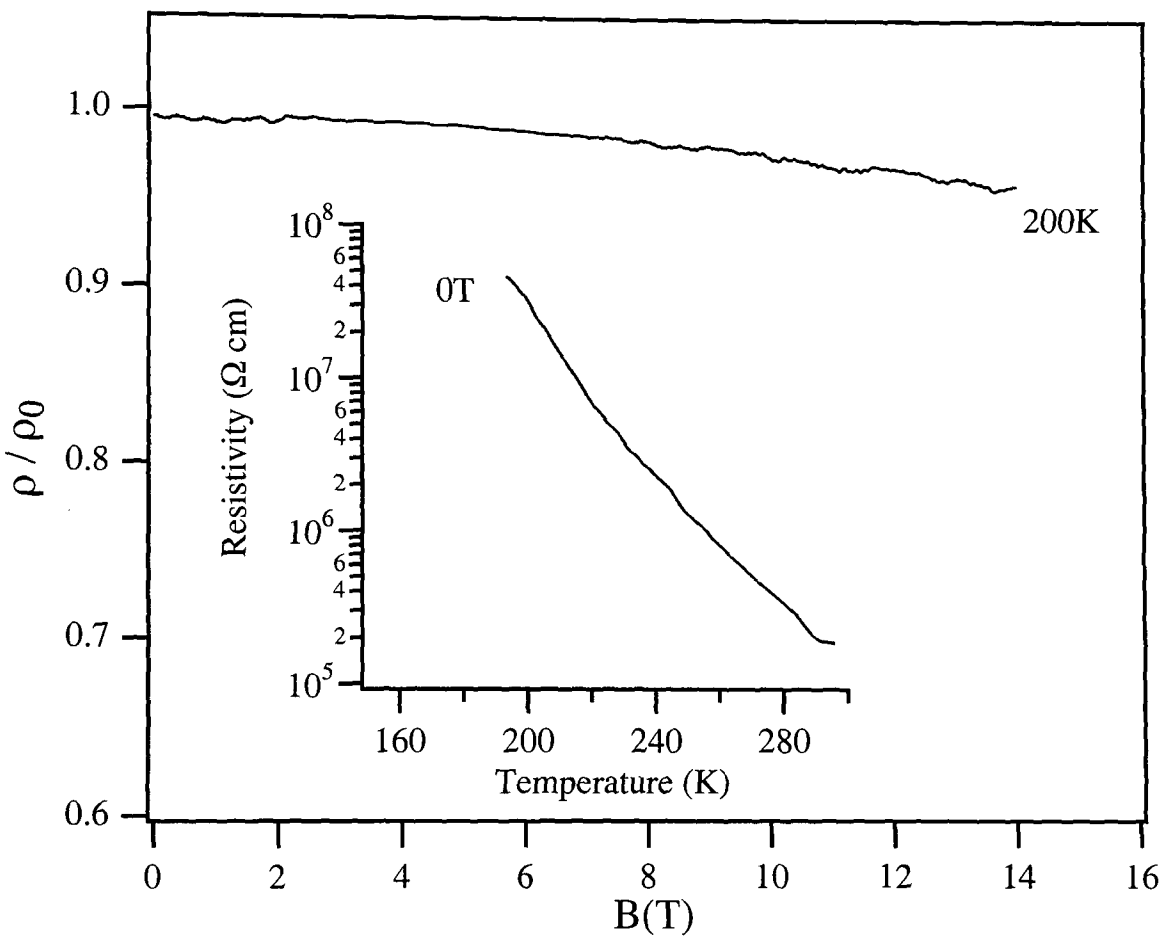


Figure 5.2.22 Field dependence of the normalised resistivity $\rho(B)/\rho(0)$ at 200K for Nd_2GaMnO_6. The inset shows the temperature dependence of resistivity at zero field.

The parameters resulting from the fit of temperature dependent resistivity data using a thermally activated conduction law, are given in Table 5.2.28. The fit itself is shown in Appendix 3, Figure 3.3 (b).

Table 5.2.28 Fit parameters for thermally activated conduction in Nd_2GaMnO_6:

Compound	Temperature range (K)	Model used	Parameter[a]
Nd_2GaMnO_6	295 to 193	$\rho \propto \exp(E_A / k_B T)$	$E_A = 271.62$ meV

[a] $1eV = 1.6022X10^{-19}J$

5.3 Discussion

It is easier to rationalise the crystallographic and magnetic properties in the La_2GaMnO_6 and Nd_2GaMnO_6 materials described above, by considering the crystallographic and magnetic modifications which have occurred, on introducing Ga^{3+} into the parent compounds $LaMnO_3$ and $NdMnO_3$. A summary of the crystallographic and magnetic properties of the $LaMnO_3$ and $NdMnO_3$ is appropriate first.

Central to the crystallographic description of $LaMnO_3$ and $NdMnO_3$, are the values of distinct Mn-O bondlengths comprising the MnO_6 octahedra in these orthorhombic (*Pnma*) perovskites. Goodenough[29] has formulated the diagram shown in Figure 5.3.1, to describe the oxygen displacements (represented by arrows) which are superimposed on MnO_6 rotations about the (110) axes in stoichiometric $LaMnO_3$. A similar distortion has been observed[18,19] in (nonstoichiometric) $NdMnO_3$. The structure axes and A-cation labelling in Figure 5.3.1 have been modified by the author to make the diagram applicable to the present study.

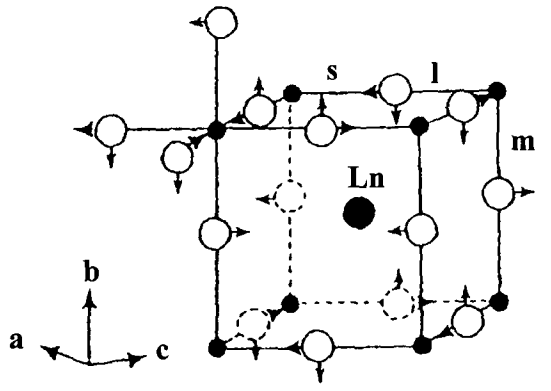


Figure 5.3.1 Oxygen displacements superimposed upon MnO_6 rotations about the (110) axes in $LaMnO_3$. (Figure reproduced, and modified from, reference [29]).

The static, cooperative JT displacements in stoichiometric $LaMnO_3$ leading to the oxygen displacements shown in Figure 5.3.1, remove the e_g orbital degeneracy and change the orthorhombic axial ratio from $\frac{b}{c} > \sqrt{2}$ to $\frac{b}{c} < \sqrt{2}$ in space group *Pnma*. The $\frac{b}{c} > \sqrt{2}$ and $\frac{b}{c} < \sqrt{2}$ regimes are often differentiated by the names O and O' structure, respectively, the O denoting orthorhombic symmetry. The resulting bondlengths arising from this static, cooperative JT distortion, are classified as long (l) and small(s) in (010) planes (i.e. equatorial Mn-O bonds), while apical Mn-O distances are medium (m) in length. Therefore, essential to

investigating the similarity between structural properties of La_2GaMnO_6 and Nd_2GaMnO_6 and the Ga-free $LaMnO_3$ and $NdMnO_3$, are the respective lengths of equatorial Mn-O(4) and apical Mn-O(5) bonds. It is interesting to observe whether they fall into the same 'small', 'medium' and 'long' subsets. This will give information regarding the nature of cooperative JT distortions, and the potential for orbital ordering, in the Mn, Ga phases.

The nature of orbital ordering, and the resulting magnetic exchange interactions, accompanying the static, cooperative Jahn-Teller distortion in stoichiometric $LaMnO_3$ was discussed briefly in the Chapter 1, with particular reference to the work of Solovyev et al.[16]. Important for the understanding of superexchange interactions accompanying a static JT distortion, is the ratio of the collective distortion modes of the octahedron[30,31], labelled 'Q_2' and 'Q_3'. These are represented graphically in Figure 5.3.2. As shown, a JT distortion of the Q_2 type displaces the equatorial oxygen atoms from their ideal positions, maintaining the lattice symmetry (*Pnma*), but modifying the cell deformation, and results in the lattice parameter ratio $\frac{b}{c} < \sqrt{2}$. The mode Q_3 is an octahedral stretching mode characteristic of a 'typically observed' apically elongated octahedron resulting from the JT effect. A breathing mode Q_1 will accompany these displacements also.

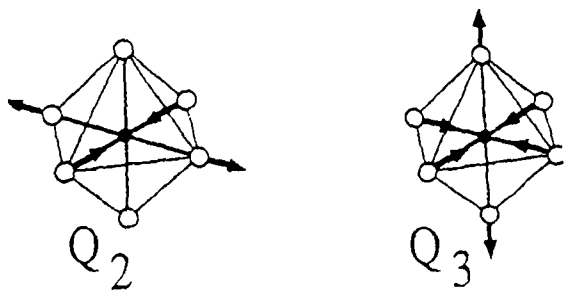


Figure 5.3.2 Collective octahedral distortion modes Q_2 and Q_3. (Figure reproduced from reference [30]).

The significance of Q_2 and Q_3 is due to their control of the degree of orbital ordering existing in an octahedral network, as explained by Feinberg et al.[32], in a study attempting to correlate magnetic ordering in the $LaMnO_3$ phase with the interplay between superexchange and JT distortions. It is proposed that the (static) JT distortions mix the $d_{3z^2-r^2}$ and $d_{x^2-y^2}$ orbitals into 'a' (lower) and 'b' (upper) orbitals with e_g symmetry, split by an energy ε, expressed as follows:

$$\varepsilon = 2g\sqrt{Q_3^2 + Q_2^2} \qquad \text{eqn. (5.3.1)}$$

The distortion Q_3 corresponds to a uniform variation of the lattice parameter along the z direction, and couples to the $d_{x^2-y^2}$ - $d_{3z^2-r^2}$ density difference. Where the lattice spacing in the z direction (y direction in *Pnma*) is shorter than the (average) spacing in the xy plane, Q_3 is negative. The distortion Q_2 is opposite on the two sublattices of the xy planes (xz in *Pnma*) and corresponds to an alternate contraction and extension of the Mn-O bonds, mixing the $d_{x^2-y^2}$ and $d_{3z^2-r^2}$ components of the a,b orbitals split by the energy given by expression 5.3.1. In the model of Feinberg et al.[32], it was found that the assumed orbital order becomes compatible with A-type AFM order in $LaMnO_3$ for a $Q_2/|Q_3|$ ratio equal or greater than approximately 2.6, when Q_3 is negative. It was deduced, that the layered A-type AFM ordering observed in $LaMnO_3$ is compatible with a sufficiently large in plane distortion Q_2.

Within this framework, the long 'Mn-O(4)' bonds in the (010) plane in $LaMnO_3$ are likely to correspond to occupied $d_{3x^2-r^2}$ and $d_{3y^2-r^2}$ orbitals, while short 'Mn-O(4)' bonds correspond to empty $d_{y^2-z^2}$ and $d_{x^2-z^2}$ as shown in Figure 1.3.4. The $d_{3x^2-r^2}$, $d_{3y^2-r^2}$, $d_{y^2-z^2}$ and $d_{x^2-z^2}$ orbitals correspond to linear combinations of $d_{3z^2-r^2}$ and $d_{x^2-y^2}$. A description of the magnetic superexchange in $LaMnO_3$ is only complete with a consideration of the half filled t_{2g} band. In the model proposed by Solovyev et al.[16] for $LaMnO_3$, the value of the inter-layer, AFM $Mn^{4+}\ t_{2g}^3$ - O^{2-} - $Mn^{4+}\ t_{2g}^3$ π superexchange interaction parameter (J_b^1 in space group *Pnma*) was suggested to decrease as the (apical) Mn-O(5)-Mn distance increases. However, both Feinberg et al. and Solovyev et al. acknowledge that taking full account of tilt distortions (and hence the non-vanishing transfer integrals $d_{x^2-y^2}$ - $d_{x^2-y^2}$ -and $d_{x^2-y^2}$ - $d_{3z^2-r^2}$ along z in *Pbnm*) is necessary to make the models more realsitic. In addition, the fact that Solovyev et al. actually invoked the AFM next-nearest-neighbour exchange to explain fully the AFM nature of inter-layer coupling present in $LaMnO_3$, suggests that a formulation based on the sign of nearest-neighbour-exchange parameters is not a realistic approach. As will be shown, these limitations make precise statements, regarding the complex superexchange interactions in Nd_2GaMnO_6 in particular, somewhat difficult.

In contrast to the magnetic properties of $LaMnO_3$, those of $NdMnO_3$ have been

studied far less extensively. However, Liu et al.[33] reported the parent $NdMnO_3$ as having two Néel temperatures, "at around 14 and 60K". Regarding the magnetic properties of the Ga containing compounds $LaGaO_3$ and $NdGaO_3$, the former is diamagnetic and Luis et al.[34] investigated the magnetic structure in orthorhombic (*Pbnm*) $NdGaO_3$, deducing that the compound "orders antiferromagnetically at $T_N \approx 1K$, with sublattice moments parallel to [001], strong antiferromagnetic intralayer exchange and weaker ferromagnetic interlayer exchange".

A particularly useful parameter with which to quantify the JT distortions present in compounds discussed in this chapter, is σ_{JT}, defined as follows:

$$\sigma_{JT} = \sqrt{\frac{1}{3}\sum_i [(Mn-O)_i - \langle Mn-O \rangle]^2} \qquad \text{eqn. (5.3.2)}$$

This parameter, along with lattice parameters and key bondlengths in $LaMnO_3$, $NdMn_{0.98(1)}O_{2.92(2)}$[18] (data are not available for a stoichiometric sample of $NdMnO_3$), $LaGaO_3$ and $NdGaO_3$, are tabulated below, to aid comparison between these phases, and those under discussion, La_2GaMnO_6 and Nd_2GaMnO_6.

Table 5.3.1 Significant room temperature structural parameters for purely Mn-, and purely Ga-containing phases.

Structural parameter	$LaMnO_3$[a]	$LaGaO_3$[b]	$NdMn_{0.98(1)}O_{2.92(2)}$[c]	$NdGaO_3$[d]
a (Å)	5.7461(2)	5.4893(1)	5.78808(4)	5.4958(1)
b (Å)	7.6637(4)	7.7701(1)	7.55640(6)	7.7060(1)
c (Å)	5.5333(2)	5.5217(1)	5.41013(3)	5.4264(1)
$\frac{b}{c}$	1.3850	1.4072	1.3967	1.4201
$\sigma_{JT} = \sqrt{\frac{1}{3}\sum_i [(Mn-O)_i - \langle Mn-O \rangle]^2}$	1.16×10^{-1}	6.14×10^{-3}	1.24×10^{-1}	2.82×10^{-2}
Mn/Ga-O(4) 'small'	1.914(3)	1.968(10)	1.912(1)	1.949(7)
Mn/Ga-O(4) 'long'	2.181(3)	1.983(10)	2.192(1)	2.018(7)
Mn/Ga-O(5) 'medium'	1.966(1)	1.976(2)	1.9512(4)	1.983(2)

a, b, c, d Structural parameters were obtained from studies described in references [13], [20], [18] and [20], respectively.

Although it is not appropriate to discuss Jahn-Teller parameters in $LaGaO_3$ and

$NdGaO_3$, in the absence of a JT cation, it is useful to calculate the σ_{JT} parameter for these two compounds, for comparative purposes. The significant Mn/Ga-O bondlengths are labelled with 'O(4)' and 'O(5)' denoting equatorial and apical bonds, respectively, using the same labelling scheme as that used for La_2GaMnO_6 and Nd_2GaMnO_6 in the current chapter. The use of 'small', 'medium' and 'long' assignments is not appropriate in all cases (for example, Ga-O bonds in $LaGaO_3$ are essentially uniform), however, again, this nomenclature is used to aid comparison with the La_2GaMnO_6 and Nd_2GaMnO_6 phases.

From the tabulated values of $\frac{b}{c}$ above, it is shown that all compounds other than $NdGaO_3$ obey the $\frac{b}{c} < \sqrt{2}$ criterion, and therefore adopt the O' structure. However, the 'short', 'medium' and 'long' classification of Ga-O bondlengths still holds in $NdGaO_3$. Whereas Ga-O distances comprising GaO_6 octahedra in $LaGaO_3$ were found to be essentially equal within experimental error in the study by Sanjuán et al.[20], small differences in equatorial Ga-O distances in $NdGaO_3$ were understood within the framework of the bond valence model. As is evident from data given for $LaGaO_3$ in Table 5.3.1, the ratio $\frac{b}{c} < \sqrt{2}$ can be achieved *even in the absence of a JT cation*, and without any significant irregularity in the octahedral network. Therefore, careful examination of the apical and equatorial bondlengths, as well as calculating the $\frac{b}{c}$ ratio, is required to confirm the presence of a static, cooperative JT distortion in La_2GaMnO_6 and Nd_2GaMnO_6. As expected, the values of σ_{JT} in $LaMnO_3$, and $NdMnO_3$ are significantly larger than those for the JT inactive Ga-containing compounds.

5.3.1 Structural and magnetic properties of La_2GaMnO_6

Firstly, it is useful to compare the structrural parameters refined for La_2GaMnO_6, with those tabulated for $LaMnO_3$, and $LaGaO_3$ in the previous section:

Table 5.3.2 Significant structural parameters for La_2GaMnO_6 at room temperature, 50 and 5K:

Structural parameter	La_2GaMnO_6[a] Room Temperature	La_2GaMnO_6 50K	La_2GaMnO_6 5K
a (Å)	5.51122(4)	5.51155(11)	5.50980(10)
b (Å)	7.80515(6)	7.79862(15)	7.79614(15)
c (Å)	5.52947(4)	5.52382(11)	5.52206(11)
$\frac{b}{c}$	1.4116	1.4118	1.4118
$\sigma_{JT} = \sqrt{\frac{1}{3}\sum_i[(Mn-O)_i - \langle Mn-O\rangle]^2}$	4.80×10^{-3}	6.80×10^{-3}	5.86×10^{-3}
σ_{JT} calculated, 50% Ga/Mn	6.07×10^{-2}	-	-
Mn/Ga-O(4) 'small'	1.9782(22)	1.9732(22)	1.9750(19)
Mn/Ga-O(4) 'long'	1.9824(22)	1.9874(22)	1.9847(19)
Mn/Ga-O(5) 'medium'	1.9898(6)	1.9878(5)	1.9890(5)

[a] Lattice parameters of La_2GaMnO_6 read from a graph in reference [17] for comparison, are a = 5.55Å, b = 7.80Å and c = 5..54Å.

As shown in Table 5.3.2, although the room temperature, 50 and 5K lattice parameters in La_2GaMnO_6 conform to the O' orthorhombic structural type according to the criterion $\frac{b}{c} < \sqrt{2}$, the 'small', 'medium' and 'long' assignments are not in the same order as in $LaMnO_3$. For example, the Mn-O(5) apical bondlength has the longest, rather than the medium length at all three temperatures, although it is the same as the longest equatorial Mn-O(4) bondlength at 50K within experimental error. The Mn-O(4) equatorial bonds alternate within the (010) planes, but have the same magnitudes within experimental error at room temperature, and show only a marginal difference at 50 and 5K. These do not correspond to the pattern of bondlengths typical of a *static, cooperative* JT distortion of the kind observed in $LaMnO_3$. For example, at room temperature the JT distortion in La_2GaMnO_6 is marginal, and is of the *apically elongated* type. This is consistent with the introduction of Ga^{3+} into the Mn^{3+}-O^{2-}-Mn^{3+} network in a random manner having destroyed the long range static cooperativity of the

JT deformations present in $LaMnO_3$. This statement is supported by the values of σ_{JT} in La_2GaMnO_6 being two orders of magnitude lower (at all three measuring temperatures), than the room temperature value quoted[35] for $LaMnO_3$. Table 5.3.2 contains a value 'σ_{JT} calculated' for room temperature La_2GaMnO_6, equal to $6.07x10^{-2}$, which is the value which would be expected for a hypothetical phase where 50% of the bonds come from $LaMnO_3$ and 50% from $LaGaO_3$. As shown, the observed room temperature parameter σ_{JT} for La_2GaMnO_6 is less ($4.80x10^{-3}$) than that which would be expected if the distortion was preserved and simply diluted. Data were not available for $LaGaO_3$ as a function of temperature, to obtain 'σ_{JT} calculated' at 50 and 5K.

A key question, in the case of the La_2GaMnO_6 compound, is the nature of JT deformations, since they do not show the static cooperativity observed in $LaMnO_3$ and (nonstoichiometric) $NdMnO_3$. The observation of significantly anisotropic oxygen thermal parameters refined at room temperature, together with the relative similarity of Mn/Ga-O distances, are consistent with the presence of *dynamic*, *cooperative* JT deformations. Figures 5.3.3 (a) and (b) illustrate the orientation of Mn/Ga-O_6 octahedra at room temperature and 5K, respectively, for part of the unit cell of La_2GaMnO_6. Significant equatorial and apical bondlengths which were included in Table 5.3.2, are marked on the diagram. The atoms are represented as 99% thermal ellipsoids in order to illustrate the change in thermal parameters, on reducing the temperature. Although only 'Mn-O' bondlengths are marked in the Figure, Ga occupies precisely 50% of these sites. The assignment of 'short', 'medium' and 'long' Mn-O bonds is clearly not appropriate, particularly at room temperature, as mentioned above, due to the similarity in their values. Figure 5.3.3 illustrates that the structure of La_2GaMnO_6 at 5K retains significant anisotropic oxygen anion displacement, suggesting that the displacements have a considerable contribution from static disorder.

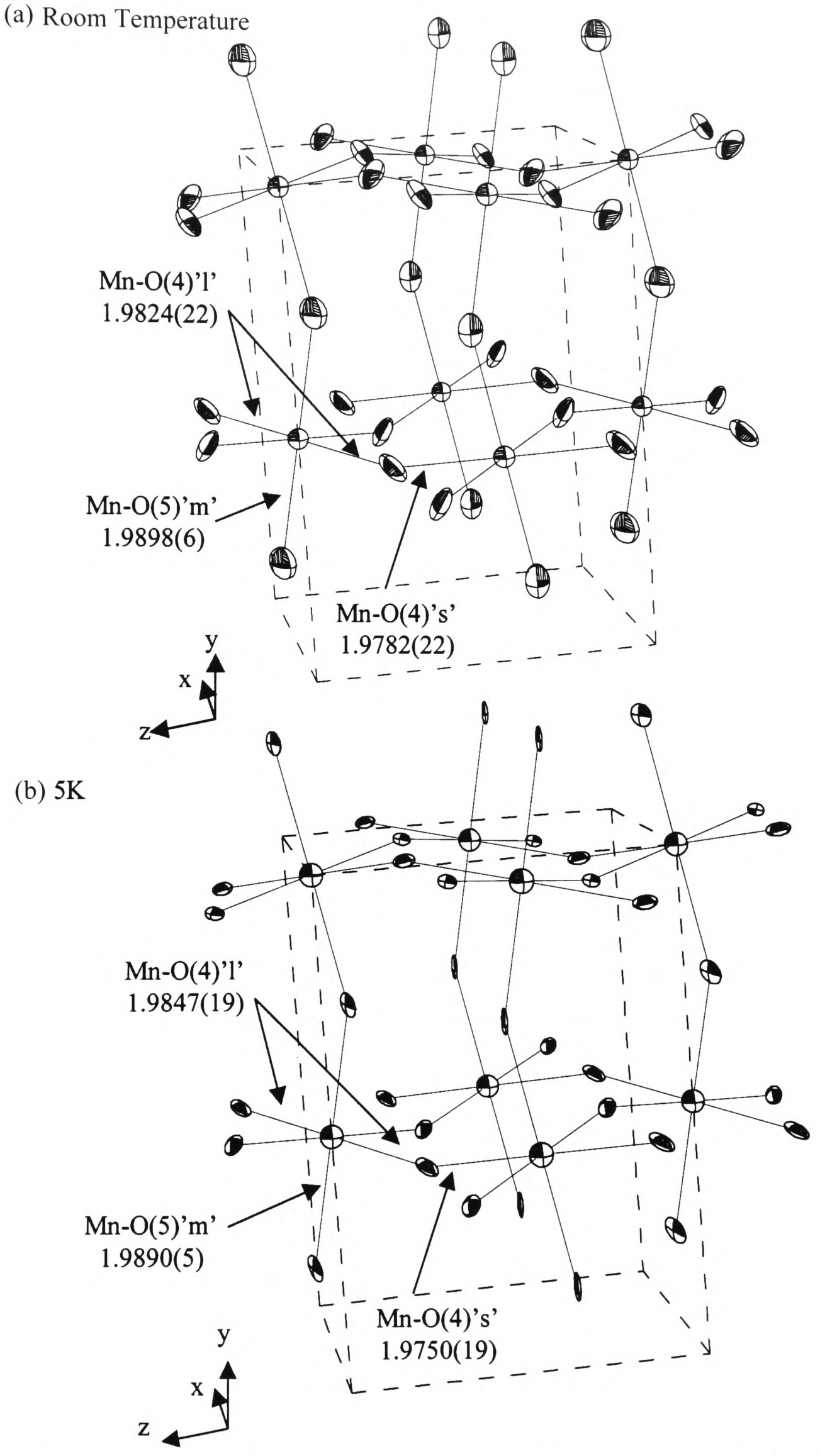


Figure 5.3.3 Representation of the atoms in La_2GaMnO_6 as 99% thermal ellipsoids, (a) at room temperature and (b) at 5K. Significant bondlengths are marked. Ga occupies 50% of all 'Mn' sites.

The results obtained for the La compound raise the issue of distinguishing *local* and *average* structure. Crystallographic techniques can measure the full extent of lattice distortions only for phases that display *coherent* orbital ordering, as is the case in stoichiometric $LaMnO_3$ or (nonstoichiometric) $NdMnO_3$. The apparent regularity of octahedra (at least relative to the Nd analogue), observed in La_2GaMnO_6, with associated large anisotropic thermal displacement parameters of oxygen anions, could indicate significant *local* JT distortion, not reflected in global atomic displacements.

For example, in a study by Radaelli et al.[36], the authors focussed on the variation of bond distances, angles and temperature factors as a function of temperature in the series $A_{1-x}A'_xMnO_3$ (A = La, Pr; A' = Ca, Sr, Ba) at a doping level, x = 0.25. The study emphasised the significance of large, low temperature oxygen Debye Waller factors, which may indicate the presence of a component of the total distortion that is otherwise masked, as it disappears on application of the *Pnma* symmetry operators (i.e. it is incoherently ordered). It is interesting to compare the elongation of the ellipsoids parallel and perpendicular to the Mn/Ga-O bonds at room temperature and 5K. For the equatorial, O(4) ellipsoids, significant elongation parallel to the Mn/Ga-O bonds appears to be retained at 5K. This would be consistent with a contribution from static disorder, afforded by the presence of a proportion of (incoherently ordered) static JT deformations. This observation is, in turn, consistent with a disordered array of Mn^{3+} (JT active) and Ga^{3+} (JT inactive) cations on B-cation sites. In the Radaelli study, low temperature (2K) oxygen Debye Waller factors of the order of U(O) ~ $1x10^{-2}$ were taken as evidence of similar, static disorder in $La_{0.5}Ca_{0.5}MnO_3$, and contrasted with the lower values obtained for $LaMnO_3$ U(O) ~ $3x10^{-3}$ at the same temperature[35]. In La_2GaMnO_6 at 5K, $U_{eq}O(4)$ takes the value $5.4x10^{-3}$ and $U_{eq}O(5)$ $9.5x10^{-3}$ by comparison. These are slightly reduced, and slightly increased, respectively, from the room temperature values where $U_{eq}O(4)$ is $6.3x10^{-3}$ and $U_{eq}O(5)$ $9.1x10^{-3}$. Therefore, these values are intermediate between those reported for $La_{0.5}Ca_{0.5}MnO_3$ and $LaMnO_3$.

Thus, it is difficult to state unambigously, the ratio of dynamic to static JT deformations in La_2GaMnO_6. Although the temperature dependence of anisotropic oxygen displacement parameters suggests a contribution from static disorder, the 'average' room

temperature crystal structure refined from neutron diffraction data does not show the order of Mn/Ga-O bondlengths typical of static, cooperative JT displacements. Interestingly, the magnetic properties of La_2GaMnO_6 suggest a high proportion of dynamic JT distortions, present at 50 and 5K, as now described.

Rationalising the magnetic and crystallographic behaviour in La_2GaMnO_6 is slightly more straightforward than in the case of the Nd analogue, since, assuming a high proportion of JT correlations in La_2GaMnO_6 to be dynamic, the compound exhibits the ferromagnetism predicted by the 'quasistatic hypothesis' in Goodenough's 1961 publication[11]. The quasistatic hypothesis was advanced in order to predict electron configurations of JT cations existing in a geometrical environment in which there are no static, cooperative JT distortions. Instead, the hypothesis relies upon the assumption that "strong coupling to the nuclear vibrations removes the orbital degeneracy and correlates the electron spin configurations of neighbouring JT ions[11]". The implication is that the electron configuration is able to 'follow' the nuclear motions, and a representation of quasistatic electron order associated with two $3d^4$ cations is given in Figure 5.3.4.

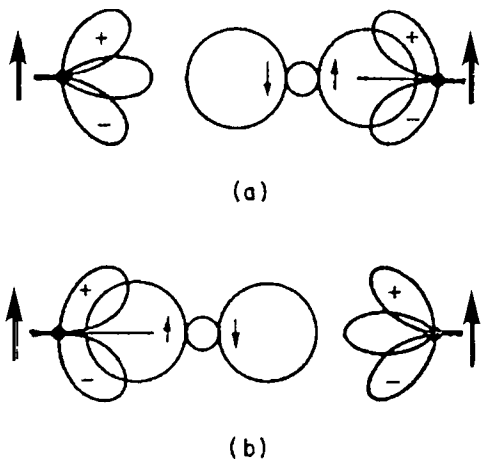


Figure 5.3.4 Schematic diagram representing quasistatic electronic ordering about $3d^4$ cations. Parts (a) and (b) show two 'extreme' relative positions of anion and cation sublattices. (Figure reproduced from reference [11].

The two 'limiting' arrangements of anion and cation sublattices correspond, according to Goodenough's rules for 180° superexchange interactions[11,29], to 'Case 3' moderate ferromagnetism. The magnetic structure obtained for La_2GaMnO_6 at 50 and 5K, does indeed exhibit isotropic ferromagnetic superexchange interactions. Hence, it is significantly different from that observed in stoichiometric $LaMnO_3$, where significant anisotropy results in

ferromagnetic planes coupling antiferromagnetically along y. The observation of isotropic ferromagnetic interactions between nearest-neighbour Mn d^4 cations at 50 and 5K is consistent with the presence of quasistatic electron order at Mn sites. Indeed, Töpfer and Goodenough state, in the 1997 study[17] of a sample of La_2GaMnO_6, (on which the results of SQUID magnetometry are very similar to those in the present study) that isotropic ferromagnetic interactions are allowed due to cooperative JT deformations enabling a rotation of the axis of ferromagnetic interaction. The rotation is assumed thus to be fast relative to the spin relaxation time to a different orientation. It is important to emphasise the requirement for *dynamic*, cooperative JT deformations of the octahedral sites, before a rationalisation of exchange interactions within the quasistatic limit can be applied. In the 1997 study[17], samples containing higher concentrations of Ga^{3+} ($1.2 \leq x \leq 2$) in the series $La_2Ga_xMn_{2-x}O_6$ than that under discussion, were judged to contain a higher ratio of dynamic to static JT deformations, on account of the saturation magnetisation approaching the theoretical value for isotropic coupling of the Mn moments. Compounds with ($1.2 \leq x \leq 2$) in the series $La_2Ga_xMn_{2-x}O_6$ were also shown to adopt the O, rather than the O' structure, emphasising a significant departure from '$LaMnO_3$ - type' behaviour. The authors did not comment on the nature of cation ordering in the samples in the 1997 study. The fact that the ferromagnetic moment expected for a high spin, octahedrally coordinated Mn^{3+} cation is reduced in our sample, (an average Mn ordered moment of 2.80(5) μ_B was obtained from the neutron study at 5K, as opposed to $4\mu_B$ from 'gS'), supports the suggestion that the 'crossover' from static to dynamic JT deformations is not complete at the x = 1 doping level in the $La_2Ga_xMn_{2-x}O_6$ series. This reduction is also consistent with the random nature of Mn nearest-neighbour interactions, afforded by the presence of Ga^{3+}.

Figures 5.3.5 (a) to (d) summarise graphically, the temperature dependence of key structural parameters, although the presence of just three points on the graph may, of course, mask more subtle variations.

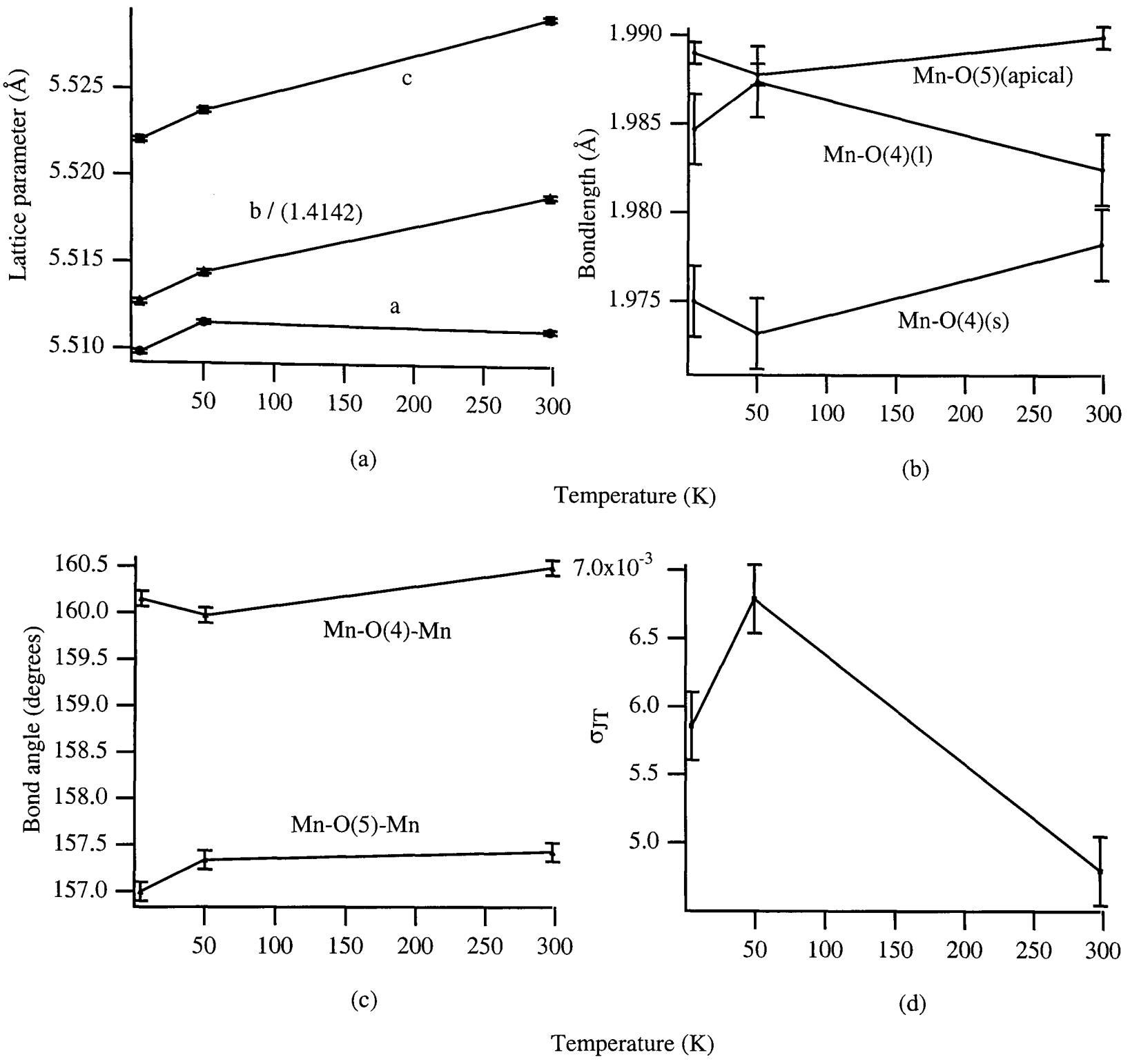


Figure 5.3.5 Temperature dependence of (a) lattice parameters, (b) Mn/Ga-O bondlengths, (c) Mn/Ga-O-Mn/Ga bond angles and (d) JT distortion parameter σ_{JT} in La_2GaMnO_6. Although only Mn cations are marked in the Figures, Ga cations occupy 50% of B-cation sites.

The explanation of the isotropic ferromagnetism observed in La_2GaMnO_6 given above, makes the variation with temperature of Mn-O bondlengths, shown in Figure 5.3.5 (b), somewhat surprising. For example, the geometry of the Mn/Ga-O_6 octahedra at room temperature corresponds to a slight apical elongation, (mode Q_3 in the 'static' formulation). However, on decreasing the temperature to 50K, there is a significant increase in the JT distortion parameter. The increase in distortion is manifested by the slight increase in Mn/Ga-O(4) (l) and marginal decrease in both Mn/Ga-O(4) (s) and Mn/Ga-O(5) bondlengths. This is

consistent with an increase in the $Q_2/|Q_3|$ ratio (again formulated in the 'static' limit), which is predicted to stabilise the A-type AFM order in $LaMnO_3$. The fact that respective Mn/Ga-O bondlengths do not vary in an *isotropic* manner as a function of temperature, indicates an electronic reorganisation typical of a system containing a fraction of static JT deformations. However, no ordered, antiferromagnetic component (which would be consistent with an increase in $Q_2/|Q_3|$) was detected in the neutron diffraction study. The variation with temperature of Mn/Ga-O bondlengths is exactly the reverse of that obtained for the majority phase in the Nd sample (as illustrated by Figure 5.3.7). However, as for majority phase Nd_2GaMnO_6, there is an anomalous reversal of the trend (although the changes are marginal within experimental error) on decreasing the temperature to 1.7K. In the 1961 publication[11], Goodenough suggested that compounds in the vicinity of the 50% Ga doping level may contain a heterogeneous mixture of static and dynamic JT effects at Mn^{3+} cations, and the variation of structural parameters presented above adds further support to this asumption for La_2GaMnO_6.

In summary, despite the 'dilution' of Mn -Mn magnetic exchange interactions afforded by the presence of 50% Ga cations on the same site, isotropic ferromagnetic correlations predominate in La_2GaMnO_6. The sign of the magnetic exchange is consistent, within the quasistatic hypothesis by Goodenough[11], with ferromagnetic correlations existing between occupied and empty e_g orbitals on adjacent Mn sites, mediated by dynamic JT correlations. However, the temperature dependence of temperature factors for oxygen anions, and the Mn/Ga-O bondlength variation with temperature, complicates the interpretation based upon the quasistatic hypothesis. This suggests that a full explanation of magnetic properties would mean invoking then superexchange interactions operative in both the quasistatic, and 'static' limit. However, the isotropic ferromagnetism observed suggests that there is a high ratio of dynamic, to static JT deformations, since ferromagnetism is predicted within the quasistatic formulation.

5.3.2 Structural and magnetic properties of Nd_2GaMnO_6

A major difference in the properties of the La_2GaMnO_6 and Nd_2GaMnO_6 compounds is evident, on comparison of structural parameters in Tables 5.3.2 and 5.3.3, respectively. The same level of Ga doping and average distribution of Mn/Ga cations in Nd_2GaMnO_6, appears to have preserved the long range static cooperativity of the local JT deformations, while in La_2GaMnO_6, Ga doping has destroyed it. This is evidenced in Nd_2GaMnO_6 at temperatures of 290, 5 and 1.7K, by the small (s), medium (m) and long (l) assignments, (in-keeping with Goodenough's formulation shown in Figure 5.3.1), of the respective lengths of equatorial and apical Mn/Ga-O bonds.

Table 5.3.3 Significant structural parameters for majority and minority phases in Nd_2GaMnO_6 at 290, 5 and 1.7K.

Majority phase parameter	Nd_2GaMnO_6 290K	Nd_2GaMnO_6 5K	Nd_2GaMnO_6 1.7K
a (Å)	5.63677(12)	5.63850(16)	5.63618(9)
b (Å)	7.65070(13)	7.63792(22)	7.63502(16)
c (Å)	5.41778(13)	5.41329(18)	5.41107(14)
$\frac{b}{c}$	1.4121	1.4110	1.4110
$\sigma_{JT} = \sqrt{\frac{1}{3}\sum_i[(Mn-O)_i - \langle Mn-O\rangle]^2}$	$6.71x10^{-2}$	$6.35x10^{-2}$	$6.47x10^{-2}$
σ_{JT} calculated, 50% Ga/Mn	$7.51x10^{-2}$	-	-
Mn/Ga-O(4) 'small'	1.9427(30)	1.9441(5)	1.9410(3)
Mn/Ga-O(4) 'long'	2.0960(26)	2.0901(4)	2.0901(2)
Mn/Ga-O(5) 'medium'	1.9679(11)	1.9707(5)	1.9692(3)
Minority phase parameter	**Nd_2GaMnO_6 290K**	**Nd_2GaMnO_6 5K**	**Nd_2GaMnO_6 1.7K**
a (Å)	5.62191(26)	5.62427(19)	5.62233(15)
b (Å)	7.66164(32)	7.64542(33)	7.64183(29)
c (Å)	5.41691(32)	5.41228(27)	5.41031(26)
$\frac{b}{c}$	1.4144	1.4126	1.4125
$\sigma_{JT} = \sqrt{\frac{1}{3}\sum_i[(Mn-O)_i - \langle Mn-O\rangle]^2}$	$5.78x10^{-2}$	$6.71x10^{-2}$	$6.56x10^{-2}$
σ_{JT} calculated, 50% Ga/Mn	$7.51x10^{-2}$	-	-
Mn/Ga-O(4) 'small'	1.938(8)	1.9341(7)	1.9387(7)
Mn/Ga-O(4) 'long'	2.074(7)	2.0888(6)	2.0880(5)
Mn/Ga-O(5) 'medium'	1.9719(25)	1.9632(9)	1.9622(7)

Therefore, Nd_2GaMnO_6 appears to show fewer structural deviations from the Ga-free $NdMnO_3$ material, than does La_2GaMnO_6 from its 'parent' compound. The parameter σ_{JT} in both phases of Nd_2GaMnO_6 is closer to that in room temperature $LaMnO_3$ and $NdMn_{0.98(1)}O_{2.92(2)}$ ($\approx 1.16x10^{-1}$), at all three measuring temperatures, than is the room temperature value for La_2GaMnO_6 ($4.80x10^{-3}$). The 290K value of 'σ_{JT} calculated' is $7.51x10^{-2}$, similar to the values observed in majority phase ($6.71x10^{-2}$) and minority phase ($5.78x10^{-2}$) Nd_2GaMnO_6. This implies the continued static distortion at the Mn site, on introduction of Ga cations.

Figure 5.3.6 illustrates the orientation of Mn/Ga-O_6 octahedra for part of the unit cell in Nd_2GaMnO_6. The bondlengths marked correspond to the 290K, majority phase values.. Since all atomic displacement parameters are isotropic at each of the three measuring temperatures in Nd_2GaMnO_6, the 99% 'ellipsoids' representing the atoms appear 'spherical', and there is no significant difference in the appearance of the low temperature structures.

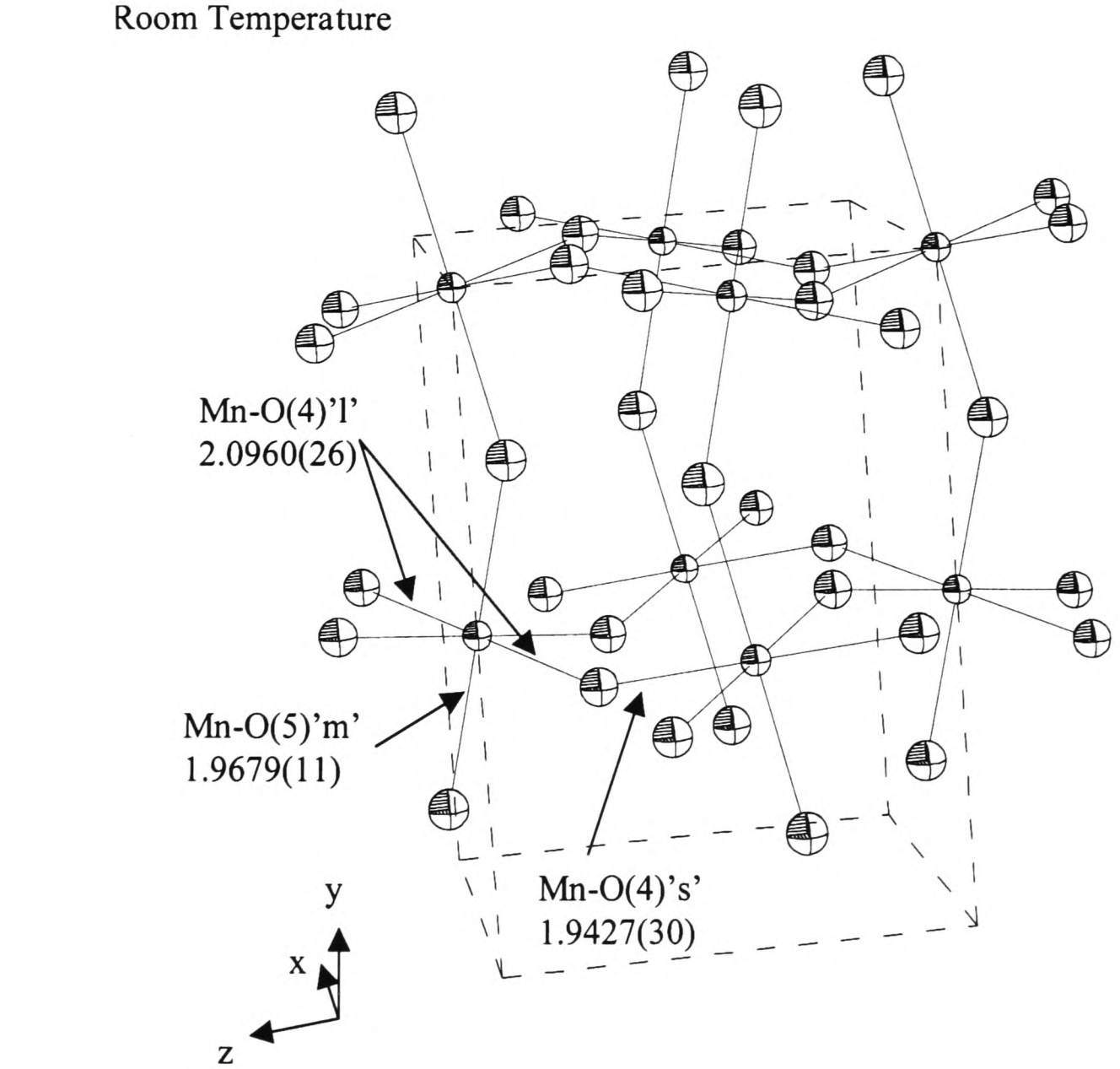


Figure 5.3.6 Representation of the atoms in Nd_2GaMnO_6 as 99% thermal 'ellipsoids' at 290K.

In their study of the series $La_{1-x}Nd_xGaO_3$, Sanjuán et al.[20] noted the increased orthorhombic distortion in the room temperature structure of $NdGaO_3$, as compared with $LaGaO_3$, attributed to the smaller size of the Nd^{3+} cation. They commented that the distortion produced a decrease in b and c lattice parameters, while a was left essentially unchanged. The authors noted that c > a for $LaGaO_3$ while c < a for $NdGaO_3$. Reference to Tables 5.3.2 and 5.3.3, reveals that these respective sizes of a and c lattice parameters are preserved in the La_2GaMnO_6 and Nd_2GaMnO_6 compounds.

The significant divergence between a and c lattice parameters in Nd_2GaMnO_6, signals significant reduction from pseudocubic symmetry as a result of the ratio of Nd-O and Mn/Ga-O bondlengths. Indeed, the separation into two distinct phases, the majority phase adopting the O' form, $\frac{b}{c} < \sqrt{2}$, and the minority phase the O form $\frac{b}{c} > \sqrt{2}$ at 290K, may have been driven by the relief of strain in the highly distorted octahedral network. The minority phase has a significantly reduced a lattice parameter, with a lower, mean Nd-O coordination distance of 2.776(1)Å, as opposed to 2.782(3)Å in the majority phase. The JT distortion is lower also in the minority phase at room temperature, σ_{JT} measuring 5.78×10^{-2}, as opposed to 6.71×10^{-2} in the majority phase.

Further treatment of the biphasic sample of Nd_2GaMnO_6 described here, by J. Burley, resulted in the formation of a single phase sample, with room temperature cell volume 234.255(1)Å. This cell volume is closer to the majority phase cell volume in the biphasic sample, (233.643(7)Å^3), than the minority (233.323(17)Å^3), but is significantly larger than either. The fact that the single phase sample was obtained after quenching the material from a firing temperature of 1400°C into liquid N_2, suggests phase separation probably occurs on cooling.

The highly distorted orthorhombic structure in Nd_2GaMnO_6 resulting from the small Nd^{3+} cation favours the accommodation of orbital ordering associated with a JT distorted octahedral geometry. Ritter et al.[10] illustrated the continuous change from a highly distorted orthorhombic, towards *quasicubic* and then to a rhombohedral structure which takes place across the $LaMnO_{3+\delta}$ series as δ (and therefore the Mn^{4+} concentration) is increased. Specifically they found that as δ increased, c and a became closer and the MnO_6 octahedra

became less distorted. Hence, they observed the loss of a *static*, cooperative JT distortion on passing to rhombohedral symmetry at a critical value of δ in the series. Although the effect in their case was driven by increasing Mn^{4+} concentration, this increased similarity in the relative magnitudes of a and c lattice parameters is reproduced on passing from Nd_2GaMnO_6 to La_2GaMnO_6. The effect observed by Ritter et al. can be initiated alternatively by aliovalent substitution, as shown in work by Urushibara et al.[37]. These authors concluded that as hole doping increases in the series $La_{1-x}Sr_xMnO_3$, the crystal structure changes from orthorhombic ($x < 0.175$) to rhombohedral ($x \geq 0.175$), with a parallel change in the JT distortion above the magnetic transition, which was shown to change from static to dynamic.

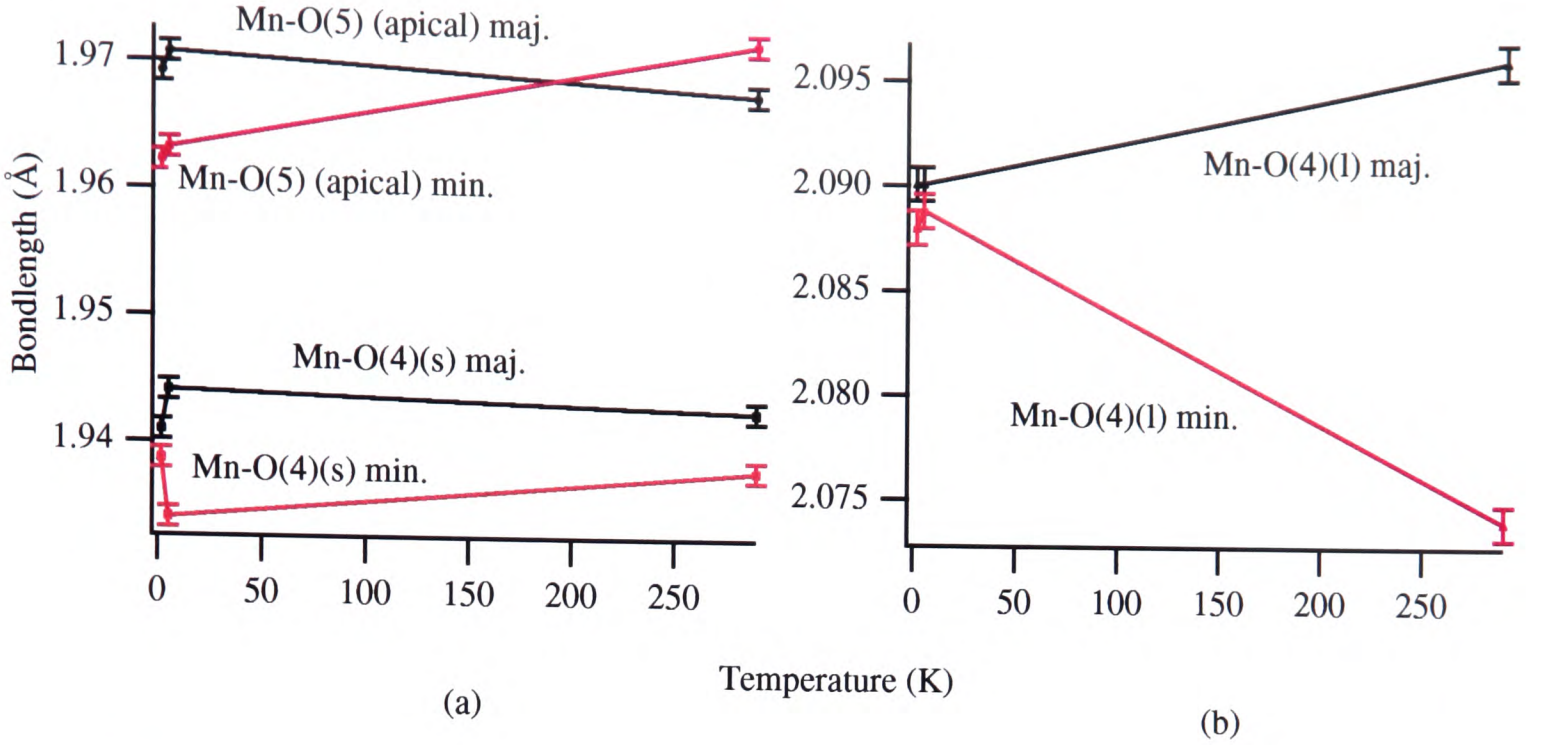
Goodenough's formulation of the changeover from the 'static' to the 'quasistatic' limit, according to the static or dynamic nature of JT distortions, has already been mentioned in the context of the magnetic properties of La_2GaMnO_6. Since it is proposed in this study, that the Mn/Ga-O bondlength alternation in Nd_2GaMnO_6 is evidence of a static, cooperative JT distortion, the magnetic properties of this compound should be interpreted, according to the rules predicted by the static limit[11].

For a random distribution of Mn and Ga, J_{Mn-Mn} is weakened, whatever its sign, by an amount depending upon the number of nearest-neighbour Mn cations present. It is possible that local 'clustering' of Mn and Ga cations occurs, on lengthscales not detected in the neutron diffraction study. Assuming there are localised regions rich in Mn cations, or at least a sufficient number of Mn-Mn nearest-neighbour interactions to drive a 'local' cooperative JT effect and orbital ordering similar to that in $LaMnO_3$, one might expect interlayer superexchange to be antiferromagnetic, and intralayer interactions to be ferromagnetic in Nd_2GaMnO_6 by analogy with $LaMnO_3$. This would result in domains containing A-type AFM structure. The magnetic structure observed (as shown in Figure 5.2.19) does consist of ferromagnetic and antiferromagnetic components, but both components act along the [010] direction of the cell. Therefore, the behaviour of Mn^{3+} in Nd_2GaMnO_6 is intermediate between its behaviour in the A-type antiferromagnet $LaMnO_3$ and the isotropic ferromagnetism observed in La_2GaMnO_6. The rationalisation of the ferromagnetic component in Nd_2GaMnO_6 is not possible, according to the quasistatic hypothesis applied in

La_2GaMnO_6, since it is proposed here that static, rather than dynamic, JT distortions occur in the Nd compound.

It is possible that the magnetic exchange interactions between Mn cations in Nd_2GaMnO_6 may be influenced further by the effects of magnetic ordering of the Nd sublattice, (shown to be ferromagnetic along y), and the potential, reorienting effect that rare earth moments can have on adjacent Mn ordered moments[38]. The presence of two distinct minima in the variation of the first derivative of Chi (FC) with respect to T(K), suggests the Mn and Nd moments might not order at the same temperature. Assuming that the ordering of Nd occurs at the temperature of the second minimum, (10K), the result of any 'reorienting' effect on the Mn moments, by the Nd, would be observed in the 5 and 1.7K magnetic structures refined from neutron diffraction data. Liu et al.[33] reported $NdMnO_3$ as having the lower of two Néel temperatures at around 14 K, similar to the value of 10K proposed to signal Nd ordering here.

Figures 5.3.7 (a) to (d) summarise changes in key structural parameters as a function of temperature in Nd_2GaMnO_6, and are useful in trying to rationalise the refined magnetic structure, on the basis of octahedral distortion, and potential orbital ordering. Again, the presence of data for just three temperatures could mask more subtle variations. The significant decrease in the JT distortion parameter between 290 and 5K in the majority phase of Nd_2GaMnO_6 appears to be manifested by the significant decrease in Mn/Ga-O(4) (l) and marginal increase of both Mn/Ga-O(4) (s) and Mn/Ga-O(5) (apical) bondlengths. These changes are mirrored by the exact reverse behaviour in the minority phase.



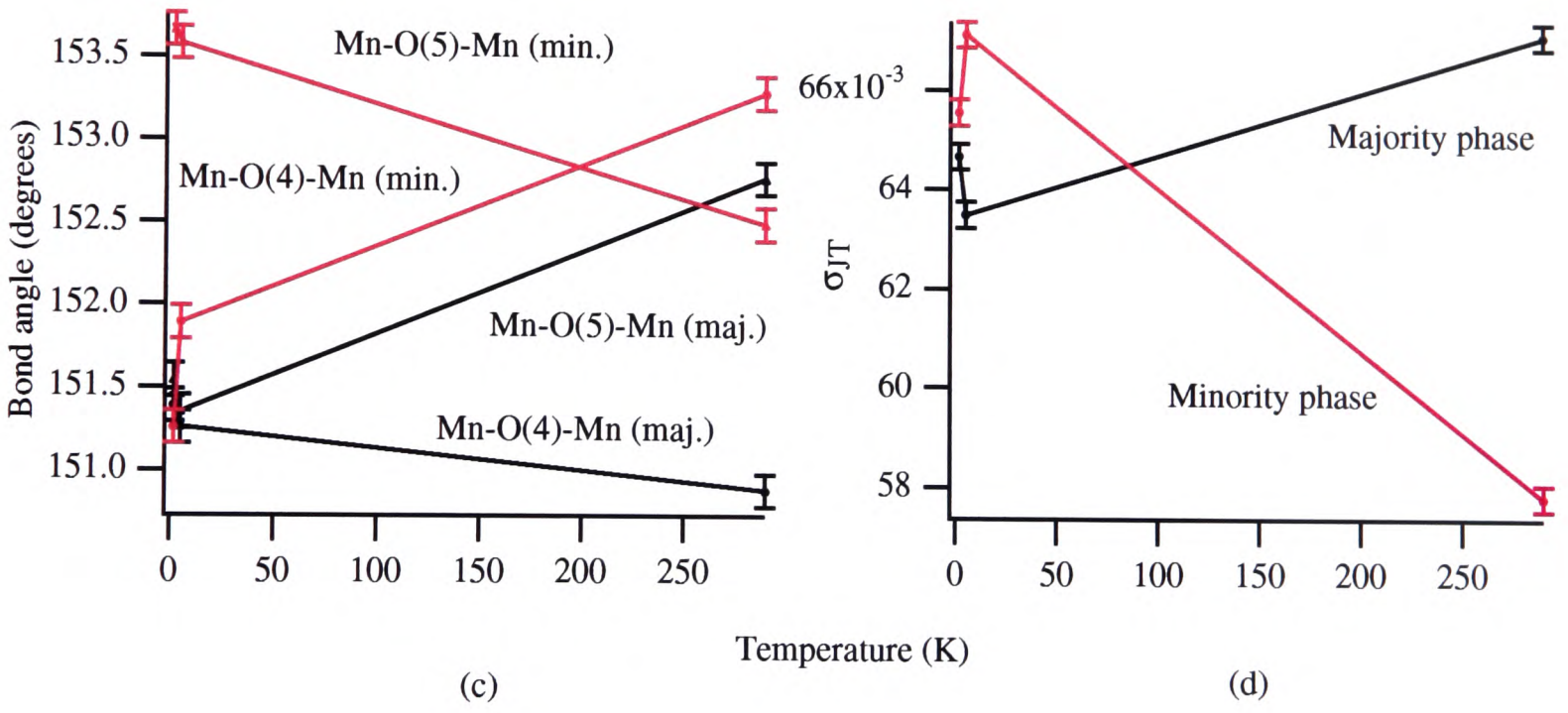


Figure 5.3.7 Temperature dependence of (a) Mn/Ga-O(5) and Mn/Ga-O(4)(s) bondlengths, (b) Mn/Ga-O(4)(l) bondlengths (c) Mn/Ga-O-Mn/Ga bond angles and (d) the JT distortion parameter σ_{JT} in majority and minority phase Nd_2GaMnO_6. Although only Mn cations are marked in the Figures, Ga cations occupy 50% of B-cation sites. Data for the minority phase are presented in purple.

This particular bondlength variation *in the majority phase* is consistent with a decrease in the ratio $Q_2/|Q_3|$, in accordance with the requirement for destabilisation of interlayer A-type AFM interactions proposed by Solovyev[16] and Feinberg[32]. Thus, it is consistent with the evolution of ferromagnetic, rather than antiferromagnetic correlation of Mn moments along y, with ferromagnetic alignment possibly enhanced by the orienting effects of parallel Nd moments, on reducing the temperature sufficiently. A similar change in Mn/Ga-O bondlengths

was observed in single phase Nd_2GaMnO_6, where the magnetic structure was also refined as '$A_X F_Y G_Z$' for the Mn sublattice and 'F_Y' for the Nd sublattice (Mx and My for Mn have values +/-1.35(4)μ_B and 2.4(1)μ_B respectively in this sample at 5K). In both majority and minority phase Nd_2GaMnO_6 described here, and in the single phase sample, the largest reduction in cell parameters occurs in the y direction, on decreasing temperature from 290 to 1.7K. However, the opposite nature of Mn/Ga-O bondlength variation in the minority phase of the Nd_2GaMnO_6 sample discussed here, (as observed from Figure 5.3.7 (a) and (b)), complicates any suggestion that the evolution of magnetic order in the bulk sample can be attributed to precise structural changes.

There is no evidence to suggest that only the majority phase exhibits long range magnetic order. The quality of diffraction data, together with the low number of magnetic Bragg peaks, do not allow refinement of the lattice parameters of the magnetic cell, without significant destabilisation of the refinement. Thus, the lattice parameters of the magnetic cell were constrained at those for the majority phase. The quality of the fit to 5 and 1.7 K data is insensitive to the phase fraction of the magnetic cell. For example, fixing the phase fraction of the magnetic cell at 65% (the majority phase fraction), results in enhanced components of Mx and My for Mn and My for Nd, but does not improve the quality of the fit.

The magnitudes of average Mn (3.00(7)μ_B) and Nd (0.93(4)μ_B) ordered moments obtained from the neutron study at 5K, are reduced from the values expected for a high spin octahedrally coordinated Mn^{3+} cation (4μ_B from 'gS'), and Nd^{3+} (3.27μ_B), and at 1.7K, a mean Mn moment of 3.15(7)μ_B is not significantly greater. The reduction in the observed moments is not surprising considering the random nature of Mn nearest-neighbour interactions, and therefore the range of orientations of ordered moments that are likely. The measurement of magnetisation as a function of field at 5K gave a value of magnetic moment of 5.59μ_B per formula unit of Nd_2GaMnO_6 in an applied field of 50kG. This value is in excess of the (total) ferromagnetic moment refined from the 5K neutron data (4.56μ_B), but is significantly reduced from that expected for a fully ferromagnetically ordered compound of this composition, suggesting not all of the Nd^{3+} moments are aligned in the direction of the applied field at 50kG. The reduction in the ordered magnetic moment observed in both

neutron diffraction and magnetisation measurements, emphasises the disruption to the magnetic structure caused by the random distribution of Mn^{3+} and Ga^{3+} over octahedral sites.

In summary, the preservation of the static, cooperative JT distortion in Nd_2GaMnO_6 is achieved despite the disordered array of Mn^{3+} and Ga^{3+} cations on B-cation sites. The variation of majority phase Mn/Ga-O bondlengths on reducing the temperature from 290 to 5K, would be consistent with the $Q_2/|Q_3|$ ratio decreasing, which in turn would lead to destabilisation of interlayer A-type AFM interactions as proposed by Solovyev et al.[16] and Feinberg et al.[32]. This is compatible with the observation of the ferromagnetic Mn component along y, detected in the neutron study. However, the reverse trends observed in the minority phase, also suggested to show long range magnetic order, invalidate this interpretation. In addition, as emphasised previously, the fact that Solovyev et al. invoked the AFM next-nearest-neighbour exchange to explain fully the interlayer AFM coupling present in $LaMnO_3$ suggests that a formulation based the sign of nearest-neighbour exchange parameters in the static limit, is not a realistic approach. It is likely that the electronic configurations at distinct Mn^{3+} cations change in a complicated manner, which is dependent upon the precise number of Ga nearest-neighbours (and possibly Mn next-nearest-neighbours), and the local structural environment. Careful examination of the microstructure in these materials may help to detect localised regions of cation ordered material by analogy with previous studies[39] and, hence, probe the 'local' rather than the 'average' structure.

5.3.3 Magnetotransport properties of La_2GaMnO_6 and Nd_2GaMnO_6

The highly insulating nature of La_2GaMnO_6 and Nd_2GaMnO_6 at fields between 0 and 14T and temperatures between 5 and 300K, supports the assertion that these materials contain minimal concentrations, if any significant amount, of Mn^{4+} cations. It is consistent also with the results of the structural study. By analogy with the results of Matsumoto et al.[40], both a static JT distortion or the presence of a dynamic JT effect and slowly fluctuating local JT distortions have a localising effect upon carriers. It is interesting to note the very similar magnitudes of negative magnetoresistance observed at 200K and 14T in the La and Nd samples (the resistivity is reduced to ~96% of the zero field value in each). This

suggests the magnetotransport behaviour is insensitive to the subtle structutral differences between the La and Nd compounds at this temperature, and insensitive to the precise nature of JT distortions in each.

La_2GaMnO_6 shows a very similar temperature dependence of resistivity as that observed in the compound of the same stoichiometry prepared by Töpfer and Goodenough in their 1997 study[17]. However, in the latter material, thermopower measurements did identify a small number of p-type carriers attributed to a small deviation from ideal stoichiometry. The calculated activation energies in the present study are 205.28meV and 271.62meV, respectively, for La and Nd samples. The fact that the activation energy in Nd_2GaMnO_6 exceeds that measured for La_2GaMnO_6, is unsurprising. The enhanced level of orthorhombic distortion has the effect of bandwidth narrowing in the former compound. As well as the energy splitting between the two e_g orbitals, the enhanced JT distortion in Nd_2GaMnO_6 modifies the transfer integral primarily through the modification of the 'long' Mn-O(4) bondlength.

The highly insulating nature of La_2GaMnO_6 and Nd_2GaMnO_6 suggests that for the purposes of developing 'double perovskites' as potential CMR materials, attention is better placed on mixed-valent Mn systems such as the recently described $La_{1.5}Sr_{0.5}RhMnO_6$ phase[26], where the introduction of Mn^{4+} cations leads to mobile charge carriers (holes). In this material, a magnetoresistance ratio of 60% has been observed in a field of 14T at 125K. In addition, the observation of significant levels of intergrain tunnelling magnetoresistance existing up to room temperature in polycrystalline, half-metallic Sr_2FeReO_6, indicates the varied potential of this class of materials.

5.4 References

[1] F Damay, C Martin, A Maignan, B Raveau *J. Magn. Magn. Mater.* **1998**, *183*, 143.

[2] MC Sanchez, J Blasco, J Garcia, J Stankiewicz, JM De Teresa, MR Ibarra *J. Solid State Chem.* **1998**, *138*, 226.

[3] X Chen, Z Wang, J Cai, B Shen, W Zhan, J Chen *J. Appl. Phys.* **1999**, *86*, 4534.

[4] B Raveau, C Martin, A Maignan *J. Alloys Compd.* **1998**, *275-277*, 461.

[5] BC Tofield, WR Scott *J. Solid State Chem.* **1974**, *10*, 183.

[6] JAM van Roosmalen, EHP Cordfunke, RB Helmholdt, HW Zandbergen *J. Solid State Chem.* **1994**, *110*, 100.

[7] JAM van Roosmalen, P van Vlaanderen, EHP Cordfunke, WL Ijdo, DJW Ijdo *J. Solid State Chem.* **1995**, *114*, 516.

[8] A Arulraj, R Mahesh, GN Subbanna, R Mahendiran, AK Raychaudhuri, CNR Rao *J. Solid State Chem.* **1996**, *127*, 87.

[9] J Topfer, JB Goodenough *Chem. Mater.* **1997**, *9*, 1467.

[10] C Ritter, MR Ibarra, JM De Teresa, PA Algarabel, C Marquina, J Blasco, J Garcia, S Oseroff, SW Cheong *Phys. Rev. B* **1997**, *56*, 8902.

[11] JB Goodenough, A Wold, RJ Arnott, N Menyuk *Phys. Rev.* **1961**, *124*, 373.

[12] R Maezono, S Ishihara, N Nagaosa *Phys. Rev. B* **1998**, *58*, 11583.

[13] F Moussa, M Hennion, J Rodriguez-Carvajal, H Moudden *Phys. Rev. B* **1996**, *54*, 15149.

[14] Y Murakami, JP Hill, D Gibbs, M Blume, I Koyama, M Tanaka, H Kawata, T Arima, Y Tokura, K Hirota, Y Endoh *Phys. Rev. Lett.* **1998**, *81*, 582.

[15] AJ Millis *Phys. Rev. B* **1997**, *55*, 6405.

[16] I Solovyev, N Hamada, K Terakura *Phys. Rev. Lett.* **1996**, *76*, 4825.

[17] J Topfer, JB Goodenough *Eur. J. Solid State Inorg. Chem.* **1997**, *34*, 467.

[18] ET Maguire, AM Coats, JMS Skakle, AR West *J. Mater. Chem.* **1999**, *9*, 1337.

[19] VA Cherepanov, LY Barkhatova, AN Petrov, VI Voronin *J. Solid State Chem.* **1995**, *118*, 53.

[20] ML Sanjuan, VM Orera, RI Merino, J Blasco *J. Phys. Condens. Matter* **1998**, *10*, 11687.

[21] M Anderson, K Greenwood, G Taylor, K Poeppelmeier *Progress in Solid State Chem.* **1993**, *22*, 197.

[22] MT Anderson, KR Poeppelmeier *Chem. Mater.* **1991**, *3*, 476.

[23] KI Kobayashi, T Kimura, H Sawada, K Terakura, Y Tokura *Nature* **1998**, *395*, 677.

[24] KI Kobayashi, T Kimura, Y Tomioka, H Sawada, K Terakura, Y Tokura *Phys. Rev. B* **1999**, *59*, 11159.

[25] A Maignan, B Raveau, C Martin, M Hervieu *J. Solid State Chem.* **1999**, *144*, 224.

[26] B Bakowski, PD Battle, EJ Cussen, LD Noailles, MJ Rosseinsky, AI Coldea, J

Singleton *Chem. Commun.* **1999**, *21*, 2209.

[27] *International Tables of Crystallography 4th Ed. Vol C*, Kluwer Academic: Dordrecht, **1995**.

[28] EF Bertaut *Magnetism Vol III*, Academic: New York, **1963**.

[29] JB Goodenough *Magnetism and the Chemical Bond*, Wiley: New York, **1963**.

[30] JL Garcia-Munoz, M Suaaidi, J Fontcuberta, J Rodriguez-Carvajal *Phys. Rev. B* **1997**, *55*, 34.

[31] H Sawada, Y Morikawa, N Hamada, K Terakura *J. Magn. Magn. Mater.* **1998**, *177-181*, 879.

[32] D Feinberg, P Germain, M Grilli, G Seibold *Phys. Rev. B* **1998**, *57*, R5583.

[33] RS Liu, JB Wu, CY Chang, JG Lin, CY Huang, JM Chen, RG Liu *J. Solid State Chem.* **1996**, *125*, 112.

[34] F Luis, MD Kuzmin, F Bartolome, VM Orera, J Bartolome *Phys. Rev. B* **1998**, *58*, 798.

[35] PG Radaelli, M Marezio, DE Cox, SW Cheong *Phys. Rev. B* **1997**, *55*, 3015.

[36] PG Radaelli, G Iannone, M Marezio, HY Hwang, SW Cheong, JD Jorgensen, DN Argyriou *Phys. Rev. B.* **1997**, *56*, 8265.

[37] A Urushibara, Y Moritomo, T Arima, A Asamitsu, G Kido, Y Tokura *Phys. Rev. B* **1995**, *51*, 14103.

[38] PD Battle, MA Green, NS Laskey, JE Millburn, PG Radaelli, MJ Rosseinsky, SP Sullivan, JF Vente *Phys. Rev. B* **1996**, *54*, 15967.

[39] M Hervieu, G Van Tendeloo, V Caignaert, A Maignan, B Raveau *Phys. Rev. B* **1996**, *53*, 14274.

[40] G Matsumoto *J. Phys. Soc. Jap.* **1970**, *29*, 606.

APPENDICES

Appendix 1

Figure 1.1[1] shows schematically the effects of anomalous scattering on F values where the difference in intensities may be rationalised as a result of the complex nature of the scattering factor for the anomalous scatterer.

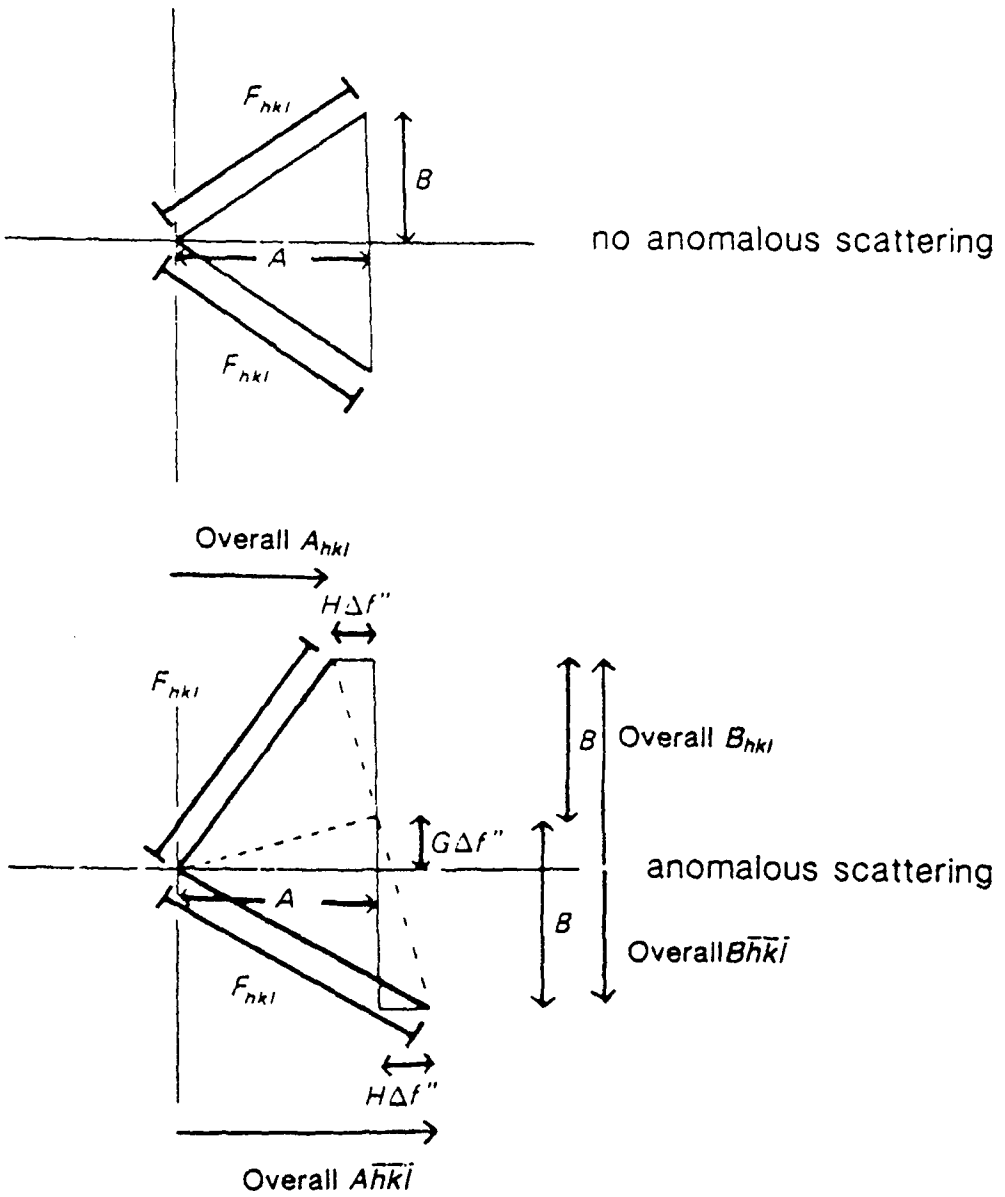


Figure 1.1 Effect of anomalous scattering on F values (see below for definitions of 'G' and 'H' notation). (Figure reproduced from reference [1]).

As shown in Chapter 2, equation 2.3.7, if there is an anomalous scatterer present, $f = f_a + \Delta f' + if'' = f' + if''$. As described by Glusker[1] and used in Figure 1.1, the following variables can be defined in order to help explain the modification of the overall structure factor,

$$A' = A + G(f_a + \Delta f') \text{ and } B' = B + H(f_a + \Delta f') \qquad \text{eqn. (1.1)}$$

where A and B refer to the normal scatterers and G and H to the anomalous scatterers. The resulting expressions for F(hkl) and F($\overline{hkl}$) are as follows[1]:

$$F(hkl) = (A' + iGf'') + i(B' + iHf'') \qquad \text{eqn. (1.2)}$$

$$= (A' - Hf'') + i(B' + Gf'')$$

Then, $$|F(hkl)|^2 = (A' - Hf'')^2 - (B' + Gf'')^2 \qquad \text{eqn. (1.3)}$$

Similarly, for F($\overline{hkl}$):

$$F(\overline{hkl}) = (A' + iGf'') - i(B' + iHf'') \qquad \text{eqn. (1.4)}$$

$$= (A' + Hf'') - i(B' - Gf'')$$

Then, $$|F(\overline{hkl})|^2 = (A' + Hf'')^2 + (B' - Gf'')^2 \qquad \text{eqn. (1.5)}$$

Therefore,

$$|F(hkl)|^2 - |F(\overline{hkl})|^2 = 4f''(B'G - A'H) \qquad \text{eqn. (1.6)}$$

The quantity in equation 1.6 is known as the Bijvoet difference[2], a function of f '' which depends on how near to the absorption edge the incident radiation is and on the positional parameters of both the anomalous scatterer and the rest of the structure.

The refinement of values for $\Delta f'$ and f '' from *powder* diffraction data is notably less precise than in the single crystal case. This is particularly true for the refinement of f '' with non-centrosymmetric space groups, due to the fact that h, k, l and $\bar{h}$, $\bar{k}$, $\bar{l}$ cannot be measured independently, precluding the use of Bijovet differences. The following structure factor expressions (used by Wilkinson et al.[3]), detail the relative sensitivity of powder diffraction data to $\Delta f'$ and f '' for both non-centrosymmetric and centrosymmetric space groups, in the simple case of one anomalous scatterer per cell. A and B refer to the rest of the structure comprised of normal scatterers[3]:

$$F(\mathbf{h}) = A + iB + (f_a + \Delta f' + if'') \exp(i2\pi(hx + ky + lz)) \qquad \text{eqn. (1.7)}$$

$$= A + iB + (a + ib)\,(\cos 2\pi \mathbf{hx} + i\sin 2\pi \mathbf{hx})$$

Similarly,

$$F^*(\mathbf{h}) = A - iB + (a - ib)\,(\cos 2\pi \mathbf{hx} - i\sin 2\pi \mathbf{hx}) \qquad \text{eqn. (1.8)}$$

$$F(\bar{\mathbf{h}}) = A - iB + (a + ib)\,(\cos 2\pi \mathbf{hx} - i\sin 2\pi \mathbf{hx}) \qquad \text{eqn. (1.9)}$$

$$F^*(\bar{\mathbf{h}}) = A + iB + (a - ib)\,(\cos 2\pi \mathbf{hx} + i\sin 2\pi \mathbf{hx}) \qquad \text{eqn. (1.10)}$$

Since the concern is the intensities,

$$F(\mathbf{h})\,F^*(\mathbf{h}) + F(\bar{\mathbf{h}})\,F^*(\bar{\mathbf{h}}) = 2A^2 + 2B^2 + 2a^2 + 2b^2 + 4\,(Aa\cos 2\pi \mathbf{hx} + Ba\sin 2\pi \mathbf{hx})$$

eqn. (1.11)

For a centrosymmetric structure (where terms involving B can be neglected), this reduces to:

$$F(\mathbf{h})\,F^*(\mathbf{h}) + F(\bar{\mathbf{h}})\,F^*(\bar{\mathbf{h}}) = 2\,(A^2 + a^2 + b^2 + 2\,Aa\cos 2\pi \mathbf{hx}) \qquad \text{eqn. (1.12)}$$

Since there are no cross terms involving b arising in either of the last two expressions, and the a^2 and aA terms (which include f ') tend to be larger than b^2, these expressions highlight the relative insensitivity of diffractrion data to variations in f ", in contrast to the sensitivity towards $\Delta f'$[4,5].

Considering the relationship between the sets of equations 1.1 to 1.6 and 1.7 to 1.12, respectively, it is useful to express F(hkl) (from equation 1.2) in full, such that,

$$F(hkl) = A + G(f_a + \Delta f') + iGf'' + i(B + H(f_a + \Delta f') + iHf'') \qquad \text{eqn. (1.13)}$$

The resulting expression for F(hkl) is:

$$F(hkl) = A + G(f_a + \Delta f') - Hf'' + i(B + H(f_a + \Delta f') + Gf'') \qquad \text{eqn. (1.14)}$$

$$= A + iB + G(f_a + \Delta f') - Hf'' + i(H(f_a + \Delta f') + Gf'') \qquad \text{eqn. (1.15)}$$

If (f_a + $\Delta f'$) is replaced by 'a' and f '' replaced by 'b', and G considered to represent cosine terms and H sine terms, the notation used in equations 1.1 to 1.6 and equations 1.7 to 1.12, respectively, is shown to be equivalent. For example, equation 1.15 would become:

$$A + iB + a\cos\theta - b\sin\theta + i\,(a\sin\theta + b\cos\theta) \qquad \text{eqn. (1.16)}$$

which is equivalent to equation (1.17), of the form used in the explanation by Wilkinson et al.[3]:

$$A + iB + (a + ib)(\cos\theta + i\sin\theta) \qquad \text{eqn. (1.17)}$$

References

[1] JP Glusker, KN Trueblood *Crystal Structure Analysis*, Wiley: New York, **1985**.

[2] JM Bijvoet *Proceedings of the K. Nederlandse Akademie van Wetenschappen* **1949**, *B52*, 313.

[3] AP Wilkinson, DE Cox, AK Cheetham *J. Phys. Chem. Solids* **1991**, *52*, 1257.

[4] GH Kwei, RB von Dreele, A Williams, JA Goldstone, AC Lawson, II, WK Warburton *J. Mol. Struct.* **1990**, *223*, 383.

[5] GH Kwei, RB von Dreele, SW Cheong, Z Fisk, JD Thompson *Phys. Rev. B* **1990**, *41*, 1889.

Appendix 2

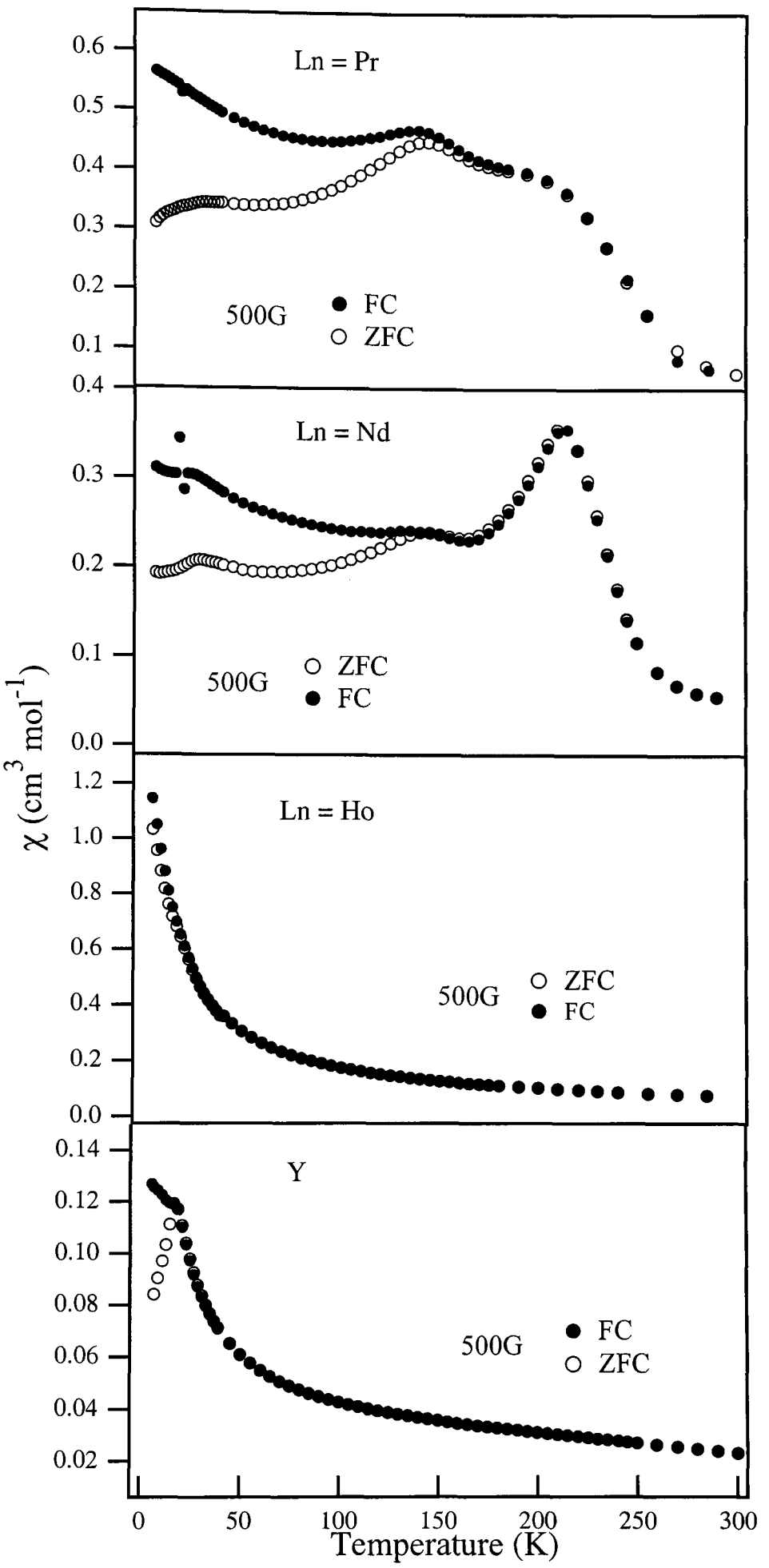


Figure 2.1 Molar magnetic susceptibility as a function of temperature, for $Sr_2LnMn_2O_{7-\delta}$ (Ln = Pr, Nd, Ho and Y). Each sample was measured in an applied magnetic field of 500G.

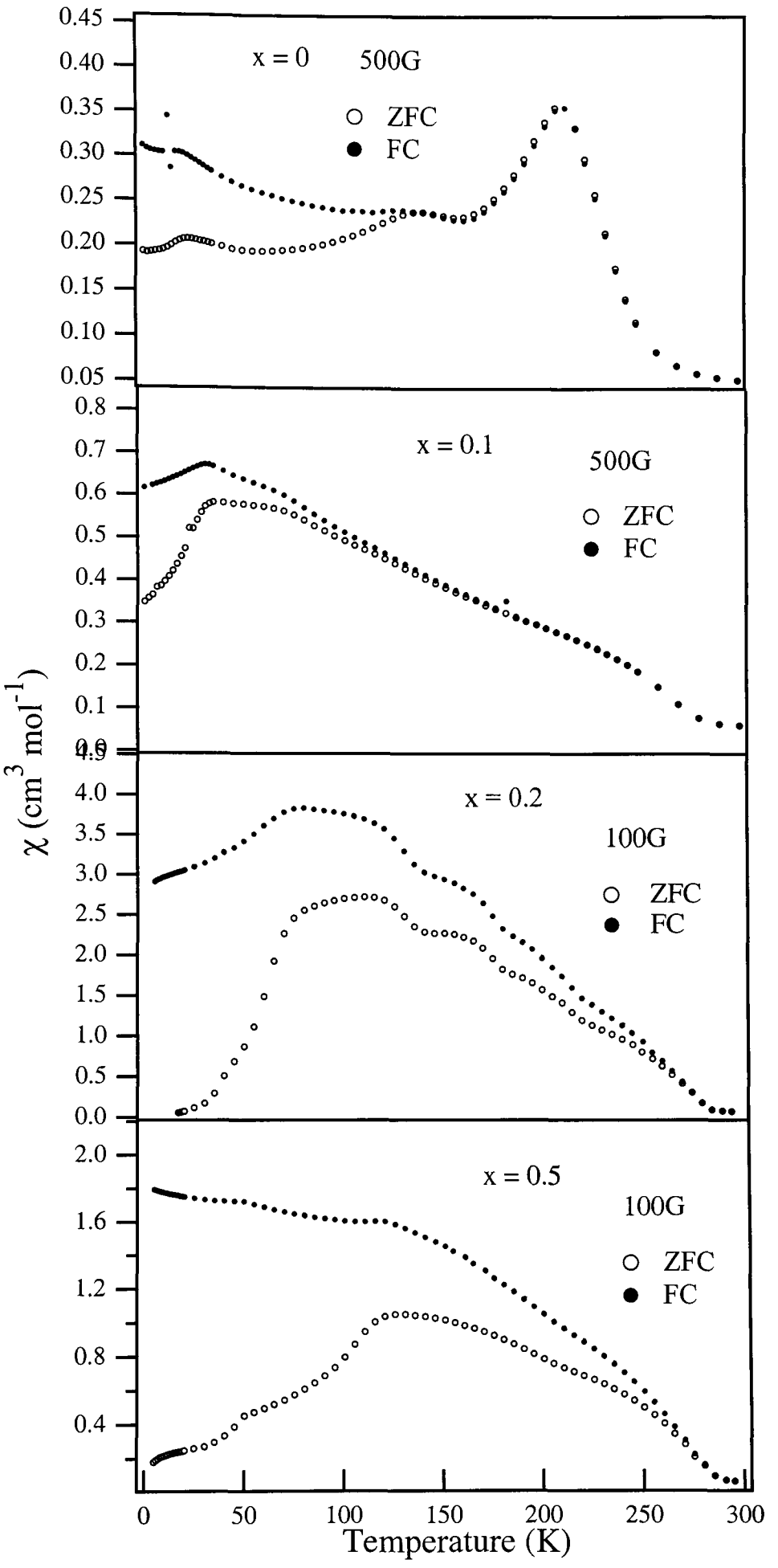


Figure 2.2 Molar magnetic susceptibility as a function of temperature, for $Sr_{2-x}Nd_{1+x}Mn_2O_{7-\delta}$ (x = 0, 0.1, 0.2 and 0.5). The x = 0 and x = 0.1 compositions were measured in an applied magnetic field of 500G, while x = 0.2 and x = 0.5 were measured in 100G.

Appendix 3

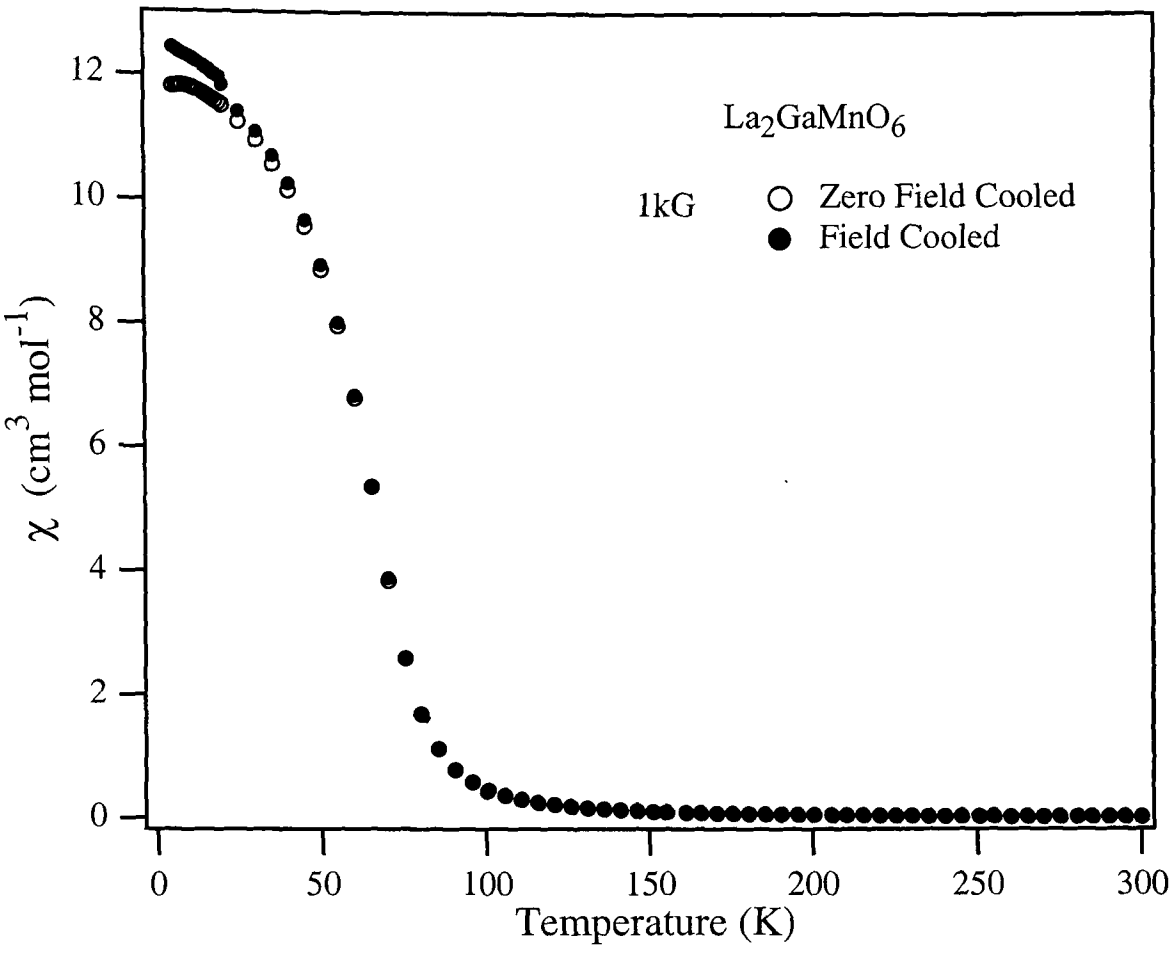


Figure 3.1 Molar magnetic susceptibility as a function of temperature for La_2GaMnO_6 at 1kG.

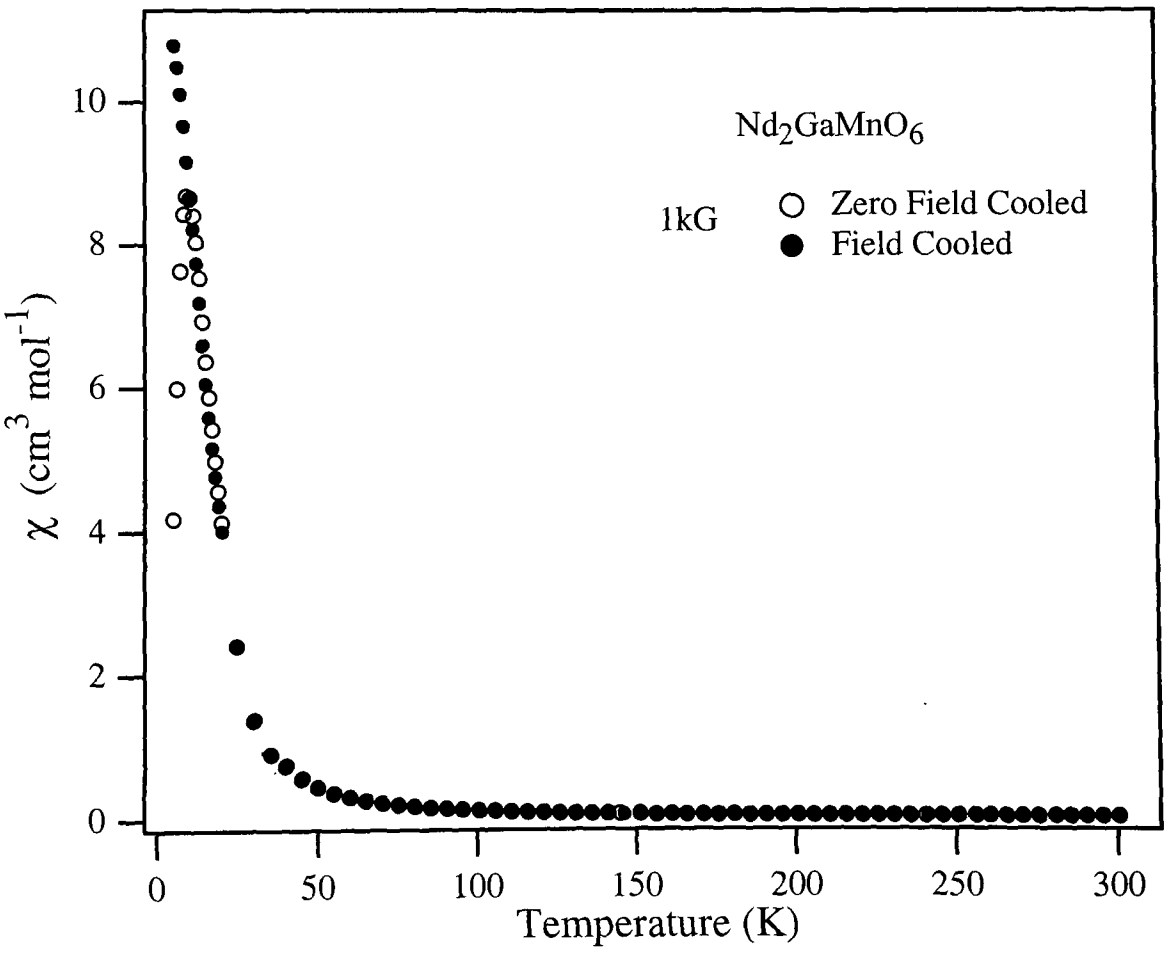


Figure 3.2 Molar magnetic susceptibility as a function of temperature for Nd_2GaMnO_6 at 1kG.

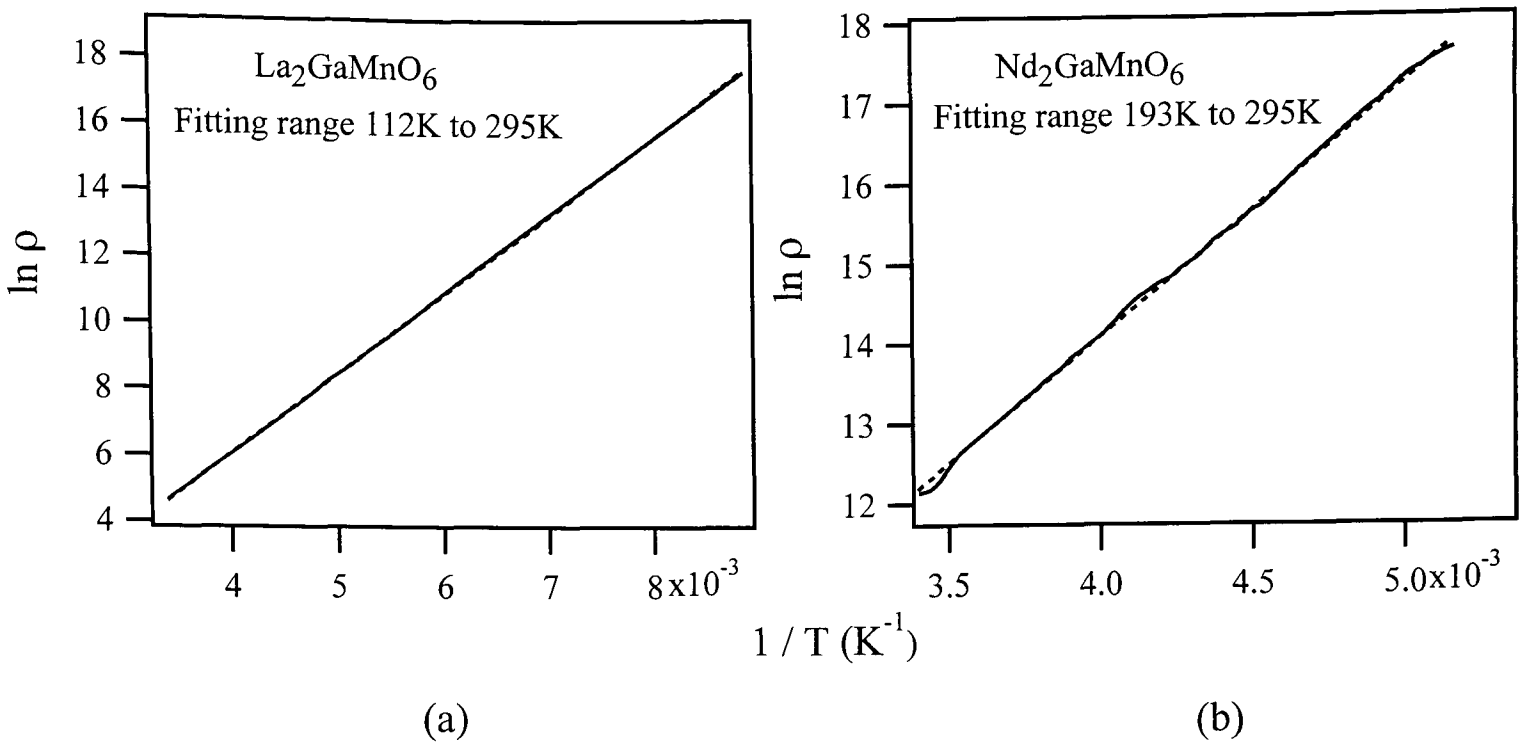


Figure 3.3 Fit of the natural logarithm of resistivity against inverse temperature, for (a) La_2GaMnO_6 in the range 112 to 295K and (b) Nd_2GaMnO_6 in the range 193 to 295K.

Summary

The properties of the Ruddlesden Popper phases described in this thesis have provided a useful insight into the requirements for CMR in layered manganites. The n = 2 RP series $Sr_{2-x}Nd_{1+x}Mn_2O_7$ ($0 \leq x \leq 0.5$), have provided the largest CMR ratios of the compounds studied[1]. The zero field resistivity signal was reduced by 2-3 orders of magnitude in a field of 14T, at ~4.2K. Moreover, these layered manganites have exhibited CMR in the absence of long range ferromagnetic order, providing a contrast to the 'typical' intrinsic CMR response of infinite layer mixed-valent manganites. The origin of the CMR effect is ascribed to local magnetic inhomogeneity[2,3], consisting of spin-aligned clusters, which are strongly susceptible to an applied magnetic field. Extrinsic contributions are also proposed to add to the size of the MR ratio, particularly in the case of $Sr_{1.8}Nd_{1.2}Mn_2O_7$, which shows LFMR below 82K in fields up to 1T. The extrinsic contributions to CMR in these materials would benefit from more extensive investigations, perhaps by controlling the grain size by modification of the synthetic conditions.

The n = 3 RP phases, based on A- and B- cation substituted derivatives of $Ca_4Mn_3O_{10-\delta}$[4], have proved more challenging, from a CMR perspective, due to the difficulties in stabilising phases containing mixed-valent Mn^{3+}/Mn^{4+} cations. Nonetheless, the orthorhombic (*Pbca*) RP phase $Ca_{3.95}La_{0.05}Mn_3O_{10-\delta}$ was synthesised using a Pechini[5] citrate gel process, and the presence of a magnetic transition at ~114K, suggested that the antiferromagnetic groundstate, with associated weak ferromagnetism arising through the DM interaction observed in $Ca_4Mn_3O_{10-\delta}$, is preserved. Unlike $Ca_4Mn_3O_{10-\delta}$ which had an immeasurably large resistivity at 4.2K, $Ca_{3.95}La_{0.05}Mn_3O_{10-\delta}$ showed CMR at 4K, with the resistivity signal reduced to 18% of the zero field value, in 14T.

B-cation substitution in $Ca_4Mn_3O_{10-\delta}$ yielded the compound $Ca_4Mn_2TiO_{9.93}$, shown to adopt orthorhombic (*Pbca*) symmetry, as observed in the parent material. This compound was characterised structurally using a combination of anomalous dispersion X-ray diffraction and neutron diffraction techniques, which enabled refinement of the Mn:Ti octahedral-site distribution. The Ti^{4+} cations were shown to undergo partial ordering onto the central

octahedral layer of the perovskite block (a Mn^{4+}:Ti^{4+} distribution of 59.8%(2.6):40.2%(2.6) and 70.1%(1.3):29.9%(1.3) across the 4b and 8c octahedral sites, respectively was observed). Neutron diffraction studies at 5K confirmed the absence of long range magnetic order in this material, which would benefit from more extensive DC, and AC magnetometry measurements. $Ca_4Mn_2TiO_{9.93}$ was shown to be highly insulating, since chemical substitution on the B-cation site in $Ca_4Mn_3O_{10-\delta}$ does not compensate the electron-localising effects of cation disorder, with the introduction of mixed-valent Mn cations.

The double perovskites, La_2GaMnO_6 and Nd_2GaMnO_6, described in Chapter 5 were shown to adopt cation disordered, orthorhombic (*Pnma*) structures. However, the decrease in size of the Ln cation on moving from La to Nd, lead to the stabilisation of a static, cooperative Jahn-Teller (JT) distortion in Nd_2GaMnO_6, characteristic of the parent $LaMnO_3$ and $NdMnO_3$ materials. This was in contrast to the mixed, static and dynamic JT distortions proposed for La_2GaMnO_6. As such, the isotropic ferromagnetic interactions observed in La_2GaMnO_6 at 50K and 5K predicted by the 'quasistatic hypothesis[6,7]' and consistent with the dynamic JT correlations, were replaced by competing ferromagnetic and antiferromagnetic superexchange interactions on the Mn sublattice along the [010] direction of the unit cell in the Nd compound. Both materials were shown to be highly insulating and neither displayed CMR, with resistivity values in each being reduced to just 96% of the zero field value at 200K, in a field of 14T. However, the Mn,Ga compositions provide an insight into the means by which introduction of diamagnetic B-cations such as Ga^{3+} influences the nature of complex superexchange interactions in Mn^{3+} systems.

References

[1] PD Battle, SJ Blundell, MA Green, W Hayes, M Honold, AK Klehe, NS Laskey, JE Millburn, LE Murphy, et al. *J. Phys. Condens. Matter* **1996**, *8*, L427.

[2] JE Evetts, MG Blamire, ND Mathur, SP Isaac, BS Teo, LF Cohen, JL Macmanus-Driscoll *Philos. Trans. R. Soc. London, Ser. A* **1998**, *356*, 1593.

[3] AI Coldea, LE Spring, SJ Blundell, J Singleton, W Hayes *J. Phys. Condens. Matter,* **1999**, *11*, 9053.

[4] PD Battle, MA Green, J Lago, JE Millburn, MJ Rosseinsky, JF Vente *Chem. Mater.* **1998**, *10*, 658.

[5] MP Pechini **1967**, US Patent No. 3 330 697.

[6] JB Goodenough, A Wold, RJ Arnott, N Menyuk *Phys. Rev.* **1961**, *124*, 373.

[7] J Topfer, JB Goodenough *Eur. J. Solid State Inorg. Chem.* **1997**, *34*, 467.